Luminescence dosimetry with ceramic materials for application to radiological emergencies and other incidents.

Eftychia C. Kouroukla

Submitted for the degree of

Doctor of Philosophy

Ustinov College, Durham University

December 2015

Abstract

The likelihood of the occurrence of radiological accidents which can induce significant health consequences to the members of the public has raised the importance of developing a personal radiation dosimetry system applicable to populations not monitored by dedicated dosemeters. Mobile phones are personal devices with high ubiquity and great potential for accident dosimetry applications. Alumina surface mount resistors (SMRs) are abundant in the printed circuit board of mobile phones and their potential as fortuitous dosemeters has been investigated using thermoluminescence (TL) and optically stimulated luminescence (OSL) techniques. The physical mechanism of the generation of luminescence of the alumina SMRs is, however, less known. The basic luminescence defects in SMRs were identified to be F-type centres and their emission process was shown to be temperature dependent and highly quenched at room temperature (RT). The trap environment of beta irradiated SMRs includes a series of closely spaced traps covering thermal depths between 0.9-1.4 eV; predicting an average lifetime for thermal fading at RT of ca 23 years. Trapped charges evicted by thermal or optical stimulation are likely to recombine at F-type centres and contribute to the luminescence response that is likely to be thermally assisted via the vibrational modes of the lattice. A phonon-assisted de-excitation of the trapped charge population could additionally be involved in the mechanism of athermal or anomalous fading. Based on the temperature dependence of the rate of fading, a model is presented for the anomalous fading observed where phonon-assisted and tunnelling effects alternate or operate simultaneously depending on the temperature of the material. A number of aspects related to the use of SMRs in dosimetry seem to benefit from the investigation of the physical processes, although for accurate dose reconstruction it is imperative to know the energy of the ionising radiation source and the position of the mobile phone relative to the direction of the source. For example, at low-energy exposures the dose may be over-estimated, not only due to the non-flat energy response of the alumina, but also due to the presence of several parts of the mobile phone which can increase the amount of energy deposited in alumina substrates due to backscatter effects. In addition, MCNP simulations indicated that for low-energy exposures, such as for ^{192}Ir, differences of up to an order-of-magnitude between resistor and whole body dose are expected. Finally, to specify the most appropriate dose conversion coefficients that can be applied to estimate whole body dose from OSL / TL determinations, the knowledge of the exposure geometry is crucial.

Table of Contents

List of Figures

kinetics (I) and a TL peak calculated using the second-order approximation (II). Note the different shape characteristics. Reprinted from Chen and McKeever, 1997.

Figure 2.6: Geometric shape characteristics of a single glow peak. The order of kinetics is determined by the geometric factor, μ_g, through the parameters T_1, T_2, and T_m. Reprinted from Pagonis *et al.*, 2006.

Figure 2.7: Examples of isothermal decay curves for (a) first-order TL peak and (b) second-order TL peak. Reprinted from Pagonis *et al.* (2006).

Figure 2.8: Representation of T_m-T_{stop} characteristics of glow curves consisted of a single (column a), several overlapping (column b), and a continuous distribution of peaks (column c). Lines B, C show the expected T_m-T_{stop} curves for first- and second-order kinetics peaks respectively. Reprinted from McKeever (1985).

Figure 2.9: Quantum mechanical electron tunnelling models of anomalous fading. In (a) an electron makes a tunnelling transition from the ground state of the trap to the nearest recombination centre. In (b) electrons are first thermally excited to higher energy level before tunnelling to the recombination centre.

Figure 2.10: Potential energy, E, of an electron in the trap as a function of distance, r, from the recombination centre used to describe the anomalous fading mechanism based on electron tunnelling through a potential barrier. E_1 is the potential energy of an electron located at the bottom of the potential well at a distance r_1. For an electron raised to an intermediate excited state the E, r are reduced to E_2 and r_2 respectively. Modified from McKeever (1985).

Figure 2.11: Localised transition model of anomalous fading. The electron trap and the recombination centre have a common excited state through which phonon-assisted excited electrons reach the ground state of the recombination centre.

Figure 3.1: Interaction mechanisms of photon energy loss in matter. The dominant process at low photon energies (i.e., <100 keV) is the photoelectric effect during which the incoming photon excites an orbital electron from its shell. The photon completely disappears producing a photoelectron which leaves the atom with energy equal to the initial photon energy (hν) minus the electron binding energy (b.e). Fluorescent radiation accompanies the photoelectric absorption

process resulting from the filling of the electron vacancy by outer shell electrons. Pair production takes place for photon energies greater than 1.02 MeV. The process is a photon-nucleus interaction in which an electron-positron (e^- - e^+) pair is created. In Compton scattering, which is important in the range between 100 keV and 10 MeV, the incoming photon is scattered through an angle θ producing a recoil electron which carries part of the initial photon energy. Reprinted from Alpen (1990).

Figure 3.2: The dependence of the three main (in the energy range of interest to dosimetry) photon interaction processes on the energy of the incoming photon beam and atomic number of the target material. The interaction cross section for photoelectric effect varies as $\tau_{ph} \sim {Z^4}/{(h\nu)^3}$. For Compton scattering, which dominates at energies 100 keV < $h\nu$ < 10 MeV, the interaction cross section varies as $\tau_c \sim Z$ whereas at photon energies above ~ 1.2 MeV pair production with $\tau_{pp} \sim Z^2$ becomes the dominant interaction process. Reprinted from Podgorsak (2006).

Figure 3.3: Relationship between absorbed dose and kerma. In (a) collision kerma is equal to the absorbed dose once CPE exists after a certain depth, z_{max}, in the medium. (b) Under conditions of TCPE the absorbed dose is constantly higher than the kerma. Reprinted from Podgorsak (2005).

Figure 3.4: Mass energy absorption coefficients of Al_2O_3 and LiF with respect to air as a function of the photon energy (NIST database).

Figure 3.5: OSL intensity as a function of time *t* for different readout modes. (a) Continuous wave OSL (CW-OSL) measures the OSL emission with a constant light source, while (b) linear-modulated (LM-OSL) monitors the light emission while ramping the intensity of the stimulation light, and (c) pulsed-OSL (POSL) stimulates the sample using short duration pulses and measures the OSL signal in between the pulses. Modified from Bøtter-Jensen, (2003).

Figure 3.6: Recovery of unknown dose, *D´*, using the SAR protocol. The TL/OSL response, *S´*, from the unknown dose is interpolated on the dose-response curve created by applying a number of doses D_1, D_2, D_3 and measuring the luminescence response S_1, S_2, S_3. The point of intersection with the x-axis gives the value of the unknown dose.

Figure 6.3: SEM micrographs of alumina resistor substrates recorded at x2000 magnification. The images of the same regions show untreated surfaces (a, b) and polished surfaces (c, d) obtained in SE (a, c) and BSE (b, d) measurement modes. The images, which show the microstructure of a type ´1206´ SMR, were acquired with an accelerating voltage of 15 kV and electron probe current of 0.5 nA.

Figure 6.4: Electron image and element maps (Al, Si, Ca, and Mg) of the polished alumina substrate sample. Ca and Si were found to be the major impurities in the lighter-coloured areas (e.g., Position 1). The darker regions (e.g., Position 2) were found to have high Mg content, whereas the minimum concentrations of Mg, Si, and Ca were found in areas such as those indicated by Position 3.

Figure 6.5: Normalised CL spectra of polished (a) Al_2O_3:C dosimetry-grade chip and (b) alumina substrate (i.e., type ´1206´ SMR) samples. The three bands at ~ 2.92, ~ 3.63, and ~ 4.08 eV obtained by fitting the spectrum using deconvolution software are also shown. The inset shows the spectrum recorded in the interval 1.5-2.5 eV with a red band-pass filter interposed to suppress the second order diffracted light. The spectra were measured with an electron beam voltage of 10 kV and corrected for the instrument response.

Figure 6.6: Panchromatic CL images of (a) Al_2O_3:C dosimetry-grade chip, and (b) alumina substrate, and monochromatic CL images of the alumina substrate measured at (c) 340Δ30 nm and (d) 394Δ30nm.

Figure 6.7: Radioluminescence emission spectra of alumina substrates measured at RT under continuous x-ray irradiation using a UV-Blue (250-450 nm) and a Blue-Green-Red (380-800 nm) spectrometer. The area between 2.25-2.5 eV (500-550 nm) is thought to be an artefact caused by the joining of the spectra obtained separately using the two spectrometers. Measurement was performed with a sample consisting of 10 type ´1206´ SMRs. The spectrum was corrected for instrument response.

Figure 6.8: Radioluminescence emission spectra of alumina substrates measured at different temperatures from -250 to 0 °C. Measurement was performed with a sample consisting of 10 type ´1206´ SMRs. All spectra were corrected for instrument response.

Figure 6.9: Radioluminescence emission spectra of alumina substrates measured at different temperatures from 50 to 350 °C plotted on a linear-log scale. Measurement was performed with a sample comprising 10 type ´1206´ SMRs.

Figure 6.10: Example of spectral deconvolution process using Gaussian-based functions. The RL emission over the 2.5-5 eV range measured at -100 °C was deconvolved into two bands with central energies at ~ 3.01 and ~ 3.88 eV. Measurement was performed with a sample comprising 10 type ´1206´ SMRs.

Figure 6.11: Temperature dependence of (a, b) central energy, and (c, d) width of the emission band components of RL in the UV-Blue range obtained following deconvolution with a Gaussian-based function. In (a, b) the uncertainty (i.e., fitting errors) in the coordinate value associated with each data point ranges from 0.04 to 0.3 eV and in (c, d) the uncertainties (fitting) are within ± 0.04 eV.

Figure 6.12: Temperature dependence of the area of fitted bands (a) band with mean central energy at ~ 3.85 eV, (b) band with mean central energy at ~ 3.01 eV, and (c) narrow emission band at ~ 1.78 eV. Measurement was performed with a sample comprising 10 type ´1206´ SMRs.

Figure 6.13: Normalised to the first data point RL intensity of (a) the ~ 3.85 eV, and (b) the ~ 3.01 eV emission bands as a function of temperature. The dashed curves show the fitting to the data points using the equation describing the thermal quenching effect, resulting in the following values: W=0.61 ± 0.02 eV and C=(2.25 ± 1.21) $x10^6$ for the ~ 3.85 eV band and W=0.19 ± 0.01 eV and C=(1.17 ± 0.69) $x10^4$ for the ~ 3.01 eV band.

Figure 6.14: Description of thermal dependence of luminescence emission (and absorption) using the configurational coordinate diagram and the electron-phonon coupling model. (a) At T=0 K the thermal energy provided by phonons is low. The absorption of photon energy (e.g., x-rays or electrons) raises an electron from a low-potential energy (E) vibrational state of the ground state to a corresponding low-potential energy vibrational state of the excited state. The return of the excited electron to the ground state results in luminescence emission. For a luminescent centre strongly interacting with the vibrational modes of the lattice both the absorption and the emission bands are broad. (b) As the temperature increases (0 K < T < Tc) the energy associated with the vibrational modes of the crystal lattice increases too introducing a

displacement of the electronic states of the emission centre to new equilibrium positions R' and Ro'. Absorption and emission can take place from higher energy vibronic states. Thermal broadening of the absorption and emission bands can be observed. (c) After a critical temperature T_c the thermal energy provided by the phonons can be high enough and the shift of the electronic states (i.e., R'', Ro'') of the centre can be significant such that the two parabolas in the CC diagram are strongly intersected. Charges excited to electronic levels located close to the crossing point of the two parabolas have more probabilities to decay to the ground state of the centre non-radiatively causing a reduction in the intensity of the luminescence emission, known as thermal quenching.

Figure 6.15: Comparison of normalised FTIR reflectance spectra of alumina substrate and dosimetry grade Al_2O_3:C single crystal. The spectra were collected at RT.

Figure 7.1: TL glow curves (5 °C s^{-1}) of alumina substrates obtained (a) no preheat treatment, (b) following thermal cleaning at various temperatures. Sample consisted of 3 type ´1206´ SMRs irradiated with 3 Gy. The TL offset at RT is due to the phosphorescence emission from shallow traps detected by the PMT prior to the onset of thermal stimulation.

Figure 7.2: Step-wise annealing curves indicating the relative thermal stability characteristics of Peaks 1 and 2. The remaining TL intensity under each peak is plotted as a function of the preheat temperature. Under the testing conditions TL Peak 1 is thermally unstable throughout the investigated temperature range, while TL Peak 2 exhibits no significant loss in intensity to ca 120 °C. Data produced with a sample consisting of 3 type ´1206´ SMRs irradiated with 3 Gy. The size of the error bars was smaller than the data symbols.

Figure 7.3: (a) TL glow curves obtained after different beta doses. The maximum temperature of all TL peaks remains unaltered as the dose increases from 1 to 10 Gy, shifting slightly to higher temperatures for larger doses. (b) Dose response characteristics of the maximum intensity of TL Peaks 1 and 2. TL Peak 1 grows sublinearly with dose, whereas TL Peak 2 grows linearly up to 20 Gy and superlinearly for higher dose levels. Data produced with a sample consisting of 3 type ´1206´ SMRs.

Figure 7.4: Phosphorescence emission associated with (a) TL Peak 1 and (b) TL Peak 2 at several sample temperatures. Data produced with a sample consisting of 4 type ´1206´ SMRs irradiated with 12 Gy.

Figure 7.5: Comparison of isothermal decay curves for a sample consisting of 4 type ´1206´ chip SMRs (filled square), a coarse- (open circle), and a fine-grain (star) sample. The samples received a dose of 12 Gy and heated to 60 and 170 °C at 5 °C s^{-1}, and held at these temperatures for 200 s.

Figure 7.6: Comparison of isothermal decay curves for a sample consisting of 4 type ´1206´ chip SMRs, a coarse grain, and a fine grain sample. The samples received a dose of 12 Gy and heated to 60 and 170 °C at 1 °C s^{-1} and held at these temperatures for 200 s.

Figure 7.7: Effect of different heating rates on the TL glow peaks of SMRs. The temperature of each peak maximum shifts to higher temperatures as the heating rate increases, and the FWHM also increases. The data are representative of a sample consisting of ~ 20 type ´0402´ SMRs.

Figure 7.8: Plots of ln (T_m^2/β) as a function of $kT_m{}^{-1}$ for TL Peak 1 and TL Peak 2 obtained using the variable heating rate method. The values of the activation energy and frequency factor are also shown. Data are representative of samples consisting of ~ 20 type ´0402´ SMRs irradiated with 4 Gy.

Figure 7.9: Examples of the application of the initial rise method on the initial rise part (i.e., up to ~10 % of maximum peak intensity) of TL Peak 2 measured at different (a) levels of dose and (b) heating rates. The plots of $ln(I)$ against kT^{-1} were fitted with linear regression lines (i.e., dashed lines), the slope of which corresponds to the value of the activation energy of the peak, *E*. The results of the IR analysis are listed in Tables 7.5 and 7.6.

Figure 7.10: Initial and remaining TL glow curves following different T_{stop} temperatures. The curves correspond to a sample consisting of 3 type ´1206´ SMRs irradiated with a dose of 3 Gy.

Figure 7.11: T_m-T_{stop} analysis of (a) TL Peak 1 in the range between 50 and 100 °C, and (b) TL Peak 2 in the range between 130 and 240 °C. The inset to (b) shows the variation in T_m of TL Peak 2 in the initial T_{stop} range from 50 to 120 °C. The error in T_m is ± 2 °C. (c) Activation energy as a function of T_{stop} calculated by analysing the remaining TL glow curves using the

initial rise method. The dashed circles indicate the possible positions of individual traps. Each data point represents the average measured or calculated quantity using several samples consisting of different number of type ´0402´ and type ´1206´ SMRs. The samples were irradiated with 3 Gy.

Figure 7.12: (a) Lost TL glow curves calculated by subtracting the remaining TL following preheat at T=25-350 °C from the initial TL glow curve. (b) Major peak components identified by subtracting each lost TL glow curve in from the next one obtained after a higher temperature preheat. For example, the lost TL_{50^oC} –where the subscript denotes the preheat temperature– was subtracted from the lost TL_{75^oC}. Data produced with a sample consisting of 3 type ´1206´ SMRs.

Figure 7.13: Schematic representation of the transitions involved in (a) semi-localised transition model, and (b) pure-localised model.

Figure 8.1: Energy band diagram showing the various OSL models: (1) direct transition from the ground state of the electron trap to the conduction band, (1') shallow trap model by Markey *et al*., (1996), (2) indirect thermally assisted OSL model by Hutt *et al*., (1988), (3) thermally assisted sub-conduction band OSL model by Poolton *et al*., (1995a,b), (4) thermally assisted model by Spooner (1994), and (5) donor-acceptor pair recombination (redrawn from McKeever *et al*., 1997).

Figure 8.2: Representative examples of room temperature CW-OSL signals measured following beta irradiation (~ 3 Gy) of a sample consisting of ~ 20 type ´0402´ SMRs using (a) blue- and (b) infrared-light stimulation.

Figure 8.3: Room temperature LM-OSL decay curves of beta irradiated (~3 Gy) alumina substrates (i.e., sample of ~ 20 ´0402´ SMRs) after 600 s of (a) blue- and (b) infrared-light stimulation. The sample was maintained at RT during optical stimulation. The influence of post-irradiation preheat treatment for some selective temperatures is also shown.

Figure 8.4: (a) Step-wise annealing curves of the CW-BOSL and IRSL signals. (b) Normalised to the initial intensity (i.e., at t=0 s) BOSL decay curves after increasing temperature of preheat treatment. The data correspond to a sample consisting of ~ 20 type ´0402´ SMRs irradiated with

~ 3 Gy and stimulated at RT. The error bars in (a) are not shown since they are comparable to the symbol size.

Figure 8.5: Examples of curve fitting of the normalised at t=0 s BOSL decay curves measured (a) without post-irradiation preheat treatment and (b) following preheat at 150 °C. In (a) a good fit was obtained assuming a linear combination of four first-order exponential decay components (i.e., C_1: *Dot*, C_2: *Dash Dot*, C_3: *Dash Dot Dot*, and C_4: *Short Dash Dot*) and a constant (i.e., y_o: *Dash*), while in (b) a second-order exponential decay function and a constant, y_o, was found to fit the experimental data adequately. The residual signals are also shown.

Figure 8.6: (a) CW-BOSL decay curves and (b) phosphorescence emission curves measured at various sample temperatures. The data were obtained using a sample consisting of 20 type ´0402´ SMRs. The dose to the sample was ~ 3 Gy.

Figure 8.7: Sample temperature dependence of the total (0-60 s) OSL light sum, phosphorescence, and Net-OSL signals during (a) blue- and (b) infrared-light stimulation. The data were obtained using a sample consisting of ~ 20 type ´0402´ SMRs. The dose to the sample was ~ 3 Gy. The data points were connected with linear curves for better visualisation. The error bars are not shown since they are comparable to the symbol size

Figure 8.8: IRSL, Phosphorescence, and Net-IRSL decay curves plotted for two sample temperatures at (a) 50 °C and (b) 75 °C. In (c), the normalised at t=0 s decay curves measured at 50, 75, and 100 °C were fitted using a single exponential function revealing an increase in the rate of decay with increasing sample temperature.

Figure 8.9: (a) Total (0-60 s) Net-BOSL light sums as a function of measurement temperature obtained after (squares) and without (circles) preheat treatment at 120 °C (10 s). The inset shows the initial (0-1 s) integrated BOSL intensity as a function of measurement temperature. The data points were connected with linear curves for better visualisation. (b) Normalised at t=0 s BOSL decay curves at selective measurement temperatures following preheat at 120 °C (10 s). The data were produced with a sample of ~ 20 type ´0402´ SMRs irradiated with ~ 3 Gy. The error bars in (a) are not shown since they are comparable to the symbol size

Figure 8.10: Dependence of photo-ionisation cross section, σ, on temperature of stimulation for the BOSL components C_2 (top panel), C_3 (middle panel), and C_4 (higher panel). The data were obtained using a sample consisting of 20 type ´0402´ SMRs.

Figure 8.11: Plot showing integrated (0-60 s) BOSL intensity vs sample stimulation temperature to 200 °C (i.e., 473 K) for a sample consisting of 20 type ´0402´ SMRs. The thermal quenching equation, $I(T) = \frac{I_o}{1+C \cdot exp^{-\frac{W}{kT}}}$, was fitted to the data (dashed curve). The average (over several samples) values of the thermal quenching parameters were found to be W = 0.53 ± 0.05 eV and C = (2.88 ± 2.4) x10^6.

Figure 8.12: Quenched (square symbols) and corrected (start symbols) data for (a) the total (0-60 s) integrated and (b) initial (0-1 s) BOSL intensity as a function of the measurement temperature. The error bars are not shown since they are comparable to the symbol size

Figure 8.13: Fit to the 0-1 s corrected data using equation $OSL(T) = OSL_o \exp(-E/kT)$ resulting an activation energy, E_a, for thermal assistance of ~ 0.11 eV. The error bars are not shown since they are comparable to the symbol size

Figure 8.14: Plot of the logarithm of photo-ionisation cross section, σ, vs kT^{-1} for components: C_2 (upper panel), C_3 (middle panel), and C_4 (lower panel) of the BOSL response. The slope of the linear part (dashed curves) of each plot corresponds to the activation energy, E_a, characterising the detrapping process during optical stimulation. The value of E_a for component C_2 is 0.061 ± 0.003 eV, 0.085 ± 0.003 eV for C_3, and 0.171 ± 0.003 eV for C_4. The plots were produced using the data shown in Figure 8.10.

Figure 9.1: Models of optical bleaching of thermoluminescence according to (a) Levy (1982), (b) Chen et al. (1990), and (c) McKeever (1994). The numbers in parentheses are explained in the text. Redrawn from McKeever (1994).

Figure 9.2: Optical bleaching of TL glow curve by blue-light stimulation. (a) Examples of remaining TL glow curves following $BOSL_{RT}$ measurements for the indicated durations (1-1000s) (b) Lost TL glow curves calculated by subtracting the bleached TL signal from the TL

obtained without illumination. The data correspond to a sample consisting of ~ 20 type ´0402´ SMRs irradiated with ~ 10 Gy.

Figure 9.3: (a) Linear-log plot showing the decrease of normalised at t=0 s integrated (50-150 °C) TL signal after storage at RT (filled squares) and storage at RT followed by blue-light optical stimulation at RT (filled circles) for different times t = 0….1000 s. The curve obtained after the remaining bleached TL was corrected for thermal fading (filled triangles) was used to derive the optical bleaching rate of the PTTL signal. The data points were connected with straight lines for better visualisation (b) Optical bleaching curve of TL Peak 1/PTTL peak (50-150 °C) plotted on a log-linear scale and fitted with a sum of three exponential functions. The time decay constants of the three exponential components are indicated in the figure.

Figure 9.4: Optical bleaching curve of the normalised at t=0 s integrated intensity of TL Peak 2 (150-290 °C). The data were fitted with a sum of three first-order exponentially decaying components with characteristic time decay constants equal to 4.5 ± 0.9 s (*Dot curve*), 41 ± 2 s (*Dash Dot curve*), and 414 ± 19 s (*Dash Dot Dot curve*).

Figure 9.5: Examples of BOSL decay curves measured during the optical bleaching process of TL. As explained in the text, the number of data points of each curve has been adjusted according to the duration of illumination. Each data point corresponds to 0.2 s of stimulation. The decay curves are representative of a sample consisting of ~ 20 type ´0402´ SMRs irradiated with ~ 10 Gy.

Figure 9.6: Variation of BOSL integral as a function of stimulation time. The lower panel shows the integrated intensity over the 1 s of stimulation, while the upper panel shows the integrated intensity over the remainder of the curve (e.g., 1-t s, where t=10, 30, 60...s). Linear curves were used to connect the data points for better visualisation. The estimated error bar of each data point is not presented due to being less than the symbol size.

Figure 9.7: Comparison of optical bleaching of TL by $BOSL_{RT}$, PH: 120 °C + $BOSL_{RT}$, and $BOSL_{120^{o}C}$ after (a) 60 s, (b) 200 s, and (c) 1000 s of stimulation. The TL glow curves correspond to a sample consisting of ~ 20 type ´0402´ SMRs.

Figure 9.8: Lost TL glow curves following annealing to 120 °C and bleaching with blue light at RT for 200 and 400 s. The position of the maximum of each lost glow peak is also indicated in the figure. The glow curves are representative of a sample consisting of ~ 20 type ´0402´ SMRs irradiated with ~ 10 Gy.

Figure 9.9: Pulse-annealing curves of alumina substrates produced by heating a sample from 100 to 290 °C using different heating rates.

Figure 9.10: (a) Numerically calculated first derivatives of pulse-annealing curves shown in Figure 4.12 smoothed using a 5-point Adjacent Averaging smoothing function. (b) Plot of ln (T_m^2/β) vs $kT_m{}^{-1}$ used to estimate the trap parameters *E, s* of the OSL traps. The T_m values were obtained by visual inspection from the maximum temperature position of the peak-shaped curves in (a).

Figure 9.11: Luminescence efficiency of TL Peak 2 as a function of maximum peak temperature, T_m, employing various heating rates analysis. The dashed curve shows the fit to the data points using the equation describing the thermal quenching effect with parameters: W = 0.61 ± 0.02 eV and C = (0.9 ± 0.3) x10^6.

Figure 10.1: (a) Short-term RT fading of TL following several time intervals between irradiation and measurement. (b) Lost TL glow curves obtained by subtracting each delayed TL glow curve from the prompt TL glow curve. The glow curves were obtained with a sample consisting of 20 type ´0402´ SMRs. The sample was irradiated with 3 Gy and heated linearly to 500 ° C at 5 ° C s^{-1}.

Figure 10.2: Fading curve of TL of Peak 1. Each data point represents the average value of the normalised remaining TL over all samples. The dose to the samples was 3 Gy.

Figure 10.3: Fading curves of TL over (a) the entire temperature range, (b) the low temperature side and (c) the high temperature side of TL Peak 2. The data points up to t ≈ 3 months were fitted with a function of type $y = 1 - b * \log(x)$ characteristic of the quantum mechanical tunnelling fading mechanism. Each data point corresponds to the average value of the normalised remaining TL of all samples. The dose to the samples was 3 Gy.

Figure 10.4: (a) Comparison of fading curves between OSL_{RT} and TL Peak 1. (b) Part of the fading rate curve of OSL_{RT} extending from 4 h to 1 year showing the logarithmic dependence on time. Each data point corresponds to the average value of the normalised remaining OSL of all samples. The dose to the samples was 3 Gy.

Figure 10.5: Fading curves of OSL at several sample temperatures produced after irradiation with 3 Gy. The set of data obtained at RT and 50 ° C sample temperature present a fast fading component from $t=t_o$ (t_o ≈1-3 minutes) to t≈4 h and a slow fading component extending from t≈ 4 h to t ≈1 year. The slow fading components were fitted with equation $y = 1 - b * \log(x)$ characteristic of the quantum mechanical tunnelling fading mechanism. The two sets of data obtained at 100 and 150 ° C sample temperature show a single fading component following a logarithmic dependence with time.

Figure 10.6: Comparison of fading curves of OSL at several sample measurement temperatures following irradiation with 3 Gy and preheat to 120 °C (10 s). The data points from $t=t_o$ (t_o ≈1-3 minutes) to t≈3 months were fitted with the equation describing the quantum mechanical tunnelling fading mechanism. Note that the rate of fading expressed by the constant *b* decreases with increasing sample temperature.

Figure 10.7: Ratio of TL measured 1 day following irradiation to the prompt TL (*t*~3 minutes) as a function of the glow curve temperature for storage temperatures of RT, 30, 30, and 90 °C.

Figure 10.8: Comparison of fading rate curves of TL at several sample storage temperatures following irradiation with 3 Gy and preheat to 120 °C (10 s). All data sets were fitted with the equation describing the quantum mechanical tunnelling fading mechanism. Note that *g* increases with increasing sample temperature.

Figure 10.9: (a) Temperature dependence of g (%/decade) of TL and OSL. (b) Arrhenius plots of the data in (a). The slope of the linear curve of each dataset corresponds to the thermal activation energy of fading.

Figure 11.1: Comparison of the TL glow curves of two samples from Group 1 (*Sample 1*: 10 resistors from mobile phone, *Sample 8*: 10 unused resistors) and two samples from Group 2

(*Sample 1*: 20 resistors from mobile phone, *Sample 8*: 20 unused resistors) measured after (a) 0.5 Gy, (b) 2 Gy, and (c) 5 Gy. The TL was detected in the UV using a Hoya U340 filter (7.5 mm).

Figure 11.2: Comparison of the OSL glow curves of two samples from Group 1 (*Sample 1*: 10 resistors from mobile phone, *Sample 8*: 10 unused resistors) and two samples from Group 2 (*Sample 1*: 20 resistors from mobile phone, *Sample 8*: 20 unused resistors) measured after (a) 0.5 Gy, (b) 2 Gy, and (c) 5 Gy. The OSL was detected in the UV with a Hoya U340 filter (7.5 mm).

Figure 11.3: Histogram of (a) $TL_{150\text{-}290^{o}C}$ and (b) OSL_{60s} sensitivity. A Gaussian probability distribution function, shown by the dashed curves, was fitted to the data. The mean and standard deviation of each Gaussian distribution are shown in the legends. The data were produced using a sample population of 100 SMRs and a dose of 20 Gy. The TL and OSL were detected in the UV with a Hoya U340 filter (7.5 mm).

Figure 11.4: BG-corrected TL glow curves of Sample 3 from (a) Group 1 and (b) Group 2 obtained once with the OSL unit located below the PMT and after removing the OSL unit. The TL was detected across the entire range of the PMT detector without any filter.

Figure 11.5: Reproducibility of normalised TL response showing the variation of the $TL_{150\text{-}290^{o}C}$ intensity as a function of ten repeated cycles of irradiation (5 Gy) and annealing (120 ° C, 10 s). The data produced using a sample consisting of 20 SMRs.

Figure 11.6: Reproducibility of OSL response following ten repeated cycles of irradiation (5 Gy) and annealing (120 ° C, 10 s). The integrated normalised to the first measurement OSL intensity over 0-10 s, 0-20 s, 0-30 s, and 0-60 s of stimulation was plotted as a function of measurement cycle. The data produced using a sample consisting of 20 SMRs.

Figure 11.7: Relationship between the TL response and the applied dose. (a) Linear plot of normalised $TL_{150\text{-}290^{o}C}$ intensity as a function of dose in the range 0.5–400 Gy, (b) log-log plot of normalised $TL_{150\text{-}290^{o}C}$ intensity over 0.5–20 Gy, and (c) log-log plot of normalised $TL_{150\text{-}290^{o}C}$ intensity over 30–400 Gy. The linear regression lines of the data in b, c are also shown from which the slopes of the lines were found to be 1.003 ± 0.004 and 1.21 ± 0.06 respectively.

Figure 11.8: Relationship between the OSL_{60s} response and the applied dose. (a) Linear plot of normalised OSL_{60s} intensity as a function of dose in the range 0.5–400 Gy, (b) log-log plot of

normalised OSL_{60s} intensity over 0.5–20 Gy, and (c) log-log plot of normalised OSL_{60s} intensity over 30–400 Gy. The linear regression lines of the data in b, c are also shown from which the slopes of the lines were found to be 0.99 ± 0.004 and 1.12 ± 0.02 respectively.

Figure 11.9: Model of a type ´0805´ SMR. The material composition of parts 1-6 are explained in Table 11.9.

Figure 11.10: Cross-section view of a simulated mobile phone consisting of (1) front and (7) back plastic case, (2) glass screen, (3, 5) aluminium covers, (4) printed circuit board, (6) battery, and two surface mount resistor components (R1, R2).

Figure 11.11: (a) Photon energy luminescence (average of TL and OSL) response of SMRs normalised to the response from ^{60}Co source gamma rays estimated following irradiation with 0.5 Gy air-Kerma dose using a range of ISO Wide Series filtered x-rays or gamma rays from a ^{137}Cs or a ^{60}Co source. (b) The MCNP-calculated relative response. (c) Theoretical (normalised to ^{60}Co) photon energy response of pure Al_2O_3 relative to air, calculated using the values of the mass energy-absorption coefficient for aluminium oxide and air (NIST, 2011). (d) The MCNP-calculated relative response of a ´bare´ SMR component (i.e., only the alumina substrate).

Figure 11.12: (a) Experimental photon energy (average of TL and OSL) response of SMRs normalised to the response from ^{60}Co source gamma rays estimated following AP irradiation of a mobile phone with 0.5 Gy air-Kerma dose using a range of ISO Wide Series filtered x-rays or gamma rays from a ^{137}Cs or a ^{60}Co source. (b) The MCNP-calculated response (average of R1 and R2) for AP irradiation of a mobile phone.

Figure 11.13: Experimental set-up used for the x-ray (High 300 Series, mean x-ray energy of 147 keV) irradiation of mobile phones, unused SMRs wrapped in light-tight black film, and TLDs placed in various locations on a whole body Rando-Alderson anthropomorphic phantom.

Figure 11.14: Experimental set-up used for the gamma (^{137}Cs) irradiation of mobile phones, unused SMRs wrapped in light-tight black tapes, and TLDs placed on each side of a water-filled ISO slab phantom.

Figure 11.15: Dose per fluence results as a function of energy for both resistors and both transport modes for a free-in-space phone exposed from the front.

List of Tables

Table 7.9: Comparison of values of activation energy, *E*, and frequency factor, *s*, of a standard SMR sample after analysing the TL glow curves (5 °C s^{-1} ; 4 Gy) using the VHR, IR, and PS methods.

Table 7.10: Values of the activation energy *E*, frequency factor *s*, and the geometric factor, μ_g, of peaks identified from the analysis of glow curves obtained following the step-wise annealing procedure described in 7.2. Data represent average values obtained using a number of samples consisting of 3 type ´1206´ SMRs.

Table 8.1: Amplitude and decay time constant characteristics of the components of the normalised BOSL decay curves after different preheat treatments. The duration of each preheat treatment was 10 s. The values shown are averages of a number of samples (n~10) consisting of ~ 20 type ´0402´ SMRs.

Table 8.2: Average (over several samples consisting of ~ 20 type ´0402´ SMRs) values of the time decay constants, τ, of the fitted components at different stimulation temperatures with and without preheat at 120 °C (10 s).

Table 9.4: Experimental sequence used to investigate the optical bleaching of TL.

Table 9.2: Kinetic parameters of lost TL and TL Peak 2 calculated using chip samples.

Table 9.3: Kinetic parameters of lost TL and TL Peak 2 calculated using fine grain samples.

Table 9.4: Experimental sequence used to determine the parameters of the OSL traps.

Table 10.1: Thermal quenching characteristics of prompt and delayed (t =5 days) OSL.

Table 10.2: TL fading. Fading rate in percentage per decade of TL Peak 2.

Table 10.3: OSL fading**.** Fading rate in percentage per decade of OSL.

Table 11.5: TL and OSL sequences for investigating the luminescence sensitivity of SMRs.

Table 11.2: Results of (a) sensitivity and (b) signal to BG ratio of the $TL_{150\text{-}290}{}^{o}{}_{C}$ and OSL signals for the samples of Group 1 and Group 2 following irradiation with 0.5 Gy.

Table 11.3: Results of (a) sensitivity and (b) signal to BG ratio of the $TL_{150\text{-}290}{}^{o}{}_{C}$ and OSL signals for the samples of Group 1 and Group 2 following irradiation with 2 Gy.

Table 11.4: Results of (a) sensitivity and (b) signal to BG ratio of the $TL_{150\text{-}290}{}^{o}{}_{C}$ and OSL signals for the samples of Group 1 and Group 2 following irradiation with 5 Gy.

Table 11.5: Comparison of the average sensitivity of $TL_{150\text{-}290}{}^{o}{}_{C}$ and $OSL_{60\ s}$ with the sensitivity of the $TL_{150\text{-}290}{}^{o}{}_{C}$ signal measured after removing the OSL unit below the PMT detector.

Table 11.6: Description of the sequence used to study the dose-response dependence of the luminescence signals.

Table 11.7: Values of LOD for the TL and OSL signals.

Table 11.8: Type, energy, and dose rate characteristics of the photon sources used to study the photon energy response of SMRs following irradiation with 0.5 Gy air-Kerma dose. The duration of each irradiation is also given.

Table 11.9: Dimensions and material composition of the various parts of an SMR.

Table 11.10: OSL measurement protocols for dose reconstruction with SMRs suggested by the MULTIBIODOSE project (Bassinet, et al., 2014).

Table 11.11: Comparison of duration and precision of OSL and TL measurement protocols specific to the equipment used in the present research (dose rate of beta irradiator 0.040 ± 0.002 Gy s^{-1}) and for the particular experimental details for a sample consisting of ~ 10 SMRs.

Table 11.12: Analytical TL and OSL measurement protocols for dose reconstruction with SMRs used in the present investigation.

Table 11.13: Results of the dose reconstruction using SMRs from mobile phones and unused SMRs attached to a Rando-Alderson anthropomorphic phantom irradiated anterior-posterior with an air-Kerma dose of 0.7 Gy at a dose rate of ~ 400 mGy h^{-1} using the ISO High 300 Series x-

rays (effective x-ray energy 147 keV). Unless indicated with asterisk, the type of SMRs used were ´0402´.

Table 11.14: Results of the dose reconstruction using SMRs from mobile phones and unused SMRs attached to a Rando-Alderson anthropomorphic phantom irradiated in a rotational geometry with a total air-Kerma dose of 0.8 Gy at a dose rate of ~ 400 mGy h^{-1} using the ISO High 300 Series x-rays (effective x-ray energy 147 keV). Unless indicated with asterisk, the type of SMRs used were ´0402´.

Table 11.15: Results of the dose reconstruction using SMRs from mobile phones and unused SMRs attached to a water-filled ISO slab phantom irradiated anterior-posterior with an air-Kerma dose of 0.71 Gy at a dose rate of ~ 11 mGy h^{-1} using a ^{137}Cs source. Unless indicated with asterisk, the type of SMRs.

Table 11.16: Values of the personal dose equivalent at a depth of 10 mm [$H_p(10)$] and 0.07 mm [$H_p(0.07)$] registered by the thermoluminescent dosemeters placed around the RA and the ISO slab phantoms.

Table 11.17: Values of the absorbed doses reconstructed using the OSL and the TL protocols for three locations on the RA and ISO phantoms.

Table 11.18: Values of the absorbed doses reconstructed using the OSL and the TL protocols for three locations about the RA and ISO phantom corrected for the fading rate effect specific to each sample.

Table 11.19: Values of the absorbed doses reconstructed using the OSL and the TL protocols for three locations on the RA and ISO phantom corrected for the photon-energy dependence effect of the alumina SMRs.

Table 11.20: Comparison between the doses reconstructed using SMRs (analysed with the OSL method) and the doses registered by the TLDs for three locations on the RA and ISO phantom.

Table 11.21: Mean doses deposited per fluence in resistors of mobile phones exposed to photons from the front or rear.

Table 11.22: Doses deposited per fluence in resistors of a mobile phone located on an ISO water-filled slab phantom and exposed to plane-parallel photon sources, and the same data given normalized to the mean of the R1 and R2 results for 0.662 MeV exposures at *AP,Out*. Fluence to personal dose equivalent conversion coefficients for AP (i.e. 0^0) exposures are also included for comparison.

Table 11.23: Absorbed dose per fluence data for organs exposed to Ir-192 from various geometries, and for FLR exposures to Cs-137 and Co-60. The red bone marrow, stomach and small intestine are considered to be the most significant organs for ARS. The main role of the remaining data is for the computation of whole body doses, $D_B{}^G$, which have been estimated as the averages of the doses to all of the organs.

Table 11.24: Estimated whole body absorbed doses per fluence data for exposures to Cs-137 and Co-60 from various geometries, and the standard deviations around these means of the absorbed doses per fluence in the organs specified in ICRP 103.

Table 11.25: Selected absorbed dose per fluence data given relative to that for the whole body, for exposures to Ir-192, Cs-137 and Co-60 from various geometries.

Table 11.26: Absolute and relative mean absorbed dose per fluence data for resistors in phones at different locations, exposed to Ir-192 photons from various geometries. The configurations that led to the greatest and smallest results are shown in bold.

Table 11.27: Absolute and relative mean absorbed dose per fluence data for resistors in phones at different locations, exposed to Cs-137 photons from various geometries. The configurations that led to the greatest and smallest results are shown in bold.

Table 11.28: Absolute and relative mean absorbed dose per fluence data for resistors in phones at different locations, exposed to Co-60 photons from various geometries. The configurations that led to the greatest and smallest results are shown in bold.

Table 11.29: Average phone and whole body doses per fluence, calibration factors, and confidence levels for each exposure. Bracketed values denote one standard uncertainty, representing just the statistical variance from the Monte Carlo calculations.

Table 11.30: Absorbed dose per fluence, averaged over both resistors in a phone located on the front or back of a slab phantom and facing away from it, and whole body dose per fluence, from which conversion factors may be derived for low energy AP and PA photon exposures; the 'reversal' of the phone datasets arises from the symmetry of the slab phantom configuration. Bracketed values denote one standard uncertainty, representing just the statistical variance from the Monte Carlo calculations.

List of Abbreviations

AP: Anterior Posterior

BG: Background

BSE: Backscattered electrons

CB: Conduction Band

CCD: Configurational Coordinate Diagram

CGCD: Computerised Glow Curve Deconvolution

CL: Cathodoluminescence

CPE: Charged Particle Equilibrium

CW: Continuous Wave

DC: Dicentric Assay

DCM: Dichloromethane

EDS: Energy Dispersive Spectroscopy

EPR: Electron Paramagnetic Resonance

ESR: Electron Spin resonance

FEG: Field Electron Gun

FISH: Fluorescence in Situ Hybridisation

FTIR: Fourier Transform Infrared

FWHM: Full Width at Half Maximum

HF: Hydrofluoric

HCP: Heavy Charged Particle

ICRP: International Commission on Radiological Protection

ICRU: International Commission on Radiological Units

ID: Isothermal Decay

IR: Initial Rise

IRSL: Infrared Stimulated Luminescence

KERMA: Kinetic Energy Released in Matter

LED: Light Emitting Diode

LET: Linear Energy Transfer

LLAT: Left-Lateral

LM: Linear modulation

LOD: Limit of Detection

MCNP: Monte Carlo N-particle

MDD: Minimum Detectable Dose

NIST: National Institute of Standards and Technology

OSL: Optically Stimulated Luminescence

OSLD: Optically Stimulated Luminescence Detector/Dosemeter

OTOR: One-Trap One-Recombination

PCB: Printed Circuit Board

PCC: Premature Chromosome Condensation

PA: Posterior Anterior

PMMA: Poly-Methyl Methalycrate

PMT: Photomultiplier Tube

POSL: Pulsed Optically Stimulated Luminescence

PS: Peak Shape

PTTL: Phototransferred Thermoluminescence

RA: Rando Alderson

RL: Radiolominescence

RLAT: Right-Lateral

ROT: Rotational

RT: Room temperature

SE: Secondary Electrons

SEM: Scanning Electron Microscope/Microscopy

SMR: Surface Mount Resistor

SR: Synchrotron

TCPE: Transient Charged Particle Equilibrium

TFT: Thin Film Transistor

TL: Thermoluminescence

TLD: Thermoluminescence Detector/Dosemeter

TR: Time Resolved

TSC: Thermally Stimulated Conductivity

TSEE: Thermally Stimulated Exoelectron Emission

TSL: Thermally Stimulated Luminescence

UV: Ultraviolet

VB: Valence Band

VD: Variable Dose

VHR: Variable Heating Rate

WDS: Wavelength Dispersive Spectroscopy

XEOL: X-ray Excited Optical Luminescence

Statement of Copyright

Acknowledgements

I wish to thank Public Health England (PHE) for the financial support provided between October 2011 and December 2014 for the production of this research.

I am extremely grateful to my academic supervisors at Durham University, Pr. Ian Bailiff and Dr Ian Terry, for the great opportunity to work on this challenging project. The help, support, critical input and comments provided throughout the duration of this thesis were of immense importance.

I am deeply thankful to my non-academic supervisors at PHE, Dr Kai Rothkamm and Dr Rick Tanner, for their encouragement, guidance, and insightful comments.

I am indebted to Mr Leon Bowen at Durham G. J. Microscopy Facility who taught me with huge patience the theoretical and experimental aspects of Scanning Electron Microscopy and assisted with his comments and ideas to produce my first publication as a postgraduate student.

A special thank you to Dr Jonathan Eakins at PHE who had been an excellent teacher of the MCNP code but also for being a great friend and advisor. I also thank Dr Adrian Finch at St. Andrews University, Dr Jan Mcclure and Mr Luke Hager at PHE for their technical assistance and helpful discussions to produce important material for my thesis.

Most of all, I thank my family. My father, mother, and brother who believed in me, supported me, and encouraged me during my entire life. And of course, a big thank you to my friends Matina, Danae, Maria, Vicky, and Nikos for brightening my life and making me smile when things did not go very well.

To my parents

Χρίστος και Ανδρομάχη

Part I: Introduction and Conceptual Framework

Chapter 1: Introduction and research objectives

1.1 Introduction

Ionising radiation, defined as wave- or particle-like radiation carrying enough energy to cause ionisation (i.e., removal of electrons from atoms or molecules) of the atoms of matter, comprises a significant part of today's human activities and needs. Sources of radioactive materials and radiation generators are widely employed in a variety of industrial sectors including the nuclear industry for the production of heat and electricity, the health industry for medical imaging and radiotherapy applications, the research and education industry as well as in a number of other less widespread activities (e.g., dating using carbon-14, food irradiation).

With exception of the medical applications (e.g., dental and chest x-ray, radiotherapy) of ionising radiation –where individuals should necessarily be exposed to ionising radiation to their benefit– exposure to ionising radiation should be avoided due to the potential of incurring serious biological health effects (e.g., cataract, erythema, cancer, genetic mutations, and death) depending on the level of absorbed dose. Examples of the health effects likely to arise at different levels of absorbed dose are given in Figure 1.1.

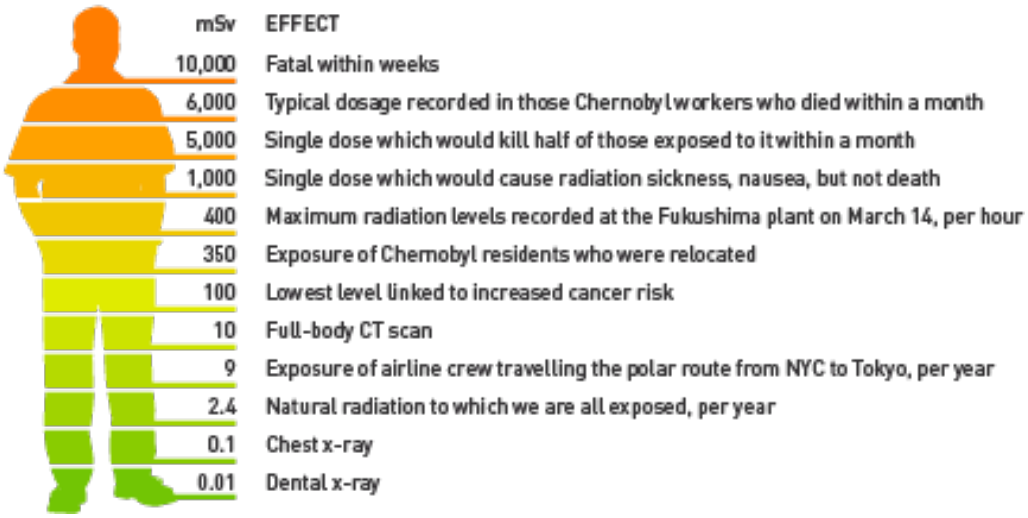

Figure 1.1: Radiation doses and potential health effects (https://cna.ca/issues-policy/radiation/quantifying-radiation).

Generally, the facilities employing radiation sources are obliged to conform to safety standards to ensure the safety and security of radioactive materials and sources (e.g., IAEA, 2004, 2006). Nevertheless, and despite the establishment of a system of control for the safe use of ionising radiation, accidents are likely to occur. A few examples of radiation or nuclear accidents that took place in the past are presented in Table 1.1 attributable mainly to equipment malfunction, lack of regular assessment and equipment maintenance, or lack of proper training or expertise of radiation workers. Accidents due to loss of control of radiation sources (i.e., 'orphan' sources) such as the Goiana incident (1987) and due to malevolent use of radioactive materials (e.g., Litvinienko polonium-210 poisoning in 2006) have also been reported (Jaworska, 2009).

Radiation or nuclear accidents may be classified into small and large scale accidents distinguished by the number of the potentially exposed individuals. The severity of an accident determined by the degree of the induced health and environmental effects may be unpredictable and heterogeneous, though. Nevertheless, it could be said that, for instance, an accident including an explosion or fire in a nuclear installation (e.g., Chernobyl nuclear power plant) is likely to result in the heterogeneous exposure of a large number of people from the public, while, of course, radiation workers in the vicinity of the accident will most likely be heavily exposed and experience the most acute and severe consequences of ionising radiation (e.g., radiation death).

Table 1.1: Examples of radiation accidents and their causes occurred around the world.

Location and date of accident	Cause
Semipalatinsk Nuclear Test Site, Kazakhstan, 1949-89	Explosions during nuclear weapon testing
Windscale fire, UK, 1957	Fire in the core of nuclear reactor
Mayak Production Facility, Former Soviet Union, 1957 (Ksysthym disaster)	Failure of cooling system of a tank storing tons of radioactive waste
Three Mile accident, USA, 1979	Nuclear reactor heat system meltdown-Operators errors
Morocco Accident, 1984	Orphan Ir-132 source
Chernobyl nuclear Power Plant, Ukraine, 1986	Explosion and fire of reactor
Goiana Accident, Brazil, 1987	Orphan radiotherapy Cs-137 source
Radiotherapy Facility, UK, 1988	Improper calibration of Co-60 therapy unit
Radiotherapy Facility, Spain, 1988	Maintenance error of clinical linear accelerator
Tamiku, Estonia, 1994	Stolen Cs-137 source from radioactive waste repository
Fukushima, Japan, 2011	Damage of reactor plants (environmental causes)

Whatever the type and severity of a radiation accident, individuals who may have been exposed need to be monitored to evaluate the likelihood of any radiation-induced health effect. Environmental monitoring is always carried out to inform the levels of radiation in the atmosphere likely to be received by people. However, to account (i.e., diagnosis and treatment) for potential acute or long term health effects individual-specific radiation monitoring is required.

Emergency or accident dosimetry aims at this purpose; to quantitatively assess shortly after the occurrence of an accident any possible exposure of humans to radiation in cases where personal dosemeters, such as thermoluminescent detectors (TLDs), were not used and to guide medical treatments (Bøtter-Jensen *et al*., 2003). In the case of a mass casualty radiation incident, the primary objective of emergency dosimetry is to determine the priority of medical intervention needed based on the level of exposure (i.e., medical triage). Emergency dosimetry methods may additionally be used to study the long-term health effects of ionising radiation and assist epidemiological patterns. In this case the reconstruction of absorbed dose is performed following a latency period (e.g., ~ 2 years for leukemia and minimum 10 years for other forms of cancer) since the onset of a radiological event and it is termed retrospective dosimetry (Simon *et al*., 2010).

The efficient management of both a small and large number of exposed individuals depends on a number of factors (e.g., identification of exposed people, immediate response of physicians), but very importantly, on the dosimetry method and the surrogate objects that could be used as dosemeters available at the time of the accident. A method which allows a large number of samples to be processed within a short time following collection and for which the experimental procedures are fast and reliable should be considered as the most suitable for emergency situations. On the other hand, the high ubiquity and the stability of the radiation-induced signal seem to be two of the most important properties of the materials performing as surrogate dosemeters. Other properties determining the suitability of objects for dosimetry applications include linear dose response, zero or minimum native background signal, low limit of detection, flat energy response, and minimum sample variability.

Emergency/accident/retrospective dose assessment can be accomplished using (1) biodosimetry methods based either on blood analysis techniques or on the electron paramagnetic resonance

(EPR) performed on biological materials, and (2) physical dosimetry methods based on luminescence techniques and EPR spectroscopy employing physical objects. Computational techniques may also be employed to reconstruct an accidental exposure taking into account the time spent by individuals in the radiation field, their motion characteristics as well as spatial and temporal characteristics of the exposure conditions (Ainsbury *et al*., 2011). Furthermore, dose modelling approaches (i.e. MCNP simulations) are often used (Bailiff, 1995, 1999) to calculate dose conversion coefficients (i.e., quantities used to relate the absorbed doses in materials to doses in air and humans) in cases where physical instead of biological materials are used as accident dosemeters. The basic principles of these techniques and their application in specific dose reconstruction problems can be found in a number of reports (Ainsbury *et al*., 2011; Alexander *et al*., 2007; Bailiff, 1995; Fattibene and Callens, 2010; Göksu and Bailiff, 2006; Haskell, 1993; Simon *et al*., 2007; Trompier *et al*., 2009; Woda *et al*., 2009). For completeness, a short review of the basic characteristics of the emergency dosimetry techniques is given below.

Biodosimetry for emergency and past exposure radiological situations can be carried out using biological (i.e., cytogenetic techniques, genetic techniques, heamotological techniques, protein biomarkers) or physical methods (i.e., EPR spectroscopy). Biologically-based techniques, through the analysis of blood samples, rely on the detection of changes in biological markers, such as chromosomes, caused by ionising radiation. The dicentric chromosome (DC) assay which measures the number of radiation-induced dicentric chromosomes (i.e., chromosomes with two centromeres) is, so far, considered the most sensitive technique for acute dose evaluations being able to detect whole body doses as low as 100 mGy (Ainsbury *et al*., 2011). However, since the number of dicentric chromosomes reduces significantly weeks or months following the exposure (i.e., fading) the DC assay is less effective for retrospective dose applications (Ainsbury *et al*., 2011; Alexander, *et al*., 2007). Also, the long culture time required is considered the main drawback of the DC assay for the management of large number of exposed populations. The premature chromosome condensation (PCC) assay is another technique for the evaluation of dose shortly after an accident permitting faster dose measurements in comparison with DC. Examples where the DC and PCC assays have been used for the acute evaluation of accident doses including the Chernobyl (1986) and the Goiana (1997) accidents can be found in Alexander *et al*., (2007). For the evaluation of past exposures and epidemiologic studies the biological method of choice is the fluorescence in situ hybridisation

(FISH) which measures the number of radiation-induced stable chromosomal translocations. The FISH method has been used to determine the level of exposure of irradiated populations following radiation accidents in sites such as the Hiroshima and Nagashaki (Kodama *et al*., 2001), Chernobyl (Jones *et al*., 2002), Semipalatinsk (Salomaa *et al*., 2002), Mayak (Wieser *et al*., 2006), and Techa River (Romanyukha *et al*., 2001) and it has been validated through comparison with dose estimates provided by personal dosemeters (Simon *et al*., 2010). A number of other biological methods have been developed to detect radiation-induced damage (Ainsbury *et al*., 2011). For instance, the newly developed protein-based biomarker ɣ-H2AX assay (Horn *et al*., 2011; Rothkamm and Horn, 2009) presents several of the characteristics (e.g., linear dose response to 100 Gy, minimum detectable dose of the order of mGy, fast sample processing and analysis, whole and partial body exposure) which are important for the rapid identification and management of large populations of accidentally exposed individuals. Nevertheless, due to the rapid loss of radiation-induced signal with time, the ɣ-H2AX assay may be a useful and reliable triage tool if performed within two days following exposure. Although the method has not yet been validated in radiation incidents, its potential in determining doses accurately was supported initially through an inter-laboratory comparison study (Rothkamm *et al*., 2013) and later via comparison with other well-established biodosimetric techniques, such as the DC assay (Rothkamm *et al*., 2014).

In the category of biodosimetry techniques, the established physically-based method is EPR (also referred to as electron spin resonance, ESR) on calcified human tissue and, specifically, tooth enamel and bones. Briefly, EPR dosimetry is based on the detection of stable paramagnetic centres (i.e., chemical elements or compounds with unpaired electrons), such as free radicals (e.g., CO_2^{-1}), created as a result of interaction with ionising radiation. The concentration of these paramagnetic centres is proportional to the amount of absorbed dose and comprises the basic principle of EPR dosimetry (IAEA, 2002; Romanyukha and Trompier, 2011).

Tooth enamel can be considered as a highly sensitive personal radiation detector due to its high n hydroxyapatite content (i.e., mineral component of teeth and bones) which gives a large number of free radicals following absorption of ionising radiation (Desrosiers and Schauer, 2001; Fattibene and Callens, 2010; IAEA, 2002) and due to the low detection limit reported to be a few hundreds of mGy (Ainsbury, *et al*., 2011; Trompier, *et al*., 2009). In addition, owing to the high

stability (~ 10^6-10^7 years at RT) of the radiation created CO_2^{-1} in tooth enamel, the method is suitable for both short and long term dose evaluations and its potential for retrospective dose assessments has been demonstrated in the reconstruction of doses of individuals accidentally exposed following the atomic bombs explosions in Hiroshima and Nagashaki (Nakamura *et al*., 1998) and in areas contaminated following the accidents in Chernobyl nuclear reactor (IAEA, 2002; Simon, *et al*., 2002, 2010), the Semipalatinsk nuclear test site (IAEA, 2002; Simon, *et al*., 2002, 2010), and the Mayak plutonium production facility (Wieser, *et al*., 2006). As with the blood analysis techniques, the method of EPR on tooth enamel can be useful in determining the real radiation-induced health risk as it provides information on the dose absorbed by biological material. However, its usefulness is limited by the fact that it is mainly applicable to extracted teeth, although there is ongoing research to set up *in vivo* EPR measurements for immediate radiation screening (Miyake *et al*., 2000; Swartz *et al*., 2007; Williams *et al*., 2010, 2014). Bone is another type of calcified human tissue which can be used for dose evaluations using the EPR method (Caracelli *et al*., 1986; Desrosiers and Schauer, 2001; Romanyukha and Trompier, 2011; Schauer *et al*., 1996). As with teeth, absorption of ionising radiation generates CO_2^{-1} species, although in smaller concentrations due to the lower amount of hydroxyapatite (Romanyukha and Trompier, 2011). Hence, the radiation sensitivity of bones is lower than that of tooth enamel resulting in a higher low detection limit (~ 1-5 Gy) which is also dependent on the type of bone (Romanyukha and Trompier, 2011). These factors together with the invasive nature of the method make them less attractive for emergency/retrospective dose evaluations.

Keratin-based human tissues, such as hair and nails, have also been tested for applications in emergency/retrospective dosimetry (Alexander *et al*., 2007; Colak and Ozbey, 2011; Romanyukha and Trompier, 2011; Romanyukha *et al*., 2011; Tepe Cam *et al*., 2014; Trompier *et al*., 2009a, b). While these biological materials offer the advantage of easy and non-invasive collection, their suitability as EPR dosemeters is restricted by the presence of significant non-radiation induced background signals placing the limit of detection to a few Gy and for hair is further limited by the presence of strong fading.

Saccharides found in the domestic environment or carried by individuals in the form of tablets (e.g., sweeteners) also provide a reliable means of estimating absorbed doses following radiation accidents (Nakajima, 1995; Fattibene *et al*., 1996; Romanyukha and Trompier, 2011; Trompier

et al., 2009) using EPR. However, despite the good linear dose response over 0.5-100 Gy and the high radiation sensitivity (i.e., detection limit of 100-200 mGy) of most types of saccharides, the sugar-EPR dosimetry method presents certain difficulties associated with complex and sugar type-dependent EPR spectra, the influence of environmental conditions (e.g., humidity and temperature) on the spectra, and the short-term instability of the radiation-induced EPR signal in the first 100 hours following irradiation (Desrosiers *et al*., 2006; Margouzui, *et al*., 2012; Romanyukha and Trompier, 2011; Trompier *et al*., 2009). Fabric materials, such as cotton and wool, have also been tested for accident dosimetry purposes with cotton showing the most promising dosimetry properties (Barthe *et al*., 1989; Kamenopoulou *et al*., 1986; Trompier *et al*., 2009). The high ubiquity of cotton in clothing represents an ideal method for personal dose assessments and dose mapping (when cotton fibres are collected from various clothes worn by individuals) but the significant background signal (making the dose response non-linear to ~ 7 Gy) and the fading (i.e., ~ 50 % loss of signal in the first 100 hours) of the EPR response need to be accounted for in the dose reconstruction process (Kamenopoulou *et al*., 1986). Extensive research has also been performed on the EPR dosimetry properties of plastics (Nakajima, 1987; Romanyukha and Trompier, 2011; Sholom and Chumak, 2010; Trompier *et al*., 2009, 2010) and glasses (Bassinet *et al*., 2010; Engin *et al*., 2006; Fattibene *et al*., 2014; Gancheva *et al*., 2006; Trompier et a., 2009; Wu *et al*., 1995); owing to their high abundance in household and personal objects. Of the broad range of objects made of plastic, or containing plastic components, buttons, watches, mobile phones and eyeglasses constitute the most useful means of determining personal doses. However, they are limited by a non-linear dose response and a significant loss of signal with time following irradiation (Trompier *et al*., 2009); although, as shown by Trompier *et al*., (2010), it may be possible to delay or reduce the fading process by storing the samples at low temperatures (e.g., - 30 °C). Exposure to ultraviolet radiation (UV) has also been shown to affect the radiation-induced EPR signals (Sholom and Chumak, 2010). Glass, particularly from the display windows of mobile phones, has recently attracted considerable scientific interest (Bassinet *et al*., 2010a; Fattibene *et al*., 2014 Trompier *et al*., 2011) for EPR emergency dosimetry. Properties such as high ubiquity, linear dose response (0-100 Gy), stable EPR signal (for measurements performed 24-48 h after irradiation), and a relatively low detection limit of ~ 2 Gy make glass from mobile phones promising candidates for emergency/retrospective dosimetry. The feasibility of using glass as an accident dosemeter was recently demonstrated in

an inter-laboratory comparison study (Fattibene *et al*., 2014), though specific issues related with the influence of parameters, including environmental conditions (e.g., UV light), on the measured EPR spectra have to be thoroughly examined and to establish the EPR method a reliable characterisation of glass samples from a wide range of mobile phones is needed.

Another method for the triage of exposed individuals and for epidemiological investigations is luminescence dosimetry which is based on the detection of thermally- or optically-stimulated light from luminescent materials that previously have been exposed to ionising radiation (Bøtter-Jensen *et al*., 2003). Luminescence techniques may be thought as the most widely used for dosimetry of radiation accidents not only because of the wide availability of objects that exhibit luminescence properties, but also because of the fact that the modern experimental systems (e.g., Risø TL/OSL reader) enable fast and simply data analysis of a large number of samples.

So far, the main application of luminescence techniques was the retrospective evaluation of accident doses using minerals (e.g., quartz) included in building materials, such as bricks, tiles, and porcelain (Bailiff, 1996, 1997; Göksu, 1997; Haskell, 1993; Stoneham, 1985). The first application of luminescence, and specifically thermoluminescence (TL), in retrospective dosimetry was the measurement of doses following the nuclear bomb denotations at Hiroshima and Nagasaki (Ichikawa *et al*., 1966; Hashizume *et al*., 1967) using bricks and tiles. Following improvements in measurement protocols, thermoluminescence measurements of cumulated doses using ceramics collected from buildings were made in various regions contaminated by the explosions of the Chernobyl nuclear power plant (Bailiff, 1995, 1999; Bailiff *et al*., 2004a; Hutt *et al*., 1993; Sato *et al*., 2002; Stoneham *et al*., 1993), in the areas affected by fallout from the Nevada Test Site (Haskell *et al*., 1994) and the Semipalatinsk Test Site (Bailiff *et al*., 2004b) as well as in settlements in the Techa River valley located near the Mayak production facility in Urals, Russia (Göksu *et al*., 2002). The newly developed optically stimulated luminescence (OSL) technique has also been employed in the retrospective dose reconstruction of settlements downwind of the Chernobyl nuclear power station (Bailiff, 1999; Ramzaev *et al*., 2008; Sholom *et al*., 2000) and the Techa River valley (Woda *et al*., 2011). Environmental/construction objects were shown to encompass several of the characteristics expected from an accident dosemeter: they are abundant, present zero background signal, allow doses of the order of mGy to be detected, show stable signal over time, and they can easily be collected and processed in a short

time (Bøtter-Jensen *et al*., 2003; Yukihara and McKeever, 2011). They can also be used to calculate shielding factors by comparing doses estimated using objects removed from interior of contaminated residences with doses estimated using objects collected from outside (Haskell, 1993) or to obtain information about the radiation field (e.g., energy distribution) by measuring dose-depth profiles using bricks from walls (Bailiff, 1997; Göksu and Bailiff, 2006).

Except for ceramics included in buildings, materials such as salt and washing powders – often found in the domestic and industrial environments – have also been investigated for dosimetry applications (Bøtter-Jensen *et al*., 2003; Göksu *et al*., 1993; Thomsen *et al*., 2002). The high radiation sensitivity and low detection capability (e.g., < 20 mGy) of these chemicals make them potential candidates for emergency dosimetry.

Nevertheless, the above mentioned luminescent materials only provide local, environmental dose information. Computational methods based on Monte Carlo simulations may enable the dose to the ceramics to be related to population's dose as long as a number of parameters related with the spatial and temporal behaviour of exposed individuals are known (Bailiff, 1997, 1999). Therefore, since human exposure can be better detected with personal objects carried by the individuals at the time of the accident the implementation of ceramic materials in objects found close to an individual's body has initiated considerable research.

In the late 70s the potential of using dental ceramics (e.g., porcelain- or glass-based ceramics used in the construction of prosthetic teeth and dental restorative materials) as accident dosemeters was demonstrated by Davies (1979) using TL and thermally stimulated exoelectron emission (TSEE) techniques. In later years additional studies were conducted by Bailiff *et al*., (2003), Veronese *et al*., (2010), and Ekendahl *et al*., (2013) who investigated several properties (e.g., dose response characteristics, photon energy response, fading, light sensitivity) of the thermally- and optically-stimulated luminescence signals of dental ceramics (e.g., crowns, prosthetic teeth). Significant reduction of the luminescence signals with time (i.e., fading) and exposure to white light were identified as the main problems for the use of dental ceramics in emergency dosimetry. The necessity to remove these materials from individuals to perform luminescence measurements may be thought of as another limitation, but since dental ceramics can be considered part of the human body they offer the possibility of using them for individual dose evaluations.

Recent investigations of personal objects that could be employed in emergency dosimetry of radiological incidents include money, clothes, and shoes (Sholom and McKeever, 2014) chip cards (Göksu, 2003; Mathur, *et al*., 2007; Woda and Spöttl, 2009) and electronic components included in portable electronic devices, such as laptops, mobile phones, data storage devices (Bassinet *et al*., 2010a, b; Ekendahl and Judas, 2012; Fiedler and Woda, 2011; Inrig, 2009; Inrig *et al*., 2008; Mrozik *et al*., 2014; Pascu *et al*., 2013; Woda *et al*., 2010).

Sholom and McKeever (2014) explored the OSL properties of a wide range of commonplace objects, such as bank notes, coins, plastic cards, shoes and clothes, possessed by individuals. Most of the tested polymers showed the potential to detect doses below 2 Gy, but also significant variability in some properties (e.g., signal instability with time was between 11-93 % 7 days following irradiation for banknotes). While the authors provided recommendations for their use in triage applications additional investigations may be needed to establish their applicability.

Of the wide variety of chip cards in the form of telephone, ID, or bank cards only those with a certain type of a translucent epoxy encapsulation containing grains of silica have the most suitable luminescence features (Göksu, 2003; Woda and Spöttl, 2009). Using, however, the TL or the OSL method a significant non-radiation induced signal was observed placing the minimum detectable dose to over 3-5 Gy (Göksu, 2003; Woda *et al*., 2009). The OSL signal obtained using blue light stimulation source was also found to exhibit a high degree of fading (i.e., ~ 60 % loss in the first day following irradiation) with storage at room temperature (Woda and Spöttl, 2009). On the other hand, lower detection limits of ~ 250 mGy and a stable luminescence signal can be obtained by measuring the infrared stimulated luminescence (IRSL) response (Göksu, 2003) making these particular types of chip cards potential candidates for emergency and retrospective individual dose monitoring.

Next to chip cards, the suitability of several types of ceramic-based electronic components (e.g., window display, resonators, inductors, resistors) of portable electronic devices has also been examined using OSL and TL techniques to establish their basic characteristics for emergency dosimetry (Bassinet *et al*., 2010a, b; Beerten and Vanhavere, 2010; Beerten *et al*., 2009; Discher and Woda, 2013; Discher *et al*., 2013; Ekendhal and Judas, 2012; Fiedler and Woda, 2011; Inrig, 2008; Inrig *et al*., 2009; Pascu *et al*., 2013). Mobile phones, in particular, potentially offer a great

versatility in terms of the parts that can be analysed with luminescence techniques and since they comprise a widespread electronic device they would allow the triage of a large number of potentially exposed individuals within an exposed population.

As mentioned earlier, glass displays in electronic devices show a prominent radiation sensitivity detectable not only by means of EPR (e.g., Bassinet *et al*., 2010a), but also by TL (Bassinet *et al*., 2010b; Discher and Woda, 2013) measurements. Following a preliminary study of the TL properties of glass from the display of mobile phones, Discher and Woda (2013) conducted a detailed investigation of the intrinsic background signal, dose response, thermal and optical stability of the TL signal and the detection limit of glass display samples obtained from 42 mobile phones. The authors identified two different types of glass which can be studied by TL: the frontside glass of a display window with a coloured pixel layer and the backside glass with a thin film transistor (TFT) structure. The latter was found to exhibit a zero dose signal of lower intensity corresponding – which however overlaps with the radiation-induced TL signal – to an equivalent dose of ~ 340 mGy and may be preferred for dosimetry applications. In a later study Discher *et al*., 2013 showed that the non-radiation induced TL signal of glass with a TFT structure can be reduced by ~ 90 % resulting a minimum detectable dose of ~ 80 mGy when the samples are chemically treated with hydrofluoric acid (HF) prior to TL analysis whereas Bassinet *et al*., (2014) showed that the strongly overlapping background signal can be reduced by a mechanically grinding the surface of the glass. Generally, all glass samples tested showed favorable properties with a linear dose response relationship between 10 mGy to 20 Gy and a reproducible TL response. Nevertheless, two important issues associated with instability and light-sensitivity of the TL signals (i.e., reduction of luminescence intensity by exposure to light) were recognised which, however, do not preclude the use of glass display as accident dosemeter if the appropriate correction factors are applied.

Except for the display, mobile phones have a number of other radiation sensitive parts that can be examined with luminescence techniques. Alumina-rich inductors, resonators, capacitors, and surface mount resistors (SMRs) have all been examined for dosimetry applications (Bassinet *et al*., 2010b; Beerten *et al*., 2009; Ekendahl and Judas, 2012; Fiedler and Woda, 2011; Inrig, 2009; Inrig *et al*., 2008; Mrozik *et al*., 2014; Pascu *et al*., 2013), but the SMR is perhaps the electronic element of the circuit board of a mobile phone that has received greater attention. The

capabilities for applications to emergency situations of a chip resistor primarily stem from the known luminescence sensitivity of its aluminium oxide substrate which physically resembles that of the known Al_2O_3:C dosimetry grade single crystal. The first investigations (Inrig, 2009; Inrig *et al*., 2008) have shown promising results (i.e. linear dose response to 100 Gy, low limit of detectability of ~ 20 mGy, reusability, dose recovery ability) indicating that the requirements of dose evaluation using alumina SMRs can be met (more detailed discussion in Chapter 3). Even though the ultimate employment of the material is restricted by the noticeable loss of signal with time (i.e. athermal fading) the recovery of accident doses can still be performed using appropriate fading correction factors (Bassinet *et al*., 2014). The experimental methodology and measurement protocols have also been established and validated by simulated radiation accidents experiments (Bassinet *et al*., 2014).

1.2 Research aims and objectives

Despite the extensive research including laboratory-based tests and a few radiological exposure trials which have undoubtedly provided solid evidence to demonstrate the applicability of SMRs from mobile phones in emergency dosimetry, there exist some open questions which, at the time of writing, have not been addressed.

To begin investigating these issues, the basic conceptual framework needed to understand and support the experimental findings, are first presented in ***Chapter 2***: Theory of Luminescence, ***Chapter 3***: Luminescence Dosimetry of Ionising Radiation, and ***Chapter 4***: Alumina Structure and Defects. The methodologies employed to direct the research questions are presented in ***Chapter 5***.

The structural and chemical environment of alumina SMRs and their potential influence on the luminescence process, as well as the defects participating in luminescence emission, have not been thoroughly examined. In a recent study (Kouroukla *et al*., 2014), x-ray chemical analysis combined with cathodoluminescence (CL) microscopy and spectroscopy techniques were employed to reveal the nature and spatial distribution of recombination centres in alumina SMRs. Further investigations using x-ray excited optical luminescence (XEOL) performed over a wide

temperature interval are presented in ***Chapter 6*** shedding more light onto the mechanism of luminescence production and the relative participation of the recombination centres during TL and OSL measurements.

The physical mechanism of TL and OSL has also been scarcely studied. The nature of trapping levels (e.g., single, multiple, discrete, continuum) involved in luminescence generation and their kinetic parameters (e.g., trap depth) – crucial to characterise specific properties, such as the thermal stability, determining the suitability of luminescence signals for dosimetry purposes – are examined in detail in ***Chapter 7*** using established TL kinetic analysis methods. The behaviour of trapped charge carriers during thermal stimulation is also examined in ***Chapter 7*** while in ***Chapter 8*** the possible detrapping and recombination pathways of trapped charges are investigated for stimulation using optical light sources [i.e., Blue and Infrared light emitting diodes (LEDs)]. Special focus is given on the influence of measurement parameters, such as the heating rate for TL (***Chapter 7***) and the sample temperature for optical stimulation (***Chapter 8***), useful to build a model for luminescence production and to decide on the most appropriate measurement protocol for dose evaluations.

The correlation of the OSL response with the TL (i.e., existence of common trapping levels) which is presupposed in the primary tests (***Chapter 8***) is established in ***Chapter 9***. By examining the optical bleaching behaviour of TL under different conditions (e.g., duration and temperature of optical stimulation) the correlation of the traps responsible for specific TL glow peaks with the OSL is revealed providing a solid ground to better explore in ***Chapter 10*** the mechanism of the undesirable loss of luminescence intensity with time after irradiation (i.e., fading). Evidence is also provided that the currently accepted model for athermal fading of quantum mechanical tunnelling may not be the most appropriate.

The basic dosimetry properties (e.g., dose-response relationship, reproducibility, limit of detection, photon energy response) of SMRs are explored in ***Chapter 11***. Though, emphasis is given to the investigation of other factors – which have not yet been considered in the existing radiological trials where well-defined and controlled irradiation conditions were employed – associated with the orientation of the mobile phone relative to the direction of the irradiation and the perturbation of the radiation field by the various parts embedded in a phone, casing and surroundings likely to affect the dose reconstruction outcome. Finally, the ability of SMRs to

provide estimates of whole body or organ doses is examined using a simulation approach and taking into account the location and orientation of the phone relative to its owner's body, the extended nature of the body with its various organs positioned at different distances from both the source and the phone.

The ultimate objective of the present investigation is to address these issues in order to gain a thorough understanding of the fundamental processes involved in the luminescence generation of alumina SMRs and to examine the influence of factors which can potentially affect the dose reconstruction procedure. The utilisation of SMRs from mobile phones as whole-body and organ-specific personal dosemeters has also been dealt with.

Chapter 2: Theory of luminescence

2.1 Introduction

The background theory of luminescence is described in this chapter using concepts which are most relevant to this study. Starting from fundamental definitions and concepts, such as the band theory of energy levels in solids and the configuration coordinate diagram (CCD), the absorption and emission processes in luminescent materials will be described. The same concepts will also be used to explain the production of luminescence in irradiated materials under thermal and optical stimulation and to produce the simplest model of luminescence Standard methods for evaluating specific thermal and optical trap parameters will be described; mainly those used in the present investigation (i.e., Chapters 7 and 8). Finally, additional concepts, such as the *thermal quenching* effect and the *fading phenomena* (i.e., thermal and athermal fading) will be reviewed, since these are known to play a significant role in the applicability of luminescent materials in dosimetry applications and were found to be present (i.e., Chapters 6 and 10) in the subject of this study (i.e., alumina substrates).

2.2 Definition of luminescence phenomena

The term luminescence is broadly used to describe the spontaneous or stimulated generation of photon emission [i.e., spectral emission of photons in the UV to near infrared (NIR) range] from solids following absorption of energy provided by external sources. It is commonly referred to as “cold light” to differentiate it from the thermal radiation produced mainly due to the vibrational motion of the internal structural constituents. Both processes may occur simultaneously in a solid with luminescence being in excess of thermal radiation. Except that thermal radiation is strongly dependent on the sample temperature according to the Stefan-Boltzmann law (Leverenz, 1968), where the intensity of the thermal energy emitted is proportional to the fourth power of the sample temperature (i.e., $\propto T^4$), it also appears to have different spectral emission characteristics which help to separate it from luminescence (Aitken, 1985; Curie, 1960; Leverenz, 1968; Yacobi and Holt, 1990).

Several luminescence phenomena exist, which are named after the source employed to excite it. Generally speaking, light emission produced by absorption of light is known as photoluminescence. Energetic electrons or cathode rays give rise to cathodoluminescence emission, whereas ionising radiations such as γ-, and x-rays, β- and other energetic particles produce radioluminescence. Excitation by an applied electric field causes the production of electroluminescence, whereas chemical reactions and mechanical processes generate chemiluminescence and triboluminescence respectively (Aitken, 1985; Curie, 1960; Leverenz, 1994; McKeever, 1985; Yacobi and Holt, 1990).

Depending on the time duration of the emission process a further distinction between fluorescence and phosphorescence is usually made. Fluorescence is mainly observed during excitation with a characteristic time τ of less than 10^{-8} s, although when fluorescence results from spin-forbidden transitions, such as th F-centre luminescence in Al_2O_3 (see Chapter 4), the lifetime of the process may be longer (i.e., ~ ms). If, however, the light emission continues after the cessation of the excitation source it is then known as phosphorescence. Over intermediate periods of time both processes may be active and in this case the different temperature dependence characteristics can be used to separate them. Phosphorescence emission is a temperature dependent process, while fluorescence is temperature independent (Aitken, 1985; Curie, 1960; McKeever, 1985; Yacobi and Holt, 1990).

While both fluorescence and phosphorescence can take place promptly during excitation, the former has a finite duration and no longer exists after the cessation of excitation. On the other hand, phosphorescence not only is a longer lasting phenomenon, but it can be activated by the application of an external stimulus in the form of heat or light. Stimulation by means of heat is known as thermally stimulated luminescence (TSL) or more simply thermoluminescence (TL). If an optical light source is used for phosphorescence stimulation the process is known as optically stimulated luminescence (OSL). It is noted here that TL and OSL are the types of luminescence which are of interest in this study.

2.3 Energy band model of luminescence

The band theory of energy levels in solids provides a generalised description of the luminescence process (Gucsik, 2009; McKeever, 1985; Yacobi and Holt, 1990). According to band theory, materials are classified into three categories based on the energy separation between the valence band (VB) and the conduction band (CB). At equilibrium conditions and T=0 K, the valence band is fully occupied by electrons while the conduction band is empty. Insulators are characterised by a large energy gap (e.g., ~ 8 eV and for alumina ~ 9 eV) where additional energy states can be created by the presence of defects (this is explained in detail in Chapter 4); a condition that is essential for the production of luminescence in many luminescent materials. Luminescence is also produced in semiconductors having a relative small energy gap (e.g., ~ 1 eV) but it is absent in metals where the two bands are not separated. In the following discussion, the various events involved in the luminescence production are treated from the scope of electron, e^-, transitions (i.e., luminescence is explained assuming that electrons are the mobile species), but similar consideration can be developed for the participation of holes, h^+ (i.e., removal of electrons from atomic positions results in formation of holes). The processes (i.e., absorption, charge transfer, and luminescent emission) described below and in Figure 2.1 are also those likely to result in TL and OSL emission.

In a perfect insulating or semiconducting crystalline material the gap between the VB and the CB (i.e., forbidden gap) will contain no electronic states. Excitation of the crystal, for example, by ionising radiation, excites valence band electrons to the conduction band from where they can fall back to the valence band and recombine directly with the holes created upon removal of the electrons (Figure 2.1-transition 1). The band-to-band recombination of electrons and holes results in emission of luminescence (i.e., also known as excitonic emission) with energy approximately equal to the energy gap (Gucsik, 2009; McKeever, 1985; Yacobi and Holt, 1990). Generally, interband transitions are mostly associated with fluorescence emission and have low probability to occur (McKeever, 1985).

In the real world, perfect crystals do not exist. Any natural or man-made material possesses several types of crystal imperfections or defects as a result of inhomogeneities in chemical composition, mixture of chemical phases, and manufacturing conditions. Imperfections such as

distorted surfaces due, for example, to mechanical treatments, displaced or missing atoms, and impurities introduce into the forbidden gap localised metastable states which are responsible for the short- and long-period phosphorescence phenomena (Leverenz, 1968; Yacobi and Holt, 1990). A distinction between traps and luminescent/recombination centres is usually made to specify if a certain defect plays the role of electron (or hole) trap or the level to which trapped charges are transported to recombine and emit luminescence. Energy states created by the presence of foreign elements (i.e., impurities) can also be found in the space between the two bands. These are either known as donor states if they contribute electrons to the conduction band or acceptor states if they contribute holes to the valence band. Usually, they appear occupied by charges prior to excitation (Yacobi and Holt, 1990).

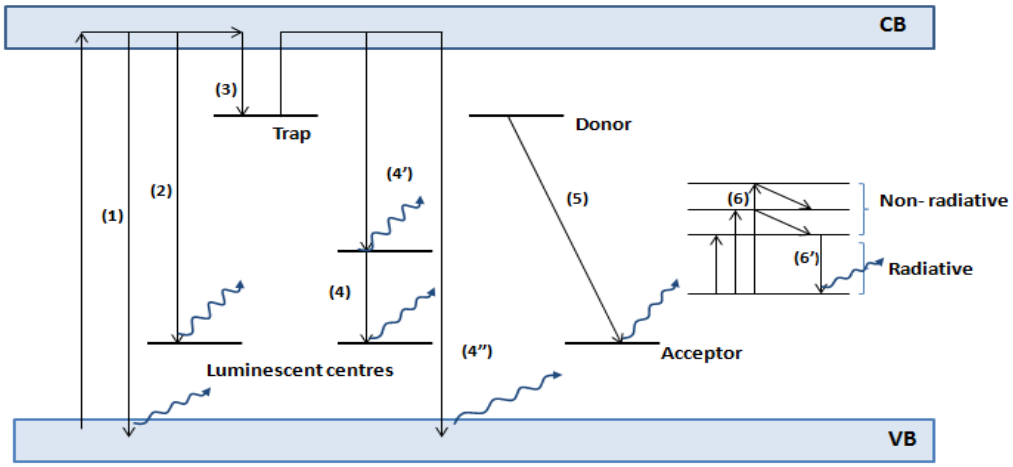

Figure 2.1: Schematic representation of the energy level diagram illustrating the absorption, charge transfer, and luminescent emission processes between the valence band (VB), the conduction band (CB), and the various localised states of a phosphor. Labels indicate: (1) band-to-band electron hole recombination, (2) fluorescence emission by direct transition of electrons from the conduction band to the recombination centre, (3) electron trapping, (4) recombination of trapped electrons excited into the conduction band with holes located at a luminescent centre via a direct transition, (4´) recombination of trapped electrons excited into the conduction band with holes located at a luminescent centre via the excited state of the luminescent centre, (4´´) recombination of trapped electrons excited into the conduction band with holes in the valence band, (5) direct donor-acceptor pair recombination, (6) electron excitation from the ground to any of the excited states of a luminescent centre, and (6´) radiative return of excited electron back to the ground state of a luminescent centre.

With the introduction of the additional localised metastable levels several promptly and stimulated radiative transitions can take place as illustrated in Figure 2.1. Following absorption of energy sufficient to cause band gap ionisation, electrons are released from the valence band leaving behind positively charged holes. Once in the conduction band, these electrons can either make a direct transition to a luminescent centre giving rise to fluorescence emission (2) or occupy an electron trap (3). Trapped electrons can then be raised by stimulation back to the conduction band from where they can finally recombine at a luminescence centre via a direct transition (4) or via the excited state of the luminescent centre (4´), or otherwise recombine with a hole in the valence band (4´´). Another possibility (5) is that of direct electron-hole or donor-acceptor pair recombination (Gucsik, 2009; McKeever, 1985; Yacobi and Holt, 1990).

The recombination processes 2, 4 and 5 may all give rise to photon emission of the same wavelength, if they happen to originate in the same luminescent centre. In such cases, the charge transfer mechanism that has preceded can possibly be identified by conductivity measurements if the conduction band is involved in the emission process or by studying the behaviour of the peak of the spectral emission as a function of the excitation intensity. For instance, donor-acceptor pair recombination is characterised by a shift of the position of the peak emission as the intensity of the excitation source varies (Yacobi and Holt, 1990).

Another radiative transition where neither the conduction band nor the valence band are involved is shown as 6 in Figure 2.1. Here, electrons that reside in the ground state of the luminescent centre are excited to any of the available excited states of the centre (Gucsik, 2009). The return to the ground state may happen in two stages involving both processes where energy is dissipated by phonons (i.e., non-radiative emission) and radiative emissions when the upper exited level has been reached (6) or only radiative emissions if excitation has raised electrons to the first excited state (6´). Very often, these luminescent centres are related to impurity ions (e.g., Cr^{3+} in Al_2O_3) providing a means to recognise them by the detection of the characteristic wavelength of the emission.

Besides the three fundamental processes of energy absorption, transfer, and energy conversion there are additional mechanisms by which luminescence may be delayed or quenched. Retrapping of stimulated charges back into the same or into other traps is very likely to occur causing a delay in the light emission or reduction if there is not sufficient energy for further

stimulation. Non-radiative mechanisms, such as multiple phonon emission, Auger effects, and recombination at the electronic states found at the surface are mainly associated with non-radiative transitions resulting in reduced luminescence efficiency. Elevated sample temperature conditions, particularly during stimulation, are known to enhance the non-radiative processes. Thermal quenching, in which the luminescence yield decreases with increasing temperature (more discussion in section 2.5), is attributed to the increased probability for radiationless transitions (McKeever, 1985; Yacobi and Holt, 1990).

2.4 Configuration coordinate model of absorption and emission

The absorption and emission processes within a luminescent centre, which is basically a fluorescence process, are conveniently described using the configuration coordinate diagram (Figure 2.2) and the Franck-Condon principle (Blasse and Grabmaier, 1994). The former represents the potential energy, *E*, of the centre as a function of a coordinate, *R*, which is usually taken to be the distance of the centre from its nearest neighbour known as internuclear distance (Blasse and Grabmaier, 1994; Gucsik, 2009; Leverenz, 1968; Yacobi and Holt, 1990) and in this model the luminescent centres are assumed to form an isolated vibronic system. In the configuration coordinate diagram horizontal transitions represent the displacement of the nucleus. According to the Franck-Condon principle electron transitions occur faster (~ 10^{-16} s) than the motion of the nucleus of the emitting centre (~ 10^{-13} s) such that the geometry of the whole system does not change appreciably. For this reason electronic transitions are represented by vertical arrows.

At thermal equilibrium (T = 0 K) electrons occupy the lowest vibrational level of the electronic ground state and upon optical excitation they can be promoted from this state to any of the vibrational levels of the excited electronic state of the centre. As a rule, the excited state that will be occupied depends on the energy of the incoming photon and the photo-ionisation cross section of the centre. The latter is the result of the interaction or coupling of the centre to the band structure. Usually, deep energy levels are said to be strongly coupled to the crystal having small photo-ionisation cross section or interaction probability. Nevertheless, in these cases the photo-

ionisation cross section can be enhanced through thermally activated processes provided by multi-phonon interactions.

The optical excitation of the electrons results in the absorption of light with energy equal to the difference between the occupied excited level and the ground vibrational level. Broad absorption and emission bands are observed in cases where the ground and excited states are separated by a distance $\Delta R=R_o-R_o'$ (Figure 2.2). In the opposite case, when the two states lay exactly above each other narrow bands are usually observed.

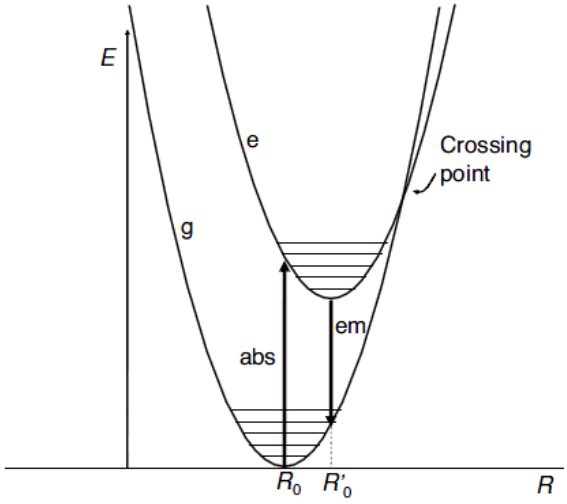

Figure 2.2: Configuration coordinate diagram showing the processes of optical absorption and emission of a luminescent centre (i.e., fluorescence emission). The potential energy *E* of the system is plotted versus its distance *R* from neighbouring atoms. Vertical transitions from the ground state (g) to excited state (e) are electronic transitions resulting in absorption of light. The return to the ground level occurs in two steps: non-radiatively from a high vibrational level (horizontal lines) to the lowest point of the excited state (i.e., ´abs´) and radiatively with emission of light to the one of the vibrational modes of the ground state (i.e., ´em´).

In the excited state the system has an excess of energy which dissipates by relaxing to the lowest most stable vibrational level of the excited state. This transition is accompanied by phonon emission to the surroundings. Radiative luminescence emission then proceeds via an electronic transition from the lowest populated level of the excited state to any of the higher vibrational

levels of the ground state, followed by a non-radiative relaxation to the equilibrium position. Due to the displacement of the two parabolic curves, resulting from the different chemical bonding of the two states, the emission bands are characterised by lower energy than the corresponding absorption bands. This phenomenon is known as the Stokes shift and explains the non-reabsorption of luminescence by the material as well as the difference between the thermal and the optical ionisation energies (Blasse and Grabmaier, 1994).

2.5 Thermal quenching mechanisms

The luminescence efficiency of a phosphor is a function of both the radiative and the non-radiative processes and it is defined as the ratio of the radiative probability to the sum of radiative and non-radiative probabilities (Curie, 1963; McKeever, 1985; Yukihara and McKeever, 2011). If $P_r = \tau_r^{-1}$ and $P_{nr} = \tau_{nr}^{-1}$ are the probability rates of radiative and non radiative transitions respectively, where $\tau_r^{-1}, \tau_{nr}^{-1}$ are the lifetimes for these transitions, the total luminescence efficiency, *n*, may be written as:

$$n = \frac{P_r}{P_r + P_{nr}} \tag{2.1}$$

The progressive loss of the luminescence efficiency with increasing sample temperature (i.e., thermal quenching effect) observed frequently during thermoluminescence (e.g., Figure 9.14), and optically stimulated luminescence (e.g., Figure 8.11) measurements has been assigned to the increased probability of non-radiative recombinations, which has an activation energy *W* (eV) and it is related exponentially to the temperature *T* (K) and the Boltzman factor *k* ($8.62 \cdot 10^{-5}$ eV K^{-1}):

$$P_{nr} = P_o \cdot \exp^{-W/kT} \tag{2.2}$$

Where P_o is a constant.

The phenomenon of thermal quenching has been widely interpreted using the Mott-Seitz model with additional reference to the configuration coordinate diagram (Figure 2.2) [Bøtter-Jensen *et al.*, 2003; Curie, 1963; Leverenz, 1968; McKeever, 1985; Yukihara and McKeever, 2011]. The

Mott-Seitz mechanism states that when an electron is thermally or optically released from a trap, it first reaches the excited level (Figure 2.1: transition 4´) of the recombination/luminescent centre before relaxation to the ground state takes place, emitting a photon. Nevertheless, as the temperature increases the parabolic potential curves of the ground and excited states of the luminescent centre approach close to each other with a high probability to intersect at a point. At high temperatures electrons gain enough energy through the vibrational motion of the atoms and they can more easily make a non-radiative transition to the ground state of the centre via the crossing point of the curves (Figure 2.2).

Schön and Klassens suggested a different mechanism for the thermal quenching effect. The Schön-Klassens model assumes that at elevated temperatures trapped holes are removed from the recombination centres by electron capture from the VB (Figure 2.3). When this happens, there are fewer radiative electron-hole recombination processes, since the centres to which electrons are transferred to have been partially depleted (Aitken, 1985; Bøtter-Jensen *et al.*, 2003; Curie, 1963; McKeever, 1985; Yukihara and McKeever, 2011).

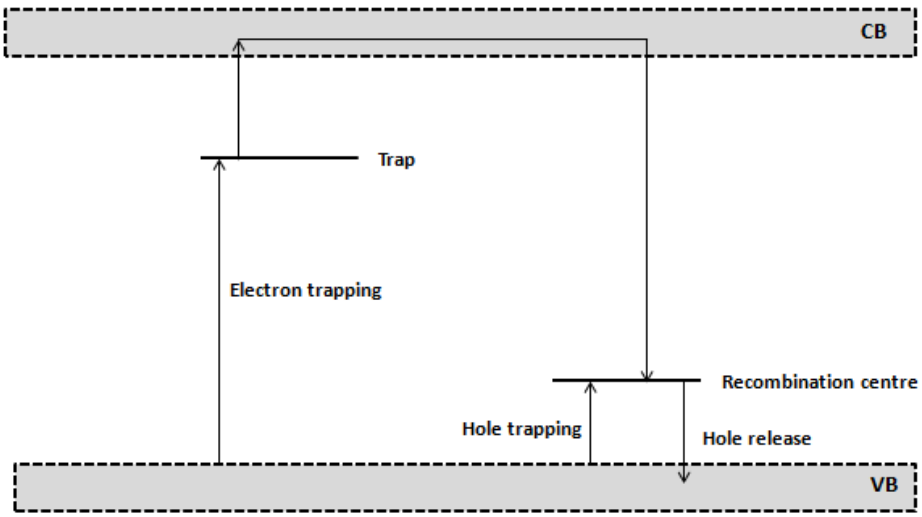

Figure 2.3: Schön-Klassens model of thermal quenching. Holes trapped at the recombination centre are thermally released leading to a reduced electron-hole recombination probability.

Common to both mechanisms described above is the mathematical expression of the phenomenon. The reduction of the luminescence intensity, *I(T)* , due to thermal quenching is given by (Bøtter-Jensen *et al.*, 2003; Yukihara and McKeever, 2011; Pagonis *et al.*, 2011):

$$I(T) = \frac{I_o}{1+C\cdot\exp^{-W/kT}} \qquad (2.3)$$

Where I_o is the unquenched luminescence intensity at a temperature T_o (K), C is a constant, and W (eV) is the activation energy of thermal quenching. A similar expression can be derived for the the dependence of the luminescence lifetime, $\tau(T)$, on the stimulation temperature (e.g., Akselrod *et al.*, 1998).

2.6 Mathematical description of luminescence

In an attempt to mathematically describe the phosphorescence phenomena each trap is assigned a parameter, known as trap depth or activation energy, *E* in units of eV (Chen and Kirsh, 1981; Chen and McKeever 1997; McKeever, 1985). This characterises the energy separation between the ground state of the trap and the bottom of the delocalised conduction band [i.e., delocalised states are those where electrons or holes are not bound to specific atoms but are shared between many atoms (IUPAC, 1994)]. Depending on the energy depth, shallow and deep trapping levels can be found within the forbidden gap of the material. The distinction between shallow and deep traps is based on the characteristic thermal depth or thermal ionisation energy (i.e., eV), but the exact energy demarcation ranges are seen to be sample dependent. However, as a practical rule of thumb, shallow traps are characterised by low thermal stability and as such charge carriers can escape from their traps at RT within a short time (i.e., seconds or minutes) following irradiation. On the other hand, the charge population in deep traps will not be released at ambient conditions unless an external stimulation is applied.

Instantaneous phosphorescence occurs at a constant temperature from traps located close to the conduction band (i.e., shallow traps) where the trapped electrons have high probability to escape even at ambient temperatures. The probability, *p*, per unit time for the thermal release of

electrons from a localised metastable state is exponentially dependent on the temperature and is given by the following expression (Randall and Wilkins, 1945):

$$p = s \cdot \exp\left(-\frac{E}{kT}\right) \qquad (2.4)$$

Where $E(\mathrm{eV})$ is the activation energy and s (s^{-1}) is a variable called the frequency factor which represents the number of times an electron interacts with the phonons of the crystal field .

Stimulated processes rely upon the existence of traps at depths greater than the energy required ($E \approx kT \sim 0.025$ eV) to allow the spontaneous release of electrons at room temperature. Trapping levels common to both TL and OSL processes are usually characterised by different activation energies; thermal and optical trap depth. The activation energy for optical stimulation is generally higher than that for thermal stimulation (Curie, 1963). The difference between the optical and the thermal activation energies is described by the the ratio of the dielectric constants, k/k_o, of the crystal for static (i.e., k) and high frequency dielectric fields (i.e., k_o) (Chen and Pagonis, 2011).

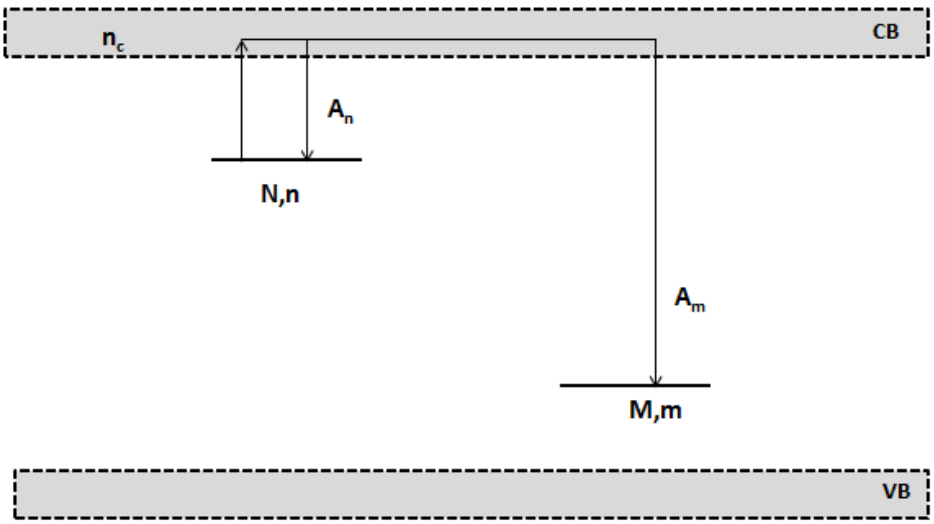

Figure 2.4: Energy level scheme of the simple one-trap one-recombination (OTOR) luminescence model. The parameters of the model are described in the text.

Randall and Wilkins (1945) developed the simplest theoretical model of phosphorescence (Figure 2.4) which consists of only one trap and one recombination centre (OTOR) [Chen and Kirsh, 1981]. In the OTOR model, it is assumed that direct transitions from the trap to the recombination centre are forbidden and the number of traps is small compared to the concentration of recombination centres. Thermal or optical stimulation releases electrons from the trap to the conduction band from which they quickly move and recombine radiatively with holes at the luminescent centre. If m and n_c denote, respectively, the concentration of trapped holes in the recombination centre and the instantaneous concentration of free electrons in the conduction band, then the luminescence intensity, I, is equal to the rate of change of the captured holes which should decrease with time according to :

$$\mathrm{I} = -\frac{\mathrm{dm}}{\mathrm{dt}} = \mathrm{A_m} \cdot \mathrm{m} \cdot \mathrm{n_c} \qquad (2.5)$$

Where A_m is the recombination probability in units of $\mathrm{cm}^3 \cdot \mathrm{s}^{-1}$ which is equal to the product of the cross section for recombination , $\sigma_m\,(\mathrm{cm}^2)$, and the thermal velocity of the free charge carriers, $u\,(\mathrm{cm} \cdot \mathrm{s}^{-1})$.

The complete mathematical presentation of the luminescence process involves equations that describe the excitation of trapped electrons into the conduction band as well as the conservation of charge neutrality. The first equation includes two terms, one of which determines the rate of change of electrons in the trap and a second term which accounts for the possibility of charge retrapping. If n is the instantaneous concentration of the electrons in the trap and N is the total number of traps, and $A_n\,(\mathrm{cm}^3 \cdot \mathrm{sec}^{-1})$ is the retrapping probability, the rate of change of the excitation of electrons is given by:

$$-\frac{\mathrm{dn}}{\mathrm{dt}} = \mathrm{n} \cdot \mathrm{p} - \mathrm{n_c}\,(\mathrm{N} - \mathrm{n}) \cdot \mathrm{A_n} \qquad (2.6)$$

The condition of charge neutrality in the case of the simple model is expressed as $\mathrm{m} = \mathrm{n} + \mathrm{n_c}$ or:

$$\frac{\mathrm{dm}}{\mathrm{dt}} = \frac{\mathrm{dn}}{\mathrm{dt}} + \frac{\mathrm{dn_c}}{\mathrm{dt}} \qquad (2.7)$$

$$\frac{\mathrm{dn_c}}{\mathrm{dt}} = \frac{\mathrm{dm}}{\mathrm{dt}} - \frac{\mathrm{dn}}{\mathrm{dt}} \qquad (2.7.a)$$

$$= A_m \cdot m \cdot n_c + n \cdot s \cdot \exp^{(-E/kT)} - n_c(N-n) \cdot A_n$$

$$= n_c[m \cdot A_m - (N-n) \cdot A_n] + n \cdot s \cdot \exp^{(-E/kT)} \qquad (2.7.b)$$

Due to the large number of unknown parameters, the simultaneous solution of the three differential equations (2.5)-(2.7) was found to be intractable and certain simplifications were thought to be necessary. The "quasi-equilibrium" assumptions whereupon (1) the concentration of free electrons is assumed to be considerably smaller than that of the trapped electrons (i.e., $n_c \ll n$) which also implies from equation 2.7 that $m \cong n$, and (2) the rate of change of the mumber of electrons in the conduction band is much smaller than the rate of recombination (i.e., $\frac{dn_c}{dt} \ll \frac{dm}{dt}$) were introduced to allow the derivation of a more simplified equation for the intensity of the luminescence at any time *t* during stimulation, which can now be expressed as:

$$I(t) = -\frac{dm}{dt} = n \cdot s \cdot \exp^{(-E/kT)} \cdot \frac{A_m \cdot m}{A_m \cdot m + A_n(N-n)} \qquad (2.8)$$

Nevertheless, while equation 2.8 is simplified it is still not capable of being solved due to the presence of several unknown variables. However, by assuming that retrapping is negligible or that the recombination probability $A_m \cdot m$ is significantly larger than the retrapping probability $A_n \cdot (N-n)$ equation 2.8 becomes:

$$I(t) = -\frac{dm}{dt} = n \cdot s \cdot \exp^{(-E/kT)} \qquad (2.9)$$

When stimulation is provided by heating in a linear manner with a constant heating rate $\beta = \frac{dT}{dt}$ $(K \cdot s^{-1})$ the luminescence emission for an intital concentration of electrons, $n_o$is expressed by:

$$I(T) = n_o \cdot s \cdot \exp^{\left(-E/kT\right)} \cdot \exp\left[-\left(\frac{s}{\beta}\right) \int_{T_o}^{T} \exp\left(-E/kT\right) dT\right] \qquad (2.10)$$

The case of negligible retrapping is known as first-order kinetics. When, however, retrapping dominates the excitation process (i.e., $A_n \cdot (N-n) \gg A_m \cdot m$) and the trap is far from saturation (i.e., $N \gg n$), and because $m \cong n$ for the simple model, the luminescence intensity follows second-order kinetics according to:

$$I(T) = -\frac{dn}{dt} = \frac{s \cdot A_m}{A_n \cdot N} \cdot n^2 \cdot \exp^{(-E/kT)} \quad (2.11)$$

The final case, which is less likely, is when the probability of retrapping is equal to that of recombination (i.e., $A_m = A_n$) which results in the following differential equation for the intensity of luminescence:

$$I(T) = -\frac{dn}{dt} = \frac{s}{N} \cdot n^2 \cdot \exp^{(-E/kT)} \quad (2.12)$$

Very often, the luminescence emission does not obey either the first- or second-order kinetics. There exist intermediate cases that can be described by the general-order expression (Chen and McKeever, 1997; Chen and Pagonis, 2011; McKeever, 1985):

$$I(T) = -\frac{dn}{dt} = \frac{s}{N} \cdot n^b \cdot \exp^{(-E/kT)} \quad (2.13)$$

In the above equation *b* is a dimensionless parameter called the kinetics order and it can take any value between 1 and 2. When *b* equals 1 equation 2.13 results in the first order approximation (i.e., equation 2.10) and when *b* equals 2 it becomes identical to the second-order kinetics (i.e., equation 2.11).

So far, the description of the rate equations of the various stages involved in the luminescence process dealt with stimulation by thermal energy which, for the model that includes only one trap, gives rise to a single peak in the glow curve (i.e., graph of luminescence intensity as a function of temperature). Multiple traps would result in a correspondingly larger number of peaks in the glow curve of the material, although it is very likely that traps will be situated in a close proximity to one another, forming a distribution of energy levels that cannot be resolved.

The maximum of the peak occurs at a characteristic temperature, T_m, which depends on the activation energy and the frequency factor of the trap, and the applied heating rate. Depending on the order of kinetics each peak displays different shape characteristics. Examples of first- and second-order TL peaks that were calculated theoretically using equations 2.10, 2.11 are presented in Figure 2.5.

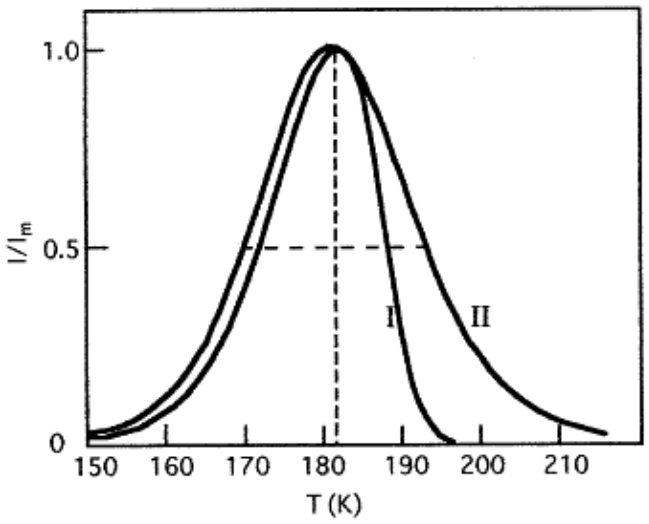

Figure 2.5: Thermoluminescence glow curves (i.e., luminescence intensity, *I*, normalised to peak maximum intensity, I_m, as a function of temperature, *T*, illustrating a TL peak of first-order kinetics (I) and a TL peak calculated using the second-order approximation (II). Note the different shape characteristics. Reprinted from Chen and McKeever, 1997.

For optical stimulation the governing equations remain similar with the exception that the exponential term in equation 2.4 which gives the probability of excitation is replaced by a parameter which is proportional to the intensity, *f*, of the light source, giving $p = f \cdot n$ (Bøtter-Jensen *et al.*, 2003; Chen and Pagonis, 2011; Yukihara and McKeever, 2011). Optical eviction of trapped electrons depends on both the energy or wavelength of the incoming photons and the power of the incident light which are related through the relationship $f = \sigma \varphi$ where φ is the photon flux (i.e., number of photons per second) and σ is the photo-ionisation cross section characterising the probability of optical transitions. The spectral dependence of this cross section can be expressed by equation 2.14, although several other expressions have been proposed (see Bøtter-Jensen *et al.*, 2003):

$$\sigma\,(hv, E_o) \infty \frac{(hv - E_o)^{\frac{3}{2}}}{(hv)^3} \qquad (2.14)$$

In equation 2.14, E_o is the minimum energy required for optical excitation in units of eV, and *hv* is the energy of the incident light. The emitted OSL intensity as a function of time when one

trapping level is emptied and recombination is the dominant process takes the form of a single exponential decay according to:

$$I(t) = -\frac{dm}{dt} = -\frac{dn}{dt} = n\sigma\varphi \qquad (2.15)$$

$$I(t) = n_o \sigma\varphi \exp(-\sigma\varphi t) = I_o \exp\left(-{}^{t}/_{\tau}\right) \qquad (2.15.a)$$

Where n_o, I_o denote, respectively, the trapped charge concentration (i.e., absorbed dose) and the OSL intensity at $t = 0$ and $\tau = 1/\sigma\varphi$ is the lifetime of the process. Deviation from an exponential decay is a common phenomenon in OSL studies, interpreted as (1) the existence of second order processes (i.e., retrapping) when the OTOR model is considered, (2) existence of a range of traps with different photo-ionisation cross sections and/or recombination centres (Bøtter-Jensen, 2003; Chen and Pagonis, 2011; Yukihara and McKeever, 2008), (3) thermal stimulation of charges from shallow traps, and (4) photo-transfer of charge carriers from deep energy states to shallower traps (Yukihara and McKeever, 2008).

In practice, the OTOR model is a rare case since the majority of materials have a great number of defects which can act as traps or recombination centres resulting in complex models (McKeever 1995; Chen *et al.*, 1997;, Chen and Pagonis, 2011; McKeever and Chen, 1997). When more complex models are considered the solution of the transport equations becomes a difficult task. However, numerical simulations can be used to provide realistic solutions. With the use of computational methods, systems that include several traps and recombination centres in which complicated charge transfer mechanisms and interaction processes are likely to occur can be approximated and validated with available experimental results.

2.7 Analysis methods for evaluating trapping parameters

The traps assocciated with the TL and OSL processes are characterised by specific parameters; that is the thermal activation energy, the frequency factor, and the order of kinetics for thermal stimulation, and the optical activation energy and the photo-ionisation cross section for optical stimulation. Knowledge of these variables is useful not only for the understanding of the luminescence production, but they also provide a means of obtaining information for some

properties which are important for the application of the TL and OSL in dosimetry (e.g., thermal stability).

2.7.1 Thermoluminescence kinetic analysis methods

A range of experimental methods including phosphorescence measurements (i.e. isothermal decay), variable heating rate (VHR) or Hoogestraaten method, variable dose (VD), initial rise (IR), peak shape (PS), as well as computerized glow curve deconvolution (CGCD) methods, are described in the literature (Aitken, 1985; Azorin, 1986; Chen and Kirsh, 1981; Chen and McKeever, 1997; Chen and Pagonis, 2011; Kirsh, 1992; McKeever; 1985; Pagonis *et al*., 2006) to evaluate the kinetic parameters activation energy, *E*, frequency factor, *s*, and order of kinetics, *b*, of a glow peak. Each of these methods has advantages and disadvantages, but all, with the exception of CGCD, require partial or complete isolation of the investigated peak from neighbouring peaks.

2.7.1.1 Order of kinetics

As a rule of thumb, the temperature of the maximum intensity, T_m, of a TL glow peak is initially examined with the VD method to identify first or second order kinetics. In the VD experiment, also known as the dose response test, a sample is repeatedly irradiated to increasing levels of dose and the temperature at which T_m occurs is noted. According to the TL theory a peak follows first order kinetics if, at a constant heating rate, the temperature at which the peak intensity is maximum does not depend on the radiation dose. A shift of T_m to lower temperatures is an indicator of second order kinetics and enhanced retrapping phenomena.

The symmetry and shape of a glow peak are additionally examined to determine the order of kinetics. A peak that is asymmetrical around T_m is of first order kinetics, while the opposite characterises a second order peak. The shape of the peak is studied through the geometric factor, μ_g, defined by Harperin & Braner (1960):

$$\mu_g = \frac{T_2 - T_m}{T_2 - T_1} \qquad (2.16)$$

where T_1 and T_2 are the temperatures on the rising and descending side of the peak respectively at which the intensity has fallen to half of the maximum value (Figure 2.6). A value of $\mu_g \sim 0.42$ is characteristic of first order kinetics and for $\mu_g \sim 0.52$ the peak follows second order kinetics. For intermediate values of the geometric factor general order kinetics is suggested.

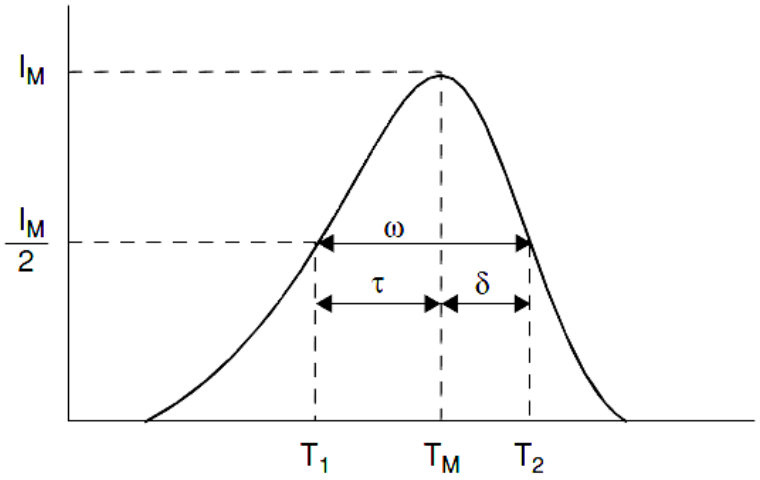

Figure 2.6: Geometric shape characteristics of a single glow peak. The order of kinetics is determined by the geometric factor, μ_g, through the parameters T_1, T_2, and T_m. Reprinted from Pagonis *et al*., 2006.

Unambiguously, the method that can be applied to identify first order kinetics is the so-called isothermal decay (ID) method which assumes that the decay of luminescence intensity with time follows an exponential law. However, exponential decay is rarely observed because a single glow peak may involve a complex structure of many discrete or a continuous distribution of energy levels likely to decay simultaneously but at different rates. Therefore, caution must be taken in interpreting the results of an ID test.

Two ways have been proposed to conduct an ID experiment (Pagonis *et al*., 2006). One way is to maintain an irradiated sample at a temperature slightly below the temperature of the peak maximum for a period of time, after which the phosphorescence emission is monitored.

Alternatively, one can perform a thermal fading test in which the sample is heated to a specific temperature, and is maintained at this temperature for some time while the remaining TL is measured. The sample is then annealed, irradiated with the same dose, kept at the same constant temperature for a different length of time and the TL signal is measured again. The process is repeated under the same experimental conditions varying only the elapsed time after irradiation. In both cases the kinetics order of a peak can be found by plotting the intensity of luminescence *I* versus time *t* on a semilog scale (Figure 2.7). A straight line is an indication of first order kinetics (Figure 2.7a) while non-linear graphs (Figure 2.7b) can be explained as being due to second order, general order or due to a continuum of trapping states.

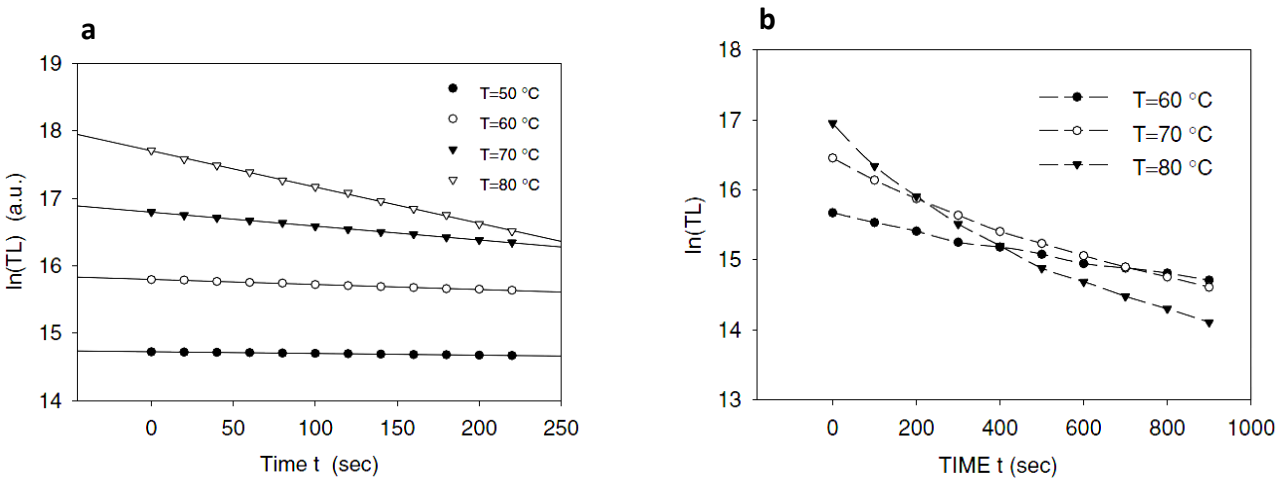

Figure 2.7: Examples of isothermal decay curves for (a) first-order TL peak and (b) second-order TL peak. Reprinted from Pagonis *et al.* (2006).

2.7.1.2 Analysis of complex TL glow peaks

As mentioned above, an apparent single peak may be composed of a number of glow peaks either well separated or closely overlapping forming a continuous distribution. The latter implies that for a given peak, there exists a continuous distribution of trapping levels each having specific kinetics parameters, but with an overall form of a single structure representative of all

the processes. A distribution of energy levels is a very common phenomenon in amorphous and polycrystalline materials and is mainly attributed to the highly disordered environment owing to the growth process and impurity content (McKeever, 1985). In these cases it is difficult to separately determine the kinetics parameters of all the overlapping components using solely experimental techniques. Instead, any attempt to evaluate the *b*, *E*, and *s* parameters will produce values that reflect the average behaviour of all the trapping states involved.

Apart from the ID method, the primary experimental procedure used to characterise complex glow peaks is known as "T_m-T_{stop}" (McKeever, 1980, 1985). This technique can be used to determine the number and T_m of each peak components in the cases of first and second order kinetics. It consists of heating a previously irradiated sample to a temperature T_{stop} that corresponds to an arbitrary point on the low temperature side of the peak, rapidly cooling down the sample to room temperature and then reheating the sample at the same linear heating rate to record the entire remaining glow curve. Here the value of T_m is noted. The sample is then annealed, irradiated and the process is repeated several times with increasing T_{stop} values in 2 to 5 °C K^{-1} steps and the new T_m values are noted. At the end, a plot of T_m against T_{stop} (Figure 2.8) is obtained that informs the number and position of overlapping peaks (if any). The appearance of plateau regions in a T_m-T_{stop} plot with the corresponding temperature range is related to specific peaks within the glow curve. If the flat regions are well separated forming a staircase structure the glow curve is first order (Figure 2.8: column a – line B). Glow curves consisting of well separated second order peaks still produce a staircase structure but the rise to the next flat region is less steep (Figure 2.8: column b – line C). Finally, if the T_m-T_{stop} graph shows a continuous increase, the glow curve is assumed to have a continuous distribution of energy levels giving rise to peaks that may be of first, second or general order kinetics (Figure 2.8: column c – line C). McKeever (1980) has given a detailed methodological plan to distinguish between different examples of peak structures and highlighted the importance of computerized fitting methods when the T_m-T_{stop} results fulfill more than one case.

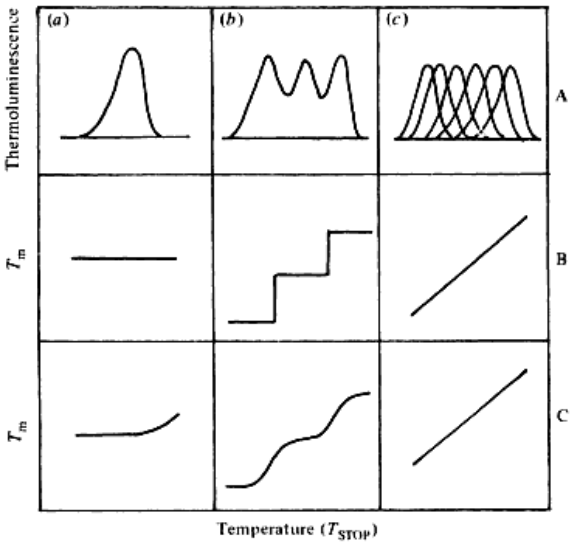

Figure 2.8: Representation of T_m-T_{stop} characteristics of glow curves consisted of a single (column a), several overlapping (column b), and a continuous distribution of peaks (column c). Lines B, C show the expected T_m-T_{stop} curves for first- and second-order kinetics peaks respectively. Reprinted from McKeever (1985).

2.7.1.3 Calculation of thermal activation energy and frequency factor

The calculation of the activation energy and frequency factor can generally be carried out using graphical- or computational- based methods. For convenience, only three will be reviewed.

The initial rise (IR) method is perhaps the only method for estimating the trap depth which does not require prior knowledge of the order of kinetics. It is based on the assumption that in the initial rise region of a TL glow peak [where $T << T_m$ and $I(T) << I_m(T)$] equation 2.10 reduces to $I(T) = \text{const} * \exp(-E/kT)$ and a plot of $ln[I(t)]$ versus $1/kT$ will result in a linear curve with slope equal to E/k (Garlick and Gibson, 1948). Nevertheless, the IR method should, generally, be applied to well-isolated peaks, and although considered one of the most accurate, it can yield lower values of the activation energy if the initial rise of the glow peak is significantly thermally quenched. In the case where the parameters of thermal quenching are known, the

method proposed by Petrov and Bailiff (1996) to correct the thermal activation energy can be applied.

A popular graphically-based method is the variable heating rate or Hoogenstraten method (Hoogenstraaten, 1958) where a range of heating rates is used. For each heating rate step the sample is exposed to the same dose and the T_m is monitored. The results are plotted as $ln\,(\frac{T_m^2}{\beta})$ versus $1/kT_m$ and a straight line is predicted. The slope of the curve is a measure of the activation energy whereas the intercept is associated with the frequency factor (Chen and Winer, 1970; Hoogenstraten, 1958). The method gives reliable results for the frequency factor because it is calculated independently of the activation energy. However, because it is based on the accurate determination of the temperature of the peak maximum, care must be taken at high heating rates to account for the effect of temperature lag. The lag is due to a temperature gradient between the heating element and the sample and if not corrected gives erroneous measurements of the temperature of the peak maximum. A formalism to correct for lag was proposed by Kitis and Tuyn (1999) given by the following expression:

$$T_m^j = T_m^i - C \cdot \ln\left(\frac{\beta_i}{\beta_j}\right) \qquad (2.17)$$

Where $T_m^j, and\ T_m^i$ are the peak maximum temperatures obtained with heating rates β_j and β_i respectively, and *C* is a constant that is calculated using two low heating rates.

Furthermore, as demonstrated by Li *et al.*, (1997) and Bulur *et al.*, (1998) the Hoogenstraaten method may also be used to estimate the thermal parameters of the traps stimulated optically. The authors suggested that by carrying out pulse-annealing measurements – where the OSL is measured after increasing post-irradiation annealing temperatures – using various heating rates, the trap parameters *E*, *s*, and *b* can be determined. For each heating rate, the reduction rate (i.e., the percentage loss of OSL at each temperature) of the OSL signal is plotted versus the annealing temperature, resulting in a peak-shaped curve. The peak maximum, T_m, is then used to produce a plot of $ln\,(\frac{T_m^2}{\beta})$ versus $1/kT_m$. Bulur *et al.*, (1998) slightly modified the analysis method by taking the first derivatives of the fractional loss of the OSL intensity at each heating rate and obtained results for the thermal activation energy and frequency factor that were similar to those calculated from the fractional TL method. It must be noted that the VHR-OSL analysis does not

result in an estimate for the optical trap depth. Rather, the thermal depth of the traps that contribute to the OSL can be calculated. The existence of common TL-OSL traps can, therefore, be inferred when the kinetic parameters derived independently from the VHR-TL and VHR-OSL are in agreement.

The peak shape method (PS) is a well-known computational method which does not involve any particular experimental procedure, but it consists of a series of mathematical expressions that can be applied to any glow peak obtained using experimental or computational techniques. The PS method, as further developed by Chen, is based on three parameters, namely T_m, T_1, and T_2, to calculate first the geometric factor μ_g, then the activation energy E, and finally the frequency factor s. Once the shape/geometric factor has been found through equation (2.16) the activation energy $E_\tau, E_\delta, E_\omega$ can be evaluated from Chen's general expressions by employing the parameters $\tau = T_m - T_1$, $\delta = T_2 - T_m$, or $\omega = T_2 - T_1$ (Figure 2.6):

$$E_\tau = \left[1.51 + 3\left(\mu_g - 0.42\right)\right]\frac{kT_m^2}{\tau} - \left[1.58 + 4.2\left(\mu_g - 0.42\right)\right]2kT_m \qquad (2.18)$$

$$E_\delta = \left[0.976 + 7.3\left(\mu_g - 0.42\right)\right]\frac{kT_m^2}{\delta} \qquad (2.19)$$

$$E_\omega = \left[2.52 + 10.2\left(\mu_g - 0.42\right)\right]\frac{kT_m^2}{\delta} - 2kT_m \qquad (2.20)$$

Finally, the frequency factor is evaluated using the formulas for first order (equation 2.21) and general order kinetics (equation 2.23):

$$s = \frac{\beta E}{kT_m^2}\exp\left[{E}/{kT_m}\right] \qquad (2.21)$$

$$s = \frac{\beta E}{kT_m^2}\left[\exp\left({E}/{kT_m}\right)\left(1 + (b-1)\right)2\frac{kT_m}{E}\right]^{\frac{b}{b-1}} \qquad (2.22)$$

2.7.1.4 Curve fitting

Computerised glow curve deconvolution (CGCD) analysis has been extensively used (e.g., Correcher *et al.*, 2008; Furetta *et al.*, 2000; Kitis *et al.*, 1998; Kitis *et al.*, 2000; Yazici *et al.*, 2002, 2003; Yazedifar *et al.*, 2012) for the determination of the characteristic parameters of

experimentally obtained and numerically simulated TL curves. It is considered an effective tool in overcoming the limitations of the experimental methods and resolving complex curves. Yet, the CGCD method is valid only for first-order kinetics where the principle of superposition can be applied (i.e. where the glow curve can be described by the superposition of independent peaks), while deconvolution of peaks following non-first-order kinetics will produce erroneous results (Bull *et al*., 1986).

For example, CGCD is able to determine simultaneously the number, position and the physical parameters of closely spaced underlying peak components that cannot be revealed through the application of T_m-T_{stop} because of instrumental limitations. The problem often arising is that the deconvolution of a given peak in its components can be successful for a number of different peak combinations and therefore a prior knowledge of the TL curve structure becomes necessary. A prediction of the order of kinetics is perhaps the most important factor that needs to be established before any curve fitting is attempted. This will determine the algorithms (i.e. first, second or general order equations) through which the analysis will be carried out. The process is usually quite laborious and the goodness of fit primarily depends on the experimental conditions used to obtain the TL glow curve. A sufficient number of data points and a well-defined curve shape with no distortions are needed to obtain good results.

2.7.2 Analysis methods of trap parameters under optical stimulation

The physical parameters of the traps associated with the OSL emission cannot be straightforwardly extracted from the analysis of the decay curves. The trap(s) that contribute to OSL may be identified approximately through a mathematical deconvolution procedure of the decay curves. The fitting process is, usually, based on the assumption of the existence of several first-order exponential decay components of the form given by equation 2.15a, each with a characteristic time decay constant τ. Using the relationship $\tau = \sigma\varphi$ the photo-ionisation cross sections can also be obtained, but the uncertainty may be large since there is no prior kowledge of the actual number of traps. In addition, this method does not provide information on the optical trap depths.

2.7.2.1 Optical activation energy

The basic approach to measure the optical activation energy of the OSL traps is by studying the luminescence response as a function of the energy or wavelength of the stimulation light. Peaks appearing in the optical excitation spectra are indicative of the existence of traps at the particular energy depth (Bailiff and Poolton, 1991; Baril and Huntley, 2003; Clark and Sanderson, 1994; Hutt *et al.*, 1988; Kars *et al.*, 2013; Spooner, 1993). The measurement technique consists of monitoring the luminescence response for a range of wavelengths from a light source over a particular detection window using a scanning monochromator or appropriate optical filters.

2.7.2.2 Photoionisation cross section

One method to estimate the photoionisation cross section is to monitor the photoconductivity as a function of the stimulation wavelength with (1) varying illumination flux, such that the photoconductivity at a wavelegth λ is maintained constant and proportional to the free charge carrier concentration, n_c or (2) constant photon flux where n_c varies with the stimulation wavelength. In either case the photoionisation cross section, $\sigma(\lambda)$, can be estimated using the following relationship (Botter-Jensen, *et al.*, 2003):

$$\sigma(\lambda) = (\frac{K}{\varphi(\lambda)})n_c \qquad (2.23)$$

Where $\varphi(\lambda)$ is the photon flux at wavelength λ and K is a constant. In approach (1) $\sigma(\lambda)$ is equal to the inverse of the required photon flux, whereas in approach (2) $\sigma(\lambda)$ is proportional to the change of n_c with wavelength. Further on, the optical activation energy of the trap(s) can be determined by fitting equation 2.14 to the resultant photoconductivity (or OSL)-wavelength curves. This was experimentally demonstrated by Whitley and McKeever (2000) for irradiated and non-irradiated Al_2O_3:C single crystals. They examined the variation of the photoconductivity and OSL over a wide range of optical excitation energies and found that the energy states, rather than being discrete levels, are distributed in energy between 1.7 and 2.5, 3.0 and 3.8, and 3.8 and 4.9 eV. The traps associated with the lowest energy interval were also found to be responsible for most of the TL-TSC peaks in the 130-230 °C range, in agreement with earlier suggestions that

the main TL-TSC peak at ~ 180 °C is due to a distribution of trapping states (Larsen, *et al.*, 1999).

A different approach to obtain absolute values of the photoionisation cross section of OSL trap(s) is the linear-modulation OSL (LM-OSL) technique. In contrast to the conventional way of measuring OSL using a constant light intensity (i.e., continuous-wave OSL, CW-OSL), LM-OSL measures luminescence by ramping the intensity of the stimulation light from zero to a maximum value. The OSL emission as a function of time increases linearly to a maximum value forming a peak and then decays to the background level. Several peaks may appear in the LM-OSL decay curve if more than one trap is emptied during measurement. The time at which the LM-OSL intensity is maximum, t_{max}, and the maximum intensity, I_{max}, can be related to the photoionisation cross section and the trap population respectively. The methodology for the LM-OSL stimulation mode was developed by Bulur (1996) for the cases of first- and general-order kinetics. For the simplest case of first-order kinetics the LM-OSL intensity can be written as:

$$\mathrm{I_{LM-OSL}(t)} = \mathrm{n_o}\,\frac{\mathrm{b}}{\mathrm{P}}\,\mathrm{t}\exp\left(-\frac{\mathrm{bt^2}}{\mathrm{2P}}\right) \qquad (2.24)$$

Where n_o is the trap population, P is the measurement time, and b is the detrapping probability which is proportional to the product of the light intensity and the photoionisation cross section ($\mathrm{b} = \sigma \mathrm{I_o}$).

From equation 2.24 one can see that the conditions of t_{max} and I_{max} are satisfied through the following relationships:

$$\mathrm{t_{max}} = \sqrt{\frac{\mathrm{P}}{\mathrm{b}}} \quad \text{and} \quad \mathrm{I_{max}} = \mathrm{n_o}\sqrt{\frac{\mathrm{P}}{\mathrm{b}}}\frac{1}{\sqrt{\mathrm{e}}} = \frac{\mathrm{n_o}}{\mathrm{t_{max}}}\frac{1}{\sqrt{\mathrm{e}}} \qquad (2.25)$$

2.8 Fading mechanisms of luminescence

2.8.1 Thermal fading

A property which can be inferred from kinetic studies is the thermal stability, or the closely related effect of thermal fading, of the TL response. A peak is considered thermally stable when the peak height or area intensity under the peak do not decay with time at room temperature (Aitken, 1985; Chen and McKeever, 1997). In the opposite case, when thermal fading occurs, phosphorescence emission may or may not be seen depending on whether the loss of the luminescence signal is due to radiative or non-radiative transitions respectively (Chen and McKeever, 1997).

As a guide, a TL glow peak is expected to be thermally stable if the temperature at which the maximum intensity is observed is higher than the temperature at which the sample is held after excitation and during the delay period before measurement (Chen and McKeever, 1997; Chen and Pagonis, 2011). More precisely, the stability is investigated through the evaluation of the lifetime, τ, which is related to the kinetic parameters E and s by the relationship:

$$\tau = s^{-1} \cdot \exp^{(E/kT)} \qquad (2.26)$$

The lifetime of a peak describes the average time spent by electrons in the trap and to ensure absence of thermal fading it should be several times longer than the duration of the irradiation and the elapsed time between irradiation and measurement (Aitken, 1985).

Peaks that tend to fade quickly at RT are not useful for TL dosimetry applications and they are eliminated by a post-irradiation annealing treatment (more detailed discussion in Chapter 7) at a temperature sufficient to remove their contribution to the glow curve but which does not affect the remaining more stable peaks. A similar approach can be applied to the OSL signal if it has been found to originate in the same peaks.

2.8.2 Athermal fading

A second mechanism by which luminescence signals display a decrease in intensity with time is that of athermal or anomalous fading. Athermal fading occurs at a rate which is faster than that predicted by the kinetic parameters of the traps and it is assumed to be associated with a mechanism other than the thermal release of trapped carriers at room temperature (Chen and McKeever, 1977; Chen and Pagonis, 2011). Quite a number of materials (e.g., diamond, feldspar, zircon, ZnS, $CaSO_4$:Dy, CaF_2:Mn, aluminas) have been found to demonstrate anomalous fading effects (Bull and Garlick, 1950; Ekendahl *et al.*, 2013; Hasan *et al.*, 1986; Hoogenstraaten, 1958; Inrig *et al.*, 2008; Kitis and Bousbouras, 1991; Kitis *et al.*, 2012; Polymeris *et al.*, 2006; Sears *et al.*, 1990; Shepherd, 1997; Spooner, 1992-93; Templer, 1986; Thomsen *et al.*, 2008; Townsend, 1968; Tsirliganis *et al.*, 2006; Tyler and McKeever, 1988; Uzun *et al.*, 2011; Visocekas, 2000; Visocekas and Ouchene, 1983; Wintle, 1977; Wheeler, 1990) and different theories have been put forward to explain the phenomena of anomalous fading.

The quantum mechanical tunnelling of trapped electrons to recombination centres was suggested by Bull and Garlick in 1950 to explain the anomalous fading of the 130 and 250 °C TL peaks in diamond. The same model was also adopted later by Hoogenstraaten (1958) who studied the decay of the luminescence from ZnS samples. The diffusion of defects which causes non-radiative electron release from traps was proposed by Townsend (1968). Nevertheless, Wintle (1977) pointed that the defect diffusion mechanism is considered unlikely to take place at ambient temperature. Wintle (1977) attempted to explain the anomalous fading behaviour in feldspars using, in addition to the previous mentioned mechanisms, a third possibility of a reduced probability of luminescence production due to the reduction of luminescent centres with time. For example, hole migration was suggested by Wintle (1977) as a possible reason for reduced recombination probability. In 1986 Templer proposed that two mechanisms may be responsible for the anomalous fading of the TL signal in zircon: the tunnelling model can explain the fading below room temperatures, whereas the localised transition model provides a quantitative and qualitative description of anomalous fading observed above room temperature. Finally, recently Chen *et al.*, (2000) used an energy band model consisting of one electron trap and three recombination centres and by means of numerical simulations they demonstrated an

earlier idea (Chen and Hag-Yahya, 1977) that anomalous fading may be normal thermal fading in disguise. This model assumes that with the addition of several recombination centres non-radiative transitions become a strongly competing process that could indirectly affect the estimation of the trapping parameters leading to an underestimation of the trap lifetime.

2.8.2.1 Tunnelling model of anomalous fading

Perhaps the most widely accepted model of anomalous fading of both TL and OSL is the quantum mechanical tunnelling of electrons. For materials in which the trapping levels are in close proximity to recombination centres the wavefunctions of the charged carriers may overlap allowing a direct tunnelling transition of electrons from the ground state of the trap to the recombination centre (Figure 2.9a).

If *r* is the distance between a trap and a recombination centre and by approximating the electron trap to a square potential well (Figure 2.10), the tunnelling probability can be expressed by (Chen and Pagonis, 2011):

$$\mathrm{P(r)} = \mathrm{P_o} \cdot \exp\left(-\alpha \mathrm{r}\right) \qquad (2.27)$$

Where P_o is a frequency factor and $\alpha = 2\frac{\sqrt{(2\mathrm{m}\cdot \mathrm{E_1})}}{\hbar}$ is the effective radius of the localised electron and relates the tunneling rate with the effective electron mass *m* and the potential energy barrier E_1 that an electron needs to overcome. Using first-order kinetics, the decrease in the population of the trapped electrons, *n*, with an initial concentration of n_o is given by:

$$\mathrm{I(t)} = -\frac{\mathrm{dn}}{\mathrm{dt}} = \mathrm{P} \cdot \mathrm{n} = \mathrm{P} \cdot \mathrm{n_o} \cdot \exp\left(-\mathrm{P} \cdot \mathrm{t}\right) \qquad (2.28)$$

At time *t* the total luminescence intensity is:

$$\mathrm{I} = \int_0^\infty \mathrm{n_o^2} \cdot \exp[-\mathrm{P(r)} \cdot \mathrm{t}]\, 4 \cdot \pi \cdot \mathrm{r}^2 \mathrm{dr} \qquad (2.29)$$

Equation 2.29 eventually leads to an expression of the form:

$$\mathrm{I} \cong \mathrm{K/t} \qquad (2.30)$$

where K is approximately constant.

The hyperbolic law dependence of the remaining luminescence intensity with time (i.e., $I \propto t^{-1}$) is one of the characteristics of the tunnelling model which also explains the rapid fading rate observed at short times followed by slower rates at longer delays. Another characteristic of the tunnelling model can be inferred from equation 2.27 which expresses the dependence of the tunnelling probability on the tunnelling distance. According to this (Huntley and Lamothe, 2001), for a random distribution of defects, tunnelling will take place first for recombination centres located close the electron traps followed by more distant sites as time progresses. Finally, as opposed to the localised model (section 2.8.2.2), anomalous fading due to electron tunnelling is expected to be temperature independent.

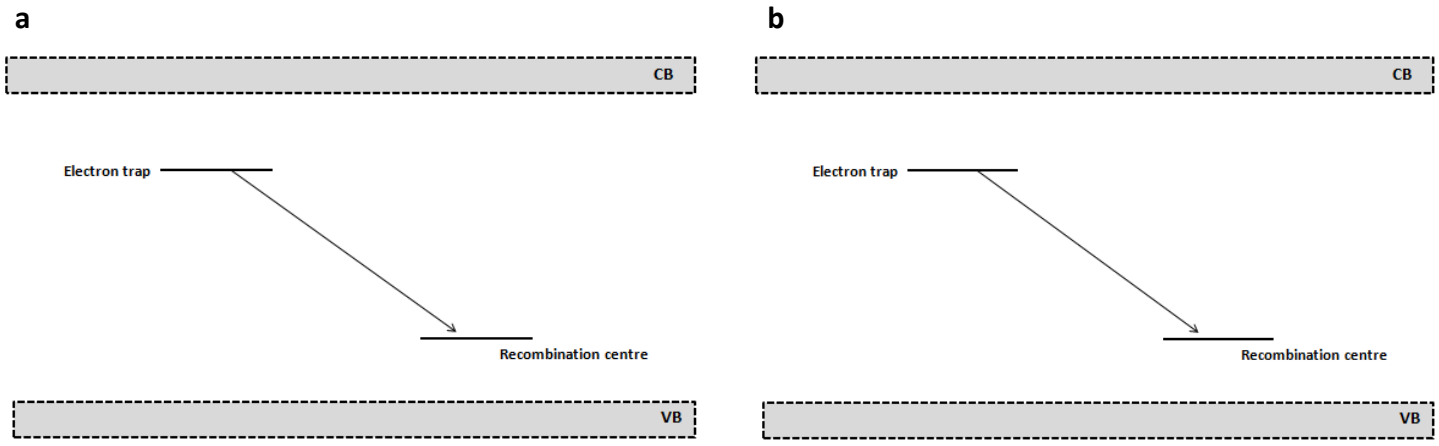

Figure 2.9: Quantum mechanical electron tunnelling models of anomalous fading. In (a) an electron makes a tunnelling transition from the ground state of the trap to the nearest recombination centre. In (b) electrons are first thermally excited to higher energy level before tunnelling to the recombination centre.

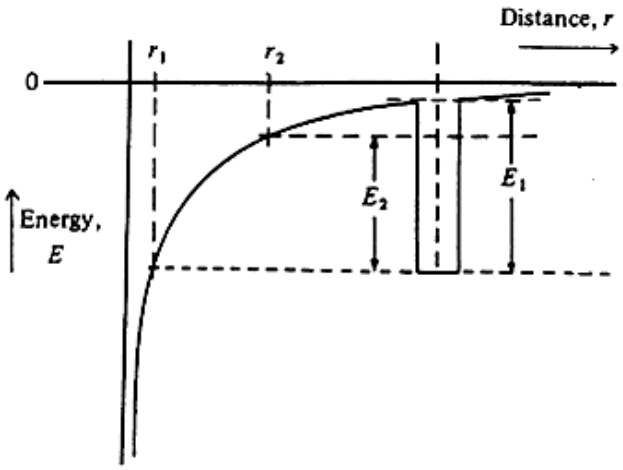

Figure 2.10: Potential energy, *E*, of an electron in the trap as a function of distance, *r*, from the recombination centre used to describe the anomalous fading mechanism based on electron tunnelling through a potential barrier. E_1 is the potential energy of an electron located at the bottom of the potential well at a distance r_1. For an electron raised to an intermediate excited state the *E*, *r* are reduced to E_2 and r_2 respectively. Modified from McKeever (1985).

Yet, Visocekas *et al.*, (1976) found that in calcite anomalous fading is accelerated with temperature and suggested a thermally assisted tunnelling model by assigning a Boltzman term to the tunnelling probability. The thermally assisted tunnelling model involves electron excitation to an energy level above the ground state of the trap and subsequent tunnelling to the recombination centre (Figure 2.9b). If n_1 *and* n_2 are, respectively, the number of electrons in the ground and excited states of the trap and $n = n_1 + n_2$, where $n_2 = n_1 \cdot \exp(-{}^{E_2}/_{kT})$, and E_2 is the thermal energy required to raise n_2 electrons to the excited state (see Figure 2.11), the total tunnelling rate is:

$$P(r) = \frac{P_o[\exp(-\alpha_1 r)+\exp(-\alpha_2 r)]}{1+\exp(-{}^{E_2}/_{kT})} \qquad (2.31)$$

Where $\alpha_1 = 2\frac{\sqrt{(2m\cdot E_1)}}{\hbar}$ and $\alpha_2 = 2\frac{\sqrt{(2m\cdot(E_1-E_2)}}{\hbar}$. Temperature dependent anomalous fading rates were also observed by Wintle (1977), Spooner (1992), and Visocekas (2000) for feldspar samples.

2.8.2.2 Localised transition model of anomalous fading

The localised transition model of anomalous fading was initially suggested to explain the decay of the TL signal in zircon (Templer, 1986; Wheeler, 1990) and, later, it was found to be applicable to other minerals (e.g., oligoclase feldspar). The model assumes that the electron trap and the closely located luminescent centre share a common excited state. Excitation of trapped electrons, usually by phonon energy, to the excited state allows an easy transition to the ground state of the recombination centre (Figure 2.11) followed by emission of phosphorescence.

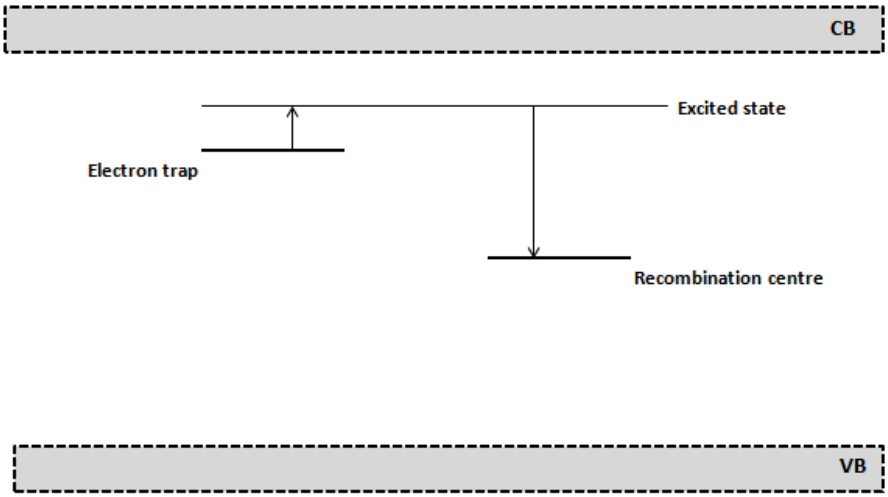

Figure 2.11: Localised transition model of anomalous fading. The electron trap and the recombination centre have a common excited state through which phonon-assisted excited electrons reach the ground state of the recombination centre.

Templer (1986) considered the existence of a uniform distribution of trap depths between a minimum (E^*_{min}) and a maximum value (E^*_{max}) and derived equations describing both the remaining TL intensity and the phosphorescence emitted during the period from the end of irradiation. In the first case, if $t^*_{min,}\ and\ t^*_{max}$ are the characteristic lifetime of the trapped electrons in E^*_{min} and E^*_{max} respectively, the remaining TL signal, *R*, as a function of time is expressed by:

$$R(t) = \frac{E_i\left\{-t/t^*_{min}\right\} - E_i\left\{-t/t^*_{max}\right\}}{E_i\left\{-t_o/t^*_{min}\right\} - E_i\left\{-t_o/t^*_{max}\right\}} \qquad (2.32)$$

E_i is an exponential integral function defined as $E_i\,(x) = -\int_{-x}^{\infty} \frac{e^{-t}}{t} dt$ and t_o is a short time after the end of irradiation.

The time dependence of phosphorescence for an initial concentration of trapped electrons n_o is:

$$I(t) = \frac{n_o k T}{t}\left\{\exp\left(-\frac{t}{t^*_{max}}\right) - \exp\left(-\frac{t}{t^*_{min}}\right)\right\} \qquad (2.33)$$

2.8.2.3 Comparison of the two models

A discussion of the different characteristics between the tunnelling and the localised models of anomalous fading has been given by Wheeler (1990) in his PhD thesis based chiefly on phosphorescence observations. Although in this study (Chapter 10), the mechanisms of fading were examined by monitoring the remaining TL and OSL responses (rather than the phosphorescence emission) as a function of the elapsed time following irradiation this discussion is provided as a guide to the reader.

According to Wheeler (1990), both models can be associated with emission of phosphorescence having distinct time and temperature dependent characteristics. The rate of decay of phosphorescence due to electron tunnelling from the ground state of the trap to the excited state of the recombination centre is expected to be greater than the *1/t* law, whereas phosphorescence due to localised transitions is expected to be lower. The same can also be seen by plotting the logarithm of the phosphorescence intensity as a function of the logarithm of time. This relationship is supralinear for the tunnelling model and sublinear for the localised model. In addition, the phosphorescence emission due to tunnelling is temperature independent (if not thermally assisted) in contrast to the thermally dependent emission in Templer's model of the localised transitions. Further on, the localised model assumes the existence of a stable component which can be isolated by appropriate thermal or optical bleaching treatments. On the other hand, if fading follows the tunnelling mechanism, it cannot be circumvented. Finally, it is

possible to detect the most likely mechanism by visual inspection of the remaining TL glow peak(s). If the loss of the signal is observed to take place from the low temperature side of the peak, it provides an indication of the localised transition model. The opposite is predicted for the tunnelling model (Chen and Mckeever, 1997).

Chapter 3: Luminescence dosimetry of ionising radiation

3.1 Introduction

Radiation dosimetry includes the procedures employed for the measurement of doses absorbed by matter as a result of exposure to various types of ionising (e.g., x-, γ-rays, neutrons) and non-ionising (e.g., UV, microwave) radiation. Personnel and environmental dose monitoring are two general areas of the field of radiation dosimetry. Both are used to estimate the cumulative dose received by populations to evaluate the likelihood of radiation-induced health effects, such as cancer. Personnel dosimetry directly calculates doses ensued from (1) occupational engagement (e.g., nuclear and medical workers) with sources of ionising radiation, (2) medical applications including imaging and cancer treatments, and (3) accidental exposure. On the other hand, environmental dosimetry is an indirect method by which the atmospheric and terrestrial radioactive activity is monitored and translated to potential human health risks.

Personal dosimetry can be exercised using a variety of synthetic materials and experimental techniques. The devices used to measure radiation dose are known as dosemeters and are broadly classified into active and passive dosemeters. Active dosemeters, such as electronic devices provide real-time indication of the accumulative absorbed dose. On the other hand, passive dosemeters, such as film badges, thermoluminescence and optically stimulated luminescence detectors, (TLD/OSLD), do not give direct estimates of the absorbed dose (Knoll, 2000; Shani, 2000). Rather, they have to be processed to indicate the total accumulated dose. The basic principle of operation of any type of dosemeter is based on the changes, induced by exposure to the radiation field, of specific physical properties of the material embedded in these devices. In the case of passive detectors, these changes can be measured post-irradiation using the relevant technique, while active dosemeters provide immediate readings. In either case, appropriate calibration factors are needed to relate the quantity measured by the dosemeter to the intended radiation protection or operational quantity. Calibration factors can be determined (IAEA, 2000) by exposing the detector (usually attached to phantoms) to known doses (measured by a reference instrument) under secondary standard laboratory conditions. The output reading of the dosemeter is then compared with the corresponding data from the reference instrument.

Calibration factors can be established for different types and geometries of irradiation. Nevertheless, since the main objective of personal dosimetry is the evaluation of human risk, dosemeters are calibrated in terms of specific radiation protection quantities [e.g., personal dose equivalent, $H_p(d)$-defined in section 3.2].

For instance, the trapping of radiation-induced electrons and holes is the fundamental effect utilised in passive luminescence detectors (i.e., TLDs and OSLDs). During thermal or optical stimulation the stored radiation energy is emitted as light following the recombination of electrons with holes. The amount of light is proportional to the absorbed dose, which can be estimated by dividing the reading given by the TLD/OSLD with the appropriate calibration factor. In the special case of accident dosimetry with luminescent materials the unknown dose is obtained by creating a calibration curve. The usual procedure involves the delivery of additional doses to the material using a calibrated source and the measurement of the TL/OSL response. The unknown dose can be found when the TL/OSL reading (e.g., integrated photon counts) from the unknown dose becomes equivalent to that from a known dose.

In this chapter, the basic principles and quantities of ionising radiation dosimetry relevant to this study are reviewed; in particular, the concepts developed for individual dose monitoring. The dosimetry of photon sources is mainly discussed, although electron dosimetry (e.g., beta particles) will be considered since the current practice of TL/OSL (accident/retrospective) dosimetry usually involves beta sources for the dose calibration process of luminescent detectors. The dosimetry with luminescent materials is of great importance for this study and is also described here. A special reference to the dosimetry characteristics and applications of Al_2O_3:C single crystals is given since this material is considered to be the most closely related material to the subjects (i.e., alumina-based resistor substrates) of this thesis. Finally, the dosimetry properties of surrogate materials and the dose recovery protocol applied in accident dosimetry will be described.

3.2 Concepts and quantities of ionising radiation dosimetry

The International Commission on Radiological Units (ICRU) and International Commission on Radiological Protection (ICRP) committees have specified several physical (ICRP, 1996), operational (ICRU, 1993b), and protection (ICRP, 1991, 2007) quantities to characterise the dosimetry of ionising radiation. Radiation monitoring instruments such as area survey meters and personal dosemeters are usually calibrated in terms of a specific operational quantity. The measurable operational quantities for area (e.g., ambient dose equivalent) and individual monitoring (e.g., personal dose equivalent) are defined at specified points and aim to control and limit the radiation exposure of individuals and workplaces in order to ensure safe working conditions. The protection quantities (e.g., equivalent dose, effective dose) are the risk-related dosimetric quantities averaged over the human body. They are used to quantify the extent of exposure of the human body by taking into account the different radiation qualities and the radiation sensitivity of organs and tissues (ICRP, 1991, 2003, 2007). Both operational and protection quantities can be related to the fundamental physical quantities, tissue absorbed dose (D_T), air kerma free-in-air (K_a), and particle fluence (Φ) through the use of conversion coefficients (ICRP, 1996).

Dosemeters measure the cumulative energy deposited in their sensitive medium resulting from the interaction of radiation with matter. Two types of interactions will be shortly discussed; those related to indirectly ionising photon radiation and those from directly ionising electron radiation. While photons are the main type of radiation considered in an emergency radiological event, the dosimetry of electrons, in particular beta particles, has to be addressed since, as mentioned above, the procedure of estimating unknown doses from potential accident luminescent detectors involves the use of laboratory-based radioactive sources (i.e., $^{90}Sr/^{90}Y$) that emit beta particles.

The energy of primary photons is transferred to secondary charged particles (i.e., electrons) of the medium through three basic interactions: the photoelectric effect at low photon energies lower than 100 keV, Compton scattering for intermediate photon energies between 100 keV and 10 MeV, and pair production which occurs at photon energies > 1.02 MeV (Figure 3.1). The energy of the incoming photons and the atomic composition of the medium determine the relative importance of each photon interaction process (Figure 3.2). The excitation and ionisation

of the atoms as well as the energy deposited by secondary particles are then responsible for the transfer of energy to the medium (Attix, 1968; Podgorsak 2005).

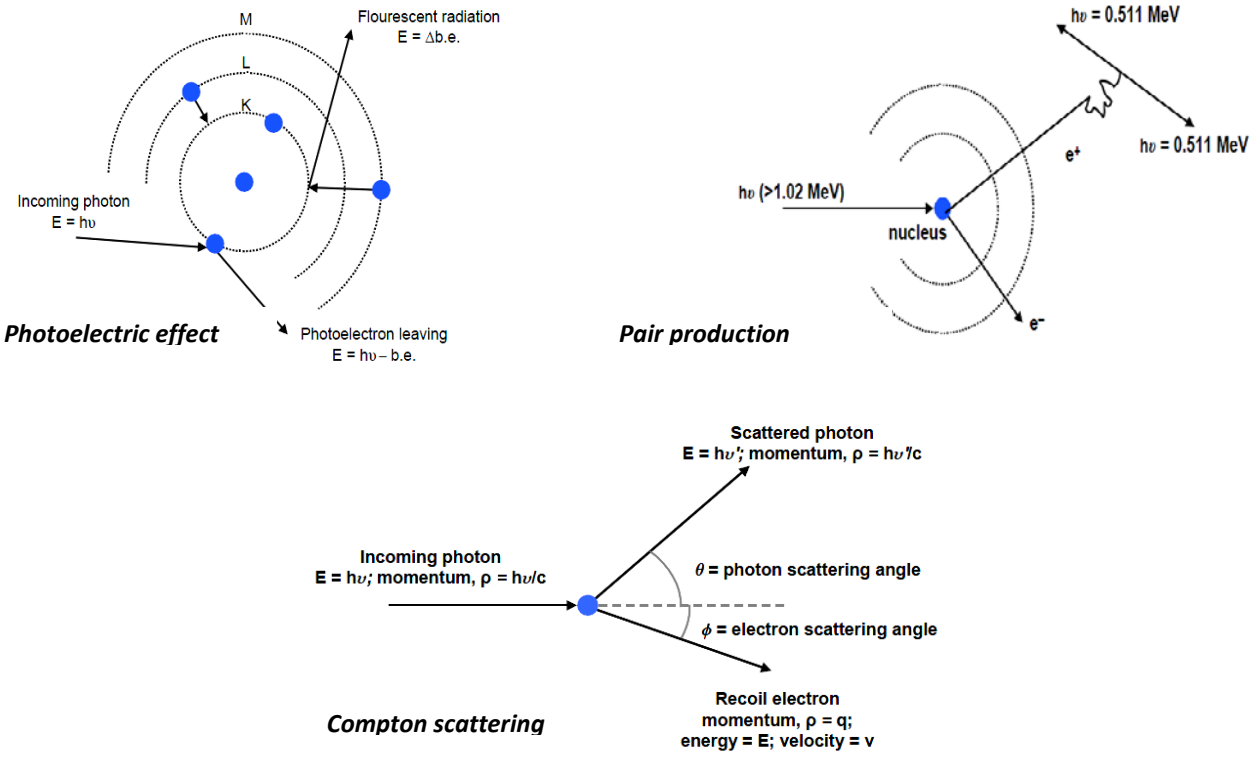

Figure 3.1: Interaction mechanisms of photon energy loss in matter. The dominant process at low photon energies (i.e., < 100 keV) is the photoelectric effect during which the incoming photon excites an orbital electron from its shell. The photon completely disappears producing a photoelectron which leaves the atom with energy equal to the initial photon energy (hν) minus the electron binding energy (b.e). Fluorescent radiation accompanies the photoelectric absorption process resulting from the filling of the electron vacancy by outer shell electrons. Pair production takes place for photon energies greater than 1.02 MeV. The process is a photon-nucleus interaction in which an electron-positron (e^- - e^+) pair is created. In Compton scattering, which is important in the range between 100 keV and 10 MeV, the incoming photon is scattered through an angle θ producing a recoil electron which carries part of the initial photon energy. Reprinted from Alpen (1990).

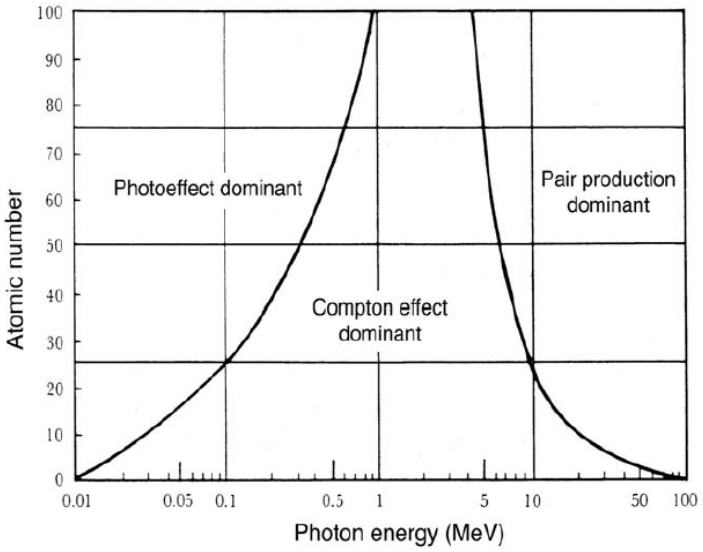

Figure 3.2: The dependence of the three main (in the energy range of interest to dosimetry) photon interaction processes on the energy of the incoming photon beam and atomic number of the target material. The interaction cross section for photoelectric effect varies as $\tau_{ph} \sim Z^4/(h\nu)^3$. For Compton scattering, which dominates at energies 100 keV < hν < 10 MeV, the interaction cross section varies as $\tau_c \sim Z$ whereas at photon energies above ~ 1.02 MeV pair production with $\tau_{pp} \sim Z^2$ becomes the dominant interaction process. Reprinted from Podgorsak (2006).

The mean kinetic energy, $d\varepsilon_{tr}$, transferred per unit mass of matter, dm, from photons to the electrons is defined as kinetic energy released in matter**, kerma, *K***:

$$K = \frac{d\varepsilon_{tr}}{dm} \qquad (3.1)$$

The unit of the quantity kerma is the gray (Gy), where $1\ Gy = 1\ J \cdot kg^{-1}$. The component of the kerma responsible for the excitation and ionisation of the atoms and the energy deposited in the medium is known as collision kerma, K_{col}. Radiative photons, particularly Bremsstrahlung radiation, generated during the slowing down of the secondary electrons define the radiative kerma, K_{rad}. The total kerma is thus equal to $K = K_{col} + K_{rad}$.

Kerma may also be defined in terms of the photon energy flow per unit area of the medium (i.e., energy fluence, Ψ) and the mass-energy transfer coefficient of the medium, μ_{tr}/ρ. For monoenergetic photons the kerma-energy fluence relationship is given by:

$$K = \Psi \frac{\mu_{tr}}{\varrho} \qquad (3.2)$$

Due to the finite range of electrons in matter, the kerma at a particular location may not always be equal to the energy absorbed and/or the absorbed dose *D* (Figure 3.3). Generally, for any photon beam there is an initial build-up region where the dose, *D*, is lower than the kerma. This is expressed by the parameter β which is the ratio of D/K_{col}, where *D* denotes the absorbed dose. In the build-up region β <1. Following this region, the absorbed dose may be equal to the kerma (Figure 3.3a) when the conditions of charged particle equilibrium (CPE) are satisfied (i.e., the flow of electrons into a small region equals the flow of electrons out of it) and the radiative losses are negligible) or, since in most cases photons experience attenuation as they propagate through the medium, the absorbed dose may be higher than the collision kerma (Figure 3.3b). This is the more realistic case, known as transient charged particle equilibrium (TCPE).

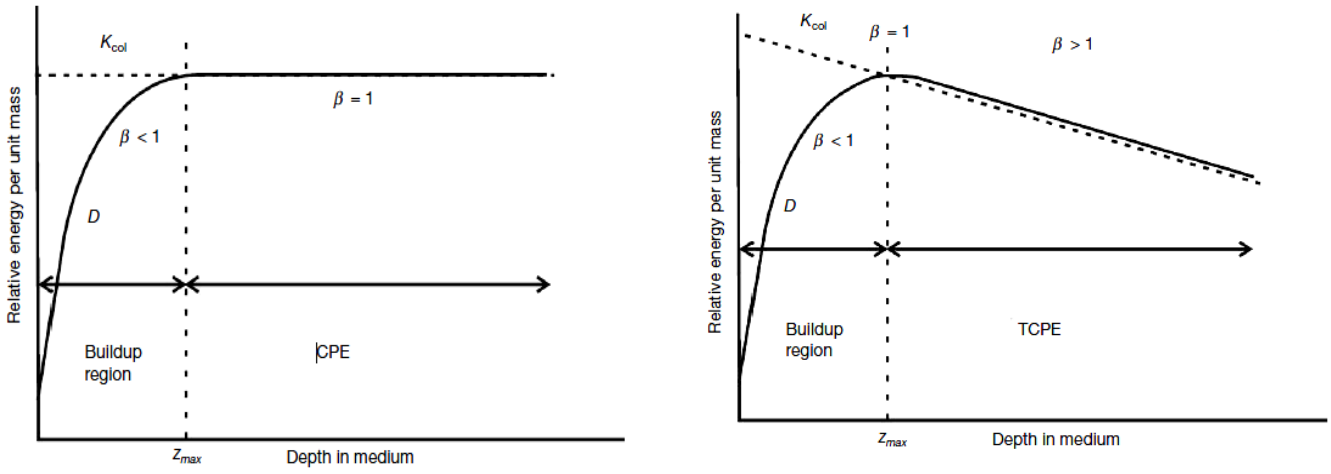

Figure 3.3: Relationship between absorbed dose and kerma. In (a) collision kerma is equal to the absorbed dose once CPE exists after a certain depth, z_{max}, in the medium. (b) Under conditions of TCPE the absorbed dose is constantly higher than the kerma. Reprinted from Podgorsak (2005).

Directly ionising charged particles, such as electrons, deposit their energy to the absorbing medium through Coulomb interactions with the constituents of the medium. Inelastic collisions with the atomic electrons or the atomic nuclei of the medium are the fundamental events resulting, respectively, in the ionisation of the atoms of the medium and the production of bremsstrahlaung radiation. These processes (i.e., radiative collisions) are also responsible for the loss of energy of the electron beam. Elastic collisions also occur as the electrons penetrate the medium affecting mainly the direction of the electrons but not the kinetic energy (Podgorsak, 2005; 2006).

In contrast to photons, electrons undergo a number of interactions as they are slowed down and as a consequence the energy of the incident electrons is distributed along their tracks. The energy transfer process of electrons, or their rate of energy loss per unit path length (dE/dx), is described by the mean collisional stopping power, $S_{col}(E)$, and it is the main quantity of interest in the dosimetry of electron beams. A similar quantity characteristic of the absorbing medium, known as mass collision stopping power, $(S_{col}/\rho)_{med}$, is used in the estimation of the absorbed dose (Podgorsak, 2005).

Turning to a more general definition, the **absorbed dose, *D*,** is the physical quantity which measures the mean amount of energy, $d\varepsilon$, deposited in the volume of interest of mass dm :

$$D = \frac{d\varepsilon}{dm} \qquad (3.3)$$

The total energy imparted to the volume of interest is equal to the energy entering the volume, $d\varepsilon_E$, minus the energy leaving the volume, $d\varepsilon_L$, and less any $d\varepsilon_R$, energy, which only increases the rest mass in the volume: $d\varepsilon = d\varepsilon_E - d\varepsilon_L - d\varepsilon_R$. The SI unit of absorbed dose is the gray (Gy).

The biological effects produced in a tissue or organ by ionising radiation are described by the protection quantity **equivalent dose, H_T**. For a given type of ionising radiation, *R*, the equivalent dose over an organ or tissue, *T*, is given by the product of the absorbed dose multiplied by a dimensionless factor, w_R, referred to as the radiation weighting factor:

$$H_T = D_T \cdot w_R \qquad (3.4)$$

The SI unit of the equivalent dose is the sievert (Sv) which is dimensionally equivalent to the gray but accounts for the biological effectiveness of different types of ionising radiations through the radiation weighting factor. Numerical values of w_R for various types of radiation and energies as specified in ICRP publication 60 (ICRP, 1991) and the more recent ICRP publication 92 (ICRP, 2003) are listed in Table 3.1. Even though the effect of neutron and heavy charged particles irradiation will not be investigated in this study, their w_R values are also presented in Table 3.1. This is just to show that, in contrast to photons and electrons, the biological effectiveness of other types of ionising radiation depends on the energy and can be significantly different from unity.

Table 3.2: Radiation weighting factors for different types and energies of ionising radiations (ICRP 1991; ICRP, 2003).

Type of ionising radiation and energy	**Radiation weighting factor, w_R (ICRP 60)**	**Radiation weighting factor, w_R (ICRP 92)**
Photons, all energies	1	1
Electrons and muons (all energies)	1	1
Protons (incident)	5	2
Neutrons:		
< 10 keV	5	Continuous function
10 keV to 100 keV	10	of energy
> 100 keV to 2 MeV	20	
> 2 MeV to 20 MeV	10	
> 20 MeV	5	
α-particles, fission fragments, heavy nuclei	20	20

The recommended individual operational quantity is the dose equivalent H_d defined as the product of absorbed dose, *D*, and the quality factor, *Q(L)*, at a specified depth *d* (ICRU, 1990):

$$\mathrm{H_d} = \mathrm{D} \cdot \mathrm{Q(L)} \qquad (3.5)$$

In the above relation the quality factor *Q(L)* is a function of the linear energy transfer (LET), L, of a charged particle in water and accounts for the relative biological effectiveness of radiation in producing biological effects. The *LET* (keV μm^{-1}) characterises the mean radiation energy, dE, lost by a charged particle per unit length of path, dl, through a material expressed by the quotient:

$$\mathrm{L} = \frac{\mathrm{dE}}{\mathrm{dl}} \tag{3.6}$$

The *Q(L)* for different *LET* ranges is expressed by the following relations (ICRU, 1990; ICRP, 2007):

$$\begin{aligned} \mathrm{Q(L)} &= 1 && (\mathrm{L} < 10) \\ \mathrm{Q(L)} &= 0.32\mathrm{L} - 2.2 && (10 < L < 100) \\ \mathrm{Q(L)} &= {}^{300}/_{\sqrt{\mathrm{L}}} && (\mathrm{L} \geq 100) \end{aligned} \tag{3.7}$$

The commonly used operational quantity for individual monitoring is the personal dose equivalent, $H_p(d)$, defined in the ICRU report 51 (ICRU, 1993b) as the dose equivalent in soft tissue at a specified depth. Personal dosemeters are typically designed and calibrated to record the dose equivalent at a depth of $\mathrm{d} = 10$ mm in soft tissue for whole body exposures from strongly penetrating radiation, or the dose equivalent at depths of $\mathrm{d} = 0.07$ mm and $\mathrm{d} = 3$ mm for skin and the lens of the eye respectively for weakly penetrating radiation (e.g., beta rays).

Several other dosimetry quantities, both for individual and area monitoring, have been developed. Nevertheless, a description of these is beyond the scope of the present investigation. Shortly, this section introduced basic concepts which are important for the assessment of the absorbed dose and the risk to populations. While the absorbed dose is the basic radiation quantity it cannot be used to assess potential radiation-induced health effects. In any exposure scenario, knowledge of the type of radiation (e.g., photons or electrons) is needed to take into account the biological effectiveness of radiation and the extent of the potential health risk (e.g., photons are more penetrating than electrons).

3.3 Dosimetry with luminescent materials

3.3.1 Materials and general properties

Passive radiation detectors that use luminescent materials are widely applied for routine individual and environmental dose monitoring involving external exposure to ionising radiation. Depending on the method of processing, luminescent detectors are classified into thermoluminescence and optically stimulated luminescence dosemeters.

Materials based on fluorides, such as lithium fluoride (LiF) and its several variations (i.e., LiF:Mg,Ti, LiF:Mg,Cu,P, CaF_2:Mn, CaF_2:Dy), oxides (i.e., Al_2O_3:C, BeO, MgO), sulphates and borates (i.e., $CaSO_4$:Dy, $CaSO_4$:Mn, $Li_2B_4O_7$:Mn, MgB_4O_7:Dy) have been investigated for applications in personal and environmental dosimetry (McKeever *et al*., 1995). Of those, the most widely used TLD dosemeter material is LiF:Mg,Ti, commercially known as TLD-100, whereas Al_2O_3:C presents not only good TLD properties, but also excellent OSLD applications.

The Commission of the European Communities published a report in 1975 (EUR 5358, 1975) specifying the technical recommendations for the use of thermoluminescence for dosimetry in individual monitoring for photons and electrons from external sources. The general performance criteria described in this early report are, however, valid for any luminescence detector. Some of the important qualities that determine the efficient use of luminescent detectors include:

- High radiation sensitivity: i.e. the luminescence response per unit absorbed dose.
- Linear dose response over a wide range of doses. The luminescence signal should be proportional to the delivered dose avoiding over- (superlinearity) or under-response (sublinearity).
- Low limit of detection: i.e. the smallest dose that can be distinguished from a zero dose reading.
- Simple annealing procedures to restore its initial conditions after irradiation.
- Luminescence response that is independent of the dose rate.
- Stable and reproducible signal that is not affected by physicochemical changes due to repeated annealing and exposure processes.

- Stable signal that is unaffected by mechanisms that cause thermal or light-induced fading.
- Flat photon energy response (defined below).
- Tissue equivalence (defined below).

3.3.2 Energy response

The energy response, $S_E(E)$, for a given absorbed dose, expresses the dependence of the response (e.g., TL/OSL reading) of a detector on the energy of the radiation responsible for the absorbed dose (Attix, 1968; McKeever *et al*., 1995). For photons, due to the dependence of the interaction cross section of each of the three photon energy loss mechanisms on the atomic number of the material and the energy of beam (Figure 3.2), the overall detector response is expected to vary with the photon energy (Podgorsak, 2006). Under electron irradiation, the response of the detector is nearly independent of the energy for electrons with E > 1 MeV, but changes significantly depending on the size and thickness of the detector for low energy electrons.

The energy dependence of a given detector, *d*, with respect to a reference material, *m*, is expressed in terms of the mass energy absorption coefficients (Attix, 1968; McKeever *et al*., 1995):

$$S_E(E) = \frac{(\mu_{en}/\rho)_d}{(\mu_{en}/\rho)_m} \qquad (3.8)$$

The $S_E(E)$ curves of any detector can be experimentally determined or produced using tables with the theoretical values of the mass energy absorption coefficients for elements with atomic number Z=1 to 92 provided by the National Institute of Standards and Technology (NIST). However, since most detectors are a mixture of elements, the weighted averages of the μ_{en}/ρ for each element are added to give the total mass energy absorption coefficient. For a detector material A_xB_y with $w_{x,y}$ the fractional weight of each element:

$$(\mu_{en}/\rho)_{A_xB_y} = \left[(\mu_{en}/\rho)_A \cdot w_x\right] + \left[(\mu_{en}/\rho)_B \cdot w_y\right] \qquad (3.9)$$

Figure 3.4 shows the photon energy dependence of two common luminescent materials, Al_2O_3 and LiF, relative to air calculated using the values of the mass energy - absorption coefficient for aluminium oxide and air (NIST database). For photon energies below about 100 keV Al_2O_3-based detectors are expected to overestimate the dose compared with the dose in air, while the photon energy dependence characteristics of LiF are only slightly greater than those in air. These effects are inherent to the detector material and particularly arise as a result of the dissimilar atomic compositions relative to air (see section below).

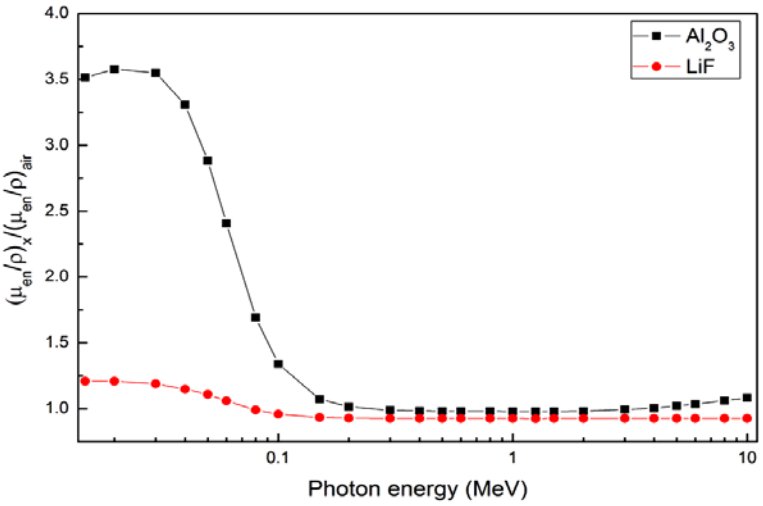

Figure 3.4: Mass energy absorption coefficients of Al_2O_3 and LiF with respect to air as a function of the photon energy (NIST database).

3.3.3 Tissue equivalence

The tissue equivalence is a property which characterises how closely the radiation response of a physical material matches that of biological tissue (EUR 5358, 1975; McKeever *et al.*, 1995). As with the (photon) energy response, tissue equivalence depends on the atomic number of the detector. For compounds the requirement for tissue equivalence is checked using the effective atomic number Z_{eff} (Yukihara and McKeever, 2011):

$$Z_{eff} = \sqrt[m]{\alpha_1 \cdot Z_1^m + \alpha_2 \cdot Z_2^m + \cdots} \quad (4.10)$$

Where α_i is the ratio of the number of electrons of each element to the total number of electrons of the compound, Z_i is the atomic number of each element, and *m* is a constant approximately equal to 3 or 4. The effective atomic number of biological tissue is approximately 7.4, while those of LiF and Al_2O_3:C are ~ 8.1 and ~ 10.2 respectively.

3.4 Measurement techniques

3.4.1 Thermally stimulated luminescence

Techniques based on the measurement of thermally stimulated luminescence were the first to be applied in luminescence dosimetry. The readout procedure of an irradiated material is performed by heating the sample to a maximum temperature with a linear heating rate and measuring the emitted light using a single photon detection system (e.g., photomultiplier tube, PMT). Heating is usually performed in a dry inert gas atmosphere (e.g., nitrogen) which helps to minimise non-radiation-induced luminescence signals (Aitken, 1985; Furetta, 2010) that can occur, for example, by the presence of impurities on the surface of the samples, (i.e., chemiluminescence) or from mechanical effects during sample preparation (i.e., triboluminescence).

Currently, a widely used instrument for TL dosimetry (and dating) research is the Risø TL/OSL automated reader manufactured at the Risø National Laboratory (Denmark). A description of the elements of the Risø luminescence reader is given in Chapter 5. Another instrument recently introduced into the market for luminescence research applications is the lexsyg TL/OSL reader designed and developed by Freiberg Instruments (Richter *et al*., 2013).

3.4.2 Optically stimulated luminescence

Optically stimulated luminescence dosimetry is based on the optical stimulation of irradiated materials using various light sources (e.g., green/blue/infrared LEDs), an optical detection system, and suitable optical filters to separate the excitation light from the emitted luminescence (Botter-Jensen *et al*., 2003; Yukihara and McKeever, 2011). Optical stimulation of the sample is available at room or elevated temperature in the Risø TL/OSL readers.

The basic mode of optical stimulation used in routine OSL dosimetry applications (also used in the present study) is the continuous-wave (CW-OSL) mode, where the intensity of the stimulation light is constant (Figure 3.5a) and luminescence is monitored continuously throughout the stimulation period (Botter-Jensen *et al*., 2003). For sufficient stimulation time the total luminescence signal can be obtained in one measurement, resulting in an exponentially decaying glow curve.

Alternative stimulation modes include pulsed OSL (POSL) and linear-modulation OSL (LM-OSL). In the former (Figure 3.5c), the luminescence intensity is measured between short duration stimulation pulses and the signal is derived by summing up the counts over several stimulation pulses (Botter-Jensen *et al*., 2003; McKeever and Akselrod, 1999; Yukihara and McKeever, 2011), while in the latter OSL is measured by linearly ramping the intensity of the stimulation light (Figure 3.5b) from zero to a maximum value (Bulur, 1996). In this case, a peak-shaped OSL decay curve is obtained.

Even though, POSL has been found to have specific advantages (e.g., allows multiple readings/dose measurements, better discrimination between the stimulation light and the emitted OSL, lower doses to be measured, and discrimination of luminescence components with different lifetimes) over the other stimulation modalities, it was not investigated in the present study since it requires a special POSL unit that has to be attached to the Risø reader. On the other hand, LM-OSL, which can be performed using the standard reader configuration, was found to have limited

applicability for dosimetry measurements, mainly because a longer measurement time is required to completely measure the OSL response.

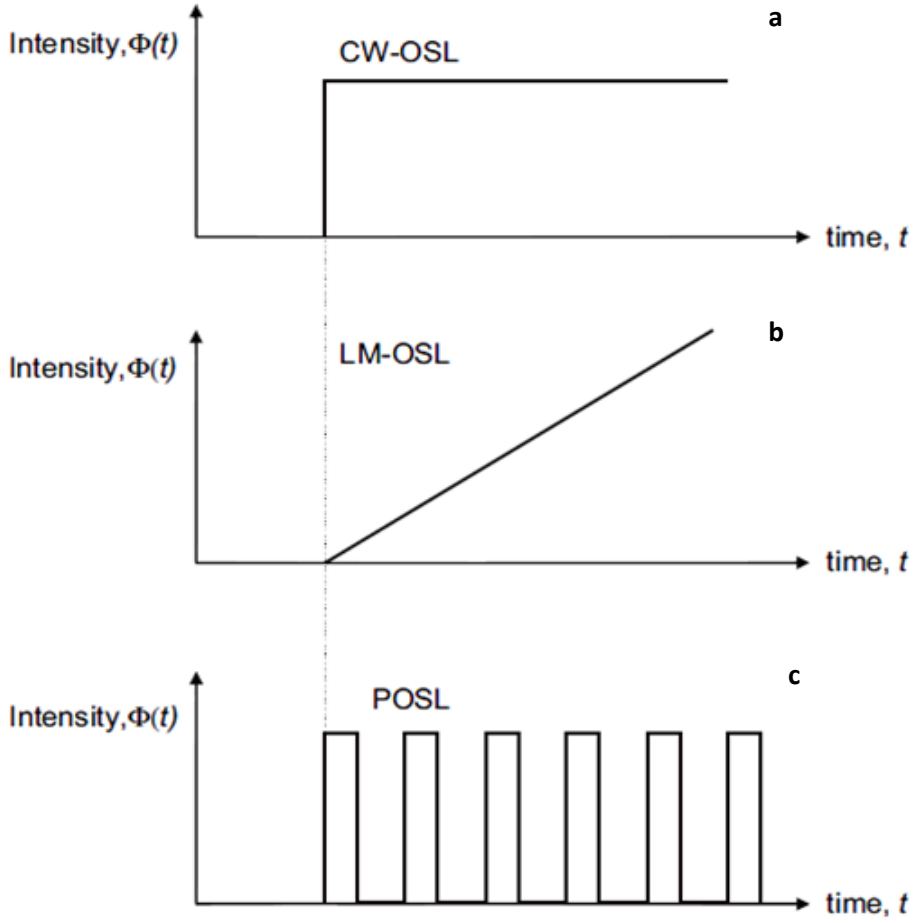

Figure 3.5: OSL intensity as a function of time *t* for different readout modes. (a) Continuous wave OSL (CW-OSL) measures the OSL emission with a constant light source, while (b) linear-modulated (LM-OSL) monitors the light emission while ramping the intensity of the stimulation light, and (c) pulsed-OSL (POSL) stimulates the sample using short duration pulses and measures the OSL signal in between the pulses. Modified from Bøtter-Jensen, (2003).

3.5 Dosimetry with Al_2O_3:C

Despite the great variety of luminescence dosemeters, up to now there is not a single material combining all of the performance criteria discussed in Section 3.3. Al_2O_3:C-based dosemeters, however, despite having specific limitations (e.g., non-tissue equivalence) are widely used for personal dose assessments in various dosimetry domains. The dosimetry characteristics and applications of Al_2O_3:C have been extensively investigated elsewhere and will be briefly discussed here. The rationale is that since Al_2O_3:C and the samples under investigation (i.e., alumina-based substrates) have similar chemical compositions, it might be possible to better understand the TL/OSL dosimetry properties of the alumina-based substrates by studying those of Al_2O_3:C. Nevertheless, as discussed in Chapter 4, there are important differences between the two materials that need to be considered.

3.5.1 Dosimetry characteristics of Al_2O_3:C

Al_2O_3:C prepared in several forms (i.e., discs, powders, tapes) has proven to be a versatile dosimetric material. Due to the high TL sensitivity (~ 40-60 times greater than that of LiF:Mg,Ti), it was initially suggested for applications in TL dosimetry (Akselrod *et al*., 1990, 1993). A notable limitation was the strong light-induced fading and light-induced TL (Akselrod *et al*., 1993; Biran and Moscovitch, 1996; Dugan *et al*., 2000; Moscovitch *et al*., 1993; Walker *et al*., 1996) which could cause, respectively, an unintentional loss of dosimetric information or an artificial TL signal uncorrelated with exposure to ionising radiation. For example, Moscovitch *et al*., (1993) reported that 95% of the TL signal fades following three hours exposure to fluorescent light. It was later demonstrated (Biran and Moscovitch, 1996) that the amount of light-induced signal loss depends on the dose and the wavelength of the light such that it is proportionally higher for small doses (Biran and Moscovitch, 1996) and short wavelengths (Walker *et al*., 1996). Nevertheless, due to the sensitivity of Al_2O_3:C to light, it was suggested that to reset the initial sensitivity of the material for subsequent uses it might be possible to optically bleach a lightly irradiated sample instead of performing a thermal anneal. Furthermore, it was suggested that dosimetry may be also carried out using the optically stimulated

luminescence (OSL) response. In fact, the OSL (CW-OSL or POSL) signal of Al_2O_3:C was found to be 3-5 times greater than the TL (Botter-Jensen and McKeever, 1997; McKeever *et al*., 1996), avoiding strong thermal quenching when the material is heated during TL readout, and presents similar dosimetric properties (e.g., dose response, limit of detection, fading in the dark, reproducibility (Akselrod *et al*., 1993; Yukihara and McKeever, 2011).

The dose response characteristics of Al_2O_3:C are dependent on the quality of radiation and the material form (e.g., discs, powder). For low *LET* radiation and Al_2O_3:C discs the relationship between the measured luminescence signal (TL and OSL) and the absorbed dose is linear in the range from 1 μGy to 10 Gy, then becoming supralinear (or superlinear) at higher doses (Akselrod *et al*., 1990, 1993; McKeever *et al*., 1995; Yukihara and McKeever, 2011). McKeever *et al*., (1996) also reported that using pulsed-OSL measurements the linear dose range of Al_2O_3:C can be extended to100 Gy. The non-linear dependence of the TL/OSL output as a function of dose has been interpreted in terms of a complex trap model which includes deep electron and hole traps competing with the main dosimetric trap(s) for charge capture during irradiation and stimulation (Pagonis *et al*., 2006; Yukihara *et al*., 2003, 2004b). For OSL measurements the dose response relationship was further found (Yukihara *et al*., 2003) to be dependent on the choice of signal (e.g., initial intensity or total integrated area) and on the detected emission band (i.e., F-centre band, UV band, or both bands).

Another characteristic of Al_2O_3:C dosemeters is the ability to monitor very low doses. It has been reported that they are capable of detecting doses lower than 0.5 μGy (Akselrod *et al*., 1990, 1993; Botter-Jensen and McKeever, 2006; Pashchenko and Barboza-Flores, 1995) independent of the dose rate, making them useful for dosimetry applications.

The energy dependence for different radiation types has also been extensively studied. While aluminium oxide exhibits an over-response for low x-ray energies (see Figure 3.4) and electron beams (e.g., Pinto *et al*., 2008), it is possible using suitable filters (i.e., thin layers of materials placed in front of the detector element to attenuate low energy photons) to obtain a smooth, independent response. In mixed fields of gamma and beta radiation it is possible to evaluate the contribution of each radiation component through dosimetry systems (detector and badge) that

include Al_2O_3:C detectors of different thickness behind a multi-element filter pack (Lee and Lee, 2001; Yukihara and McKeever, 2011). The readings from each detector can then be combined using mathematical algorithms and the doses due to beta or gamma radiation can be determined separately. However, in working environments, such as nuclear power plants, where neutron radiation can make a significant contribution to the mixed radiation field, different detectors sensitive to each radiation component need to be enclosed within the same dosimetry badge in order to account for the lack of neutron sensitivity of Al_2O_3:C. A different approach that has been investigated is the use of two Al_2O_3:C detectors, one of which is covered or mixed with neutron converters (e.g., Gd_2O_2, ^{6}LiF) (Mittani *et al*., 2007; Mukherjee *et al*., 2011; Yukihara *et al*., 2008). In a mixed gamma-neutron field the bare detector will detect primarily the gamma radiation, whereas the modified detector is expected to monitor both the radiation component due to the neutron-induced interactions and the gamma radiation component. So far, Al_2O_3:C mixed with lithium-6 enriched compounds have been found to result in the best neutron sensitivity.

Other attractive properties of Al_2O_3:C-based TLDs and OSLDs are the low fading during storage in the dark (less than 5% in a year), good reproducibility and reusability, simple readout and optical annealing procedures.

3.5.2 Dosimetry applications of Al_2O_3:C

Personal dosimetry is one of the many applications of Al_2O_3:C-based detectors. The high radiation sensitivity, low detection threshold, extended linear dose response, and good reproducibility are the key characteristics for the suitability of Al_2O_3:C in individual dose monitoring. In combination with suitable filters to correct for the non-flat energy dependence and the slightly high effective atomic number (~ 10.2), Al_2O_3:C detectors are used for whole body photon dose assessment [i.e., $H_p(10)$] in various workplaces (Akselrod *et al*., 1990,1993; Bøtter-Jensen and McKeever, 1996; Lee and Lee, 2001; Yukihara and McKeever, 2011).

TL dosimetry with Al_2O_3:C is usually carried out using discs of 5 mm in diameter by 0.9 mm thickness cut from single crystal rods, whereas detectors for OSL measurements, OSLDs, are

manufactured in tapes containing a thin layer of Al_2O_3:C powder (McKeever *et al*., 1995; Yukihara and McKeever, 2011). The OSLD form was found to have less sample-to-sample variability in sensitivity compared with the TLD form due to the inhomogeneous distribution of defects along the length of the original crystal rod. Monitoring of beta radiation for skin and extremity (e.g., lens of the eyes or fingers) dosimetry [i.e., $H_p(0.07)$, $H_p(3)$] has also been shown (Akselrod *et al*., 1993, 1996, 1999; Lee and Lee, 2001; Pinto *et al*., 2008) to be possible with thinner detector elements or powders (e.g., surface density of ≤ 10 mg cm^{-2}). Suitable filters placed in front of the detector element are required to provide a more uniform energy response to beta radiation.

Assessment of environmental doses from gamma and/or mixed gamma-beta radiation fields is another potential use of Al_2O_3:C with applications extending also to luminescence archaeological dating and retrospective dosimetry (Akselrod *et al*., 1996; Botter-Jensen *et al*., 1997, 1999; Burbridge *et al*., 2003; Goedicke, 2006; Goksu *et al*., 1999, 2002; Pashchenko and Barboza-Flores, 1995).

In the field of clinical dosimetry, Al_2O_3:C OSLDs show promising capabilities. A number of studies have been conducted to characterise the dosimetric properties of Al_2O_3:C for *in vivo* dosimetry in external photon-, electron-, and proton-beam radiotherapy (Jurinsic, 2007; Reft, 2009; Viamonte, 2008; Yukihara *et al*., 2005, 2008, 2010), and diagnostic x-ray procedures (Lim *et al*., 2011; Yukihara *et al*., 2010). Al_2O_3:C OSLDs were found to have a linear dose response up to ~ 3 Gy, with negligible sensitivity changes after repeated exposures, independent of the energy for megavoltage photon- (e.g., 6 and 18 MV x-rays), electron- (in the range 6-20 MeV), and proton-beams (E > 100 MeV). The angle and dose-rate or dose-per-pulse (for linear accelerators) dependence were also studied by Jurinsic (2007) and shown to be insignificant. *In vivo* (e.g., treatment plan verification, skin dose measurements) and *in vitro* (i.e., phantom measurements) dose verifications in radiotherapy procedures using the prompt radioluminescence (RL) and OSL signals emitted from Al_2O_3:C crystals attached to an optical fibre cable is another recent application of the Al_2O_3:C-based OSLDs. A more detailed description of the characteristics and applications of the fibre-dosimetry technique can be found in Aznar *et al*., (2004), Gaza *et al*., (2004), and Akselrod *et al*., (2007).

Medical dosimetry applications involving heavy charged particle (HCP) beams (Gaza *et al*., 2004; Reft, 2007; Yukihara *et al*., 2004a) as well as space dosimetry (Sawakuchi *et al*., 2008a ; Yasuda *et al*., 2002; Yukihara *et al*., 2006) may also be carried out using Al_2O_3:C. The basic limitation, however, is the reduction of the luminescence efficiency of Al_2O_3:C with increasing radiation *LET*. Contrary to low *LET* radiations such as x-rays, high *LET* charged particles produce dense ionisation events along their tracks resulting in a saturation of the trapping states, reduced luminescence response, and deviation from linearity as the dose increases (Gaza *et al*., 2004; Yukihara *et al*., 2004). The dose response characteristics and luminescence efficiency for various types of HCP relative to that from ^{60}Co gamma rays have been determined for both TL and OSL measurement modes (Sawakuchi *et al*., 2008a.b; Yukihara *et al*., 2004). It was found that the relative TL/OSL efficiency depends on the type of particle, *LET* value, measurement technique, material form, and the choice of signal in the case of OSL. Changes in the form of the OSL decay curves expressed as a faster decay rate with increasing *LET* value have also been noticed (Yasuda *et al*., 2002; Yukihara *et al*., 2004; Yukihara and McKeever, 2011) and proposed as a means of identifying the radiation quality in mixed HCP fields.

3.6 Dosimetry with surrogate luminescent materials

3.6.1 Dosimetry properties of surrogate materials

In section 3.3, the most desirable properties of luminescent detectors for routine personal monitoring were presented. The dosimetry characteristics of Al_2O_3:C detectors, a widely used personal dosimetry system, were also reviewed mainly because the synthetic material used in the construction of the detector has some similarities with the sintered alumina substrates investigated in this study for emergency/retrospective dosimetry. In this section, the general properties of the objects that could be employed for emergency/retrospective dosimetry are presented.

In the event of an unplanned and uncontrolled release of radioactive materials and of ionising radiation, where occupational and non-occupational individuals may be subjected to various levels of exposure, objects of general use are sought that could substitute for the synthetic dosemeters that have been developed for routine dosimetry. In addition to the general requirements listed above (Haskell, 1993), materials that are used as accident or fortuitous dosemeters should be widely and readily available and easily identifiable (Woda *et al*., 2009). Where area monitoring is concerned, objects with common properties that can be found at different locations around the exposed area would be preferred, allowing the generation of dose profiles providing further information concerning the nature of the radiation field. Individual monitoring further requires objects be in close proximity to the human body, as this would more conveniently provide an estimate of the personal absorbed dose. While for most dose reconstruction purposes a low limit of detection (i.e., mGy) is the desirable, when samples are collected from locations where high doses may be found, such as in the vicinity of a radiological incident, the dose response of surrogate materials should be linear over a wider range, but for triage < 10 Gy is sufficient.

3.6.2 General procedure of dose recovery in accident/retrospective dosimetry

In the special case following an accidental exposure, absorbed doses can be estimated using a *dose recovery test*. This is similar to the procedure described in Section 3.1 for establishing a dosemeter's calibration factor. In accident and retrospective dose assessments the single aliquot regenerative (SAR) dose protocol developed for quartz is most often employed (Bøtter-Jensen *et al*., 2003). The luminescence response, S' – which can be the total area under a glow peak or the height of the peak for TL measurements, or the initial intensity or the total integrated area under the glow curve for OSL measurements (Yukihara and McKeever, 2011) – due to the accident dose, D', is initially measured. A number of doses (i.e., D_1, D_2, D_3..) over a wide range are sequentially delivered to the sample followed by TL or OSL readout (i.e., S_1, S_2, S_3..). An annealing (usually thermal) procedure is carried out following TL or OSL readout to avoid accumulation of doses from the previous irradiation. A dose response curve (i.e., calibration curve) is then created by plotting the TL or OSL response from each dose as a function of the delivered dose, and the unknown dose is estimated by interpolating the luminescence response

(of the unknown dose) to the dose-response curve. A simplified representation of the SAR protocol is shown in Figure 3.6. The full SAR dose protocol consists of additional intermediate steps which help to check that the sensitivity of the sample does not change during the dose recovery procedure. A more detailed description of the SAR procedure is given in Chapter 6.2.5.

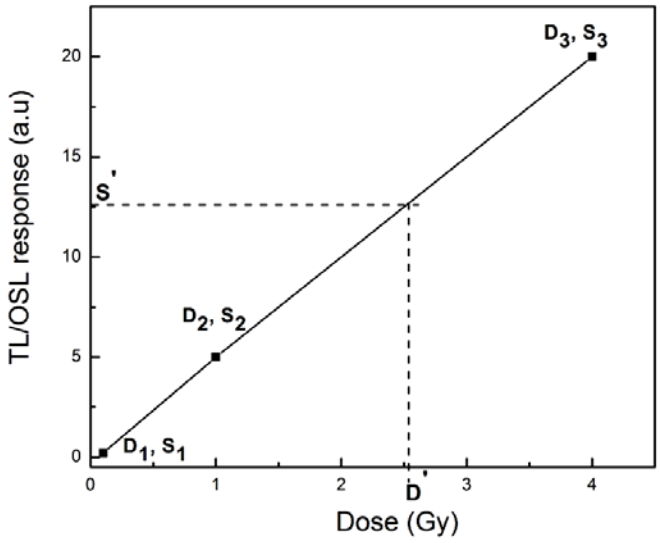

Figure 3.6: Recovery of unknown dose, D´, using the SAR protocol. The TL/OSL response, S´, from the unknown dose is interpolated on the dose-response curve created by applying a number of doses D_1, D_2, D_3 and measuring the luminescence response S_1, S_2, S_3. The point of intersection with the x-axis gives the value of the unknown dose.

An important consideration for accurate determination of the absorbed dose is that the radioactive source or, specifically, the dose rate of the source has been calibrated for the specific sample. The procedure of calibrating the beta sources attached to the Risø TL/OSL reader involves two steps. Initially, the sample of interest is irradiated with a dose from a standard calibrated gamma-ray source (e.g., ^{60}Co) and the luminescence response is measured. The dose recovery protocol is then used to determine the irradiation time from the beta source needed to produce the same TL or OSL response. The ratio of the TL or OSL signals due to the dose from

the standard gamma source and due to the dose (i.e., irradiation time) from the beta source determines the dose rate of the source.

Usually, dose rates are quoted in terms of air kerma (i.e., amount of kerma in a unit mass of air) which by convention is assumed to be equivalent to the absorbed dose in air. As a consequence, the doses to the surrogate materials correspond to air doses. Conversion to personal doses can then be achieved by applying conversion coefficients to relate the physical quantity measured by the ´dosemeter´ to the required radiation protection or operational quantity [e.g., personal dose equivalent, $H_p(d)$]. These conversion coefficients are also specific to the material in use and are usually established using radiation transport codes, where the conditions (e.g., type of radioactive source, geometry of irradiation, location of dosemeter) of the accidental exposure should, as precisely as possible, be simulated. A more thorough discussion of the methodology employed in the calculation of dose conversion coefficients is given in Chapter 11.

Chapter 4: Alumina structure and defects

4.1 Introduction

Alumina is a ceramic oxide with a unique combination of mechanical, electric, and optical properties. Powders of alumina are used in the production of materials for a wide variety of industrial uses. Polycrystalline alumina materials which are produced via a thermally assisted process where powders are compacted into solid dense objects (i.e., sintering) are employed for the majority of mechanical (e.g., abrasives, cutting tools), structural (e.g., tiles), and electronic (e.g., insulating substrates) applications (Peelen, 1977). More demanding applications, such as the production of transparent gem stones (i.e., ruby crystals) and the synthesis of personal radiation detectors (i.e., α-Al_2O_3:C TLD-500), require single crystal structures which are obtained using sophisticated manufacturing methods, and highly controlled growth conditions. The quality of the starting material as specified by the shape and size, and chemical composition of the grains, as well as the manufacturing conditions, determine the number and the nature of the defects introduced into the crystal structure, which in turn control several properties of the final product.

In the manufacturing process of α-Al_2O_3:C dosimetry grade single crystals the purity of the alumina powder and the growing conditions (e.g., temperature, pressure, heating and cooling rate) are carefully selected such that specific types of defects (i.e., oxygen vacancies) are formed in the crystal lattice. Traditionally, the Czochralski, Stepanov or Vernuil crystal growth techniques were employed in the fabrication of α-Al_2O_3:C dosimetry grade materials (Akselrod *et al*., 1990; McKeever *et al*., 1995), although in recent times alternative methods have also been tried (Yong *et al*., 2013). On the other hand, sintered polycrystalline alumina substrates that are used to support passive electronic components, such as surface mount resistors, always contain small amounts of impurities, such as chromium, and dopants which likely introduce additional extrinsic defects. For instance, small concentrations of magnesia (MgO) are commonly added to Al_2O_3 during the sintering process as a means of improving densification and controlling abnormal grain growth (Peelen, 1977). Also, the presence of structural disorder (i.e., grain

boundaries and porosity) in the microstructure of polycrystalline ceramics possibly has an effect on the defect concentration.

The optical properties of alumina and in particular the production of luminescence emission are influenced by the imperfections of the crystal structure. In the following, the most important kinds of defects in various forms of alumina materials will be discussed emphasising those associated with the generation of the luminescence phenomena.

4.2 The crystal structure of α-alumina

There are several metastable crystallographic forms/transitions of alumina, denoted by the Greek letters γ-, δ-, ε-, η-, θ-, κ-, χ- (Shackelford and Doremus, 2008; Riedel and Chen, 2010). Each transition possesses dissimilar structural arrangement characteristics and material properties. The thermodynamically stable transition used in most ceramic applications is the alpha alumina (α-Al_2O_3) which is obtained by a nucleation and growth process through a phase transformation cycle ($\gamma \rightarrow \ldots \rightarrow \alpha$) at progressively increasing heating temperatures (Levin and Brandon, 1998).

Alpha alumina exhibits the structure of corundum (Figure 4.1), in which the oxygen ions (O^{2-}) are arranged in a slightly distorted close stacking with trivalent aluminium cations (Al^{3+}) occupying two thirds of the octahedral interstitial positions (Atkinson *et al.*, 2003; Boch and Niepce, 2007; Jacobs and Stewart, 1982; Moulson and Herbert, 2003; Riedel and Chen, 2010; Shackelford and Doremus, 2008). In this configuration, each oxygen anion is positioned between four aluminium cations while each aluminium cation is surrounded by six oxygen anions.

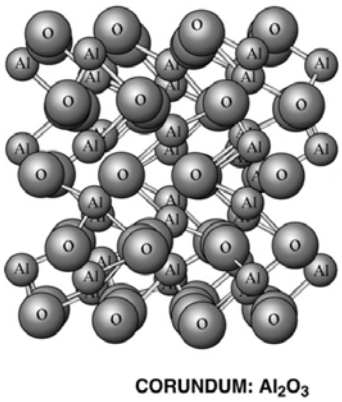

Figure 4.1: Crystal structure of corundum. The oxygen ions (O) form a hexagonal close packing with the aluminium ions (Al) occupying two thirds of the interstitial sites. Modified from Shackelford and Doremus (2008).

4.3 Point defects in alumina

Point or lattice defects in crystals occur as a consequence of the absence or displacement of lattice atoms or due to the presence of impurities and dopants. The first class of crystal imperfections are referred to as intrinsic point defects and may exist naturally (i.e., non-stoichiometry), while those introduced by foreign elements belong to the class of extrinsic point defects (Stoneham, 2001). Sometimes, doping with a particular atomic element does not cause the formation of extrinsic defects but brings about increased concentrations of a particular type of intrinsic defect.

4.3.1 Intrinsic point defects

The most common types of intrinsic point defect in ionic compounds are the *Shottky* and the *Frenkel* defects (Figure 4.2). A *Shottky* defect is formed when both the cation and the anion are missing from regular lattice positions resulting in pairs of negatively charged cationic vacancies and positively charged anionic vacancies (Boch and Niepce, 2007; Carter and Nortor, 2007; Kang., 2005; Rahaman, 2005; Riedel and Chen, 2010). Electrical charge neutrality of the crystal is preserved since the vacancies are created in a stochiometric ratio. A *Shottky* defect in alumina

can be described using the Kronger-Vink notation by the following reaction (Atkinson *et al*., 2003; Kang, 2005):

$$2Al_{Al}^{x} + 3O_{O}^{x} \leftrightarrow 2V_{Al}'' + V_{O}^{\cdot\cdot} + Al_2O_3 \quad (4.1)$$

The symbols $x, V_{Al}'', and\ V_{O}^{\cdot\cdot}$ denote a neutral effective charge, a negatively charged aluminium vacancy, and a positively charged oxygen vacancy respectively.

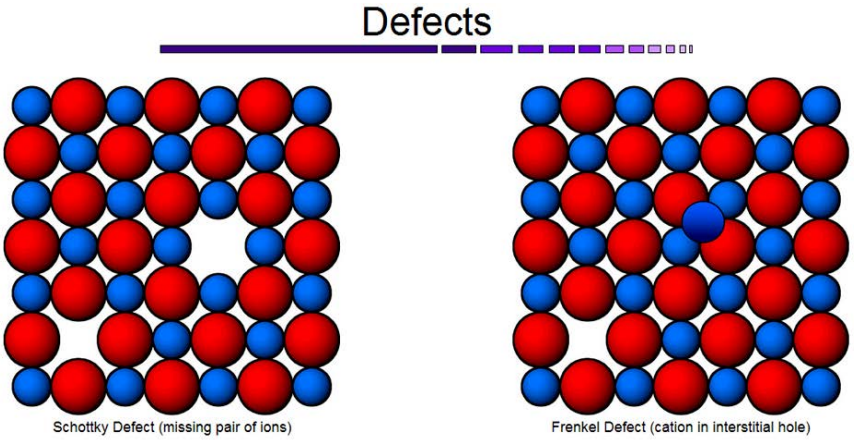

Figure 4.2: (a) Shottky and (b) cation Frenkel defects in ionic compounds. A Shottky defect consists of a pair of cation and anion vacancies while a cation Frenkel defect comprises a cation vacancy and a cation interstitial (http://education.mrsec.wisc.edu/SlideShow/slides/contents/defects.html).

Frenkel-type defects are formed when the ions are displaced from their regular lattice sites and occupy interstitial positions (Boch and Niepce, 2007; Carter and Nortor, 2007; Kang, 2005; Rahaman, 2005; Riedel and Chen, 2010). Vacancies are again formed in the position of previously occupied crystal sites. Both cation *Frenkel* and anion *Frenkel* defects may occur depending on which atomic species is displaced. Cation and anion *Frenkel* defects in alumina are expressed as (Atkinson *et al*, 2003; Kang, 2005):

$$Al_{Al}^{x} \leftrightarrow V_{Al}''' + Al_{i}^{\cdot\cdot\cdot} \quad (4.2)$$

$$O_{O}^{x} \leftrightarrow V_{\ddot{O}} + O_{i}'' \quad (4.3)$$

Whether the *Shottky* or the *Frenkel* disorder is dominant in the crystal structure of alumina is not yet clear. However, the formation energies of *Shottky* and anion *Frenkel* are lower than that of cation *Frenkel* defects (Atkinson, 2003; James and Stewart, 1982; Kotomin and Popov, 1998) which may favour their appearance in the host lattice. In addition, luminescence studies that have been carried out using numerous configurations of alumina materials indicated the prevalence of the oxygen vacancies; which also points to the existence of *Shottky* or anion *Frenkel* defects.

In general, the concentration of native point defects as a result, for example, of the non-stochiometry or imperfect crystallisation is expected to be small at low temperatures (~ 1000 °C), but increases considerably at higher temperatures (~ 1600 °C) and in the presence of specific impurities (Kroger, 1984). For example, polycrystalline aluminas which are usually sintered at temperatures above 1400 °C (Shackelford and Doremus, 2008) and dosimetry grade Al_2O_3:C single crystals (McKeever *et al*. 1995) which are heated close to the melting point of alumina (i.e., ~ 2000 °C) are expected to have large concentration of point defects. In addition, impurities introduced during fabrication, such as Mg in polycrystalline and C in single crystals, should also contribute to the formation of point defects.

4.3.2 Extrinsic point defects

Extrinsic lattice defects in alumina compounds result, mainly, from the substitution of the Al^{3+} atom by elements of similar or different valence state (Atkinson *et al*, 2003; Kroger, 1984; Rahaman, 2005). Some extrinsic point defects are attributed to trace levels of impurities (e.g., Cr^{3+}) present even in the most pure alumina powders, while others are created by the intentional doping of the material. Incorporation of elements with the same valence state (i.e., isovalent) as that of Al^{3+} does not require charge compensation and usually does not increase the concentration of the intrinsic point defects (Atkinson *et al*., 2003; Kroger, 1984). It is possible, however, for these elements to generate electronic levels within the large band gap of ~ 9 eV (Kroger, 1984; Nassau, 1978) of the alumina that can play an important role in the charge trapping/detrapping and recombination mechanisms of the various luminescence processes. Aliovalent elements with a valence state lower or higher than that of the host metal – acting as acceptors and donors respectively – necessitate the formation of cationic or anionic vacancies for

charge compensation (Atkinson *et al*., 2003; James and Stewart, 1982; Kroger, 1984; Rahaman., 2005). For example, the synthesis of dosimetry grade single crystals α-Al_2O_3:C, as well as the manufacturing of polycrystalline alumina substrates used in electronic components, involves the incorporation of divalent dopants; carbon in α-Al_2O_3:C (Akselrod *et al*., 1990) and magnesium in α-Al_2O_3 substrates (Boch and Niepce, 2007; Carter and Nortor, 2007; Kang, 2005; Moulson and Herbert, 2003; Riedel and Chen, 2010). In both cases, an anion vacancy compensation mechanism has been suggested to take place resulting in excess formation of oxygen vacancies (Atkinson *et al*, 2003; James and Stewart, 1982; Moulson and Herbert, 2003).

For α-Al_2O_3:C dosimetry crystals, it was initially suggested (Akselrod *et al*., 1990) that the two-valent carbon ions (C^{2-}) replace the three-valent aluminium cations leading to to the formation of oxygen vacancies acting as hole trapping centres. According to a different theory by Yang *et al*., (2008), carbon ions, having a valence state of four (C^{4-}), substitute the two-valent oxygen ions, O^{2-} and charge compensation is retained through the formation of oxygen vacancies. In a similar manner, the formation of oxygen vacancies induced by incorporation of MgO into α-Al_2O_3 is expressed by the following reaction (Atkinson *et al*., 2003):

$$Al_2O_3 \overset{MgO}{\Longleftrightarrow} 2Mg'_{Al} + V_O^{\cdots} + Al_2O_3 \qquad (4.4)$$

4.4 Formation mechanisms of point defects in single crystal and polycrystalline alumina

Point defects are always present in ionic compounds in thermodynamic equilibrium (Carter and Nortor, 2007). However, for certain applications it is desirable to increase the number of vacancies or interstitials. Generally, the formation of point defects in crystalline compounds requires the displacement of the atoms from regular lattice positions. To do so, energy must be provided to the crystal to break the bonds holding the elements together. For example, energies in the ranges 20-50 eV and 50-90 eV are required to displace aluminium and oxygen atoms respectively from normal lattice positions (Agnew, 1992; Arnold and Compton, 1960; Lee and Crawford, 1979; Zinkle and Kinoshita, 1997). Irradiation with beams of energetic particles is an efficient method to introduce vacancies and interstitial ions through, mainly, elastic collisions with the atoms (Hannay, 1975). Studies conducted with single crystals of pure alumina

bombarded with neutrons as well as heavy charged particles indicated that oxygen vacancies are predominantly formed (Evans and Stapelbroek, 1978; Lee and Crawford, 1979), the properties of which, as examined by the optical absorption and emission profiles, were found to be similar. In contrast, exposure to low LET radiation such as β-, γ-, or X-rays may change the charge state of existing defects without causing significant radiation damage.

Thermochemical processes can also be used to introduce specific crystal defects (Hannay, 1975). This is the case for α-Al_2O_3:C dosemeters which are heated at high temperatures (~ 2000 °C), close to the melting point of alumina, under reducing conditions in the presence of graphite; a process which results in the removal of oxygen ions from the crystal lattice and the formation of high concentrations of oxygen vacancies of the order of ~ 10^{16}-10^{17} per unit volume (Akselrod and Kortov, 1990; Akselrod *et al*, 1990; McKeever *et al*., 1995). The reduction reaction of alumina that creates oxygen vacancies in the lattice and liberates electrons in the conduction band can be written as (James and Stewart, 1982; Rahaman, 2005):

$$2O_O^{2-} \rightarrow O_2(g) + 2V_O + 4e_c \qquad (4.5)$$

Alternatively, oxygen deficient crystals can be produced by heating the material in an atmosphere of aluminium vapor (Lee and Crawford., 1978, 1979). This procedure produces oxygen vacancies through an excess of aluminium cations in the crystal lattice.

Polycrystalline alumina materials also contain oxygen vacancies, but their formation does not involve bombardment with energetic particles or sophisticated and expensive manufacturing processes. As already mentioned in the introduction, polycrystalline alumina substrates are processed via sintering methods (i.e., solid-state or liquid-phase sintering). This refers to a thermally activated process during which powders are compacted into solid dense bodies and then fired at high temperatures (> 1400 °C) (Boch and Niepce, 2007; Carter and Nortor, 2007; Kang, 2005; Moulson and Herbert, 2003; Riedel and Chen, 2010). The final product has a complex microstructure with grain boundaries and pores. Very often, other oxides such as MgO, CaO, and SiO_2 or combinations of these are added at small concentrations as sintering aids to minimise porosity, assist densification at lower temperatures, and suppress abnormal grain growth (Boch and Niepce, 2007; Kang, 2005; Moulson and Herbert, 2003; Riedel and Chen, 2010). The driving force of sintering is the transport of atoms by various diffusion paths such as

surface, lattice, and grain boundary diffusion (Boch and Niepce, 2007; Kang, 2005; Rahaman, 2005). Lattice and grain boundary diffusion are the dominant atom movement mechanisms and depend significantly on the temperature and the concentration of point defects (Rahaman, 2005). For example, oxygen diffusion is faster at the grain boundaries (Boch and Niepce, 2007); the regions where there is a preferential segregation of additives (Altay and Gulgun, 2003; Soni *et al*, 1995). This is also in agreement with the enhanced diffusion of oxygen with Mg^{2+} doping (Atkinson *et al*., 2003; Boch and Niepce, 2007; Kang, 2005). It can, thus, be concluded that the presence of the dopants is expected to influence significantly the nature and concentration of point defects in polycrystalline alumina materials.

4.5 Luminescence-colour centres

In the preceding discussion oxygen vacancies considered to be the main and most abundant point defects in alumina compounds. The reason is that oxygen vacancies are the crucial constituents that predominantly give rise to coloration effects in crystalline materials (Nassau, 1978). This term is used to describe the appearance of light absorption and emission phenomena in otherwise optically transparent crystals (Carter and Nortor, 2005; Kotomin and Popov, 1998; Nassau, 1978; Schulman and Compton, 1962; Sole *et al*., 2005). Colour effects in minerals appear as a result of charge localisation – usually electrons – at impurity ions, groups of atoms or vacancies. Physical optical effects such as light scattering by internal structural components may be another cause for the appearance of colours (Nassau, 1978) and this is likely to be more important in polycrystalline materials with irregular distribution of grains, grain boundaries and pores.

Alumina doped with chromium or titanium ions (i.e., Cr^{3+}, Ti^{3+}) is known as ruby or sapphire respectively due to the specific colours introduced by these impurities. The colour in these cases is the result of the interaction of light with the unpaired electrons of the impurity ions (Shackelford and Doremus, 2008). In pure alumina samples the most common types of colour centre are those caused by the trapping of one or two electrons by an oxygen vacancy resulting in positively charged F^+- or electrically neutral *F*-colour centres respectively; where the letter *F* is derived from the German word Farbe (i.e., colour). The defect environment of the alumina is expected to be complex, consisting of vacancies and interstitials of either ion species and clusters

of these defects are likely to give rise to cation vacancies occupied by holes that produce *V*-colour centres (Jacobs and Kotomin, 1994; Kotomin and Popov, 1998). Like F^+- and *F*-centres, localisation of holes at aluminium vacancies can give rise to a V^{2-}- centre (i.e., single hole trapped on an oxygen ion nearly an aluminium vacancy) or a *V* centre which consists of a V^{2-}-centre which has trapped a second hole (Summers, 1984). Hole trapping by impurity atoms replacing aluminium cations has also been found to generate *V*-centres and a V_{Mg} centre consisting of a magnesium ion that has occupied a regular lattice cation site was experimentally shown to exist (Kotomin and Popov, 1998; Kulis *et al*., 1981; Summers, 1984). However, the electronic properties of *V*-colour centres in alumina compounds are less well known and their role is often not taken into account in explaining certain luminescence processes.

The formation mechanisms of colour centres are similar to those of oxygen vacancies. The synthesis of single crystal α-Al_2O_3:C dosemeters under reducing conditions results in a non-stoichometric compound with an excess of aluminium cations and a number of unbound valence electrons. The vacancies generated due to the removal of the oxygen ions can trap the electrons liberated by the metal ion forming *F*-type centres maintaining crystal charge neutrality. In addition, the intentionally doping of the material with carbon atoms in amounts of 100-5000 ppm increases the concentration of oxygen vacancies and provides charge compensation for the formation of F^+-centres (Akselrod *et al*., 1990; McKeever *et al*., 1995; Muthe *et al*., 2008). The above process is usually termed subtractive coloration, but the principles are equally applied to the additively coloured method in which (Lee and Crawford. 1978, 1979) oxygen vacancies are created due to an excess of aluminium atoms.

High energy radiation incident on crystals can also produce colour centres. The energy transferred by charged or uncharged particles through the various interaction mechanisms is sufficient to excite valence band electrons which are liberated and produce *F*-colour centres once they encounter anion vacant sites. At the same time, holes are generated in the valence band which are also free to move producing *V*-colour centres, through capture at cation vacancies (Hannay, 1975; Jacobs and Kotomin, 1994).

As discussed by Lee and Crawford (1978, 1979), the colour properties of the *F*-type centres created by thermochemical methods are similar to those induced by energetic particle bombardment, but the thermal annealing characteristics of materials in which they have been

generated can be significantly different. The thermochemically produced colour centres are thermally stable up to 1400 °C whereas the colour centres produced by irradiation can be completely removed by annealing at 900 °C.

Numerous experimental and theoretical calculations have been carried out to establish the electronic structure, absorption, and emission properties of the *F*-type colour centres. Since, they are not unique to alumina, having been identified in a several oxide crystals (e.g., MgO, CaO, BeO), their optical properties are expected to depend on the host lattice environment. In the case of alumina, an understanding of the characteristics of these electron centres is important since, as discussed above, they comprise the main sites for radiative recombination during several types of stimulation processes (e.g., thermally- and optically-stimulated luminescence, thermally stimulated conductivity).

Knowledge of the electronic structure of the positively charged F^+-centre was acquired experimentally by Evans and Stapelbroek (1978) by investigating the UV-excited optical absorption and emission spectra of high purity crystalline Al_2O_3 samples. Following fusion-neutron irradiation the samples revealed absorption bands at 4.8, 5.4, and 6 eV. Upon excitation with 4.8 and 5.4 eV light a strong luminescence emission band centered at 3.8 eV (~ 330 nm) was detected. This band, which was found to be weaker during 6 eV illumination was attributed to the F^+-centre. The resemblance of the three absorption bands with the three degenerate excited states of an F^+-centre, as well as the absence of the 3.8 eV emission band in oxygen (O^+) implanted crystals, led the authors to suggest a model based on neutron irradiation induced F^+-centres to explain the observed optical properties. The energy levels of the F^+-centre are schematically shown in Figure 4.3. According to the F^+-centre model, the 4.8, and 5.4 eV absorption bands are assigned to electronic transitions from the ^1A ground state of the F^+-centre to the ^1B and ^2A excited states respectively. The third absorption band near 6 eV was tentatively assigned to the $^1A \rightarrow {}^2B$ transition although it was believed to belong to the presence of the *F*-centre. The 3.8 eV emission band was assigned to the fast (~ 7 ns) $^1B \rightarrow {}^1A$ relaxation transition. The positions of the ground and the excited states of the F^+-centre with respect to the valence and the conduction bands of the alumina crystal have also been calculated by means of theoretical methods (Kotomin and Popov, 1998; Stashans *et al.*, 1994). Kotomin *et al.*, (1998) simulated successfully the energy levels of an F^+-centre that was found to lie 3.1 eV above the

top of the valence band with the ^1B, ^2A, and ^2B excited states being well localised within the band gap at about 2.26, 3.39, and 5.15 eV above the ^1A state. The room temperature excitation and emission properties of the *F*-type centres in Al_2O_3 crystals are illustrated in Figure 4.4.

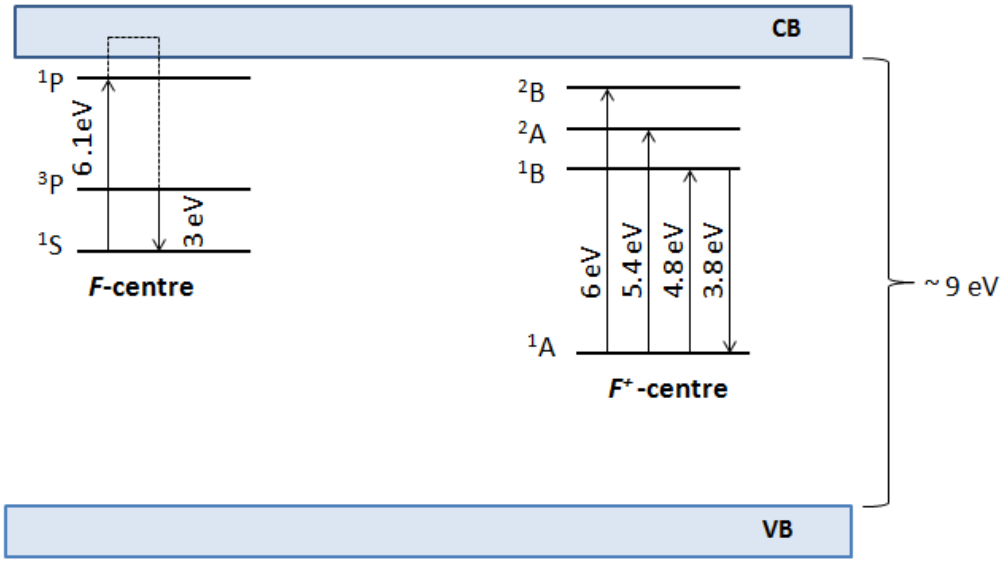

Figure 4.3: Energy levels for absorption and emission of the *F*- and F^+-centre in the band structure of α-Al_2O_3 crystal.

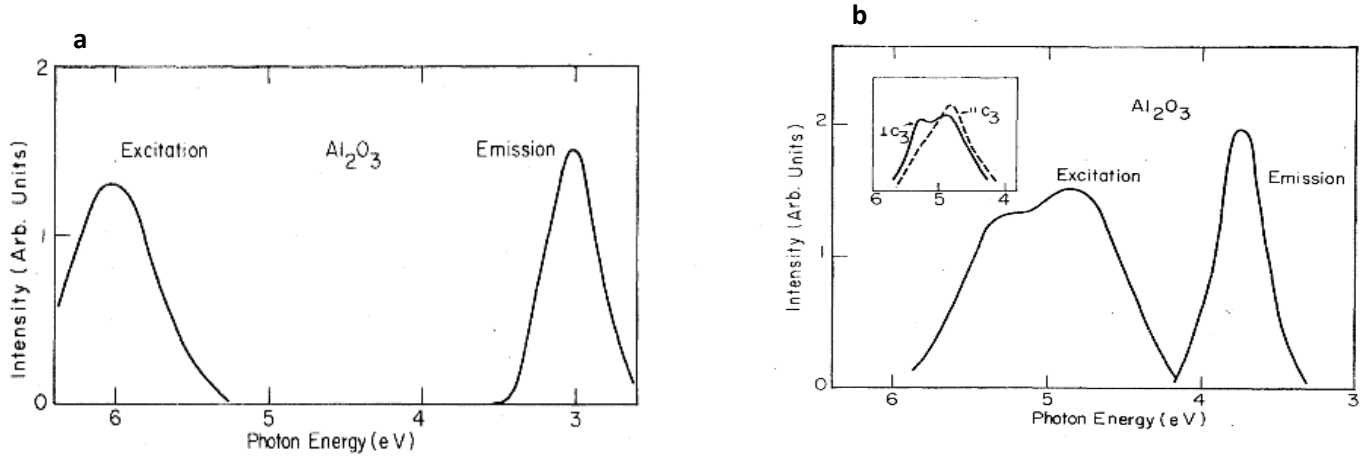

Figure 4.4: Room temperature excitation and emission spectra of (a) an *F* - centre and (b) an F^+ - centre in subtractively colored Al_2O_3 crystals Reprinted from Lee and Crawford (1979).

On the basis of the results obtained from optical absorption and emission studies in as-grown sapphire crystals and crystals coloured using thermochemical (i.e., additive and subtractive coloration) and high energy particle irradiated methods, Lee and Crawford (1978, 1979) determined the luminescence features of the *F*-centres. The subtractively coloured Al_2O_3 samples showed, in addition to the absorption bands at 4.8 and 5.4 eV of the F^+-centres, a band at 6.1 eV. In the additively coloured samples as well as in crystals coloured by electron or neutron bombardment only the 6.1 eV absorption band could be detected. Nevertheless, the emission spectra of all coloured samples consisted of the 3.8 eV band due to F^+-centres and a 3.0 eV (~ 420 nm) band with a characteristic radiative lifetime of about 36 ms. The long lifetime of the emission process and the large Stokes shift (i.e., difference in wavelength between the maximum of the absorption and the maximum of the emission bands) are usually indicative of a forbidden transition. Indeed, by comparison with other metal oxides, the authors attributed the new bands to the presence of *F*-centres, the electronic structure of which (Figure 4.3) resembles that of a helium atom. The 6.1 eV absorption band is attributed to the excitation of electrons from the ^1S ground state to the ^1P excited state. The de-excitation of electrons involves a two-step process: a temperature dependent non-radiative transition (i.e., $^1P \rightarrow {}^3P$) and a temperature-independent radiative transition from the ^3P state to the ^1S ground state of the *F*-centre which explains the 3.0 eV emission band. According to Hund's selection rules for emission (Blasse and Grabmaier, 1994), the $^3P \rightarrow {}^1S$ transition is spin forbidden and is expected to be associated with a long radiative lifetime; in agreement with the experimental results. The ground state of the *F*-centre is placed 5.3 eV above the top of the valence band, while the ^1P excited state should lie close or within the conduction band to account for the experimentally observed photoconductivity response at 6.1 eV (Draeger and Summers, 1979; Kotomin and Popov, 1998; Lee and Crawford, 1979; Stashans *et al.*, 1994).

4.6 Studies of luminescence processes in α-Al_2O_3 compounds

Following the early investigations on the role of colour centres in the luminescence of α-Al_2O_3, a number of spectroscopic studies were conducted to determine the absorption and emission characteristics in alumina samples of variable origin (i.e., growth, composition). Although good

agreement concerning the contribution of the *F*-type centres in the various luminescence phenomena observed was achieved, most of the conclusions were drawn for single crystalline materials produced using either ultra high pure (> 99.99%) alumina or samples deliberately doped with known amounts of additives while limited data exist for polycrystalline ceramics (Kortov *et al*., 2008; Nagabhusana *et al*., 2008; Sato *et al*., 1999).

A few examples of experimental data that identify the luminescence characteristics of various alumina samples are presented below where both the *F*-type and the impurity-related luminescence are demonstrated. Even though variations have been observed from sample to sample, there exist some common findings that can be used to assign the defect structure and processes involved in the generation of luminescence of analogous materials (e.g., polycrystalline alumina substrates) that lack specific analysis. The basic conversion processes between *F*- and F^+-centres under optical- and electron-stimulation are also reviewed.

4.6.1 F-type luminescence

Emission spectra measured during x-ray irradiation (i.e., radioluminescence, RL) of an undoped and three commercially available Al_2O_3 detectors (Al_2O_3:C, Al_2O_3:Si,Ti, and Al_2O_3:Mg,Y) were analysed by Peto (1996). In the RL spectra of all samples two bands at 310 nm and 695 nm were detected and associated with F^+-centres and Cr^{3+} impurities respectively. In particular, the F^+ emission was found to be the most intense in all but the Al_2O_3:C RL spectrum that was dominated by a band at 420 nm attributed to *F*-centres. Although less intense, the 420 nm band was present in the spectrum of the other doped materials. A different interpretation was given in the case of the Al_2O_3:Si,Ti detector where it was suggested that the presence of Ti^{3+} ions rather than of oxygen vacancies are responsible for the 420 nm emission. More complicated emission spectra were found for the Al_2O_3:Mg,Y sample with several additional bands appearing between 460 – 580 nm likely to be associated with Y^{3+}.

Kristianpoller *et al*., (1998) studied the photoluminescence (PL), X-ray excited (XL) and thermoluminescence emission spectra of beta-, x- and UV- irradiated samples of pure, carbon and rare earth doped α-Al_2O_3. They identified emissions due to F/F^+ centres (i.e., 410 nm / 330

nm) and characteristic impurity related emission bands such as the narrow Cr^{3+} red peak at 698 nm. Interestingly, only the *F*-type emission was detected in the pure samples, whereas C-doped Al_2O_3 presented both *F*-type bands. Generally, *F* and F^+ emissions were more pronounced in the α-Al_2O_3:C sample confirming the role of carbon atoms in creating a high concentration of oxygen vacancies.

The luminescence of single crystals of α-Al_2O_3 was also analysed using cathodoluminescence (CL) techniques by Sato *et al*., (1999) and Ghamnia *et al*., (1997, 2003). In Ghammia *et al*., (1997) the emission spectra obtained under electron irradiation of energy 4 keV and 10^{-3} A·cm^{-2} current density consisted of peaks that were attributed to excitation of F^+-centres (330 nm), Cr^{3+} (695 nm) and Ti^{3+} (750 nm) impurities. The authors also showed that by varying the electron beam density from 10^{-3} to 10^{-5} A·cm^{-2} new bands were observed at 275 nm and 418 nm that correspond to $F_{cations}$- and neutral *F*-centres. They suggest that $F_{cations}$-centres are formed when divalent elements such as Mg^{2+} or Ca^{2+} exist in the material, possibly as native impurities of the raw powder and these usually lead to enhanced F^+ emission as they produce luminescence in the same spectral region (i.e., ~ 300 nm) of the F^+ centre. Although, the influence of the electron beam density on the emission process was not investigated in detail, it seems that by changing the beam density which determines the amount of dose delivered to the sample and also the diffusion length of electron-generated charge carriers, different recombination centres were activated, and reduction of the electron beam density from 10^{-3} to 10^{-5} A·cm^{-2} probably decreased the participation of deep lying centres in the emission process. This also implies that luminescent centres closer to the surface of the sample have a higher likelihood of being detected. The concentrations of these ´surface´ centres, attributed by Ghamnia *et al*. (1997) to Mg^{2+} or Ca^{2+}, are expected to be lower than that associated with *F* and F^+ type emission, an assumption which appears reasonable given that Mg^{2+} or Ca^{2+} were identified as trace impurities.

The suggestion of enhanced F^+ luminescence due to the presence of Mg^{2+} was confirmed experimentally by Akselrod and Kortov (1990) and more recently by Rodriguez *et al*., (2011) who studied the luminescence efficiency of Al_2O_3 doped with C and Mg and compared it with the published values for TL/OSL emission of single crystal Al_2O_3:C dosemeter. They concluded that the incorporation of atoms of Mg^{2+} induces new bands at ~ 520 nm and ~ 750 nm and enhances the F^+-centre emission. As explained in other studies (e.g., Summers, 1984; Kotomin *et*

al., 1998), Mg^{2+}-doped Al_2O_3 contains V_{Mg} centres which act as hole traps. Release of holes from the V_{Mg} centres during TL or OSL and capture by F-centres produce excited F^+-centres which de-excite by emission of ~ 330 nm luminescence. Increased F^+ concentration is generally favoured because it allows more $F^+ \rightarrow F$ conversions.

Ghamnia *et al*., (1997) also observed a mechanism of $F^+ \leftrightarrow F$ interchange upon varying the experimental conditions in an scanning electron microscope (SEM) such as focus/defocus of electron beam, high and low electron beam current. F^+-centre emission was found to increase in intensity at the expense of the *F* band at high current density and for a focused electron beam. That was interpreted as being due to the excitation of pre-existing single (e.g., *F*-centres) and/or double (e.g., F_2^{2+}-centres) oxygen vacancies which change into excited F^+-centres that de-excite by emission of a photon of 330 nm wavelength. A similar mechanism is supported for the $F^+ \rightarrow F$ conversion that was observed at lower current density. Conversion processes between the F^+- and the *F*-centre have been reported by several researchers (e.g., (Flerov *et al*., 1996; Ghamnia *et al*., 1997; Ghamnia *et al*., 2003; Jonnard *et al*., 2000; Kotomin and Popov, 1998; Surdo and Kortov, 2004; Kotomin *et al*., 1994; Lee and Crawford, 1979; Summers, 1984; Surdo and Pustovarov, 2005). Lee and Crawford (1979) showed that the intensity of the F^+-centre emission increases upon bleaching with 6.1 eV light due to excitation of an *F*-centre electron. The conversion reactions between the *F*- and the F^+-centre under optical or particle-stimulation are expressed according to:

$$F + (excitation) \rightarrow (F^+)^* + e^-$$

$$(F^+)^* \rightarrow F^+ + hv\ (330\ nm) \qquad (4.6)$$

$$F^+ + (excitation) \rightarrow (F)^*$$

$$(F)^* \rightarrow F + hv\ (420\ nm) \qquad (4.7)$$

The *F*-type luminescence of Al_2O_3 crystals and the influence of experimental conditions on the emission spectra have also been explored by Jonnard *et al*., (2000). Using single crystals with known impurity content (e.g., Si, Ca, Fe, Ti, Cr, Na, Mg, K etc) annealed at different temperatures, optical CL spectroscopy following electron beam irradiation was carried out for different electron beam energies and densities. For the sample annealed at 1000 ºC only the F^+ band was observed at 4 keV while at lower electron beam energies (1.9 and 1 keV) optical

emissions of the *F*-centre at 420 nm and a Cr^{3+} impurity at 693 nm were detected. As with the effect of electron beam density discussed earlier, the energy of the electron beam affects the penetration profile of the electrons in the sample. Generally, the penetration depth of the electrons decreases with decreasing beam energy and the luminescence of the surface states is expected to be more pronounced particularly when material is opaque. A second sample (annealed at 1500 ºC) revealed the same spectral modifications as a function of the incident beam energy, with the addition of a small structure at 4.1 eV associated with divalent metal impurities (e.g., Ca^{2+}) at the lowest electron energy (i.e., 1 keV). The emission from a third sample (annealed at 1700 ºC) was spectrally analysed under 4 keV excitation and using two electron beam densities (0.15 mA cm^{-2} and 1.5 mA cm^{-2}). When the density of the incident electron beam increased tenfold the intensity of the emission bands associated with the chromium ions and *F*-centres reduced significantly, the 4.1 eV peak disapperared and the F^+-centre peak narrowed (well separated from the *F* peak) but preserved its initially intensity. The differences in the spectral characteristics in relation to the incident electron beam parameters were interpreted as an $F^+ \leftrightarrow F$ interchange mechanism where several factors like the relationship between the excitation and ionisation cross sections, the density of the electron beam, the number of excited $(F^+)^*$ centres, the number of the available electrons in the conduction band and the decay probability of F^+-centre are contributing factors.

In a study by Surdo *et al*., (2005) using a synchrotron (SR) source, the impurity and intrinsic defect luminescence of anion-deficient α-Al_2O_3 crystals was explored using steady-state and time-resolved spectroscopic methods. The primary luminescence of the *F*- and F^+-centres was detected under CW x-ray excitation. Additional emission bands observed at 1.79 eV (~ 693 nm), 1.75 eV (~ 709 nm), and 2.4 eV (~ 517 nm) were attributed to Cr^{3+}, Ti^{3+} and interstitial aluminium ions (Al^+) centres. The authors also studied the time decay constants of the radiative relaxation processes. In agreement with earlier predictions (Evans and Stapelbroek, 1978), F^+-centre emissions, measured under pulsed excitation, were characterised by a fast relaxation/decay time in the nanosecond range (i.e., 2 - 7 ns) and the decay time of the impurity centres associated with titanium and interstitial aluminium ions was in the microsecond range (3.5 and 56 μs respectively), while lastly Cr^{3+}- and *F*-centres relaxed radiatively with decay times in the millisecond range (4 ms for Cr^{3+}- and 34 ms for *F*-centres). The value for the

recombination lifetime of the *F*-centre found by Surdo *et al*. (2005) is very close to the value of 36 ms calculated by Lee and Crawford (1979).

4.6.2 Impurity-related luminescence

The strong influence of impurities in the defect environment of alumina can be confirmed from the studies discussed above. Reports regarding other impurities are rather limited in comparison with chromium and titanium ions which can be found even in the most pure Al_2O_3 single crystalline materials. Consequently their effect on absorption and emission characteristics have been particularly examined using intentionally doped alumina samples.

When chromium is incorporated into alumina, even in trace quantities, it gives characteristically sharp emissions located at ~ 1.8 eV (~ 695 nm), with smaller satellite bands. Absorption occurs in the visible part of the spectrum at 3.1 eV (~ 400 nm) and 2.2 eV (~ 550 nm) due to internal transitions from the $^2A_2$ ground level to the $^4T_1$ (i.e., 3.1 eV) and the $^4T_2$ (i.e., 2.25 eV) excited levels of the Cr atom (Blasse and Grabmaier, 1994). The red emission (known as R-line) results from either the capture of hole by Cr^{2+} or the capture of electrons by Cr^{4+} ions according to Lapraz *et al*. (1991), Pokorny and Ibarra. (1994) and Summers (1984):

$$Cr^{2+} + h^{+} \rightarrow (Cr^{3+})^{*} \rightarrow Cr^{3+} + hv\,(695\,nm) \qquad (4.8)$$

$$Cr^{4+} + e^{-} \rightarrow (Cr^{3+})^{*} \rightarrow Cr^{3+} + hv\,(695\,nm) \qquad (4.9)$$

The role played by chromium impurities in the luminescence of aluminium oxide samples was thoroughly examined by Lapraz *et al*., (1991), who compared the TL and fluorescence spectra obtained after x-ray irradiation at 77 K of a series of ruby (i.e., Cr doped Al_2O_3) crystals with different concentrations of Cr with those from nominally pure α-Al_2O_3. It was observed that the fluorescence spectra of all samples exhibit the characteristic red emission due to Cr^{3+} ions and this was accompanied by weaker lines at ~ 701 nm and ~ 704 nm attributed to interactions of neighbouring Cr^{3+} ions and a wide band at ~ 774 nm that was related to aggregates of more than two Cr^{3+} ions. The fluorescence yield of the R-line and the two satellite lines was found to

increase with increasing impurity concentration, reaching a maximum around 4000 ppm and then decreased for higher concentrations. The intensity of the ~ 774 nm showed a continuous increase with increasing chromium quantity. Also the TL intensity of the 260 K peak in the region of the *F* and F^+ emission bands was found to decrease progressively (i.e., F/F^+ emission quenching) with increasing concentrations of Cr^{3+} ions and finally disappeared.

Titanium is another impurity that can have an influence on the luminescence processes in Al_2O_3. Incorporation of Ti impurities into the structure of alumina crystals can either cause higher sensitivity owing to the blue-green emission of Ti ions, or lower sensitivity when the infrared (IR) emission of Ti ions is more pronounced (Evans and Stapelbroek, 1994; Mikhailik *et al*., 2011; Molnar *et al*., 2001). The primary emission of Ti ions is in the IR part of the spectrum near 730-760 nm (Flerov *et al*., 1996; Mikhailik *et al*., 2011; Surdo *et al*., 1999). However, in samples of Ti-doped Al_2O_3, emission bands in the UV (~ 290 nm) and visible (~ 425 nm) region have been observed and attributed to the presence of Ti^{3+}. Recently, Mikhailik *et al*., (2011) demonstrated that the luminescence emission of Al_2O_3:Ti depends on the concentration of titanium impurities. They used pure and titanium doped Al_2O_3 and analysed the SR-induced excitation and emission spectra. The ~ 730 nm band appeared in the emission spectra of all samples indicating that Ti^{3+} impurity ions can be present even in the pure samples. The emissions of the *F*- and F^+-centres were detected after excitation with 5.9 eV both at low (i.e., T = 8 K) and room temperature. The sample with low Ti concentration (i.e., 10 ppm) showed enhanced *F*- (420 nm) and infrared emissions (730 nm) but reduced F^+ -luminescence as compared with the undoped sample. The enhancement of the intensity of the blue band at ~ 420 nm was explained as being due to the Ti^{3+} ions acting as electron donors at low concentrations (Flerov *et al*., 1996; Mikhailik *et al*., 2011). The mechanism involves electron release from Ti^{3+} ions and recombination with F^+-centres followed by *F*-light emission according to the reactions:

$$Ti^{3+} + (excitation) \rightarrow Ti^{4+} + e^- \qquad (4.10)$$

$$F^+ + e^- \rightarrow (F)^* \rightarrow F + hv\,(420\,nm) \qquad (4.11)$$

As the dopant concentration increased (e.g., 50, 100, 500 ppm) the intensity of the F/F^+-bands gradually weakened while the ~ 730 nm band showed an increasing trend. As explained, at high concentrations titanium ions act as recombination centres that can capture free electrons resulting

in infrared emission. Therefore, the number of electrons available for capture by the F^+-centres and the associated emissions are limited by the competing action of titanium centres (Mikhailik *et al*., 2011; Molnar *et al*., 2001):

$$Ti^{4+} + e^- \rightarrow (Ti^{3+})^* \rightarrow Ti^{3+} + hv\ (730\ nm) \qquad (4.12)$$

Although as discussed in Chapter 6 titanium was not detected in the emission spectra of the sintered alumina substrates, it still remains a possible emission.

4.7 TL and OSL spectral emission characteristics of α-Al_2O_3

For synthetic phosphors to be useful for general TL and OSL dosimetry applications they need to exhibit a radiation sensitive response capable of being detected. As discussed above, while the environment of alumina combines intrinsic- and extrinsic-defect related radiative processes extending over the entire visible and UV range of the electromagnetic spectrum only certain emissions can be associated with TL/OSL emission.

The association of the *F*-type and impurity-related luminescence centres with the TL peaks and the OSL decay curves of alumina materials has been investigated by performing TL and/or OSL spectral emission analysis and evidence for the nature of the traps from which charge carriers are thermally or optically released prior to recombination at luminescent centres has been found only in a few cases (Summers., 1984). Nevertheless, so far there is insufficient evidence to identify the trap(s) involved in the generation of the principal TL peak at 160-200 °C (the position of the peak maximum depends on the applied heating rate), which has been associated with both electron (e.g., Molnar *et al*., 1999) and hole (e.g., Akselrod and Gorelova, 1993) traps. OSL spectral emission studies, using continuous-wave and time-resolved (TR) methods, have also been carried out (e.g., Markey *et al*., 1995; Pagonis *et al*., 2013; Rodriguez *et al*., 2011; Yukihara and McKeever, 2006). Common emission characteristics were detected in the TL and OSL spectra which enabled the development of a general luminescence model.

4.7.1 TL spectral emission characteristics

Depending on the properties of the alumina material (e.g., growth conditions, impurity content), the TL glow curve can be composed of a number of different peaks over a wide temperature range between 260 to 430 °C (Summers, 1984). A peak centered within the range 160-200 °C has been detected in Al_2O_3 crystals and suggested for TL dosimetry. Analysis of the spectral composition of this peak have revealed various emission bands in the UV, blue, and near IR range as well as a strong dependence on the impurity content of the material. Olster *et al*., (1994), Peto (1996), and Kristianpoller *et al*., (1998) examined the x-ray irradiated emission characteristics of the TL peaks of nominally pure and doped Al_2O_3 crystals. The peak near 180-200 °C which appeared in the glow curve of all Al_2O_3:C samples showed a dominant emission at 410-420 nm attributed to *F*-centres and weaker emissions at 325-330 nm (Kristianpoller *et al*., 1998; Olster *et al*, 1994) and 695-700 nm (Olster *et al*., 1994; Peto., 1996) due to F^+- and Cr^{3+}-centres respectively. In contrast, in pure Al_2O_3 samples the spectral emission of the 180 °C TL peak was found to coincide with that for the F^+-centre or Cr^{3+}-centre luminescence, with a much weaker contribution of the *F*-centre. The TL emission spectra of undoped and Al_2O_3:C crystals recorded by Peto (1996) are shown in Figure 4.5. These results provide strong indication that common defects present in alumina materials are associated with the properties of the host lattice rather than the quality or growth conditions. The latter possibly determine the concentration and the intensity of the luminescence emission of each defect species.

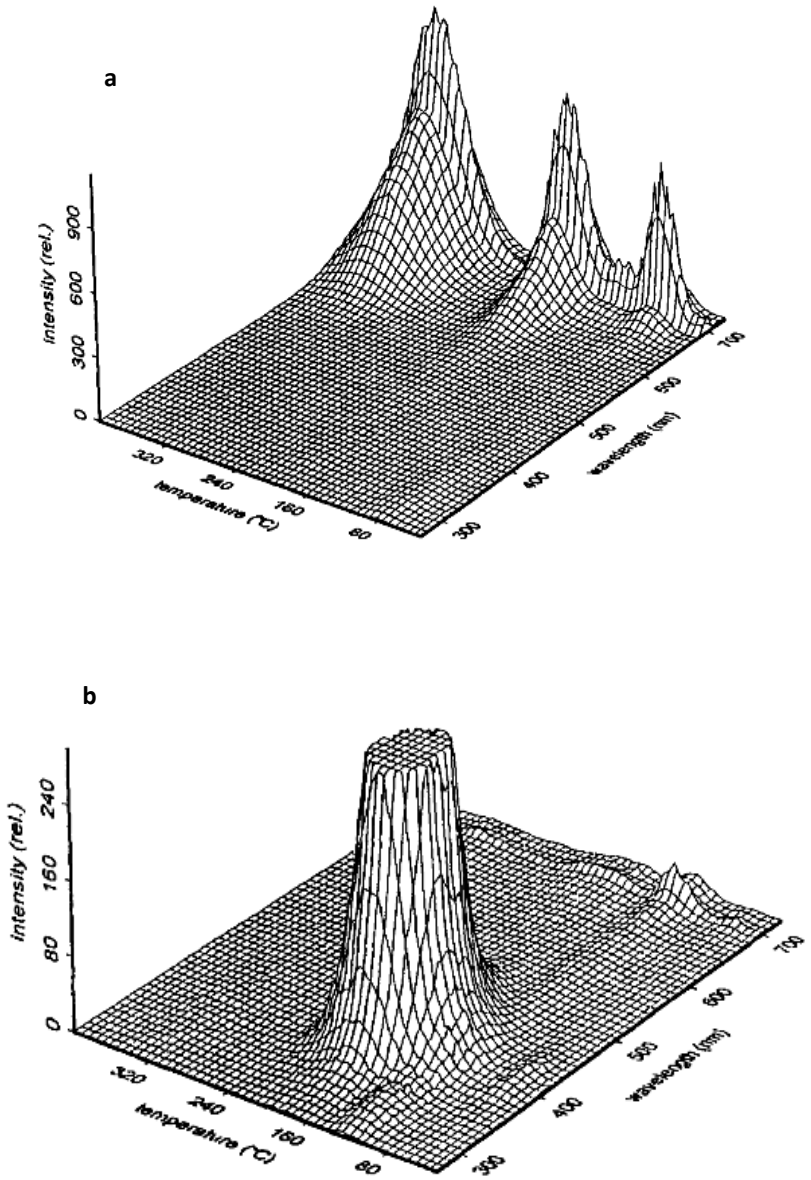

Figure 4.5: Spectral emission (luminescence intensity as a function of temperature and wavelength) characteristics of the TL peaks in (a) undoped Al_2O_3, and (b) Al_2O_3:C, Reprinted from Peto (1996).

The development of the Al_2O_3:C by Akselrod *et al*., (1990) as a highly sensitive TL/OSL detector came after previous attempts to grow Al_2O_3 with several additives (see McKeever *et al*., 1995). Improved TL properties were noticed for the carbon-doped crystals owing to a significant enhancement of the concentration of the intrinsic point defects (i.e., oxygen vacancies) and of the

F-colour centre (Akselrod *et al*., 1990; Yang *et al*., 2008). For dose assessment with α-Al_2O_3:C single crystals the peak at ~ 200 ºC is used, the spectral characteristics of which coincide primarily with the emission of the *F*-centres at ~ 420 nm (Akselrod *et al*., 1990; McKeever *et al*., 1995; Peto., 1996; Yukihara and McKeever, 2006). The F^+ luminescence may also contribute to the TL emission but it is more difficult to observe because of the dominant *F* band (Summers, 1984). As mentioned above, F^+-centres are oxygen vacancies with one electron and therefore are positively charged with respect to the crystal lattice. The addition of carbon atoms into the crystal provides charge compensation and facilitates the increase of the concentration of the F^+-centres, which in turn result in enhanced *F* luminescence as they act as recombination sites according to:

$$F^+ + e^- \rightarrow F^* \rightarrow F + hv\ (420\ nm) \qquad (4.13)$$

Unlike the preceding studies, where single crystalline materials were used, Nagabhusana *et al*., (2008) synthesized polycrystalline alumina samples and studied the TL and PL characteristics after heavy γ-irradiation. The TL glow curve was composed of two peaks at ~ 210 ºC and ~ 350 ºC. Spectral analysis of the 210 ºC peak revealed the emission to be due to *F*-centres and the material was suggested for dosimetry applications.

Knowledge of the emission wavelength of a TL peak primarily describes the nature of the recombination site(s) and potentially indicates the sign of the delocalised charge. For example, the *F*-centre ~ 420 nm luminescence resulting from electron capture at an F^+-centre, suggests that the trap(s) emptied during thermal or optical stimulation is an electron trap. Consistent with an electron trap model of the main dosimetric peak in α-Al_2O_3:C is the decrease of the F^+-centre concentration in the temperature range of the peak, the photo-ionisation of the *F*-centre following illumination with UV light (Yukihara *et al*., 2003), and intense exoelectron emission (Molnar *et al*., 1999). Likewise, TL emissions due to radiative relaxations of the F^+-centres can be explained by a release of holes from hole traps and subsequent trapping at an *F*-centre according to Equation 4.14 or by the capture of electrons at F^{2+}-centres (Equation 4.15). Nevertheless, the electron trap model of the F^+ emission calls for the existence of stable, empty oxygen vacancies; a fact that has not been evidenced yet (Yukihara and McKeever, 2006). Finally, as explained above, the contribution of Cr^{3+} recombinations centres can be due to electron capture by Cr^{4+} or hole capture by Cr^{2+} ions according to Equations 4.8 and 4.9. By means of optical absorption

measurements the most probable mechanism for the chromium band is likely to be revealed. If electron traps are emptied during TL then an increase in the absorption band of Cr^{4+} should be detected following irradiation (Pokorny and Ibarra., 1994).

$$F + h^+ \rightarrow (F^+)^* \rightarrow F^+ + hv\,(330\,nm) \qquad (4.14)$$

$$F^{2+} + e^- \rightarrow (F^+)^* \rightarrow F^+ + hv\,(330\,nm) \qquad (4.15)$$

Taking the factors discussed into account, the simultaneous detection of the *F*, F^+, and Cr^{3+} emissions in the main peak of α-Al_2O_3 cannot sufficiently be explained by an electron trap model only. McKeever *et al*., (1999) argued that one possibility is that a simultaneous release of electrons and holes may take place in the same temperature range, or that a series of traps exist that release electrons and holes resulting in radiative recombinations at *F*-, F^+-, and Cr^{3+}-centres. According to Surdo *et al*., (2004), at least three types of traps empty thermally in the temperature range of the 200 °C peak of additively coloured α-Al_2O_3 crystals and a simultaneous release of electrons and holes can take place within the range of the low temperature side of the TL peaks (i.e., 90-200 °C), resulting in the formation of defect-bound excitons at F^+- and *F*-centres (i.e., $e^0_{F^+}, e^0_F$) and luminescence according to equations 4.16 and 4.17. The high temperature part of the peak between 170 and 210 °C is related to recombination of electrons at F^+-centres that were freed from traps with an optical depth of ~ 2.8 eV (Equation 4.16).

$$F^+ + e^0_{F^+} \rightarrow (F^+)^* \rightarrow F^+ + hv\,(3.8\ eV) \qquad (4.16)$$

$$F + e^0_F \rightarrow F^* \rightarrow F + hv\,(3.0\ eV) \qquad (4.17)$$

Identification of traps

An understanding of the luminescence mechanisms requires knowledge of both the traps and the recombination centres and their environments in the material. While the main recombination centres involved in the TL and (OSL) emission processes of α-Al_2O_3 crystals have more or less been determined, the origin, identity, and the distribution of traps, have not been fully identified. Pickard and Davis (1970) carried out thermally stimulated conductivity (TSC) measurements using polycrystalline and single crystalline alumina materials. By looking at the number of the

TSC peaks they concluded that polycrystalline materials contain several discrete traps with a trap density about an order of magnitude higher than that in single crystals.

As for the origin of the traps, Akselrod and Kortov (1990) had suggested that the 420 nm emission of the dosimetric peak in α-Al_2O_3:C single crystals is due to traps created by carbon impurities, but this is unlikely given that the emission due to *F*-centres is observed in similar TL peaks of undoped or samples doped with different impurities. Springis *et al*., (1995) also discussed the type of traps in Al_2O_3 from which electrons are thermally stimulated to produce the *F* emission of the 160 °C TL peak (the heating rate used by each researcher may result in the appearance of the main peak at temperatures lower or higher than 200 °C). For crystals growth under reducing conditions it was proposed that the electron traps are associated with hydrogen or acceptor impurities such as Ca, Mg, Na, K.

Finally, a review of a number of experimental studies conducted to identify the traps involved in several low and high temperature TL peaks has been given by Summers (1984). The author discusses the influence of growing conditions (i.e., redaxion/oxidation history) on the spectral properties of the TL peaks in single crystals of alumina, but due to confounding results he does not reach explicit conclusions regarding the identity of the traps. However, in agreement with the findings of Flerov *et al*., (1995), it appears that the TL peaks in oxidized corundum samples are associated with the release of holes from different types of *V*-centres, while those in reduced samples are attributed to electron traps.

4.7.2 OSL spectral emission characteristics

OSL spectrally resolved experiments have also been conducted (e.g., Bailiff and Clark, 1999; Denis *et al*., 2011; Markey *et al*., 1995; Pagonis *et al*., 2013; Rodriguez *et al*., 2011; Yukihara and McKeever, 2006) with dosimetry grade α-Al_2O_3:C crystals or analogous materials, such as Mg-doped α-Al_2O_3:C that was also proposed for personal dosimetry. The spectral components of the OSL emission were examined in CW-OSL, POSL, and TR-OSL modes of excitation. In CW-OSL spectroscopy the luminescence emission is monitored throughout stimulation, usually, with conventional light sources (e.g., green/blue LEDs) of constant intensity (Bøtter-Jensen., 1997;

Yukihara *et al*., 2011). POSL spectra are obtained between short duration laser pulses (Bøtter - Jensen, 1997; McKeever and Akselrod, 1999). In the course of a TR-OSL experiment the radiative emissions are detected during and between short pulses of stimulation provided by high power laser sources. With POSL and TR-OSL not only the wavelength range but the relaxation lifetimes of the emissions can be extracted. Temporal discrimination of emission bands with different lifetimes is better achieved by means of TR-OSL (Yukihara *et al*., 2011).

Whichever the method used, the reported conclusions are in an excellent agreement in that the OSL spectra exhibit emissions characteristic of the fast (< 7 ns) relaxation decay of the F^+-centres and of the slower (~ 35 ms) *F*-centre luminescence. More intense UV emissions at ~330 nm due to F^+-centres were observed for the α-Al_2O_3:C,Mg crystals due to enhanced F^+-centre concentration induced by the magnesium atoms. An example of the CW-OSL spectra of beta-particle irradiated α-Al_2O_3:C and α-Al_2O_3:C,Mg crystals during stimulation with 540 nm light is shown in Figure 4.6.a. As seen, the F^+ band of α-Al_2O_3:C is relatively weak in the CW-OSL and in the TR-OSL (Figure 4.6.b) spectra acquired between a series of pulses (channel B) possibly due to the very fast lifetime of the process and the very strong *F* emission. Nevertheless, it is clearly detected in the TR-OSL spectra obtained during laser pulses (channel A).

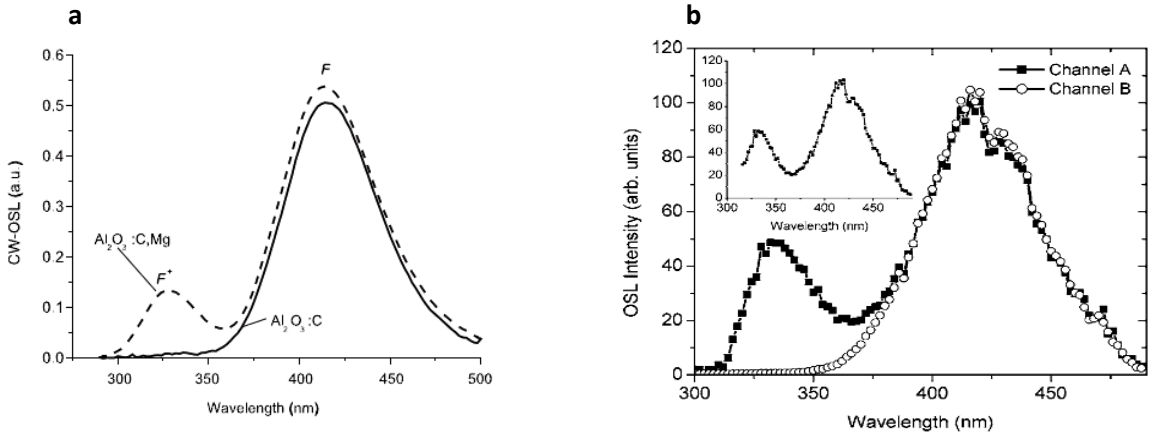

Figure 4.6: (a) CW-OSL emission spectrum for α-Al_2O_3:C, and α-Al_2O_3:C,Mg single crystals measured following beta irradiation and stimulation with a 540 nm light source (reprinted from Denis *et al*., 2011). (b) TR-OSL emission spectra of gamma-irradiated α-Al_2O_3:C single crystals detected during (channel A) and between (channel B) laser pulses from the 532 nm line of a Nd:YAG laser. Reprinted from Yukihara and McKeever (2006).

A similar mechanism that involves optical release of electrons from electrons traps was suggested to explain the OSL emission of the *F*-centres. However, and as explained above, an electron trap model cannot account for the F^+-centre emission. In this case the simultaneous release of electrons and holes may be assumed which also involves transfer of energy between the *F* - the F^+-centers (McKeever *et al.*, 1999; Yukihara and McKeever, 2006).

4.8 Conclusions

Complex processes participate in the production of luminescence in anion deficient α-Al_2O_3 materials. More is known about the recombination sites as revealed by the characteristic wavelengths of the luminescence emissions than about the trapping states. Generally, the luminescence phenomena are controlled by structural defects; the nature and concentration of which depend on the sample and growth variables. Of the different types of defects, oxygen vacancies are considered the most important constituents for the production of luminescence in alumina materials. These lattice point defects may be found naturally in the crystal structure (non-stoichiometry effect) but primarily are related to the growth and fabrication conditions and the presence of impurities.

α-Al_2O_3:C single crystals that are specifically produced for applications in dosimetry contain high concentrations of oxygen vacancies arising from the combined effect of high temperature treatment and carbon doping. The formation of *F*-type colour centres by electron capture at oxygen vacancies has been found to be responsible for the high TL and OSL sensitivity of α-Al_2O_3:C detectors. It has been established that the commonly detected luminescence emission in alumina single crystals is the *F* band in the blue region (~ 420 nm) of the electromagnetic spectrum. A weaker broad band in the UV (~ 330 nm) due to the F^+-centres and a sharp emission at ~ 695 nm characteristic of Cr^{3+} ions commonly present in alumina compounds have also been reported. The detection of these emissions seems to depend only on the properties of the material since they have been identified using a wide range of spectroscopic techniques and different modes of excitation (e.g., UV-, β -, γ - , x- rays).

The spectral emission characteristics of the main TL peak (~ 160-200 °C) and the CW-OSL decay curve of α-Al_2O_3:C also coincide with *F* band emission. Electrons from traps of (yet) unknown origin are thermally or optically stimulated and recombine at F^+-centres producing luminescence centred at ~ 420 nm. On the other hand, in undoped (i.e., ´´pure´´) materials the UV (~ 330 nm) and the Cr^{3+} (~ 695 nm) bands dominate the luminescence emission spectra. This would be expected on the basis of a lower oxygen vacancy and F^+-centre concentration, a possibly higher concentration, and the use of less pure powders with higher concentration of Cr^{3+} impurities. Lower TL/OSL yields are also expected for pure aluminas due to lower concentration of recombination centres while the long wavelength emission of Cr^{3+} is not be efficiently detected by commonly used instruments.

Currently, only a small volume of luminescence studies for polycrystalline sintered alumina has been published. In the polycrystalline, not purposely doped α-Al_2O_3 materials, it is assumed that small amounts of sintering additives based on divalent metal oxides (e.g., MgO and CaO_2) account for the creation of oxygen vacancies and, hence, of the luminescent centres. Structural defects such as grain boundaries and pores are also expected to play an important role, not only in the transport mechanisms of defects, but also in the total trapping environment. The various types of emission spectra (e.g., TL, OSL, RL) of alumina substrates are expected to be dominated by the F^+- and the Cr^{3+}- bands and the TL or OSL efficiency is anticipated to be even lower owing to the complex microstructure and the opacity of sintered aluminas.

This Chapter has introduced some key concepts and factors influencing the process of luminescence emission in different variants of alumina materials. In the context of previous experimental and theoretical studies, it has been demonstrated that luminescence emission in crystals is significantly controlled by the types of defects (intrinsic- and impurity-related) created during the fabrication process. It was additionally discussed that the production of luminescence may also be affected by the arrangement of the different phases within a crystal (i.e., microstructure). These data together with well-established microscopy, spectroscopy, and analytical techniques will be used to address particular research questions of the present thesis. Specifically, it will be examined in Chapter 6 how the microstructure and the elemental composition influence the generation process of luminescence in sintered polycrystalline alumina

substrates. In addition, the potential influence of the physical characteristics of the sintered alumina substrates on dosimetry properties will be addressed.

Part II: Characterisation of sintered alumina

Chapter 5: Methodology

5.1 Introduction

This Chapter introduces the samples, measurement techniques, instrumentation, as well as, theoretical approaches employed in characterising the luminescence characteristics of sintered alumina substrates.

5.2 Description of samples

The basic research material utilised in this study is known commercially as a surface-mount chip resistor. This is a passive electronic component used in various electronic devices (e.g., mobile phones, personal computers). SMRs are, generally, abundant in printed circuit boards (PCB), but smaller quantities may be found in other parts of the electronic circuit. Figure 5.1 shows part of a PCB of a mobile phone with two SMRs indicated in red circles.

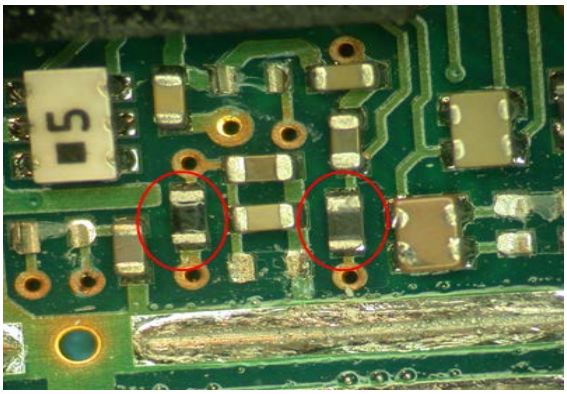

Figure 5.1: Part of a printed circuit board of a mobile phone. The presence of surface mount resistors is indicated with red circles.

The design of a typical SMR is illustrated in Figure 5.2. A high purity (~ 96% Al_2O_3) white alumina substrate is used as the host body, upon which the resistive element is deposited. The top black surface of the SMR was found to have very low TL and OSL sensitivity compared with the

bottom white surface which is almost uncoated and, therefore, used for all measurements. SMRs are manufactured according to several standard sizes (Table 5.1), but those most commonly encountered in personal electronic equipment, and particularly in mobile phones have typical dimensions of 1.0x0.2x0.35 mm (i.e., type ´0402´) or smaller.

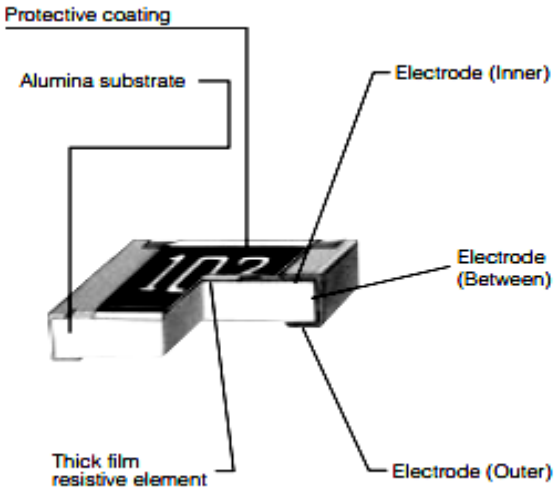

Figure 5.2: Construction of a typical surface-mount chip resistor. Obtained from Panasonic datasheet.

Table 5.3: Standard dimensions of different types of surface-mount chip resistors.

Resistor type	**Dimensions mm (length×width×thickness)**
0201	0.6×0.30×0.25
0402	1.0×0.50×0.35
0603	1.6×0.80×0.45
0805	2.0×1.25×0.60
1206	3.1×1.55×0.60

Samples of surface-mount resistors obtained both as unused components from different manufacturers and components extracted from discarded mobile phones were used throughout this study. Mobile phones of both ´old´ and ´advanced´ (i.e., smartphones/touch screen devices) technology manufactured by different companies were examined to obtain a rough idea of the

number and sizes of the SMRs in the PCB. The general characteristic of the PCB of ´old´ generation mobile phones is the presence of a large number (~ 30) of type ´0402´ SMRs and a smaller amount of larger resistor types (e.g., ´0805´). Smartphones were found to have a relatively smaller amount (≤ 20) of type ´0402´ SMRs and approximately an equal quantity of smaller resistors (type ´0201´). Exceptions to these limits were, of course, detected in a number of mobile phones.

Initially, a wide range of SMRs of variable physical size was investigated. Qualitatively, all were found to have similar microscopic, spectroscopic and elemental characteristics, whereas the luminescence sensitivity was found to be quite dissimilar. Taking into account these facts, it was decided that, with exception of the studies related to the dosimetry characteristics where mostly type ´0402´ resistors were used, some of the TL/OSL and spectroscopic measurements would be carried out using larger resistor types (i.e., ´1206´). This helped to reduce the amount of the delivered dose and, therefore, minimise possible dose-related sensitisation effects (i.e., increase in luminescence sensitivity). Generally, the results are presented as average values using samples of varying number of resistors. Where necessary, for quantitative comparison of experimental data, the number of resistors per sample will be defined.

Dosimetry-grade Al_2O_3:C chips (Laundauer Stillwater Crystal Growth Division, Stillwater, OK, USA) in the form of discs of ca ~ 5 mm diameter cut from single crystal rods were also employed in the initial stages of the project.

5.3 Sample preparation

5.3.1 TL/OSL with chip components

The samples used for TL and OSL measurements were analysed without any special preparation treatment. Nevertheless, those resistor components extracted from mobile phones were immersed into dichloromethane (DCM) for a few minutes to remove most of the solder paste used to attach the resistors to the PCB. Without this treatment the white ceramic substrate was found to turn

black as the solder paste melted during TL readout to 500 °C, which could potentially reduce the sensitivity of the samples.

The alumina resistor components were placed directly into sample carriers in the form of ~ 12 mm diameter cups made of nickel alloy (Figure 5.3a). A thin layer of silicone oil was deposited on to the cups to keep the samples fixed during the various stages of measurement. The potential influence of silicone oil on the luminescence of the samples was tested separately by comparing the TL and OSL signals between cups with silicone oil and clean cups. It was found that silicone oil did not produce a spurious signal that interfered with the TL and OSL from alumina components.

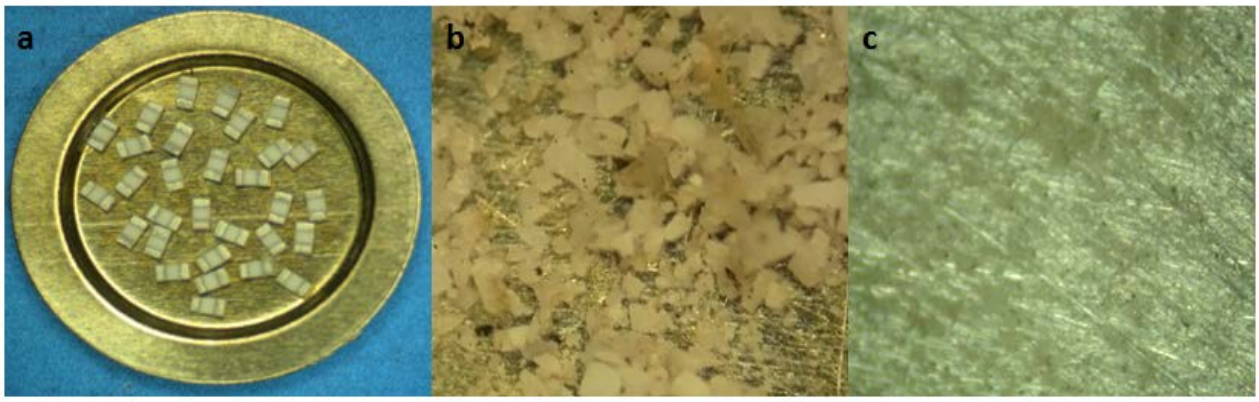

Figure 5.3: (a) The majority of TL and OSL experiments was performed using SMRs samples placed in nickel cups. The phenomenon of temperature lag was investigated using (b) coarse grains (> 20 μm) of the alumina substrate part of SMRs, and (c) powder consisting of 2-10 μm grains deposited onto aluminium discs.

5.3.2 TL analysis using fine grains from chip components

The difference in the temperature between the heating element and the actual temperature of the sample (i.e., thermal lag) can have a significant effect in the accurate determination of the trapping parameters of luminescent materials (e.g., Kitis and Tuyn, 1999). It was also suggested (Jain *et al*., 2008) to be responsible for the appearance of a build-up region in the isothermal or phosphorescence decay curves. The effect of temperature lag, however, is expected to be less

pronounced in thin solid samples and coarse or fine grain samples due to improved contact with the heater plate. To investigate the effect of temperature lag, fine grain preparation technique (Aitken, 1985) was employed in this study.

A number of type ´1206´ resistors were initially etched using aqua regia to remove the contacts from the top, bottom, and side surfaces of the alumina substrates. The top surface of the components was further processed to remove the ruthenium oxide layer and the polymer coating that were found to be resistant to aqua regia. The clean components were then roughly crushed using a mortar and pestle to obtain a small amount of coarse grains with grain size greater than 20 μm (Figure 5.3b). The remaining sample was further crushed to produce a uniform powder. The powder was placed into a glass test tube, filled with acetone up to ~ 6 cm, and left to settle for 2 minutes to separate the grains larger than 10 μm. After 2 minutes the material suspended in the tube was poured into a second glass tube and allowed to settle for another 20 minutes during which grains with size lower than 2 μm are expected to suspend in the tube. This material was poured into a third tube and left at RT to evaporate the acetone.

The second tube with the remaining material (i.e., grain size: 2-10 μm) was filled with acetone, shaked well to give a uniform mixture, and deposited using a pipette onto flat bottom tubes containing on the base ~ 10 mm diameter aluminium discs (Figure 5.3c). The discs had been previously roughened with abrasive paper to create suitable surface for the deposition of fine grains and washed in methanol to remove any residue. Finally, the prepared discs were placed into the oven at 40 °C and left overnight to evaporate the acetone.

5.3.3 SEM microscopy and spectroscopy

The samples used in SEM studies, to examine the surface morphology, chemical composition, and emission spectra of the alumina substrate were optically polished using standard techniques. To obtain optically polished flat surfaces, the samples were mounted on resin blocks, ground on rotating wheels with silicon carbide papers of different grit size (P800 and P1200) and polished mechanically by means of diamond abrasives of decreasing grain size (6 μm and 1 μm). To ensure that the surface was free from residual polishing paste, the samples were washed in

methanol. In the final stage of preparation, the samples were inserted into a Cressington model 207 carbon coater and coated with a thin conducting layer (< 20 nm) of carbon in order to reduce the charging effect of the surface. Unpolished samples were also examined.

5.4 Physical characterisation and cathodoluminescence spectroscopy

Characterisation of the microstructure of the surface of resistor alumina substrates was carried out using an SEM featuring additional specialised detectors for collection of cathodoluminescence (CL) emission spectra. Analysis of the elemental composition of the bulk and the surface was also performed by means of energy dispersive spectroscopy (EDS) and wavelength dispersive spectroscopy (WDS) using x-rays detection systems available in the SEM.

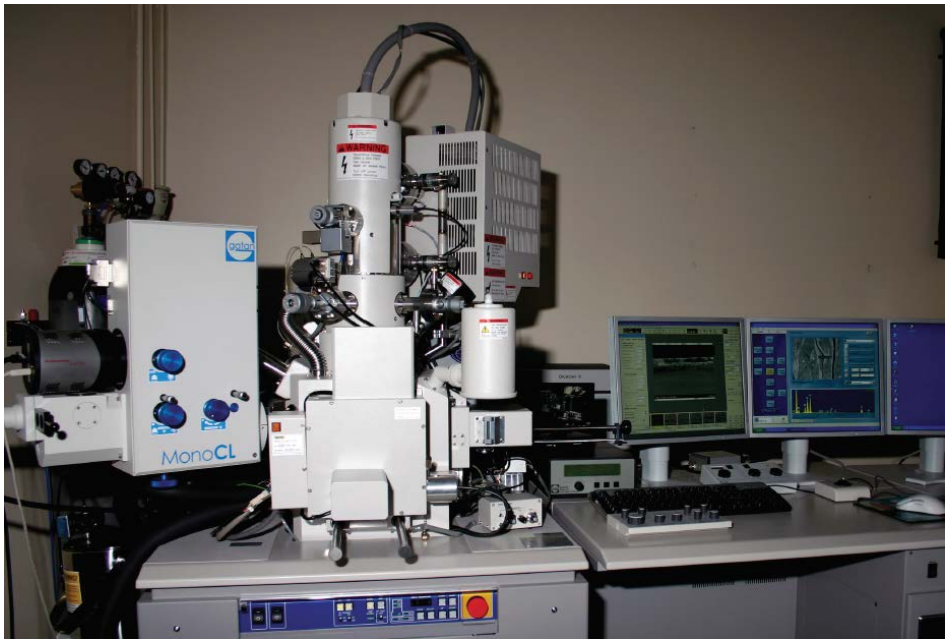

Figure 5.4: Photograph of the Hitachi SU-70 FEG SEM at the GJ Russell Microscopy Facility at Durham University.

The instrument used was a Hitachi SU-70 field electron gun (FEG) SEM at the GJ Russell Microscopy Facility at Durham University (Figure 5.4) which is an ultra-high resolution instrument that produces focused electron beams (accelerating voltage: 0.5-30 kV, probe current: >150 nA) by a Schottky field emission electron gun. The instrument is equipped with an in-column secondary electron detector, a retractable backscattered electron detector, an Oxford Instruments energy dispersive x-ray system (INCA x-act LN_2-free Silicon Drift detector), an Oxford Instrument wavelength dispersive x-ray spectrometer (INCA-Wave 700) and a Gatan MonoCL3 cathodoluminescence system. The basic components of the MonoCL3 system are: (1) retractable diamond turned parabolic mirror with 1 mm aperture, (2) Czerny-Turner monochromator, (3) standard PMT (spectral range: 185-850 nm), (4) Pixis CCD camera, (5) beam control and image processing Digiscan system, and (6) filter housing with circular 1 inch diameter colour filters.

5.5 X-ray excited emission spectroscopy

Luminescence emission spectra were also obtained as a function of temperature from -250 to 400 °C in response to continuous x-ray irradiation, radioluminescence (RL)..

The spectrally resolved RL was measured on a system at the University of St Andrews (Facility for the Luminescence of Minerals) based on the system that was originally designed at Sussex by Luff and Townsend (1993). The main components of the system are shown in Figure 5.5. The RL instrument consists of (1) an x-ray generator emitting Cu Ka x-rays at 10 Gy min^{-1}, (2) a UV-blue (250 - 550 nm) spectrometer on the left, and (3) a blue-green-red (380-850 nm) spectrometer on the right. The blue-green-red spectrometer runs with a 400 nm long pass filter to remove second order effects in the UV-blue. The spectrometers work as high-sensitivity image plates onto which sample luminescence is diffracted, producing a strip across the image plate. The signal (counts against wavelength) is obtained from the image by integrating the counts vertically down the plate in the central region. Independent system corrections are applied to the data from each spectrometer giving data that overlap and should, in principle, match in the centre. A cryostat sample holder (4) and a high temperature (not shown in Figure 5.5) sample

holder are available in the system. Sample heating is performed linearly at a constant heating rate of 10 K min^{-1}.

Figure 5.5: Photograph of the RL/TL system at the Facility for the Luminescence of Minerals at the University of St Andrews. The basic components of the instrument are (1) power supply of x-ray generator emitting Cu Ka x-rays, (2) UV-blue (250-550 nm) spectrometer (3) blue-green-red (380-850 nm) spectrometer, (4) cryogenic sample holder. Courtesy of Dr Adrian Finch.

5.6 TL/OSL measurements – The Risø Reader

All TL and OSL measurements were performed at Durham University with a Risø TL/OSL Luminescence reader (model DA-12) designed and produced at Risø DTU National Laboratory, Denmark. A picture of a similar Risø TL/OSL reader (model DA-20) is shown in Figure 5.6. A light detection system, a thermal and optical stimulation unit, and a radioactive source are the

basic components of a Risø reader. A schematic drawing showing the main components is presented in Figure 5.7. A motor driven rotating carousel with maximum occupancy of 48 positions is used to accommodate the samples in the sample chamber which are usually placed in stainless steel discs or nickel cups. The chamber can be evacuated or maintained in a nitrogen atmosphere (Bøtter-Jensen *et al.*, 2003; Guide to the ´´Risø TL/OSL reader´´, 2013).

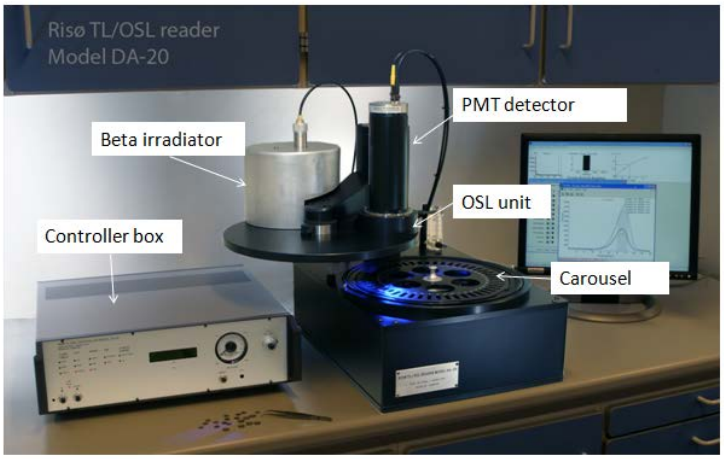

Figure 5.6: Photograph of a Risø TL/OSL Luminescence reader (model DA-20) showing the basic components. Modified from Guide to the ´´Risø TL/OSL reader´´ (2013).

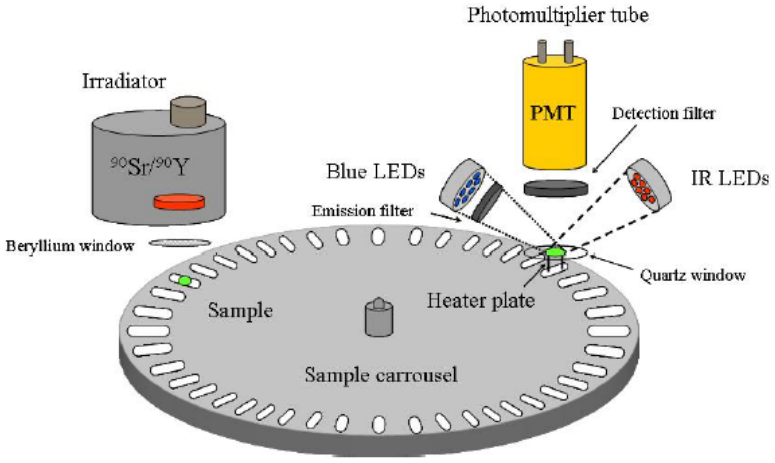

Figure 5.7: Schematic representation of the basic components of a Risø TL/OSL Luminescence reader. Reprinted from Guide to the ´´Risø TL/OSL reader´´ (2013).

Single photon light detection system

A PMT combined with suitable optical filters is used for the detection of the emitted luminescence. The installed PMT is a bialkali EMI 9235QA showing maximum detection efficiency in the wavelength range from 200 to 400 nm, although its response is extended to longer wavelengths (Figure 5.8). Shielding of the detector from scattered stimulation light is achieved using detection filters placed in front of the PMT photocathode. Depending on the energy of the stimulation light source different filters or filter combinations can be used. The Hoya U-340, Schott BG39 and Corning 7-59 are the standard filters in the Risø TL/OSL readers (Bøtter-Jensen *et al*, 2003; Guide to the ´´Risø TL/OSL reader´´, 2013). Their transmission characteristics are shown in Figure 5.9. Unless otherwise stated, the Hoya U340 filter (7.5 mm), with maximum transmission at ~ 340 nm, was used in the present investigation both for OSL and TL measurements.

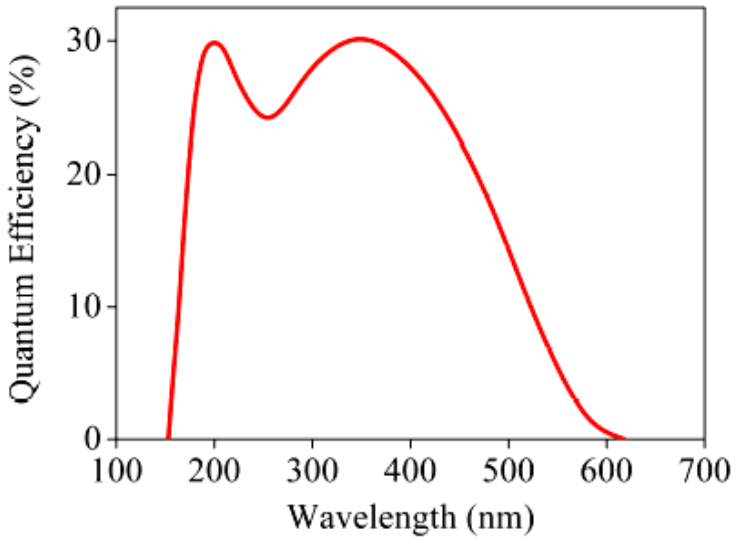

Figure 5.8: Graph showing the quantum efficiency of the PMT (EMI 9235QA) detector as a function of the photon wavelength. Reprinted from Guide to the ´´Risø TL/OSL reader´´ (2013).

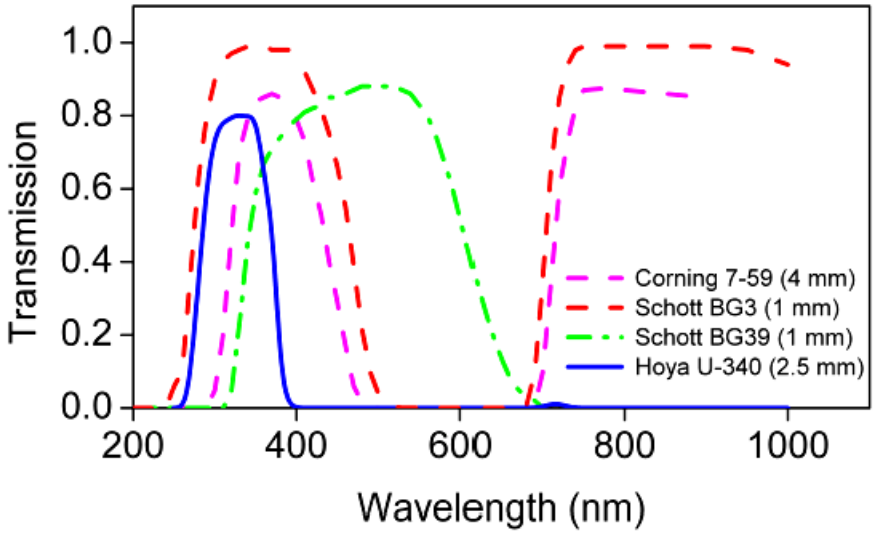

Figure 5.9: Transmission curves of the standard detection filters accompanying the Risø TL/OSL readers. Reprinted from Guide to the ´´Risø TL/OSL reader´´ (2013).

Luminescence stimulation units

Thermal stimulation was performed using a heater plate located below the PMT (Figure 5.7). The heating element, which is made of a high resistance alloy (i.e., Kanthal), is able to heat the samples from RT up to 700 °C at linear heating rates ranging from 0.1 to 20 K s^{-1}. Another function of the heating element is to lift the sample to the measurement position (Bøtter-Jensen *et al.*, 2003; Guide to the ´´Risø TL/OSL reader´´, 2013).

An alternating current passes through the heating element to enable heating. Feedback control of the temperature is accomplished by means of a low-mass Chromel-Alumel thermocouple located underneath the heater. A non-switching continuous full sine wave generator operating at 20 kHz is used to control heating. The heating process is usually performed in an atmosphere of nitrogen flow allowing cooling of the heating element and protection of the heating system from oxidation at high temperatures (Bøtter-Jensen *et al.*, 2003; Guide to the ´´Risø TL/OSL reader´´, 2013).

Optical stimulation is achieved using an add-on OSL unit consisting of arrays of blue and infrared LEDs placed below the PMT at a distance of ~ 20 mm above the sample. The blue LEDs emitting at 470 nm with a bandwidth, Δ, of 20 nm are usually arranged in four clusters each containing seven individual LEDs (i.e., 28 LEDs). The maximum intensity delivered to the sample from the 28 blue LEDs is approximately 30 mW cm^{-2}. In addition to the filters placed in front of the PMT, a CG-420 green long pass filter is incorporated in front each blue LED cluster reducing further the amount of directly scattered light from reaching the detector. IR light (870 nm Δ 40 nm) is delivered by an array of three clusters each containing 7 individual IR LEDs. The total intensity at the sample position from these 21 IR LEDs is approximately 145 mW cm^{-2} (Bøtter-Jensen *et al*, 2003; Guide to the ´´Risø TL/OSL reader´´, 2013). The emission characteristics of each LED source in combination with the transmission curves of the available filters are displayed in Figure 5.10.

Since the OSL unit is attachable to the system it can easily be removed for TL measurements. This is expected to decrease the sample to PMT distance and increase the TL sensitivity of samples. In fact, it was observed (Chapter 11) that the TL output of alumina substrates to a given dose increases by a factor of ten when the OSL unit was removed.

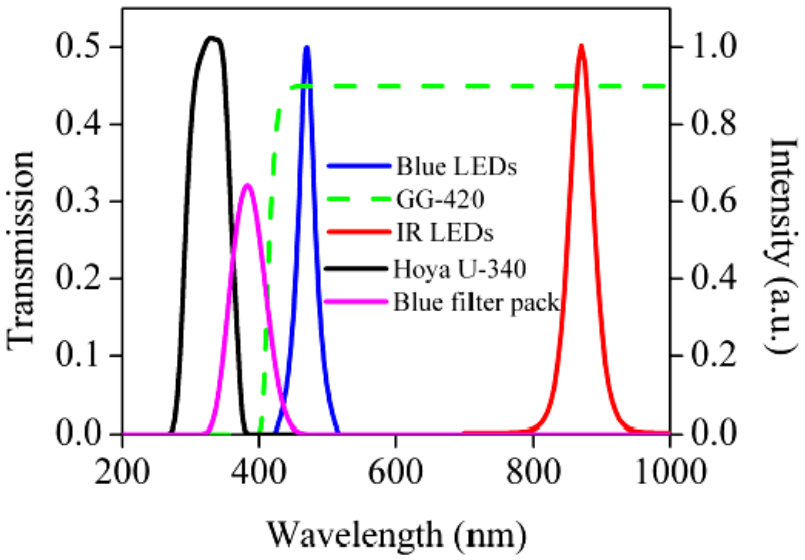

Figure 5.10: Emission spectra of the blue and IR LEDs displayed together with the transmission curves of the detection filters of the Risø TL/OSL readers. Reprinted from Guide to the ´´Risø TL/OSL reader´´ (2013).

Irradiation sources

The Risø TL/OSL reader at the Luminescence Dating and Dosimetry Laboratory, Department of Archaeology, Durham University is equipped with a beta source. The beta irradiator (Figure 5.6) is located above the sample chamber (~ 5 mm source-sample distance) consisting of a 1.48 GBq (40 mCi) $^{90}Sr/^{90}Y$ beta source emitting beta particles with a maximum energy of 2.27 MeV. The sample chamber is separated from the source by a beryllium window (0.125 mm thick) acting as a vacuum interface (Bøtter-Jensen *et al*., 2003; Guide to the ´´Risø TL/OSL reader´´, 2013).

In October 2011, the beta source delivered a dose rate to quartz grains (90-150 μm) at the sample position of 0.054 ± 0.002 Gy s^{-1}. The dose rate in substrate chips (type ´0402´ and ´1206´) was separately determined using the procedure described in Section 3.7 and found to be 0.04 ± 0.002 Gy s^{-1} (October 2012).

It is noted that except for the beta source of the Risø TL/OSL reader, additional radiation sources (i.e., x- and gamma-rays) available at Public Health England (PHE) facilities were employed for the irradiation of SMRs. The details of the radiation sources are given in the chapter where measurements are discussed.

5.7 Computational procedures

Radiation transport simulations

Monte Carlo methods are used for solving complex mathematical problems using repeated random processes. The Monte Carlo N-Particle Transport (MCNP) code developed by Los Alamos National Laboratory is often applied in radiation sciences to reproduce theoretically the transport and the interactions of nuclear particles (e.g. neutrons, electrons, photons). It does so by simulating the behaviour of each individual particle and by recording specific aspects, known as tallies, of their average behaviour. MCNP codes use cross-section data and physics models to give approximate solutions to the equations governing the particle transport through matter by simulating the particle history life from its emission from the source until all its energy has dissipated in the absorbing medium (MCNP5 Manual, 2008).

In this study, the MCNP Version 5 code was used for two purposes: (1) to validate the theoretically produced models of a SMR and a mobile phone through comparison with experimental data, and (2) to study the behaviour of SMRs as accident personal dosemeters by simulating an accident scenario where the suitability was tested through comparison between the absorbed dose to the alumina substrate and organ absorbed dose.

Simulations were generally carried out by considering photon irradiation in which electron generation and transport were also taken into account. This is known as the detailed physics treatment which assumes that all photon interactions (i.e., photoelectric effect, Compton scattering, pair production) except coherent scattering (i.e., interaction of photons with matter change the direction of the primary photons but does not reduce their energy) produce electrons whose transport and interactions are also included in the simulation process. This model, although it is computationally inefficient, provides more accurate estimates of the absorbed dose, especially for high energy photons. The simple physics model where electrons are produced as photons travel through matter but it is assumed that are locally deposited (i.e., kerma approximation) was also tested (MCNP5 Manual, 2008) and mostly employed in the voxel phantom calculations presented in Chapter 11.

Part III: Results

Chapter 6: Physical characterisation and luminescence spectroscopy of alumina SMRs

6.1 Introduction

While the dosimetry properties of the alumina substrates of SMRs have been investigated in a number of publications (e.g., Beerten *et al*., 2009, 2010; Ekendahl and Judas, 2011; Inrig, 2009) their physical form and the fundamental processes associated with the emission of luminescence have previously not been examined. Polycrystalline ceramics are expected to be structurally and compositionally distinctively different from the analogous single crystalline materials due to different manufacturing methods and conditions (Chapter 4). Nevertheless, their luminescence characteristics (at least, not all) may not differ considerably, depending on which defect states are actively involved in the emission process. As an example, the polycrystalline alumina substrates of SMRs and the single crystalline Al_2O_3:C dosemeters present similarities in their emission spectra (i.e., see Section 6.4 below) and the TL and OSL responses indicating, at first sight, that both materials share some common types of recombination and trapping centres. On the other hand, markedly different properties (e.g., athermal stability) can be found between the two materials (Akselrod, *et al*., 1993; Inrig, 2009) suggesting that the overall luminescence process (i.e., trapping, detrapping, recombination, and their competition) is controlled by various defects introduced in a material by the manufacturing process.

To begin investigating these issues certain microscopic and spectroscopic characteristics of alumina-based SMRs and Al_2O_3:C dosemeters (Laundauer Stillwater Crystal Growth Division, Stillwater, OK, USA) were compared using surface probing techniques available with a SEM. To characterise the morphology and microstructure of the outermost layers of the surface of polished and unpolished samples, energy- and wavelength- dispersive x-ray analysis methods (EDXRF and WDXRF respectively) were employed to determine the elemental composition of the materials. Cathodoluminescence and radioluminescence emission spectra were measured to study the nature of surface and bulk defects participating in the luminescence processes stimulated in the volume penetrated by the ionising radiation.

6.2 Scanning Electron Microscopy – Cathodoluminescence

6.2.1Surface Morphology – SEM Microscopy

The microstructure of the surfaces of polished and unpolished alumina substrate samples and dosimetry grade Al_2O_3:C crystals were evaluated using the secondary electron (SE) and backscattered electron (BSE) signals provided by the detectors attached to the SEM. The former (i.e., SE signal) is produced as a result of the inelastic scattering of the incident electron beam by weakly bound (valence band) electrons. They are low energy (0-50 keV) electrons, the emission of which originates a few nanometers below the surface of the specimen and are particularly useful for high spatial resolution imaging (Goldstein *et al*., 1981; Gucsik, 2009; Holt *et al*., 1974; Yacobi and Holt, 1990). Backscattered electrons are elastically scattered by the nuclei of surface atoms. These high energy (> 50 keV) electrons are mainly used for microscopic analysis providing compositional contrast information since the BSE coefficients depend strongly on the atomic number of the specimen. In BSE images, regions of high atomic number appear brighter compared to regions of low atomic number (Goldstein *et al*., 1981; Gucsik, 2009; Holt *et al*., 1974; Yacobi and Holt, 1990).

Selected SEM micrographs of the specimens, acquired with an accelerating voltage of 15 kV and electron probe current of 0.5 nA, are shown in Figures 6.1 and 6.2 for alumina substrates of SMRs and dosimetry grade Al_2O_3:C discs cut from single crystals, respectively. The images of the same regions show untreated surfaces (a, b) and polished surfaces (c, d) obtained in SE (a, c) and BSE (b, d) measurement modes. Figure 6.3 shows additional SEM images of the polished and unpolished substrate specimens acquired at a higher magnification (i.e., x2000). The SEM images shown are representative of a type ´1206´ SMR, although similar microstructural features were identified for the ´0402´ type SMR (Appendix A1); the type of SMR most commonly found in the PCB of mobile phones.

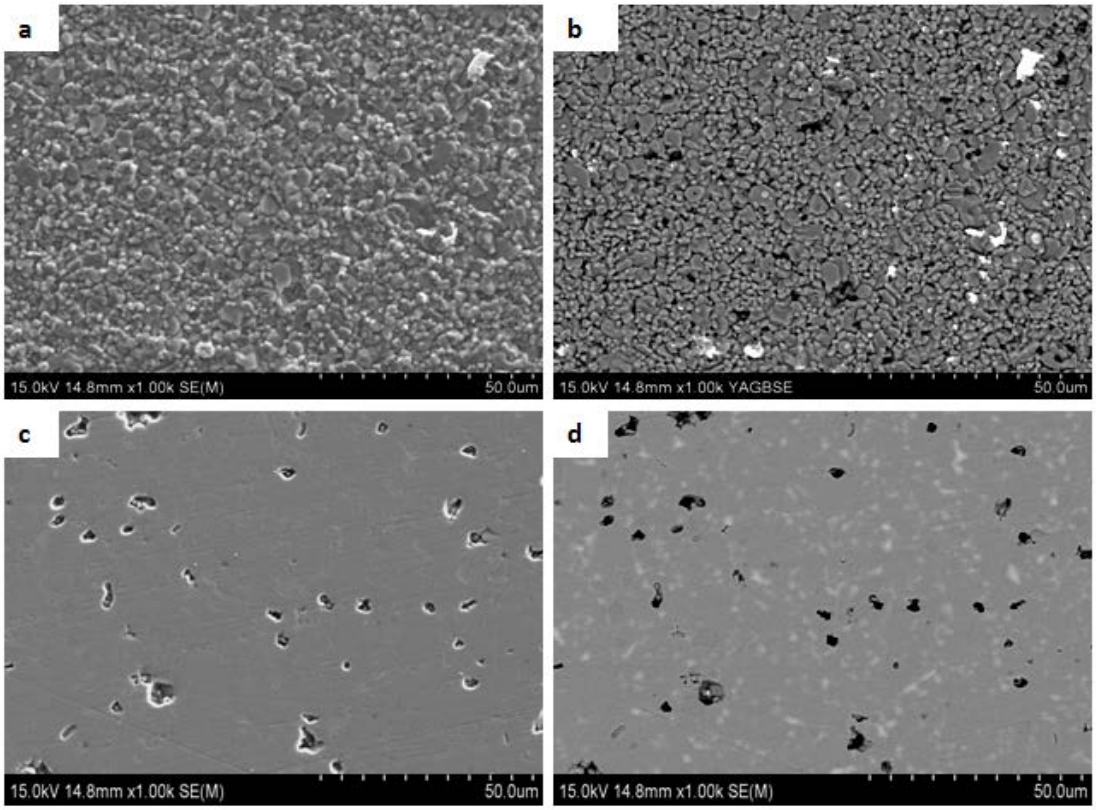

Figure 6.1: SEM micrographs of alumina resistor substrates recorded at x1000 magnification. The images of the same regions show untreated surfaces (a, b) and polished surfaces (c, d) obtained in SE (a, c) and BSE (b, d) measurement modes. The images which show the microstructure of a type ´1206´ SMR were acquired with an accelerating voltage of 15 kV and an electron probe current of 0.5 nA.

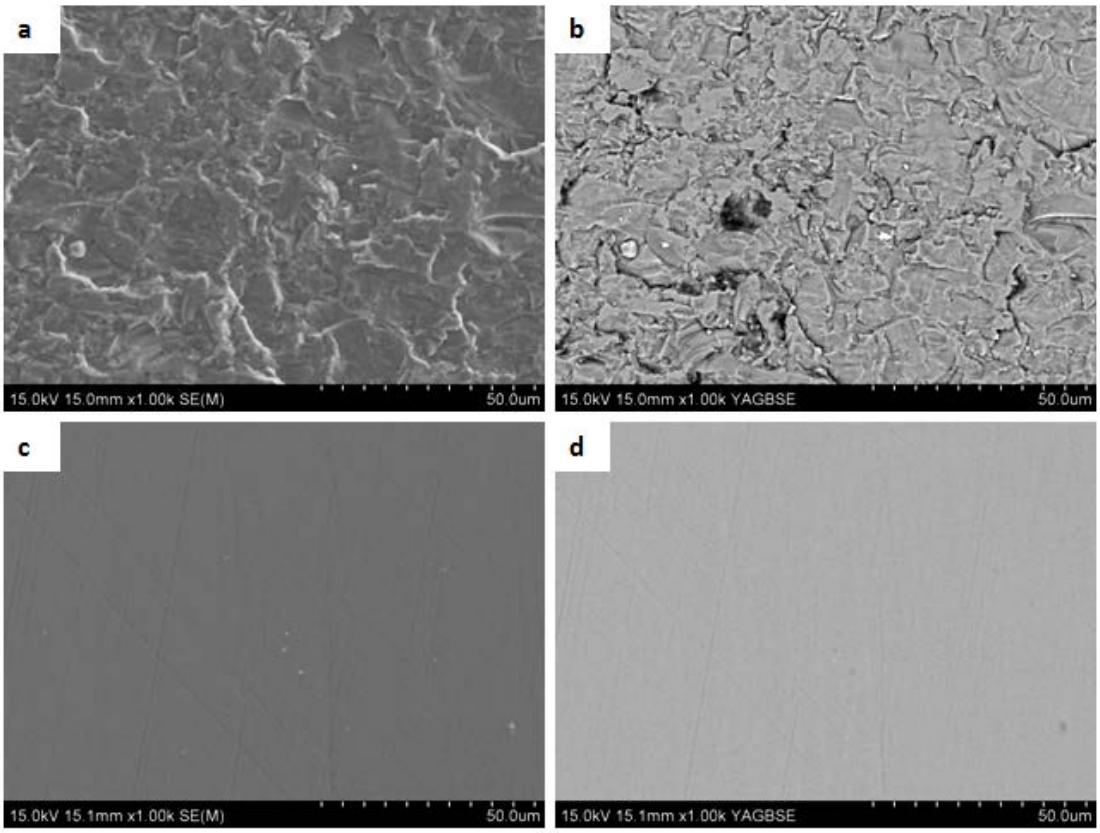

Figure 6.2: SEM micrographs of dosimetry grade Al_2O_3:C chip cut from single crystal (Laundauer Stillwater Crystal Growth Division, Stillwater, OK, USA) recorded at x1000 magnification. The images of the same regions show untreated surfaces (a, b) and polished surfaces (c, d) obtained in SE (a, c) and BSE (b, d) measurement modes. The images were acquired with an accelerating voltage of 15 kV and electron probe current of 0.5 nA.

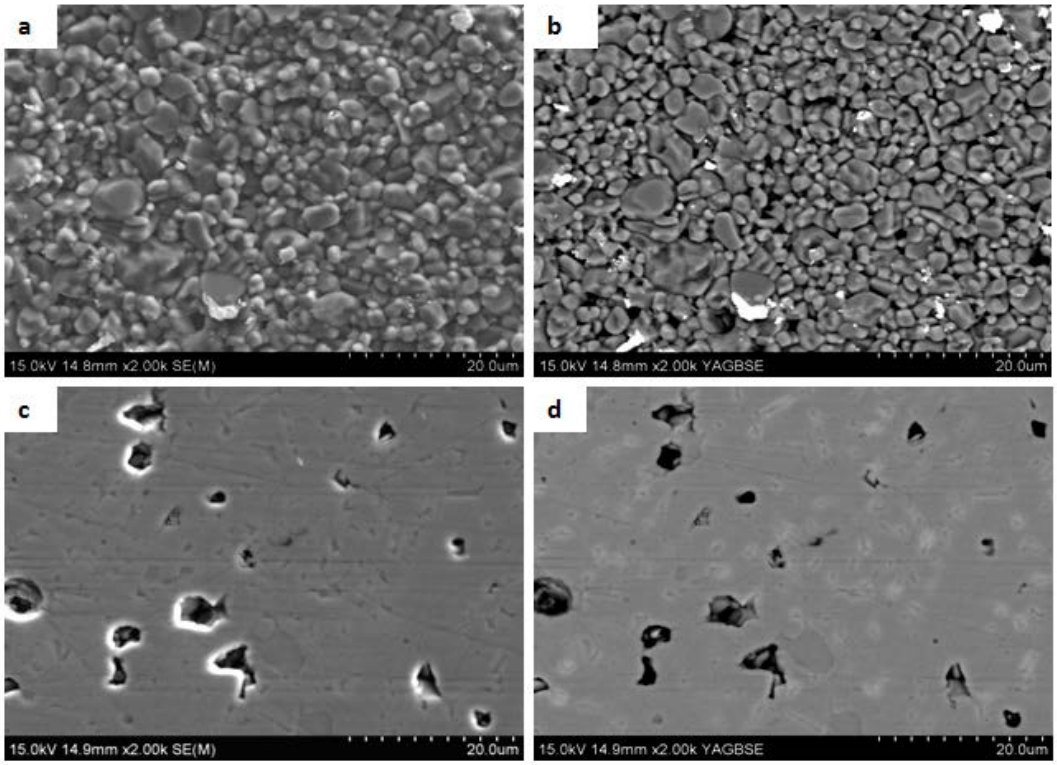

Figure 6.3: SEM micrographs of alumina resistor substrates recorded at x2000 magnification. The images of the same regions show untreated surfaces (a, b) and polished surfaces (c, d) obtained in SE (a, c) and BSE (b, d) measurement modes. The images, which show the microstructure of a type ´1206´ SMR, were acquired with an accelerating voltage of 15 kV and electron probe current of 0.5 nA.

The surface of the unpolished alumina substrates (Figures 6.1a,b and 6.3a,b) appears heterogeneous, consisting of irregularly shaped grains that are randomly oriented and grain boundaries and pores can also be identified in both the SE and BSE images, although the latter images provide better contrast and visualisation details of the grain boundaries and the pore distribution. The grain structure is less obvious in the surface of the polished sample (Figures 6.1c,d and 6.3c,d), but a random distribution of voids indicated by darker areas is revealed and bright spots can also be observed distributed across the sampled surface. Nevertheless, as observed later in section 6.2.3 using a different imaging mode (i.e., CL imaging), the same structural arrangement is, in fact, maintained both in the surface and in the bulk of the samples.

Contrary to the unpolished samples, the BSE images of the polished specimen display areas of different contrast which indicate variations in elemental concentrations.

The surface of the unpolished dosimetry-grade Al_2O_3:C (Figure 6.2a,b), supplied as a cut chip, does not present the grain morphology seen in alumina substrates and porosity is absent. After polishing, a flat homogeneous surface was obtained as shown in Figure 6.2c,d and comparison of the BSE image of both the polished and unpolished surfaces did not reveal significant compositional variation between the surface and the interior.

6.2.2 Elemental Analysis – ED/WD Spectroscopy

The elemental composition of the samples was analysed using the energy (energy dispersive spectroscopy, EDS) and the wavelength (wavelength dispersive spectroscopy, WDS) of the characteristic x-rays emitted from the samples under electron irradiation (beam voltage of 15 kV). Semi-quantitative elemental analysis confirmed that the dosimetry-grade Al_2O_3:C crystal was free of major impurities, with weight percent concentrations of 57% aluminium and 43% oxygen. Using a number of different SMR components obtained from various manufacturers it was found that the alumina substrate contained on average of 97% Al_2O_3 (i.e., 53% aluminum and 44% oxygen) and 3% of other oxygen compounds based on the elements Mg, Ca, and Si.

Chemical mapping of the alumina substrates was also performed to reveal the density distribution of selected elements throughout the scanned sample region. These measurements, however, were carried out using only the polished specimens, since the sensitivity of the technique relies on the use of flat, polished surfaces.

A typical BSE image of the alumina substrate that was used to carry out spot x-ray microanalysis is shown in Figure 6.4. Comparison of the BSE image with the maps of Al, Si, Ca, and Mg was used to elucidate the location of the elements. X-ray analysis in the lighter-coloured areas (e.g., Position 1) revealed the presence of the elements Ca and Si as additional major constituents. The darker regions (e.g., Position 2) were found to have high Mg content. Also, there were areas (e.g., Position 3) where minimum concentrations of Mg, Si, and Ca were found. It is clear that the impurity concentrations are highly heterogeneous and this may be a consequence of Mg, Ca,

and Si being spatially distributed along grain boundaries as observed in previous studies of sintered alumina substrates (Soni *et al*., 1995; Altay and Gulmun, 2003).

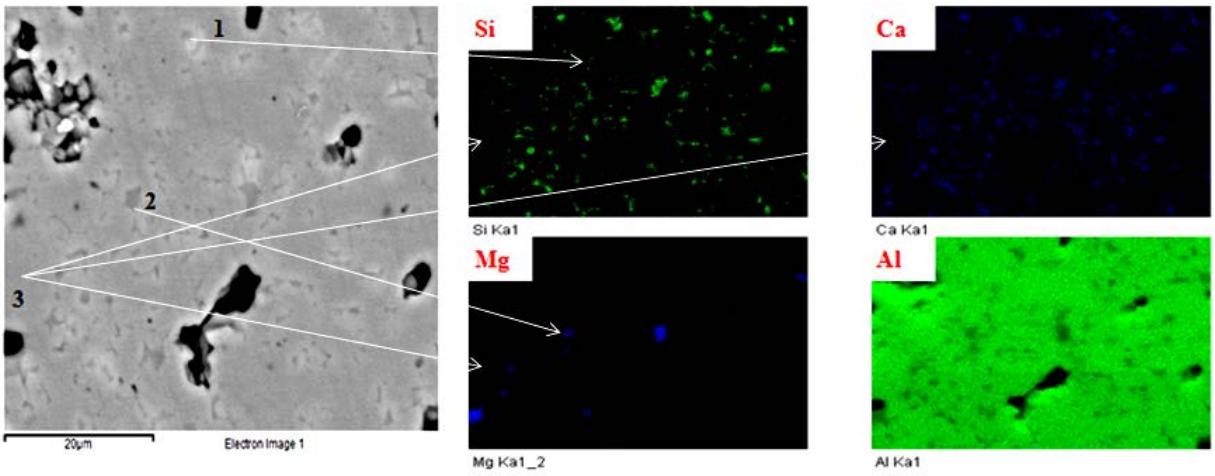

Figure 6.4: Electron image and element maps (Al, Si, Ca, and Mg) of the polished alumina substrate sample. Ca and Si were found to be the major impurities in the lighter-coloured areas (e.g., Position 1). The darker regions (e.g., Position 2) were found to have high Mg content, whereas the minimum concentrations of Mg, Si, and Ca were found in areas such as those indicated by Position 3.

6.2.3 Cathodoluminescence Spectroscopy

CL emission spectra were collected at RT using a coupled MonoCL3 (Gatan Ltd, Oxford) scanning monochromator that incorporates a PMT detector (Hamamatsu R374) operated in single photon counting mode and a 1200 lines/mm diffraction grating; the entrance and exit slits of the monochromator were set to 5 mm (30 nm FWHM). All spectra were acquired with an acceleration voltage of 10 kV, a step size of 0.5 nm, and a dwell time of 1 s and corrected for the instrument reponse. It is noted that the uncertainties in the reported wavelength values reflect fitting errors.

A typical CL emission spectrum of a polished dosimetry-grade Al_2O_3:C crystal is shown in Figure 6.5a. The spectrum contains two emission bands centered at ~ 3.69 ±0.04 eV (~ 336 ± 5 nm) and ~ 2.97 ± 0.05 eV (~ 417 ± 6 nm). In contrast, the CL spectral emission for the polished

Al_2O_3 substrate (Figure 6.5b) contains a broad distribution of emission extending from ~ 2.4 to ~ 5 eV (~ 250 to ~ 450 nm) and a narrow band centered at ~ 1.78 eV (~ 697 ± 4 nm) shown in the inset to Figure 6.5b. The form and width of the spectrum in the blue-UV suggests that it comprises several component bands. Measurements with a smaller band pass indicated the presence of an emission band at ~ 4.13 (~ 300 nm) and a combination of bands located at ~ 4.08 ± 0.71 eV (~ 304 ± 5 nm), ~ 3.63 ± 0.43 eV (~ 342 ± 5 nm) and ~ 2.92 ± 0.11 eV (~ 425 ± 3 nm) were indicated by fitting the spectrum using deconvolution software. The above values of the central wavelength of the emission bands are the mean values obtained from the deconvolution process using a number of alumina substrate samples and the uncertainties represent the standard deviation of the mean.

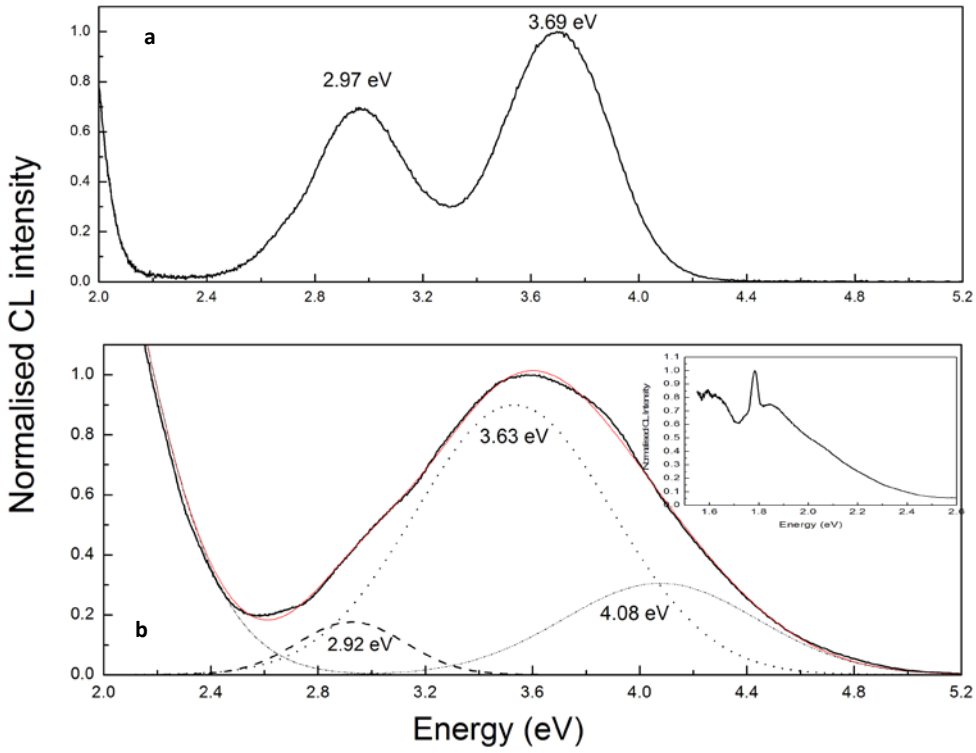

Figure 6.5: Normalised CL spectra of polished (a) Al_2O_3:C dosimetry-grade chip and (b) alumina substrate (i.e., type ´1206´ SMR) samples. The three bands at ~ 2.92, ~ 3.63, and ~ 4.08 eV obtained by fitting the spectrum using deconvolution software are also shown. The inset shows the spectrum recorded in the interval 1.5-2.5 eV with a red band-pass filter interposed to suppress the second order diffracted light. The spectra were measured with an electron beam voltage of 10 kV and corrected for the instrument response.

CL spectra of unpolished alumina substrate samples (not shown) revealed the same emission features indicating that mechanical surface treatment (i.e., polishing) did not introduce additional defects on the surface of the samples.

6.2.4 Cathodoluminescence imaging

Cathodoluminescence imaging is a valuable capability of the SEM-CL technique that can be used to obtain information about the spatial distribution of the luminescence emission either in the entire spectral range of the detector (i.e., panchromatic mode) or at fixed wavelengths (i.e., monochromatic mode). In addition, details about the morphological origin of the emissions can be obtained when the detector operates in the monochromatic mode.

Figures 6.6a and b show the panchromatic CL images of the polished specimens, indicating the total luminescence emission from the scanned sample area (i.e., panchromatic images). The surface of the dosimetry-grade Al_2O_3:C crystal is characterised by uniform light emission, with some areas appearing brighter where deep scratches have been induced by mechanical polishing. The alumina substrate presents areas of variable brightness. Some regions appear brighter, mainly those associated with small grains, while areas formed by the union of several grains display a reduced light intensity. Dark areas in the image are also observed across the surface, indicating regions of reduced luminescence emission.

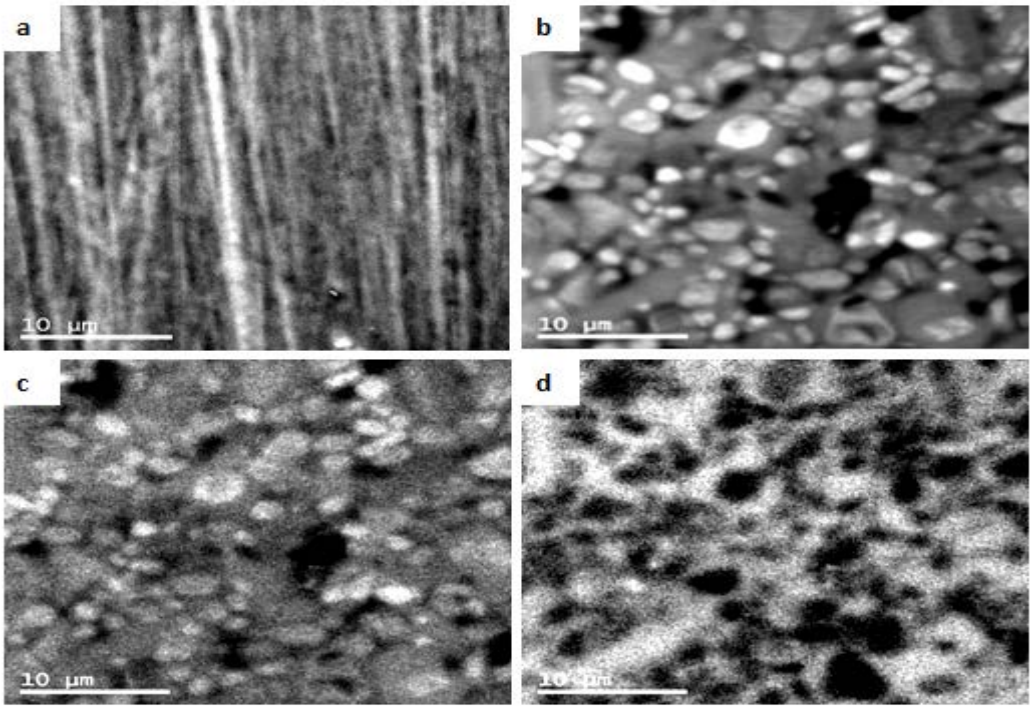

Figure 6.6: Panchromatic CL images of (a) Al_2O_3:C dosimetry-grade chip, and (b) alumina substrate, and monochromatic CL images of the alumina substrate measured at (c) 340Δ30 nm and (d) 394Δ30nm.

Monochromatic images of the same area were also obtained (Figure 6.6b,c) by adjusting the monochromator to pass wavelengths within the selected emission band. It appears that the emission from small grains is dominated by the UV band, whereas the more extended structural features are correlated with the blue band.

6.2.5 Discussion

Morphology

The structural arrangement of the surfaces is substantially different between the two forms of alumina-based materials, in particular, the existence of porosity in the alumina substrates which is likely to arise from the low temperatures applied during the sintering stage of the synthesis process. Apart from the mechanical properties (e.g. hardness, toughness) which are greatly

controlled by the density, grain size, porosity, and the nature of the additives, optical properties are also affected by the structural parameters of the ceramic body. For instance, the polycrystalline alumina substrates are significantly more opaque than the dosimetry grade Al_2O_3:C crystals. Opacity in polycrystalline ceramics is caused when incident light passing through the material undergoes multiply scatterings as a result of changes in the refractive indexes at the grains, pores, grain boundaries and compound additives usually located at the grain boundaries (Carter and Nortor, 2007). The effect of porosity/opacity and therefore reduced light transmission is that in a luminescence measurement even though all stimulated volumes are actively involved, the light emitted may not be detected due to optical self-absorption and as a consequence the efficiency of light emission is affected. In addition, the existence of extended defects on the surfaces of the alumina substrates, such as grain boundaries and voids, may be associated with enhanced non-radiative recombination processes.

Elemental composition

As discussed further in Chapter 4, magnesium, silicon and calcium – identified as the main impurities of the alumina substrates – are known to be added as sintering additives during the manufacturing process. These impurity elements are added to facilitate sintering to theoretical density and to produce translucent specimens by eliminating discontinuous grain growth, suppressing pore-grain boundaries separation and decreasing the grain growth rate. Since alumina has a very limited solubility for most cations, these elements are expected to be found along the grain boundaries. Figure 6.4 indicated that Si and Ca are concentrated near the edges of grains, but Mg is mainly concentrated in a few small regions. Furthermore, comparison of the element maps showing the distribution of aluminium and magnesium atoms indicates that magnesium is in excess in the aluminium deficient locations. This can be expected to arise in cases where the concentration of the dopant is higher than the solubility limit such that Mg could substitute for the aluminium cations. Also, the presence of divalent impurities, such as Ca^{2+} and Mg^{+2}, has been found to affect the luminescence process in Al_2O_3 compounds (Chapter 4; Section 4.6), which, as explained below, could be the case in the alumina SMRs.

CL Spectroscopy

In previous studies (section 4.6) aluminium oxide materials have been found to exhibit two main luminescence emission bands, one at ~ 310-340 nm (3.65-4 eV) and one at ~ 410-420 nm (2.95-3.03 eV), which are attributed to the presence of F^+- and F- centres, respectively, and associated with intrinsic defects created by oxygen vacancies that have captured one electron (F^+) and two electrons (F). In dosimetry grade single crystals, the concentration of F- and F^+-centres is optimised by growing the material in a highly reducing atmosphere in the presence of carbon (Akselrod *et al*., 1990; McKeever *et al*., 1995). Using different alumina based materials it was found that the luminescence of the F-centres is more pronounced in the single crystalline (Sato *et al*., 1999) and carbon-doped materials (Akselrod and Kortov, 1990; Kristianpoller *et al*., 1998; Olster *et al*., 1994), whereas pure Al_2O_3 materials have a dominant ~ 310-340 nm band (Kristianpoller *et al*., 1998; Olster *et al*., 1994). Moreover, the presence of divalent elements such as Mg^{2+} or Ca^{2+} can cause the formation of $F_{cations}$-centres which produce luminescence at ~ 300 nm or ~ 4 eV (Kulis *et al*., 1981; Ghamnia *et al*., 2003) and also result in enhanced F^+ emission (Ghamnia *et al*., 2003).

The spectrum shown in Figure 6.6b indicates that the currently accepted model of recombination at F^+ and F intrinsic defect centres in Al_2O_3:C also applies to the alumina substrate. Nevertheless, the broad CL emission spectrum observed in the substrate suggests additional recombination sites have been created by the presence of impurities which may be the result of a modification of the local environment of F^+ (or F) centres. Moreover, since the CL spectrum is also dominated by emissions of wavelengths below 400 nm (or with energies above 3.1 eV), both an enhancement of the F^+-centre emission and the presence of $F_{cations}$-centres in the alumina substrate can also be suggested. The detection of both magnesium and calcium in the EDS-WDS measurements support this interpretation of the data.

The CL measurements also revealed a narrow emission band at ~ 1.78 eV (~ 697 nm) that is characteristic of emission associated with Cr^{3+} ion impurities (Chapter 4; Section 4.6). Although chromium was not detected in the previous EDS-WDS analysis, it can exist at trace quantities in the starting powder of aluminium oxide materials.

CL Imaging

Cathodoluminescence imaging of the polished substrate samples confirmed that the complex microstructure of the surface (i.e., grains, grain boundaries, and pores), seen mainly in the SE and BSE images of the unpolished sample, is maintained also in the bulk of the substrate (i.e., Figure 6.6). In addition, the segregation of emission type with grain size suggests a complex process of defect modification during the manufacturing process of these ceramics that is likely to have been influenced by the annealing applied during the sintering process. Compositional fluctuations between the smaller and the bigger grains could also be responsible for the spatial variation of the CL emission.

6.3 X-ray Excited Optical Luminescence

6.3.1 Radioluminescence spectroscopy

The optical emission characteristics of alumina substrate samples were also studied under continuous x-ray irradiation (i.e., radioluminesence) in the temperature range from -250 to 400 °C (10 °C s^{-1}) using the apparatus described in Chapter 5 (Section 5.4) and in Brooks *et al*., (2002) and Luff and Townsend (1993). The RL emission from the samples was detected separately in the UV-blue (200-450 nm) and the blue-green-red (380-800 nm) part of the spectrum, corrected for the spectral response of the system, and joined together using the overlapping region (i.e., 380-450 nm) of the spectrometers. It is noted, however, that the absolute sensitivity of each detector is different and, thus, only the major features of the spectra, such as the central wavelength of the emission bands, were examined. The results presented below were obtained using two samples each consisting of ~ 10 type ´1206´ SMRs. The values of the central wavelength of the emission bands represent the average estimate over the samples studied. The absolute uncertainty in the wavelengths due to the spectrometers estimated to be several nm. A typical example of the RL spectrum obtained at RT is presented in Figure 6.7. The radioluminescence spectrum from 1.5 to 5 eV is dominated by a single broad emission band at ~ 4 eV (~ 310 nm), although as indicated by the dashed circle a weaker band seems to be present at longer wavelengths. A a sharp peak at ~ 1.78 eV (~ 697 nm) can also be seen. Finally, the band

in Figures 6.7, 6.8, and 6.9 between 2.25-2.5 eV centered at ~ 2.38 eV is a cross-over artefact caused by the joining of the spectra obtained separately using the two spectrometers and, therefore, has not been further studied.

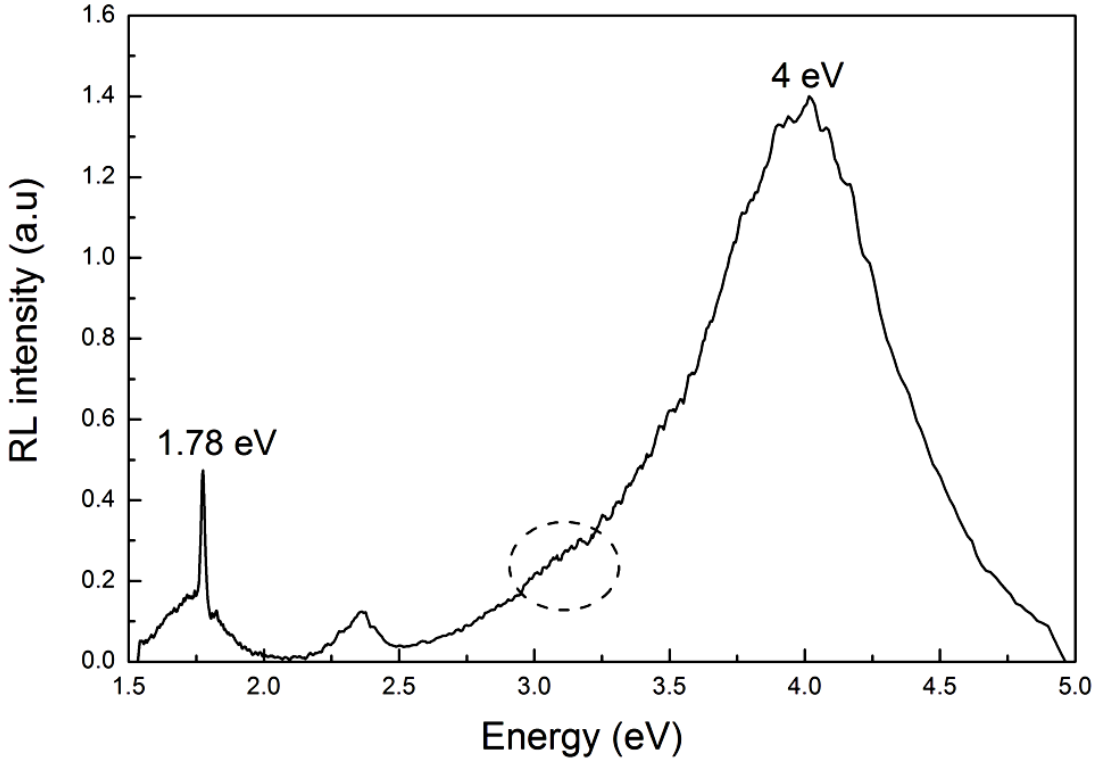

Figure 6.7: Radioluminescence emission spectra of alumina substrates measured at RT under continuous x-ray irradiation using a UV-Blue (250-450 nm) and a Blue-Green-Red (380-800 nm) spectrometer. The area between 2.25-2.5 eV (500-550 nm) is thought to be an artefact caused by the joining of the spectra obtained separately using the two spectrometers. Measurement was performed with a sample consisting of 10 type ´1206´ SMRs. The spectrum was corrected for instrument response.

Selected examples of RL spectra obtained at different temperatures over the intervals from -250 to 0 °C (i.e., low temperature range) and from 40 to 350 °C (i.e., high temperature range) are presented in Figures 6.8 and 6.9 respectively. From Figure 6.8 one can see that in the low temperature range, and specifically from -250 to -100 °C, the existence of two bands with

maxima at ~ 3.91 eV (~ 317 nm) and ~ 3.03 eV (~ 409) nm are clearly identified. At temperatures higher than -100 °C and up to the maximum temperature investigated (i.e., 400 °C) the intensities of both the ~ 3.91 and the ~ 3.03 eV emission bands (i.e., Figures 6.8 and 6.9) appear to decrease. The emission band at ~ 1.78 eV (~ 697 nm) exhibits a complicated dependence on the temperature and this is discussed in the following section. A three dimensional representation of the RL emission as a function of temperature in the low- and high-temperature range is shown in Appendix A2.

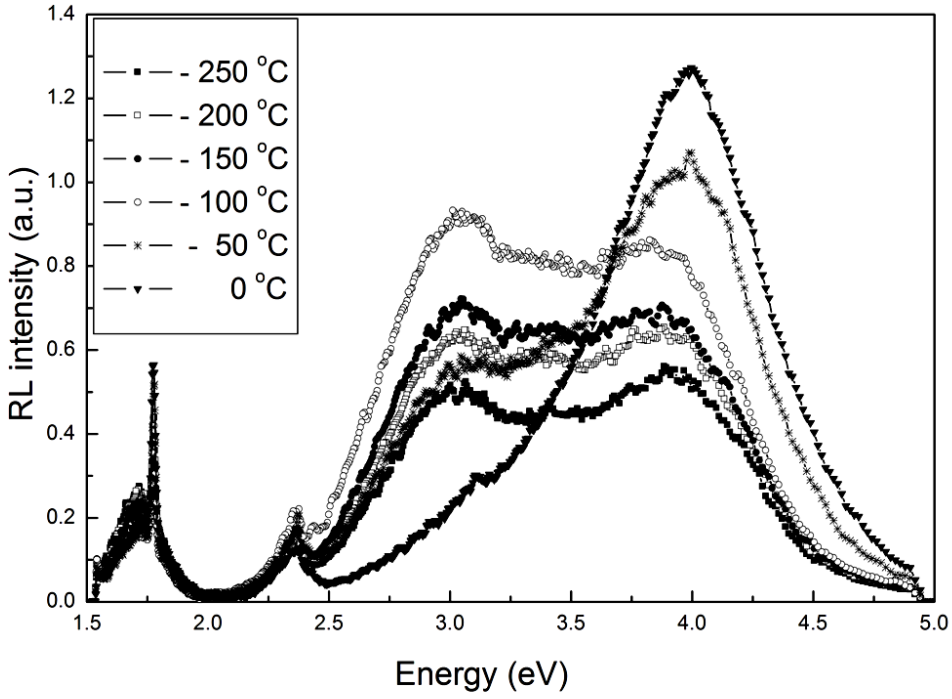

Figure 6.8: Radioluminescence emission spectra of alumina substrates measured at different temperatures from -250 to 0 °C. Measurement was performed with a sample consisting of 10 type ´1206´ SMRs. All spectra were corrected for instrument response.

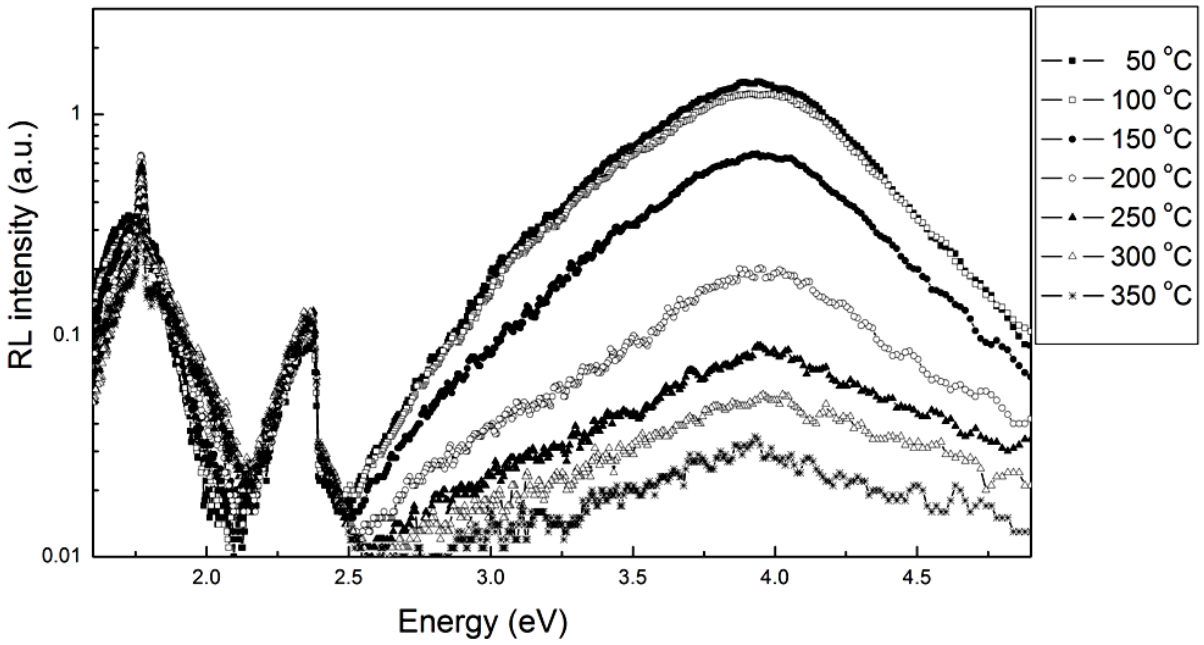

Figure 6.9: Radioluminescence emission spectra of alumina substrates measured at different temperatures from 50 to 350 °C plotted on a linear-log scale. Measurement was performed with a sample comprising 10 type ´1206´ SMRs.

6.3.2 Temperature dependence of RL emission

The temperature dependence of the RL emission in the UV-Blue range was examined following a deconvolution process assuming that each spectral band is described by a Gaussian function. An example is shown in Figure 6.10 for the RL emission obtained at -100 °C where the Gaussian fitting process indicated the presence of two components at ~ 3.01 eV (~ 412 nm) and at ~ 3.88 eV (~ 320 nm). For the low temperature range (i.e., -250 to 0 °C) the central energy and width of each emission band are noted and presented in Figure 6.11. As seen in Figure 6.11a,c, the position of the maximum central energy and the width of the first component of the UV-Blue RL changes slightly as the sample temperature increases from -250 to - 100 °C having, respectively, mean values of ~ 3.01 eV (~ 412 nm) and ~ 0.72 eV. At temperatures between - 100 °C and 0 °C both the maximum energy of the peak and the width of the band increase and at temperatures

higher than 0 °C they seem to decrease. Similarly, the peak energy of the second component (Figure 6.11b) of the UV-Blue RL is stable at ~ 3.85 eV (~ 322 nm) from -250 to -100 °C starting to increase at higher temperatures. The width of the same band (Figure 6.11d) is initially stable at ~ 0.87 eV from -250 to -100 °C and at higher temperatures started to decrease. In the high temperature range (i.e., T > 0 °C) the central energy and width of the emission band at ~ 3.85 eV (~ 322 nm) did not change significantly with temperature (results not shown), whereas the characteristics of the emission at ~ 3.01 eV (~ 412 nm) could not be examined due to the unresolved nature of the band (see Figures 6.7 and 6.9).

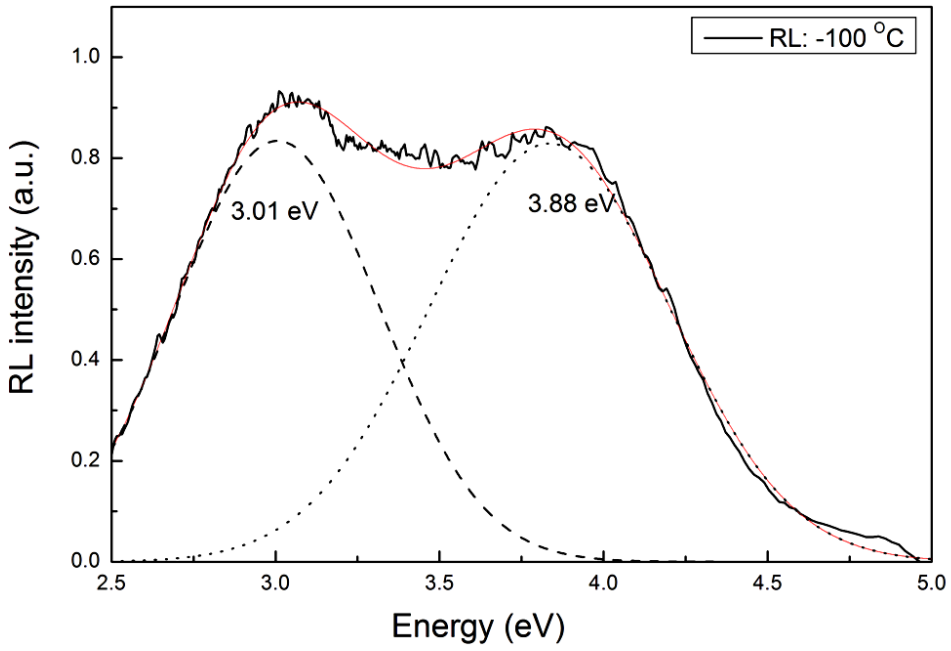

Figure 6.10: Example of spectral deconvolution process using Gaussian-based functions. The RL emission over the 2.5-5 eV range measured at -100 °C was deconvolved into two bands with central energies at ~ 3.01 and ~ 3.88 eV. Measurement was performed with a sample comprising 10 type ´1206´ SMRs.

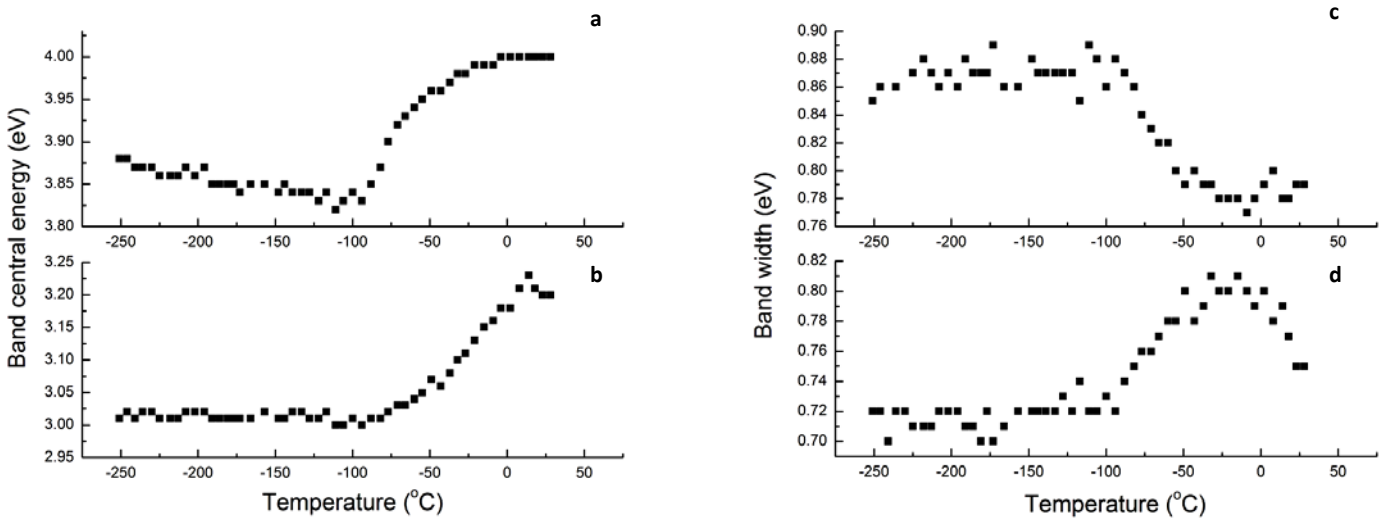

Figure 6.11: Temperature dependence of (a, b) central energy, and (c, d) width of the emission band components of RL in the UV-Blue range obtained following deconvolution with a Gaussian-based function. In (a, b) the uncertainty (i.e., fitting errors) in the coordinate value associated with each data point ranges from 0.04 to 0.3 eV and in (c, d) the uncertainties (fitting) are within ± 0.04 eV.

The temperature dependence of the integrated area of each band was also studied and the results are presented in Figure 6.12. From -250 to -80 °C the ~ 3.01 eV and ~ 3.85 eV nm emission bands increase continuously and then both decrease from -80 °C to 0 °C (Figure 6.12a,b). The band at ~ 3.85 eV continues to decrease up to ~ 300 °C, while at T > 300 °C it nearly disappears. The temperature dependence of the area of the ~ 3.01 eV band was not investigated at temperatures higher than 0 °C (Figure 6.12b) since it was too weak to define its wavelength range.

As discussed in Chapter 2 (section 2.5), the most likely reason for the decrease of the RL emission with temperature is the thermal quenching effect, the parameters of which (i.e., activation energy *W* and frequency factor *C*) can be determined from the plot showing the luminescence intensity as a function of T (K) using an equation of the form $I(T) = \frac{I_o}{1+C\cdot\exp^{-W/kT}}$.

The thermal quenching effect of the ~ 3.85 eV band was studied in the temperature range 40-200 °C (Figure 6.13a) and the thermal quenching parameters calculated (W=0.61 ± 0.02 eV and C=(2.25 ± 1.21) x10^6). For the ~ 3.01 eV band the phenomenon of thermal quenching was

investigated in the range -90 to -20 °C (Figure 6.13b) resulting an activation energy of W=0.19 ± 0.01 eV and a frequency factor of C=(1.17 ± 0.69) x10^4.

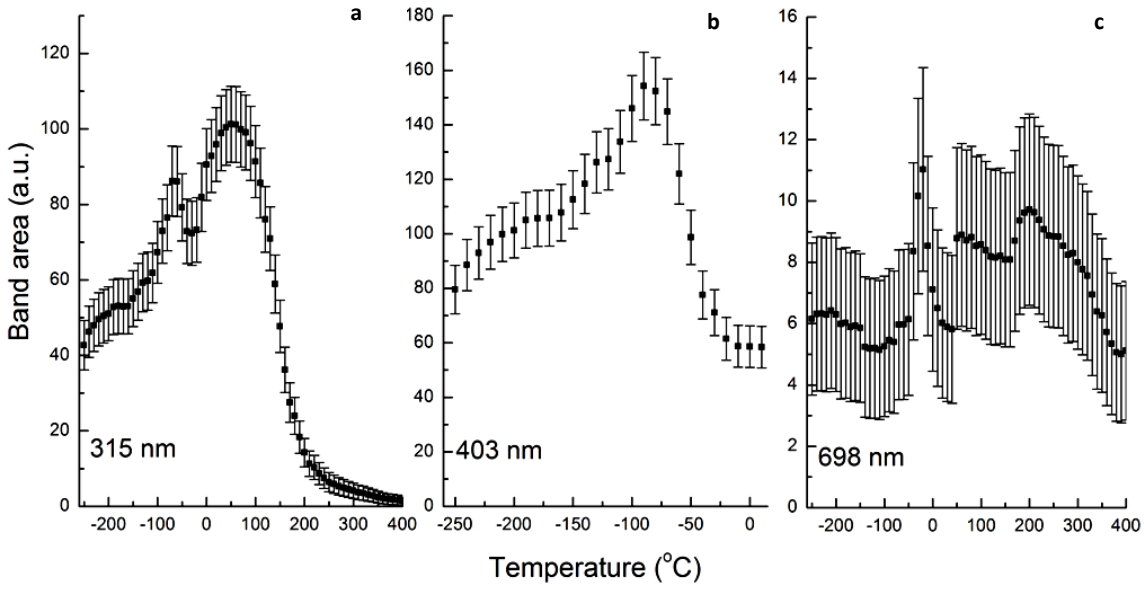

Figure 6.12: Temperature dependence of the area of fitted bands (a) band with mean central energy at ~ 3.85 eV, (b) band with mean central energy at ~ 3.01 eV, and (c) narrow emission band at ~ 1.78 eV. Measurement was performed with a sample comprising 10 type ´1206´ SMRs.

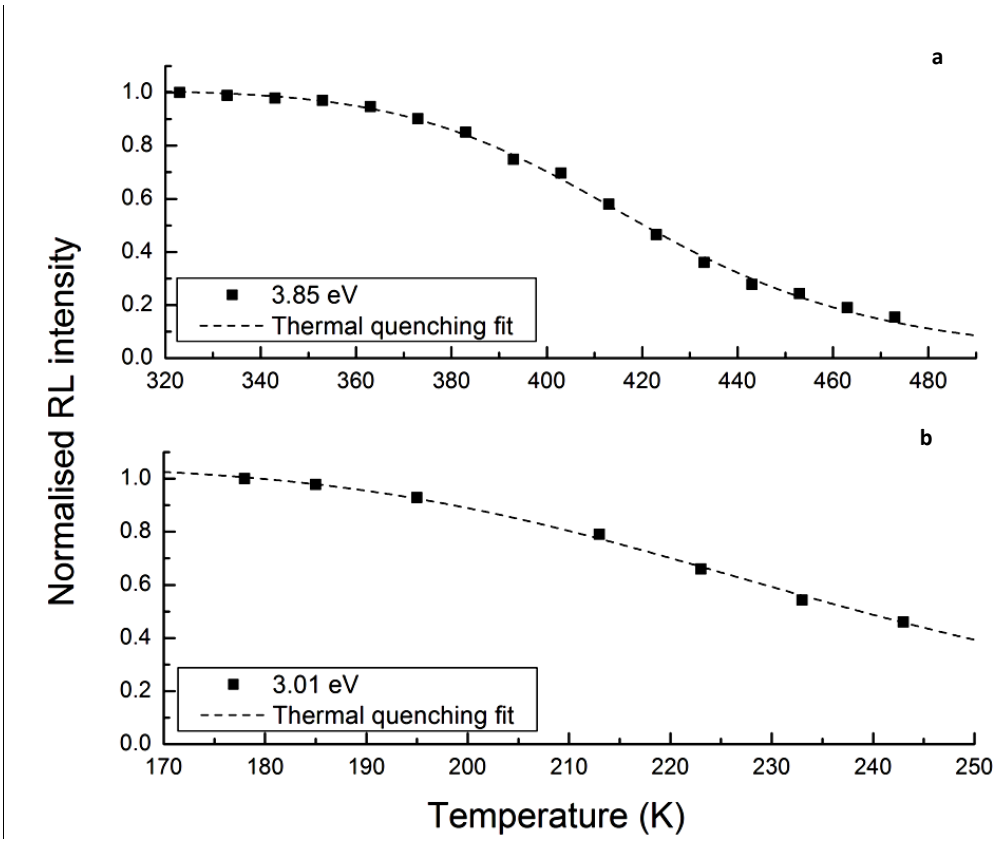

Figure 6.13: Normalised to the first data point RL intensity of (a) the ~ 3.85 eV, and (b) the ~ 3.01 eV emission bands as a function of temperature. The dashed curves show the fitting to the data points using the equation describing the thermal quenching effect, resulting in the following values: W=0.61 ± 0.02 eV and C=(2.25 ± 1.21) x10^6 for the ~ 3.85 eV band and W=0.19 ± 0.01 eV and C=(1.17 ± 0.69) x10^4 for the ~ 3.01 eV band.

A similar analysis was performed for the narrow emission band at ~ 1.78 eV (~ 697 nm) which showed insignificant variation in the peak central energy and width as a function of temperature. The area (i.e., 690-710 nm) of this band, however, demonstrated a complex dependence on temperature as shown in Figure 6.12c. Nevertheless, due to the significant statistical error associated with each data point it was not possible to draw conclusions about its behaviour, although it seems that the intensity of the ~ 698 nm emission shows a slight increase in the low temperature range (Figures 6.8 and 6.12c) and a steady decrease when the temperature exceeds ~ 200 °C (Figure 6.12c).

6.3.3 Discussion

Radioluminescence spectroscopy

On further examination the RL spectrum (Figure 6.7) has bands in common with those in the CL spectrum (Figure 6.5). The deconvolution process indicated that the CL spectrum can be fitted with three Gaussian bands at ~ 2.92, ~ 3.63, and ~ 4.08 eV; and the RL spectrum fitted with two bands at ~ 3.01and ~ 3.85 eV which could be a composite of two CL bands at ~ 4.15 and ~ 3.75 eV, but which appear as a single band in the RL spectrum with mean peak energy at ~ 3.85 eV.

One possible reason for the difference in the number of fitted components between the RL and the CL spectrum may be found by reviewing the production of luminescence in each case. For example, RL differs from CL in that it mostly characterises the radiative recombination processes particularly of the bulk of the samples (i.e., the bulk of the grains in the case of polycrystalline materials). On the other hand, due to the limited penetration (i.e., ~ μm) depth of electrons compared with x-rays, CL can be considered as a relatively surface process. In the CL spectrum it was suggested that the additional UV band (~ 4.08 eV, ~ 300 nm) may be associated with divalent impurity ions, such as Mg and Ca (see also Chapter 4), which are also assumed to be concentrated mainly on the surface of the grains and at the grain boundaries. Considering that CL arises mostly from the surface of the material it would be anticipated that the ~ 300 nm band or the F_{cation}-centres most likely associated with this band would be more pronounced in the CL emission. The omission of the ~ 300 nm band in the measured RL spectrum does not necessarily indicate that it is absent from the alumina substrates or that the theory of creation of additional F-type centres due to the presence of divalent impurities is invalid. Instead, it suggests that the environment of F^{+}-centres has been modified causing a shift of the emission band to shorter wavelengths if these impurities have, for instance, entered the bulk of the grains. This can occur in cases where the concentration of dopants is higher than the solubility limit of aluminium. Given the inhomogeneous distribution of Mg, Ca, and Si (Figure 6.4) and taking into account that chemical mapping was performed using polished alumina substrates that revealed the interior of grains, it would be reasonable to assume that these elements can be found elsewhere in the sample; yet their maximum concentrationis expected to be across the outermost layers and

near the grain boundaries, their associated luminescence emissions of which could be better studied by the CL method.

Temperature dependence of RL emission

Several conclusions about the relaxation processes involved in the generation of luminescence can be made following the measurement of the radioluminescence emission over the wide temperature interval from -250 to 400 °C.

The broadening of the 2.5-5.0 eV emission observed from -250 to about -100 °C which, as indicated by the deconvolution process, is primarily caused by the increase of the width of the band at ~ 3.01 eV, and the strong thermal quenching effect of both emission centres (i.e., F- and F^+-centres) are characteristics of materials in which strong electron-phonon interaction mechanisms take place. However, due to the strong overlapping of the two bands in the UV-Blue region it cannot be excluded that the ~ 3.85 eV band also exhibits similar behaviour; in agreement with observations (Bonnelle and Jonnard, 2010; Brewer *et al*., 1980; Draeger and Summers, 1979; Evans and Stapelbroek, 1978) made using other forms of Al_2O_3 crystals where both the F- and the F^+-emissions revealed the temperature dependence phenomena observed in this study for the polycrystalline alumina substrates.

The interpretation of the phenomena of thermal broadening and thermal quenching of luminescence emission based on the coupling of the electronic states of the luminescent centres to the vibrational modes (i.e., phonons) of the crystalline lattice can be made using the configurational coordinate diagram (Figure 6.14 and Chapter 2; Section 2.2). As already described in Chapter 2, in the CC diagram the lower parabola corresponds to the ground state of the luminescent centre with the upper parabola being equivalent to the excited sate of the same defect. A number of vibrational levels (i.e., vertical lines) are also assumed to exist above the minima of each state. The coupling between the electronic and the vibronic states is assumed to be strong. This assumption is valid for the F- and F^+-centres of Al_2O_3 single crystals based on measurements of the magnitude of a parameter known as Huang-Rhys factor *S* (Brewer *et al*., 1980; Evans and Stapelbroek, 1978). Furthermore, the absence of sharp emissions (i.e., zero-phonon lines) in the spectra of Al_2O_3 single crystals even at very low temperatures (e.g., liquid

nitrogen) was explained by these authors using the large Huang-Rhys factor and the assumption of strong electron-lattice interaction. Although, the magnitude of the Huang-Rhys factors of the F-type centres for the alumina substrates of SMRs is not known, the broad nature of the RL bands measured in the low temperature range suggests that it corresponds to a value characteristic of strong electron-phonon coupling.

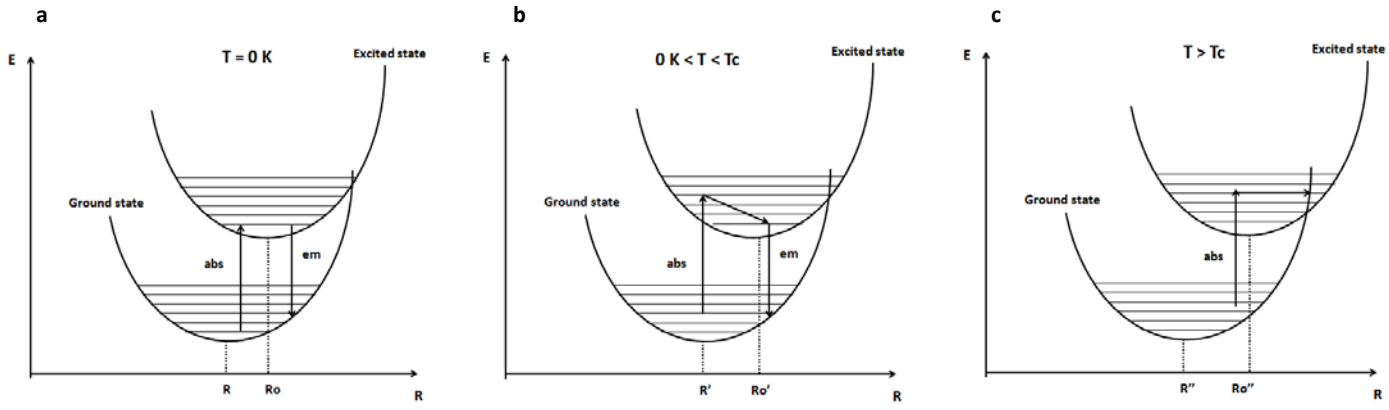

Figure 6.14: Description of thermal dependence of luminescence emission (and absorption) using the configurational coordinate diagram and the electron-phonon coupling model. (a) At T=0 K the thermal energy provided by phonons is low. The absorption of photon energy (e.g., x-rays or electrons) raises an electron from a low-potential energy (*E*) vibrational state of the ground state to a corresponding low-potential energy vibrational state of the excited state. The return of the excited electron to the ground state results in luminescence emission. For a luminescent centre strongly interacting with the vibrational modes of the lattice both the absorption and the emission bands are broad. (b) As the temperature increases (0 K < T < Tc) the energy associated with the vibrational modes of the crystal lattice increases too introducing a displacement of the electronic states of the emission centre to new equilibrium positions R' and Ro'. Absorption and emission can take place from higher energy vibronic states. Thermal broadening of the absorption and emission bands can be observed. (c) After a critical temperature T_c the thermal energy provided by the phonons can be high enough and the shift of the electronic states (i.e., R'', Ro'') of the centre can be significant such that the two parabolas in the CC diagram are strongly intersected. Charges excited to electronic levels located close to the crossing point of the two parabolas have more probabilities to decay to the ground state of the centre non-radiatively causing a reduction in the intensity of the luminescence emission, known as thermal quenching.

Both the CL and RL processes arise from the radiative relaxation of charges (i.e., electrons) from one of the vibrational levels of the ground state to one of the vibrational levels of the excited state of the recombination centre. Different vibrational levels are occupied by the electrons depending on the thermal energy (i.e., temperature) of the centre. At T=0 K (-273 °C) and, more generally, low temperatures (e.g., -250 to -100 °C in this study) the most likely transitions are those from the low energy levels of the ground and excited state. For example, the most likely optical transition at T=0 K (-273 °C) resulting in absorption of luminescence occurs from the lowest energy point of the ground state to (usually) the lowest energy point of the excited state (Figure 6.14a). The return of the electron from an excited to the ground state is responsible for the emission of luminescence. As the temperature increases the energy associated with the vibrational modes of the crystal lattice increases introducing a displacement of the electronic states of the emission centre (Ridley, 1988). In addition, higher vibronic states are likely to be occupied (Figure 6.14b). These phenomena together are responsible for the thermal broadening of the emission bands. When temperature exceeds a critical temperature T_c (e.g., -90 °C for the F- and 40°C for the F^+-centres of alumina substrates), and so does the vibrational/thermal energy, the shift of the electronic states of the centre can be significant such that the two parabolas in the CC diagram are strongly intersected. Charges excited to electronic levels located close to the crossing point of the two parabolas have a higher probability to decay to the ground state of the centre non-radiatively as indicated in Figure 6.14c (Blasse and Grabmaier, 1994; Ridley, 1988). The latter process is then responsible for the reduction in the intensity of the luminescence emission (i.e., thermal quenching).

Although a quantitative comparison of the thermal broadening and thermal quenching effects between the emission attributed to F-centres and that due to F^+-centres may be inaccurate because of the overlapping nature of these bands, it is clear from Figures 6.8 and 6.9 that the F-band demonstrated stronger temperature dependence and consequently stronger thermal quenching. On the basis of the previous discussion, it could be argued that the F-centres exhibit stronger electron-lattice coupling, in accordance with the results reported for single crystals [i.e., the Huang-Rhys factor for the F- was found to be higher than that of the F^+-centre (Brewer *et al.*, 1980; Evans and Stapelbroek, 1978)]

Finally, it is worth mentioning that the value of the activation energy for thermal quenching of the F^+-centre (E=0.61 eV) agrees very well with theoretical calculations (E=0.6 eV) conducted by Stashans *et al*. (1994), although Evans and Stapelbroek (1978) calculated the activation energy to be ~ 0.4 eV in Al_2O_3 single crystals. So far it appears that similar calculations have yet to be performed for the F-centre.

FTIR measurements

To obtain additional information about the phonon modes of the alumina substrates, the vibrational spectra of the material were collected using an FTIR technique. The IR spectroscopy measurements were carried out at RT in a Perkins Elmer Spectrum 2 FTIR spectrometer in the 400-1500 cm^{-1} wavenumber range. Due to the significant thickness (i.e., several mm) of the samples FTIR spectra were recorded in the reflectance mode, where the reflected IR light is collected by the detector.

Figure 6.15 shows a typical reflectance spectrum (i.e., IR reflectance as function of wavenumber) of alumina substrates. For comparison, the FTIR spectrum of a dosimetry grade Al_2O_3:C single crystal was also collected and presented in the same figure.

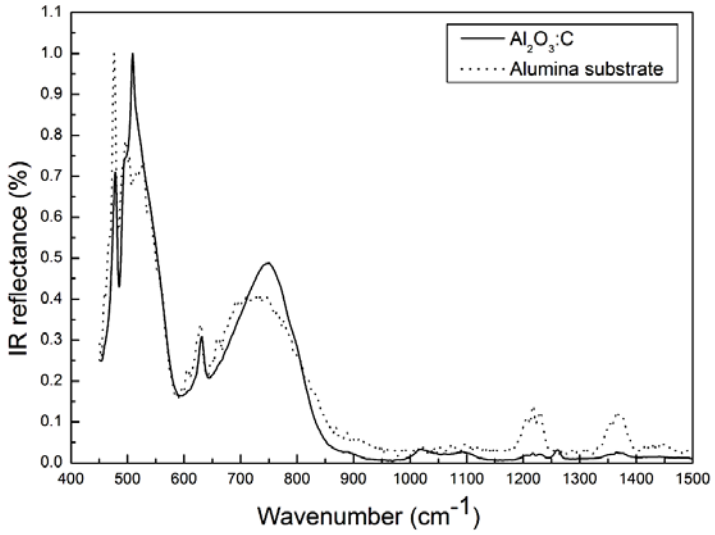

Figure 6.15: Comparison of normalised FTIR reflectance spectra of alumina substrate and dosimetry grade Al_2O_3:C single crystal. The spectra were collected at RT.

The first observation is that the features of the FTIR reflectance spectra of the alumina substrate and the Al_2O_3:C single crystal are comparable. However, in both cases due to the broadening of the reflectance spectra, it was not possible to resolve clearly and characterise the phonon modes. In general, both spectra contain some sharp peaks at ~ 478, ~ 500, and ~ 630 cm^{-1} and some broad IR bands at ~ 740, ~ 900, ~ 1220, and ~ 1370 cm^{-1} corresponding, respectively, to phonon energies of ~ 0.059, ~ 0.062, ~ 0.078, ~ 0.092, ~ 0.112, ~ 0.151, and ~ 0.170 eV.

6.4 Conclusions

The luminescence in alumina substrates generated by electron or x-ray excitation is produced by intrinsic defects, such as the oxygen vacancies occupied by one (i.e., F^+-centres) and two electrons (i.e., F-centres), and extrinsic defects associated with impurities (e.g., Mg, Cr). The F-type luminescent centres are common in aluminium oxide compounds, although their concentration and relative contribution would generally depend on the manufacturing conditions, form, and purity of the starting material. Extrinsic- or impurity-related luminescence can either arise from the intentional doping of the material or from the presence of trace amounts of elements in the initial powder used for the fabrication of the ceramic.

The divalent impurities of Mg and Ca, identified in the x-ray chemical analysis, are believed to have been intentionally added to the alumina substrates to aid the stage of densification during the sintering process. Based on existing literature (Chapter 4) and the deconvolution of the CL spectrum their presence could be associated with some types of centres, known as $F_{cations}$, producing luminescence in the spectral range of the F^+-centres (~ 3.7 eV). Yet, as suggested by the comparison of RL and CL spectra measured at RT, the contribution of the emission band from $F_{cations}$ may be dependent on the depth of the recombination centres below the surface of the grains from which the luminescence is emitted. It appears that near the surface of the grains, where the concentration of Mg and Ca is higher, the $F_{cations}$ emission is more pronounced and possibly makes a stronger contribution to the CL spectrum, whereas the luminescence arising from greater depths (i.e., radioluminescence) cannot be distinguished from the F^+-emission.

Additional recombination centres introduced by Cr ions were also detected in the RL and CL spectra. Chromium, which produces luminescence in the red region of the spectrum, although not detected in the chemical analysis of the alumina substrates, may exist as native impurities. Nevertheless, all dopants do not necessarily produce active luminescent centres. This is the case of dosimetry grade Al_2O_3:C single crystals which, although usually doped with carbon, did not exhibit extrinsic luminescence associated with the carbon ions since the main role of carbon is to increase the concentration of the native intrinsic oxygen centres.

Whereas in dosimetry grade Al_2O_3:C single crystals where the F- and F^+-bands can be clearly resolved, similar emission bands were found to overlap and produce a broader spectrum within the range ~ 2.5-5.0 eV in both the CL and RL spectra of the alumina substrates tested. The modification of the local environment of the F-type centres due to the highly disordered structure of alumina substrates could account for the broadened nature of the luminescence spectra and the strong thermal quenching of the ~ 2.5-5.0 eV emission may also contribute to this general broadening of the bands.

A model based on the strong coupling of the electronic states of the luminescent centres to the vibrational modes of the crystal lattice is suggested to account for the temperature dependence of luminescence. The implication of the strong thermal quenching effect is that if these centres participate as recombination centres during TL and OSL measurements (as has been found for the dosimetry grade Al_2O_3:C single crystals), the luminescence efficiency is expected to be significantly reduced and the temperature dependence of the TL and OSL is investigated in the following chapters. On the other hand, the emission at ~ 1.78 eV (~ 697 nm) due to Cr^{3+} impurities seems remarkably robust to changes in temperature, suggesting a potential for TL and OSL dosimetry applications.

Chapter 7: Thermally stimulated processes in alumina SMRs

7.1 Introduction

Materials considered for dosimetry applications usually present complex luminescence signals reflecting the competition between the various trapping, detrapping, and recombination processes. Aside from the spectroscopic methods which, as demonstrated in the previous chapter, mainly provide information about the defect environment and emission/recombination characteristics, analysis of the TL and OSL responses under various laboratory conditions can be used to obtain an insight into the physical mechanism of luminescence production as well as to define various properties (e.g., thermal stability, optical sensitivity) for reliable dosimetry uses. Further on, the kinetic analysis methods (Chapter 2) and correlation studies between TL and OSL offer the possibility to obtain knowledge about the behaviour of charge carriers in the trapping levels involved in luminescence emission and, thus, to decide on the most suitable signal for dosimetry application.

In this chapter, the form of luminescence emission of alumina substrates from SMRs following beta irradiation, under thermal stimulation and thermal annealing conditions will be inspected. The fundamental parameters of the traps (i.e., order of kinetics, activation energy, and frequency factor) associated with the TL glow peaks of the alumina substrates will be determined using standard kinetic analysis methods, including the variable heating rate/Hoogenstraaten method, the peak shape method, and the initial rise method. The existence of multiple trap components within the TL glow curve will also be examined using thermal cleaning procedures (i.e., TL measurements following preheat to increasing end temperatures).

It is to be noted that data presented in the following sections usually correspond to a specific sample, where the number and type of SMRs will be clearly specified. These, however, are to be considered representative of the wider sample population investigated and the values of the kinetic parameters calculated are average estimates of the samples examined, whereas the errors represent the standard deviation of the mean value. In all cases the TL was detected in the UV range with a Hoya U340 filter (7.5 mm).

7.2 Thermoluminescence response: General features

Before the description of more analytical procedures which will help to unfold the complex nature of the TL glow curves of SMRs, the general features of TL will be presented.

The form of the TL response of the alumina substrates was examined first by administrating to a set of samples (i.e., cups consisting of variable numbers of types ´1206´ and ´0402´ SMRs) to a beta dose of ~ 3 Gy and reading out immediately the TL signal without any post-irradiation thermal or optical treatment. The thermal stability of the TL signal was further investigated using a thermal cleaning procedure – also known as step-wise annealing – during which the samples were beta irradiated, preheated to a given temperature for 10 s – sufficient to heat the sample homogeneously given the finite thickness of the substrate, but not long enough to produce significant thermal escape of the trapped charge carriers – after which the TL response was measured. At the end of the sequence the samples were annealed to 500 °C and the TL measured, re-irradiated, and preheated to a higher temperature. Measurement of the TL response to a test dose equal to ~ 0.5 Gy, delivered at the beginning and at the end of the annealing test, showed that any sensitivity change induced by the repeating cycles of dose and preheat was negligible for the alumina substrates tested.

A typical TL glow curve obtained with a sample of 3 type ´1206´ SMRs from 25 to 500 °C at a rate of 5 °C s^{-1} is shown in Figure 7.1a. Based on visual inspection and using a simple deconvolution procedure, a combination of three nearly symmetrical peaks centred at ~ 100 °C (Peak 1), ~ 210 °C (Peak 2), and ~ 360 °C (Peak 3) could be used to describe the measured glow curve. The position of the TL peaks varies with the heating rate as well as the thickness of the samples due to temperature lag (discussed below). Moreover, of these peaks, only TL Peak 2 is potentially suitable for dosimetry on a long timescale, TL Peak 1 was found to be thermally unstable at RT (i.e., mean lifetime of ca 10 minutes), and TL Peak 3 may be of practical use after high radiation exposures.

The TL glow curves obtained following a step-wise annealing treatment at various temperatures between 25 and 300 °C are presented in Figure 7.1b. The position of TL Peak 1 shifts to higher temperatures, and progressively its intensity reduces, disappearing when the preheat temperature exceeds 150 °C. The intensity of TL Peak 2 is not significantly affected by preheat treatment up

to approximately 120 °C, but decreases notably and the peak shifts to higher temperatures for preheats greater than 150 °C. Above 250 °C only TL Peak 3 appears in the TL glow curve. The thermal stability of TL Peak 1 and TL Peak 2 calculated using data obtained from step-wise annealing curves (total area under each TL peak versus the preheat temperature) are presented in Figure 7.2. Consistent with Figure 7.1b, TL Peak 1 shows a continuous decrease with annealing temperature, while the integrated light sum of TL Peak 2 shows a plateau up to ~ 120 °C followed by a decreasing trend.

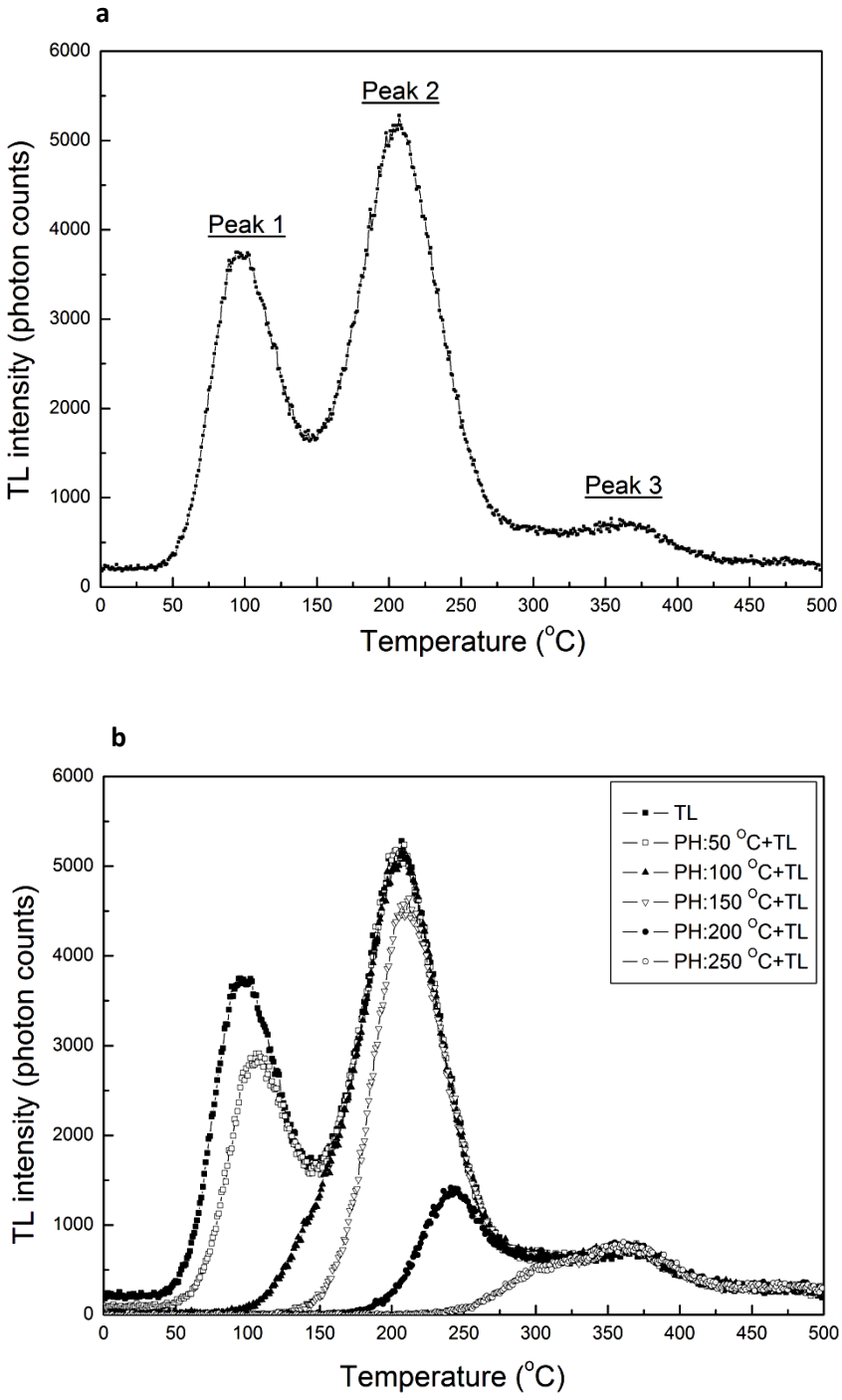

Figure 7.1: TL glow curves (5 °C s^{-1}) of alumina substrates obtained (a) no preheat treatment, (b) following thermal cleaning at various temperatures. Sample consisted of 3 type ´1206´ SMRs irradiated with 3 Gy. The TL offset at RT is due to the phosphorescence emission from shallow traps detected by the PMT prior to the onset of thermal stimulation.

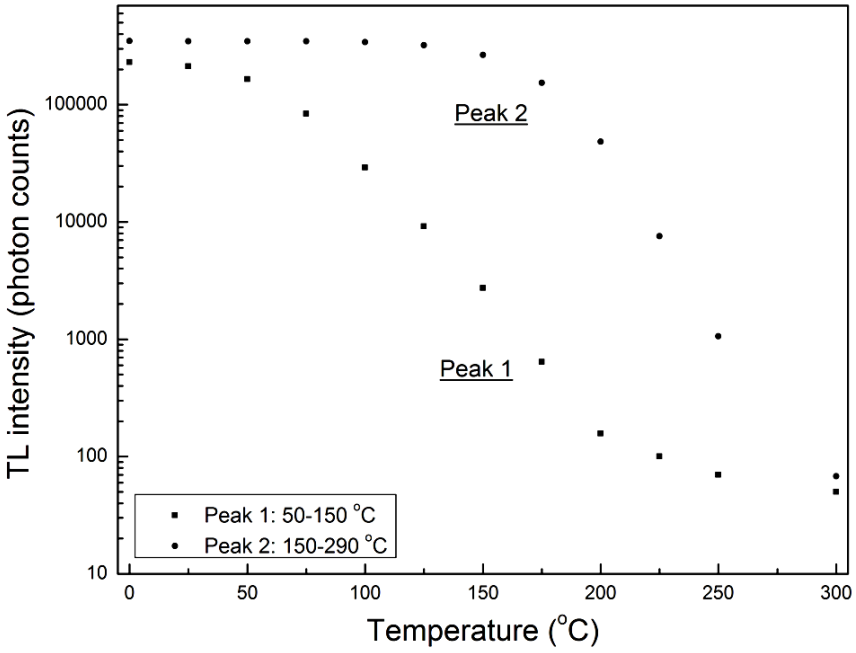

Figure 7.2: Step-wise annealing curves indicating the relative thermal stability characteristics of TL Peaks 1 and 2. The remaining TL intensity under each peak is plotted as a function of the preheat temperature. Under the testing conditions TL Peak 1 is thermally unstable throughout the investigated temperature range, while TL Peak 2 exhibits no significant loss in intensity to ca 120 °C. Data produced with a sample consisting of 3 type ´1206´ SMRs irradiated with 3 Gy. The size of the error bars was smaller than the data symbols and it's not shown.

Unless otherwise stated, TL measurements were carried out without any thermal pretreatment except in the case of the evaluation of the trap parameters of TL Peak 2 where a thermal cleaning procedure consisting of a 10 s heat treatment at 120 °C was applied to the post-irradiated samples to isolate it from TL Peak 1. The choice of this annealing regime was made after examining the experimental results from the previous thermal stability test. Preheating the sample at 120 °C removes TL Peak 1 without significantly affecting the intensity and shape of TL Peak 2 as indicated by the results of Figure 7.2.

7.3 Evaluation of trapping parameters

As discussed in Chapter 2, most of the kinetic analysis methods developed to calculate the activation energy and frequency factor of a TL peak require prior knowledge of the order of kinetics. For example, the VHR was developed to provide accurate values of the trapping parameters for TL peaks following first-order kinetics, although it also has been found to be reliable for second- and general-order kinetics peaks. The correct choice of expressions (Chen and McKeever, 1997) in the peak shape method also relies on previous determination of the order of kinetics. Perhaps, the only method that is independent of the order of kinetics is the initial rise method.

The order of kinetics *b* of the TL Peaks 1 and 2 of the alumina substrates was initially investigated using the peak shift method (Pagonis *et al*., 2006) which consists of examining the behaviour of the maximum of the peak at different dose levels. As discussed in Chapter 2, the position of the glow peak maximum of peaks that follow first-order kinetics is expected to remain constant as the dose varies, and second- and general-order kinetics TL peaks generally shift to lower temperatures with increasing dose level. Also, the intensity of the isothermal decay curve of a first-order TL peak decreases exponentially with the time of thermal pretreatment during isothermal measurement, but non-first-order peaks and peaks due to a distribution of traps show non-exponentially isothermal decay curves. In addition, the symmetry of the TL peaks expressed by the geometric factor μ_g was studied to obtain additional information on the order of kinetics. As suggested by Chen (Chen *et al*., 1990) the value of the geometric factor for first-order peaks is ~ 0.42, that of second-order peaks is ~ 0.52, while intermediate values correspond to general-order kinetics.

Finally, values for the activation energy *E* and frequency factor *s* of each peak were finally calculated using the VHR, the IR, and PS methods on the TL glow curves obtained under various experimental conditions as discussed in the following sections.

7.3.1 Order of kinetics

Peak shift with dose

The variation of the maximum temperature, T_m, of TL Peak 1 and TL Peak 2 with dose was studied in the range between 1 and 60 Gy. As shown in Table 7.1 and Figure 7.3a both peaks display an insignificant shift within experimental error (± 2 °C) as the dose increases from 1 to 10 Gy and this is indicative of first order kinetics. Nevertheless, at higher dose levels a small shift towards higher temperatures is indicated. Since both peaks are accompanied by adjacent peaks on the high-temperature side, the existence of another peak could potentially explain this behaviour. On the other hand, the presence or overlapping peak components within each peak each with different dose response characteristics also looks reasonable. The growth of the peak maximum intensity, I_m, with dose is also presented in Figure 7.3b. TL Peak 1 grows slightly sublinearly with dose, whereas TL Peak 2 displays a linear-superlinear dose response. More about the dose response characteristics of the luminescence response is presented in Chapter 11 dealing with the dosimetry properties of alumina substrates.

Table 7.1: Intensity and shape characteristics of TL Peak 1 and TL Peak 2 for various dose levels. I_m and T_m denote, respectively, the peak maximum intensity and peak maximum temperature, while T_1, T_2 are, respectively, the temperatures on the rising and descending side of the peak at which the intensity has fallen to half the maximum value. $\mu_g=(T_2-T_m)/(T_2-T_1)$ is the so-called geometric or symmetry factor characteristic of the order of kinetics. Data in this table represent average values produced using several samples consisting of 3 type ´1206´ SMRs.

	TL Peak 1					**TL Peak 2**				
Dose (±0.12Gy)	**I_m (photon counts)**	**T_m (±2 °C)**	**T_1 (±2 °C)**	**T_2 (±2 °C)**	**μ_g**	**I_m (photon counts)**	**T_m (±2 °C)**	**T_1 (±2 °C)**	**T_2 (± 2°C)**	**μ_g**
1	1380±37	98	71	126	0.51±0.05	1700±41	202	166	238	0.50±0.05
2	2340±48	98	71	126	0.51±0.05	3370±58	203	168	238	0.50±0.05
4	4640±68	99	72	126	0.50±0.06	6940±83	203	168	238	0.50±0.05
8	8720±93	100	75	126	0.51±0.06	14000±118	204	168	240	0.50±0.04
10	10750±104	101	76	128	0.52±0.06	17777±133	205	169	244	0.52±0.04
15	14950±122	103	78	127	0.49±0.06	26980±164	205	168	244	0.51±0.04
20	19980±141	103	79	127	0.50±0.06	36731±192	206	170	242	0.50±0.04
40	32680±181	105	80	128	0.48±0.06	77930±279	208	171	248	0.52±0.04
60	44880±212	106	81	128	0.47±0.06	125663±354	209	172	249	0.52±0.04

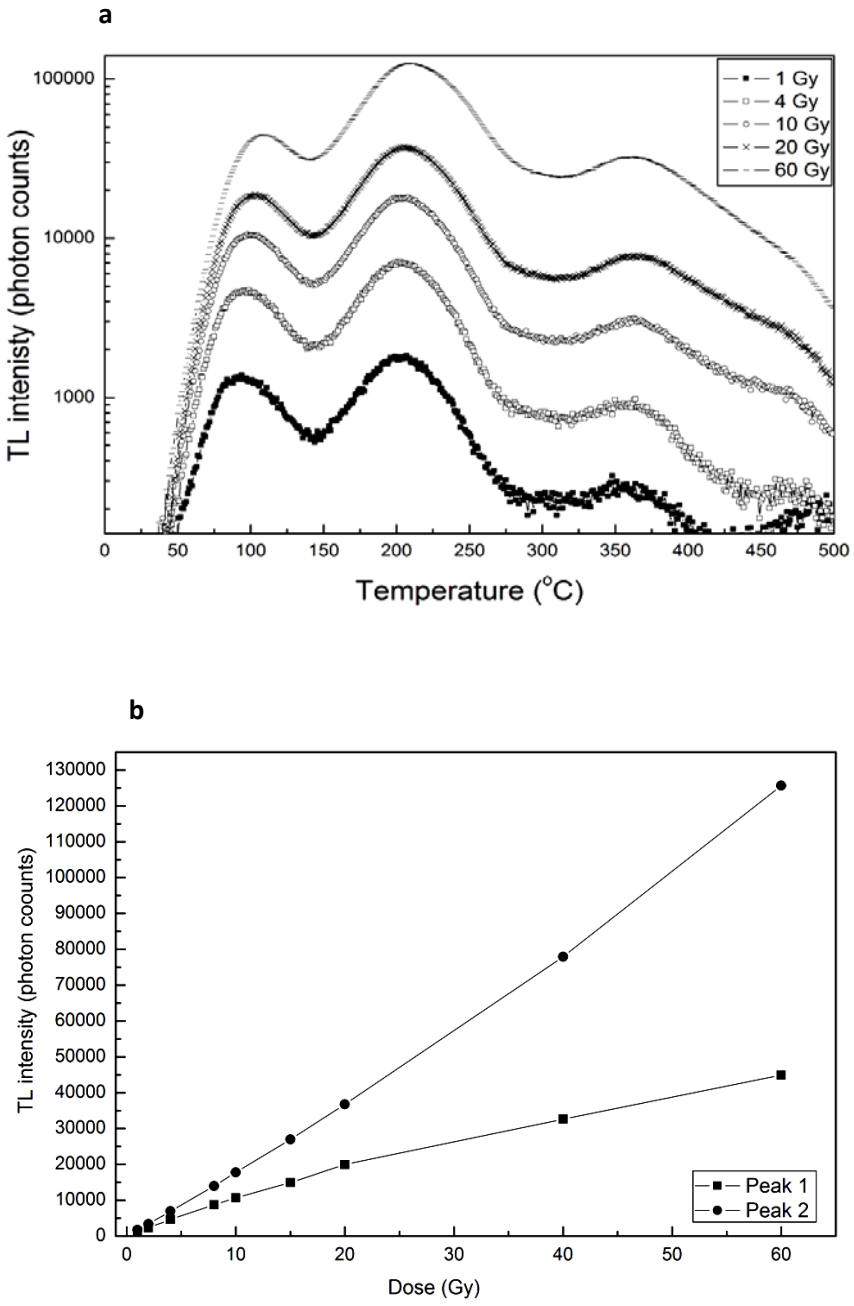

Figure 7.3: (a) TL glow curves obtained after different beta doses. The maximum temperature of all TL peaks remains unaltered as the dose increases from 1 to 10 Gy, shifting slightly to higher temperatures for larger doses. (b) Dose response characteristics of the maximum intensity of TL Peaks 1 and 2. TL Peak 1 grows sublinearly with dose, whereas TL Peak 2 grows linearly up to 20 Gy and superlinearly for higher dose levels. Data produced with a sample consisting of 3 type ´1206´ SMRs.

Peak shape

An indication of the order of kinetics was also obtained by estimating the symmetry factor using the T_m, T_1 and T_2 (i.e., the temperatures on the low and high temperature side of the peak respectively corresponding to half the maximum intensity) parameters of the peaks listed in Table 7.1. Despite the results from the peak shift method, where an insignificant shift of the peak maximum temperature points to first-order kinetics (< 10Gy), the symmetry factor of both peaks at any dose level is characteristic of either second- or general-order kinetics, with values of μ_g in the range 0.50 – 0.52.

Isothermal decay

The isothermal decay curves were produced by monitoring the phosphorescence emission for 200 s at different sample temperatures between 50 and 90 °C for Peak 1 and 170 to 190 °C for Peak 2 (using a heating rate of 5 °C s^{-1} to reach the selected temperature). To make sure that sufficient phosphorescence intensity was obtained, especially at the lower temperatures, the samples were irradiated with a dose of ~ 12 Gy. The form of the phosphorescence emission of both peaks is shown in Figure 7.4 on a log-linear scale. Instead of a monotonic exponential or non-exponential decay predicted by first- or non-first order kinetics respectively, a peak followed by non-exponential decay curve is visible in the isothermal plots of both peaks. As discussed later, the origin of such peaks may be the result of complex kinetics or arise from experimental artifacts (e.g., temperature lag). The latter, particularly the effect of temperature lag (Chapter 2; Section 2.7.1.3), was examined using thin samples and the results are presented in the following section.

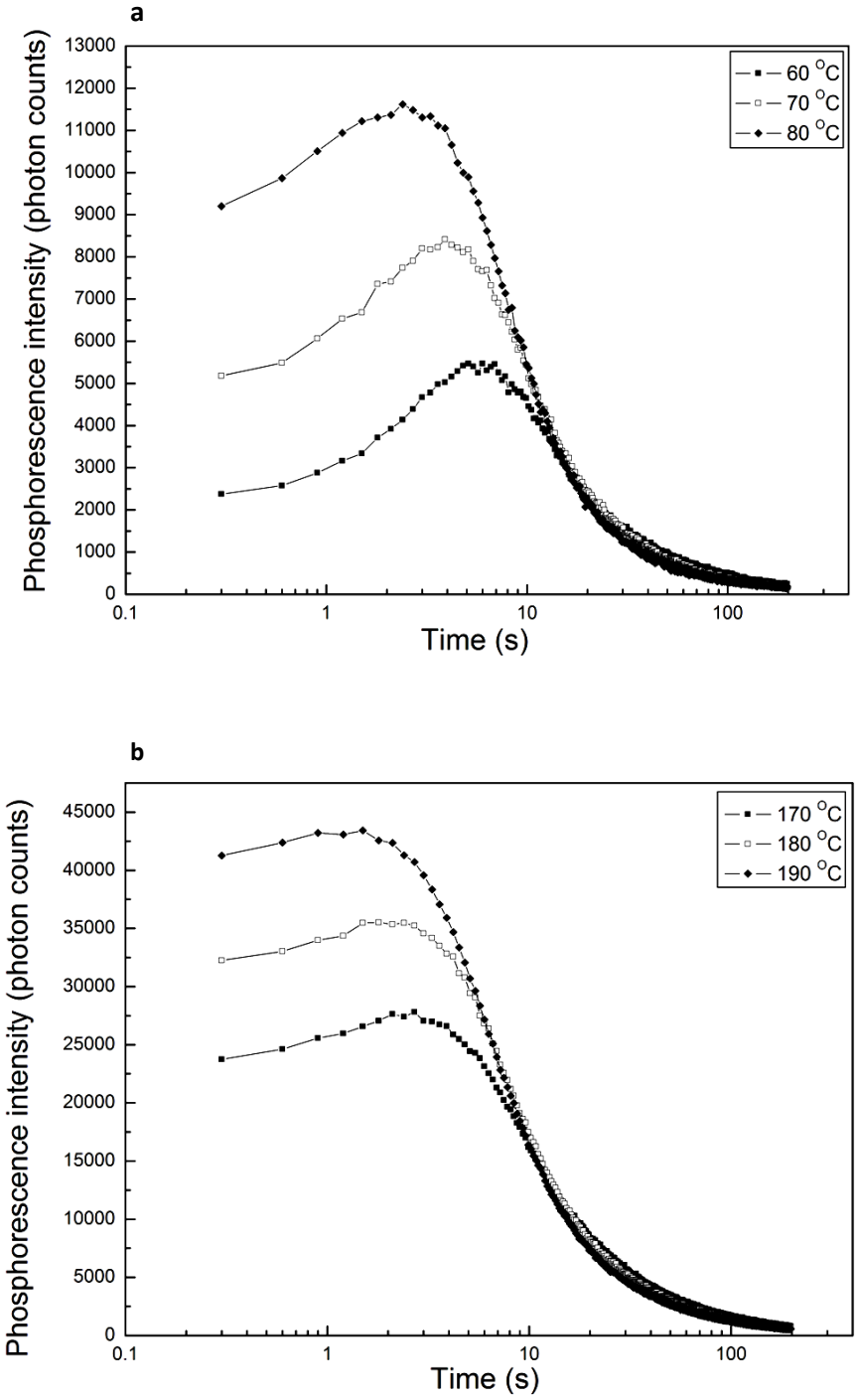

Figure 7.4: Phosphorescence emission associated with (a) TL Peak 1 and (b) TL Peak 2 at several sample temperatures. Data produced with a sample consisting of 4 type ´1206´ SMRs irradiated with 12 Gy.

7.3.2 Temperature lag effect

Regarding the initial rise in each ID curve, three possibilities have been previously considered by Jain *et al*., (2007) to explain a peak-shaped structure observed in the isothermal signals of quartz. The first reason for the appearance of delayed isothermal emissions is the existence of a single trap and two luminescence centres with recombination probabilities that differ by several orders of magnitude. According to Franklin *et al*., (1993), the measurement of the isothermal decay starts once the chosen temperature is attained. However, even if the selected temperature is reached instantaneously there can be an initial period where the concentration of electrons in the conduction band still rises. Therefore, in the case of two recombination centres, electrons already present in the conduction band will recombine first with (almost all) the holes in the centre with the larger recombination probability while electrons which reach the conduction band more slowly will recombine with the holes in the other centre, though more slowly since their concentration is still rising (Franklin *et al*., 1993; Jain *et al*., 2007). This can result in a peak in the ID plot.

The other possibility, which has been primarily used to interpret similar observations in OSL signals, assumes that there exists a thermally unstable trap (i.e., shallow trap) which competes for charge capture during thermal stimulation (Jain *et al*., 2007; McKeever *et al*., 1997). However, as suggested by Jain *et al*., (2007), if non-first-order kinetics is responsible for the initial rise in the isothermal decay curve then it is expected that the position of the peak maximum will vary with dose or duration of pre-measurement annealing due to variations in the concentration of charges in the available traps. The effects of higher irradiation dose (i.e., increase of trapped charge population) and preheat (i.e., decrease of trapped charge population) were therefore tested (results are not shown) where it was found that the maxima of the ID peaks remained the same.

A different effect related to temperature lag was also considered by Jain *et al*., (2007) and earlier by Bailey (1998) for the OSL curves of quartz measured at elevated temperatures. These authors attributed the initial build-up to the effect of thermal lag between the heater element and the sample. In the Risø reader the temperature of the sample may be different from that of the heater plate, due, mainly, to the finite thickness of the alumina substrates and the presence of cups. However, isothermal measurements start at the point the heater element reaches the final

temperature, while the sample temperature may still be ramping causing the initial build-up in the ID signal. Jain *et al.*, (2007) carried out a range of experimental tests and numerical simulations to describe the characteristics of the ID peaks due to thermal lag. In particular, the authors showed that the peak (1) is nearly absent for powdered samples, (2) move to longer measurement time with increasing heating rate, and (3) disappears when the measurement temperature exceeds that maximum temperature of the peak responsible for the isothermal signal.

Investigation of predictions (2) and (3) using alumina substrates chips showed that the peak maxima of the isothermal signals shift to longer measurement time as the heating rate increases and both vanish at T > 100 °C and T > 200 °C, the maximum temperatures of Peak 1 and Peak 2 respectively. Measurements performed using coarse and fine grain samples, prepared as described in the methodology section, also confirmed the behaviour predicted by Jain *et al.*, (2007). In particular, the ID curves measured at a heating rate of 5 °C s^{-1} with both the coarse- and the fine-grain samples still displayed a peak structure, although the maxima were observed at significantly shorter measurement times. Furthermore, when a lower heating rate was applied (i.e., 1 °C s^{-1}), the initial rise in the ID curves was found to be absent in most of the investigated temperatures. In Figures 7.5 and 7.6 the ID curves measured at 60 and 170 °C using two different heating rates (i.e., Figure. 7.5: 5 °C s^{-1}; Figure. 7.6: 1 °C s^{-1}) are compared for all three types of samples. The temperatures were selected because the build-up effect was more pronounced at these values.

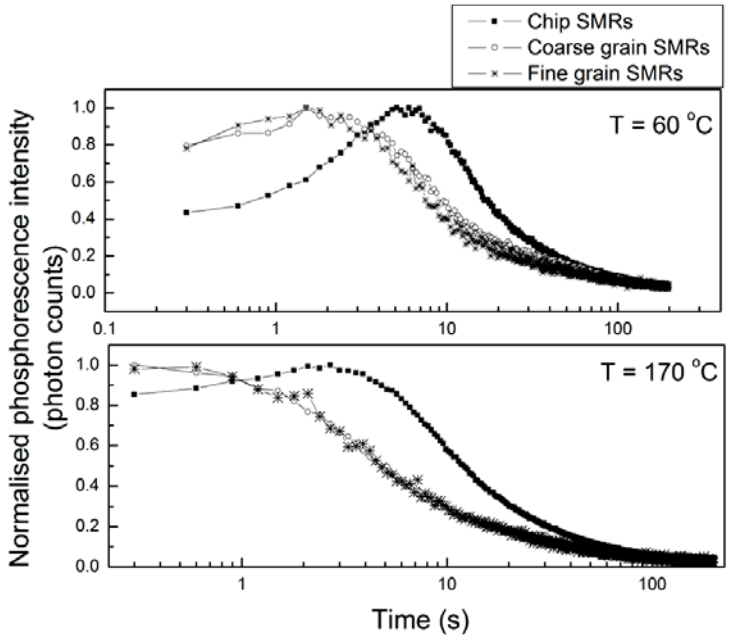

Figure 7.5: Comparison of isothermal decay curves for a sample consisting of 4 type ´1206´ chip SMRs (filled square), a coarse- (open circle), and a fine-grain (star) sample. The samples received a dose of 12 Gy and heated to 60 and 170 °C at 5 °C s^{-1}, and held at these temperatures for 200 s.

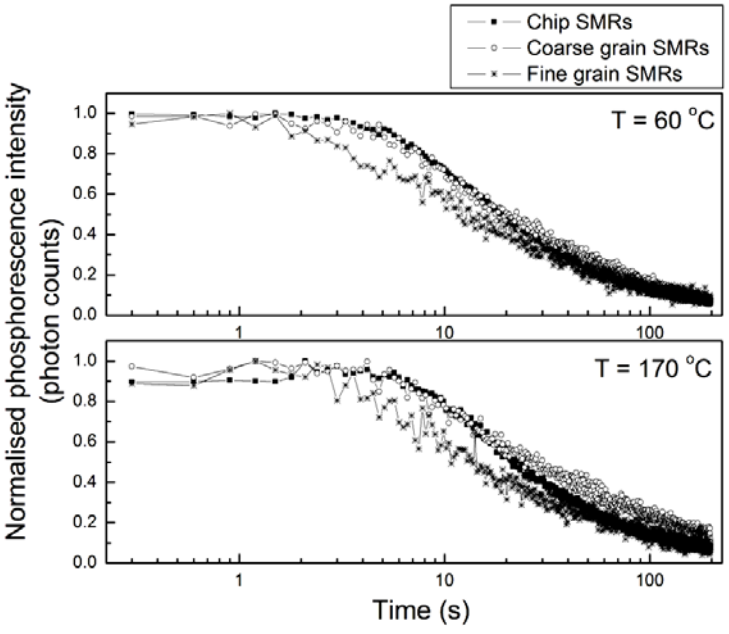

Figure 7.6: Comparison of isothermal decay curves for a sample consisting of 4 type ´1206´ chip SMRs, a coarse grain, and a fine grain sample. The samples received a dose of 12 Gy and heated to 60 and 170 °C at 1 °C s^{-1} and held at these temperatures for 200 s.

Although it was demonstrated that the build-up effect in the ID curves of the coarse- and fine-grain specimens is not due to non-first-order kinetics, the phosphorescence emission still does not decay according to the first-order kinetics mechanism. It could, therefore, be reasonably argued that both TL peaks follow non-first-order kinetics.

7.3.3 Activation energy and frequency factor

So far the nature of the order of kinetics of the TL peaks of alumina substrates is unclear. Although the isothermal decay measurements presented in the previous section indicate non-first order kinetics, there can be a number of reasons for departure from exponential decay. The presence of overlapping components within a TL peak due to several trapping states could also potentially explain most of the experimental data. Nevertheless, for the purpose of extracting the physical parameters and until more solid evidence for the multiple trap structure of the peaks is found, they will be treated as individual TL peaks of second-order kinetics.

Variable heating rate method

The variable heating rate was first used to calculate the activation energies and frequency factors of TL Peak 1 and 2 (Section 2.7.1). The maximum temperature, T_m, the full width at half maximum, (FWHM), and the total light sum of each peak was examined for a range of heating rates between 1 and 12 °C s^{-1} following the administration of a dose of 4 Gy. As expected from theory (Kitis *et al*., 1994), T_m shifts to higher values with increasing heating rate, the FWHM slightly increases, and the total light sum (i.e., peak integral) decreases (Figure 7.7 and Table 7.2).

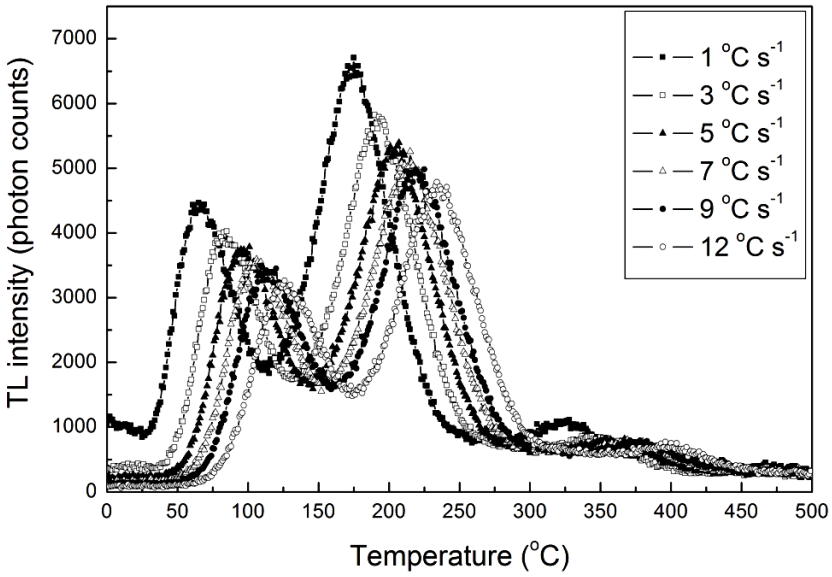

Figure 7.7: Effect of different heating rates on the TL glow peaks of SMRs. The temperature of each peak maximum shifts to higher temperatures as the heating rate increases, and the FWHM also increases. The data are representative of a sample consisting of ~ 20 type ´0402´ SMRs.

Table 7.2: Variation of the maximum temperature T_m, FWHM, and luminescence integral of TL Peak 1 and 2 at different heating rates.

	TL Peak 1			TL Peak 2		
Heating rate ($^oC\ s^{-1}$)	**T_m (±2 ^oC)**	**FWHM**	**Peak integral[a] (50-150 ^oC)**	**T_m (±2 ^oC)**	**FWHM**	**Peak integral[a] (150-290 ^oC)**
1	69	55	1	175	65	1
2	80	57	0.94	186	67	0.92
3	87	59	0.90	194	68	0.89
4	92	57	0.89	202	67	0.85
5	99	57	0.85	205	68	0.82
6	104	59	0.81	212	68	0.81
7	109	57	0.81	214	67	0.78
8	112	58	0.80	216	69	0.76
10	119	58	0.77	226	71	0.76
12	128	61	0.73	238	71	0.73

[a]The peak integral at each heating rate was normalised to that obtained with a heating rate of 1 $^oC\ s^{-1}$

The values of *E* and *s* were determined graphically from the slope and the intercept of a plot of ln (T_m^2/β) vs ${kT_m}^{-1}$ (Figure 7.8). In this graph, each T_m value represents the peak maximum temperature corrected for temperature lag (Chapter 2; equation 2.17). This is because using the values of T_m taken directly from the recorded glow curves the plots of ln (T_m^2/β) vs ${kT_m}^{-1}$ were significantly curved and the estimation of *E* and *s* would be incorrect, since he relationship between ln (T_m^2/β) and ${kT_m}^{-1}$ should be linear.

An estimate of the lifetimes at RT of the electrons in the trap(s) responsible for each TL peak was made using the following expression which mainly determines the remnant luminescence intensity at any time *t* following irradiation if thermal decay at temperature *T* has occurred.

$$\tau = s^{-1}\exp(E/kT) \qquad (7.1)$$

Although the use of the above expression is considered valid in the case of first-order kinetics – since only in this case the relationship between remaining intensity and time *t* will be exponential (Chen and McKeever, 1997; McKeever, 1985) – it is also used to describe the thermal stability of non-first-order kinetics peaks. Discrepancies are, of course, expected (e.g., Singh, 2013; Singh *et al*., 2013), but unless the order of kinetics of a peak is precisely known the above expression could provide a reasonable compromise to determine, at least, a general upper limit for the timescale a peak is expected to be thermally stable at a given temperature.

As shown in Figure 7.8, TL Peak 1 has a very short lifetime of about 10 minutes at RT. This result supports a thermal fading mechanism (Chapter 10) for the observed fast decay of the peak when there is a delay between irradiation and measurement of the TL signal. The calculated mean lifetime at RT of TL Peak 2 is ~ 3 years making it more suitable for dosimetry use. Nevertheless, as will be shown later (Chapter 10), TL Peak 2 suffers strong signal loss at RT.

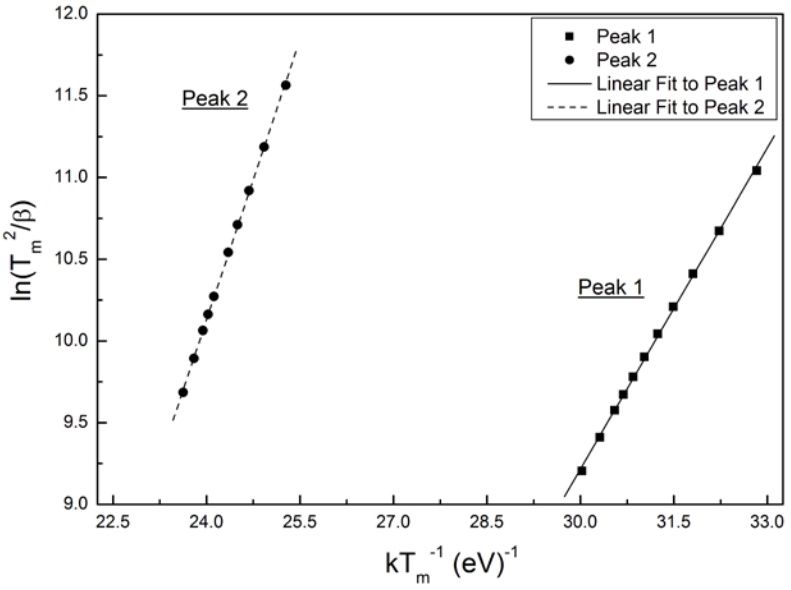

Parameter	TL Peak 1	TL Peak 2
E (eV)	0.65±0.01	1.14±0.01
s (s^{-1})	(2.55±0.57)x10^{8}	(4.36±1.16)x10^{11}
τ (RT)	9.90 minutes	2.96 years

Figure 7.8: Plots of ln (T_m^2/β) as a function of kT_m^{-1} for TL Peak 1 and TL Peak 2 obtained using the variable heating rate method. The values of the activation energy and frequency factor are also shown. Data are representative of samples consisting of ~ 20 type ´0402´ SMRs irradiated with 4 Gy.

Due to the significance of the correction for the temperature lag effect in determining the correct values of T_m of the peaks, it was thought sensible to repeat the VHR test using the fine- or coarse-grain samples. The data obtained with a heating rate of up to 8 °C s^{-1} were slightly affected by temperature lag resulting in average (over 4 samples) values of *E* (Table 7.3) close to those obtained using the standard chip samples. Using the whole data set and applying the lag correction approach, the new values of the trap depth were by ca 14 % higher than those obtained using the standard chip samples. More noteworthy differences were, however, found for the values of *s* and *τ*.

Table 7.3: Average values of the trap parameters of TL Peak 1 and 2 estimated with the VHR method using coarse- and fine-grain samples. In the ´Without temperature lag correction´ case only the data obtained with heating rate up to 8 °C s^{-1} were used, whereas in the other case the entire data set (β = 1-12 °C s^{-1}) was analysed. The values represent the average estimated quantity over 4 samples (i.e., 2 coarse- and 2 fine-grain samples).

	Without temperature lag correction		**With temperature lag correction**	
Parameter	**TL Peak 1**	**TL Peak 2**	**TL Peak 1**	**TL Peak 2**
E (eV)	0.70±0.02	1.22±0.04	0.74±0.01	1.32±0.03
s (s^{-1})	(9.25±0.43)x10^{8}	(6.89±0.60)x10^{12}	(3.44±0.63)x10^{9}	(9.03±1.06)x10^{13}
τ (RT)	30 minutes	8.70 years	43 minutes	23 years

Initial rise and peak shape methods

The IR and PS methods were also used to calculate the activation energies and frequency factors of both peaks obtained after the variable dose and the various heating rate experiments. In the IR method the values of the activation energy were obtained from the slope of the plots of $ln\,(I)$ versus kT^{-1} which in the initial rise part of the peak where the TL intensity is ~ 10 % of the maximum intensity yields a linear curve (Figure 7.9).

For the peak shape method the expressions for second-order kinetics were used. In particular, the activation energy was calculated applying all three peak-shape factors (i.e., $\delta = T_2 - T_m$, $\tau = T_m - T_1$, $\omega = T_2 - T_1$). In all cases, the frequency factor was determined using the second-order expression (Chapter 2; equation 2.22) by substituting the calculated value of *E*. Tables 7.4 and 7.5 list the values of the *E* and *s* parameters after the application of the IR method measured at different dose levels (Table 7.5) and at different heating rates (Table 7.6). The results from the application of the PS analysis on the same glow curves are given in Table 7.7 and 7.8 respectively. All results represent the average estimates of *E* and *s* calculated using a number of different samples of types ´1206´ and ´0402´ SMRs.

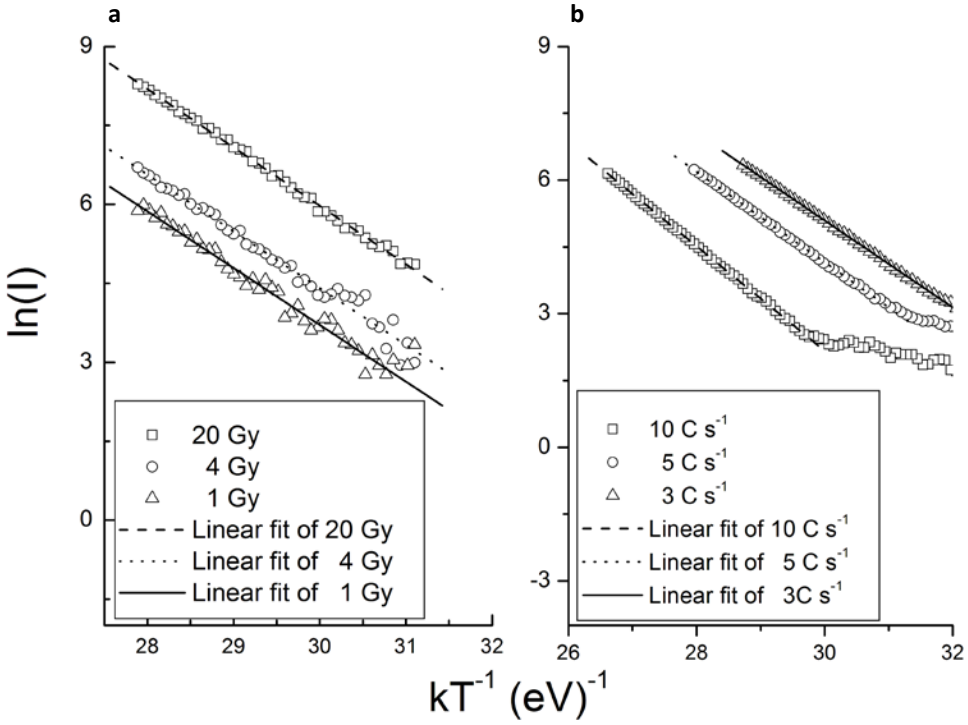

Figure 7.9: Examples of the application of the initial rise method on the initial rise part (i.e., up to ~10 % of maximum peak intensity) of TL peak 2 measured at different (a) levels of dose and (b) heating rates. The plots of *ln(I)* against kT^{-1} (*I-intensity*) were fitted with linear regression lines (i.e., dashed lines), the slope of which corresponds to the value of the activation energy of the peak, *E*. The results of the IR analysis are listed in Tables 7.5 and 7.6.

Table 7.5: Initial Rise method.
Activation energy and frequency factor values of TL Peak 1 and TL Peak 2 at different dose levels.

	TL Peak 1		TL Peak 2	
Dose (±0.12Gy)	**E (eV)**	**s (s^{-1})**	**E (eV)**	**s (s^{-1})**
1	0.60±0.02	$(3.21\pm0.21)\times10^{7}$	1.10±0.02	$(1.31\pm0.05)\times10^{11}$
2	0.62±0.02	$(6.22\pm0.20)\times10^{7}$	1.10±0.02	$(1.31\pm0.05)\times10^{11}$
4	0.65±0.01	$(1.58\pm0.05)\times10^{8}$	1.10±0.03	$(1.24\pm0.07)\times10^{11}$
8	0.68±0.01	$(3.97\pm0.12)\times10^{8}$	1.08±0.02	$(7.00\pm0.26)\times10^{10}$
10	0.67±0.02	$(2.69\pm0.02)\times10^{8}$	1.08±0.02	$(7.00\pm0.25)\times10^{10}$
15	0.67±0.02	$(2.38\pm0.14)\times10^{8}$	1.11±0.01	$(1.33\pm0.02)\times10^{11}$
20	0.74±0.02	$(2.30\pm0.12)\times10^{9}$	1.11±0.01	$(1.25\pm0.02)\times10^{11}$
40	0.80±0.01	$(1.38\pm0.03)\times10^{10}$	1.12±0.01	$(1.51\pm0.03)\times10^{11}$
60	0.81±0.01	$(1.77\pm0.04)\times10^{10}$	1.11±0.02	$(9.82\pm0.35)\times10^{10}$

Table 7.6 Initial Rise method.
Activation energy and frequency factor values of TL Peak 1 and TL Peak 2 at different heating rates.

	TL Peak 1		TL Peak 2	
Heating rate (° C s^{-1})	**E (eV)**	**s (s^{-1})**	**E (eV)**	**s (s^{-1})**
1	0.62±0.01	$(7.44\pm0.24)\times10^{7}$	0.91±0.02	$(8.31\pm0.36)\times10^{8}$
2	0.66±0.01	$(3.12\pm0.10)\times10^{8}$	0.93±0.02	$(1.52\pm0.07)\times10^{9}$
3	0.69±0.01	$(7.49\pm0.22)\times10^{8}$	1.02±0.01	$(1.52\pm0.03)\times10^{10}$
4	0.74±0.01	$(4.29\pm0.11)\times10^{8}$	1.00±0.02	$(7.69\pm0.10)\times10^{9}$
5	0.71±0.02	$(1.10\pm0.06)\times10^{9}$	1.05±0.02	$(2.57\pm0.38)\times10^{10}$
6	0.76±0.01	$(4.70\pm0.12)\times10^{9}$	1.14±0.01	$(2.19\pm0.10)\times10^{11}$
7	0.72±0.02	$(1.22\pm0.07)\times10^{9}$	1.18±0.01	$(6.15\pm0.10)\times10^{11}$
8	0.79±0.01	$(1.31\pm0.03)\times10^{10}$	1.18±0.01	$(5.42\pm0.14)\times10^{11}$
10	0.85±0.01	$(1.01\pm0.02)\times10^{11}$	1.18±0.02	$(4.20\pm0.10)\times10^{11}$
12	0.86±0.01	$(8.75\pm0.20)\times10^{10}$	1.26±0.01	$(1.48\pm0.02)\times10^{12}$

Table 7.7: Peak shape method.

Activation energy and frequency factor values of (a) TL Peak 1 and (b) TL Peak 2 at different dose levels.

a **TL Peak 1**

Dose (±0.12Gy)	E_ω (eV)	E_δ (eV)	E_τ (eV)	s_ω (s^{-1})	s_δ (s^{-1})	s_τ (s^{-1})
1	0.69±0.03	0.69±0.05	0.67±0.06	(4.64±0.31)x10^8	(7.12±0.85)x10^8	(2.23±0.31)x10^8
2	0.69±0.03	0.69±0.05	0.66±0.06	(4.51±0.29)x10^8	(7.17±0.76)x10^8	(2.21±0.25)x10^8
4	0.68±0.03	0.69±0.05	0.65±0.06	(3.95±0.25)x10^8	(6.77±0.80)x10^8	(1.58±0.21)x10^8
8	0.72±0.03	0.73±0.06	0.68±0.07	(3.70±0.26)x10^9	(4.90±0.70)x10^9	(1.90±0.27)x10^9
10	0.73±0.03	0.70±0.06	0.82±0.07	(4.91±0.34)x10^9	(5.70±0.65)x10^9	(2.99±0.34)x10^9
15	0.74±0.04	0.74±0.07	0.73±0.07	(2.61±0.11)x10^9	(4.23±0.46)x10^9	(1.17±0.16)x10^9
20	0.73±0.04	0.76±0.07	0.72±0.06	(1.10±0.05)x10^{10}	(1.45±0.05)x10^{10}	(5.02±0.50)x10^9
40	0.74±0.04	0.74±0.08	0.71±0.07	(2.12±0.12)x10^9	(3.72±0.42)x10^9	(8.29±0.75)x10^8
60	0.73±0.05	0.75±0.09	0.71±0.06	(1.53±0.09)x10^9	(2.74±0.28)x10^9	(5.43±0.53)x10^8

b **TL Peak 2**

Dose (±0.12 Gy)	E_ω (eV)	E_δ (eV)	E_τ (eV)	s_ω (s^{-1})	s_δ (s^{-1})	s_τ (s^{-1})
1	0.83±0.03	0.84±0.05	0.79±0.07	(2.12±0.29)x10^8	(1.13±0.15)x10^8	(4.20±0.50)x10^7
2	0.85±0.03	0.86±0.06	0.82±0.06	(3.95±0.24)x10^8	(2.28±0.30)x10^8	(8.70±0.50)x10^7
4	0.85±0.03	0.87±0.06	0.82±0.06	(2.85±0.30)x10^8	(2.30±0.28)x10^8	(8.96±x0.78)10^7
8	0.83±0.04	0.85±0.05	0.81±0.06	(2.29±0.18)x10^8	(1.28±0.22)x10^8	(4.65±0.55)x10^7
10	0.85±0.04	0.86±0.05	0.83±0.07	(3.02±0.21)x10^8	(1.99±0.24)x10^8	(7.49±0.75)x10^7
15	0.82±0.04	0.84±0.05	0.80±0.06	(1.70±0.10)x10^8	(1.01±0.24)x10^8	(3.85±0.29)x10^7
20	0.83±0.03	0.85±0.05	0.81±0.06	(2.45±0.12)x10^8	(1.37±0.18)x10^8	(5.20±0.37)x10^7
40	0.83±0.03	0.86±0.04	0.82±0.07	(1.75±0.08)x10^8	(1.21±0.19)x10^8	(5.45±0.40)x10^7
60	0.84±0.04	0.85±0.05	0.82±0.06	(1.85±0.15)x10^8	(1.28±0.10)x10^8	(5.78±0.43)x10^7

Table 7.8: Peak shape method.

Activation energy and frequency factor values of (a) TL Peak 1 and (b) TL Peak 2 at different heating rates.

a **TL Peak 1**

Heating rate (° C s^{-1})	E_ω (eV)	E_δ (eV)	E_τ (eV)	s_ω (s^{-1})	s_δ (s^{-1})	s_τ (s^{-1})
1	0.59±0.02	0.56±0.04	0.62±0.05	(2.59±0.20)x10^7	(7.90±1.05)x10^6	(6.79±1.17)x10^7
2	0.61±0.02	0.55±0.04	0.66±0.05	(4.58±0.35)x10^7	(6.81±0.44)x10^6	(2.86±0.95)x10^8
3	0.68±0.02	0.53±0.04	0.69±0.05	(4.79±0.35)x10^7	(3.92±1.05)x10^6	(6.87±0.51)x10^8
4	0.68±0.03	0.62±0.05	0.74±0.06	(5.25±0.41)x10^8	(6.53±0.63)x10^7	(3.96±0.93)x10^9
5	0.70±0.03	0.64±0.05	0.71±0.05	(3.76±0.28)x10^8	(1.10±0.15)x10^8	(1.01±0.16)x10^9
6	0.69±0.03	0.63±0.05	0.76±0.06	(6.17±0.46)x10^8	(8.13±0.66)x10^7	(4.33±1.12)x10^9
7	0.74±0.03	0.65±0.05	0.72±0.05	(4.23±0.31)x10^8	(1.26±0.16)x10^8	(1.11±0.17)x10^9
8	0.74±0.03	0.69±0.05	0.79±0.06	(2.12±0.16)x10^9	(3.81±1.51)x10^8	(9.90±0.54)x10^9
10	0.78±0.03	0.71±0.05	0.85±0.07	(6.64±0.51)x10^9	(7.22±0.90)x10^8	(5.70±1.03)x10^{10}
12	0.78±0.03	0.70±0.05	0.86±0.07	(3.53±0.26)x10^9	(2.97±0.66)x10^8	(4.37±0.40)x10^{10}

b **TL Peak 2**

Heating rate (° C s^{-1})	E_ω (eV)	E_δ (eV)	E_τ (eV)	s_ω (s^{-1})	s_δ (s^{-1})	s_τ (s^{-1})
1	0.78±0.03	0.72±0.04	0.84±0.05	(2.65±0.16)x10^7	(5.75±0.16)x10^6	(1.30±0.53)x10^8
2	0.91±0.03	0.80±0.05	1.01±0.07	(8.42±0.55)x10^8	(5.69±0.19)x10^7	(1.39±0.67)x10^{10}
3	0.85±0.03	0.80±0.05	0.90±0.06	(1.71±0.10)x10^8	(3.98±0.71)x10^7	(5.99±0.45)x10^8
4	0.85±0.03	0.74±0.04	0.98±0.06	(1.99±0.12)x10^8	(1.13±0.58)x10^7	(4.64±0.12)x10^9
5	0.88±0.03	0.83±0.05	0.92±0.05	(3.50±0.21)x10^8	(1.11±0.99)x10^8	(8.59±0.12)x10^8
6	0.98±0.03	0.94±0.06	1.00±0.06	(3.46±0.22)x10^9	(1.41±0.76)x10^9	(6.29±0.17)x10^9
7	1.01±0.03	0.99±0.06	1.02±0.06	(8.92±0.57)x10^9	(5.29±0.13)x10^9	(1.10±0.66)x10^{10}
8	1.01±0.03	0.91±0.05	1.10±0.07	(7.48±0.47)x10^9	(7.10±0.98)x10^8	(7.58±0.81)x10^{10}
10	1.03±0.03	0.90±0.05	1.16±0.08	(1.08±0.67)x10^{10}	(5.12±0.38)x10^8	(2.88±0.57)x10^{11}
12	1.05±0.03	0.98±0.06	1.11±0.07	(1.22±0.74)x10^{10}	(2.35±0.61)x10^9	(5.06±0.27)x10^{10}

The above measurements were also performed using the coarse- and the fine-grain samples (results are not shown), and similar to the VHR analysis, the *E* values were found to be on average 13 % higher, whereas the *s* values showed a considerably larger percentage difference.

7.3.4 Summary – Discussion

General features

According to the TL theory (Randall and Wilkins, 1945), each peak in the TL glow curve corresponds to a particular trap in the energy band structure of the luminescent material. It can, therefore, be assumed that three traps giving rise to TL peaks at ~ 100 ° C (TL Peak 1), ~ 210 ° C (TL Peak 2), and ~ 360 ° C (TL Peak 3) participate in the thermally stimulated luminescence of beta particle irradiated alumina substrates. Nevertheless, thermal annealing at progressively higher temperatures indicates that TL Peak 1 and TL Peak 2 may be more complex consisting of several components related to either discrete energy levels or arising from a distribution of trapping states.

TL Peak 1, defined in the range 50-150 °C, displays a considerable reduction in intensity accompanied by a shift of the peak maximum temperature even for thermal treatments as low as 50 °C. The former can be explained as being due to the thermal depletion of the charge population from the traps responsible for the peak, whereas the latter usually implies the existence of overlapping peak components.

In the step-wise annealing experiments the onset of a decrease in the intensity of TL Peak 2 (150-290 °C) and a shift in peak maximum temperature is evident at ca 120 °C, the changes progressively increasing as the temperature reaches 150 °C. As with TL Peak 1, this could be explained assuming several components under the main peak. Nevertheless, one would anticipate this to take place at annealing temperatures exceeding 150 °C. One explanation would be to assume that TL Peak 1 and TL Peak 2, since they are not well separated, share common traps such that annealing at 150 °C results in the total destruction of TL Peak 1 but also in the removal of a component from TL Peak 2 producing the above effects. The existence of overlapping components and/or traps will be explored in the following section.

TL Trap parameters

The basic kinetic parameters of TL Peak 1 and TL Peak 2 were evaluated using a number of approaches. The order of kinetics was initially examined to help evaluate the validity of the methods used to calculate the activation energy and frequency factor and to obtain an indication of the various processes that can take place during thermal stimulation. First-order kinetics indicative of direct thermal detrapping/recombination or minimum retrapping processes could not be verified for either peak. Aside from the values of geometric factor which significantly deviate from that expected for a first-order peak the strongest evidence for non-first-order kinetics resulted from the measurement of the isothermal response. Using coarse and fine grain samples to minimise the effect of temperature lag, seen as build-up in the ID curves (Figure 7.5), it was shown that the phosphorescence emission from SMRs decays in a non-exponential manner; inconsistent with first-order kinetics.

Following the determination of the order of kinetics, the *E* and *s* values of each glow peak were calculated using several approaches. From a practical point of view, the analysis of the kinetic parameters of the traps is needed for the estimation of the lifetime, τ, of a given peak which will define its usable timescale for dosimetry applications. The predicted lifetime is calculated at a specified temperature using the calculated values of *E* and *s* and the expression $\tau = s^{-1}\exp(E/kT)$, with *T* being equal to 293 K (i.e., 20 °C). Knowing τ is equivalent to the time the charge population remains in the traps before thermal release at RT commences. In addition, the lifetime is a useful parameter for distinguishing between the mechanisms of thermal and athermal loss of the trapped charge carriers. Therefore, it is important that at a given temperature the lifetime τ does not change with, for example, the experimental conditions. This in turn implies that *E* and *s* are invariable parameters. Nevertheless, the expectation of *E* and *s* being constant may not be realistic, since these parameters are estimates derived from experimental values likely representing an average behaviour of a combination of different physical parameters.

As shown above, the kinetic parameters of the traps of the TL peaks of alumina substrates, studied both as standard chip or as coarse- and fine-grain samples, calculated by the PS and IR methods demonstrated a small variation with heating rate and only for TL Peak 1 a small

variation of *E* and *s* with dose was observed using the IR method Specifically,the activation energy of TL Peak 1 calculated using the IR method increased from ~ 0.60 to ~ 0.80 eV with increasing dose and from ~ 0.60 to ~ 0.90 eV with increasing heating rate for both the IR and the PS method. On the other hand, the *E* values of TL Peak 2 calculated using either the IR or the PS method remained relatively constant with dose at ~ 1.10 eV and ~ 0.85 eV respectively, but increased as the heating rate increased. In the same manner, the frequency factor also varied with dose and heating rate. Overall, values lower by about 15 % were obtained by the PS analysis.

The heating rate is perhaps the most important variable of TL affecting not only the duration of the measurement but several properties of the glow peaks. In accordance with theoretical predictions (Kitis *et al*., 1994), the three most important effects produced (e.g., Figure 7.7 and Table 7.2) when the heating rate increased from 1 to 12 ^{o}C s^{-1} were (1) a shift of maximum peak temperature to higher values, (2) a slight increase of the width [or full width at half maximum (FWHM)] of a peak, and (3) a decrease of the peak total light sum (i.e., peak integral). Such variations may result in inaccuracies in the determination of the parameters of the peak (e.g., T_m, T_1, T_2) and therefore in the trap parameters. This will be more evident for methods based on the shape characteristics, such as the PS method, rather than the IR method. More important, however, is a different effect that takes place as the heating rate increases. This is thermal lag which, as explained above, manifests itself as a delay between the temperature of the heating element and the sample temperature, resulting in poor control of the true temperature range of a peak. Usually, under the influence of temperature lag, T_m appears larger than would be expected from kinetic theory, giving rise to higher values of *E* and *s*. The increase in *E* and *s* with heating rate was also observed earlier by Gokce *et al*. (2009) and attributed to the temperature lag phenomenon.

A different interpretation has been suggested for the change of trapping parameters with dose. In an early study, Levy (1984) using computerised generated TL glow curves showed that some characteristics of single glow peaks which are not expected from the standard first- and second-order kinetics may be interpreted on the basis of an interactive trap model. According to this model, if a luminescent system contains several types of traps, some of the charges excited from ´lower temperature´ traps during thermal stimulation will be captured by traps associated with the high temperature side of a peak, and this leads to a dependence of the calculated values of *E*

and *s* on radiation dose. More recently, Furetta *et al*. (2000) explained the changes in the activation energy, maximum temperature, and order of kinetics with increasing dose by assuming a continuous distribution of trapping states. The authors used the term ´effective´ activation energy and peak maximum temperature to describe the parameters of a peak which is not due to a single trapping level. They proposed that, at small doses, the shallow energy levels are primarily filled, whereas the filling of deeper traps is partially incomplete. As the dose increases the trapped concentration of the deeper energy levels increases and as a consequence E_{eff} and T_{meff} shift toward higher values. Similar effects have been reported by other researchers (e.g., Agersnap *et al*., 1999; Ogundare *et al*., 2006; Walker *et al*., 1996) and also explained based on the assumption of several overlapping components with different dose-dependent growth rates.

In general, the results obtained with the standard chip samples using the VHR, the IR, and the PS methods do not differ significantly, if comparison is made for a given dose and heating rate. This is more evident in Table 7.9 which includes the activation energy and the frequency factor of the glow curves obtained at 5 °C s^{-1} for a dose of 4 Gy. It can be seen that there is a good agreement between the methods used, although the PS method gives systematically lower values. This might be due to the fact that the accurate calculation of the T_1 and T_2 is affected by the presence of adjacent peaks which are not possible to be removed using a thermal cleaning procedure.

Table 7.9: Comparison of values of activation energy, *E*, and frequency factor, *s*, of a standard SMR sample after analysing the TL glow curves (5 °C s^{-1} ; 4 Gy) using the VHR, IR, and PS methods.

	TL Peak 1		**TL Peak 2**	
Method	**E (eV)**	**s (s^{-1})**	**E (eV)**	**s (s^{-1})**
VHR	0.65±0.01	(2.55±0.57) x10^{8}	1.14±0.01	(4.36±1.16)x10^{11}
IR (Variable Dose)	0.65±0.01	(1.58±0.05)x10^{8}	1.10±0.03	(1.24±0.07)x10^{11}
IR (VHR)	0.71±0.02	(1.100.06)±x10^{9}	1.05±0.02	(2.57±0.38)x10^{10}
PS (Variable Dose)-average over ω,δ,τ	0.67±0.05	(4.11±0.42)x10^{8}	0.85±0.05	(2.02±0.45)x10^{8}
PS (VHR)-average over ω,δ,τ	0.68±0.04	(4.99±0.07)x10^{9}	0.88±0.04	(4.40±0.44)x10^{8}

On the other hand, for the coarse- and the fine-grain samples the values between the VHR. the IR, and PS methods were found to not agree perfectly and the reasons are not clear at this srtage The VHR method resulted higher values for *E* and *s* and a significantly larger and more realistic

value for the lifetime of TL Peak 2. A final remark which may further support that the VHR using the thinner samples resulted the most representative estimates of the trap parameters is that IR even though it is considered one of the most reliable methods for the evaluation of the kinetic parameters it often gives lower values since it is based on the intensity at the maximum of the TL peak which appears reduced due to thermal quenching. This, however, was not observed when the standard chip samples were measured, but it can be seen in the data obtained with the coarse- and fine-grain samples. Since, as will be demonstrated in the following sections, TL Peak 2 suffers from thermal quenching it could be assumed that in all cases the values of E using the IR method are lower due to the thermal quenching effect.

In summary, both TL Peak 1 and 2 follow non-first-order kinetics which is most likely caused by the presence of multiple trapping states. The most reliable kinetic parameters, describing the average behaviour of all traps involved, seem to be those estimated using the VHR method and the samples less affected by temperature lag. As suggested in the beginning of this chapter, TL Peak 1 cannot be considered for dosimetry uses because even if samples are maintained at RT prior to TL readout the trapped charge population will fade thermally. In contrast, TL Peak 2 seems to arise from a trap population with sufficient thermal depth (~ 1.32 eV) to prevent the thermal escape of charge carriers at RT.

7.4 Multiple trap TL glow peaks

As indicated in the preceding analysis, the TL signal of alumina substrates most probably arises from a complex rather than a single trap environment. The main observations expected in the case of a multiple trap model are (1) a shift of the TL peak maximum to higher temperatures with increasing dose levels, (2) the movement of T_m during the step-wise annealing test, and (3) non-exponential isothermal decay

To better resolve the nature of each TL peak two further types of analysis were carried out. The method of T_m-T_{stop} (Chapter 2) was used as a first instance to check the existence and the number of overlapping peak components. Experimentally it is similar to a step-wise annealing procedure, but in this case the sample is heated to a temperature T_{stop}, cooled down immediately (i.e., no

hold), and the remaining TL is measured. This procedure is repeated several times on the same sample – irradiated again with the same dose – by increasing the T_{stop} value by a small step. For every T_{stop} the T_m value of the remaining TL glow peak is noted and used to produce the T_m-T_{stop} graph. The presence of plateau regions within a T_{stop} range is usually indicative of an individual peak (McKeever, 1985). The T_m-T_{stop} method was tested using several aliquots consisting of different number of type ´0402´ and type ´1206´ SMRs, irradiated with ~ 3 Gy and heated sequentially from 50 to 300 °C by increasing the T_{stop} by 5 °C. Figure 7.10 shows an example of remaining TL glow curves after a series of T_{stop} temperatures.

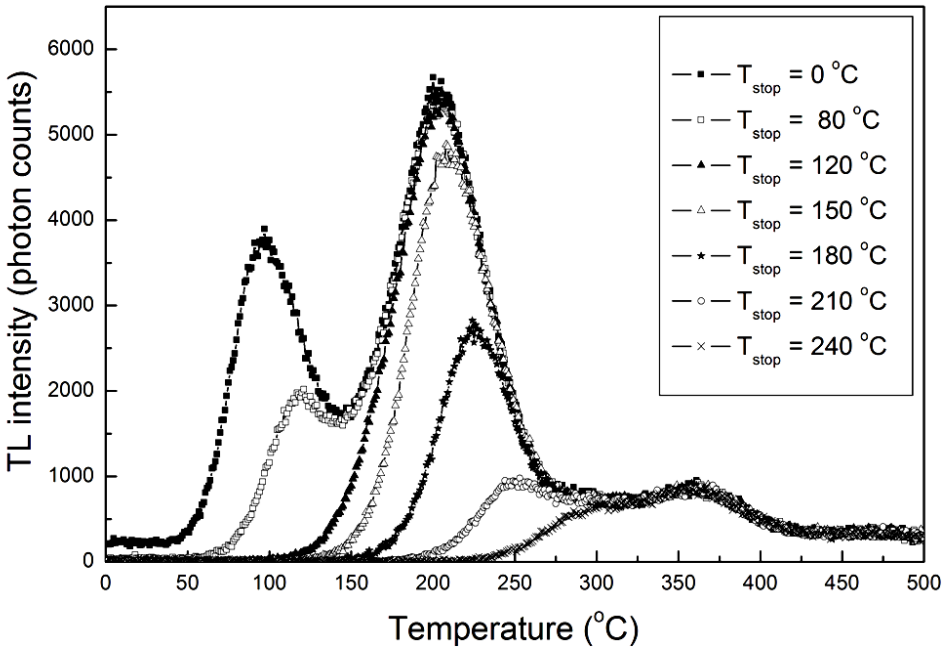

Figure 7.10: Initial and remaining TL glow curves following different T_{stop} temperatures. The curves correspond to a sample consisting of 3 type ´1206´ SMRs irradiated with a dose of 3 Gy.

TL Peak 1 was resolved only in the 50-100 °C T_{stop} range where the T_{m1} demonstrates a continuous rise from ~ 105 °C to ~ 134 °C (Figure 7.11a). Consistent with the previous step-wise annealing test (Section 7.2), the T_{m2} of TL Peak 2 remains approximately constant at ~ 205 °C from 50 °C to ~ 130 °C (inset to Figure 7.11b), increases monotonically to 298 °C for T_{stop}

between 130-240 °C (Figure 7.11b) and vanishes after higher T_{stop} values. Although it is likely that the T_{stop} step used was not sufficient to resolve the individual components, the results suggest the presence of several overlapping peaks possibly arising from a continuous distribution of trapping states or several closely spaced traps. Nevertheless, by performing IR analysis on the remaining TL glow curves following each pulse anneal some flat regions with approximately the same activation energy were able to be identified. As seen in Figure 7.11c, from 50 to 100 °C there appear two plateau regions indicated by dashed circles at 50-70 °C and 80-100 °C corresponding to trap depths of ~ 0.73 eV and ~ 0.94 eV respectively. A third plateau between 115-125 °C can also be seen indicating the existence of another trap with activation energy of ~ 1.11 eV. Above 130 °C the activation energy exhibits a nearly continuous increase from ~ 1.18 to ~ 1.33 eV until another flat region at ~ 1.38 eV is reached for T_{stop} between 175 and 205 °C.

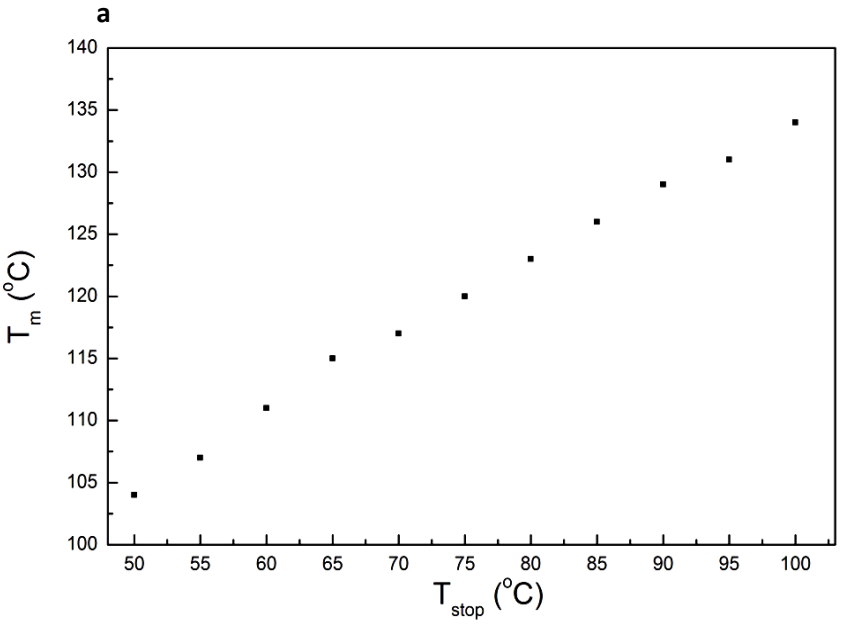

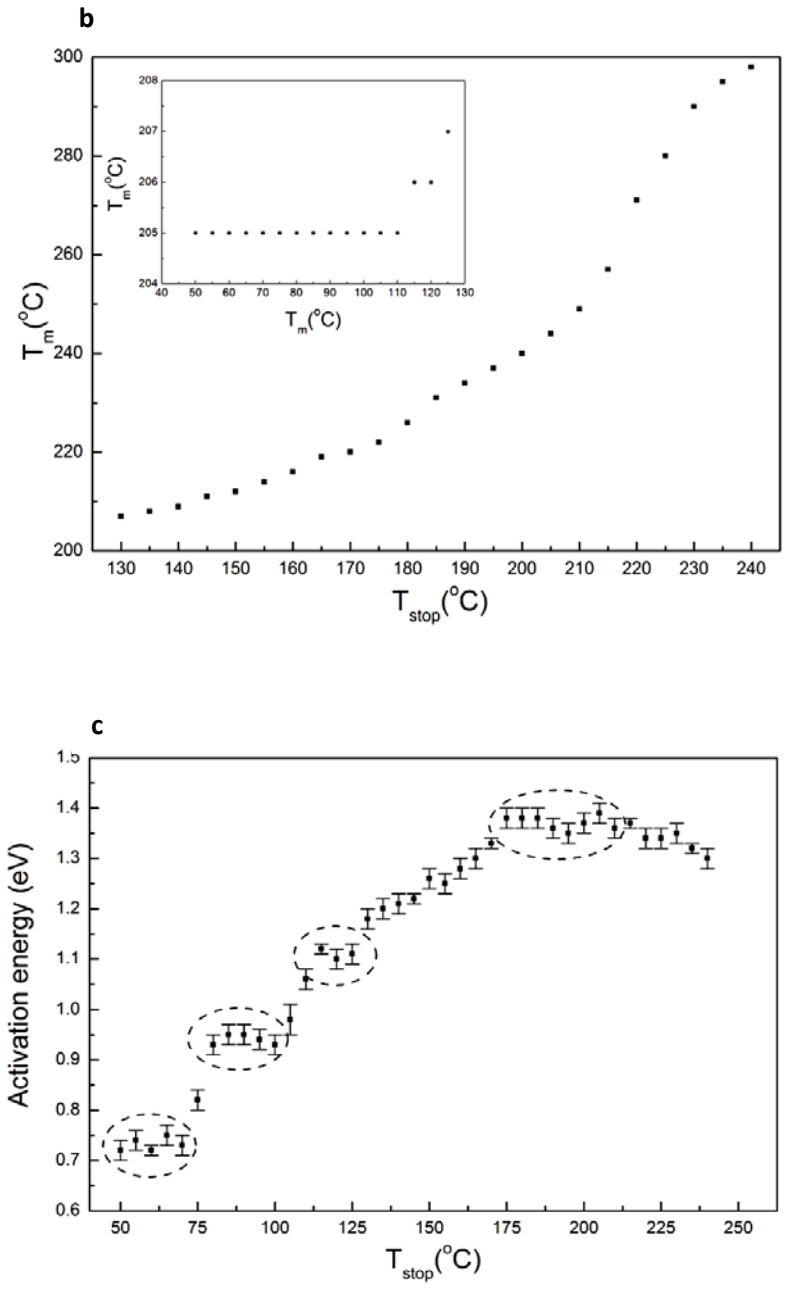

Figure 7.11: T_m-T_{stop} analysis of (a) TL Peak 1 in the range between 50 and 100 °C, and (b) TL Peak 2 in the range between 130 and 240 °C. The inset to (b) shows the variation in T_m of Peak 2 in the initial T_{stop} range from 50 to 120 °C. The error in T_m is ± 2 °C. (c) Activation energy as a function of T_{stop} calculated by analysing the remaining TL glow curves using the initial rise method. The dashed circles indicate the possible positions of individual traps. Each data point represents the average measured or calculated quantity using several samples consisting of different number of type ´0402´ and type ´1206´ SMRs. The samples were irradiated with 3 Gy.

Owing to the stronger evidence for the existence of multiple peaks under the entire TL glow curve a second method was employed to confirm the results of the T_m-T_{stop} method and, if possible, to identify more overlapping components. The second method is based on the deconvolution of the TL glow curves obtained in the step-wise annealing test described in Section 7.2.

The lost TL glow curves were initially calculated by subtracting the TL remaining after each annealing step from the original untreated glow curve (Figure 7.12a). Subsequently, each ´lost´ TL glow curve was subtracted from the next one obtained after a higher temperature preheat. For example, the lost $TL_{50}{}^{o}{}_{C}$ – where the subscript denotes the preheat temperature – was subtracted from the lost $TL_{75}{}^{o}{}_{C}$. The idea was that, for example, the TL lost after annealing at 75 °C already includes the TL component lost after annealing at 50 °C and as such their difference will likely reveal the part of the TL only affected by the higher preheat temperature. Figure 7.12b shows the major peaks identified following the above analysis. TL Peak 1 was found to have three components at ~ 86 °C ($TL_{86}{}^{o}{}_{C}$), ~ 101 °C ($TL_{101}{}^{o}{}_{C}$), and ~ 122 °C ($TL_{122}{}^{o}{}_{C}$) plus a peak component at ~ 145 °C ($TL_{145}{}^{o}{}_{C}$) shared between TL Peak 2. Similarly, TL Peak 2 was found to be composed of four components at ~ 181 °C ($TL_{181}{}^{o}{}_{C}$), ~ 204 °C ($TL_{204}{}^{o}{}_{C}$), ~ 220 °C ($TL_{220}{}^{o}{}_{C}$), and ~ 244 °C ($TL_{244}{}^{o}{}_{C}$). The higher temperature part of the glow curve was fitted with one peak at ~305 °C ($TL_{305}{}^{o}{}_{C}$) shared between TL Peak 2 and another one at ~ 366 °C ($TL_{366}{}^{o}{}_{C}$) corresponding to TL Peak 3. The kinetic parameters of the resulting peaks were finally estimated using the IR and PS methods. The results are presented in Table 7.10.

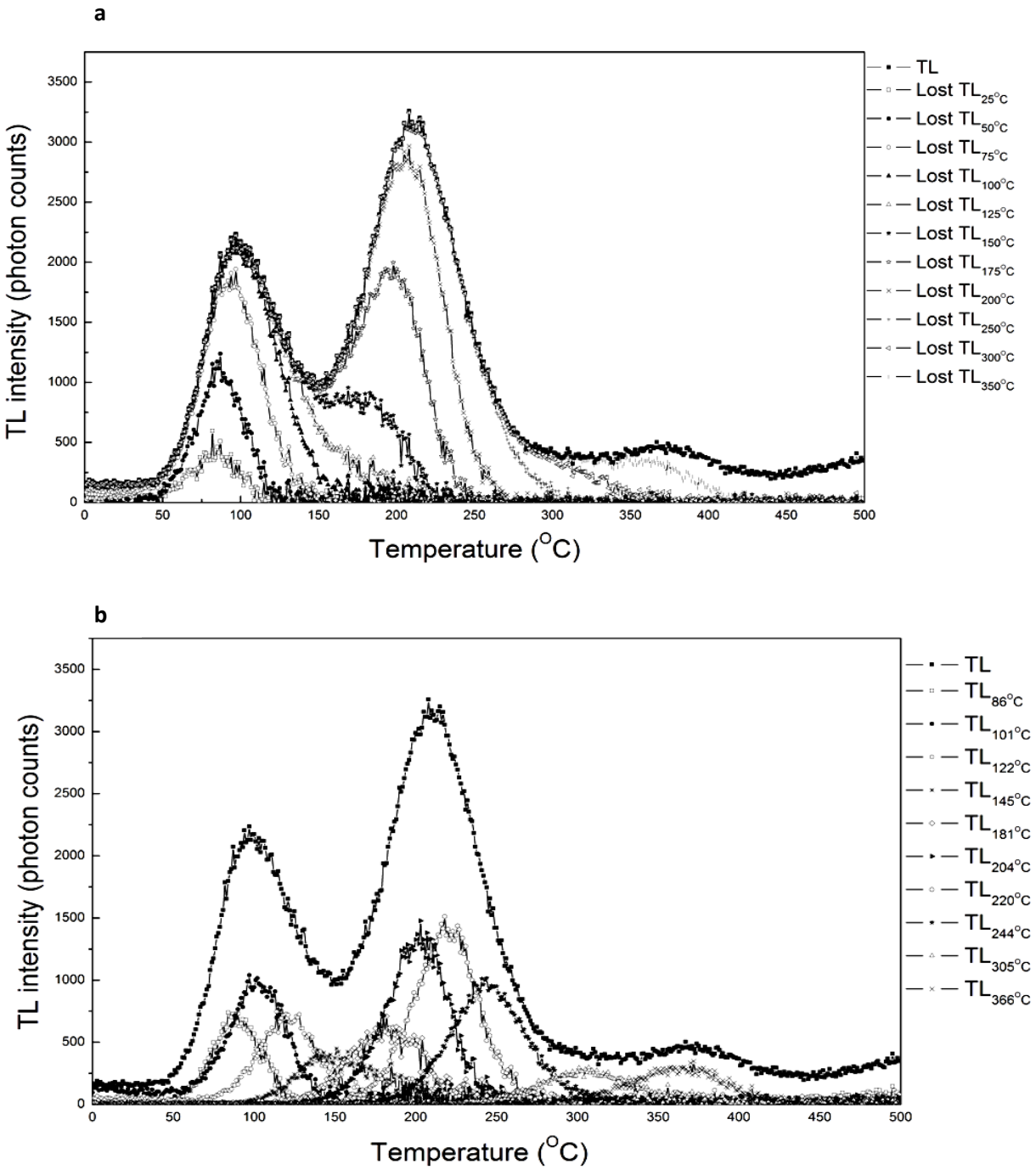

Figure 7.12: (a) Lost TL glow curves calculated by subtracting the remaining TL following preheat at T=25-350 °C from the initial TL glow curve. (b) Major peak components identified by subtracting each lost TL glow curve in from the next one obtained after a higher temperature preheat. For example, the lost $TL_{50^{o}C}$ – where the subscript denotes the preheat temperature – was subtracted from the lost $TL_{75^{o}C}$. Data produced with a sample consisting of 3 type ´1206´ SMRs.

Table 7.10: Values of the activation energy *E*, frequency factor *s*, and the geometric factor, μ_g, of peaks identified from the analysis of glow curves obtained following the step-wise annealing procedure described in 7.2. Data represent average values obtained using a number of samples consisting of 3 type ´1206´ SMRs.

	Peak Shape			Initial Rise	
Peak	**E (eV)**	**μ_g**	**s (s^{-1})**	**E (eV)**	**s (s^{-1})**
TL_{86^oC}	0.94±0.10	0.54±0.08	$(6.87\pm1.53)\times10^{12}$	1.00±0.04	$(4.64\pm0.19)\times10^{13}$
TL_{101^oC}	1.03±0.11	0.52±0.07	$(2.68\pm0.59)\times10^{13}$	1.00±0.03	$(1.17\pm0.07)\times10^{13}$
TL_{122^oC}	0.99±0.10	0.47±0.07	$(1.46\pm0.28)\times10^{12}$	1.05±0.02	$(9.16\pm0.35)\times10^{12}$
TL_{145^oC}	0.94±0.08	0.54±0.05	$(5.73\pm0.96)\times10^{10}$	0.95±0.02	$(8.35\pm0.35)\times10^{10}$
TL_{181^oC}	1.07±0.09	0.50±0.05	$(2.09\pm0.34)\times10^{11}$	0.94±0.04	$(6.65\pm0.57)\times10^{9}$
TL_{204^oC}	1.28±0.11	0.43±0.06	$(1.09\pm0.18)\times10^{13}$	1.30±0.01	$(1.70\pm0.02)\times10^{13}$
TL_{220^oC}	1.43±0.13	0.47±0.06	$(1.37\pm0.24)\times10^{14}$	1.35±0.02	$(1.92\pm0.06)\times10^{13}$
TL_{244^oC}	1.51±0.13	0.51±0.06	$(1.77\pm0.30)\times10^{14}$	1.36±0.02	$(5.02\pm0.15)\times10^{12}$
TL_{305^oC}	1.53±0.11	0.52±0.05	$(5.27\pm0.73)\times10^{12}$	1.45±0.08	$(1.04\pm0.11)\times10^{12}$
TL_{366^oC}	1.48±0.08	0.44±0.04	$(9.48\pm1.07)\times10^{10}$	1.54±0.12	$(2.86\pm0.45)\times10^{11}$

As seen in Table 7.10, except for the first peak between 50-70 °C, the remaining three peaks found from the T_m-T_{stop} method have also been identified by the deconvolution method. The agreement in the values of the activation energy is also very good.

In summary, both the deconvolution process and the T_m-T_{stop} method substantiate the initial assumption for the existence of a series of closely spaced mixed-order kinetics peaks within each TL glow peak. Nevertheless, it would be very optimistic to attempt determining the exact number, position, and kinetic parameters of each trap/peak, arguably because different results would be produced by varying the experimental parameters, such as the heating rate or the T_{stop} step. On the other hand, it is speculated that the actual distribution of energy levels is more complex, and although it cannot be precisely uncovered, it can account for most of the characteristics of the thermoluminescence response. As already explained in the relevant sections, the overall behaviour of an apparently single peak consisting of several components (i.e., traps) will most likely deviate from first-order kinetics. Interaction between trapping levels during thermal stimulation of the trapped charge population is also expected which might be one reason for non-first-order kinetics (e.g., retrapping of thermally excited charges into deeper traps is the basic characteristic of second-order processes). On the basis of a multiple trap model the

variation of trap parameters with dose as well as the superlinear dose-response of TL Peak 2 can also be interpreted.

7.5 Comparison of kinetics parameters of alumina SMRs with single crystal Al_2O_3:C dosemeter

TL kinetic analysis studies may provide some insight into the dosimetry properties (e.g., thermal stability) of the trapping levels involved in the generation of luminescence, but also of the defect environment of the phosphor. Contrary to established dosemeters where the types of defects are controlled during the manufacturing process to ensure the most suitable dosimetry properties, fortuitous dosemeters can have a variety of defects which can modify the trapping environment and the relevant luminescence characteristics. This could be corroborated, for example, by comparing the kinetic parameters of the trapping states between two analogous materials. For alumina-based SMRs the most appropriate reference material is the dosimetry grade Al_2O_3:C single crystal.

With the exception of a few studies (e.g., Kitis *et al*., 1994; Kortov *et al*., 1994), it has been suggested (Agersnap *et al*., 1999; Walker *et al*., 1996; Whitley and McKeever, 2000; Yazici, *et al*., 2003; Zahedifar *et al*., 2012) that the main dosimetry peak of Al_2O_3:C is composed of several overlapping components. For instance, Agersnap *et al*., (1999) identified a distribution of first-order traps with activation energies ranging from ~ 1.28 to ~ 1.43 eV. Zahedifar *et al*., (2012) identified mainly three mixed-order kinetics peaks with activation energies between 1.12 and 1.3 eV. Yazici *et al*., (2003) showed that the peak components and kinetic parameters of the main dosimetry peak of Al_2O_3:C vary with dose, although they distinguished two dominant general-order kinetics peaks with mean energies around 1.43 and 1.37 eV. On the other hand, Kitis *et al*., (1994) concluded that the main TL peak is due to a single trap at a depth of 1.5 eV and $s \sim 10^{16}$ s^{-1} and follows general order kinetics, while Kortov *et al*., (1994) suggested that the order of kinetics of the main TL peak is 2, the activation energy is 1.31 eV and the frequency factor varies in the range 10^{12}-10^{14} s^{-1}. The kinetics of the low temperature secondary TL peaks of Al_2O_3:C have also, in a few instances, been determined. Recently, Chithambo and Seneza (2014) characterised the kinetic parameters of the 46 °C peak measured with a heating rate of 1 °C s^{-1}

and concluded that it follows first order kinetics with E ~ 0.7 eV and s ~ 10^{10} s^{-1}. In an earlier study, Kortov *et al*., (2005) showed that the 80 °C peak (β=5 °C s^{-1}) is a first-order kinetics peak having a trap depth of ~ 0.81 eV and frequency factor of ~ 10^{11} s^{-1}.

Despite the slight disagreement, these values can be considered quite similar and close to the kinetic parameters of the TL peaks of alumina-based SMRs reported earlier. Specifically, based on the evaluation of trapping parameters obtained from the VHR method and using the coarse- and fine-grain samples, and assuming that both peaks are due to a single trapping level, it was shown that Peak 1 has a mean *E* of 0.74 eV and *s* of 10^{9} s^{-1}, while the corresponding kinetic parameters of Peak 2 were found to be equal to ~1.32 eV and ~10^{13} s^{-1}. Assuming that Peak 2 is due to several overlapping components, it was found that these second-order components are distributed in energy from ~ 0.94 to 1.5 eV (and *s* ranging from ~ 10^{10} to ~ 10^{14} s^{-1}) which is also in good agreement with the findings for the dosimetry grade single crystal Al_2O_3:C.

Based on the satisfactory agreement between the kinetic parameters of the two alumina-based materials it could be argued that common traps participate in the luminescence process or that similar type of defects (as also indicated from the emission spectra in Chapter 6) exist in both materials. Yet, in the alumina SMRs the additional structural and compositional defects are expected to modify the trap environment resulting in different dosimetry characteristics.

7.6 A TL model for alumina substrates

On the basis of the available experimental results discussed above, the model that may describe the mechanism of thermoluminescence production in alumina substrates more accurately is a semi-localised model. In the semi-localised model, electrons may simultaneously move to the CB and the excited state of the trap from where they can be further transported to the CB or tunnel to a recombination centre (Kumar *et al*., 2006, 2007; Mandowski, 2005). As summarised in Kumar *et al*. (2006), TL glow peak properties such as (1) non-first order kinetics, (2) a dose-dependent T_m, and (3) linear, sub-linear or supra(super)-linear dose response curves are predicted by a semi-localised recombination model. As both TL Peaks 1 and 2 exhibit these properties, a semi-localised recombination model can be used to describe their behaviour.

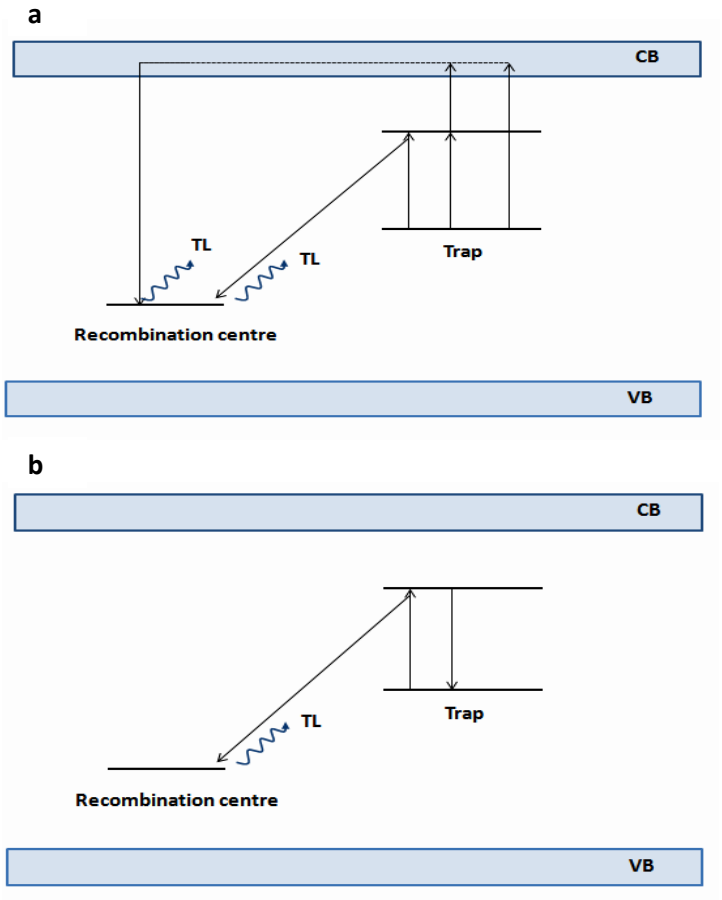

Figure 7.13: Schematic representation of the transitions involved in (a) semi-localised transition model, and (b) pure-localised model.

The pure-localised model (Kumar *et al*., 2006, 2007), where electrons are not transported to the CB either from the excited or the ground state of the trap is less likely (Figure 7.13b). According to this model, the form of the isothermal decay of TL is exponential and the order of kinetics always one but, as discussed above, the form of the isothermal TL decay of alumina substrates is not exponential.

It may be possible to obtain stronger evidence that the delocalised band participates in the recombination processes by measurement of TSC currents which are measured under the action of an applied voltage. TSC characterises the detrapping process of charge carriers and mainly arises from an increase in the conductivity of the material due to a transfer of electrons into the

conduction band during thermal stimulation (Chen and McKeever, 1997). Consequently only a semi-localised transition model would result in such conductivity.

7.7 Thermoluminescence response: Conclusions

The main conclusions of the analysis of the TL response of alumina substrates can be summarised as follows:

a) A number of trapping levels contribute to the TL signal as indicated by the step-wise annealing experiments where a shift of TL peak maxima to higher temperatures with increasing dose and the non-exponential nature of the isothermal decay curves were observed.
b) The results obtained using the T_m-T_{stop} method support a multiple trap model, and provide additional information regarding the number and thermal depth of the traps.
c) The traps responsible for TL Peak 1 at ~ 90 ± 5 °C are relatively shallow having an average ´effective´ trap depth of ~ 0.74 ± 0.01 eV and frequency factor of ~ 10^9 s^{-1}. These values, when combined, result in an average lifetime at RT of about 43 minutes.
d) The trap population associated with the main TL peak at ~ 200 ± 5 °C has a greater calculated thermal stability (i.e., τ ~ 23 years) arising from the larger average ´effective´ trap depth of ~ 1.32 ± 0.03 eV and frequency factor of ~ 10^{13} s^{-1}.
e) The most likely model describing the luminescence process in alumina substrates appears to be one where the conduction band participates in the recombination process either by direct electron transitions or via an intermediate state. The dominance of retrapping or recombination cannot be directly inferred as both are likely, depending on the occupancy of the energy levels, in an interactive trap model.

Chapter 8: Optically stimulated luminescence characteristics of alumina SMRs

8.1 Introduction

During optical (and thermal) stimulation trapped charges may undergo a number of different transitions before radiative or non-radiative recombination takes place. One possibility is a direct transition from the ground state of a trap to the conduction band followed by retrapping to the same or other traps or recombination in a luminescence centre [Figure 8.1 (1)]. Alternatively, recombination may take place following an indirect thermally-activated transition [e.g., Figure 8.1 (2) and (4)].

Thermally assisted recombination models have been suggested by Hutt *et al*., (1988), Spooner (1994), and Poolton *et al*., (1995a,b) for the IR stimulated luminescence in feldspars. The model by Hutt *et al*., (1988) – depicted as (2) in Figure 8.1 – involves an optical transition from the ground to the excited state of the trap followed by phonon assisted escape into the conduction band. Spooner (1994) proposed that a thermally assisted transition takes place first into some states lying very close to the ground state of the trap followed by optical excitation into the conduction band [Figure 8.1 (3)]. This model configuration resembles the vibrational levels that exist in the electronic ground state of a luminescent centre (i.e Chapter 2; section 2.2). A third thermally-activated but sub-conduction band recombination process [Figure 8.1 (4)] was suggested by Poolton *et al*., (1995a,b). The authors considered the existence of an array of band-tail states just below the conduction band to which charges are optically excited. Recombination at luminescent centres takes place following thermally-assisted hopping through the band-tail states. A basic characteristic of the thermally assisted OSL models is the activation energy, E_a, of the detrapping process and this parameter can be determined experimentally.

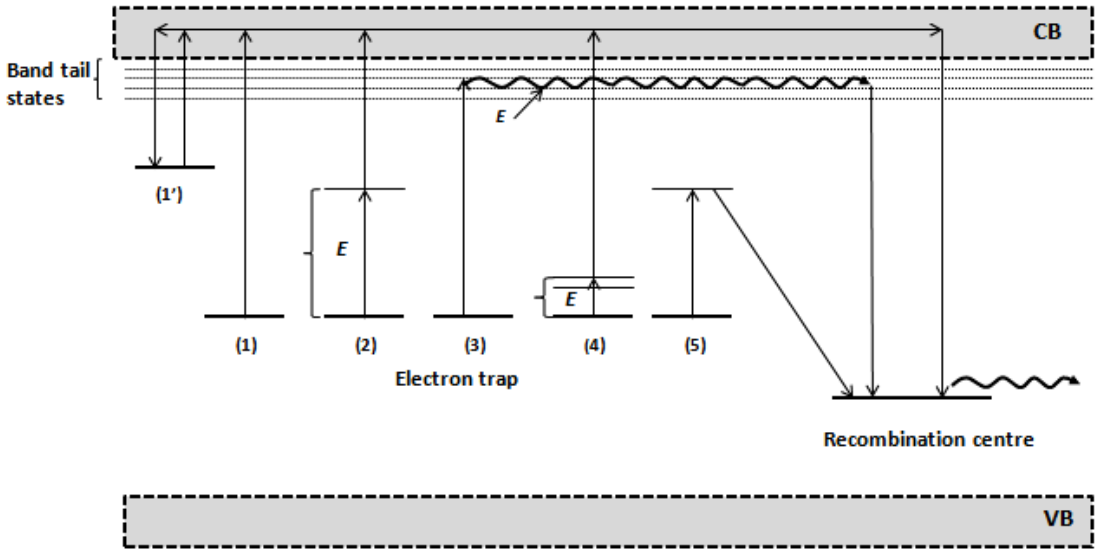

Figure 8.1: Energy band diagram showing the various OSL models: (1) direct transition from the ground state of the electron trap to the conduction band, (1') shallow trap model by Markey *et al*., (1996), (2) indirect thermally assisted OSL model by Hutt *et al*., (1988), (3) thermally assisted sub-conduction band OSL model by Poolton *et al*., (1995a,b), (4) thermally assisted model by Spooner (1994), and (5) donor-acceptor pair recombination (redrawn from McKeever *et al*., 1997).

The first indication of a thermally assisted mechanism is the increase in the luminescence intensity as the sample temperature is progressively increased. Nevertheless, shallow traps may also give rise to enhanced OSL production. The shallow trap model [Figure 8.1 (1')] was used by Markey *et al*., (1996) to explain the temperature dependence of the green stimulated OSL in α-Al_2O_3:C single crystals. The model assumes that shallow traps can be refilled by phototransfer of charges from deeper OSL traps. The charges will remain trapped until they are optically or thermally released again into the conduction band. However, as the sample temperature rises, the probability of thermal excitation is higher and, if radiative recombination routes are available, enhanced OSL emission can be produced. A similar effect is expected if during the duration of OSL measurement optical eviction of charges in shallow traps, followed by radiative recombination takes place.

Another indication of a thermally assisted mechanism can be obtained by examining the rate of decay of the OSL curves at different sample temperatures. An increase of the decay rate with

increasing stimulation temperature excludes the direct conduction band and shallow trap models. Yet, there is still a possibility of the participation of another non-thermally assisted sub-conduction band mechanism, that of the donor-acceptor (d-a) pair recombination [Figure 8.1 (5)] which can also account for the change in the rate of decay. For the IR stimulated luminescence in feldspars and for closely separated d-a pairs, Poolton *et al*., (2009) suggested that stimulation promotes electrons to the excited state of the donor centre from which the probability of direct recombination (i.e., via tunnelling) at the acceptor centre is higher due to an overlap of the wavefunctions between the donor and acceptor. Nevertheless, the d-a pair recombination is considered a non-thermally activated process, in contrast to the other thermally-assisted processes. Therefore, a thermally-assisted process may be identified if, while performing OSL measurements at different temperatures, an increase in the rate of decay of OSL curves is observed and an activation energy E_a can be calculated.

In this chapter, the general features of the OSL of alumina substrates, including the form of OSL under different stimulation modes (i.e., CW- and LM-OSL) and under various preheat conditions will first be introduced. Nevertheless, the main objective is to examine the influence of the temperature of the samples, T_s, during optical stimulation on the efficiency of OSL production. A model for the OSL of alumina substrate SMRs will then be unfolded based (1) on the criteria developed to distinguish between the various models in other luminescent materials, and (2) on considerations of the properties of the crystal lattice alone (e.g., electron-phonon coupling).

As explained in the previous chapter, all graphical examples presented in the following sections correspond to a specific sample with the number and type of SMRs will be clearly specified, but these can be considered representative of the wider sample population investigated. The values of the relevant parameters given in the tables and elsewhere are average estimates over all the samples examined, whereas errors represent the standard deviation of the mean value. OSL was detected in the UV range with a Hoya U340 filter (330 ± 40 nm, 7.5 mm) and, unless otherwise stated, OSL decay curves were measured for 60 s using a measurement interval of 0.3 s.

8.2 Optically Stimulated Luminescence response: General features

8.2.1 Continuous Wave OSL

The luminescence response of alumina substrates under optical stimulation was first investigated in the CW mode and subsequently (Section 8.2.2) by linearly ramping the intensity of the LED sources. Each sample (i.e., typically consisting of ~ 20 type ´0402´ SMRs) was irradiated (β ~ 3 Gy) and while maintained at RT it was optically stimulated using blue light (470 ± 30 nm). Following annealing to 500 °C, the sequence was repeated using the infrared light source (880 nm ± 40 nm). The decay curves, representing the detected luminescence light as a function of the duration of stimulation, obtained in the CW mode are shown in Figure 8.2a,b on a linear-log scale. The blue-stimulated signal (BOSL) is characterised by a non-exponential fast-decaying curve followed by a slowly decaying long tail, while the infrared-stimulated signal (IRSL) exhibits a peak-like structure followed by a nearly exponentially decaying part. Since the same samples – annealed at 500 °C and re-irradiated – and the same optical detection system configuration were used for all measurements a comparison of the strength of the OSL signals is possible, although for a more correct comparison, the strength of each stimulation source needs to be taken into account. Overall, the total integrated (0-60 s) BOSL signal is about ten times stronger than the IRSL and has a background signal (average counts of last 10 s) over five times higher.

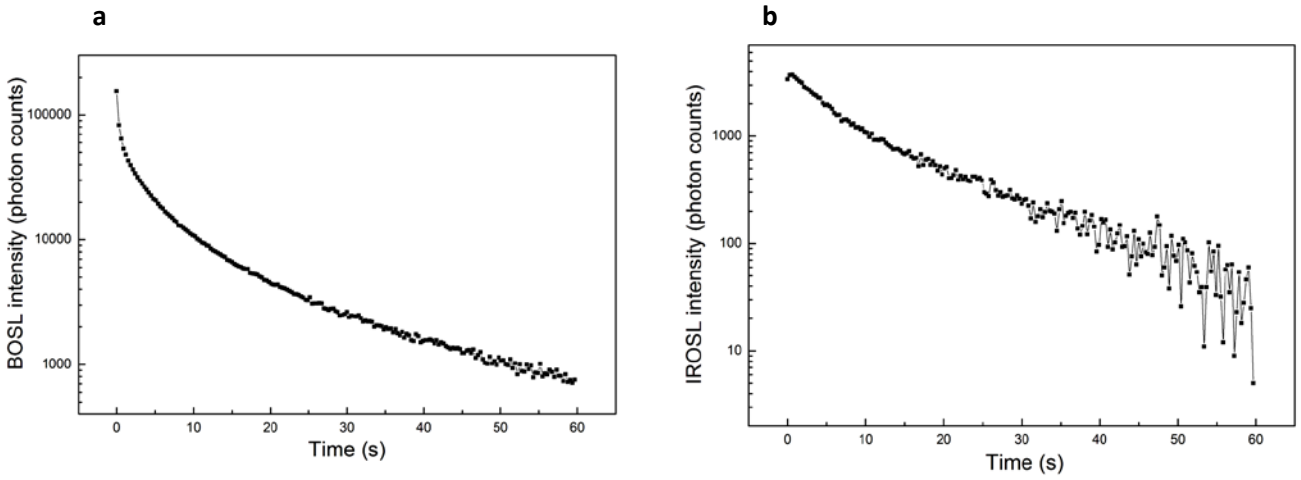

Figure 8.2: Representative examples of room temperature CW-OSL signals measured following beta irradiation (~ 3 Gy) of a sample consisting of ~ 20 type ´0402´ SMRs using (a) blue- and (b) infrared-light stimulation.

As mentioned in Chapter 2 (Section 2.2.2), a number of reasons such as the existence of second order processes (i.e., retrapping), the participation of a series of traps with differing photo-ionisation cross section and/or recombination centres (Botter-Jensen, 2003; Chen and Pagonis, 2011; Yukihara and McKeever, 2008), the thermal stimulation of charges from shallow traps, and the photo-transfer of charged carriers from deep to shallower traps (Yukihara and McKeever, 2011) may be responsible for the non-exponential behaviour of the OSL decay curves. Although, at this stage, it is unclear which one or combination of these prevails in the production of BOSL in alumina substrates, the existence of a series of traps with different photo-ionisation cross sections was roughly tested initially by measuring the LM OSL responses and subsequently by performing curve fitting analysis on the decay curves measured (1) following various preheat treatments (Section 8.3) and (2) using various sample stimulation temperatures, T_s (Section 8.4).

8.2.2 Linearly Modulated OSL

The LM-OSL signals were measured for 600s using similar irradiation and readout parameters employed in the measurement of CW-OSL. Figure 8.3a shows the LM-BOSL decay curve which exhibits a sharp peak at ~ 10 s accompanied by a broad peak-like shoulder that decays slowly to the instrumental background level at the end of the stimulation period. Under IR stimulation, however, only a broad peak cantered at about 40 s can be seen (Figure 8.3b). The influence of selective preheat treatments at different temperatures on the LM-OSL decay curves is also shown in Figure 8.3a,b and a discussion of this treatment is provided later in section 8.3.2.

Since, according to the theoretical model (Chapter 2; section 2.6.2.2), each LM-OSL peak corresponds to a particular trap, broad structures usually indicate the existence of a distribution of trapping levels. It could, therefore, be argued that the BOSL originates in, at least, two different trap populations corresponding to a sharp peak at ~ 10 s and a broad peak-shaped component respectively, while the IRSL arises from a single trap population.

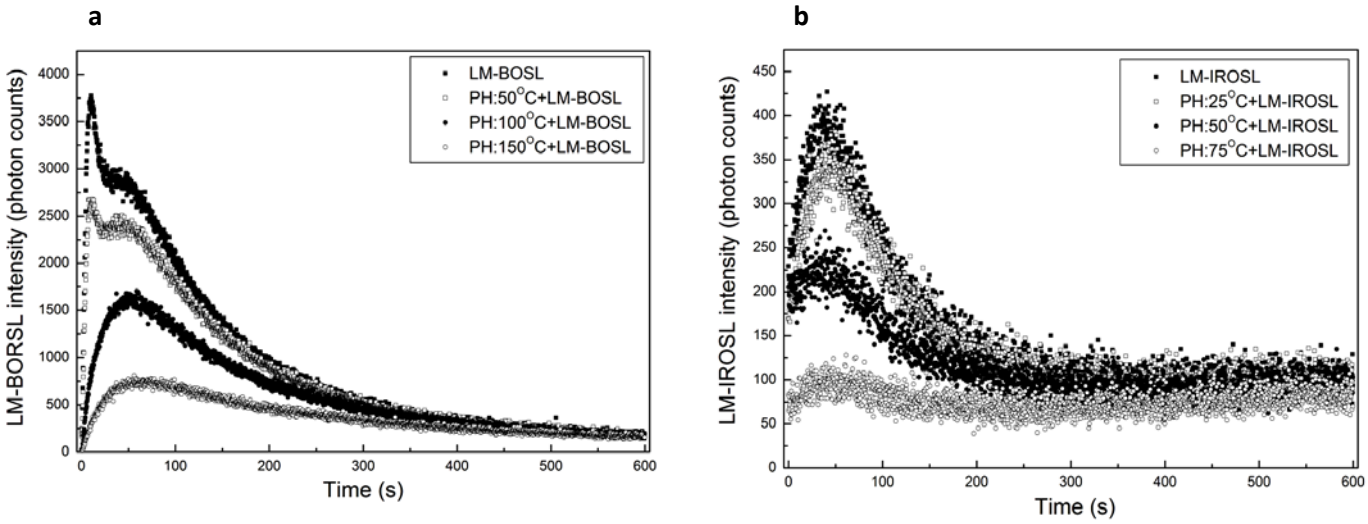

Figure 8.3: Room temperature LM-OSL decay curves of beta irradiated (~3 Gy) alumina substrates (i.e., sample of ~ 20 ´0402´ SMRs) after 600 s of (a) blue- and (b) infrared-light stimulation. The sample was maintained at RT during optical stimulation. The influence of post-irradiation preheat treatment for some selective temperatures is also shown and discussed later in section 8.3.2.

8.3 Step-wise annealing OSL

8.3.1 Theoretical considerations

Step-wise annealing experiments are helpful in studying the thermal stability and identifying the origin of trap(s) associated with OSL in relation to the TL response. In step-wise annealing experiments, it is reasonable to assume that the reduction of the OSL intensity is due to the thermal release of charge population from optically sensitive traps. What is not known is whether the thermally evicted charges recombine radiatively, non-radiatively or are transferred to thermally stable and optically inaccessible energy levels. Likewise, preheating a sample to high temperatures may generate the thermal transfer processes of charges from, usually, deep thermally accessible but optically insensitive traps to traps that can more easily be emptied by optical stimulation. The occurrence of thermal transfer processes from deep thermally stable traps induced following preheating alone (basic transfer mechanism suggested by Rhodes, 1988) or optical bleaching combined with preheating (i.e., the recuperation mechanism proposed by Aitken and Smith, 1988) was not investigated in detail, but this ought to be justified by a basic test for recuperation/thermal transfer by examining for the presence of regenerated signal after heating alone. But for the purpose of developing a reliable luminescence model it will be assumed that thermal transfer processes are insignificant, especially at the temperatures and durations used for dosimetry applications (i.e., 120 °C, 10 s).

A different interpretation of the decrease of OSL with increasing preheat temperature has been suggested by Jain and Ankjaergaard (2011). These authors proposed that preheat does not remove electrons from optically active traps, rather it reduces the concentration of holes in the luminescent centres by recombination with electrons thermally ejected from traps which are not associated with the OSL signal.

8.3.2 Experimental method and analysis

A step-wise annealing sequence similar to that described in Chapter 7 (section 7.2) for the TL response was used to investigate the influence of various preheat temperatures on the OSL signals. The duration of post-irradiation (typically 3 Gy) preheat was 10 s and OSL measurements were carried out at RT. After the completion of each cycle comprising dose, preheat and OSL measurement, the sample was heated to 500 °C to measure the TL and remove any remaining trapped charge. Monitoring of sensitivity changes was made by delivering a small dose (~ 0.5 Gy) once at the start and at the end of the experimental sequence; an average increase in sensitivity of less than 3 % was observed. Unless otherwise stated, OSL signals comprised the integrated counts recorded during the first 60 s of stimulation less a background calculated on the basis of the average count–rate recorded during the last 10 s of stimulation.

As indicated in Figure 8.4a, thermal cleaning at progressively higher temperatures to 200 °C reduces the intensity of the CW-OSL signals. In particular, the IRSL integral decreases in the same range where TL Peak 1 also reduces by preheating, suggesting that IRSL and TL Peak 1 may use common traps. Within the same temperature range, the BOSL response decreases at a slower rate and retains a measurable signal even after preheating at 300 °C. It was found that only after annealing above 500 °C the BOSL signal becomes undetectable.

Moreover, as shown in Figure 8.4b, the decay rates of the BOSL curves become slower as the temperature of preheat increases to 150 °C reversing to a faster decay rate at higher annealing temperatures. In all cases, a non-exponential decay trend can be observed. If a linear combination of first-order exponential components is assumed the BOSL decay curves up to a preheat of about 100 °C can be fitted with four first-order exponentially decaying components (Figure 8.5a), while those measured following higher preheat temperatures can be better fitted using a third- or second-order exponential decay function (Figure 8.5b). By comparison with the TL response, it might be assumed that the first very fast (0-1 s of BOSL) exponential component is related to TL Peak 1 since above 100 °C both are practically absent, while the remaining three components likely represent different traps.

An alternative fitting of the BOSL decay curves using a hyperbolic decay function of the form $BOSL\ (t) = a + (1 + bt)^{-1/c} + d$, with a, b, c, d empirical constants, was also attempted. Yet, in

all cases the quality of the fit was found to be poorer in comparison with that obtained assuming a sum of exponential decay functions. These results contradict earlier findings (Woda, *et al*., 2010) where the BOSL decay curves were described by a hyperbolic decay function, but interpreted assuming a multi-exponential decay model representing a distribution in optical ionisation cross sections.

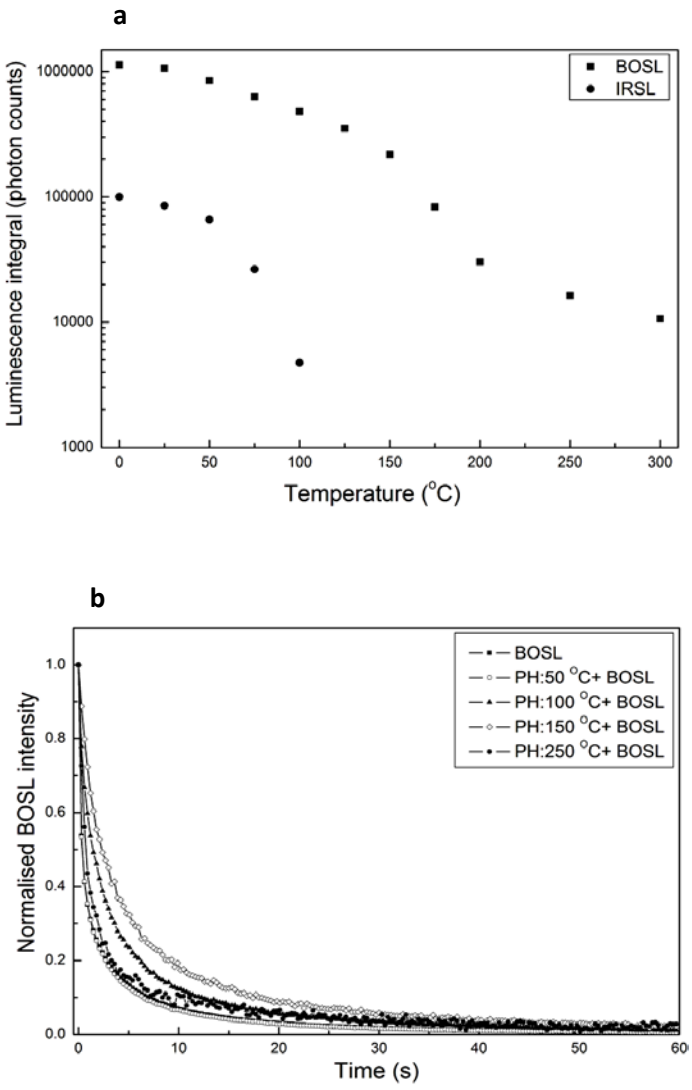

Figure 8.4: (a) Step-wise annealing curves of the CW-BOSL and IRSL signals. (b) Normalised to the initial intensity (i.e., at t=0 s) BOSL decay curves after increasing temperature of preheat treatment. The data correspond to a sample consisting of ~ 20 type ´0402´ SMRs irradiated with ~ 3 Gy and stimulated at RT. The error bars in (a) are not shown since they are comparable to the symbol size.

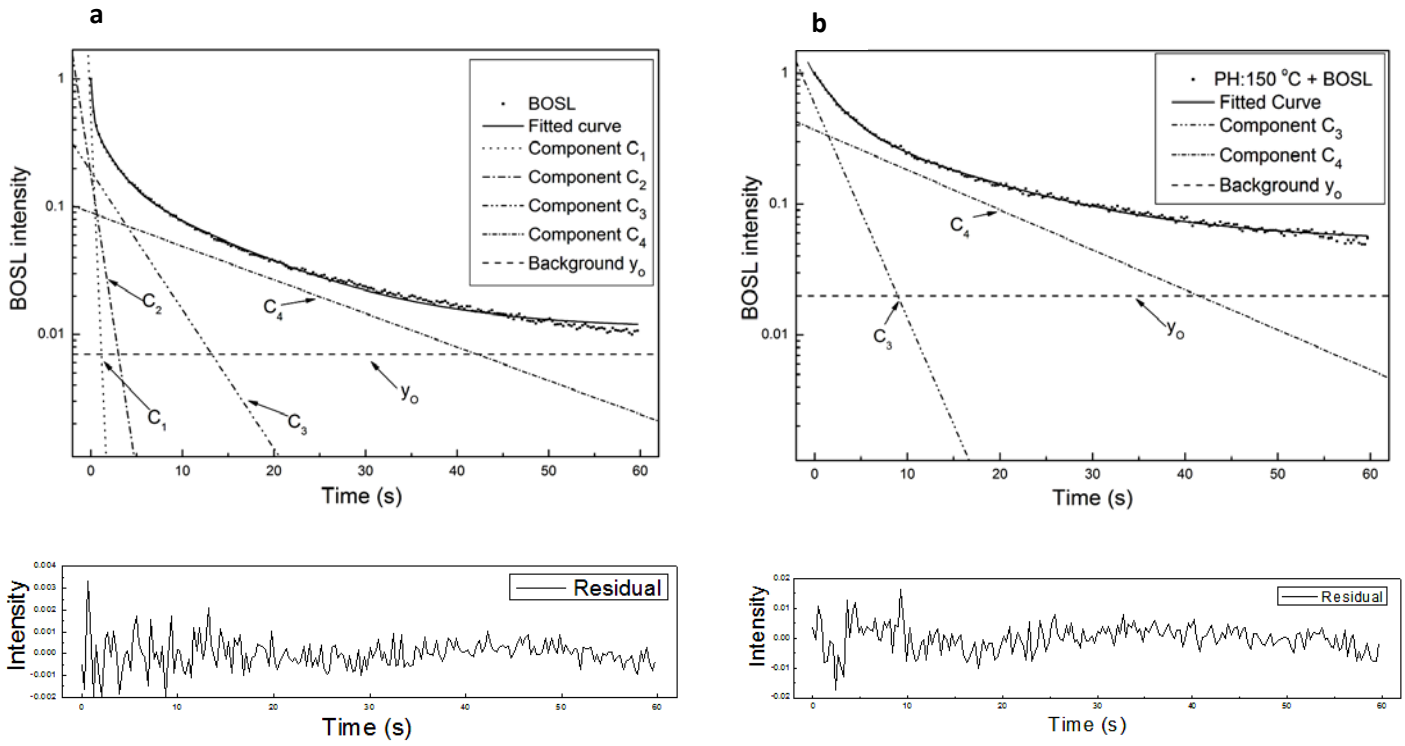

Figure 8.5: Examples of curve fitting of the normalised at t=0 s BOSL decay curves measured (a) without post-irradiation preheat treatment and (b) following preheat at 150 °C. In (a) a good fit was obtained assuming a linear combination of four first-order exponential decay components (i.e., C_1: *Dot*, C_2: *Dash Dot*, C_3: *Dash Dot Dot*, and C_4: *Short Dash Dot*) and a constant (i.e., y_o: *Dash*), while in (b) a second-order exponential decay function and a constant, y_o, was found to fit the experimental data adequately. The residual signals are also shown,

The amplitude (A_i) and time decay constant (τ_i) characteristics of the BOSL decay curve components derived using an expression of the form $BOSL\,(t) = y_o + A_1 \exp\left(-{}^{t}/_{\tau_1}\right) + A_2 \exp\left(-{}^{t}/_{\tau_2}\right) + \cdots$ are listed in Table 8.1. It is noted that these results are specific to the wavelength and intensity of the LED source in the Risø system. BSOL curves measured after preheating the samples from 25 to100 °C present a very fast component (C_1: *Dot*) identified in the first second (0-1 s) of stimulation and three additional components (C_2: *Dash Dot*, C_3: *Dash Dot Dot*, and C_4: *Short Dash Dot*) in the remaining 60 s. Component C_1 is not observed in the

BOSL curves obtained following annealing above 100 °C, whereas also component C_2 is absent from the BOSL signals obtained with preheat higher than 150 °C.

Table 8.1: Amplitude and decay time constant characteristics of the components of the normalized BOSL decay curves after different preheat treatments. The duration of each preheat treatment was 10 s. The values shown are average of a number of samples (n ~ 10) consisting of ~ 20 type ´0402´ SMRs.

	Component 1 (C_1)		**Component 2 (C_2)**		**Component 3 (C_3)**		**Component 4 (C_4)**		**Constant**
Preheat (°C)	**A_1**	**τ_1 (s)**	**A_2**	**τ_2 (s)**	**A_3**	**τ_3 (s)**	**A_4**	**τ_4 (s)**	**(y_o)**
0	0.550±0.003	0.270±0.002	0.16±0.03	0.96±0.06	0.19±0.02	4.00±0.12	0.09±0.03	16.2±0.45	0.01
25	0.530±0.003	0.270±0.002	0.18±0.04	0.93±0.06	0.19±0.02	4.00±0.10	0.09±0.04	16.5±0.53	0.01
50	0.560±0.003	0.260±0.003	0.19±0.03	1.29±0.07	0.17±0.03	4.60±0.30	0.07±0.06	18.4±1.02	0.01
75	0.480±0.005	0.330±0.003	0.21±0.04	1.19±0.07	0.21±0.03	4.40±0.20	0.09±0.06	18.0±0.95	0.01
100	0.340±0.006	0.520±0.005	0.21±0.06	1.19±0.13	0.31±0.05	4.14±0.20	0.13±0.06	18.4±0.98	0.01
125	-	-	0.25±0.02	1.07±0.008	0.50±0.01	4.00±0.20	0.23±0.01	17.8±1.02	0.02
150	-	-	-	-	0.58±0.05	2.66±0.05	0.37±0.01	14.2±0.32	0.05
175	-	-	-	-	0.41±0.01	1.67±0.10	0.45±0.01	13.4±0.40	0.14
200	-	-	-	-	0.45±0.02	2.37±0.16	0.38±0.01	16.7±1.09	0.17

In a similar manner, step-wise annealing at progressively higher temperatures results in the removal of the sharp peak in the LM-BOSL curve leaving only a broad-peak which also decreases with increasing preheat temperature (Figure 8.3a). In particular, the sharp LM-BOSL peak, the BOSL component, C_1, and TL Peak 1 all vanish for annealing temperatures above 100 °C. Finally, in accordance with the behaviour of the CW-IRSL, the LM-IRSL curves (Figure 8.3b) show a drastic decrease followed by extinction at preheat temperatures greater than 100 °C. The thermal stability curves of the integrated LM-OSL signals have been omitted since they were found to be similar to those obtained after CW stimulation (i.e., Figure 8.4a).

8.4 Temperature dependence of OSL signals

8.4.1 Measurement considerations

The temperature, T_s, at which the samples are maintained during OSL measurements can have some profound effects in the efficiency of luminescence production (Aitken, 1998; McKeever *et al*., 1997; Murray and Wintle, 1998; Wintle and Murray, 2000). For example, as the temperature increases the luminescence efficiency reduces due to the thermal quenching effect. However, countering this effect is an enhancement in the rate of trapped charge eviction and of charge transport to shallow traps (i.e., phototransferred TL; PTTL). The first effect, known as thermally-assisted OSL, results in shorter stimulation times which is useful for dosimetry applications, and in the second, the transfer of charges to shallow traps can give rise to delayed radiative recombination as well as to a slowly decaying phosphorescence tail (McKeever *et al*, 1997; Wintle and Murray, 2000). The optimum stimulation temperature should therefore (1) minimize the effect of shallow traps, (2) keep thermal quenching to a minimum, and (3) avoid thermal eviction of charges from optically sensitive traps.

8.4.2 Experimental method and analysis

The temperature dependence of the CW-BOSL and IRSL was investigated using the following procedure. The samples were irradiated with 3 Gy and optically stimulated while maintained at RT. Following annealing to 500 °C by TL measurement, the same dose was delivered and the OSL response was measured at a sample temperature, T_s, increased by 25 °C. A total of ten sample temperatures in the 25-300 °C range were obtained. To make sure that the measured OSL signals were not due to the thermal release of charge (i.e., phosphorescence) as the temperature rose, the experiment was repeated by measuring only the phosphorescence emission. In those cases where significant thermal release was found to have occurred, the Net-OSL signal was calculated by subtracting the phosphorescence component. Sensitivity changes were monitored using the procedure described earlier.

Examples of the CW-BOSL decay curves and the phosphorescence emission curves for selected sample temperatures are shown in Figure 8.6a,b for a sample consisting of ~ 20 type ´0402´ SMRs. Significant phosphorescence emission is seen (Figure 8.6b) to take place above 50 °C, increasing with stimulation temperature to 100 °C, after which it shows a considerable drop at ~ 150 °C. It is interesting to note that the form of the phosphorescence curves resembles that of the CW-IRSL response (Figure 8.3b) where a build-up is observed the first moments of stimulation. As demonstrated earlier (Chapter 7) for the isothermal luminescence emission, the initial rise showing in the phosphorescence is most likely attributed to the thermal lag effect. It is also anticipated that the build-up showing in the IRSL decay curves to be removed following subtraction of the phosphorescence component.

The temperature dependence characteristics of the BOSL, phosphorescence, and Net-BOSL responses created by plotting the total signal (i.e., integral 0-60 s less the BG) under the curve versus the sample temperature are shown in Figure 8.7a. A reduction in the total Net-BOSL intensity is observed with increasing sample temperature; which is what expected from the thermal quenching effect. Although above 150 °C the rate of decrease becomes less pronounced, the BOSL remaining when stimulation is carried out at 200 °C is less than 10 % of the $BOSL_{RT}$. The latter is probably due to the combined influence of thermal quenching and the increased thermal eviction of trapped charges.

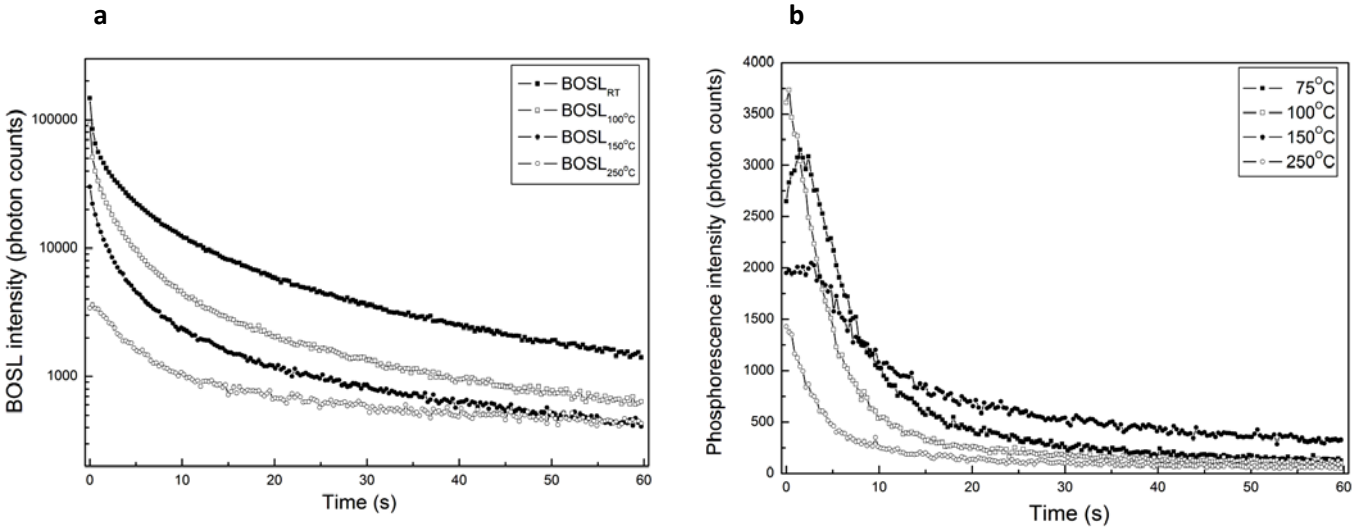

Figure 8.6: (a) CW-BOSL decay curves and (b) phosphorescence emission curves measured at various sample temperatures. The data were obtained using a sample consisting of 20 type ´0402´ SMRs. The dose to the sample was ~ 3 Gy.

The variation of the IRSL and the phosphorescence light sums with stimulation temperature are shown in Figure 8.7b. Both the IRSL and the phosphorescence signal display a complex behaviour with temperature. The thermal dependence of the IRSL curve shows two maxima at ~ 50 °C and ~ 175 °C corresponding approximately to the temperatures at which the phosphorescence emission is at its maximum intensity. The light sum of the Net IRSL decay curves, after subtraction of phosphorescence, decreases with sample temperature up to 150 °C, and above this temperature the IRSL is practically indistinguishable from the phosphorescence emission. These results are similar to those obtained in the previous section where the IRSL response was found to be not detectable after preheating at temperatures above 150 °C.

Figure 8.8a,b shows the IRSL, phosphorescence, and Net IRSL decay curves obtained at 50 °C and 75 °C. It is characteristic that the peak-shaped structure disappears from the decay curve after subtraction of the phosphorescence component leaving a first-order exponentially decaying curve. The rate of decay also increases. This is clearly shown in Figure 8.7c where the normalised IRSL decay curves at 50, 75 and 100 °C are shown together with their fitted functions. The time decay constant, τ, obtained from the fitting procedure decreases from 5.61 ± 0.13 s, at 50 °C to 2.25 ± 0.03 s at 75 °C to 1.42 ± 0.02 s at 100 °C confirming the expected increase in the rate of decay.

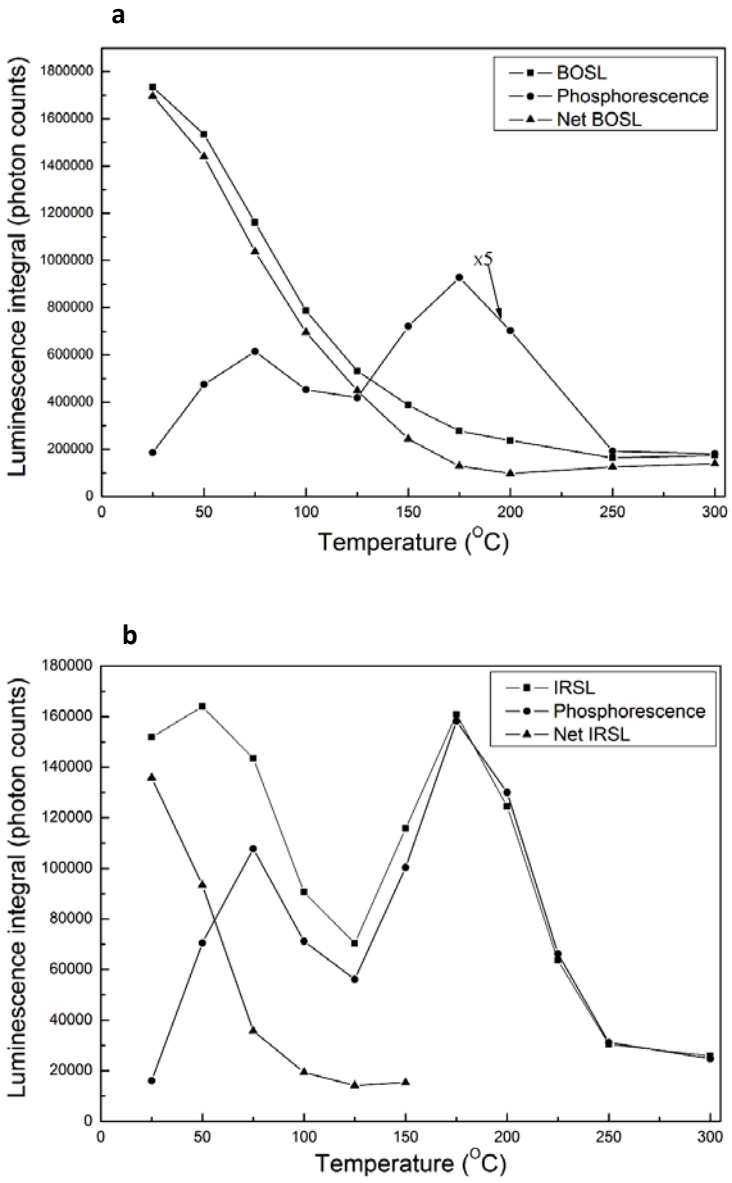

Figure 8.7: Sample temperature dependence of the total (0-60 s) OSL light sum, phosphorescence, and Net-OSL signals during (a) blue- and (b) infrared-light stimulation. The data were obtained using a sample consisting of ~ 20 type ´0402´ SMRs. The dose to the sample was ~ 3 Gy. The data points were connected with linear curves for better visualisation. The error bars are not shown since they are comparable to the symbol size.

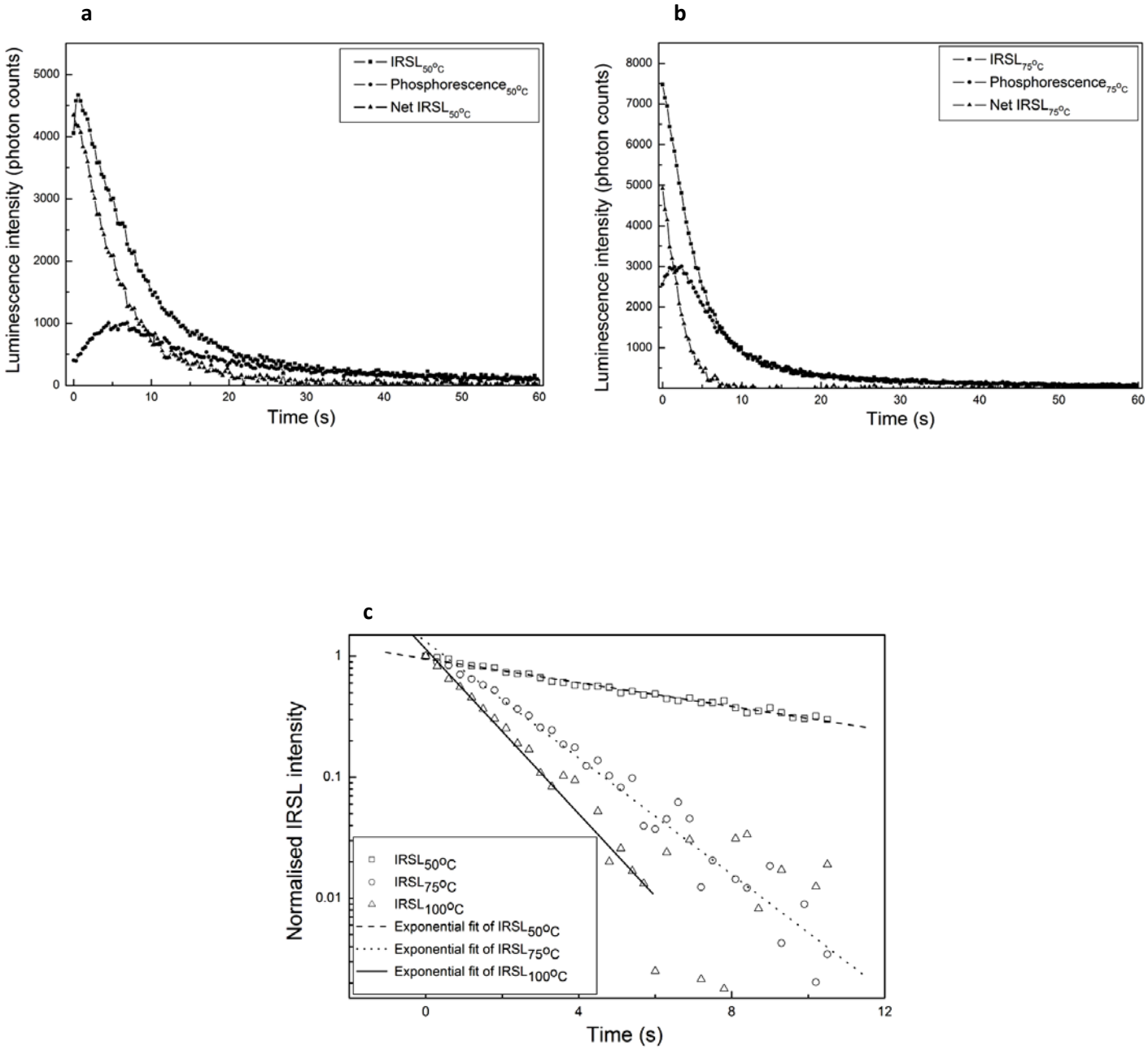

Figure 8.8: IRSL, Phosphorescence, and Net-IRSL decay curves plotted for two sample temperatures at (a) 50 °C and (b) 75 °C. In (c), the normalised at t=0 s decay curves measured at 50, 75, and 100 °C were fitted using a single exponential function revealing an increase in the rate of decay with increasing sample temperature.

To investigate the possible influence of shallow traps associated with the first TL peak at ~ 100 °C, the above experiments were repeated by preheating the samples to 120 °C for 10 s after which the OSL and phosphorescence emissions were measured. For measurement temperatures between 25 and 100 °C the IRSL was barely detectable, whereas at higher temperatures the signal obtained was due entirely to phosphorescence. This observation provides further evidence for the IRSL being related to the first TL peak and further indicates that thermally-assisted IRSL emission from deeper traps does not contribute significantly to the observed IRSL.

On the other hand, the integral of the Net-BOSL signal (Figure 8.9a) was found to decrease more slowly in the range 25-125 °C than when measured without post-irradiation preheat, while both reach the same value at higher temperatures. The slower rate of decrease of the BOSL integral after annealing at 120 °C indicates the absence of, or smaller contribution of, a thermally unstable component which could also be associated with trap(s) associated with the first TL peak. Another interesting feature was noted when the initial intensity recorded during the 1 s of optical stimulation was plotted as a function of stimulation temperature (inset to Figure 8.9a). The initial intensity of the BOSL response shows a slight increase in the range 25-100 °C that is followed by a decrease at higher temperatures. This feature, which was barely noticeable in the data obtained from the non-preheated sample, is usually attributed to the presence of shallow traps or to thermally-assisted eviction of charges leading to radiative recombinations. Finally, another effect became visible when the Net-OSL curves were normalised to the initial intensity as shown in Figure 8.9b. The rates of decay of the OSL curves recorded between RT and 200 °C were found to increase significantly with increasing stimulation temperature and above 200 °C the Net-BOSL curves (not shown) displayed a peak similar to the data obtained without the application of post-irradiation preheat. As discussed below (Section 8.6), this behaviour is characteristic of a thermally activated detrapping process.

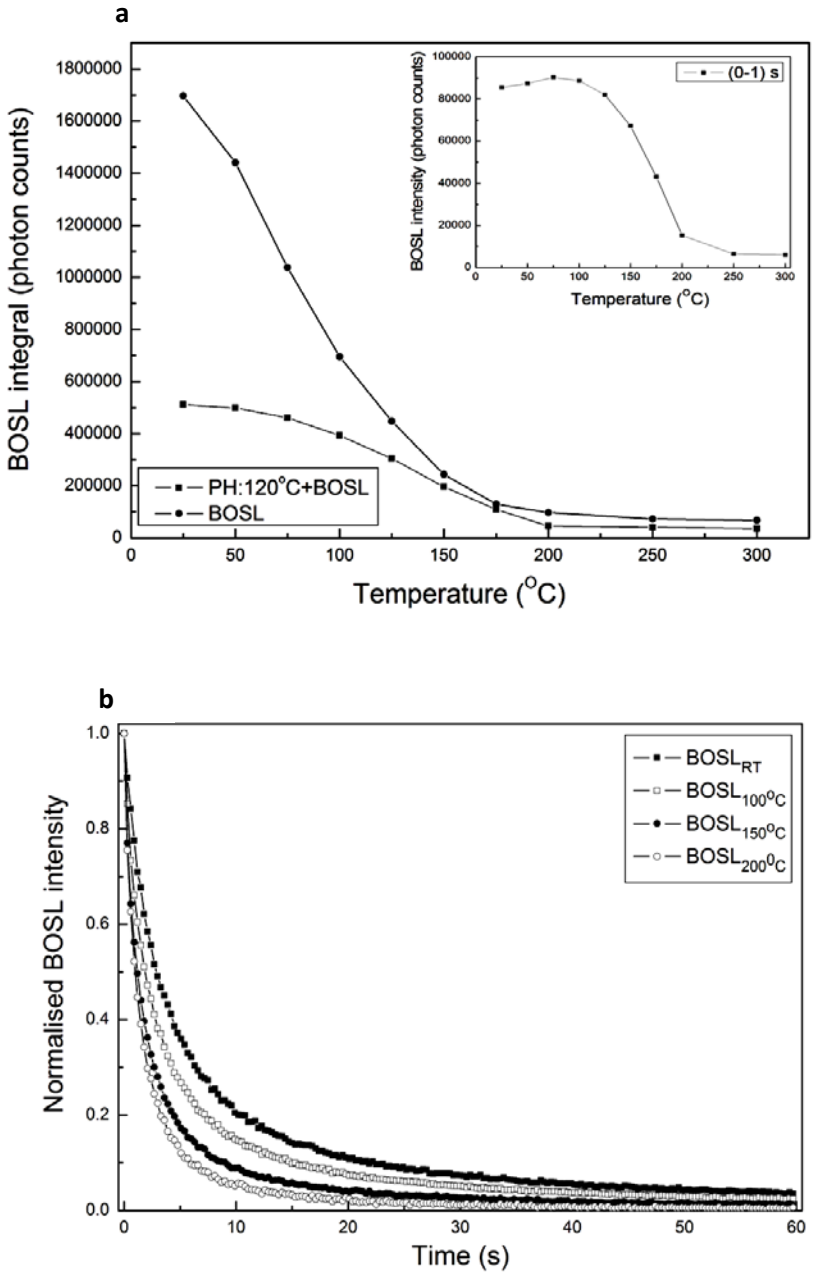

Figure 8.9: (a) Total (0-60 s) Net-BOSL light sums as a function of measurement temperature obtained after (squares) and without (circles) preheat treatment at 120 °C (10 s). The inset shows the initial (0-1 s) integrated BOSL intensity as a function of measurement temperature. The data points were connected with linear curves for better visualisation. (b) Normalised at t=0 s BOSL decay curves at selective measurement temperatures following preheat at 120 °C (10 s). The data were produced with a sample of ~ 20 type ´0402´ SMRs irradiated with ~ 3 Gy. The error bars in (a) are not shown since they are comparable to the symbol size.

Deconvolution of the Net-BOSL curves using a combination of several first-order exponential decay components was performed to examine the variation of the time decay constant with stimulation temperature. The results are presented in Table 8.2 together with the decay constants of the components derived from fitting the BOSL curves measured without preheat treatment. As demonstrated above, preheating at temperatures above 100 °C removes the very fast component C_1 from the decay curves. In the case of the preheated sample, the time decay constants of the remaining three components are generally lower and decrease monotonically with stimulation temperature up to 200 °C. In the non-annealed case, components C_2 and C_3 also decrease as the sample temperature increases but component C_4 displays an irregular behaviour. It is assumed that the variations in the time decay constant of the last component are introduced by the presence of charges in shallow energy levels at the beginning of stimulation which become delocalised as temperature increases resulting in a slowly decaying component.

Table 8.2: Average (over several samples consisting of ~ 20 type ´0402´ SMRs) values of the time decay constants, τ, of the fitted components at different stimulation temperatures with and without preheat at 120 °C (10 s).

	Component 1 (C_1)		**Component 2 (C_2)**		**Component 3 (C_3)**		**Component 4 (C_4)**	
Stimulation temperature (°C)	**No PH**	**PH:120 °C**	**No PH τ (s)**	**PH:120 °C τ (s)**	**No PH τ (s)**	**PH:120 °C τ (s)**	**No PH τ (s)**	**PH:120 °C τ (s)**
25	0.28±0.02	-	1.40±0.26	1.30±0.09	4.38±0.34	4.34±0.23	16.4±0.50	19.3±1.10
50	0.26±0.02	-	2.06±0.14	1.27±0.07	6.63±0.81	4.29±0.22	14.9±0.50	18.1±0.99
75	0.24±0.02	-	1.51±0.13	0.71±0.02	4.54±0.36	3.17±0.07	14.6±0.60	15.2±0.40
100	0.26±0.03	-	1.28±0.09	0.55±0.02	4.24±0.27	2.71±0.06	17.2±1.26	13.9±0.36
125	0.38±0.01	-	1.28±0.09	0.38±0.01	3.83±0.29	2.25±0.04	15.5±0.95	12.0±0.30
150	-	-	1.05±0.02	0.40±0.02	2.79±0.34	1.95±0.05	17.2±1.30	10.4±0.44
175	-	-	-	-	1.62±0.05	1.56±0.05	17.5±1.50	10.9±0.74
200	-	-	-	-	0.96±0.06	1.01±0.02	11.0±0.90	11.3±0.86

While the decay constant is a parameter that directly can be derived from the fitting process, it does not provide information about the optical properties of the traps involved in the OSL process. However, since $\tau = 1/\sigma\varphi$ the photo-ionisation cross sections, σ, of the traps can be estimated and the dependence of σ on the stimulation temperature examined. Having estimated

the number of photons per unit time per unit area (i.e., photon flux, φ) emitted from the blue-LEDs (Choi *et al*., 2006) the values of the photo-ionisation cross sections for components C_2, C_3, and C_4 were calculated and plotted as a function of the stimulation temperature. It should be noted that, due to the inverse dependence of σ on τ, component C_2 corresponds to the highest photo-ionisation cross section (i.e., $\sigma_{RT} \sim 10^{-17}$ cm^2), while C_4 corresponds to the lowest value (i.e., $\sigma_{RT} \sim 10^{-18}$ cm^2).

As seen in Figure 8.10, the photoionisation cross sections of all components increase with increasing measurement temperature. The temperature dependence of the optical cross section has, in most cases, been interpreted in terms of a two-step excitation process which involves a thermally activated transition into an intermediate excited state followed by optical excitation to the CB (Kuhns *et al*., 2000; Mishra *et al*., 2011; Soni *et al*., 2012; Spooner, 1993). In this case, the rate of detrapping may be increased by thermal assistance and is exponentially dependent on temperature (i.e., $\sigma(T,\lambda) \propto \exp(-E/kT)$).

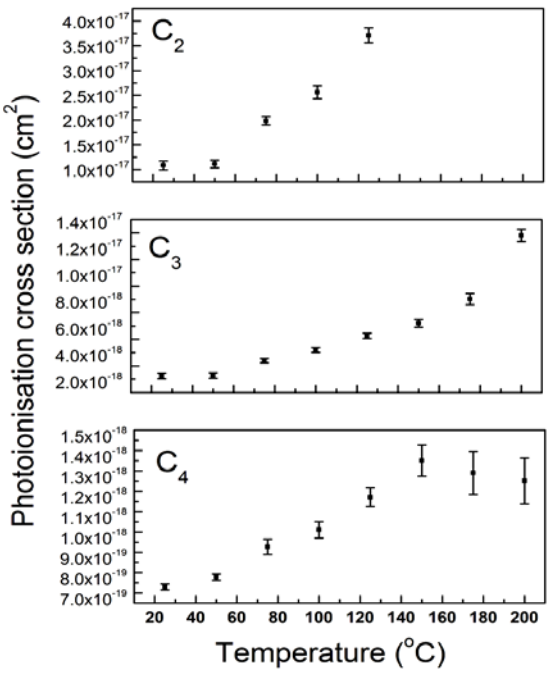

Figure 8.10: Dependence of photo-ionisation cross section, σ, on temperature of stimulation for the BOSL components C_2 (top panel), C_3 (middle panel), and C_4 (higher panel). The data were obtained using a sample consisting of 20 type ´0402´ SMRs.

As already discussed in the introduction of this Chapter, various thermally-assisted models have been put forward to explain the thermal effects associated with OSL production. One of the central assumptions of these models is that the energy of stimulation photons is less than the optical trap depth and delocalisation of trapped charge can take place via an intermediate excited state. However, Cruscinska (2010) argued that the temperature dependence of the photo-ionisation cross section as well as other temperature related effects (e.g., increase of initial OSL intensity) can be explained by a coupling of energy levels in the crystal lattice and the strong electron-phonon interactions at temperatures higher than 0 K (-273 °C). Using the electron-phonon interaction model by Noras (1980), in which the optical cross section is a function of the optical trap depth E_o, the stimulation energy $h\nu$, the phonon energy $\hbar\omega$, and the temperature T, Cruscinska (2010) simulated numerically the temperature effects of OSL production considering initially the simple one-trap one recombination (OTOR) model and subsequently a model consisting of two electrons traps. Direct excitation of electrons into the conduction band was assumed in both models. Without rejecting the validity of the thermally assisted models, Cruscinska demonstrated the potential of the electron-phonon interaction model in explaining the observed changes in the shape and intensity of the OSL curve. Most importantly, she showed that such consequences can be observed even when stimulation is carried out with photon energy greater than the optical trap depth.

In the following section the temperature effects of the BOSL curves will be examined using specific OSL models developed for other luminescent materials (e.g., quartz, feldspar, α-Al_2O_3:C). And since measurements of the optical depth(s) of the trap(s) associated with the OSL production in alumina substrates have not been made, two cases will be considered. In the first instance, it will be assumed that the excitation energy $h\nu$ is smaller than E_o such that direct excitation of electrons out of the trap(s) is less probable. Later, it will be discussed the case where $h\nu > E_o$ leading to an electron-phonon coupling model will be discussed.

8.5 Thermally assisted BOSL

8.5.1Measurement considerations

As shown in section 8.4.2, the BOSL curves of the alumina substrates become faster and the initial (i.e., 0-1 s) intensity is enhanced as the measurement temperature increases (Figure 8.9). Both observations are consistent with a thermally assisted eviction model. The activation energy of this process can be calculated using an Arrhenius equation of the form $OSL(T) = OSL_o \exp(-E/kT)$ (Chen and McKeever, 1997). In practice, the data obtained from the measurement of the OSL as a function of sample temperature are plotted on a log-linear scale and the data in the linear part of the plot are fitted to the above equation. The slope of the linear fit gives the value of the activation energy. However, because the effect of thermal quenching can be strong it is generally better to correct the data for thermal quenching before the activation energy for thermal assistance is calculated. This procedure was adopted by Murray and Wintle (1998) who studied the temperature effects of the green-light stimulated OSL in quartz. The authors investigated the OSL decay curves of quartz at temperatures from 25 to 500 °C and observed a small increase in the OSL signal during the first 0.4 s of stimulation with temperature up to 100 °C and a continuous decrease of the total (0-100 s) OSL integral. Initially, they calculated the parameters of thermal quenching and used their values to correct both the initial (0.4 s) and the total (100 s) integrals. Afterwards, they estimated the thermal assistance activation energy using only the data from the first 0.4 s.

8.5.2Experimental method and analysis

The thermal quenching parameters of the BOSL response in alumina substrates were calculated by fitting the data from the total light sum (Figure 8.9a) as a function of stimulation temperature (i.e., 25-200 °C) with the equation that describes the thermal quenching efficiency (i.e., Chapter 2; equation 2.3). Based on the assumption that most of the BOSL signal is associated with the main TL peak at ~ 200 °C, the data obtained at higher stimulation temperatures were not

included in the fitting process since the effect of thermal depletion of the BOSL signal becomes very important. Figure 8.11 shows an example of the original BOSL data and the thermal quenching fit. Following analysis of a number of samples, the average values of the thermal quenching parameters were found to be W = 0.53 ± 0.05 eV and C = (2.88 ± 2.4) x10^6. The W and C values were then used to correct the BOSL data. As shown in Figure 8.12a the total integral corrected for thermal quenching, is now nearly constant with temperatures from 25 to 125 °C while the signal from the first 0-1 s (Figure 8.12b) displays a noticeable increase. This behaviour is in agreement with a thermally assisted process which is expected to leave unaffected the total integrated signal, but affects the initial decay (Murray and Wintle, 1998). The activation energy, E_a, of thermal assistance was found from the plot of $ln(BOSL_{0\text{-}1\ s})$ versus kT^{-1} to be ~ 0.11 eV (Figure 8.13).

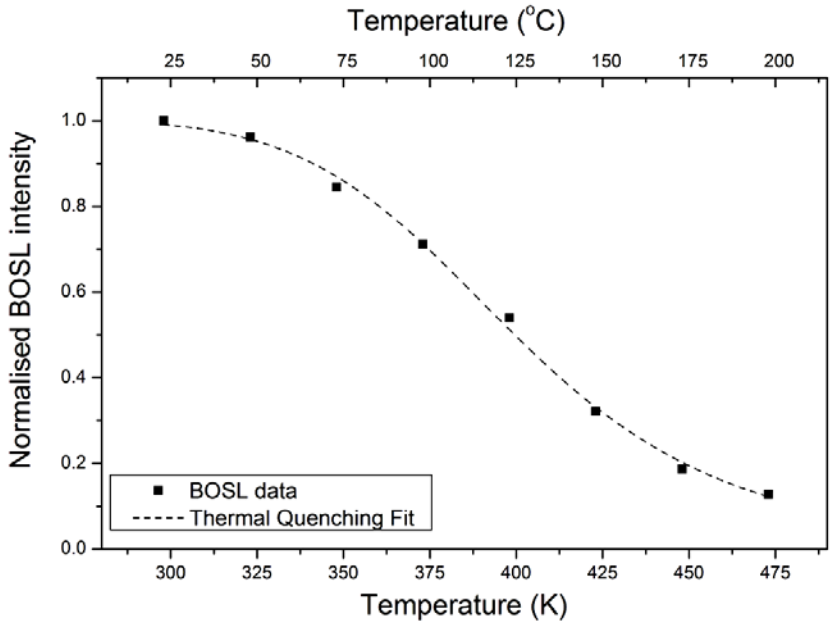

Figure 8.11: Plot showing integrated (0-60 s) BOSL intensity vs sample stimulation temperature to 200 °C (i.e., 473 K) for a sample consisting of 20 type ´0402´ SMRs. The thermal quenching equation, $I(T) = \frac{I_o}{1+C \cdot exp^{-\frac{W}{kT}}}$, was fitted to the data (dashed curve). The average (over several samples) values of the thermal quenching parameters were found to be W = 0.53 ± 0.05 eV and C = (2.88 ± 2.4) x10^6.

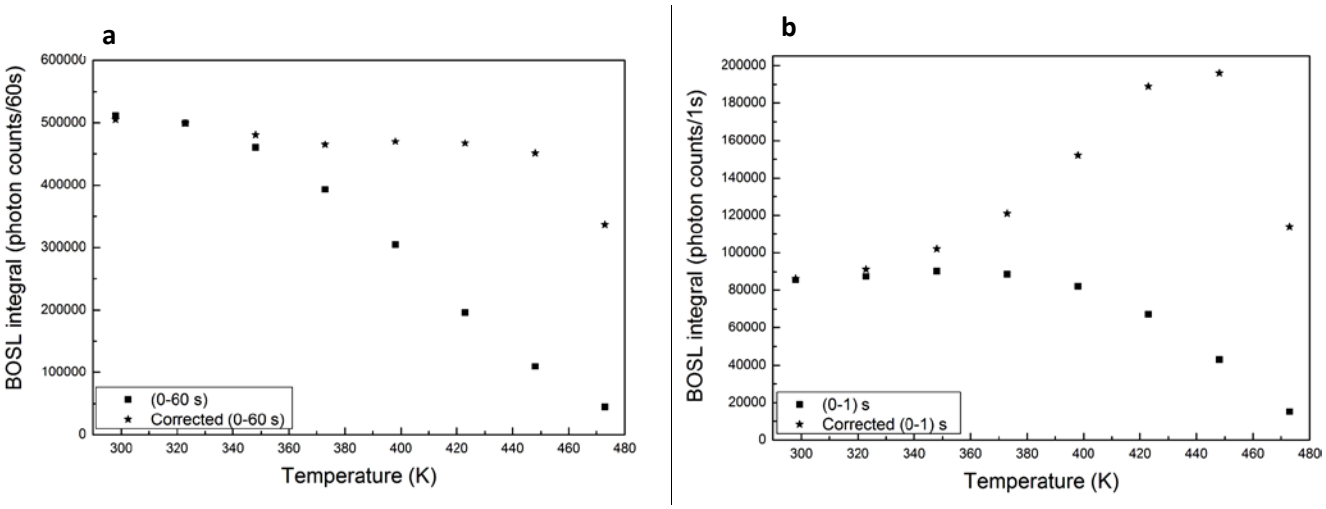

Figure 8.12: Quenched (square symbols) and corrected (start symbols) data for (a) the total (0-60 s) integrated and (b) initial (0-1 s) BOSL intensity as a function of the measurement temperature. The error bars are not shown since they are comparable to the symbol size.

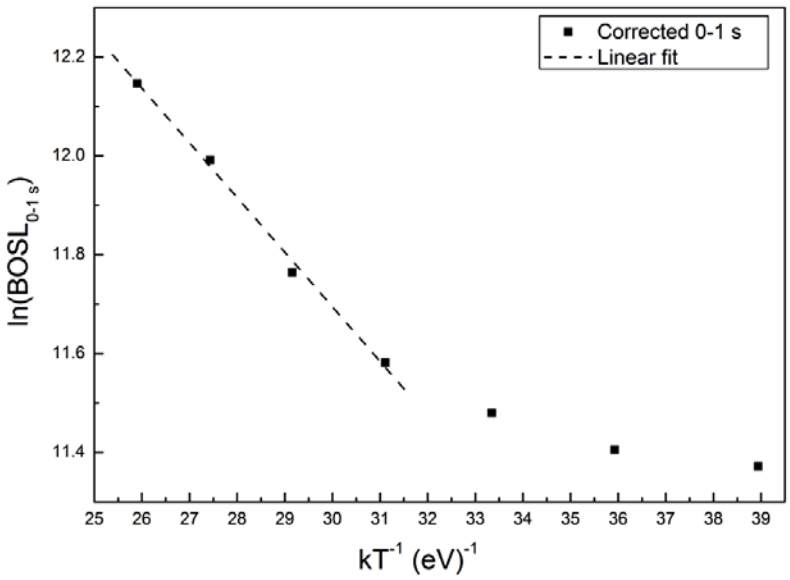

Figure 8.13: Fit to the 0-1 s corrected data using equation $OSL(T) = OSL_o \exp(-E/kT)$ resulting an activation energy, E_a, for thermal assistance of ~ 0.11 eV. The error bars are not shown since they are comparable to the symbol size.

A single value for the activation energy, E_a, should imply the existence of one trap optically depopulated during measurement at elevated temperatures between 25 and 200 °C. Nevertheless, the fitting procedure in section 8.3 suggests that the $BOSL_{25\text{-}200\ °C}$ following a preheat to 120 °C is described by the sum of at least three components with distinct values of the photo-ionisation cross section. Assuming that the three components represent different traps and that production of luminescence proceeds via an intermediate state, then a unique activation energy for each trap should be possible to calculate. The method employed to determine the activation energy of the components is based on the work by Singarayer (2002) who examined the variation of the photo-ionisation cross section, σ, as a function of stimulation temperature, T_S, for the components resolved by curve fitting the LM-OSL curves in quartz samples. By plotting the logarithm of σ against kT^{-1} an activation energy can be obtained from the slope of the linear part of the plot.

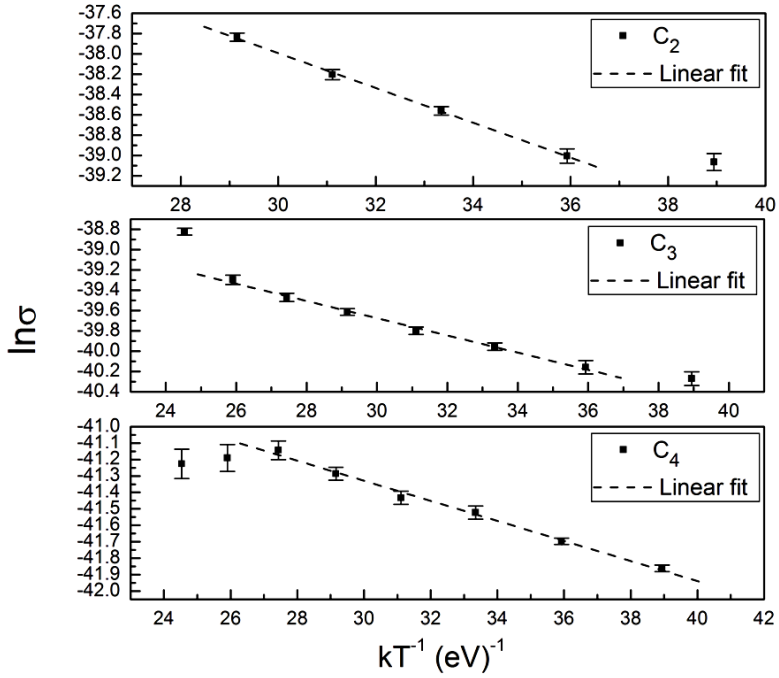

Figure 8.14: Plot of the logarithm of photoionisation cross section, σ, vs kT^{-1} for components: C_2 (upper panel), C_3 (middle panel), and C_4 (lower panel) of the BOSL response. The slope of the linear part (dashed curves) of each plot corresponds to the activation energy, E_a, characterising the detrapping process during optical stimulation. The value of E_a for component C_2 is 0.061 ± 0.003 eV, 0.085 ± 0.003 eV for C_3, and 0.171 ± 0.003 eV for C_4. The plots were produced using the data shown in Figure 8.10.

The above analysis was performed using the data shown in Figure 8.10. The plot of $ln\sigma$ vs kT^{-1} of each component (Figure 8.14) produced three distinct values for the activation energy corresponding to 0.061 ± 0.003 eV for C_2, 0.085 ± 0.003 eV for C_3, and 0.171 ± 0.003 eV for C_4. The average of these values is equal to 0.106 ± 0.003 eV in good agreement with the activation energy found using the integral of the initial intensity. These findings support the existence of a multiple trap OSL model in accordance with a multiple trap TL model proposed in Chapter 7.

8.6 Discussion and Summary

The preceding investigation into the optically stimulated luminescence responses of alumina substrates revealed further details regarding the mechanism of OSL production, showing that OSL in alumina substrates can be generated using both blue and infrared light, although the characteristics of these optical signals were found to be quite different. The former (i.e., BOSL) exhibits a non-exponentially decaying curve and the latter (i.e., IRSL) is characterised by a nearly exponential decaying part. The results of the step-wise annealing procedure together with the deconvolution of the OSL decay curves suggested that the different forms of the BOSL and IRSL could arise from the contribution of charges in traps of different thermal depths. Quite dissimilar characteristics were also found following OSL measurements using a range of stimulation temperatures.

Step-wise annealing effects on BOSL response

The total area under the BOSL curve was found to decrease continuously with increasing preheat temperature, while the rate of decay was seen to progressively increase for preheat treatments to ~ 150 °C, and then to decrease at higher temperatures. The temperature range at which these changes occur coincide with the temperature range over which TL Peak 1 was defined. Curve fitting analysis also revealed that the fast exponentially decaying component (i.e., component C_1) disappears following annealing above 100 °C. This observation could also be taken as evidence of the contribution of TL Peak 1 to the BOSL signal. Finally, the disappearance of the sharp peak at ~ 10 s from the LM-BOSL decay curves (Figyre 8.3a) following preheating at

temperatures greater than 100 °C further supports the connection of TL Peak 1 with the BOSL. Nevertheless, the BOSL response also seems to be associated with the traps related to the other TL peaks and in particular with TL Peak 2 at ~ 200 °C, as suggested by the strong reduction in the BOSL following preheating at temperatures between 150 and 200 °C. A connection with the traps associated with TL Peak 3 at ~ 350 °C was also implied by the step-wise annealing data since a measurable BOSL signal is obtained even after preheat treatments above 300 °C.

Step-wise annealing effects on IRSL response

In contrast to the characteristics of BOSL, preheat at temperatures above 150 °C resulted in complete removal of the IRSL supporting the suggestion that the trap(s) responsible for the TL Peak 1 may also contribute to the IRSL signal. Additional evidence for the close relationship of the IRSL with the first TL peak was obtained by studying the thermal fading characteristics at RT. Both signals were found to decrease quickly and at the same rate when measurement was performed following various delayed periods from the administration of the dose.

Sample temperature effects on BOSL response

BOSL measurements at elevated temperatures revealed interesting information that could help identify the mechanism of OSL production. Summarising, optical stimulation at progressively higher sample temperatures was found to (1) strongly reduce the total integrated luminescence intensity, (2) slightly increase the initial (0-1 s) integrated intensity between 25-100 °C, (3) increase the rate of decay of the BOSL curves, and (4) significant increase the phosphorescence emission.

The first effect, common to luminescent materials (e.g., quartz, Wintle and Murray, 1988; feldspar, Poolton *et al*., 1995; α-Al_2O_3, Akselrod *et al*., 1998), is thermal quenching, although thermal erosion of the trapped charge population may also contribute to the enhanced decrease of the OSL output at high temperatures. For this reason and based on the results from the step-wise annealing test, the thermal quenching parameters of the BOSL in alumina substrates were calculated using data obtained for temperatures up to 200 °C.

On the assumption that the optical depth of the traps associated with the BOSL response is larger than the energy of photons from the excitation source, a *thermally assisted* recombination model could more appropriately account for the temperature effects of the BOSL decay curves. Although as will be shown later, shallow traps do play a role in the production of BOSL in alumina and can account for the enhanced OSL produced at elevated temperatures, their influence will be excluded from the interpretation of the thermal effects. The main reason for this is the observed increase in the rate of decay of OSL curves which does not conform with the expectations of a shallow trap model. Donor-acceptor pair recombination also seems less likely for the BOSL mechanism since, generally, d-a transitions are expected to be temperature independent and, hence, a thermal activation energy is not expected. As described above, both the enhanced luminescence emission and the change (i.e., increase) of the rate of decay are predicted in the models proposed by Hutt *et al*., (1988), Spooner (1994), and Poolton *et al*., (1995), although it may be difficult to differentiate between them. Of these models, the band-tail state mechanism may be less probable due to observed phototransfer TL (PTTL) effects (see next Chapter) accompanying BOSL production. PTTL is thought to be produced when optically evicted charges are retrapped at shallower energy levels. This mechanism is more efficient when the charge pathway is via the conduction band. Between the Hutt *et al*. and the Spooner models no definite conclusions can be made unless the energy separation between the excited state and the conduction band is known. If the energy gap is larger than the calculated activation energies the model suggested by Hutt *et al*. can no longer be applicable. The validity of the Hutt *et al*. model may also be tested by repeating the temperature dependence experiment using different excitation wavelengths. As discussed by Poolton *et al*. (1995), the Hutt *et al*. model cannot explain a potential dependence of thermal activation energy on the optical excitation energy. In other words, the thermal activation energy of the trap should be stable and independent of the stimulation wavelength. Unfortunately, using the LED light sources built into the Risøe reader it was not possible to examine the wavelength dependence of the thermal activation energy since, as already mentioned, infrared light is able to stimulate only part of the charge population associated with the traps in the range from RT to ~ 120 °C.

Nevertheless, there is still the possibility that the temperature induced changes in the BOSL curves are caused by the variation of the photo-ionisation cross section with temperature. In this case it is necessary to assume that the energy of photons (~ 2.6 eV) from the blue LED source is

higher than the optical trap(s) depth(s). Even though this piece of knowledge appears to be missing for the alumina substrates when searching the literature it was found that in the closely related α-Al_2O_3:C material the traps that contribute more than 90 % of the OSL signal are distributed in the energy range 1.7-2.5 eV (Whitley and McKeever, 2000). Adopting this energy range for the optical depths of the traps in alumina substrates, it could be hypothesized that during blue-light stimulation all transitions from the ground state of the traps place electrons directly into the conduction band. Then, due to electron-phonon interactions the probability of these transitions is enhanced because the elevated temperature during measurement increases the photo-ionisation cross section. The thermal activation energies now correspond to the vibrational or phonon energies of the traps. An assumption that could hold true when comparing the E_α calculated for OSL with the vibrational energies measured with the FTIR technique in Chapter 6. Another, evidence for electron-phonon interactions may be obtained by spectral emission measurements. For example, thermal broadening of emission bands is usually attributed to electron-phonon coupling (Bonnelle and Jonnard, 2010; Brewer *et al*., 1980). As noted in Chapter 6 (section 6.3.2), the width of the ~ 330 and ~ 410 nm radioluminescence emission bands was found to increase with increasing sample temperature from -250 to ~ -100 °C and this provides strong support for the importance of electron-phonon interaction processes in the luminescence emission of alumina substrates. The last thermal effect observed – that of phosphorescence emission – is not closely correlated with the mechanism of OSL production, but it can significantly influence the practical usefulness of BOSL for dosimetry. The phosphorescence component was found to be negligible for measurements carried out at RT, but significant thermal release was detected at elevated temperatures affecting both the intensity and the shape of the final OSL curve. Therefore, it is important, when OSL measurements are performed at elevated sample temperatures, to evaluate the phosphorescence component under the same conditions and extract it in order to acquire the optically stimulated signal.

Sample temperature effects on IRSL response

In the case of IRSL, the properties and the mechanism of luminescence production could not be easily assessed mainly due to the strong thermal instability of the IRSL response. Nevertheless, the change in the decay rate with stimulation temperature (i.e., Figure 8.8c) suggests a thermally

assisted recombination model, although the activation energy could not be evaluated because, as indicated in the step-wise annealing test, the charge population giving rise to IRSL is subject to strong thermal erosion, as the stimulation temperature increases. Also, because of thermal erosion the thermal quenching effect (i.e., Figure 8.7b) could not be evaluated above RT. The latter also prevented the correction for thermal quenching of the data in Figure 8.7b to obtain a value for the activation energy.

Summary

IRSL is likely associated with shallow traps; arguably the traps that give rise to the peak components of the first TL glow peak at ~ 100 °C. Nevertheless, the exponentially decaying nature of the (Net) IRSL curves and the single peak structure observed in the LM-OSL curves indicate that IRSL is most likely associated with a single peak (trap) component of the TL Peak 1. Although, the optical depth of the IRSL trap is not known, it is suspected to be greater than the energy of the stimulation light (i.e., ~ 1.4 eV). Furthermore, the change in the rate of decay with sample temperature suggests a recombination mechanism which involves the excited state of the trap or a phonon-assisted process.

The traps responsible for the BOSL response have a spectrum of thermal depths located from RT to ~ 400 °C. Those located at levels corresponding to TL peaks below 120 °C (i.e., TL Peak 1) contribute a very fast thermally unstable component which can be removed by a short duration preheat to temperatures equal or greater than 120 °C. The most important contribution to BOSL is from the traps in the range 150-220 °C (i.e., first half of TL Peak 2). Although the exact mechanism of luminescence production could not be identified, a thermally activated charge eviction process through an intermediate level was identified as the most likely mechanism for the production of OSL if the traps have an optical depth greater than 2.6 eV. Alternatively, luminescence could be produced by electron transitions directly into the conduction band assisted by the phonons of the crystal lattice produced by the vibrational modes.

The production of BOSL was found to be thermally quenched at temperatures exceeding ~ 100 °C and the activation energy of thermal quenching was calculated to be ~ 0.53 ± 0.05 eV. This value is very close to the thermal activation energy of the F^+-centre (i.e., 0.61 ± 0.02 eV)

estimated in Chapter 6, suggesting that the recombination of blue-light optically stimulated charges occurs at the F^+-centres.

Finally, for practical dosimetry applications, BOSL seems to be more suitable since IRSL thermally fades quickly at RT.

Chapter 9: Correlation between the TL and OSL signals in alumina SMRs

9.1 Introduction

As a matter of fact, the number of traps or the extent to which these traps participate in luminescence emission may not be common under thermal or optical stimulation since different parameters (i.e., frequency factor, photo-ionisation cross section) dictate the interaction or, specifically, the probability of charge detrapping during stimulation. When the excitation of the material is dominantly optical rather than thermal, the characterisation of specific properties of the traps is not very straightforward. This limitation, however, can to some extent be overcome through the correlation of OSL with the TL response. TL-OSL correlation studies are carried out to identify common trap components from which the properties of the same traps under optical stimulation can be evaluated.

The most common approach that has been used by several researchers (e.g., Akselrod and Akselrod, 2002; Bruce *et al*., 1999; Dallas *et al*., 2010; Kitis *et al*., 2010; Polymeris *et al*., 2006; Singh *et al*., 2012) to identify common traps involves examination of the residual TL levels following optical bleaching, usually with the same light source used for OSL measurements. Deconvolution of the TL glow curves and the OSL decay curves based on various luminescence models have also been employed in most of these studies to quantitatively and qualitatively relate specific glow peaks with the mathematically resolved OSL components.

The correlation between the TL glow curve and the BOSL signal in alumina substrates was investigated by varying (1) the duration of optical stimulation prior to TL readout and (2) the sample temperature during optical stimulation prior to TL readout. Additional approaches were used to determine the most appropriate optical bleaching mechanism. The thermal stability and lifetime of the energy levels participating in the generation of OSL were also examined using the method of various linear heating rates suggested by Li *et al*., (1997).

The correlation between IRSL and TL was also investigated using similar experimental procedures. The results (not shown) confirmed previous suggestions that the IRSL response is

associated with the trap(s) population giving rise to TL Peak 1, while optical bleaching using infrared light does not affect the characteristics (e.g., T_m, width, intensity) of the remaining TL glow curve.

9.2 Theoretical aspects

In the simplest case, the optical bleaching of TL can be explained by considering that during optical stimulation trapped charges are evicted depleting the charge population in those traps participating in the TL process and this is reflected in reduced TL intensity. OSL production may or may not accompany optical bleaching depending on whether excited charges recombine radiatively or non-radiatively or transferred to optically insensitive traps.

Photo-transferred TL and OSL production are two phenomena closely related to the optical bleaching of TL. PTTL is observed when certain TL peaks, which are easily bleached by optical stimulation, reappear in the TL glow curve. It is commonly observed as a result of photo-transfer of charges from deeper to shallower traps (Chen and McKeever, 1997). As with TL, PTTL peaks may decrease during prolonged illumination, but at a rate that is faster than predicted if only thermal excitation were allowed. The reduction in the PTTL signal is usually ascribed to (1) optical stimulation of trapped charges from the relevant traps (Wintle and Murray, 1997), (2) depletion of holes in the recombination centres (McKeever, 1994; McKeever and Morris, 1994), and (3) a combination of the two effects (McKeever, 1994).

Three models have been developed to explain the reduction of TL as a function of the duration of optical stimulation. A review of these models can be found in McKeever (1994) who examined the relevance of each model for the behaviour of TL in quartz following optical stimulation. The earliest model discussed by McKeever (1994) is that of Levy (1982) illustrated in Figure 9.1a who considered the presence of several participating electron traps (represented as 1,2,3 in Figure 9.1a). Electrons in these traps are optically excited followed by retrapping into the same traps or recombination with holes in the recombination centre. The latter process causes a decrease in the number of holes which is the main reason for the reduction of the TL response. Levy's model is appropriate for non-first-order kinetics TL peaks and predicts a zero peak and

PTTL signal if illumination continues for prolonged durations. The argument of McKeever (1994) against the model by Levy is that since the bleaching rate is wavelength dependent, the TL should decay to zero at any wavelength. However, this has not always been observed in experiments (e.g., Spooner *et al*., 1988).

Non-zero residual levels independent of irradiation dose and intensity of illumination are predicted in the model proposed by Chen *et al*., (1990). This model (Chen and McKeever, 1997; Chen and Pagonis, 2011; Chen *et al*., (1990), McKeever, 1994) assumes a single electron trap and single recombination centre (Figure 9.1b). Optical stimulation can not only remove electrons from the electron trap, but also from the recombination centre if this is located close to the valence band (i.e., below the Fermi level).

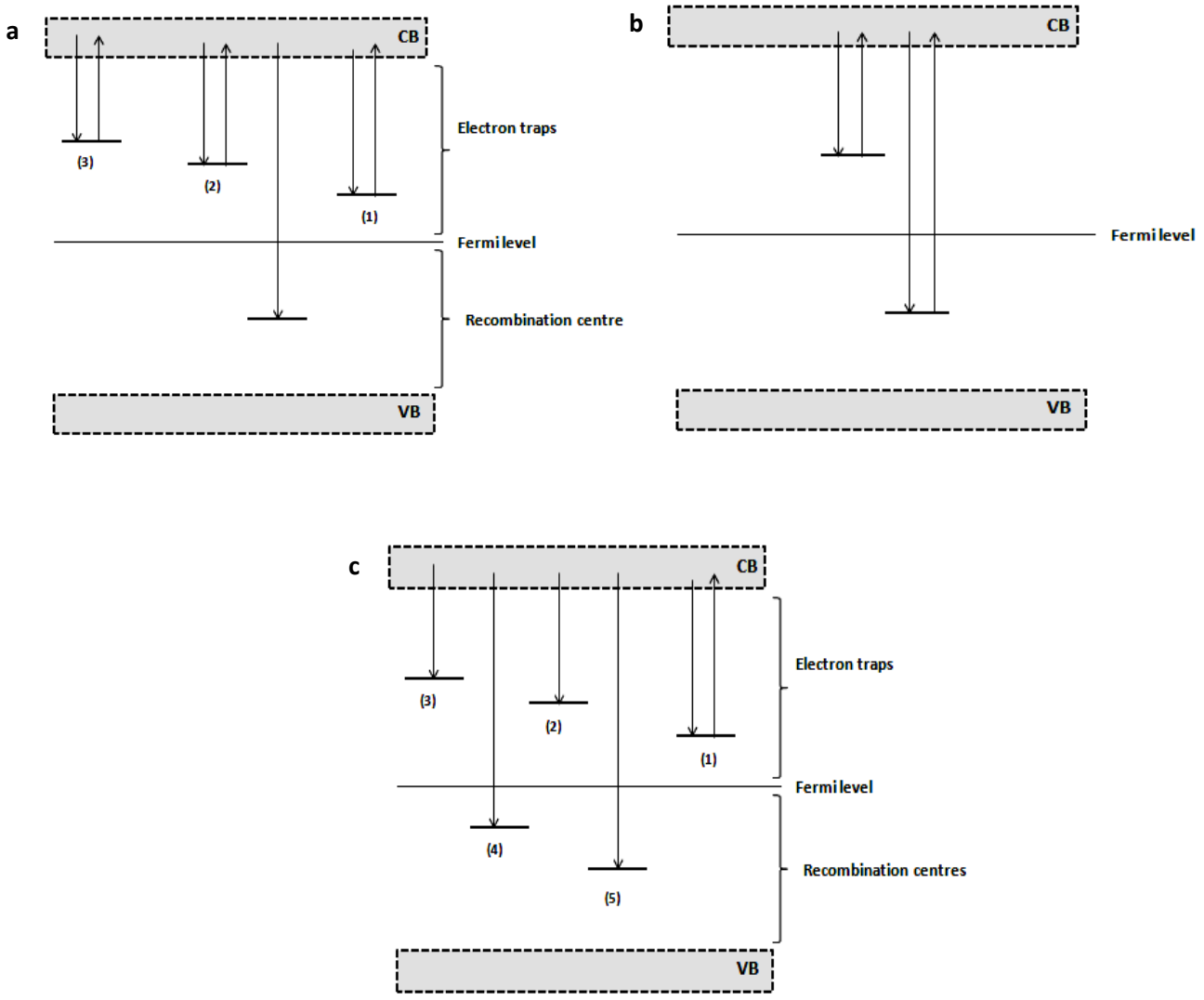

Figure 9.1: Models of optical bleaching of thermoluminescence according to (a) Levy (1982), (b) Chen *et al*., (1990), and (c) McKeever (1994). The numbers in parentheses are explained in the text. Redrawn from McKeever (1994).

In McKeever's model (1994), multiple electron traps and loss of recombination centres are used to account for the optical bleaching of TL. In this model, the basic assumption is made that that light removes electrons from traps which are optically sensitive, but thermally inaccessible. The model represented schematically in Figure 9.1c includes (1) a shallow trap, (2) a thermally sensitive trap, (3) a thermally inaccessible trap, and two recombination centres (4, 5) one of

which is non-radiative (5). Illumination delocalises electrons in the thermally insensitive trap and these radiatively recombine with the holes in the recombination centres (4). This process results in a reduction of the concentration of holes in the recombination centres and, as a consequence, in the subsequent TL intensity since the same number of electrons in the thermally active trap has a smaller quantity of available holes at recombination centres. Some characteristics expected from this model are: the presence of an unbleachable residual level, the dose dependence of the residual level, and the wavelength dependence of the bleaching rate if additional thermally inaccessible traps are added to the model.

.

9.3 Experimental method and analysis

The sensitivity to light of TL in alumina substrates was investigated using the measurement sequence shown in Table 9.1.

Table 9.4: Experimental sequence used to investigate the optical bleaching of TL.

Step number	Treatment
1	Test beta dose: 1 Gy
2	TL readout to 500 °C (5 °C s^{-1}) to obtain the initial TL sensitivity of the sample
3	Beta dose: 10 Gy
4	TL readout to 500 °C (5 °C s^{-1}) to obtain the unbleached TL glow curve, followed by a second TL readout for background measurement
5	Beta dose: 10 Gy
6	BOSL at RT for 1 s
7	TL readout to 500 °C (5 °C s^{-1}) to obtain the residual TL glow curve
8	Repeat steps 5 to 7 by varying the duration of BOSL between 1 and 1000 s
9	Repeat steps 1 and 2 to obtain the final TL sensitivity of the sample

To examine the relative efficiency of PTTL production and further investigate the relationship between TL and BOSL, two modifications of the above measurement sequence were tested. In the first, a preheat step of 120 °C (10 s hold) was added after the administration of dose in steps 1 and 5, while in the second the BOSL bleaching step 6 was carried out at a temperature of 120 °C.

At the end of Step 9 of each sequence it was found that the sensitivity of the sample to the test dose was higher by about 30 % which corresponds to ~ 2 % per cycle (i.e., beta dose + BOSL + TL). The sensitised TL glow curves at Step 4 were corrected by taking into account the cumulative increase in sensitivity from the first cycle.

The experiments presented in the following sections were conducted using a sample population each consisting of ~ 20 type ´0402´ SMRs. The graphical examples presented correspond to a specific sample but are considered representative of the average behaviour of all the samples investigated. The values of the relevant parameters given in the tables and elsewhere are averages of all the samples examined, whereas errors represent the standard deviation of the mean value. Unless otherwise stated, OSL and TL were detected in the UV range with a 7.5 mm Hoya U340 filter.

9.3.1 Case I: $BOSL_{RT}$

The effect of blue-light (LED, 470 nm) stimulation on the TL glow curve of a sample of alumina substrates (~ 20 type ´0402´ SMRs) is shown in Figure 9.2a. The initial and bleached TL glow curves are presented following the measurement of $BOSL_{RT}$ for various durations. Their difference, representing the lost TL signal, is also shown in Figure 9.2b. As can be seen, the entire range of the TL glow curve is affected by blue-light stimulation, although the degree to which each TL peak is reduced is different.

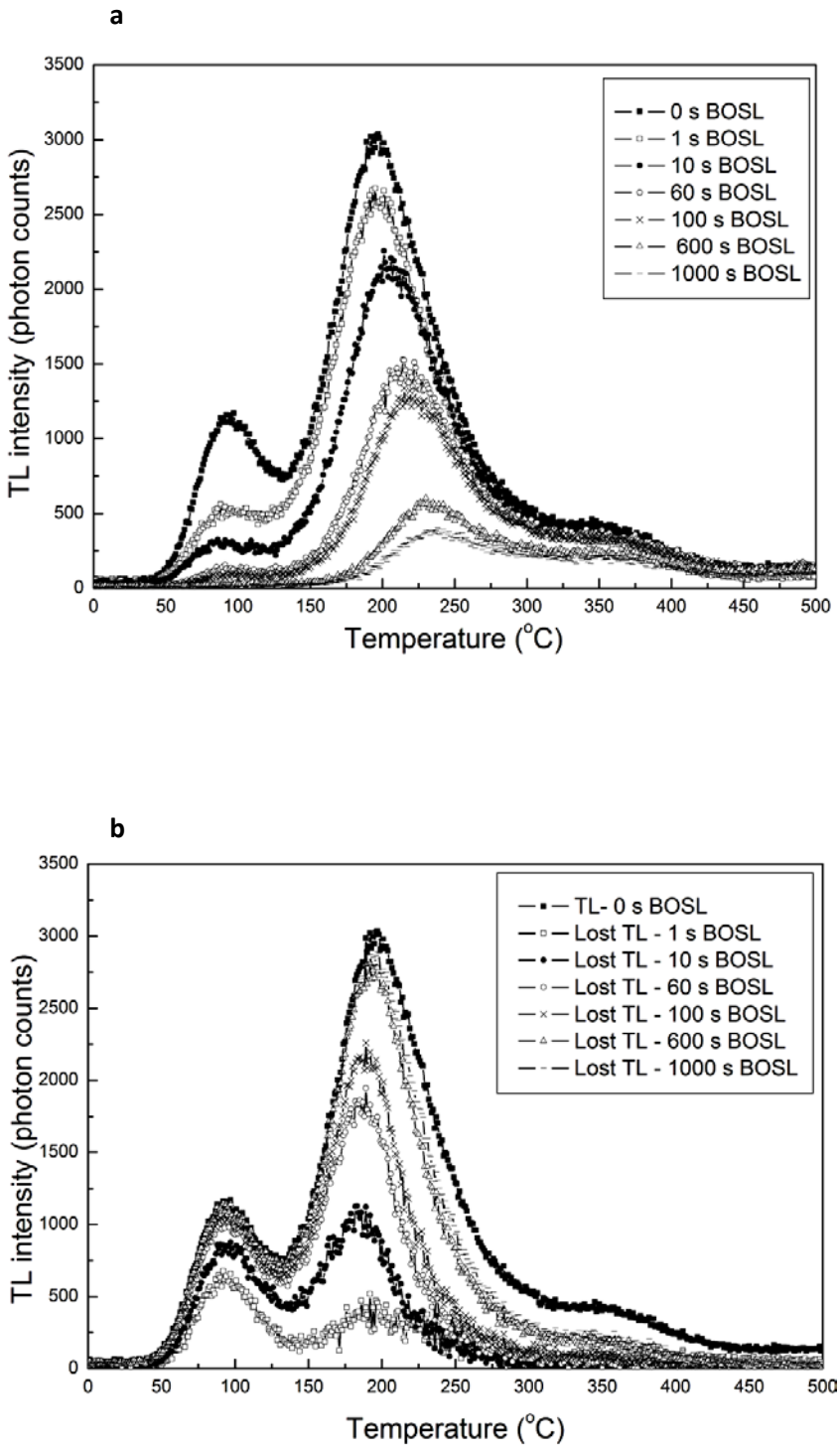

Figure 9.2: Optical bleaching of TL glow curve by blue-light stimulation. (a) Examples of remaining TL glow curves following $BOSL_{RT}$ measurements for the indicated durations (1-1000s) (b) Lost TL glow curves calculated by subtracting the bleached TL signal from the TL obtained without illumination. The data correspond to a sample consisting of ~ 20 type ´0402´ SMRs irradiated with ~ 10 Gy.

TL Glow Curve: 50–150 °C

The immediate impression from Figure 9.2a is that blue light strongly reduces the intensity of TL Peak 1. Nevertheless, as found from subsequent tests (e.g., Section 9.3.2), the remaining TL Peak 1 is in fact a photo-transfer peak (i.e., PTTL). The latter was demonstrated when the sequence was repeated following post-irradiation preheat at 120 °C. This thermal treatment, as shown in the step-wise annealing experiments (Chapter 7; Section 7.2), would cause complete removal of TL Peak 1, such that optical bleaching would not be expected to produce any effect on this part of the glow curve. This, however, was not observed. In contrast, it was found that $BOSL_{RT}$ regenerates a smaller part of Peak 1, presumably, by transferring charges from deeper traps. Following preheating to 200 °C (sufficient to remove most of TL Peak 2) the PTTL peak was not observed suggesting that the most likely source are those traps that contribute to TL Peak 2. An absence of PTTL was also noted when BOSL was measured at elevated temperature (i.e., 120 °C) which is expected given that the lifetime of the charges in the shallow traps is very short at the elevated sample temperature used in the experiment (it is to be noted that the lifetime of trapped charges is exponentially dependent on temperature through the Boltzman factor E/kT).

Therefore, and on the basis of a multiple trap model suggested in Chapter 7 for the TL Peak1, it is likely that part of the TL Peak 1 is bleached quite fast after 1 s (or less) of $BOSL_{RT}$ stimulation while at the same time part of it (likely associated with different trap population) is restored as a PTTL signal by removing charges from the traps of TL Peak 2. As the duration of illumination increases, the charge transfer process from TL Peak 2 to TL Peak 1 by a phototransfer mechanism reduces significantly. As discussed earlier, reasons such as optical excitation of charges out of the TL Peak 1/ PTTL traps or reduction in the concentration of recombination centres, may contribute to a decrease of the PTTL signal. Thermal release (i.e., thermal fading) of charges from the traps associated with TL Peak 1 may be another factor assisting the decrease of the PTTL signal as the illumination time increases. The thermal fading of TL Peak 1 was investigated by holding the sample at RT for the same periods of time as the duration of the optical bleaching step. The proportion of thermal loss of TL Peak 1 (50-150 °C) was measured and subtracted from the PTTL signal (50-150 °C). This procedure enabled the measurement of the rate of bleaching of PTTL due to optical stimulation alone. The results are shown in Figure 9.3a.

The optical bleaching characteristic of the PTTL signal for bleaching times to 100 s was fitted using a summation of three exponential functions (Figure 9.3b) plus a constant (not shown in Figure 9.3b), plotted on a log-linear scale. The time decay constants of these components obtained from the curve fitting were: 0.36 ± 0.02 s (*Dot curve*), 4.6 ± 0.5 s (*Dash Dot curve*), and 35.2 ± 2.4 s (*Dash Dot Dot curve*). The multi-exponential nature of the bleaching characteristic can be taken as an indication of the presence of several traps and this is consistent with the complex structure of TL Peak 1 (Chapter 7; section 7.4).

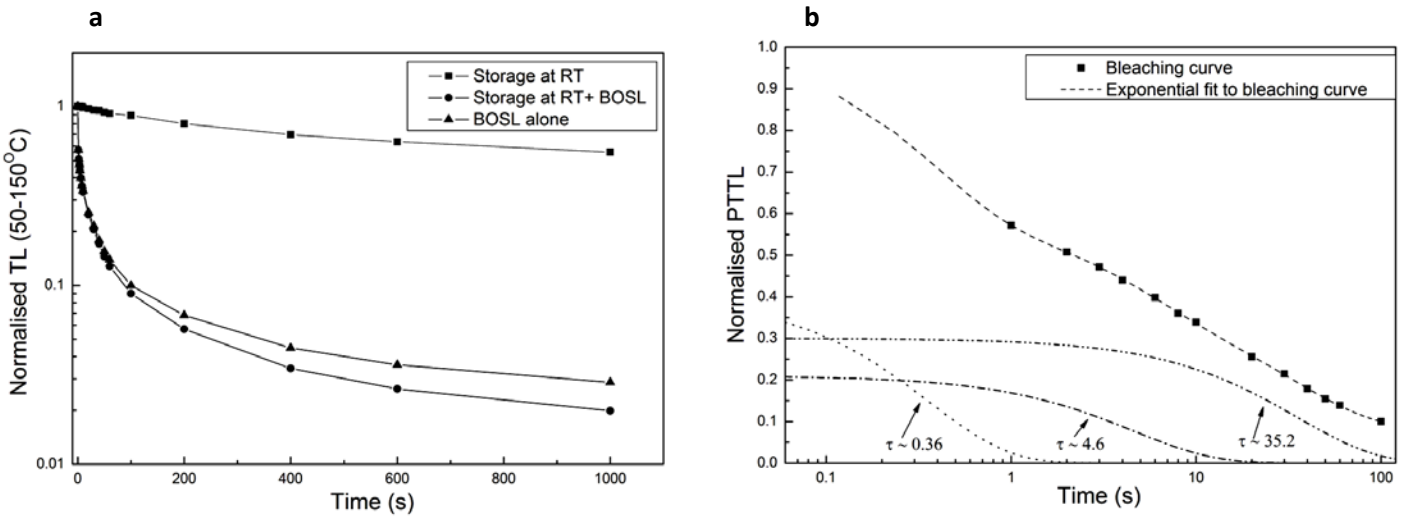

Figure 9.3: (a) Linear-log plot showing the decrease of normalised at t=0 s integrated (50-150 °C) TL signal after storage at RT (filled squares) and storage at RT followed by blue-light optical stimulation at RT (filled circles) for different times t = 0….1000 s. The curve obtained after the remaining bleached TL was corrected for thermal fading (filled triangles) was used to derive the optical bleaching rate of the PTTL signal. The data points were connected with straight lines for better visualisation (b) Optical bleaching curve of TL Peak 1/PTTL peak (50-150 °C) plotted on a log-linear scale and fitted with a sum of three exponential functions. The time decay constants of the three exponential components are indicated in the figure. The error bars in (b) are not shown since they are comparable to the symbol size.

TL Glow Curve: 150–450 °C

The remainder of the TL glow curve also decreases with increasing illumination time, but appears to be more resistant than the TL Peak 1/PTTL peak. As indicated in Figure 9.2a, most signal loss takes place in the first half of TL Peak 2 (i.e., 150-200 °C). Furthermore, as shown in

Figure 9.2b, the temperature of the maximum of the 'lost' TL curves shifts towards higher values (i.e., for t=10 s T_m=185 °C, for t= 1000 s T_m =194 °C) as the bleaching duration increases. This behaviour could be characteristic of a peak that follows non-first-order kinetics (Murray *et al*., 2009) or could indicate the presence of several components. These indications are consistent with the conclusions of Chapter 7 where it was found that TL Peak 2 is composed of several non-first order kinetics peaks.

The optical bleaching curve of TL Peak 2 created by plotting the normalised remaining TL intensity over 150-290 °C as a function of bleaching time on a log-linear scale is presented in Figure 9.4. Due to insignificant thermal fading of TL Peak 2 for the duration of the measurement (1000 s), the data have not been corrected for thermal loss. TL Peak 2 demonstrates a fast decrease the first 60 s of BOSL followed by a slower rate at longer bleaching periods and its optical bleaching can be described by the sum of three first-order exponential decaying components with characteristic time decay constants equal to 4.5 ± 0.9 s, 41 ± 2 s, and 414 ± 19 s plus a constant (not shown in Figure 9.4) which likely represents an unbleachable or hard-to-bleach component. The lost TL signal over the same temperature range exhibits similar behaviour (results are not shown) while also the peak temperature of the 'lost' TL moves to higher temperatures with increasing illumination time suggesting a complex peak structure. This is also consistent with the findings of Chapter 7 (i.e., Section 7.4)

The high temperature (~ 300-450 °C) part of the TL glow curve exhibits behaviour similar to that of TL Peak 2, but a detailed analysis of the optical bleaching behaviour of Peak 3 was prevented by its low intensity.

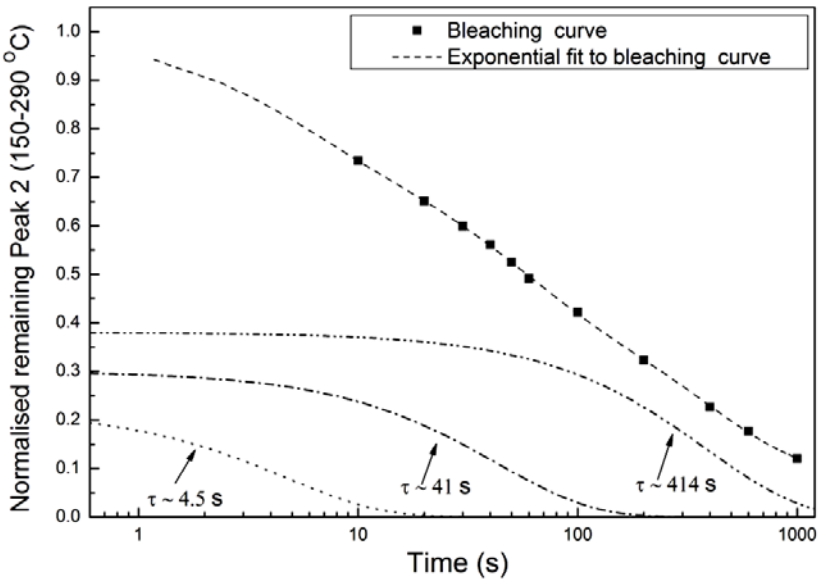

Figure 9.4: Optical bleaching curve of the normalised at t = 0 s integrated intensity of Peak 2 (150-290 °C). The data were fitted with a sum of three first-order exponentially decaying components with characteristic time decay constants equal to 4.5 ± 0.9 s (*Dot curve*), 41 ± 2 s (*Dash Dot curve*), and 414 ± 19 s (*Dash Dot Dot curve*). The error bars are not shown since they are comparable to the symbol size.

BOSL emission

During the bleaching process of TL, the BOSL emission was concomitantly monitored. The intention was to understand if the optical bleaching of TL and the reduction in the PTTL are accompanied by an increase in the BOSL emission.

Examples of the BOSL decay curves measured during the bleaching process of TL are shown in Figure 9.5. The number of data points in each curve was adjusted so that each one corresponds to 0.2 s of stimulation. For example, the BOSL measured for 1 s has only 5 data points (5 x 0.2 = 1 s) while that measured for 100 s has 500 data points (500 x 0.2 = 100 s).

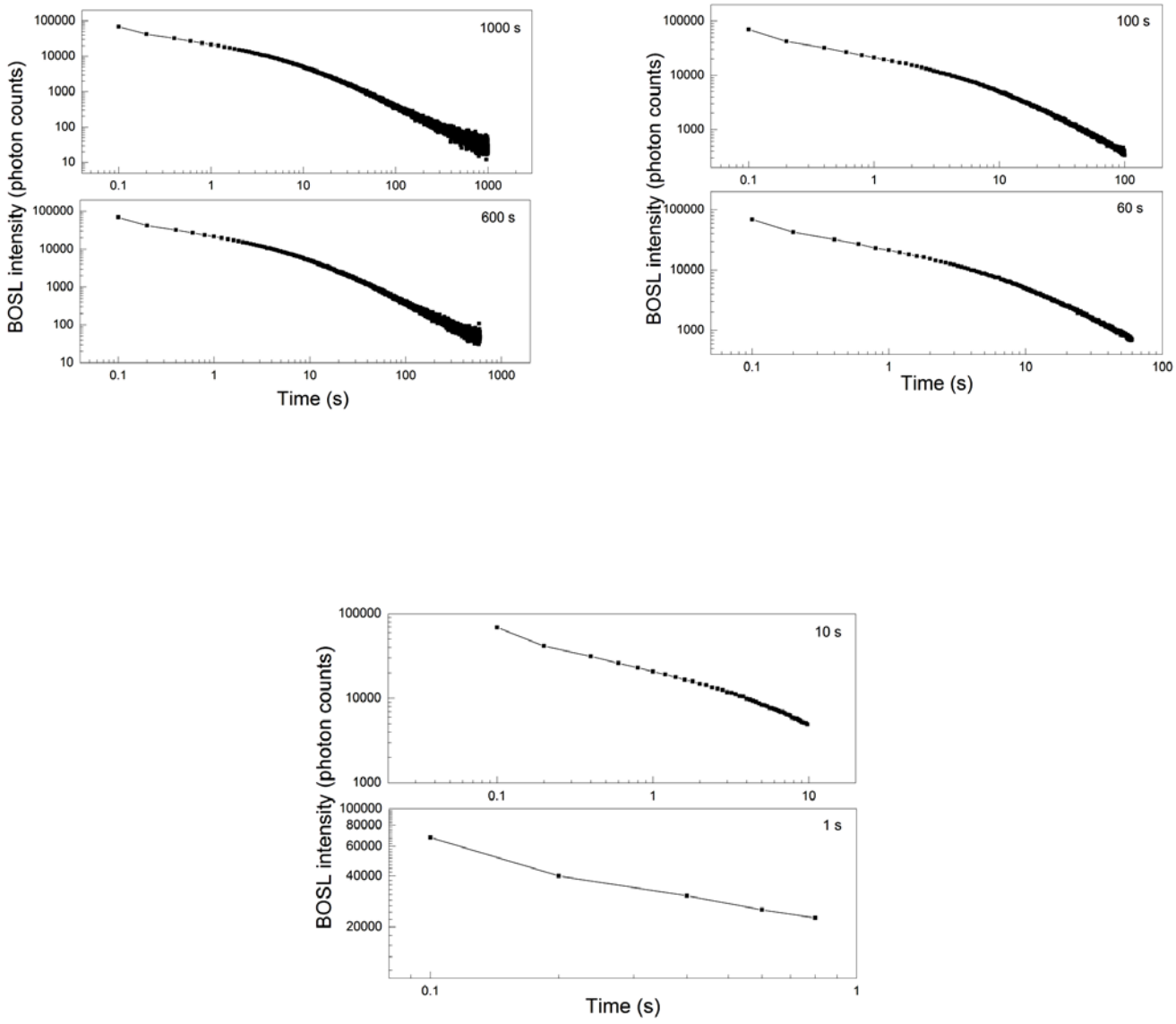

Figure 9.5: Examples of BOSL decay curves measured during the optical bleaching process of TL. As explained in the text, the number of data points of each curve has been adjusted according to the duration of illumination. Each data point corresponds to 0.2 s of stimulation. The decay curves are representative of a sample consisting of ~ 20 type ´0402´ SMRs irradiated with ~ 10 Gy.

To examine how the BOSL signal varies with stimulation time, each decay curve was integrated over two regions; the first corresponds to the integrated intensity over 1 s of stimulation and the second is equal to the integrated intensity over the remainder of the curve (e.g., 1-t s, where t=10,

30, 60...s). The background was estimated by exposing an unirradiated sample to blue-light stimulation for the same period of time as the duration of the BOSL measurements yielding an average value of 30 counts per 0.2 s which has been subtracted from the measured signal integral.

Figure 9.6 shows the variation of BOSL integral as a function of stimulation time. The 1–t s integral (upper panel) displays an increasing trend when time increases from 1 to ~ 200 s. For longer stimulation periods it does not show further increase and seems to be stable around a mean value of 1087 ± 1 kcounts. On the other hand – given the statistical error in the measured photon counts – the initial intensity over the 1 s (lower panel) demonstrates an insignificant average increase (i.e., less than 1 %) having a mean value of 192 ± 0.4 kcounts. These observations are consistent with Figure 9.5 which indicates that while the initial part of the decay curve does not seem to vary importantly, additional components are added to the curve as the time of stimulation increases. In addition, these results suggest that complete emptying of OSL trap(s) occurs for stimulation time longer than 200 s.

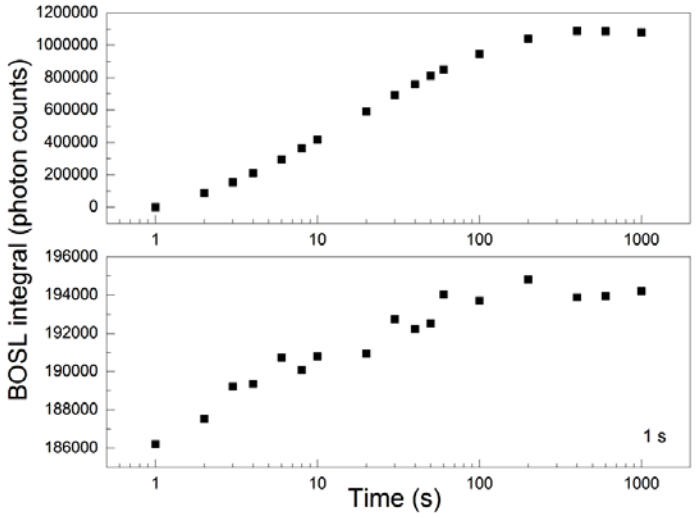

Figure 9.6: Variation of BOSL integral as a function of stimulation time. The lower panel shows the integrated intensity over the 1 s of stimulation, while the upper panel shows the integrated intensity over the remainder of the curve (e.g., 1-t s, where t=10, 30, 60...s). Linear curves were used to connect the data points for better visualisation. The estimated error bar of each data point is not presented due to being less than the symbol size.

In Chapter 8 (section 8.3) several pieces of evidence were presented to support the relationship between TL Peak 1 and BOSL. It was also assumed that TL Peak 1 contributes to the initial part of the decay curve. In agreement with these assumptions, it was shown above that Peak 1 is very quickly (within 1 s) removed by optical stimulation, while part of it is regenerated as PTTL. The nearly constant level of the 1 s integral further supports that TL Peak 1 is completely bleached by short duration stimulation and the remaining TL seen in Figure 9.2 is a PTTL signal.

9.3.2 Case II: PH: 120 °C + $BOSL_{RT}$

The main effect of the application of preheat prior to optical stimulation in these experiments was to reduce considerably the reservoir of charge available to produce PTTL. On the other hand, the optical bleaching behaviours of TL Peak 2 and TL Peak 3 appeared to be similar to the case without preheat, as seen in Figure 9.7 where the remaining TL signal after $BOSL_{RT}$ measurements for different durations of stimulation is compared for the preheated and the non-preheated sample.

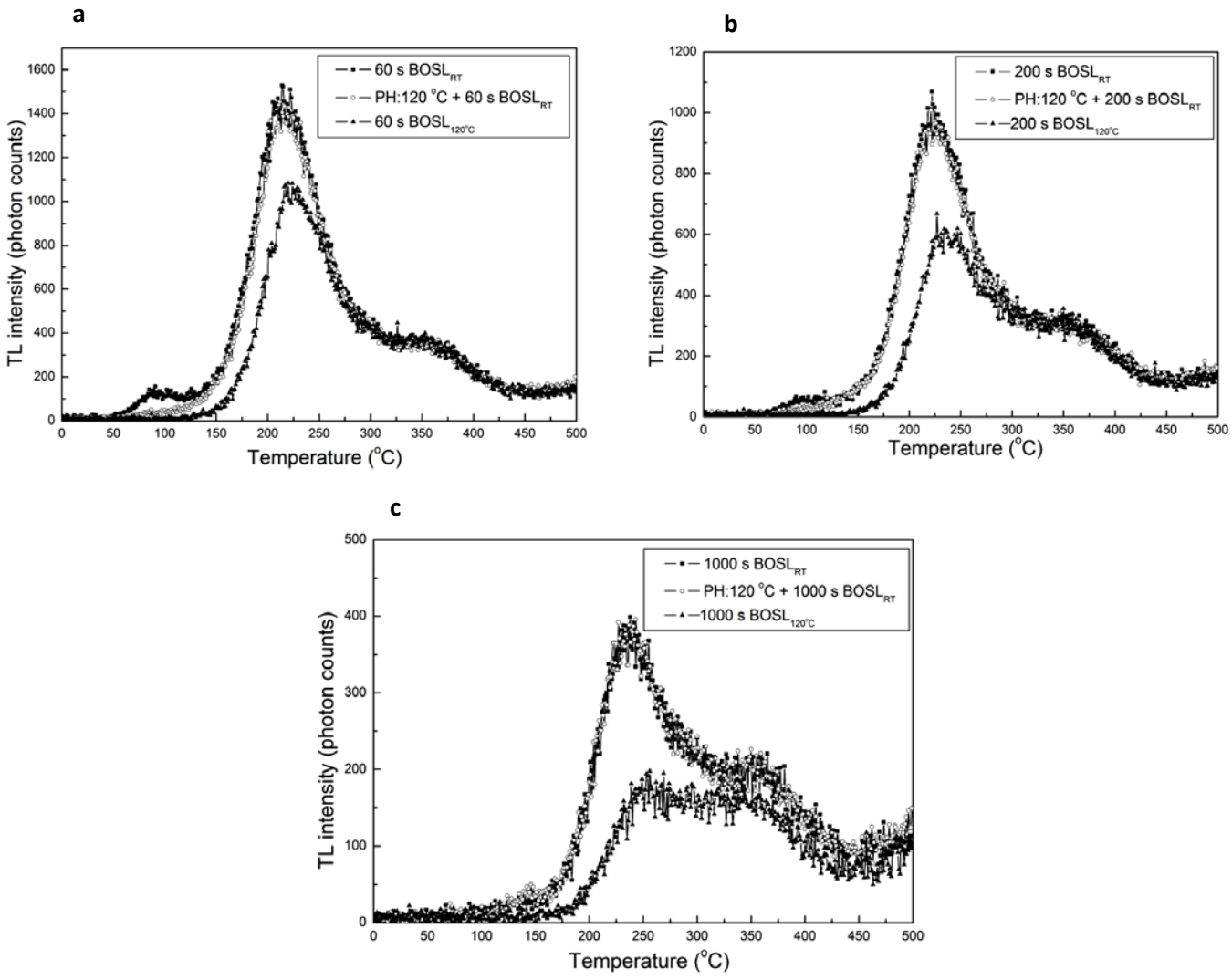

Figure 9.7: Comparison of optical bleaching of TL by $BOSL_{RT}$, PH: 120 °C + $BOSL_{RT}$, and $BOSL_{120\,^{o}C}$ after (a) 60 s, (b) 200 s, and (c) 1000 s of stimulation. The TL glow curves correspond to a sample consisting of ~ 20 type ´0402´ SMRs.

9.3.3 Case III: $BOSL_{Ts}$

When optical stimulation was carried out at elevated sample temperature T_S the TL Peak 1 arising from a phototransfer process could not be detected (Figure 9.7), since as explained earlier, photo-transfer of charges from deep to shallow traps still takes place but the time these charges spend in the traps is very short. Once excited (most likely thermally) the probability of

radiative recombination is high (the concentration of holes in the luminescent centre is considered to be large prior to optical bleaching) increasing, therefore, the intensity of BOSL. However, as shown in Section 8.4, a decrease in intensity is observed, likely, due to a competing thermal quenching effect.

Also, from Figure 9.7, it can be seen that the bleaching efficiency of TL, in particular of TL Peak 2, is accelerated by the elevated temperature optical stimulation. This would be expected given that BOSL was found to be a thermally assisted process (i.e., the probability of charge detrapping is enhanced at elevated sample temperature, since the photo-ionisation cross-section is greater). It must be noted, however, that the increased reduction efficiency of TL may be due to the combined effect of thermal and optical stimulation.

9.4 Discussion

In previous studies (e.g., Polymeris *et al*., 2006; Spooner, 1993, 1994) it was implicitly assumed that the lost TL (following optical stimulation/bleaching) and the emitted OSL (during optical stimulation) light sums are directly proportional if derived from the same trap population. Nevertheless, such assumption could be questioned not only because it is likely that the same trapped charge population behaves differently under thermal or optical stimulation (i.e., different detrapping routes may become available) but also because, the effect of thermal quenching may be different for TL and OSL which inevitably affects the luminescence response. For these reasons, in this study the correlation between TL and OSL was studied only qualitatively.

In relation to the TL glow curve, the $BOSL_{RT}$ seems to originate from the recombination of the charge population evicted from the traps responsible for the TL over the temperature range 50-220 °C. When an irradiated alumina substrate sample is optically stimulated – during the initial part of the stimulation (t < 10 s) – the total electron population of the traps associated with the TL Peak 1 and part of the electron population of the traps associated with the TL Peak 2 are optically evicted to the conduction band. Some of the mobile charges recombine radiatively with holes at luminescent centres producing OSL and others are transferred to shallow traps giving rise to PTTL or to deeper traps.

As the duration of optical stimulation increases, the detrapping process of charges associated with TL Peak 2 increases too, enhancing also the magnitude of BOSL. At the same time, the charges optically transferred to shallow traps (i.e., PTTL) may also be optically evicted (the thermal fading of TL/PTTL at RT is too small to account for the decrease of PTTL observed) and contribute to BOSL causing the reduction of TL Peak 1/PTTL peak. If the reduction of PTTL as the duration of optical stimulation increases is responsible for the increase of the integrated BOSL intensity it would be expected to contribute a slowly-decaying component to the BOSL decay curve (the initial part should remain unchanged, as evidenced by comparing the 1 s integral at different stimulation periods). This was tested by examining the BOSL curves measured for t > 400 s at RT and 120 °C (after 200 s most PTTL has decayed to a level equivalent to the instrumental background so that the full extent of the contribution to BOSL can be better observed at longer stimulation periods). It was found that those curves measured at elevated sample temperature decay faster (for t > 1 s) with time and eventually reach the background level. In contrast, the $BOSL_{RT}$ includes a slowly decaying component and takes longer stimulation time to reach the same background level.

Together with the reduction of the TL Peak 1/PTTL peak, the TL throughout the entire glow curve decreases with illumination time. Having assumed that BOSL excites electrons from thermally active traps (i.e., the temperature range of TL measurement) and further assuming that all traps associated with the TL over the range 50-450 °C use the same type of recombination centre, the optical bleaching of TL could be mostly due the decreased concentration of available holes in the radiative recombination centre(s). Specifically, the reduction of the population of holes could be mainly due to radiative recombinations of electrons evicted from optically sensitive traps. In this case, during the measurement of TL, evicted charges either recombine non-radiatively, or are transported to deep traps (i.e., traps associated with the TL above 500 °C). Complete emptying of the optically sensitive trap population of TL Peak 2 was observed to take place when bleaching is performed for t > 200 s. Nevertheless, for longer stimulation times – where the integrated BOSL signal no longer increases – the TL integral continues to reduce, although at a slower rate. It could, thus, be assumed that the optical stimulation of the charge population of thermally sensitive traps and their subsequent recombination is not the only factor influencing the bleaching process of TL. If it was the only factor, then, following blue stimulation for t > 200 s, a constant residual level of TL would be expected.

An assumption that could be made is that there exists an additional luminescent centre where only charges from traps that do not contribute to OSL (i.e., the trap population that gives rise to TL over 220-450 °C). The reduction of TL in this temperature range, which is not associated with OSL production, could therefore be attributed to the effect of hole removal from the recombination centre, rather than electron removal from the traps. This effect likely occurs even for short duration optical stimulation but it can more easily be noticed after prolonged illumination once the charge population in the optically sensitive traps has been depleted.

The behaviour of optical bleaching described above resembles the mechanism proposed by Chen *et al*., (1990), where blue stimulation empties TL traps which are optically sensitive rather than thermally disconnected traps as suggested by McKeever (1994). Based on this model, the higher reduction rate of TL can be attributed to the effect of electron removal from both the electron traps and the recombination centre(s). These effects are likely to occur simultaneously during optical stimulation, but the effect of electron removal from the RC may be more easily be noticed once the charge population in optically sensitive traps has been depleted. To acquire additional evidence the experiment was repeated, initially lowering the excitation dose to 3 Gy and subsequently by increasing it to 40 Gy. It was found, supporting the model of Chen *et al*., (1990) that the residual level is independent of the initial trap occupation.

Even though, longer stimulation periods were not investigated to test the applicability of the simplest bleaching model suggested by Levy (1982) which predicts that a given TL peak reduces to the instrumental background level following prolonged illumination it was thought to be less applicable. The main reason is the argument by McKeever (1994) that since the optical bleaching rate is wavelength dependent, the TL should decrease to a minimum at any wavelength. By using the IR-light source (LED, 880 nm) of the Risø reader it was found that no measurable reduction of TL above 120 °C could be obtained, no matter how long the stimulation was applied for.

In summary, the optical sensitivity of thermoluminescence (particularly of TL Peak 2) of alumina substrates can be described by the following flow chart showing only the radiative recombination processes responsible for the optical bleaching of TL. However, it is almost certain that some of the optically evicted charges as well as charges evicted thermally during TL measurement will recombine non-radiatively.

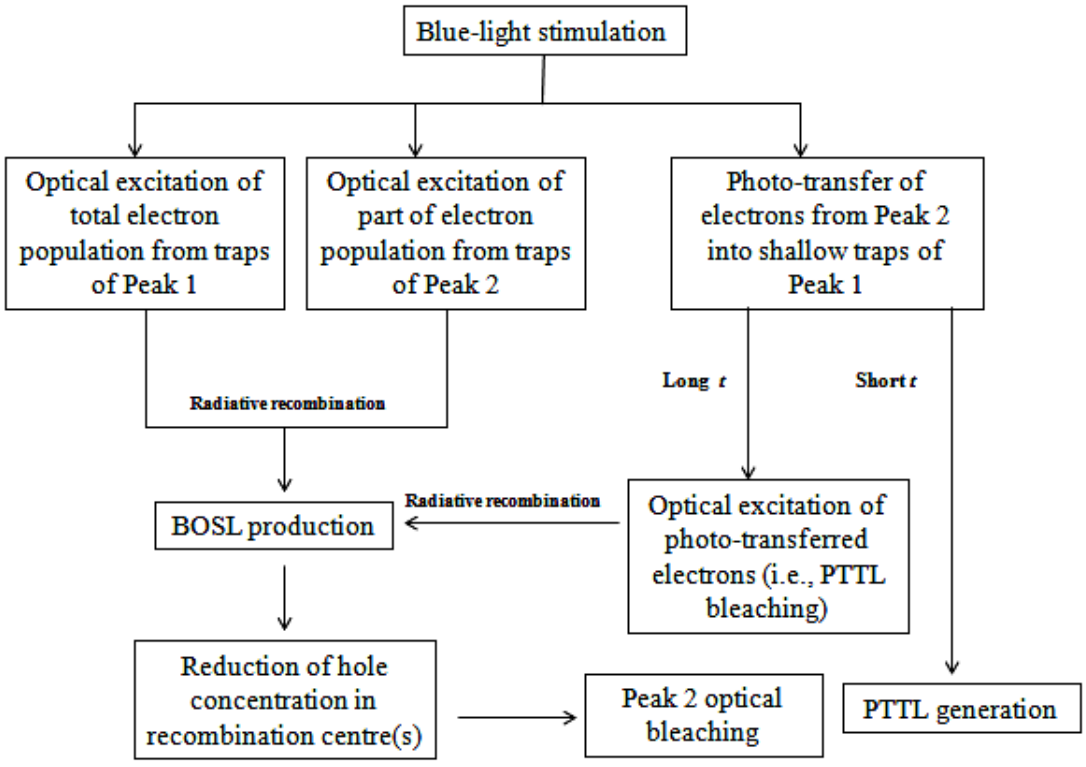

9.5 Identification of trap origin of BOSL

If, as already suggested, the production of BOSL and TL are associated with similar energy levels (i.e., traps and recombination centres) it might be anticipated that the kinetic parameters of the traps will be comparable. Two methods were used to estimate the parameters *E* and *s* of the traps associated with OSL. Initially, the lost TL glow peaks obtained following annealing to 120 °C (in order to isolate TL Peak 2 from TL Peak 1) and optical bleaching were analysed using the initial rise method. Subsequently, the method of various linear heating rates suggested by Li *et al*., (1997) was employed to independently determine the trap parameters.

Since, as proposed earlier, the bleaching of TL Peak 2 due to optical excitation of electrons from the relevant traps is completed when stimulation is carried out for t > 200 s, the initial rise method was applied only to the lost TL glow peaks following blue light stimulation for 200 and 400 s. These lost TL glow curves (Figure 9.8) were expected to reflect the total charge population emptied during optical stimulation. Table 9.2 includes the values of the activation

energy and frequency factor calculated after the application of the initial rise method. It should be noted that for the calculation of the frequency factor, the second-order kinetics expression (i.e., Chapter 2; equation 2.23) was applied, using the values of the geometric factor which were found to be 0.50 ± 0.05 and 0.52 ± 0.04 for the lost TL glow peaks following 200 and 400 s of blue stimulation respectively. Using the values of E and s, the predicted lifetime, τ [where $\tau = s^{-1}\exp\left(E/kT\right)$], of OSL traps at 20 °C is 2.2 years. For comparison, the trap parameters of TL Peak 2 estimated in Chapter 7 (Section 7.3) are also presented in the table where it can be seen that the agreement is very good. In particular, the first half of TL Peak 2, corresponding to a TL glow peak centered at about 190 ± 2 °C (5 °C s^{-1}), seems to be responsible for the majority of OSL emission.

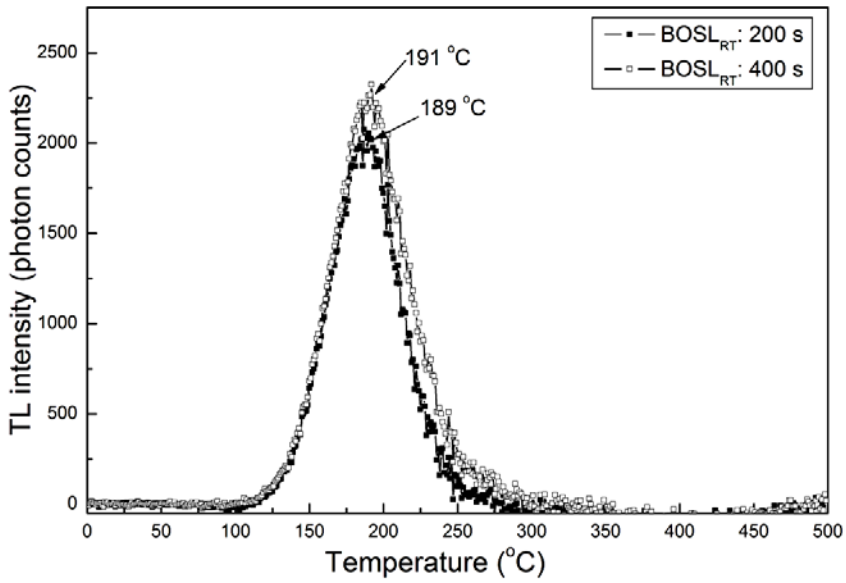

Figure 9.8: Lost TL glow curves following annealing to 120 °C and bleaching with blue light at RT for 200 and 400 s. The position of the maximum of each lost glow peak is also indicated in the figure. The glow curves are representative of a sample consisting of ~ 20 type ´0402´ SMRs irradiated with ~ 10 Gy.

Table 9.2: Kinetic parameters of lost TL and TL Peak 2 calculate using chip samples.

Lost TL (150-290 °C)				TL Peak 2 (150-290 °C)			
Method	**E (eV)**	**s (s^{-1})**	**$\tau_{20\,^\circ C}$ (years)**	**Method**	**E (eV)**	**s (s^{-1})**	**$\tau_{20\,^\circ C}$ (years)**
IR : $BOSL_{RT}$ 200 s	1.16±0.01	(1.15±0.14)x10^{12}	2.16	**IR**	1.10±0.03	(1.24±0.15)x10^{11}	2.14
IR : $BOSL_{RT}$ 400 s	1.15±0.01	(7.79±0.32)x10^{11}	2.16				
VHR	1.12±0.02	(2.68±0.16)x10^{11}	2.18	**VHR**	1.14±0.01	(4.36±0.22)x10^{11}	2.96

The same analysis was performed using the fine grain samples, since as pointed in Chapter 1 the true values of the kinetic parameters of the TL glow peaks are likely those obtained when the temperature lag effect is minimised. The kinetic parameters of the lost TL calculated in this case (Table 9.3) are also consistent with those found in Chapter 7.

Table 9.3: Kinetic parameters of lost TL and TL Peak 2 calculate using fine grain samples

Lost TL (150-290 °C)				TL Peak 2 (150-290 °C)			
Method	**E (eV)**	**s (s^{-1})**	**$\tau_{20\,^\circ C}$ (years)**	**Method**	**E (eV)**	**s (s^{-1})**	**$\tau_{20\,^\circ C}$ (years)**
IR : $BOSL_{RT}$ 200 s	1.29±0.02	(4.45±0.74)x10^{13}	23	**IR**	1.28±0.02	(5.82±0.91)x10^{13}	23
IR : $BOSL_{RT}$ 400 s	1.31±0.03	(5.21±0.82)x10^{13}	23				
VHR	1.30±0.02	(3.74±0.56)x10^{13}	23	**VHR**	1.32±0.03	(9.03±1.06)x10^{13}	23

The method of various heating rates has already been described in Chapter 2 (Section 2.6.1). Essentially, it is a pulse annealing test (i.e., similar to a step-wise annealing procedure, though in this case the sample is immediately cooled after being heated to the measurement temperature T_{stop}) which is repeated using a range of increasing heating rates. The experimental procedure used to determine the parameters of the OSL traps is indicated in Table 9.4.

Table 9.4: Experimental sequence used to determine the parameters of the OSL traps.

Step number	Treatment
1	Test beta dose: 1 Gy
2	BOSL at a sample temperature of 100 °C for 60 s to obtain the initial sensitivity of
3	TL readout to 500 °C (5 °C s^{-1}) to erase any remaining signal
4	Beta dose: 5 Gy
5	Heat to temperature T_o = 100 °C with a heating rate of 1 °C s^{-1}
6	BOSL at a sample temperature of 100 °C for 60 s
7	TL readout to 500 °C (5 °C s^{-1}) to erase any remaining signal
8	Repeat steps 4 to 7, increasing the sample temperature in step 5 by 10 °C to 290 °C
9	Repeat steps 1 and 2 to obtain the final sensitivity of the sample
10	Repeat steps 1 to 9 using a series of increasing heating rates (β: 1-10 °C s^{-1}).

Figure 9.9 shows the pulse annealing curves for different heating rates where each data point represents the remaining BOSL signal after each annealing temperature. To produce these curves, at each heating rate the total BOSL intensity – representing the integrated luminescence signal over 60 s less a background calculated using the number of counts recorded during the last 10 s – measured following annealing to temperature $T_i > T_o$ (i=100...290 °C) was normalised to the BOSL integral obtained at T_o = 100 °C.

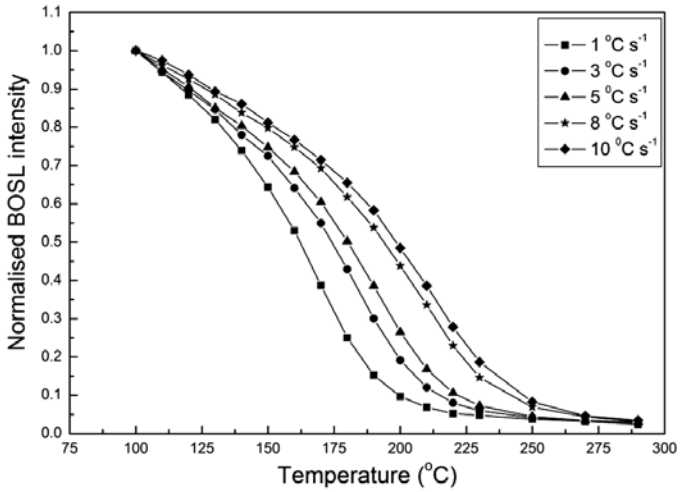

Figure 9.9: Pulse-annealing curves of alumina substrates produced by heating a sample from 100 to 290 °C using different heating rates.

The estimation of the trap parameters using the various linear heating rates method is based on the comparable approach applied to TL measurements (TL-VHR). The activation energy and frequency factor were obtained from the slope and the intercept of the plot of ln (T_m^2/β) vs. $kT_m{}^{-1}$. Two methods have been previously used to convert each pulse-annealing curve into a peak-shaped curve from which the T_m (i.e., temperature at which the peak-shaped curves reach a maximum) values can be obtained, (Li *et al*., 1997; Li *et al*., 2011; Fu *et al*., 2012) plotting the reduction rate of the OSL signal as a function of the annealing temperature. By reduction rate was calculated as the percentage difference between the signal measured after annealing to $T_o+\Delta T$ and the signal measured at T_o, where T_o is the starting annealing temperature of the experiment and ΔT is the temperature increment for the next annealing step. Bulur *et al*. (1998) applied a slightly different form of analysis of the data, taking the first derivative of the remaining OSL curves and this approach was employed here. The first derivative of the pulse annealing curves obtained at each heating rate were calculated numerically and smoothed using a 5-point Adjacent Averaging smoothing function (OriginPro7). These are presented in Figure 9.10a for selected heating rates. The values of T_m were then determined from each peak-shaped curve and used (after corrected for thermal lag) to produce a plot of ln (T_m^2/β) vs $kT_m{}^{-1}$ (Figure 9.10b), from which the calculated values of activation energy and the frequency factor were found to be 1.10 ± 0.02 eV and 2.68 x10^{11} s^{-1} respectively. These values are not statistically different to those estimated earlier (Table 9.2). They were inserted into the following equation (Fu *et al*., 1998)

$$E/_{kT}\exp\left(E/_{kT}\right) = sT/_{\beta} \qquad (9.1)$$

with which a peak maximum temperature, T_m, of 188±2 ^{o}C (β= 5 ^{o}C s^{-1}) was evaluated.

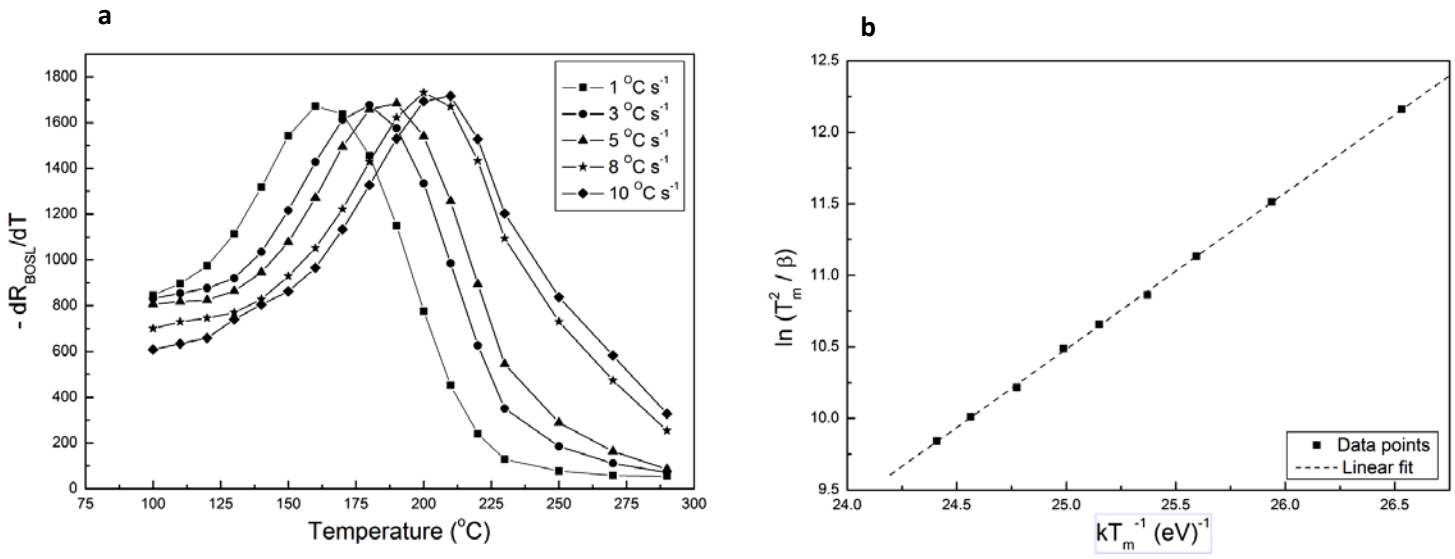

Figure 9.10: (a) Numerically calculated first derivatives of pulse-annealing curves shown in Figure 9.9 smoothed using a 5-point Adjacent Averaging smoothing function. (b) Plot of ln (T_m^2/β) vs $kT_m{}^{-1}$ used to estimate the trap parameters *E*, *s* of the OSL traps. The T_m values were obtained by visual inspection from the maximum temperature position of the peak-shaped curves in (a) and corrected for the thermal lag effect.

9.6 Identification of common TL and OSL recombination centres

From the analysis so far and the very good agreement in the kinetic parameters, it can be suggested that the OSL signal in annealed alumina substrates is derived from the same type of traps responsible for a TL peak at ~ 190 ^{o}C. In this section, the thermal quenching efficiencies of TL and OSL were investigated to further examine whether common recombination centres are used in the production of TL and OSL.

Even though there are two types of thermal quenching mechanism, the model developed by Mott-Seitz – according to which thermal quenching is attributed to the increased probability of non-radiative recombination as the temperature of measurement is raised (for more detailed description of the mechanism the reader is referred to Chapter 2; section 2.4) – is most frequently encountered in the literature and has, in addition, been used to explain the thermal quenching effect in the Al_2O_3:C dosimetry grade materials (e.g., Akselrod *et al*., 1998).

In practice, the thermal quenching effect is expressed as a reduction of the luminescence efficiency with increasing sample temperature. OSL and spectral radioluminescence measurements (Chapter 7; Section 7.3.2) performed over a range of increasing temperatures can directly provide a means to determine the extent of thermal quenching by measuring relative changes in luminescence efficiency. From an analysis of the thermal quenching effect of the BOSL signal of alumina substrates (Chapter 8), the following quenching parameters were evaluated: W = 0.53 ± 0.05 eV and C = (2.88 ± 2.40) x10^6. For the thermal quenching of TL, the method is less straightforward and it is based on the observed shift of T_m and the reduction of peak integral as a function of the heating rate (Kitis *et al*., 1994; Akselrod *et al*., 1998), using a VHR procedure and plotting the integrated intensity under the peak as a function of T_m.

The data from Section 7.3 were used to generate the graph shown in Figure 9.11 which was fitted using the function $I(T) = \frac{I_o}{1+C \cdot \exp^{-W/kT}}$ resulting in the following values for *W* and *C*: W = 0.61 ± 0.02 eV and C = (0.9 ± 0.3) x10^6. The similarity of the thermal quenching parameters of TL and BOSL suggests that thermally and optically excited charges likely recombine at the same luminescent centre(s).

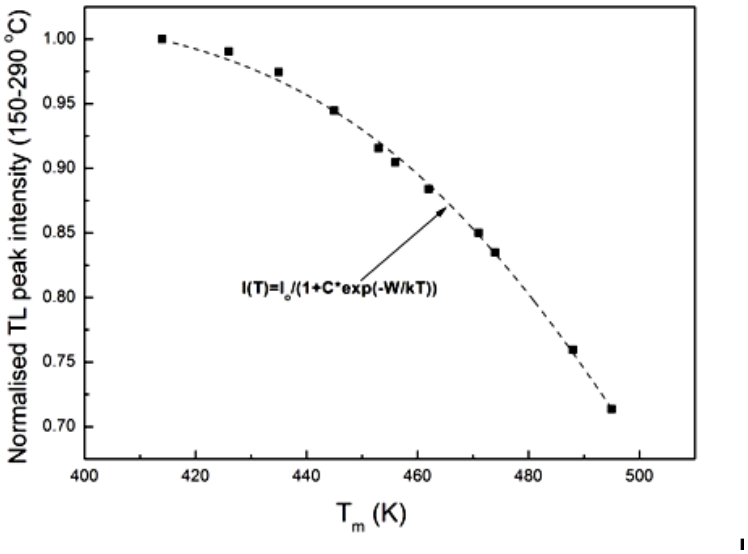

Figure 9.12: Luminescene efficiency of TL Peak 2 as a function of maximum peak temperature, T_m, employing various heating rates analysis. The dashed curve shows the fit to the data points using the equation describing the thermal quenching effect with parameters: W = 0.61 ± 0.02 eV and C = (0.9 ± 0.3) x10^6.

9.7 Summary

The TL and OSL signals measured with alumina substrates from SMRs are well correlated as indicated from the optical bleaching tests of TL using blue light stimulation.

The most likely bleaching mechanism of TL involves optical eviction of the trapped electron population followed by radiative recombination. However the increased rate of TL reduction observed after prolonged illumination indicates that the bleaching process is assisted by another mechanism and optical eviction of electrons out of the recombination centre(s) could be responsible; in accordance with the model proposed by Chen *et al*., (1990).

The BOSL signal is associated with the same trapping levels that give rise to TL Peak 2. The most likely source of BOSL is the trap population associated with a TL peak at ~ 190 ° C with a thermal depth of 1.30 ± 0.02 eV and lifetime of ~ 23 years at RT (calculated using fine- and coarse-grain samples).

An examination of the relative change in luminescence efficiency indicated the presence of common TL/OSL recombination centre(s), although, spectrally-resolved measurements are needed to verify this. Furthermore, it could be argued, based on the close agreement of the parameters of the thermal quenching effect between the TL and OSL (i.e., $W \approx 0.6$ eV, $C \approx 10^6$) and the F^+ emission centre [i.e., $W = 0.61$ eV, $C = 10^6$ (Chapter 6)], that the thermally or optically evicted charges recombine at F^+ centres. The extent to which the F^+ band (~ 250-350 nm) contributes to the measured TL and/or OSL signal should depend on the choice of the detection filters used. Since, the majority of TL/OSL measurements in this thesis were carried using a Hoya U340 filter with transmission between ~ 260-390 nm the luminescence emission associated with recombinations at F^+ centres is expected to be dominant. Smaller contribution to the measured luminescence signals may also arise from recombinations at F centres (~ 350-450 nm), although this emission band was found to exhibit significant thermal quenching at RT.

The findings of the present chapter may ultimately be useful to develop an understanding of other properties (e.g., athermal stability) of the luminescence of alumina-based SMRs which can empirically be better characterised using the TL instead of the OSL response.

Chapter 10: Thermal and athermal stability of luminescence

10.1 Introduction

As will be demonstrated in the following chapter most of the basic dosimetry properties (e.g., linear dose response, low detection limit) can be reproduced using SMRs from electronic equipment (e.g., mobile phones). Nevertheless, there exists an important limitation for the use of this material for radiation dosimetry applications. Significant fading of the luminescence response following laboratory irradiation was identified in the early studies (Inrig, 2009; Inrig *et al*., 2008) and methods to avoid it including the detection of a signal component that is stable over time or the application of specific pre-measurement conditions (e.g., preheat, optical bleaching) – suggested by Templer (1985) to overcome the anomalous fading in zircon – were proven ineffective in the case of alumina-based SMRs (unpublished personal work). As a consequence, unless the reconstruction of unknown doses is carried out within a very short period (i.e., < 1 h) from the exposure, correction for the amount of luminescence loss must be applied to obtain reliable estimates of the doses. The most accurate approach would require the determination of sample-specific fading correction factors, which might be practical when the delay between irradiation and readout is only a few hours. In cases where the potential radiation-induced health effects to individuals have to be assessed within short periods from exposure but longer delays are involved the use of universal fading correction factors has been adopted. Radiological exposure trials (Bassinet *et al*., 2014; Inrig, 2009), based on previously determined fading correction functions (i.e., not sample-specific), have shown that as long as fading is measured with the same experimental sequence used in the dose reconstruction protocol, the accident doses can be estimated with a good degree of accuracy. An issue that is raised here is that TL or OSL dosimetry should be performed using the same readout parameters adopted in fading measurements. Modifications, for example, in the preheat temperature and the readout temperature should be avoided since these may affect the measured rate of fading; though, the actual fading which is believed to be inherent to the material and it is related with the trapping and/or recombination environment is not going to be influenced.

Thermal and athermal mechanisms have been suggested (Inrig, 2009) to explain the instability of the luminescence of SMRs. The component of fading due to thermal escape of charge carriers at RT was mainly detected in the low temperature TL glow peak. The fading of the main dosimetry peak was attributed to an athermal quantum mechanical tunnelling mechanism; although due to the complex nature of the 200 °C peak it could not be excluded that there can be an underlying component which fades thermally with the rest following a tunnelling model. Similar considerations were put forward to explain the instability of the OSL response, but in this case the identification of thermal fading was based on the observed decrease in the rate of fading with increasing preheat temperature. Specifically, the most significant improvement in the measured fading rates was obtained following a preheat at 120 °C

The thermal and athermal stability of the TL and OSL of alumina-based SMRs is investigated in this chapter. The dependence of fading rates on measurement parameters and the physical mechanism of athermal/anomalous fading will also be explored

10.2 Experimental method

The procedure of determining the fading rate is rather simple, though it is lengthy and requires a careful consideration of the laboratory conditions (e.g., light, temperature). The samples are given a dose and the luminescence response is measured shortly after irradiation (i.e., $t_o \approx$1-3 minutes) corresponding to the non-faded prompt signal F_o. The same dose is delivered to the samples, followed by a period of storage $t_i > 0$ at temperature T. At the end of time t_i the luminescence response is measured again corresponding to the faded/delayed signal F_i. The plot of the ratio of F_i / F_o (i.e., the normalised remaining luminescence) as a function of elapsed time t can be used to derive the rate of fading.

In the initial experiments it was found that the rate of fading is independent of the size of the samples (i.e., number of SMRs per cup). Fading tests were performed using ca 100 samples each consisting of ~ 10 or ~ 20 type ´0402´ SMRs both unused and extracted from mobile phones. Of the total sample population, 20 samples were used to study the short-term (i.e., 30 minutes–1 month) TL and OSL fading, initially by measuring the fading of the TL signal and subsequently,

using the same samples, the fading of the OSL. The remaining 80 samples were divided into two groups (one for each stimulation mode) and used to measure the long-term fading extending from 2 months to 1 year. The handling and preparation of the samples was performed under red light conditions. The samples were irradiated with a beta dose of 3 Gy and subsequently stored inside light-tight boxes at RT.

10.3 Fading of TL at RT

To determine the fading behaviour of all glow peaks of SMRs both the prompt and delayed TL were measured without preheat. Figure 10.1a shows the remaining TL glow curves of a sample consisting of ~ 20 type ´0402´ SMRs measured following storage for different time intervals. The TL lost during each storage period is depicted in Figure 10.1b.

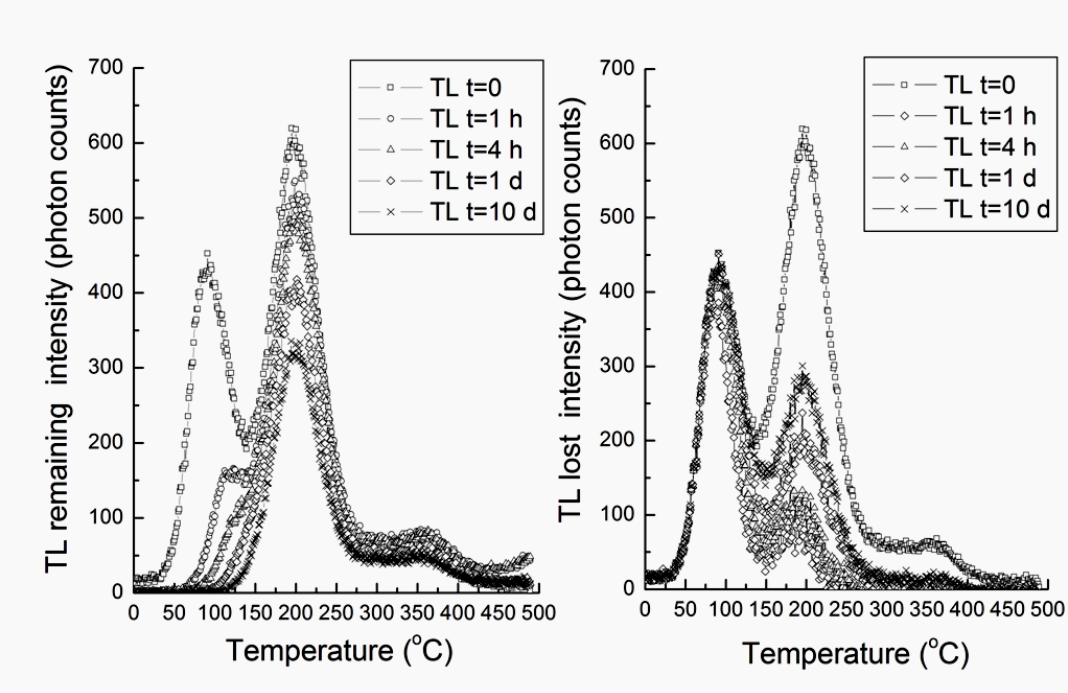

Figure 10.1: (a) Short-term RT fading of TL following several time intervals between irradiation and measurement. (b) Lost TL glow curves obtained by subtracting each delayed TL glow curve from the prompt TL glow curve. The glow curves were obtained with a sample consisting of 20 type ´0402´ SMRs. The sample was irradiated with 3 Gy and heated linearly to 500 ° C at 5 ° C s^{-1}.

Inspection of Figure 10.1a indicates that the TL of SMRs is unstable over the entire temperature range. Nevertheless, TL Peak 1 presents the most striking fading behaviour. The intensity over 50-150 ° C reduces to ~ 30 % of its initial value just 1 hour after irradiation and completely diminishes for delays greater than 1 day. The total fading of TL Peak 1 is illustrated in Figure 10.2 where the normalised to the first measurement (i.e., $t = t_o$, with $t_o \approx$ 1-3 minutes) remaining TL intensity was plotted as a function of the elapsed time since the end of irradiation. Each data point was obtained by averaging the results over all samples.

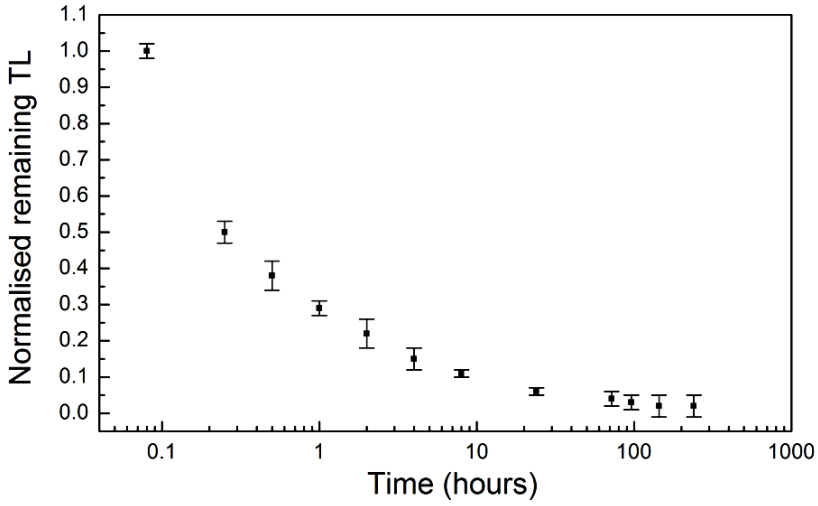

Figure 10.2: Fading curve of TL Peak 1. Each data point represents the average value of the normalised to the first measurement (i.e., $t = t_o$,with $t_o \approx$1-3 minutes) remaining TL over all samples. The dose to the samples was 3 Gy.

The increased fading of TL Peak 1 in comparison with the remaining TL glow curve as well as the complete disappearance after 1 day suggests the involvement of a process which should be less active in TL Peaks 2 and 3. Thermal fading, for instance, could provide a solid explanation for the above observations and has also been suggested by Inrig (2009), although without providing sufficient justification. The common approach to verify the presence of thermal fading is by estimating the lifetime at RT of charges in the trap(s), which for TL Peak 1 was found to be

close to 40 minutes (Table 7.3). It could, therefore, be argued that the fading of TL Peak 1 is attributed to the thermal release of charge carriers from shallow traps.

TL Peak 2 demonstrates greater stability with time than TL Peak 1. In particular, the TL over 150-290 ° C decreases by more than 30 % after 1 day storage at RT, followed by slower rate of fading at longer delay periods. As indicated in Figure 10.1b, the maximum loss of luminescence originates from a peak component centred at ~ 200 °C. In addition, fading tests carried out over a period of 1 year showed that while the reduction of TL Peak 2 seems to proceed continuously, the remaining intensity –given the statistical error of the data– tends to follow a lower rate of loss after ~ 3 months. In other words, it is possible that beyond 1000 h there is another slow fading component which, although it may not be useful for short-term emergency dosimetry, it has the potential to be used for retrospective dosimetry applications. However, if this slow fading component needs to be used in retrospective dosimetry, the rate of fading and the fading correction function beyond ~ 1000 h have to be calculated separately.

Figure 10.3 shows the TL fading curves produced using the data over the entire temperature range of TL Peak 2 (Figure 10.3a), the first half between 150 and 220 ° C (Figure 10.3b), and the second half between 220 and 290 ° C (Figure 10.3c). With the aim to determine whether the quantum mechanical tunnelling mechanism – considered the dominant mechanism responsible for the fading of the main TL peak of SMRs – participates in the fading process of TL Peak 2 the data sets in Figure 10.3 were fitted with an equation of the form $y = 1 - b * \log(x)$ where the *y* is equivalent to the normalised remaining intensity, *b* is a constant characteristic of the fading rate, and *x* is the ratio of t_i/t_o. According to a tunnelling-type fading model, the relationship between signal loss and the logarithm of time is expected to be linear. This behaviour can be observed in Figure 10.3a-c for the data obtained following storage up to 3 months, while for longer durations between irradiation and readout the relationship between remaining TL and time is no longer linear.

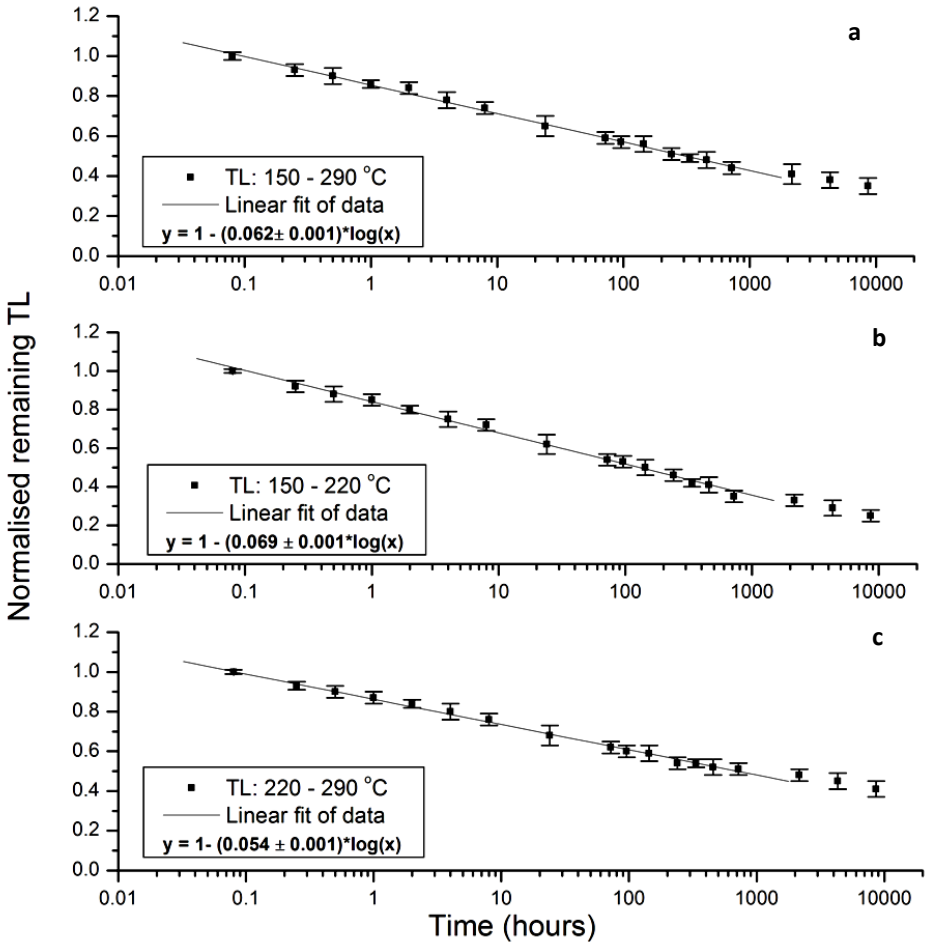

Figure 10.3: Fading curves of TL over (a) the entire temperature range, (b) the low temperature side and (c) the high temperature side of TL Peak 2. The data points up to $t \approx 3$ months were fitted with a function of type $y = 1 - b * \log(x)$ characteristic of the quantum mechanical tunnelling fading mechanism. Each data point corresponds to the average value of the normalised remaining TL of all samples. The dose to the samples was 3 Gy.

Concerning the fading mechanism and following the discussion above, the instability of TL Peak 2 may not be solely due to an athermal mechanism. As proposed earlier (Chapter 7; section 7.4), TL Peak 2 is likely made up of several non-first-order peak components, although the number and position of which were not fully resolved since the method employed in section 7.4 may be considered somehow arbitrary. In addition, based on the kinetic analysis results presented in section 7.4, TL Peak 2 is expected to be stable at RT. However, and as long as the actual number

and kinetic parameters of the components are not precisely known the lifetimes for thermal fading cannot be accurately determined. In turn, this implies that thermal fading cannot be excluded. Instead, it could be assumed that the initial (i.e., 1-2 days) fast rate of fading may be partly assigned to the thermal decay of one of the components of TL Peak 2. Moreover, the rate of fading of the first half (i.e., 150-220 ° C) of the peak – expressed by the constant *b* in Figure 10.3 – is about 20 % higher than that of the second half (i.e., 220-290 ° C). This fact could also be taken as an indication of thermal fading contribution, although such fading characteristics are also expected by the localised transition model (Templer, 1986). In any case, it seems that the dominant fading effect is caused by an anomalous-type process. The very good fit of the fading rate curve with the tunnelling-type equation suggests that quantum mechanical tunnelling is the most likely mechanism contributing to the fading process of TL Peak 2. On the other hand, following storage for $t > 3$ months a potential second TL fading component with lower rate of loss is observed that cannot be explained based on the tunnelling model. Additional experiments performed at elevated storage temperature may help to elucidate the origin of fading process.

Finally, TL Peak 3 displays the lowest fading behaviour compared with TL Peaks 1 and 2. The TL intensity over 300–450 ° C begins to decrease after ~ 1 day from the end of irradiation and demonstrates a slow rate of decay with time. However, for reasons given in Section 7.2, this part of the glow curve is not considered suitable for dosimetry application in this study and its fading characteristics will not be further investigated.

10.4 Fading of OSL at RT

The fading behaviour of OSL is expected to present similar characteristics with that of TL since, as suggested in previous parts of this work, the TL and OSL of SMRs are strongly correlated. It was shown above that the instability of TL is attributed to a combination of thermal and athermal mechanisms. The thermal fading of TL is mainly associated with the low-temperature TL peak (50-150 °C) which is also source of the OSL (Chapter 9; section 9.12). In the case of TL, the contribution of this unstable component can be excluded from the calculation of the fading rate (and in dose measurements using the SAR protocol) simply by selecting the integrated range which corresponds to the stable TL. Such analysis, however, is not possible using the OSL

response, where all components appear in a single decay curve. Heating the samples to 120 ° C for 10 s was found (Inrig, 2009) to be adequate to eliminate the thermally unstable component. Higher temperature thermal treatments were found to cause small reduction in the fading, unless the preheat was raised to 260 °C. However, such high preheat treatment causes considerably thermal erosion leaving a statistically poorly defined OSL signal.

In this study, the fading of OSL of SMRs was initially measured a) without thermal treatment to identify the presence, if any, of thermal fading and b) following a preheat to 120 ° C (10 s). The influence on the rate of fading of the temperature of the sample during optical stimulation was investigated too. OSL measurements were carried out for 60 s and the fading curves were produced by integrating the intensity from the first 10 s of stimulation less a background equal to the average counts of the last 10 s. Different integration intervals were also analysed, but the rate of fading was found to be statistically invariable.

10.4.1 Fading of OSL without preheat

Figure 10.4a presents the fading of the OSL_{RT} measured without preheat treatment. The fading of Peak 1 is also shown for comparison. The rate of fading of OSL_{RT} can be described by a fast fading component for delays up to ~ 4 h followed by a slower fading component showing logarithmic dependence on time (Figure 10.4b). The resemblance between the first fading component of OSL_{RT} and the fading rate curve of TL Peak 1 is noticeable suggesting a similar fading mechanism and further confirming the existence of common traps. Nevertheless, the absolute vales of the normalised remaining intensity do not perfectly agree which is due to the fact that the OSL_{RT} is derived simultaneously from the traps responsible for TL Peak 1 and TL Peak 2 and, as suggested above, TL Peak 2 fades predominantly according to an athermal mechanism.

Thermal release of trapped charges at RT is the most likely cause of the fast reduction in intensity of OSL occurring within short period following irradiation. Once the influence of thermal fading is complete, the remaining OSL decreases according to a different mechanism. Quantum mechanical tunnelling could be responsible for the long-term fading process of OSL

and the linear relationship between the normalised remaining intensity and the logarithm of time provides some evidence for this.

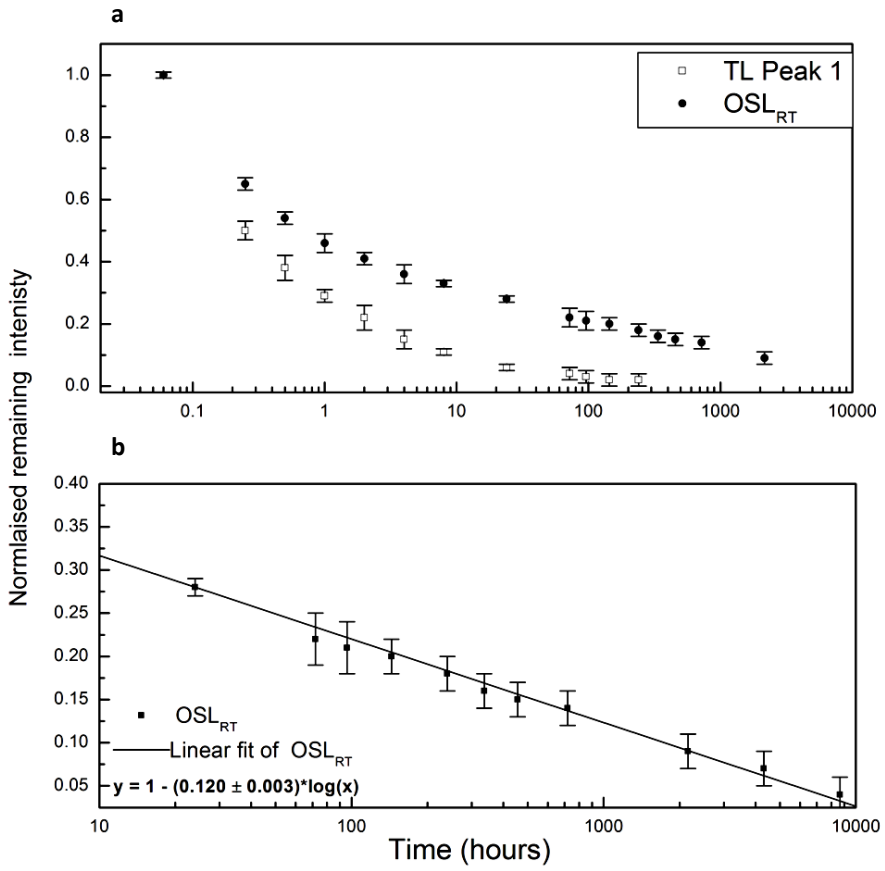

Figure 10.4: (a) Comparison of fading curves between OSL_{RT} and TL Peak 1. (b) Part of the fading rate curve of OSL_{RT} extending from 4 h to 1 year showing the logarithmic dependence on time. Each data point corresponds to the average value of the normalised remaining OSL of all samples. The dose to the samples was 3 Gy.

The results presented above were obtained while the samples were maintained at RT during optical stimulation. Nevertheless, it is common to perform OSL measurements at elevated sample temperature, since as demonstrated in Section 8.10, the effect of charge trapping into shallow traps can be prevented and a thermally-assisted enhancement of the OSL is observed. Changing the temperature of the sample during optical stimulation may, however, affect the rate of fading. To test this effect and to determine the appropriate corrections factors, the fading rate of non-preheated samples was measured for various readout temperatures between RT and 150

°C. The results of these measurements are shown in Figure 10.5. The OSL fading rate curve measured at a sample temperature of 50 °C presents features similar to those measured at RT. The rate of fading of the slow component – expressed by the constant *b* – is approximately the same in both cases. The sets of data obtained while the samples were stimulated at a sample temperature of 100 and 150 °C exhibit a single fading component showing logarithmic dependence on the time. The rate of fading of the samples stimulated at 150 °C (b = 0.059 ± 0.001) is ca 20 % lower than that at 100 °C (b = 0.075 ± 0.002).

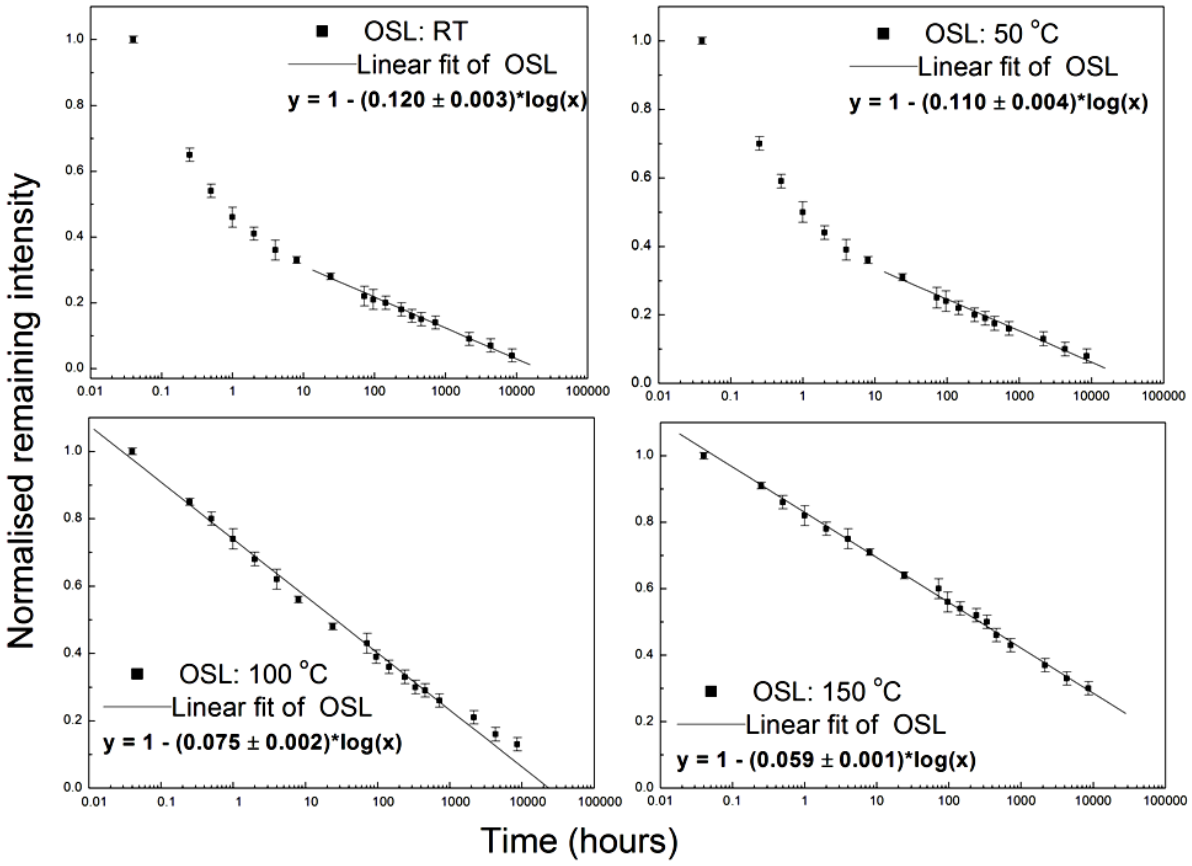

Figure 10.5: Fading curves of OSL at several sample temperatures produced after irradiation with 3 Gy. The set of data obtained at RT and 50 ° C sample temperature present a fast fading component from $t=t_o$ to $t \approx 4$ h and a slow fading component extending from $t \approx 4$ h to $t \approx 1$ year. The slow fading components were fitted with equation $y = 1 - b * \log(x)$ characteristic of the quantum mechanical tunnelling fading mechanism. The two sets of data obtained at 100 and 150 ° C sample temperature show a single fading component following a logarithmic dependence with time.

The main problem associated with OSL measurements carried out at elevated sample temperatures between RT and ca 100 °C is the lack of an appropriate function describing the relationship between the remaining OSL and the time which could be used as a means to correct for the loss of luminescence. The data from $t=t_o$ ($t_o \approx$1-3 minutes) to $t \approx 4$ h display a non-linear behaviour with time potentially because they contain a significant contribution from the thermally unstable OSL component. This component is expected to be absent from the delayed OSL following a radiological accident exposure, but it is expected to contribute to the OSL measured promptly (due to regenerative doses) during the application of the SAR procedure. As a consequence, if this component is not eliminated from the prompt measurements the calculation of accident doses will be highly inaccurate.

One way to remove the thermally unstable OSL is to modify the SAR protocol such as between the administration of each regenerative dose and the readout process a delay period of ~ 4 h is introduced. However, this method would significantly extend the total measurement time and would be impractical, for example, in emergency cases where a large number of samples has to be analysed. Alternatively, the OSL measurements can be carried out at elevated sample temperature (i.e., $T > 100$ °C), since, as the sample is heated to the specified temperature before the beginning of optical stimulation, the charges trapped in shallow traps are thermally removed and do not contribute to the total OSL. This effect is similar to applying a preheat step immediately after irradiation.

By increasing the temperature of the sample from 100 to 150 °C the apparent rate of fading was seen to decrease by ca 20 %. Additional measurements (results not shown) carried out at even higher temperatures (e.g., 200 and 250 °C) showed that the fading rate can be further reduced, but the effects of thermal quenching and thermal depletion caused considerable reduction in both the delayed and the prompt OSL measurements.

One possible explanation for the reduction in fading rate with increasing stimulation temperature is that during the period between irradiation and measurement, charges not lost, for instance, by radiative or non-radiative recombination processes are transported to deeper, more stable trapping levels that can be accessed by higher temperature stimulation (i.e., thermally assisted detrapping). The existence of thermal assistance can be verified by comparing the normalised to RT $OSL_{50^oC,}$ OSL_{100^oC}, and OSL_{150^oC} measured promptly and following a delay between

irradiation and readout. In other words, if thermal assistance is responsible for the reduction in the rate of fading the thermal quenching properties (i.e., luminescence efficiency as a function of T_s) of the prompt and the delayed OSL are likely to differ and this involves the presence of deeper traps. Table 10.1 gives the values of the ratio OSL_{RT}/OSL_{Ts} when there is no delay (i.e., $t=t_o$) and after the samples have been stored for t = 5 days before measurement. The effects of thermal quenching are not the same for both OSL signals measured at the same temperature, and in the second case, following a delay, competition with a different process appears to stimulate a greater population of charges resulting in higher luminescence efficiency. This is more evident at temperatures above 50 °C where, for example, the prompt $OSL_{100°C}$ is 45 % of the prompt OSL_{RT}, whereas the delayed $OSL_{100°C}$ is 81% of that measured at RT.

Table 10.1: Thermal quenching characteristics of prompt and delayed (t =5 days) OSL.

Sample temperature, T_s (°C)	**OSL_{RT}/OSL_{Ts} (prompt)**	**OSL_{RT}/OSL_{Ts} (delayed)**
RT	1.00	1.00
50	0.91	1.00
100	0.45	0.81
150	0.30	0.50

10.4.2 Fading of OSL with preheat

The fading of OSL following a preheat to 120 °C (10 s hold) for sample measurement temperatures ranging from RT to 150 °C is presented in Figure 10.6. As expected, the component of fading associated with thermal escape of charges from shallow traps is absent from all sets of data while the production of OSL seems to be thermally assisted; consistent with the results presented earlier for the non-preheated samples.

The equation describing the quantum mechanical tunnelling model was successfully fitted to the data points from $t = t_o$ ($t_o \approx$ 1-3 minutes) to $t \approx$ 3 months. The divergence in the fitted data observed for $t >$ 3 months, in accordance with the results of the TL in Figure 10.3, likely

indicates the presence of a different fading component with lower rate of loss. Comparison of the slopes (i.e., constant *b*) of the linear fits clearly indicates that the rate of fading decreases with increasing readout temperature. Though, this decrease becomes significant only at $T > 100$ °C. In particular, the rate of fading at 50 °C and 100 °C is, respectively, 3 and 5 % lower than that at RT but decreases by ca 23 % when the temperature of the sample during stimulation is 150 °C.

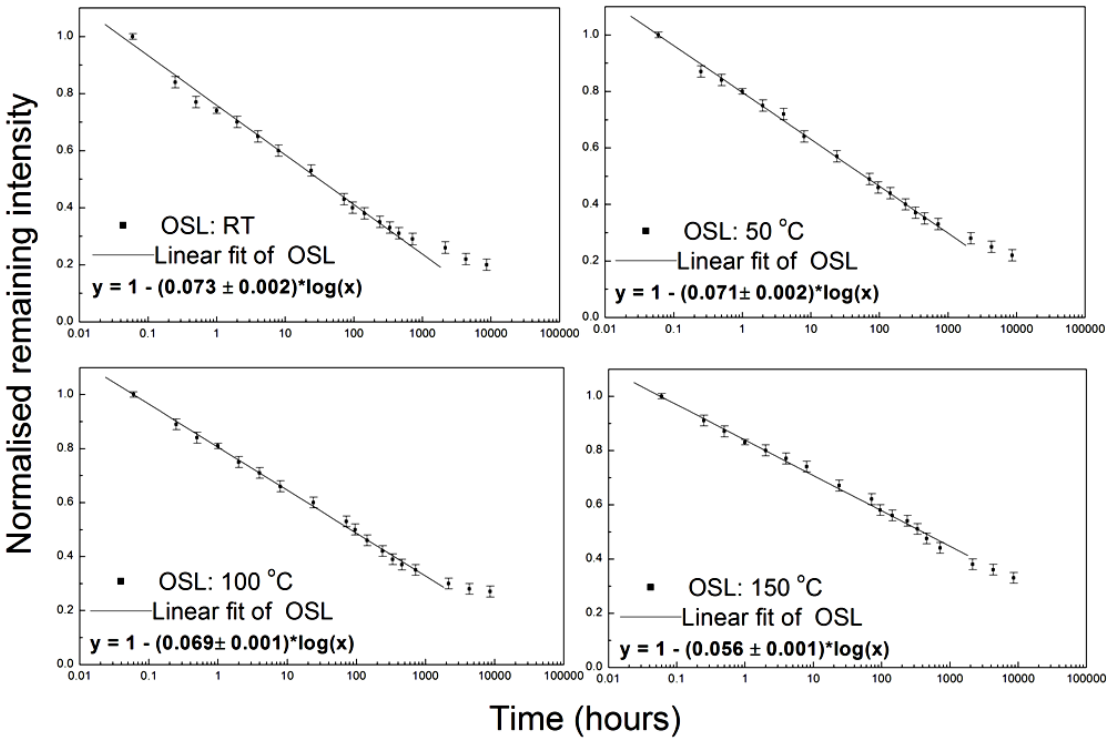

Figure 10.6: Comparison of fading curves of OSL at several sample measurement temperatures following irradiation with 3 Gy and preheat to 120 °C (10 s). The data points from $t = t_o$ ($t_o \approx$ 1-3 minutes) to $t \approx 3$ months were fitted with the equation describing the quantum mechanical tunnelling fading mechanism. Note that the rate of fading expressed by the constant *b* decreases with increasing sample temperature.

10.5 Comparison of fading behaviour of TL and OSL signals

Having assumed that the main dosimetry signal – which for TL is the ~ 200 °C peak and for OSL is the emission following preheat to 120 °C – fades according to a quantum mechanical tunnelling mechanism, the fading characteristics of TL and OSL can be directly compared. The

most common way to express the anomalous fading of luminescence is the use of the quantity g defining the percentage fading rate per decade of time (Aitken, 1985). For a tunnelling model g can be obtained from the slope of the plot of the remaining luminescence intensity vs the logarithm of the time elapsed since irradiation through the expression $g = 230.2 * slope$. The values of g of the TL and OSL are summarised in Tables 10.2 and 10.3. The difference in the values of g between the TL Peak 2 (150–290 °C) and the OSL data is within 15 % indicating that common traps are involved in the production of luminescence under thermal or optical stimulation. In particular, the fading rate of OSL measured at 100 °C following a preheat to 120 °C is in excellent agreement with the fading rate of TL over 150–220 °C, while when the sample temperature increases to 150 °C, the rate of fading becomes closer to that of TL over the second half of the peak. As explained earlier, the higher sample temperature temperature is able to stimulate the population of traps showing a lower rate of fading.

Finally, the fading rates of $OSL_{100°C}$ and $OSL_{150°C}$ measured without preheating the samples differ by less than 10 % from those measured after the application of 120 °C preheat indicating that a preheat could be omitted. However, a potential problem associated with elevated sample temperature measurements is phosphorescence emission which has to measured separately and subtracted from bothe the prompt and the delayed measurements.

Table 10.2: TL fading.
Fading rate in percentage per decade of TL Peak 2.

Peak range (°C)	g (%/decade): TL
150-290	14.2±0.2
150-220	15.9±0.2
220-290	12.4±0.2

Table 10.3: OSL fading.
Fading rate in percentage per decade of OSL.

Sample temperature (°C)	g (%/decade): OSL without preheat	g (%/decade): OSL with preheat
RT	-	16.8±0.5
50	-	16.3±0.5
100	17.3±0.2	15.9±0.2
150	13.6±0.2	12.9±0.2

10.6 Fading of TL and OSL at elevated storage temperature

The evaluation of fading at elevated storage temperature can provide information to identifying the physical mechanism of the luminescence instability. For example, according to a ´classical´ tunnelling model the rate of fading of luminescence is temperature independent and fading cannot be altered by thermal treatment. In contrast, in the localised transition model and the thermally assisted tunnelling model the rate of fading can be thermally accelerated. The localised transition model also predicts a stable remnant luminescence level by an appropriate thermal treatment.

The effect of elevated storage temperature on the rate of fading of TL and OSL was assessed using a subset of the samples used in the previous measurements. The samples following irradiation with 3 Gy and preheat to 120 °C (10 s hold) were placed inside aluminium containers and left for durations between 0.5 and 48 hours in a Sanyo Gallenkamp OMT oven at various controlled temperatures T between 18 and 90 °C before measurement.

Figure 10.7 shows an example of the ratio of TL measured 1 day following beta irradiation to the TL measured promptly (i.e., $t_o \approx$ 1-3 minutes) following irradiation as a function of the glow curve temperature for storage temperatures of to 18 ± 2 (RT), 30 ± 2, 60 ± 2, and 90 ± 2 °C. As indicated in the figure, the temperature at which the sample is held during storage enhances the fading of TL especially that associated with the lower temperature side of the peak.

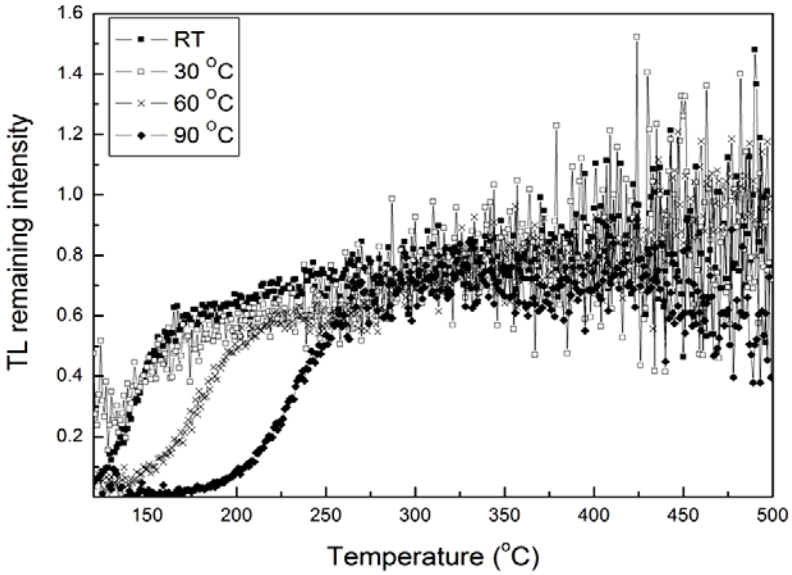

Figure 10.7: Ratio of TL measured 1 day following irradiation to the prompt TL (t ~ 3 minutes) as a function of the glow curve temperature for storage temperatures of RT, 30, 60, and 90 °C.

The enhancement of fading of TL Peak 2 (150-290 °C) with increasing storage temperature can also be observed in Figure 10.8 by the progressive increase in the value of g. The normalised to the prompt TL measurement remaining intensity is plotted as a function of the logarithm of time after irradiation. As earlier (Figure 10.6), a logarithmic function was fitted to all data sets and the g values were obtained. Similar plots (not shown) were produced for OSL measured at 100 °C sample temperature.

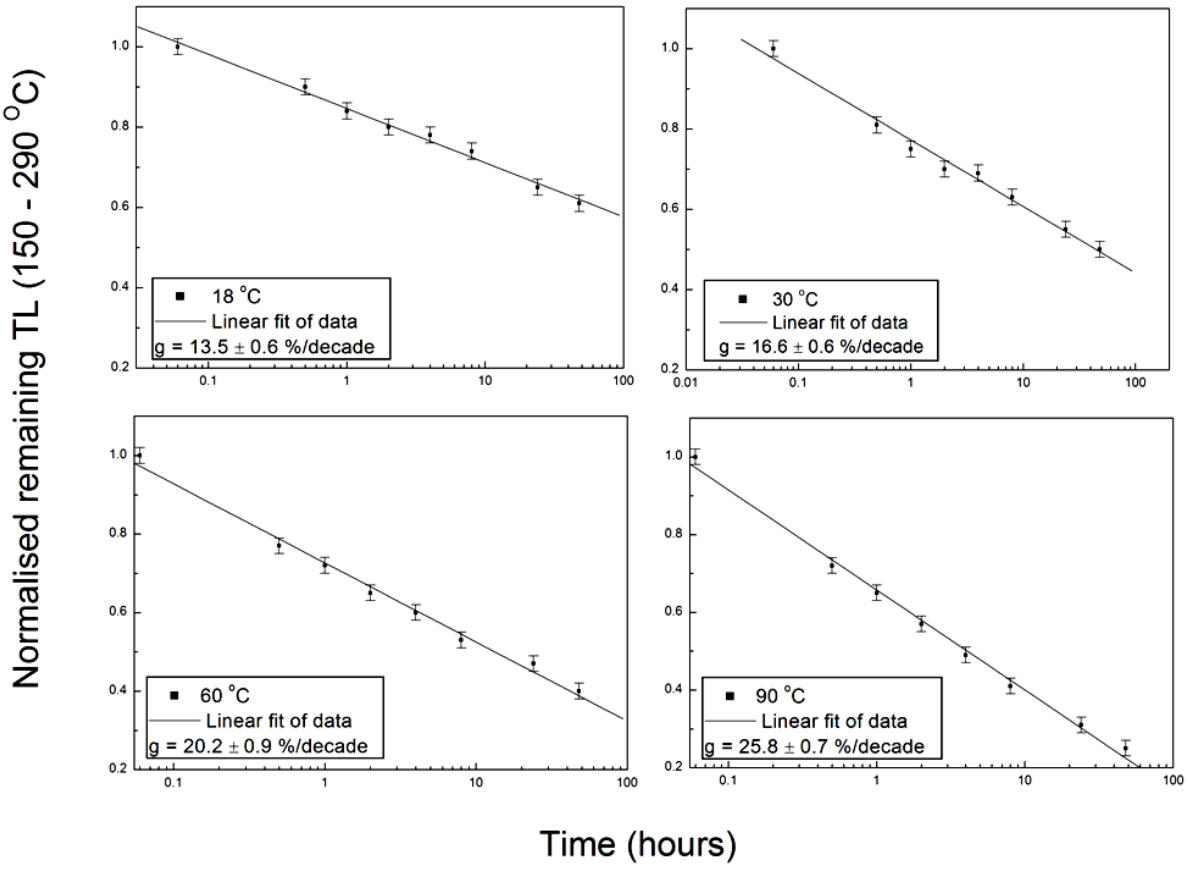

Figure 10.8: Comparison of fading rate curves of TL at several sample storage temperatures (18, 30, 60, and 90 °C) following irradiation with 3 Gy and preheat to 120 °C (10 s). All data sets were fitted with the equation describing the quantum mechanical tunnelling fading mechanism. Note that *g* increases with increasing sample temperature.

The temperature dependence of *g* for both TL and OSL is presented in Figure 10.9a as a function of storage temperature T (°C). Supposing that fading is a thermally activated process it might be possible to obtain the thermal activation energy by plotting the data using an Arhenius plot, as shown in Figure 10.9b. As far as a plot of ln(g) vs 1/T results in a straight line, the thermal activation energy of the given process can be found by multiplying the slope of the straight line with the Boltzmann factor (i.e., $k = 8.617 \times 10^{-5}$ eV K^{-1}).

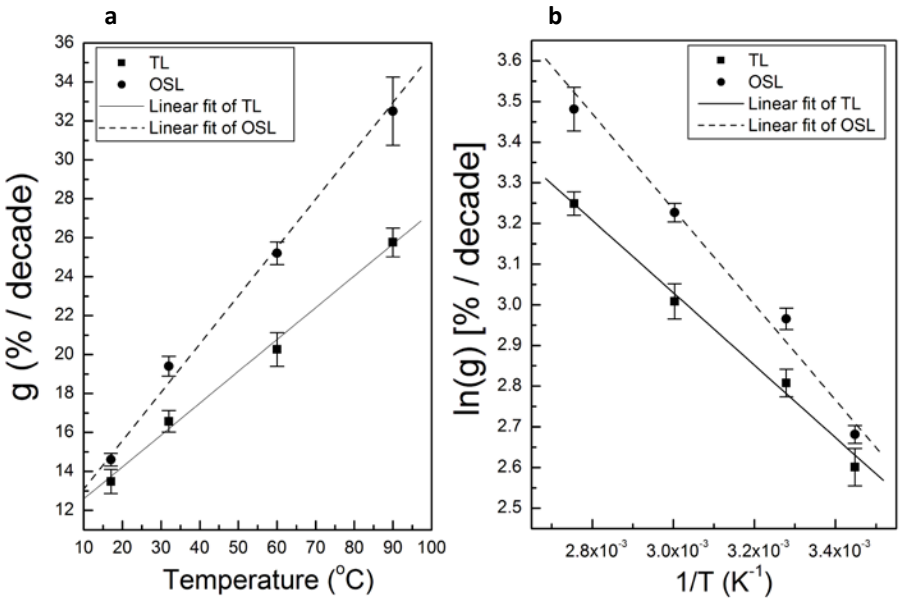

Figure 10.9: (a) Temperature dependence of g (%/decade) of TL and OSL. (b) Arrhenius plots of the data in (a). The slope of the linear curve of each dataset corresponds to the thermal activation energy of fading.

As indicated in Figure 10.9a, in both cases, *g*, increases linearly with temperature. The effect of storage temperature on *g* is stronger for OSL compared with that obtained for the TL glow peak (150-290 °C). Such observation was expected given that, as demonstrated in Section 8.12, the OSL response is mostly correlated with the initial temperature part of TL Peak 2 (150-220 °C) which shows slightly larger *g* values (Table 10.2). Also, Figure 10.9b indicates that anomalous fading is a thermally assisted process with average (for TL and OSL) thermal activation energy of 0.085 ± 0.007 eV. The value of the activation energy for thermal assistance correlates well with some of the energies of the vibrational modes (e.g., ~ 0.078, ~ 0.092, and ~ 0.112 eV) calculated from the FTIR measurements (Chapter 6) providing additional support for a thermally-assisted fading mechanism.

10.7 Fading of TL and OSL for samples stored in a magnetic field

In the presence of a strong magnetic field (i.e., several tesla, *T*) the wavefunctions of two interacting states (e.g., trap-recombination centre) may be shrinked (shrinkage effect) leading to

less strong interactions (Filin *et al*., 1995). Concerning the quantum mechanical tunnelling mechanism of fading which is based on the tunnelling of trapped charges from the traps to nearby recombination centres due to overlap of wavefunctions of the electrons in the traps and the holes in the recombination centres, it would be expected the shrinkage effect to cause a reduction in the tunnelling probability and, hence, in the rate of loss of luminescence signals.

This shrinkage effect was shortly investigated by measuring the fading of TL and OSL signals for delay periods of 1 and 2 days for samples (n = 5) held in a magnetic field of 4 T at RT. The loss of both luminescence signals for these samples was found to be statistically similar to the average fading calculated in the previous sections for TL and OSL, suggesting that, under the particular experimental conditions employed, a shrinkage effect likely does not take place.

10.8 The mechanism and origin of anomalous fading of luminescence in alumina substrates

10.8.1 The mechanism of anomalous fading at RT

The preliminary work of Inrig (2009) on the stability of luminescence of SMRs had attributed the anomalous fading effect to a quantum mechanical tunnelling mechanism, possibly because the intensity of the remaining luminescence *I* was related to time *t* by a hyperbolic law (i.e., $I \propto t^{-1}$). However, it could be argued that these early conclusions were speculative because other factors affecting fading, such as the storage temperature, were not investigated. The objectives of the experiments presented in the previous sections were, first, to monitor the fading over laboratory timescales using various measurement protocols to determine the appropriate correction functions and, second, to test the validity and accuracy of a tunnelling model. Having already established a relationship between TL and OSL in SMRs, it was realised that the results following TL fading tests would be more helpful to explore how well the various types of charge escape mechanisms can account for the fading behaviour observed in the alumina substrates.

Direct tunnelling from the trap to the recombination centre

To begin with, the results of the TL and OSL fading tests carried out while the samples were stored at RT could be interpreted in terms of a quantum mechanical tunnelling model. The logarithmic dependence of signal loss on the elapsed time since irradiation and the rapid fading rate observed at short times followed by a slower rate at longer delay times are all in accordance with a quantum mechanical tunnelling model. In this case, electrons in the ground state of the traps tunnel through a potential barrier to the excited state of a recombination centre located at a distance r away and recombine radiatively (phosphorescence emission is expected) or non-radiatively. Assuming that the trapping levels are in close proximity to recombination centres, significant overlap of the wavefunctions of the initial (trap) and final (recombination centre) electronic states make the direct tunnelling transition probable.

However, the hypothesis of the classical tunnelling mechanism seems to fail when (1) the fading behaviour of TL Peak 2 is analysed over different temperature intervals, and (2) the relationship between the remaining luminescence intensity and the logarithm of time is examined for prolonged duration of storage. Specifically, the higher rate of fading obtained for the rising part (i.e., 150–220 °C) of TL Peak 2 cannot be accounted for by the quantum mechanical tunnelling model which predicts that fading will be more rapid for the high temperature side of a peak where deeper trapping levels are assumed to exist. This is a consequence of the exponential dependence of the rate of tunnelling on the trap depth (see Equation 2.28 and Chen and McKeever, 1997). Also, the presence of a very slow fading component for $t > 3$ months could be indicative of the attainment of a stable remnant luminescence level which is not in accordance with this model. Of course, the first observation could be the result of thermal fading of charges in some comparable shallow energy levels (yet, the conclusions of the evaluation of kinetic parameters indicated that all traps between 150 and 290 °C are sufficiently deep to fade thermally) and the second observation may ensue from the fact that the fading at prolonged storage periods is quite small resulting in a false plateau region.

A third indication that a quantum mechanical tunnelling mechanism may not be the dominant mechanism for the fading of luminescence at RT could be taken from the fading tests performed with samples stored in a magnetic field, where the shrinkage effect on the wavefunction of the

charged carriers would likely cause lower rate of loss. However, as discussed in section 10.7, the fading of TL and OSL is the same at RT independent of the presence of a magnetic field.

Localised transition from the trap to the excited state of recombination centre

On the other hand, the above characteristics could be interpreted using the alternative localised transition model of anomalous fading whereupon the loss of trapped charge population proceeds via the excited state of the trap shared with the recombination centre (Templer, 1986). The transition from the ground to the excited state of the trap is likely to be mediated by some thermal energy provided by the vibrational modes of the lattice (i.e., phonons). Following Templer's argument (for zircon) that there exists a distribution of trap depths from E_{min} to E_{max} the low temperature side of a TL peak could be expected to fade faster since it is this part which is associated with the shallow traps (i.e., E_{min}). In addition, a localised transition model predicts the existence of a fading component following a t^{-1} dependence and the presence of a non-fading component. Yet, this stable luminescence component may not be observed over the laboratory timescale fading monitored in these experiments.

10.8.2 The behaviour of anomalous fading at elevated storage temperature

Given the above discussion, it may not be easy to determine the exact mechanism of fading since both the classical quantum mechanical tunnelling and the localised transition model could reasonably explain the experimental findings. Nevertheless, measurements of fading at elevated storage temperature indicated the presence of an acceleration of the rate of fading which immediately makes a purely quantum mechanical tunnelling model less applicable since the rate of tunnelling is expected to be temperature independent. The contribution of thermal assistance to the increased rate of fading also seems less likely since, although this scenario could potentially explain the higher rate of fading of the low temperature half of TL Peak 2, the fading rate of the high temperature side of the peak would be expected to remain relatively unaffected and as shown above, even at 30 °C the loss of luminescence from the second half of TL Peak 2 is ~ 20 % higher than that at RT.

While, in contrast, a localised model and a modified thermally-assisted tunnelling model of anomalous fading predict a dependence of the fading rate on the storage temperature, the thermal dependence of the fading process requires a fundamentally different interpretation of the transport of charges carriers.

In a localised transition model the probability, p, of trap emptying is related to the temperature by an Ahrhenius relationship of the form $p \sim exp(-E/k_{\beta}T)$, where in this case E denotes, not the trap depth, but the energy separation between the ground and the excited state of the trap. By raising the temperature of the samples during storage, the probability of escape increases resulting in a faster rate of fading.

In a thermally-assisted tunnelling model the probability of direct transition from the trap to the recombination centre depends primarily on the separation distance r (i.e., width of the potential barrier) and the frequency factor a (see Equation 2.28) which describes the extent to which the wavefunctions overlap (Hurd, 1985). Neither of these parameters includes a temperature factor to account for the thermal dependence of the rate of fading. However, Visocekas *et al*., (1976) suggested that if there is an intermediate state within the potential barrier the probability of tunnelling recombination increases since the width of the barrier decreases. In this two-step tunnelling process thermal activation is expected only to occur for those charges transferred from the ground state of the traps to the energy level located within the potential well. The final stage where pure tunnelling takes place is temperature independent.

Alternative charge transport processes

The temperature dependence of tunnelling has also been treated by Hurd (1985) who considered two different cases. The concepts provided by Hurd were developed to explain the electronic transport – and related phenomena, such as the conductivity – in semiconductors, but similar considerations can be applied to elucidate the behaviour of other processes associated with the movement of electrons in insulators. Hopping over the potential barrier separating two sites (e.g., trap and recombination centre) is one way by which transport can take place and is thermally activated according to an Arrhenius law. The activation energy of the transport of particles due to hopping can be found by plotting the natural logarithm of the rate of transport as a function of

the inverse temperature. This relationship is expected to be linear and the slope of the *ln(transport rate)* vs T^{-1} will be equivalent to the activation energy.

If tunnelling proceeds through the potential barrier the temperature dependence is introduced assuming that the overlap of the wavefunctions in the two sites increases with temperature due to thermal oscillations of the barrier width. This case looks similar to the thermally-assisted model suggested by Visocekas *et al*., (1976), although it differs in two points. First, instead of assuming the presence of an intermediate energy level within the barrier, the model makes use of the so-called coincidence event (Emin, 1975) in which the electronic energy of a charge carrier in one site (i.e., trap) becomes equal to that if it were located in the neighbouring site to which it tunnels (i.e., recombination centre). The coincidence of the two sites is a thermally dependent process since as the instantaneous position of a charge carrier in a site (e.g., trap) changes constantly with temperature – because the position of the atoms changes due to the vibrational modes of the lattice which increases with temperature – the electronic energy also changes. This effect introduces a thermal dependence in the overall transport process [i.e., $\sim exp(-U/k_{\beta}T)$ with U being the activation energy for displacement], yet the tunnelling probability through the barrier is again temperature independent. In addition, Hurd (1985) states that when coincidence is satisfied (i.e., when direct tunnelling is allowed) and under conditions of a strongly vibrating potential barrier (i.e, *vibrating barrier model*) the overall tunnelling probability can also be temperature dependent. This, however, appears to be a complicated case controlled by several factors. In addition, a number of assumptions need to be introduced and the effect under investigation (e.g., anomalous fading) should be examined over a wide temperature range to investigate the temperature dependence of the tunnelling probability. It is characteristic of this model that at high enough temperatures it eventually reduces to the hopping model.

10.8.3 Temperature dependence of fading rate

When trying to distinguish, for example, between the quantum mechanical tunnelling and the localised transition model based exclusively on the assumption that the former is temperature independent while the latter is not, the conclusions can be ill founded. Rather, the temperature of the sample determines which process should dominate the fading of luminescence. For instance,

if fading measurements were to be made at temperatures close to absolute zero, then, the most likely mechanism is that of a quantum mechanical tunnelling through the potential barrier since all thermal mechanisms will be suppressed due to the absence of thermal energy (e.g., phonons). Some preliminary fading tests (results are not shown) performed for a delay period of 1 day with samples stored at ~ -263 °C (~ 10 K) showed that the amount of TL/OSL signal loss is not significant different (i.e., ~ 10 % lower) from that measured for samples stored at RT, indicating that the fading process in the temperature range from ~ -263 °C to RT is likely temperature independent supporting a classical quantum mechanical mechanism. At RT knowledge of the energy separation between the ground state and the excited state of the trap for the localised model or the height of the barrier for the hopping model is required to decide whether these processes can occur. At even higher temperatures it would be reasonable to assume that thermally-activated processes are dominant over tunnelling, although both may be active at the same time.

A possible answer to differentiating between all these transport mechanisms lie in examining the dependence of the fading rate on temperature. Assuming that the rate of fading is proportional to the rate of transfer of captured carriers from one site to the other, the rate of fading will be linearly dependent on the temperature or $ln(\text{fading rate}) \propto T^{-1}$ (Hurd, 1985; Wheeler, 1990) for the localised model and the hopping (over the potential barrier) model. In the vibrating barrier model the relationship becomes $ln(\text{fading rate}) \propto T$ and, as proposed by Hurd (1985), this relationship is more appropriate to describe the behaviour where the Arrhenius plots show significant curvature. As shown in Figure 10.9, the rate of fading of both TL and OSL increases linearly with the temperature [or $ln(\text{fading rate}) \propto T^{-1}$] of the samples during storage and hence it is likely that the mechanism of the anomalous fading of luminescence in SMRs above RT is thermally activated.

10.8.4 The origin of anomalous fading

Polycrystalline alumina can be considered a disordered material, presenting a random distribution of grains, grain boundaries, pores, and impurities where together generate a complex and massive network of defects and, possibly, an equivalent concentration of localised states

(e.g., traps and recombination centres) creating additional pathways for the movement of captured charge carriers. Arguments that anomalous fading in feldspar, is correlated with the state of structural disorder have also been proposed (Hasan *et al*., 1986; Huntley and Lian, 2003; Sears *et al*., 1990). Furthermore, Sears *et al*., (1990) demonstrated that anomalous fading reduces in samples by annealing at high temperatures (i.e., 1000 °C) to lower the degree of disorder In a few instances (Huntley and Lian, 2006; Spooner, 1993) the influence of elemental composition of feldspars on fading was also examined. Except for plagioclase feldspar where a positive correlation between calcium content and fading rate was identified, a clear trend between specific element and fading could not be found.

If anomalous fading is associated with the escape of electrons from traps, then, it could be argued that in a disordered material there can be strong interaction between the trapped charges facilitating the detrapping process (Bonnelle, 2010). In addition, given that there is strong indication (i.e., large width of emission bands seen in CL and RL results) that in SMRs the electron-lattice interaction is strong, multiphonon electronic transitions can occur enhancing the movement of electrons (Bonnelle, 2010). In short, in a material with a high density of defects and strong electron-phonon coupling the possibility, even at RT, that electrons move from one site to the other (i.e., tunnelling model) or make phonon-assisted transitions from the ground to excited state of the trap (i.e., localised transition) is highly probable, and so is fading.

Chapter 11: Dosimetry with alumina SMRs

11.1 Introduction

The basic dosimetry characteristics (e.g. TL/OSL response, minimum detectable dose, fading) of alumina SMRs were investigated by several research groups (e.g., Beerten *et al*., 2009, 2010; Ekendahl and Judas, 2011; Inrig, 2009; Pascu *et al*., 2013) while, in a few instances (Beerten and Vanhavere, 2010; Ekendahl and Judas, 2011) the photon energy dependence of alumina substrates was also reported. In a more recent interlaboratory study (Bassinet *et al*., 2014) the sample preparation methodology (e.g., procedure of extracting SMRs from mobile phones) and the analytical measurement OSL protocols were validated in a series of blind tests where the participating laboratories had no prior knowledge of the administered dose.

However, there are still a number of issues to be considered to establish the complete deployment of SMRs for emergency dosimetry. For instance, there is the possibility that significant discrepancies in the evaluation of the unknown doses may arise if the nature (e.g., acute or protracted) and the energy distribution of the accidental exposure is not known. An irradiation which is protracted, rather than acute, would require a consideration of fading likely to have occurred during the exposure. Furthermore, due to the lack of tissue equivalence of the alumina, the doses would significantly be overestimated if the radiation field is composed entirely of low energy photons (i.e., < 100 keV). Other potential sources of uncertainty, not considered in the existing radiological trials are associated with the orientation of the mobile phone relative to the direction of the irradiation and the perturbation of the radiation field by the phone's insides, casing and surroundings.

The location and orientation of the phone relative to its owner's body, the extended nature of the body with its various internal organs positioned at different distances from both the source and the phone, and the potentially time-dependent orientation of the body relative to the radiation source, could all lead to significant differences between the dose deposited in an alumina SMR within a phone and that deposited in a given organ.

To validate a personal accident dosimetry system a comparison of organ or whole body doses and the doses measured by the dosimetry materials for a number of exposure scenarios has to be performed. Experimentally, this can be accomplished using realistic anthropomorphic phantoms (e.g., Rando-Alderson phantom) or slab phantoms made of materials that simulate the absorption and scattering properties of human tissue. Usually, the dose deposited at the location of interest (e.g., organs, skin) is estimated using physical dosemeters with well-established dosimetry properties, such as thermoluminescence detectors (TLDs), and compared with the dose estimates obtained using the objects under investigation placed in equivalent positions. To avoid these time-consuming and practically complicated procedures the use of mathematical models of the human body (i.e., voxel phantoms) together with computer codes simulating the transport and energy deposition processes of radiation in the human body (e.g., Monte Carlo methods) are used and compared with the results of experimental measurements to validate the results. For instance, Zankl (1999) investigated theoretically the doses received by TLDs positioned at a variety of locations around the body, and considered how their responses compare with organ doses, Hervé *et al*., (2007) examined the relationship between organ and whole body doses and the doses measured by two materials (i.e., dental enamel and sugar) suggested for retrospective dosimetry with electron spin resonance (ESR), while Takahashi *et al*., (2001, 2003) performed Monte Carlo calculations and experiments with a realistic head phantom to establish the relationship between teeth dose estimated by ESR and organ doses for external photon exposures. However, no group has yet considered the issues specifically relevant to accident dosimetry using mobile phones, or derived explicit calibration factors relating doses absorbed in resistors to the doses absorbed by the body.

In the first part of this chapter (11.2-11.6), basic properties (e.g., sensitivity, dose response, detection threshold, reproducibility) determining the suitability of the TL and OSL of alumina-based SMRs from mobile phones in accident/retrospective dosimetry will be examined. An evaluation of the photon energy response of the resistor components will also be presented in section 11.7 based on both experimental results and radiation transport simulations (i.e., MCNP). This is followed (section 11.9) by the presentation of the results of dose reconstruction procedures for mobile phones irradiated attached to an anthropomorphic phantom, as well as to a slab phantom, under different irradiation conditions (geometry of exposure and photon energy). Monte Carlo modelling of different exposure situations has been performed, considering various

photon exposures of mobile phones positioned off-phantom, on a slab phantom, and at different locations around a voxel phantom model of the International Commission on Radiological Protection (ICRP) reference male (ICRP, 2008). The dose per applied fluence in resistors within these phones were calculated, and compared against the concurrent doses per applied fluence in the various organs of the body. Some of the doses to the organs of the body are directly comparable to those in the ICRP reference values set (ICRP, 2010), providing important quality assurance of the calculation method. However, additional geometries are used that replicate accident/terrorist scenarios that could not be taken directly from the reference data. The following are discussed in section 11.10 First, a description of the phone model is given, with results then presented that consider the effects of its geometry on dosimetry, with particular foci on the positions of the resistors within the phone and whether the phone is exposed from the front or the back. Finally, the impact of the phone location is considered, with the implications of this for an emergency dosimetry service discussed.

11.2 Selection of SMRs from mobile phones

As mentioned in Chapter 5, the majority of TL and OSL dosimetry tests were performed using type ´0402´ SMRs. They are more easily identifiable among the variety of other electronic components (e.g., capacitors, resonators) included in PCB of mobile phones. This was especially the case under the dim red-light laboratory conditions employed during the entire procedure (extraction and measurement) to protect the samples from exposure to white-light and avoid possible light-induced signal loss. Unused SMRs of the same type were also used.

11.3 Luminescence variability and sensitivity

11.3.1 Measurement considerations

While the dosimetry properties of both TL and OSL of SMRs have been systematically examined, the TL technique has not yet been considered for dose assessments, arguably because the sensitivity (i.e., luminescence output per unit absorbed dose) of TL is lower than that of OSL.

In a recent inter-laboratory comparison study (Bassinet *et al*., 2014), the ability of SMRs (mainly of type ´0402´) extracted from ^{60}Co-irradiated mobile phones to reconstruct doses in three ranges (i.e., < 1 Gy, 1-2 Gy, and > 2 Gy) was evaluated between 13 laboratories using OSL procedures. Participants (included the Durham Laboratory) were instructed to use 10 resistors to reconstruct the unknown doses. Within experimental uncertainty, there was good agreement between estimated and nominal doses indicating, at least, that the sensitivity of the recommended number of resistors per sample would be adequate to allow small doses (e.g., < 1 Gy) to be detected.

While using only 10 resistors may have some practical advantages (e.g., less preparation time, possibility to use remaining SMRs for retrospective dose assessment) there can be an important reason for increasing the number of components per measurement. It could be argued, for instance, that the uncertainty in the estimation of dose can be decreased by increasing the number of resistors since the luminescence sensitivity is expected to be higher. Nevertheless, there exist other factors, such as the stimulation method employed (TL or OSL), the SAR dose protocol used and most importantly the fading correction factor applied, that can significantly impact the accurate evaluation of the accident dose.

This section is not intended to study specifically the sensitivity and variability of SMRs in view of the fact that this would be practically unfeasible given the great diversity of manufacturers. Instead, the TL and OSL sensitivity of SMRs will be compared for a limited number of components with the purpose of identifying the assets of each stimulation mode.

11.3.2 Experimental method and results

To cover the possibility of having to deal with both ´old´ and ´advanced´ technology mobile phones the TL and OSL sensitivity of type ´0402´ SMRs was investigated for a maximum number of 20 resistors per analysis (typical to be found in the majority of mobile phones). Components extracted from seven mobile phones, as well as unused components, were divided into two groups consisting of 10 (Group 1) and 20 (Group 2) SMRs. The luminescence sensitivity of each group was measured for three levels of dose (i.e., 0.5, 2, and 5 Gy) using the sequences shown in Table 11.1. The reason for applying the 120 ° C preheat treatment (Step 2) was to remove the contribution of the thermally unstable signal associated with traps between 50 and 150 ° C (see Chapter 7; section 7.2). Furthermore, a final annealing step (Step 4) was applied at the end of each cycle to remove any remaining TL, OSL or photo-transferred OSL signal from Step 3.

Table 11.5: TL and OSL sequences for investigating the luminescence sensitivity of SMRs.

Step 1	Step 2	Step 3	Step 4
Beta dose: 0.5, 2, 5 Gy	Preheat: 120 °C, 10 s (5 ° C s^{-1})	TL: RT-500 ° C (5 ° C s^{-1})	Annealing to 500 ° C (5 ° C s^{-1})
Beta dose: 0.5, 2, 5 Gy	Preheat: 120 °C, 10 s (5 ° C s^{-1})	BOSL: 100 ° C, 60 s, 0.3 s /data point	Annealing to 500 ° C (5 ° C s^{-1})

Selected examples of the TL glow curves and OSL decay curves of each group are presented in Figure 11.1a-c and Figure 11.2a-c. The average, over multiple measurements, background signals estimated using the sequences in Table 11.1 without Step 1 (i.e., TL, OSL signal from unirradiated sample holders without resistors) are also shown. The TL glow curves measured after irradiation with 0.5 Gy present significant statistical noise. Nevertheless, the statistical fluctuation in the detected counts is seen to improve with increasing sample size and dose level.

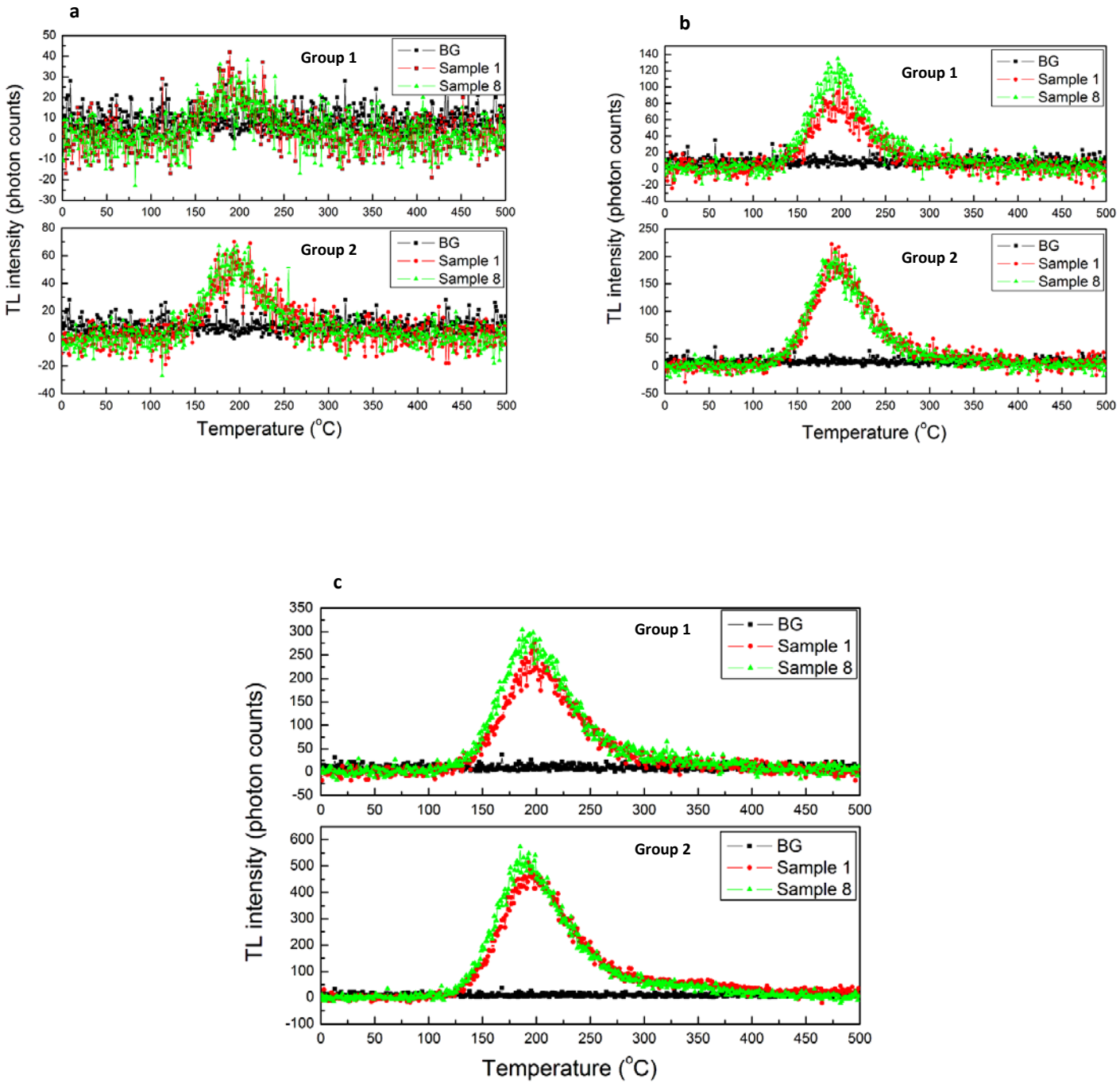

Figure 11.1: Comparison of the TL glow curves of two samples from Group 1 (*Sample 1*: 10 resistors from mobile phone, *Sample 8*: 10 unused resistors) and two samples from Group 2 (*Sample 1*: 20 resistors from mobile phone, *Sample 8*: 20 unused resistors) measured after (a) 0.5 Gy, (b) 2 Gy, and (c) 5 Gy. The TL was detected in the UV using a Hoya U340 filter (7.5 mm).

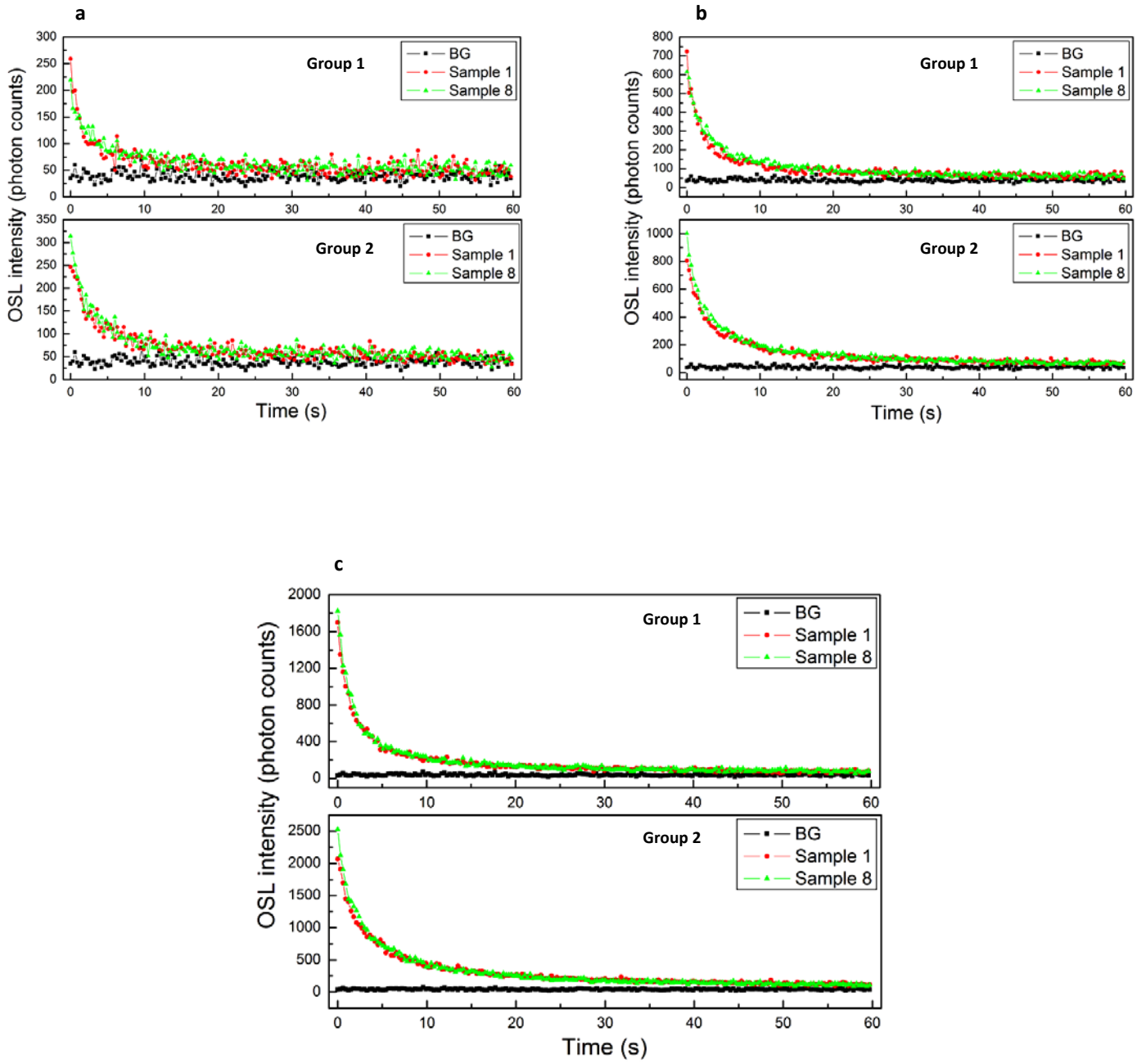

Figure 11.2: Comparison of the OSL glow curves of two samples from Group 1 (*Sample 1*: 10 resistors from mobile phone, *Sample 8*: 10 unused resistors) and two samples from Group 2 (*Sample 1*: 20 resistors from mobile phone, *Sample 8*: 20 unused resistors) measured after (a) 0.5 Gy, (b) 2 Gy, and (c) 5 Gy. The OSL was detected in the UV with a Hoya U340 filter (7.5 mm).

The luminescence sensitivities of the samples – calculated as the BG-corrected[1] integrated luminescence signal (photon counts) per unit dose – as well as the TL/BG and OSL/BG ratios are given in Tables 11.2-4. TL was integrated over the range 150-290 °C, but since OSL dosimetry can be carried out using any part of the decay curve, OSL was integrated over different time intervals (i.e., 0-10 s, 0-20 s, 0-30 s, and 0-60 s) to examine any possible sensitivity variation.

The luminescence sensitivity of both groups is substantially better for the OSL_{60s} signals. Specifically, the samples of Group 1 show initially a difference in sensitivity between $TL_{150\text{-}290^{o}C}$ and OSL_{60s} of ~ 60 % at 0.5 Gy, but as the dose increases this difference drops to 47 and 43 % at 2 and 5 Gy, respectively. This is because, as the dose to the samples increases, the signal to BG ratio increases too. Yet, the increase of $TL_{150\text{-}290^{o}C}$/BG (i.e., 0.5 Gy: 2.6, 2 Gy: 6.4, 5 Gy: 13.7) is more notably than that of OSL_{60s} /BG (i.e., 0.5 Gy: 1.6, 2 Gy: 2.7, 5 Gy: 4.9) which is believed to be responsible for the reduction in the difference of the sensitivity between $TL_{150\text{-}290^{o}C}$ and OSL_{60s}. Another reason for the observed differences in the signal to BG ratio between TL and OSL could be attributed to the different BG levels associated with each stimulation method. In TL the BG signal includes mainly the dark counts of the PMT, while in OSL, despite the use of filters, a significant amount of scattered stimulation light can reach the detector and contribute to the BG signal.

For the samples of Group 2, which exhibit higher sensitivity than Group 1, the difference in sensitivity between OSL_{60s} and $TL_{150\text{-}290^{o}C}$ does not seem to depend much on the dose and it is stable around 30 %. The increased $TL_{150\text{-}290^{o}C}$ and OSL_{60s} sensitivities of Group 2, as well as, the absence of dose dependence of their difference are likely related to the fact that the samples of Group 2 consisting of a larger number of resistors result in a considerably improved signal to BG ratio. The latter is particularly evident for the TL signals which, although they still present a high degree of statistical noise, especially at low doses (< 2Gy), they are characterised by better-resolved glow curves (Figure 11.1a).

Finally, the difference in sensitivity between TL and OSL signals reduces as the OSL integration interval decreases and becomes comparable when the OSL intensity of the initial 10 s of the

[1] The BG-corrected TL and OSL signals were obtained by subtracting the TL and OSL signal of the unirradiated samples from those obtained following irradiation.

decay curves are used. Nevertheless, the OSL/BG significantly improves with decreasing integration interval.

Furthermore, as expected, the increase in sensitivity is nearly proportional to the increase in the number of resistors. Except for the OSL signals measured at 0.5 Gy where the increase in sensitivity between Group 1 and 2 is only 20 %, possibly due to significant statistical variation in the detected counts, in the remaining cases the TL and OSL sensitivities of Group 2 are, respectively, ~ 40 and ~ 50 % higher than that of Group 1.

Table 11.2: Results of (a) sensitivity and (b) signal to BG ratio of the $TL_{150\text{-}290^{o}C}$ and OSL signals for the samples of Group 1 and Group 2 following irradiation with 0.5 Gy.

a	Group 1					Group 2				
0.5 Gy	$TL_{150\text{-}290^{o}C}$	$OSL_{10\,s}$	$OSL_{20\,s}$	$OSL_{30\,s}$	$OSL_{60\,s}$	$TL_{150\text{-}290^{o}C}$	$OSL_{10\,s}$	$OSL_{20\,s}$	$OSL_{30\,s}$	$OSL_{60\,s}$
Sample1 (MP)	3482±59	4291±66	5821±76	6703±82	9379±97	7918±89	6001±77	8145±90	9303±96	12085±110
Sample2 (MP)	4818±69	5417±74	7397±86	8629±93	9693±98	8838±94	6531±81	8807±94	10245±101	12241±111
Sample3 (MP)	4724±69	4511±67	7605±77	9581±98	10781±104	8820±94	6373±80	8557±93	11619±108	11855±109
Sample4 (MP)	4558±68	4393±66	5943±77	6563±81	8705±93	8110±90	7891±89	9167±96	10469±102	11875±109
Sample5 (MP)	4610±68	4529±67	6399±80	7455±86	10511±103	7426±86	6739±82	8609±93	9843±99	12987±114
Sample6 (MP)	3492±59	4683±68	6209±79	7095±84	9507±98	8372±91	5989±77	8207±91	9215±96	11685±108
Sample7 (MP)	3246±57	4481±67	6039±78	6879±83	9461±97	7630±87	6039±78	8003±89	9207±96	11991±110
Sample8 (NEW)	3106±56	4299±66	5809±76	6767±82	9213±96	8220±91	5943±77	8067±90	9183±96	11603±108
Sample9 (NEW)	3564±60	4397±66	5949±77	6827±83	8985±95	7986±89	6043±78	8105±90	9481±97	11851±109
Sample10 (NEW)	4974±71	4867±70	6452±80	7321±86	10285±101	7567±87	6867±83	8952±95	10321±102	10285±101
Average	**3956±63**	**4587±68**	**6363±80**	**7382±86**	**9581±98**	**8089±90**	**6442±80**	**8462±92**	**9889±99**	**12019±110**
SD	**736**	**340**	**641**	**975**	**673**	**489**	**610**	**414**	**787**	**672**
CV (%)	**19**	**7**	**10**	**13**	**7**	**6**	**10**	**5**	**8**	**6**

b	Group 1					Group 2				
0.5 Gy	$TL_{150-290^{o}C}$/BG	$OSL_{10\ s}$ /BG	$OSL_{20\ s}$ /BG	$OSL_{30\ s}$ /BG	$OSL_{60\ s}$ /BG	$TL_{150-290^{o}C}$/BG	$OSL_{10\ s}$ /BG	$OSL_{20\ s}$ /BG	$OSL_{30\ s}$ /BG	$OSL_{60\ s}$ /BG
Sample1 (MP)	2.43±0.08	2.59±0.08	2.08±0.05	1.88±0.04	1.61±0.02	4.42±0.14	3.22±0.10	2.52±0.06	2.21±0.04	1.79±0.03
Sample2 (MP)	2.95±0.12	3.19±0.10	2.79±0.09	2.68±0.07	1.81±0.04	4.69±0.15	3.41±0.11	2.64±0.06	2.34±0.04	1.86±0.03
Sample3 (MP)	2.96±0.10	2.67±0.09	2.41±0.06	2.38±0.05	1.76±0.03	4.80±0.15	4.09±0.17	3.03±0.12	2.96±0.09	2.08±0.06
Sample4 (MP)	2.96±0.10	2.62±0.08	2.10±0.05	1.86±0.04	1.57±0.02	4.59±0.15	4.30±0.18	3.58±0.13	3.27±0.10	2.39±0.04
Sample5 (MP)	2.92±0.10	2.67±0.09	2.19±0.05	1.97±0.04	1.69±0.02	4.13±0.13	3.49±0.11	2.61±0.06	2.28±0.04	1.85±0.03
Sample6 (MP)	2.44±0.08	2.73±0.09	2.15±0.05	1.93±0.04	1.62±0.02	4.39±0.14	3.21±0.10	2.53±0.06	2.20±0.04	1.76±0.03
Sample7 (MP)	2.24±0.07	2.66±0.09	2.12±0.05	1.90±0.04	1.62±0.02	3.82±0.12	3.23±0.10	2.49±0.06	2.20±0.04	1.78±0.03
Sample8 (NEW)	2.28±0.08	2.59±0.08	2.07±0.05	1.89±0.04	1.60±0.02	4.82±0.16	3.19±0.10	2.50±0.06	2.20±0.04	1.76±0.03
Sample9 (NEW)	2.47±0.08	2.63±0.08	2.10±0.05	1.89±0.04	1.59±0.02	4.15±0.13	3.23±0.10	2.51±0.06	2.24±0.04	1.77±0.03
Sample10 (NEW)	2.82±0.10	2.82±0.10	2.45±0.07	2.5±0.07	1.83±0.04	4.71±0.15	3.58±0.14	2.45±0.07	2.5±0.05	1.83±0.04
Average	**2.63±0.09**	**2.72±0.09**	**2.25±0.06**	**2.09±0.04**	**1.67±0.03**	**4.45±0.14**	**3.50±0.12**	**2.69±0.07**	**2.44±0.05**	**1.89±0.03**
SD	**0.3**	**0.18**	**0.24**	**0.31**	**0.10**	**0.33**	**0.39**	**0.36**	**0.37**	**0.20**
CV (%)	**11**	**7**	**10**	**15**	**6**	**7**	**11**	**13**	**15**	**11**

Table 11.3: Results of (a) sensitivity and (b) signal to BG ratio of the $TL_{150-290^{o}C}$ and OSL signals for the samples of Group 1 and Group 2 following irradiation with 2 Gy.

a	Group 1					Group 2				
2 Gy	$TL_{150-290^{o}C}$	$OSL_{10\ s}$	$OSL_{20\ s}$	$OSL_{30\ s}$	$OSL_{60\ s}$	$TL_{150-290^{o}C}$	$OSL_{10\ s}$	$OSL_{20\ s}$	$OSL_{30\ s}$	$OSL_{60\ s}$
Sample1 (MP)	2961±54	3286±57	4226±65	4867±70	6207±79	7148±85	5168±72	6848±83	7882±89	9979±100
Sample2 (MP)	3244±57	3323±58	5466±74	6245±79	6408±80	7486±87	5483±74	7406±86	8517±92	10743±104
Sample3 (MP)	3853±62	2664±52	3956±63	4954±70	6905±83	7785±88	5988±77	8541±92	9007±95	10397±102
Sample4 (MP)	4086±64	3632±60	4825±69	5473±74	6805±82	7022±84	6552±81	8989±95	10724±104	11858±109
Sample5 (MP)	3541±60	3238±57	4366±66	5053±71	6615±81	6870±83	5854±77	7699±88	8829±94	10800±104
Sample6 (MP)	3059±55	3344±58	4250±65	4782±69	6056±78	7106±84	5095±71	6912±83	7917±89	9830±99
Sample7 (MP)	3109±56	3365±58	4248±65	4756±69	5881±77	7331±86	5227±72	7018±84	8042±90	10006100
Sample8 (NEW)	3050±55	3399±58	4339±66	4878±70	6105±78	7360±86	5150±72	6867±83	7918±89	9870±99
Sample9 (NEW)	3148±56	3459±59	4369±66	4967±70	6244±79	7028±84	5104±71	6823±83	7842±89	9812±99
Sample10 (NEW)	3348±58	3144±56	4886±70	5387±73	7304±85	7532±87	5144±72	7886±89	8387±92	10320±102
Average	**3339±58**	**3286±57**	**4493±67**	**5136±72**	**6358±80**	**7237±85**	**5477±74**	**7499±87**	**8507±92**	**10361±102**
SD	**375**	**255**	**440**	**458**	**446**	**287**	**497**	**772**	**884**	**639**
CV (%)	**12**	**8**	**10**	**9**	**7**	**4**	**10**	**10**	**10**	**6**

b	Group 1					Group 2				
2 Gy	$TL_{150-290^{\circ}C}$/BG	$OSL_{10\ s}$ /BG	$OSL_{20\ s}$ /BG	$OSL_{30\ s}$ /BG	$OSL_{60\ s}$ /BG	$TL_{150-290^{\circ}C}$/BG	$OSL_{10\ s}$ /BG	$OSL_{20\ s}$ /BG	$OSL_{30\ s}$ /BG	$OSL_{60\ s}$ /BG
Sample1 (MP)	5.88±0.18	5.89±0.17	4.18±0.09	3.53±0.06	2.62±0.04	12.7±0.38	8.70±0.25	6.17±0.13	5.09±0.09	3.61±0.05
Sample2 (MP)	6.61±0.26	7.24±0.25	4.64±0.14	4.39±0.10	2.68±0.06	13.6±0.41	9.17±0.26	6.59±0.14	5.42±0.09	3.81±0.05
Sample3 (MP)	6.85±0.20	5.96±0.15	3.97±0.09	3.57±0.07	2.91±0.04	14.3±0.43	9.40±0.27	8.67±0.26	6.84±0.18	4.42±0.`0
Sample4 (MP)	7.00±0.24	6.41±0.19	4.63±0.10	3.84±0.07	2.78±0.04	12.0±0.35	10.37±0.31	7.79±0.16	6.56±0.11	4.18±0.06
Sample5 (MP)	6.65±0.20	5.82±0.17	4.28±0.09	3.62±0.07	2.73±0.04	13.3±0.41	9.72±0.28	6.81±0.14	5.58±0.10	3.82±0.05
Sample6 (MP)	6.21±0.20	5.98±0.18	4.20±0.09	3.48±0.06	2.58±0.03	12.7±0.38	8.59±0.25	6.22±0.13	5.11±0.09	3.57±0.05
Sample7 (MP)	6.28±0.20	6.01±0.18	4.19±0.09	3.47±0.06	2.54±0.03	13.4±0.41	8.79±0.25	6.30±0.13	5.17±0.09	3.61±0.05
Sample8 (NEW)	5.90±0.18	6.06±0.18	4.26±0.09	3.53±0.06	2.60±0.03	12.6±0.37	8.67±0.25	6.18±0.13	5.11±0.09	3.58±0.05
Sample9 (NEW)	6.24±0.19	6.15±0.18	4.29±0.09	3.58±0.07	2.63±0.04	12.0±0.35	8.60±0.25	6.15±0.13	5.07±0.09	3.56±0.05
Sample10 (NEW)	6.34±0.21	6.45±0.18	4.89±0.16	3.87±0.08	2.96±0.07	12.2±0.40	7.45±0.18	5.89±0.16	4.87±0.08	3.78±0.06
Average	**6.40±0.21**	**6.20±0.18**	**4.35±0.10**	**3.69±0.07**	**2.67±0.04**	**12.89±0.39**	**8.95±0.18**	**6.68±0.15**	**5.48±0.10**	**3.79±0.06**
SD	**0.37**	**0.42**	**0.28**	**0.28**	**0.14**	**0.76**	**0.78**	**0.88**	**0.68**	**0.29**
CV (%)	**6**	**7**	**6**	**8**	**5**	**6**	**9**	**13**	**12**	**8**

Table 11.4: Results of (a) sensitivity and (b) signal to BG ratio of the $TL_{150\text{-}290^{\circ}C}$ and OSL signals for the samples of Group 1 and Group 2 following irradiation with 5 Gy.

a	Group 1					Group 2				
5 Gy	$TL_{150-290^{\circ}C}$	$OSL_{10\ s}$	$OSL_{20\ s}$	$OSL_{30\ s}$	$OSL_{60\ s}$	$TL_{150-290^{\circ}C}$	$OSL_{10\ s}$	$OSL_{20\ s}$	$OSL_{30\ s}$	$OSL_{60\ s}$
Sample1 (MP)	2935±54	3144±56	3979±63	4507±67	5507±79	7170±85	5109±71	6905±83	7972±89	9903±100
Sample2 (MP)	3218±57	4429±67	5123±72	5318±73	6123±78	7647±87	5557±75	7433±86	8588±93	10706±103
Sample3 (MP)	3813±62	3348±58	3275±57	3944±63	5576±75	7969±89	6494±81	8475±92	9218±96	11663±108
Sample4 (MP)	4181±65	3665±61	4790±69	5487±74	6762±82	7132±84	6275±79	8355±91	9723±99	12570±112
Sample5 (MP)	3671±61	3189±56	4208±65	4854±70	6067±78	6952±83	6015±78	7858±89	8928±94	10866±104
Sample6 (MP)	3174±56	3362±58	4215±65	4738±69	5757±76	7355±86	5080±71	6787±82	7882±80	9775±99
Sample7 (MP)	3128±56	3321±58	4208±65	4736±69	5812±76	7401±85	5041±71	6825±83	7901±89	9804±99
Sample8 (NEW)	3140±55	3336±58	4227±65	4770±69	5832±76	7406±86	5049±71	6823±83	7898±89	9815±99
Sample9 (NEW)	3219±57	3328±58	4175±65	4703±69	5737±76	7220±86	5126±72	6862±83	7963±89	9879±99
Sample10 (NEW)	3354±58	3768±61	4678±68	4921±70	5967±77	7532±86	5768±76	5678±75	8921±94	10352±102
Average	**3433±59**	**3489±59**	**4288±65**	**4798±69**	**5912±77**	**7378±86**	**5551±75**	**7200±85**	**8499±92**	**10533±103**
SD	**384**	**382**	**501**	**421**	**355**	**298**	**556**	**844**	**671**	**1000**
CV (%)	**12**	**11**	**12**	**9**	**6**	**4**	**10**	**12**	**8**	**10**

b	Group 1					Group 2				
5 Gy	$TL_{150-290^{\circ}C}$/BG	$OSL_{10\,s}$ /BG	$OSL_{20\,s}$ /BG	$OSL_{30\,s}$ /BG	$OSL_{60\,s}$ /BG	$TL_{150-290^{\circ}C}$/BG	$OSL_{10\,s}$ /BG	$OSL_{20\,s}$ /BG	$OSL_{30\,s}$ /BG	$OSL_{60\,s}$ /BG
Sample1 (MP)	12.05±0.34	12.73±0.36	8.52±0.18	6.84±0.12	4.60±0.06	30.58±0.89	20.06±0.56	14.07±0.28	11.32±0.19	7.47±0.09
Sample2 (MP)	13.87±0.58	15.53±0.49	10.58±0.25	7.48±0.18	5.20±0.09	30.25±0.85	21.74±0.61	15.07±0.31	12.12±0.20	7.99±0.10
Sample3 (MP)	15.28±0.43	11.76±0.28	9.18±0.15	6.11±0.11	4.64±0.06	35.62±1.06	24.94±0.88	17.53±0.52	14.95±0.36	8.52±0.09
Sample4 (MP)	14.58±0.58	14.68±0.41	10.06±0.21	8.11±0.14	5.42±0.07	29.19±0.83	24.42±0.78	16.82±0.34	13.59±0.23	9.21±0.11
Sample5 (MP)	15.12±0.48	12.90±0.37	8.95±0.18	7.29±0.13	4.96±0.06	29.42±0.86	23.45±0.65	15.87±0.32	12.56±0.21	8.10±0.10
Sample6 (MP)	12.98±0.37	13.54±0.38	8.97±0.18	7.14±0.12	4.76±0.06	29.75±0.85	19.96±0.56	13.84±0.28	11.21±0.19	7.39±0.09
Sample7 (MP)	13.05±0.38	13.39±0.38	8.95±0.18	7.14±0.12	4.80±0.06	32.42±0.96	19.81±0.56	13.91±0.28	11.23±0.19	7.40±0.09
Sample8 (NEW)	13.17±0.38	13.45±0.38	8.99±0.18	7.18±0.12	4.81±0.06	30.89±0.89	19.84±0.56	13.91±0.28	11.23±0.19	7.41±0.09
Sample9 (NEW)	13.30±0.38	13.42±0.38	8.89±0.18	7.09±0.14	4.77±0.06	32.54±0.96	20.13±0.56	13.98±0.28	11.31±0.19	7.45±0.09
Sample10 (NEW)	14.02±0.41	12.87±0.37	9.43±0.18	7.86±0.13	4.87±0.06	31.52±0.93	18.87±0.37	12.43±0.18	10.86±0.13	7.75±0.10
Average	**13.71±0.44**	**13.43±0.38**	**9.25±0.19**	**7.22±0.13**	**4.88±0.06**	**31.22±0.91**	**21.22±0.62**	**14.74±0.31**	**12.04±0.21**	**7.87±0.10**
SD	**1.03**	**1.05**	**0.62**	**0.54**	**0.25**	**2.04**	**2.18**	**1.56**	**1.32**	**0.64**
CV (%)	**8**	**8**	**7**	**8**	**5**	**7**	**10**	**11**	**11**	**9**

Concerning the inter-sample variability of each group – determined by the coefficient of variation (i.e., ratio of the standard deviation to the average value) – it could be said that it is overall small and seems to be independent of whether the resistors were extracted from mobile phones or not. The samples of Group 2 demonstrate a variation in TL and OSL sensitivity of ~ 10 %. In contrast, the samples of Group 1 are, generally, characterised by higher coefficient of variation which is most likely caused by the smaller signal to BG ratio. Nevertheless, the number of the samples studied here is very small and the results are not necessarily representative of a wider population.

To obtain an idea of the variability in the luminescence output that can be met in reality, the individual sensitivity of 100 SMRs selected randomly from several mobile phones and from batches of unused components was measured following irradiation with a relatively high dose (i.e., 20 Gy) to ensure sufficient counting statistics. The distribution of $TL_{150\text{-}290^{o}C}$ and OSL_{60s} sensitivity is represented by the histograms in Figure 11.3a,b. Each set of data was found to follow the Gaussian probability distribution, shown by the dashed curves. Again, although the sample population is small it is evident that the luminescence sensitivity can vary greatly between samples. For this particular sample population, the OSL and TL sensitivities were found to differ by ~ 20 %.

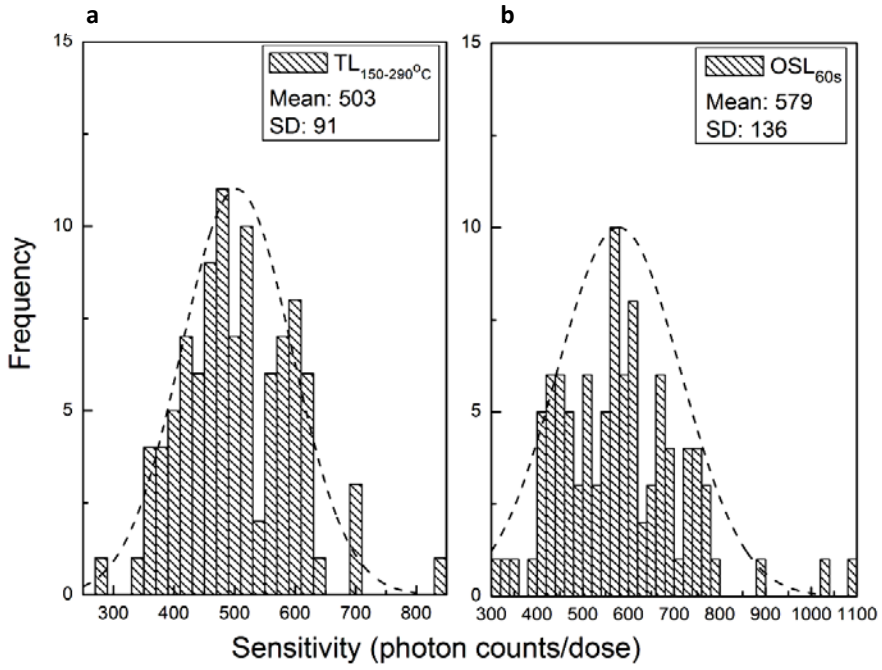

Figure 11.3: Histogram of (a) $TL_{150\text{-}290^{o}C}$ and (b) OSL_{60s} sensitivity. A Gaussian probability distribution function, shown by the dashed curves, was fitted to the data. The mean and standard deviation of each Gaussian distribution are shown in the legends. The data were produced using a sample population of 100 SMRs and a dose of 20 Gy. The TL and OSL were detected in the UV with a Hoya U340 filter (7.5 mm).

In conclusion, it could be argued that the OSL signal of SMRs has superior sensitivity capabilities than the TL counterpart and, in cases where a small number of resistors is available, OSL may be the preferred stimulation technique for the evaluation of accident doses. Nevertheless, the TL method offers significantly improved detection capabilities (i.e., signal to BG ratio), but apparently it requires samples consisting of a greater number of SMRs. While both sensitivity and detectability are important factors governing the suitability of a radiation detector it should be realised that the choice of the stimulation mode has to be made following an examination of other properties of the dosemeter. For example, as evidenced in the previous chapter, the luminescence signals of the alumina substrates suffer significant fading at RT implying that the signal to BG ratio will be lower following a delay between irradiation and measurement. In this case, TL may be more suitable than OSL.

In spite of that, it is speculated that the TL sensitivity and detection capability of SMRs may further be improved by removing the OSL unit. To justify this, the TL sensitivity of the samples was measured again without the OSL unit below the PMT. As seen in Figure 11.4a,b and Table 11.5, the TL signal per unit dose increases importantly by bringing the samples closer to the detector. In particular, the TL sensitivities of both groups increase by approximately a factor of 11, while the $TL_{150\text{-}290^{o}C}$/BG ratio is also greater than before by a factor of 7. In addition, compared with OSL_{60s} the TL signal appears ~ 6 times more sensitive (Table 11.5). These results indicate the possibility of measuring low doses with adequate sensitivity using a small number of resistors. Also, retrospective dose evaluations will be more possible using the remaining SMRs.

Table 11.5: Comparison of the average sensitivity of $TL_{150\text{-}290^{o}C}$ and $OSL_{60\ s}$ with the sensitivity of the $TL_{150\text{-}290^{o}C}$ signal measured after removing the OSL unit below the PMT detector.

	Group 1			**Group 2**		
Dose (Gy)	**$TL_{150\text{-}290^{o}C}$ (without OSL unit)**	**$TL_{150\text{-}290^{o}C}$**	**$OSL_{60\ s}$**	**$TL_{150\text{-}290^{o}C}$**	**$TL_{150\text{-}290^{o}C}$ (without OSL unit)**	**$OSL_{60\ s}$**
0.5	43986±210	3956±63	7382±86	85356±292	8089±90	12019±110
2	38786±197	3339±58	6358±80	75406±275	7237±85	10361±102
5	39759±199	3433±59	5912±77	77569±279	7378±86	10533±103
Average	40844±202	3576±60	7284±85	79444±282	7568±87	11092±105

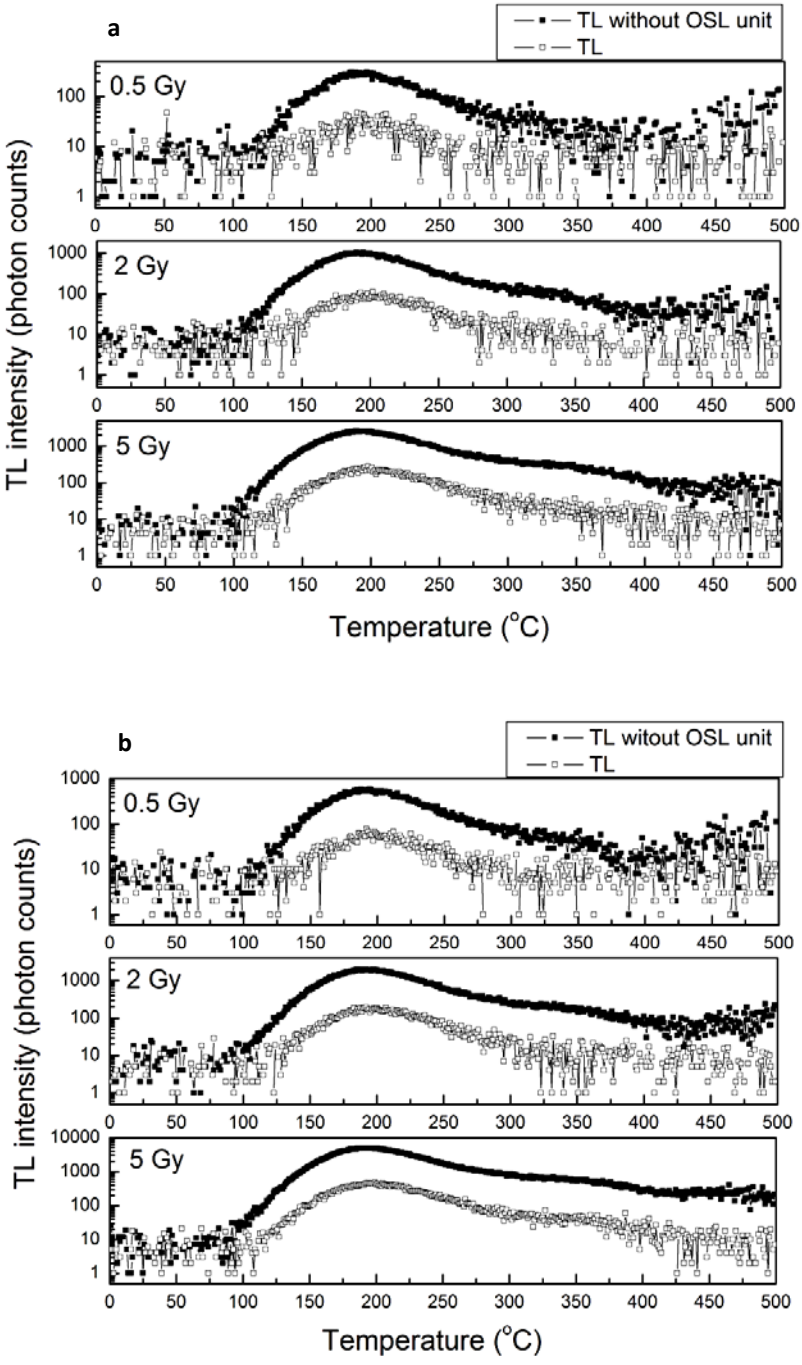

Figure 11.4: BG-corrected TL glow curves of Sample 3 from (a) Group 1 and (b) Group 2 obtained once with the OSL unit located below the PMT and after removing the OSL unit. The TL was detected across the entire range of the PMT detector without any filter.

11.4 Luminescence reproducibility

11.4.1 Introduction

During the application of the SAR technique, luminescence materials are subjected to a series of successive preheat treatments and irradiations to reconstruct the unknown dose or equivalent dose (i.e., laboratory dose required to regenerate a luminescence signal that matches the signal derived from the unknown dose; Bøtter-Jensen *et al*., 2011). The combination of annealing and irradiation over several repetitions may, however, cause changes in the sensitivity of the material which, in turn, can affect the accuracy of the dose estimate. It is, hence, required that the material presents a constant and reproducible radiation response. Nevertheless, sensitisation (i.e., sensitivity increase) or desensitisation (i.e., sensitivity decrease) effects are more likely to occur following irradiation to high doses or annealing at high temperatures (e.g., > 500 ° C). Dose sensitisation usually results from the filling of competing deep traps that can be subsequently excited increasing the response of the material, while high temperature annealing may affect the sensitivity of a material by inducing impurity dissipation and defect clustering reactions (Chen and McKeever, 1997). Even if the regenerative doses and the thermal treatments involved in SAR protocols are not significant to cause sensitisation/desensitisation, it is a common practice to monitor sensitivity changes by delivering to the samples a small test dose after each regenerative dose.

11.4.2 Experimental method and results

The reproducibility of TL and OSL was tested using two samples (one for each stimulation technique) consisting of ~ 20 SMRs removed from mobile phones. The sequences indicated in Table 11.1 were repeated 10 times for a test dose of 5 Gy. TL glow curves were integrated, as usual, over the 150-290 °C range and OSL over 0-10 s, 0-20 s, 0-30 s, and 0-60 s. The measured $TL_{150\text{-}290^{o}C}$, OSL_{10s}, OSL_{20s}, OSL_{30s}, and OSL_{60s} integrated intensities were normalised to the first measurement and plotted against the number of measurement cycles and are shown in Figures 11.5 and 11.6. The results indicate small sensitivity changes. The $TL_{150\text{-}290^{o}C}$ signal in each

measurement cycle varies by ~ 1 % from the first measurement, while the OSL signals vary by ~ 2 %. It could be concluded that the resistors present fairly reproducible luminescence signals, at least for doses up to 5 Gy.

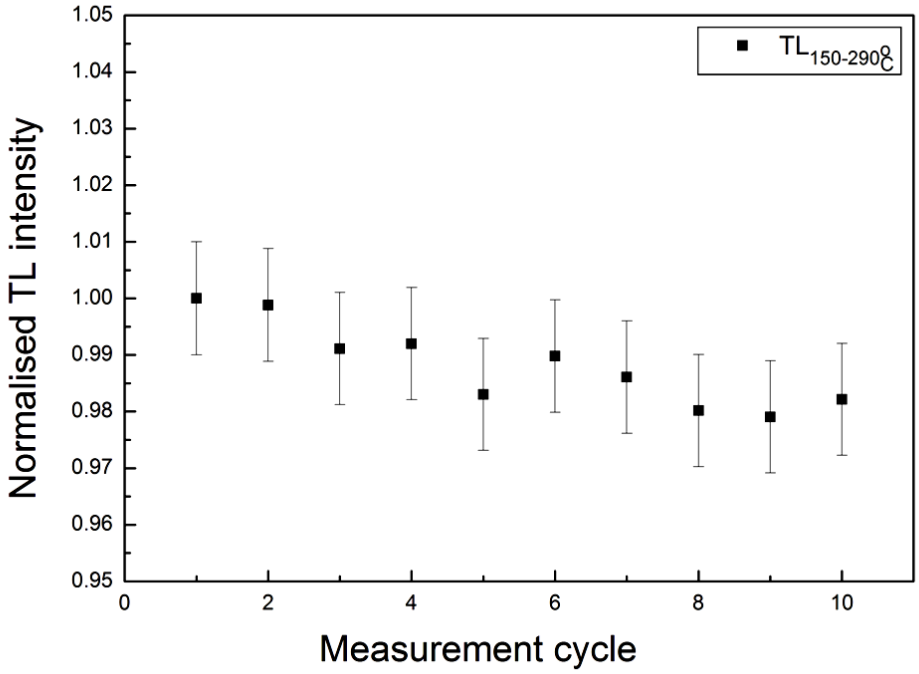

Figure 11.5: Reproducibility of normalised TL response showing the variation of the $TL_{150\text{-}290}{}^{o}{}_{C}$ intensity as a function of 10 repeated cycles of irradiation (5 Gy) and annealing (120 ° C, 10 s). The data produced using a sample consisting of 20 SMRs.

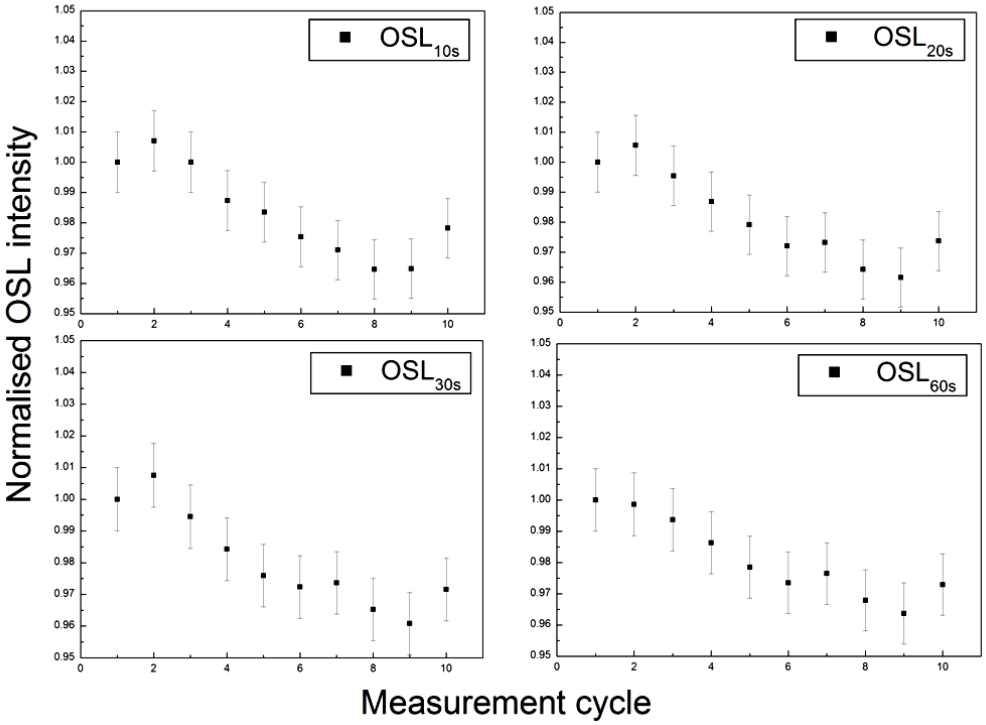

Figure 11.6: Reproducibility of OSL response following 10 repeated cycles of irradiation (5 Gy) and annealing (120 ° C, 10 s). The normalised to the first measurement integrated OSL intensity over 0-10 s, 0-20 s, 0-30 s, and 0-60 s of stimulation was plotted as a function of measurement cycle. The data produced using a sample consisting of 20 SMRs.

11.5 Luminescence dose response

11.5.1 Experimental method and results

The dose-response relationship of the luminescence of the two samples from Group 2 used in section 11.3 was examined for a dose ranging between 0.5 and 400 Gy using the sequence shown in Table 11.6, which is similar to that employed previously (i.e., Table 11.1) except that an additional irradiation-preheat-readout cycle has been added following the measurement of luminescence from the doses of interest. This step always includes the same test dose and is used

to monitor sensitivity changes and correct the luminescence response by normalising the signal in Step 4 to the signal in Step 8.

Table 11.6: Description of the sequence used to study the dose-response dependence of the luminescence signals.

Step		Description
1.	Annealing to 500 °C by TL readout at 5 °C s^{-1}	Remove trapped charges from previous use
2.	Beta dose: 0.5 – 400 Gy (2.3 Gy s^{-1})	Sample irradiation
3.	Preheat to 120 °C for 10 s	Remove charges from thermally unstable traps
4.	TL readout to 500 °C (5 °C s^{-1}): Sample 1 OSL readout (100 °C, 60 s): Sample 2	Measurement of luminescence response associated with thermally stable traps
5.	Annealing to 500 °C by TL readout at 5 °C s^{-1}	Remove remaining charges from Step 4
6.	Test dose: 1 Gy	Sensitivity monitor
7.	Preheat to 120 °C for 10 s	Remove charges from thermally unstable traps
8.	TL readout to 500 °C (5 °C s^{-1}): Sample 1 OSL readout (100 °C, 60 s): Sample 2	Measurement of luminescence response from test dose
9.	Repeat steps 1-8 for a new beta dose	

The TL and OSL dose response curves were constructed by plotting the normalised (to the test dose) luminescence signals against the amount of administrated dose. TL signals were integrated over 150-290 °C and OSL over 0-60 s, since it was found that the dose-response characteristics are similar, independent of the integral used. Figure 11.7a shows the TL dose-response curve using the whole data set plotted on a linear scale, while Figure 11.7b,c presents the dose-response relationships from 0.5-20 Gy and from 30-400 Gy, respectively, plotted on a logarithmic scale together with their linear regression lines. Similar graphs were produced for the OSL_{60s} normalised response and are shown in Figure 11.8a-c.

The dependence of the TL and OSL responses on the applied doses presents two slightly distinct behaviours. From 0.5 to 20 Gy the relationship is linear becoming super-linear at higher dose levels. The linear and super-linear dependencies can be confirmed through the acquisition of the values of the slopes of the linear regression lines in the logarithmic graphs. In the first dose region (i.e., 0.5-20 Gy) the slopes of the linear fits to the data are, respectively, 1.003 ± 0.004 for TL and 0.99 ± 0.004 for OSL; indicative of linear dose-response relationship (Chen and McKeever, 1997; McKeever *et al*., 1995). On the other hand, the linear regression lines fitted to the second dose region (i.e., 30-400 Gy) have slopes greater than unity (i.e., 1.21 ± 0.06 for TL and 1.12 ± 0.02 for OSL) characteristic of super-linear behaviour. The slightly higher super-linear behaviour of TL could be assigned to the fact that the TL signal is derived from a greater number of traps, while, as suggested in Section 9.2.4, OSL is mostly associated with the energy levels between 150-200 °C. In fact, if the integration interval of TL is limited to the 150-200 °C range the slope of the *LogTL* vs *LogDose* curve in the 30-400 Gy region is reduced to 1.16 ± 0.003. This value is closer to the corresponding slope of the OSL curve.

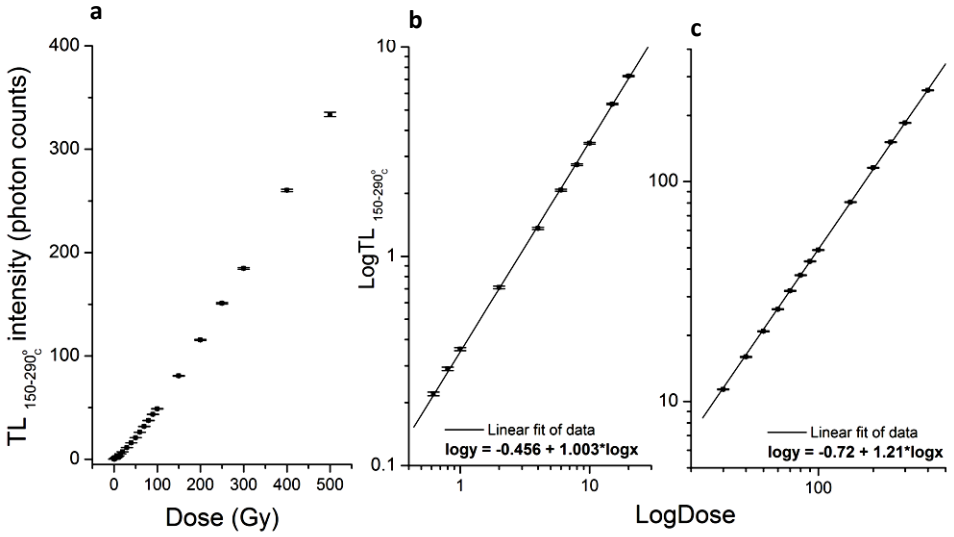

Figure 11.7: Relationship between the TL response and the applied dose. (a) Linear plot of normalised $TL_{150\text{-}290^{o}C}$ intensity as a function of dose in the range 0.5–400 Gy, (b) log-log plot of normalised $TL_{150\text{-}290^{o}C}$ intensity over 0.5–20 Gy, and (c) log-log plot of normalised $TL_{150\text{-}290^{o}C}$ intensity over 30–400 Gy. The linear regression lines of the data in b, c are also shown from which the slopes of the lines were found to be 1.003 ± 0.004 and 1.21 ± 0.06 respectively.

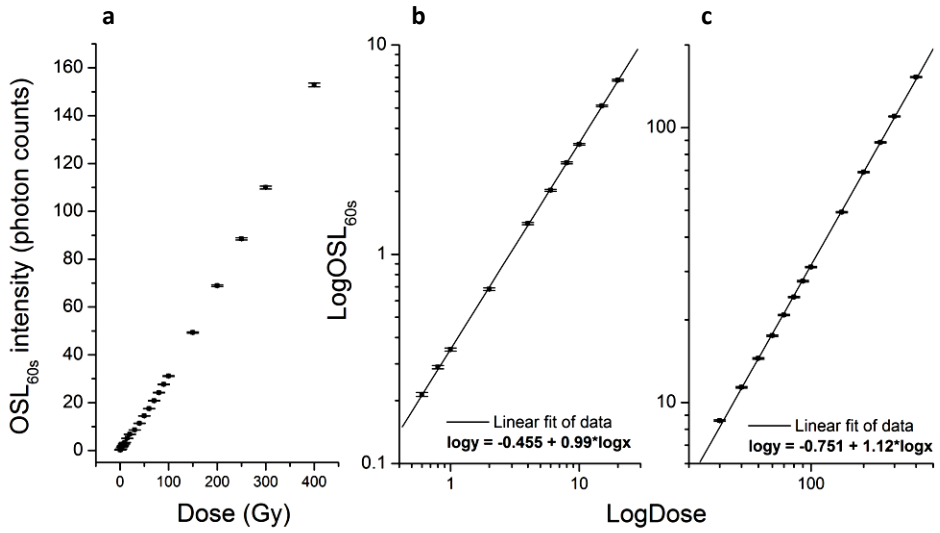

Figure 11.8: Relationship between the OSL_{60s} response and the applied dose. (a) Linear plot of normalised OSL_{60s} intensity as a function of dose in the range 0.5–400 Gy, (b) log-log plot of normalised OSL_{60s} intensity over 0.5–20 Gy, and (c) log-log plot of normalised OSL_{60s} intensity over 30–400 Gy. The linear regression lines of the data in b, c are also shown from which the slopes of the lines were found to be 0.99 ± 0.004 and 1.12 ± 0.02 respectively.

The physical mechanisms that have been suggested to account for super-linear dose-response functions are associated with the range and the properties of trapping levels present in the material acting as competitors for charge trapping during irradiation or stimulation (Chen and McKeever, 1997; Pagonis and Chen, 2011).

Superlinear dose dependence due to competition during irradiation can be explained assuming the presence of disconnected traps that do not participate in the production of luminescence. It is further assumed that the concentration of these competing energy levels is lower and their trapping probability is higher than that of the active traps. At low doses both types of traps are filled linearly. After a certain dose level, the competing traps are expected to be completely occupied (i.e., saturation) and any additional increase in the dose will not affect their concentration. Nevertheless, the available charge population will now have more probabilities of being captured by the active traps causing an over-response with dose. If only competition

during irradiation is assumed the dose-response of luminescence is expected to be linear at low doses, followed by a region of superlinearity at higher doses.

In the second case of competition during stimulation, the competition arises from a second thermally stable trap population with high probability of electron capture (Kristianpoller *et al*., 1974). During stimulation some of the excited charges instead of recombining with holes may get trapped in the competing energy levels. The fewer recombinations imply that there are more holes in the recombination centre and since the response is proportional to both the initial concentration of electrons and holes a superlinear growth with dose is expected to set in at the point where the occupancy of the competing centre approaches saturation.

The possible effect of one type of active luminescence traps and two recombination centres, one of which playing the role of competitor, has also been considered to interpret the dose dependence phenomena of luminescence. Numerical simulations performed by Chen *et al*., (1996) exemplified the different dose-response behaviours expected from a model with two energy levels (i.e., traps) and a model with two recombination centres. The first model will result a quadratic dose dependence followed by superlinearity, while a linear-superlinear dose-response relationship is anticipated from the second model.

Nevertheless, it should be recognised that the superlinearity effect observed at high doses is, in fact, an under-response at low doses. In other words, the luminescence sensitivity is not enhanced as the dose increases, but it is depressed since the effect of competition is more pronounced at low doses. This could be justified with experiments where the competition produced by the additional traps or recombination centres is removed by appropritate thermal annealing procedures or by administrating large dose to the samples prior to measurements of the luminescence sensitivity (Chen and McKeever, 1997).

Based on the experimental findings above, it would not be easy to determine the exact mechanism being responsible for the dose-dependence characteristics of the luminescence signals of alumina-based SMRs. While the model which includes competition between two energy levels can be excluded since it predicts a quadratic relationship with dose (at low doses), there isn’t sufficient evidence to decide between the model of competition during irradiation and

competition between two luminescent centres. Besides, one should not neglect that combined competition during irradiation and readout may occur simultaneously.

As a final point, the linear dose-response relationship of TL and OSL up to 20 Gy supports the suitability of SMRs for dose reconstruction purposes where the dose range of interest is from 0 to ~ 10 Gy, although the results are not in accordance with earlier findings (e.g., Inrig *et al*., 2008; Inrig, 2009) that the response is linear up to 100 Gy. Initially, it was hypothesised that the sensitivity changes observed at doses exceeding 20 Gy were not sufficiently corrected. To check this hypothesis, the methodology employed in the SAR technique to confirm that the luminescence signals have been adequately corrected for sensitivity changes was adopted here. Following the last dose of the dose-response sequence, the TL and OSL responses were measured again by delivering a dose equal to one of the initial dose points (e.g., 5 Gy). The ratio of the sensitivity-corrected signals to this dose, delivered once in the beginning and at the end of the whole sequence, was found to be close to unity (i.e., 0.98 ± 0.04), suggesting that sensitivity changes were accurately monitored and corrected.

Another reason for the discrepancy between the results presented here and those by Inrig *et al*., (2008) may be related to the different properties of the resistors used. To check the consistency of the results, the experiment was repeated using different samples. The same linear-superlinear behaviour was noted without exception. Nevertheless, it cannot be excluded that other set of resistors may display different dose response relationship.

11.6 Limit of detection

11.6.1 Introduction

A challenging property of any dosimetry system is the capability of detecting low levels of radiation exposure. Previous studies (Ekendahl and Judas, 2011; Inrig, 2009; Inrig *et al*., 2008) indicated that the minimum detectable dose (MDD) or limit of detection (LOD) associated with resistor components from mobile phones is of the order of mGy. The MDD or LOD characterises the smallest dose that can be distinguished with a given level of confidence from the background

dose (i.e., signal of an unexposed blank sample converted into units of dose). According to the International Union of Pure and Applied Chemistry (IUPAC, 1997), the LOD is given by an equation of the form $LOD = a + k\sigma_{BG}$, where a corresponds to the mean of counts from blank measurements, σ_{BG} is the standard deviation of the blank measurements (i.e., BG), and k is a factor chosen to express the desired confidence level and is usually taken to be equal to 3.

Since the values of the LOD depend on the BG signal it has to be separately determined for TL and OSL. This is because, as mentioned earlier, the BG associated with TL measurements is caused mainly by the dark counts of the PMT, whereas the BG of OSL is further enhanced by the scattered light from the stimulation source.

11.6.2 Experimental method and results

The TL and OSL BG signals of empty sample cups were measured fifty times using the sequences in Table 11.1 without the irradiation step. The mean, $\overline{BG}$, and standard deviation, σ_{BG}, of all measurements are shown in Table 11.7. The BG dose and LOD were then estimated by inserting the values of columns 2 and 4 into the equations describing the dose response relationship of TL and OSL taken from Figure 11.7. For OSL a second estimate of the LOD was made using a sample carrier filled with 20 SMRs since, contrary to TL, the scattering of the stimulation light by the SMRs may also contribute to the BG signal.

Table 11.7: Values of LOD for the TL and OSL signals.

Stimulation mode	$\overline{\mathbf{BG}}$ (counts)	$\boldsymbol{\sigma_{BG}}$ (counts)	$\overline{\mathbf{BG}} + 3\boldsymbol{\sigma_{BG}}$ (counts)	BG dose (Gy)	MDD (Gy)
TL(empty/filled cup)	1248	69	1456	0.120±0.002	0.14
OSL_{10s} (empty cup)[a]	724	60	904	0.150±0.001	0.17
OSL_{10s} (filled cup)[a]	1404	92	1680	0.220±0.002	0.25
OSL_{60s} (empty cup)[b]	4352	310	6745	0.420±0.006	0.59
OSL_{60s} (filled cup)[b]	8087	568	9789	0.690±0.012	0.82

a The normalised OSL_{10s} signal are described by the equation: $\boldsymbol{y = (0.018 \pm 0.008) + (0.340 \pm 0.001)x}$,
b The normalised OSL_{60s} signal are described by the equation: $\boldsymbol{y = (0.01 \pm 0.009) + (0.340 \pm 0.001)x}$

As already noted, TL is associated with lower BG level than OSL which, in addition, is independent of the presence of SMRs in the sample carriers. For the specific instrument in use the BG dose was found to be equal to 0.120 Gy and the minimum dose that can be distinguished at a confidence level of 95 % (i.e., $3\sigma_{BG}$) is 0.140 Gy. An alternative way of expressing the MDD is to say that approximately 20 mGy above the background dose would produce a TL signal that enables exposure to be detected. It is also worth noting that similar MDD was estimated for TL measurements without the OSL unit.

On the other hand, the MDD of OSL seems to depend on the selected integration interval and if the sample holders are empty or filled with SMRs. For filled cups and when the intensity from the total length of stimulation is used ~ 13 mGy are needed to generate a signal than can be distinguished from the instrumental BG, while, correspondingly, ~ 30 mGy are needed if the intensity of the first 10 s of stimulation is analysed. In the case of empty cups the lower limit of detection is close to 20 mGy either for the 10 or 60 s signals.

The calculated values of the MDD are in good agreement with the range reported in previous studies. Nevertheless, a direct comparison of the absolute values would be inappropriate since this would require the use of the same read-out instrument and measurement protocols.

11.7 Photon energy response

11.7.1 Introduction

Personal dosimetry budges usually contain several passive luminescent detectors for the assessment of different operational protection quantities in mixed radiation fields (e.g., personal dose equivalent: $H_p(d)$, d=10, 3, 0.07 mm). The detector material is selected to reproduce most of the dosimetry requirements mentioned above (e.g., linear dose response, reproducibility, stability) but also ideally to provide a radiation response similar to biological tissue (i.e., tissue equivalence). In most cases the effective atomic number (Chapter 3; section 3.3.3) of the detector material (e.g. LiF:Mg,Cu,P) is higher than that of tissue (i.e., Z_{eff} ~ 7.4), producing an over-response following exposure to low energy photons (Chapter 3: Figure 3.4). Filters of

appropriate chemical composition and geometry (e.g., thickness) are placed in front of the detector not only to provide the equivalent tissue thickness needed for the estimation of particular dose quantity [e.g., filters to provide 10 mm tissue equivalence for the $H_p(10)$ dose], but they are also used to flatten the energy response function of the detector. Also, the badge holder containing the detectors and filters – which may also comprise an integral part of the filtration (Eakins *et al*., 2008) – is carefully designed such that it improves the radiation response. The development of the final dosimetry system (holder, detector, and filters) is accomplished using a series of irradiation experiments and computational modelling (e.g., MCNP simulations) where the energy response properties of various combinations are tested (Chase and Hirning, 2008; Eakins, 2010; Jung *et al*., 2004).

On the other hand, accident/retrospective dosimetry for personal dose evaluation is performed using materials carried by individuals that are not designed for dosimetry applications. The radiation sensitive element employed is usually embedded within another structure that may alter the overall performance as a detector. Since, it is not possible to optimise the construction of the surrogate materials employed as dosemeters, it is necessary to examine how they perform when irradiated, especially using sources of low energy radiation. Sintered alumina, as the dosimetry grade Al_2O_3:C single crystal, is non-tissue equivalent (Z_{eff} ~ 10.2) and also SMRs exhibit an increased (~ 4 times) luminescence response when irradiated with photon energies below 100 keV (Beerten and Vanhavere, 2010; Ekendahl and Judas 2011). While the SMRs used in previous studies had been extracted from mobile phones, the photon energy response of SMRs when irradiated in situ with the phones was also investigated in this study.

Computational modeling using MCNP simulations was also performed using simplified geometry models of a SMR and a mobile phone to explore the effects of the position of mobile phones relative to the source to provide key data for converting the dose registered in SMRs external to the mobile phone.

11.7.2 Experimental investigation

The photon energy response measured by TL and OSL of SMRs from mobile phones was studied using two approaches. In the first, two samples (one for each stimulation mode) consisting of ~ 20 SMRs extracted from two mobile phones were placed in strips containing suitable positions to hold the resistors fixed, wrapped in a thin light-tight black bag, and placed directly in the direction of the radiation source. In the second case, the strips with the samples (without the black bag) were returned to the mobile phones in contact with the circuit board and behind the battery and irradiated first with the screen of the mobile phones facing the sources [anterior-posterior geometry, (AP)] and subsequently (following readout and annealing) with the battery facing the sources [posterior-anterior geometry, (PA)].

In both cases, the SMRs or the mobile phones were exposed to an air-Kerma dose of 0.5 Gy delivered by a gamma source (^{137}Cs or ^{60}Co) or a range of ISO Wide Series filtered x-ray beams produced by a high frequency 300 kV constant potential x-ray generator (x- and gamma-ray facilities at PHE, Chilton). The total number, energies, and dose rates of all photon sources used are listed in Table 11.8.

All irradiations were performed free in-air at a distance of 0.7 or 0.65 m from the x-ray generator or the gamma sources respectively. A 2 mm thick poly-methyl methacrylate (PMMA) sheet was placed in front of the gamma-irradiated materials to ensure charged particle equilibrium. Finally, the luminescence readout of the SMRs was performed using the sequences indicated in Table 11.1 with a minimum delay after irradiation of ~ 1 hour. Where the duration of irradiation was significant such that fading during irradiation could take place, the total elapsed time was estimated as (Auclair *et al*., 2003):

$$[delay\ time\ prior\ to\ readout + (duration\ of\ irradiation)/2].$$

Table 11.8: Type, energy, and dose rate characteristics of the photon sources used to study the photon energy response of SMRs following irradiation with 0.5 Gy air-Kerma dose. The duration of each irradiation is also given.

Source type	Source effective x-rayenergy (keV)[a]	Air-Kerma dose rate (Gy h^{-1})	Duration of irradiation (h)
ISO Wide Series x-rays	45	1.21	0.41
ISO Wide Series x-rays	58	0.88	0.57
ISO Wide Series x-rays	79	1.35	0.37
ISO Wide Series x-rays	104	2.27	0.22
ISO Wide Series x-rays	134	2.22	0.22
ISO Wide Series x-rays	169	2.21	0.23
ISO Wide Series x-rays	202	2.35	0.21
^{137}Cs	662	0.065	7.64
^{60}Co	1253	0.024	20.6

a For an x-ray beam with a spectrum of energies the effective energy is defined as the energy of a monoenrgetic x-ray beam with the same half value layer (HVL).

11.7.3 Computational modelling – MCNP simulation

The photon energy responses of SMRs and SMRs in mobile phones were calculated using the general purpose Monte Carlo radiation transport code MCNP5 (X-5, 2008).

A simplified model of a SMR was constructed using specifications provided by various manufacturers (e.g., Panasonic Thick Film Chip resistors). The SMR (Figure 11.9) consists of a rectangular shaped ceramic body made of sintered aluminium oxide (Al_2O_3), one face of which is coated with the resistive element (i.e., RuO_2) and a thin layer of an insulating material (i.e., epoxy). The bottom face of an unused SMR is uncoated, whereas those embedded in mobile phones are fixed onto the PCB with a solder paste. The side surfaces of the ceramic body are usually covered by three layers of electrical contacts. The dimensions and material composition of each part of the simulated SMR component are listed in Table 11.9. The modelled resistor corresponds to a type ´0805´ SMR, which is slightly larger than the ones (i.e., type ´0402´)

commonly encountered in most modern mobile phones. It should be noted that the material composition of the various parts of the SMR is not representative of all the commercially available SMRs. In the initial design of the model a number of alternative material combinations were considered for the terminations and the resistive element. For each SMR model the photon energy response of the alumina substrate was determined considering the possible effect of attenuation of the photons by the various layers above the alumina substrate and how this may vary by changing their chemical composition as well as the effect of backscatter. Nevertheless, it was found that the differences in the photon energy response arising from changing the elemental composition were insignificant and, therefore, only one case was considered for the study of the final model.

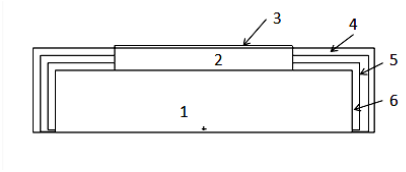

Figure 11.9: Model of a type ´0805´ SMR. The material composition of parts 1-6 are explained in Table 11.9.

Table 11.9: Dimensions and material composition of the various parts of an SMR

SMR part	Dimensions (cm)			Material
	Length	Width	Thickness	
1.Ceramic substrate	0.2	0.125	0.04	Aluminium oxide (Al_2O_3)
2.Resistive element	0.1	0.125	0.015	Ruthenium oxide (RuO_2)
3.Insulating coating	0.1	0.125	0.0005	Epoxy
4.Outer termination	0.06	0.125	0.005	Tin-Silver (Sn-Ag)
5.Middle termination	0.06	0.125	0.005	Nickel (Ni)
6.Inner termination	0.06	0.125	0.005	Palladium-Silver (Pd-Ag)

A three dimensional model of a touch-screen mobile phone –typical of the designs of phone currently available– was also developed (Figure 11.10). Schematically, the phone had approximate outer dimensions 10×8×1 cm, comprising a 1.17 g cm^{-3} plastic case (1, 7) fronted by a 2.23 g cm^{-3} glass screen (2), and containing a printed circuit board (4) which was modelled as a homogenous slab of appropriate typical average chemical composition. The lower half of the phone was half-filled with a ~ 0.4 cm thick slab of density 3.13 g cm^{-3} that represented the phone battery (6). Two metallic covers (3, 5) made of pure aluminium (2.70 g cm^{-3}) were also added;

one above the PCB, and the second in contact with the battery. Finally, two identical SMRs (labelled ´R1´ and ´R2´) were included within the phone: ´R1´ was located in the lower half of the phone behind the battery, whereas ´R2´ was located away from the battery in the top half of the phone. The specifications of the phone design and the chemical and physical characteristics of its constituent parts were determined by examining a mobile phone using a Hitachi Analytical Table Top Microscope model TM3000 with XRF probe. Trace amounts of some heavy elements incorporated into the circuit board and battery were derived from Cui and Zhang (2008), Li *et al*., (2007), Williams (2010), and Yamane *et al*., (2011).

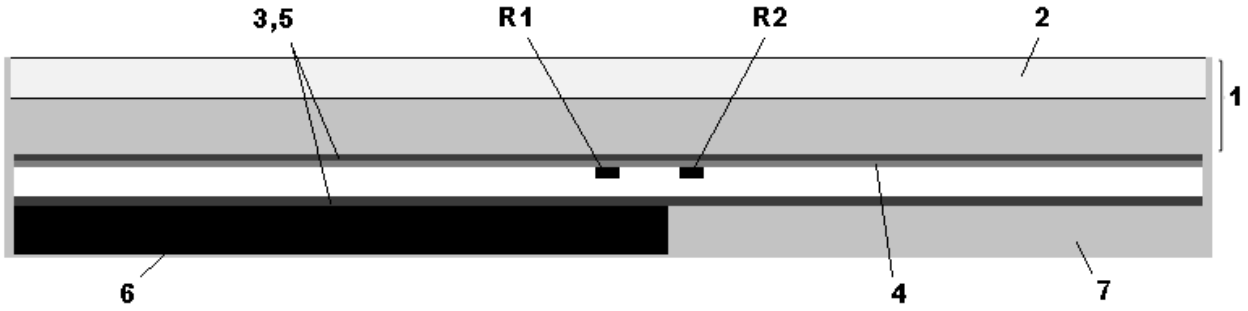

Figure 11.10: Cross-section view of a simulated mobile phone consisting of (1) front and (7) back plastic case, (2) glass screen, (3, 5) aluminium covers, (4) printed circuit board, (6) battery, and two surface mount resistor components (R1, R2).

The final geometry (SMR alone, or SMRs in mobile phone) was surrounded by a vacuum. All simulations were performed with photons only (MCNP '*mode p*') using either plane-parallel monoenergetic (i.e., from 400 to 2000 keV) sources or the ISO Wide Series x-ray spectra (ISO, 1999) taken by the Physicalisch Technische Bundesanstalt (PTB-Dos-34). In all cases, the dimensions of the sources were adjusted to completely cover the modelled geometry. The photon energy response of SMRs was calculated by simulating the energy deposited per mass using the MCNP ´f6:p' kerma tally (i.e., track length estimate of energy deposition in a SMR divided by its mass) normalised to the photon fluence through the SMR that was calculated (MCNP ´f4:p' tally) by repeating the simulation with all materials set to a vacuum. To obtain results that could directly be compared with the experimental data, the normalised ´f6:p' tally results per fluence for the SMRs were further normalised to the air-Kerma ´f6:p' tally values per applied fluence.

These latter data were estimated separately for each of the incident photon beams by repeating the simulations using the same problem geometry but replacing all materials with air of density ~ 0.012 g cm^{-3}. Two irradiation geometries were finally considered. In the first, particles were incident on the front face of the targets [i.e., anterior posterior (AP) geometry] while in the second the source particles started towards the direction of the back surface of the targets [i.e., posterior anterior (PA) geometry]. Each simulation was performed by simulating the transport of ~ 10^8 source particles, resulting in relative statistical errors of less than 5 % for all results.

11.7.4 Photon energy response of SMRs: Results

The measured luminescence and MCNP-calculated responses of alumina-based SMRs as a function of photon energy, normalised to the responses from exposures to ^{60}Co source gamma rays (mean energy: 1253 keV), are shown in Figure 11.11a,b. Since the TL and OSL data were found to be statistically similar, their average response was plotted.

As expected, due to the high effective atomic number of Al_2O_3 and the predominance of the photoelectric effect at low photon energies (Chapter 3; sections 3.3.2 and 3.3.3), the SMRs present an enhanced response per unit absorbed dose for photon energies below about 100 keV, showing a maximum relative response of ~ 4 at 45 keV. At higher photon energies the luminescence response can be considered energy independent. The agreement between the MCNP-calculated and experimental data is also very good, providing strong evidence that the simulated model of the SMR accurately describes the physical system.

Nevertheless, both the MCNP-calculated and the experimental photon energy responses are slightly higher than the theoretical-based one (Figure 11.11c) in the low-energy region (40-100 keV). The difference is likely due to the fact that the calculated photon energy response is derived using the mass-energy absorption coefficients for pure Al_2O_3 [available from the National Institute of Standards and Technology (NIST, 2011)] whereas in the present investigation the alumina substrate, although it does not contain impurities, is adjacent to various layers of high density and high atomic number materials (Table 11.10) that can modify the radiation field, for example, by producing scattered radiation or secondary charged particles that

also deposit their energy into the ceramic body. The MCNP simulations were, therefore, repeated using a ´bare´ SMR component (i.e., only the alumina substrate) and the results (Figure 11.11d) verified the initial assumption.

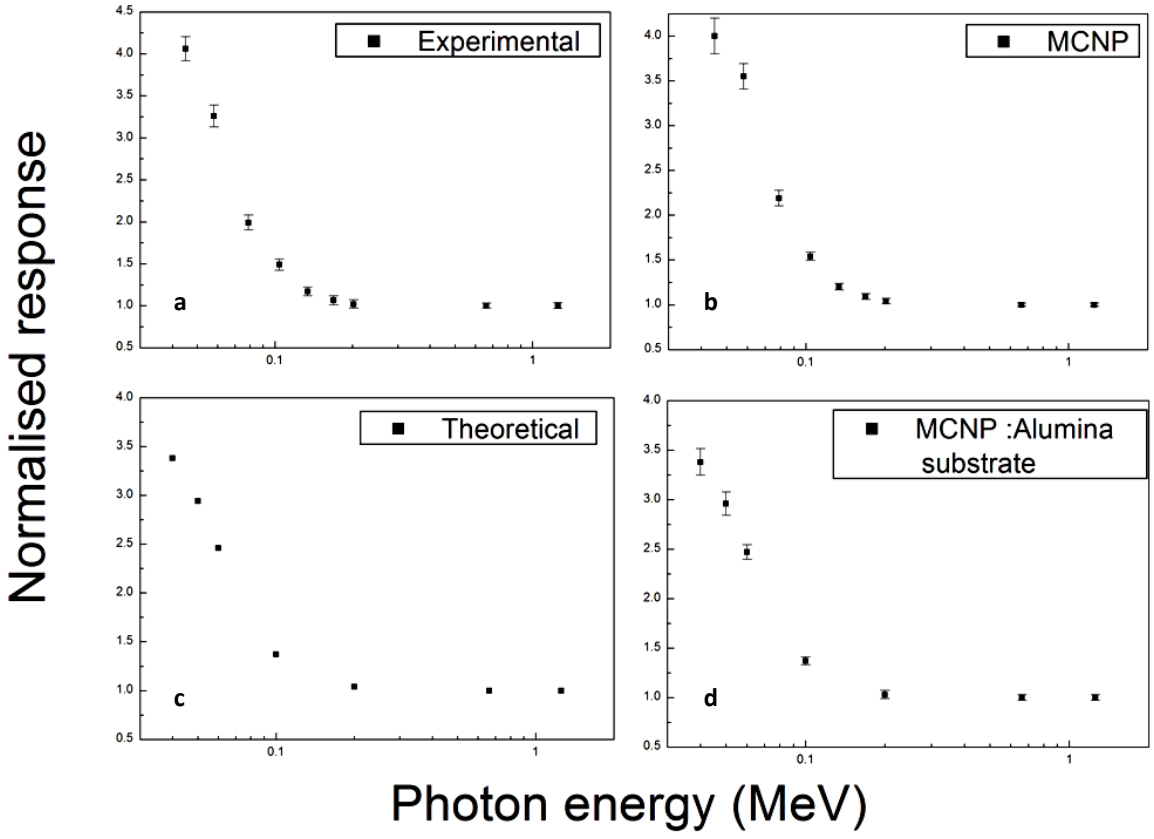

Figure 11.11: (a) Luminescence (average of TL and OSL) response of SMRs normalised to the response from ^{60}Co source gamma rays estimated following irradiation with 0.5 Gy air-Kerma dose using a range of ISO Wide Series filtered x-rays or gamma rays from a ^{137}Cs or a ^{60}Co source. (b) The MCNP-calculated relative response. (c) Theoretical (normalised to ^{60}Co) photon energy response of pure Al_2O_3 relative to air, calculated using the values of the mass energy-absorption coefficient for aluminium oxide and air (NIST, 2011). (d) The MCNP-calculated relative response of a ´bare´ SMR component (i.e., only the alumina substrate).

11.7.5 Photon energy response of SMRs in mobile phones: Results

The experimental and MCNP-calculated photon energy dependence of SMRs when the mobile phone is irradiated from the front (i.e., AP irradiation) are shown in Figure 11.12a,b. The experimental data were plotted using the average luminescence response (TL and OSL), whereas the MCNP data correspond to the average response of R1 and R2. Overall, both data sets agree to within 10 % indicating that the modelled geometry and physics provide, respectively, a quite reliable picture of a realistic mobile phone and irradiation conditions. Also, both the experimental and the MCNP photon energy response of the SMRs irradiated inside the mobile phone are in good agreement with those obtained when the SMRs where irradiated outside the phone.

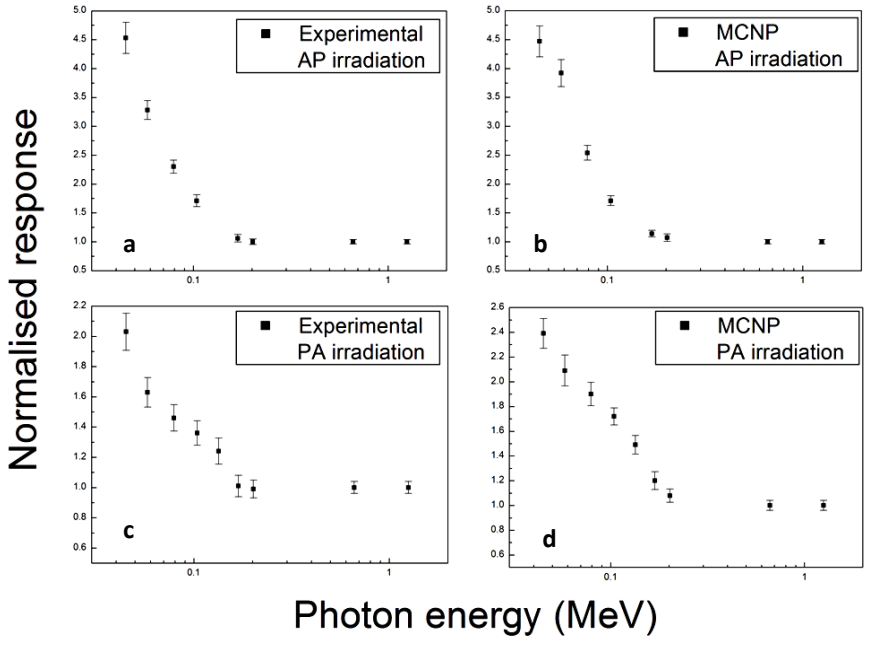

Figure 11.12: (a) Experimental photon energy (average of TL and OSL) response of SMRs normalised to the response from ^{60}Co source gamma rays estimated following AP irradiation of a mobile phone with 0.5 Gy air-Kerma dose using a range of ISO Wide Series filtered x-rays or gamma rays from a ^{137}Cs or a ^{60}Co source. (b) The MCNP-calculated response (average of R1 and R2) for AP irradiation of a mobile phone. (c) Same data as in (a) but for PA irradiation. (d) The MCNP-calculated response of R1 for PA irradiation.

For PA irradiation (Figure 11.12c,d) the photon energy response follows a similar trend as for the AP case, although the absolute values show important differences at low photon energies. The experimental data and MCNP data for resistor R1 show a maximum difference of ~ 50 % at 45 keV and 58 keV (i.e., lower photon energy response). The difference between the AP and PA data, however, decreases as the photon energy increases, and disappears above 100 keV. These results indicate that photons in the 40-100 keV range can be significantly attenuated by the battery of the phone, reducing the amount of energy deposited to the components located behind it. This was also confirmed when the MCNP-calculated photon energy response of resistor R2 (results not shown) located on the top half of the phone, away from the battery, was obtained. In this case it was found that R2 does not show the decreased photon energy dependence found for R1.

Finally, it was found that for the PA irradiation geometry and low photon energies, the MCNP data are ~ 20 % higher than the corresponding experimental data. The discrepancy is probably due to differences in the dimensions and material composition of the battery between the modelled and the real case.

11.8 Conclusions

The TL method –which, so far, has not been adopted in accident dosimetry with SMRs– could be an alternative to OSL offering improved sensitivity and counting statistics (i.e., signal to BG ratio) when measurements are performed without the optical stimulation unit located underneath the PMT detector of the Risø reader.

Some of the basic dosimetry properties of SMRs, such as the reproducibility of the luminescence response, the linearity of the response with dose to 20 Gy, and the capability of detecting low dose of the order of a few mGy were found to be in accordance with the requirements for dose assessment.

Since the main TL and OSL dosimetry signals are unstable at RT, showing a continuous reduction with time delay following irradiation, it is possible to reconstruct an accident dose by applying the appropriate fading correction factors.

Except for knowledge of the onset and duration of an accidental exposure that is required to correct the luminescence data for fading, knowledge of the energy spectrum of the radiation field is also required due to the dependence of the luminescence response of SMRs on the energy of the photon source. In addition, for photon energies lower than 100 keV, the location of the mobile phone relative to the source, as well as the position of SMRs within the phone, requires more investigation since the absorbed dose is likely to differ depending on the positions of the SMRs tested and the configuration of shielding within the phone relative to the source(s), and this is discussed further in the next section.

Finally, it is worth noting that in most cases the alumina SMRs will register photon dose and not beta or alpha because of their shielded locations within the mobile phone.

11.9 Dose reconstruction using mobile phones: Experimental approach

11.9.1 Measurement considerations

In the case of a mass casualty radiological accident the processing of a large number of mobile phones within a short period would be needed. Analysis of the conditions under which the accidental exposure took place and of the properties of the surrogate objects selected as accident dosemeters are crucial factors for reliable estimation of the accident dose. To increase the response capacity to a large scale radiological accident a close collaboration with other laboratories may be needed. On the basis of establishing an accident, an interlaboratory study in the framework of the EU-FP7 MULTIBIODOSE project (Bassinet, *et al.*, 2014) involving several laboratories was completed in 2014. The main objectives were to provide basic training on the various steps involved in the preparation of samples (e.g., SMR identification) and to test and validate the applicability of two OSL measurement protocols.

The procedure of extracting the SMRs from the mobile phones, even though it has to be performed under red light conditions, is generally not very tedious for a trained individual; SMRs are easily identifiable [i.e., they are flat with a black cover on top of the white alumina substrate (Figures 5.1 and 5.3)] between the remaining components of the printed circuit board

and they can be removed without difficulty using a sharp tool (e.g., scalpel or knife). To reduce the preparation time per sample, the smallest number of SMRs recommended by the MULTIBIODOSE project (Bassinet, *et al*., 2014) is 10 type ´0402´, although in cases where the smallest type SMRs (i.e., ´0201´) are included in the PCB the number of components per sample/cup must be increased. The results of the study demonstrated that the size of the sample provided adequate radiation sensitivity not only in the intermediate (1-2 Gy) and high (> 2 Gy) dose range, but also in the low (< 1 Gy) dose range. Nevertheless, as shown above, the luminescence sensitivity per unit absorbed dose can increase by ~ 50 % for a sample consisting of ~ 20 type ´0402´ SMRs. The precision in the evaluation of the unknown dose is expected therefore to improve; though, of course, the overall preparation time per sample will increase too.

Regarding the influence of the measurement protocol on the duration and precision of the dose reconstruction, a full SAR protocol (see Part I: Chapter 3; section 3.7) consisting of several calibration points and additional steps to check for sensitivity changes would significantly increase the measurement time per sample providing, though, better precision in the dose estimates. At the time of writing, the OSL method and the protocols proposed by the MULTIBIODOSE project (Table 11.10) have been more widely tested. These protocols, even though they are based on a single dose calibration point for time-efficient measurements, they were found to provide adequate agreement between the delivered and the measured absorbed doses. In the first protocol – termed *"fast mode"* protocol – the sample is not preheated prior to OSL acquisition (Steps 1 and 4) so that measurements are much faster. However, after the administration of the calibration dose (Step 2) the OSL signal will contain the thermally unstable component. Since this component of the OSL signal is absent from the OSL measured in Step 1 (due to the delay between the accident exposure and measurement), it also should be removed from the OSL in Step 4. The usual approach is to preheat the sample prior to OSL measurement or to let the thermally unstable component fade normally at RT for a few minutes. When a large number of samples are processed the OSL (Step 4) of each sample is not measured immediately after the administration of the calibration dose. Instead, the remaining samples are processed sequentially (Steps 1 and 2) which gives enough time for the thermally unstable component to fade. The second protocol (i.e., "*full mode*" protocol), is based on the same principles, but a preheat treatment proceeds each OSL measurement making the procedure slower since for each

sample the full measurement cycle (Step 1 to 5) is first completed before the next sample is analysed.

Table 11.10: OSL measurement protocols for dose reconstruction with SMRs suggested by the MULTIBIODOSE project (Bassinet, *et al*., 2014).

Step	Fast mode OSL protocol	Full mode OSL protocol
1	OSL acquisition at RT for 30 s	Preheat: 10 s at 120 °C (2 °C s^{-1} heating rate)
2	Calibration dose: 5 Gy	OSL acquisition at 100 °C (5 °C s^{-1}, wait 5 s prior to start OSL measurement) for 30 s
3	Minimum delay between irradiation (calibration dose) and measurement: 10 min (only if only one sample is measured)	Calibration dose: 5 Gy
4	OSL acquisition at RT for 30 s	Preheat: 10 s at 120 °C (2 °C s^{-1} heating rate)
5	-	OSL acquisition at 100 °C (5 °C s^{-1}, wait 5 s prior to start OSL measurement) for 30 s

To examine the extent of potential discrepancies introduced by the size of the sample, the measurements for a dose reconstruction were performed using samples of variable number of SMRs. Three protocols were applied: the "*full mode*" OSL protocol suggested by the MULTIBIODOSE project (Table 11.10), a "*full SAR*" OSL protocol including four calibration points (Table 11.2), and a "*fast mode*" TL protocol (Table 11.12). Table 11.11 lists the characteristics of each protocol in terms of duration and precision applicable to the specific equipment used (dose rate of beta irradiator 0.040 ± 0.002 Gy s^{-1}).

Table 11.11: Comparison of duration and precision of OSL and TL measurement protocols specific to the equipment used in the present research (dose rate of beta irradiator 0.040 ± 0.002 Gy s^{-1}) and for the particular experimental details for a sample consisting of ~ 10 SMRs.

Protocol	Details	Duration per sample	Precision
"*full mode*" OSL	Calibration beta dose: 5 Gy	~ 10 minutes	± 17 % of D_o
"*full SAR*" OSL	Test beta dose: 0.7 Gy	~ 40 minutes	± 10 % of D_o
"*fast mode*" TL	Calibration beta dose: 5 Gy	~ 8 minutes	± 16 % of D_o

Table 11.12: Analytical TL and OSL measurement protocols for dose reconstruction with SMRs used in the present investigation.

Fast TL

Step	Description
1	TL acquisition to 500 °C (5 °C s^{-1})
2	Calibration dose: 5 Gy
3	TL acquisition to 500 °C (5 °C s^{-1})

Full SAR OSL

Step	Description
1	Preheat: 10 s at 120 °C (5 °C s^{-1} heating rate)
2	OSL acquisition at 100 °C (5 °C s^{-1}, wait 5 s prior to start OSL measurement) for 30 s
3	Test dose: 0.5-1 Gy
4	OSL acquisition at 100 °C (5 °C s^{-1}, wait 5 s prior to start OSL measurement) for 30 s
5	First calibration dose: $D_1 > D_o$ (where D_o is the unknown/accident dose)
6	Preheat: 10 s at 120 °C (5 °C s^{-1} heating rate)
7	OSL acquisition at 100 °C (5 °C s^{-1}, wait 5 s prior to start OSL measurement) for 30 s
8	Test dose: 0.5-1 Gy
9	Preheat: 10 s at 120 °C (5 °C s^{-1} heating rate)
10	OSL acquisition at 100 °C (5 °C s^{-1}, wait 5 s prior to start OSL measurement) for 30 s
11	Repeat steps 1-10 three times for a new calibration dose $D_{2,3,4} > D_o$

11.9.2 On-phantom irradiation of mobile phones: Experimental set-up

A series of experiments were conducted under radiation exposure conditions which were considered to more closely simulate a radiological accident. A number of mobile phones, strips of unused SMRs wrapped in light-tight black bags, and TLDs containing LiF:Mg,Cu,P with different filters designed for the detection of $H_p(10)$ and $H_p(0.07)$ personal dose equivalent were attached to a whole body Rando-Alderson (RA) anthropomorphic phantom (Figure 11.13) available at Public Health England Centre for Radiation, Chemicals, and Environmental Hazards (CRCE) at Chilton, Oxfordshire.

Figure 11.13: Experimental set-up used for the x-ray (High 300 Series, mean x-ray energy of 147 keV) irradiation of mobile phones, unused SMRs wrapped in light-tight black film, and TLDs placed in various locations on a whole body Rando-Alderson anthropomorphic phantom.

The phantom was placed at a distance of 4 m from the ISO High 300 Series x-ray generator (mean energy 147 keV). The first set of samples was irradiated AP with an air-Kerma dose – estimated at the position of the centre of the phantom torso in the absence of the phantom to be of 0.7 Gy (± 5 %) where the dose rate was ~ 400 mGy h^{-1}. At the end of the irradiation, lasting ~

2 hours, the samples were removed from the phantom and left at RT until their measurement. The phantom was then loaded with a second set of samples and irradiated four times each with an air-Kerma dose of 0.2 Gy (± 5 %) at a dose rate of ~ 400 mGy h^{-1}. The first irradiation was performed with the front of the phantom facing the source (i.e., AP) and the other three by turning the phantom each time by 90 ° [i.e., PA, left-lateral (LLAT), and right-lateral (RLAT)] and administrating a total dose of 0.8 Gy (± 5 %). This sequential rotational (ROT) geometry, is likely to be more representative of a real emergency, where individuals are likely to move both translationally and rotationally relative to the source, leading to them (and their phones) becoming exposed to radiation from a wide range of directions.

A similar experiment was performed using gamma photons from a ^{137}Cs source. However, in this case a water-filled ISO slab phantom [i.e., a 30 x 30 x 15 cm^3 cubic structure made of PMMA used to represent the human torso (ISO, 1999)] was used. The experimental set-up is shown in Figure 11.14. The phantom was placed at a distance of 1.6 m from the source and irradiated anterior-posterior with an air-Kerma dose – estimated at the front face of the phantom in the absence of the phantom – of 0.71 Gy (± 5 %) at a dose rate of ~ 11 mGy h^{-1}. The total exposure time was 237900 s.

Figure 11.14: Experimental set-up used for the gamma (^{137}Cs) irradiation of mobile phones, unused SMRs wrapped in light-tight black tapes, and TLDs placed on each side of a water-filled ISO slab phantom.

11.9.3 Analysis and Results

The main objectives of the experiments described above were to investigate the influence of the presence and orientation of the human body (simulated using the phantoms) as well as the influence of the location of mobile phones on the human body on the evaluated accident doses; which would further increase the validity of the suggested accident dosimetry method. Furthermore, to enable the establishment of the currently proposed measurement methodology (Bassinet, *et al*., 2014) the analysis was, for the most part, performed according to the specifications defined by the MULTIBIODOSE project and, in particular, using the "*full mode*" OSL protocol considered to be more accurate than the "*fast mode*" protocol. The other protocols listed in Table 11.12 were also tested, but in cases where the number of SMRs extracted from mobile phones was not sufficient only the "*full mode*" OSL protocol was applied. Yet, as indicated in the previous section, unused components are expected to present similar behaviour with those included in mobile phones when irradiated with photons of energy above 100 keV.

Therefore, the unused SMRs attached to the phantoms were mainly used to test the full SAR OSL protocol and the TL protocol and also to examine the influence of the sample size on the accuracy of the dose estimates.

The results of the dose reconstruction procedure are presented in Tables 11.13, 11.14, and 11.15 for the AP irradiation geometry using the x-ray source, the ROT irradiation using the x-ray source, and the AP irradiation using the ^{137}Cs source, respectively. Each table includes the type of the sample (SMRs from phones or unused), its location on the phantom, the number of components per measurement, the delay period between the end of irradiation and readout, the protocol used, and the estimated dose in Gy. The dose results correspond to the corrected for anomalous fading doses. In the cases where the "*full mode*" OSL protocol was employed the fading correction factors determined by the MULTIBIODOSE project were applied which, however, are insignificantly different from those presented in Chapter 10.

The doses measured using the TLD materials placed in positions equivalent to those of mobile phones are listed in Table 11.16, where the results refer to the personal dose equivalent at a depth of 10 mm, Hp(10), and 0.07 mm, Hp(0.07), below the surface of the phantom. The values of the measured quantities are given in units of Sv which is equivalent to Gy for photons of all energies (Chapter 3; section 3.2).

Table 11.13: Results of the dose reconstruction using SMRs from mobile phones and unused SMRs attached to a Rando-Alderson anthropomorphic phantom irradiated anterior-posterior with an air-Kerma dose of 0.7 Gy at a dose rate of ~ 400 mGy h^{-1} using the ISO High 300 Series x-rays (effective x-ray energy 147 keV). Unless indicated with asterisk, the type of SMRs used were ´0402´.

Sample type	Location	No of SMRs	Delay (days)	Protocol	Dose (Gy)
SMRs from MPs	Right hip	20*	12	"*full mode*" OSL	1.11±0.15
Unused SMRs	Right hip	20	18	"*full mode*" OSL	1.07±0.15
Unused SMRs	Right hip	20	18	"*full SAR*" OSL	1.00±0.10
Unused SMRs	Right hip	20	18	"*fast mode*" TL	2.29±0.18
SMRs from MPs	Left hip	10	12	"*full mode*" OSL	1.16±0.17
SMRs from MPs	Left hip	15	12	"*fast mode*" TL	2.15±0.15
Unused SMRs	Left hip	20	18	"*full mode*" OSL	1.11±0.15
Unused SMRs	Left hip	20	18	"*full SAR*" OSL	1.06±0.14
Unused SMRs	Left hip	20	18	"*fast mode*" TL	2.20±0.17
SMRs from MPs	Right chest	10	12	"*full mode*" OSL	1.18±0.16
SMRs from MPs	Right chest	15	12	"*fast mode*" TL	2.23±0.14
Unused SMRs	Right chest	20	18	"*full mode*" OSL	1.09±0.15
Unused SMRs	Right chest	20	18	"*full SAR*" OSL	1.05±0.15
Unused SMRs	Right chest	20	18	"*fast mode*" TL	2.30±0.13
SMRs from MPs	Left chest	20*	12	"*full mode*" OSL	1.24±0.18
Unused SMRs	Left chest	20	18	"*full mode*" OSL	1.19±0.17
Unused SMRs	Left chest	20	18	"*full SAR*" OSL	1.12±0.16
Unused SMRs	Left chest	20	18	"*fast mode*" TL	2.60±0.12
SMRs from MPs	Right side	10	12	"*full mode*" OSL	0.97±0.11
SMRs from MPs	Right side	15	12	"*fast mode*" TL	1.98±0.16
Unused SMRs	Right side	20	18	"*full mode*" OSL	0.90±0.10
Unused SMRs	Right side	20	18	"*full SAR*" OSL	0.86±0.08
Unused SMRs	Right side	20	18	"*fast mode*" TL	2.16±0.17
SMRs from MPs	Left side	20*	12	"*full mode*" OSL	1.16±0.10
Unused SMRs	Left side	20	18	"*full mode*" OSL	1.08±0.08
Unused SMRs	Left side	20	18	"*full SAR*" OSL	0.99±0.07
Unused SMRs	Left side	20	18	"*fast mode*" TL	2.32±0.12
SMRs from MPs	Back	20*	12	"*full mode*" OSL	0.35±0.07
SMRs from MPs	Back	10	12	"*full mode*" OSL	0.39±0.05
SMRs from MPs	Back	15	12	"*fast mode*" TL	1.25±0.18
Unused SMRs	Back	20	18	"*full mode*" OSL	0.36±0.09
Unused SMRs	Back	20	18	"*full SAR*" OSL	0.33±0.05
Unused SMRs	Back	20	18	"*fast mode*" TL	1.13±0.12

*The type of SMRs extracted from mobile phones (MPs) was ´0201´

Table 11.14: Results of the dose reconstruction using SMRs from mobile phones and unused SMRs attached to a Rando-Alderson anthropomorphic phantom irradiated in a rotational geometry with a total air-Kerma dose of 0.8 Gy at a rate of ~ 400 mGy h^{-1} using the ISO High 300 Series x-rays (effective x-ray energy 147 keV). Unless indicated with asterisk, the type of SMRs used were ´0402´.

Sample type	Location	No of SMRs	Delay (days)	Protocol	Dose (Gy)
SMRs from MPs	Right hip	10	5	"*full mode*" OSL	1.17±0.13
SMRs from MPs	Right hip	15	5	"*fast mode*" TL	2.56±0.11
Unused SMRs	Right hip	20	8	"*full mode*" OSL	1.10±0.11
Unused SMRs	Right hip	20	8	"*full SAR*" OSL	1.02±0.05
Unused SMRs	Right hip	20	8	"*fast mode*" TL	2.36±0.13
SMRs from MPs	Left hip	20*	5	"*full mode*" OSL	1.20±0.14
Unused SMRs	Left hip	20	8	"*full mode*" OSL	1.10±0.12
Unused SMRs	Left hip	20	8	"*full SAR*" OSL	0.99±0.12
Unused SMRs	Left hip	20	8	"*fast mode*" TL	2.50±0.14
SMRs from MPs	Right chest	10	5	"*full mode*" OSL	1.18±0.12
SMRs from MPs	Right chest	15	5	"*fast mode*" TL	2.44±0.15
Unused SMRs	Right chest	20	8	"*full mode*" OSL	1.09±0.06
Unused SMRs	Right chest	20	8	"*full SAR*" OSL	0.97±0.06
Unused SMRs	Right chest	20	8	"*fast mode*" TL	2.32±0.16
SMRs from MPs	Left chest	20*	5	"*full mode*" OSL	1.10±0.14
Unused SMRs	Left chest	20	8	"*full mode*" OSL	1.00±0.11
Unused SMRs	Left chest	20	8	"*full SAR*" OSL	0.92±0.09
Unused SMRs	Left chest	20	8	"*fast mode*" TL	2.84±0.18
SMRs from MPs	Right side	10	5	"*full mode*" OSL	1.18±0.14
SMRs from MPs	Right side	15	5	"*fast mode*" TL	2.64±0.15
Unused SMRs	Right side	20	8	"*full mode*" OSL	1.11±0.11
Unused SMRs	Right side	20	8	"*full SAR*" OSL	0.99±0.07
Unused SMRs	Right side	20	8	"*fast mode*" TL	2.48±0.12
SMRs from MPs	Left side	20*	5	"*full mode*" OSL	1.18±0.14
Unused SMRs	Left side	20	8	"*full mode*" OSL	1.10±0.12
Unused SMRs	Left side	20	8	"*full SAR*" OSL	1.02±0.11
Unused SMRs	Left side	20	8	"*fast mode*" TL	2.78±0.11
SMRs from MPs	Back	20*	5	"*full mode*" OSL	1.21±0.14
SMRs from MPs	Back	10	5	"*full mode*" OSL	1.16±0.12
SMRs from MPs	Back	15	5	"*fast mode*" TL	2.68±0.10
Unused SMRs	Back	20	8	"*full mode*" OSL	1.12±0.14
Unused SMRs	Back	20	8	"*full SAR*" OSL	0.98±0.10
Unused SMRs	Back	20	8	"*fast mode*" TL	2.44±0.16

*The type of SMRs extracted from mobile phones (MPs) was ´0201´

Table 11.15: Results of the dose reconstruction using SMRs from mobile phones and unused SMRs attached to a water-filled ISO slab phantom irradiated anterior-posterior with an air-Kerma dose of 0.71 Gy at a dose rate of ~ 11 mGy h^{-1} using a ^{137}Cs source. Unless indicated with asterisk, the type of SMRs used were ´0402´.

Sample type	Location	No of SMRs	Delay (days)	Protocol	Dose (Gy)
SMRs from MPs	Front	20*	10	"*full mode*" OSL	0.78±0.11
SMRs from MPs	Front	10	10	"*full mode*" OSL	0.74±0.10
SMRs from MPs	Front	15	10	"*fast mode*" TL	2.18±0.10
Unused SMRs	Front	20	10	"*full mode*" OSL	0.75±0.12
Unused SMRs	Front	20	10	"*full SAR*" OSL	0.72±0.11
Unused SMRs	Front	20	10	"*full SAR*" OSL	0.72±0.11
SMRs from MPs	Back	10	10	"*full mode*" OSL	0.33±0.07
SMRs from MPs	Back	10	10	"*fast mode*" TL	2.23±0.09
SMRs from MPs	Back	15	10	"*fast mode*" TL	0.71±0.11
SMRs from MPs	Back	15	10	"*fast mode*" TL	0.58±0.12
Unused SMRs	Back	20	10	"*full mode*" OSL	0.41±0.09
Unused SMRs	Back	20	10	"*full SAR*" OSL	0.38±0.06
Unused SMRs	Back	20	10	"*fast mode*" TL	0.62±0.13
SMRs from MPs	Right side	20*	10	"*full mode*" OSL	0.53±0.11
Unused SMRs	Right side	20	10	"*full mode*" OSL	0.48±0.10
Unused SMRs	Right side	20	10	"*full SAR*" OSL	0.44±0.08
Unused SMRs	Right side	20	10	"*fast mode*" TL	1.65±0.13
SMRs from MPs	Left side	10	10	"*full mode*" OSL	0.44±0.10
SMRs from MPs	Left side	15	10	"*fast mode*" TL	1.81±0.10
Unused SMRs	Left side	20	10	"*full mode*" OSL	0.48±0.12
Unused SMRs	Left side	20	10	"*full SAR*" OSL	0.40±0.10
Unused SMRs	Left side	20	10	"*fast mode*" TL	1.88±0.15

*The type of SMRs extracted from mobile phones (MPs) was ´0201´

Table 11.16: Values of the personal dose equivalent at a depth of 10 mm [$H_p(10)$] and 0.07 mm [$H_p(0.07)$] registered by the thermoluminescent dosemeters placed around the RA and the ISO slab phantoms.

Location	Irradiation type	Irradiation	Air-Kerma dose	$H_p(10)$	$H_p(0.07)$
Front of RA phantom	ISO High 300 Series x-rays	AP	0.70	0.65	0.78
Back of RA phantom	ISO High 300 Series x-rays	AP	0.70	0.27	0.32
Left of RA phantom	ISO High 300 Series x-rays	AP	0.70	0.66	0.53
Front of RA phantom	ISO High 300 Series x-rays	ROT	0.80	0.78	0.98
Back of RA phantom	ISO High 300 Series x-rays	ROT	0.80	0.81	1.00
Left of RA phantom	ISO High 300 Series x-rays	ROT	0.80	0.72	0.89
Front of ISO phantom	^{137}Cs gamma rays	AP	0.71	0.63	0.78
Back of ISO phantom	^{137}Cs gamma rays	AP	0.71	0.32	0.40
Left of ISO phantom	^{137}Cs gamma rays	AP	0.71	0.56	0.73

Discussion

The first observation to be noted from the results presented above is that the values of the doses estimated using the SMRs are, generally, higher than the air-Kerma dose. This is particularly evident for the doses evaluated using the TL method. However, before discussing the possible reasons giving rise to the over-estimation of the absorbed doses it would be worth mentioning that:

1. Within the calculated uncertainties, the doses obtained using the SMRs extracted from mobile phones do not differ from those obtained with the unused components, confirming the earlier indications that the various parts of the mobile phone do not affect the energy deposited to the resistors for photon energies above ~ 100 keV. Furthermore, and specifically for the irradiations conducted using the RA phantom, there is good agreement between the value of dose obtained for the right and left hip, the right and left chest, and the right and left side of the phantom.
2. The results obtained using samples consisting of higher number (i.e., ~ 20) of SMRs per measurement are ~ 10 % lower (i.e., closer to the delivered doses) than those measured with smaller sample sizes (i.e., ~ 10). Although this difference may not be considered significant, it could provide greater confidence if lower doses were to be measured.

3. The "*full SAR*" OSL protocol resulted in dose values closer by ~ 10-15 % to the delivered doses. Given the significantly higher amount of time needed to complete the full measurement cycle per sample in comparison with the "*full mode*" OSL fast protocol, its omission could be tolerated in a rapid-response dosimetry system.

As a consequence of (1) and in order to compare the reconstructed doses with those measured using the TLDs three regions of interest on the phantoms were defined: front, back, and the sides. The average values of the doses for each region are shown in Table 11.17.

Table 11.17: Values of the absorbed doses reconstructed using the OSL and the TL protocols for three locations on the RA and ISO phantoms.

	OSL METHOD				**TL METHOD**		
Location	**RA phantom**	**RA phantom**	**ISO phantom**	**Location**	**RA phantom**	**RA phantom**	**ISO phantom**
Front	1.12±0.15	1.07±0.10	0.75±0.11	Front	2.30±0.15	2.50±0.14	2.20±0.10
Back	0.36±0.07	1.12±0.12	0.39±0.08	Back	1.19±0.20	2.63±0.16	0.64±0.12
Sides	0.99±0.09	1.10±0.11	0.66±0.10	Sides	2.42±0.15	2.56±0.13	1.78±0.12
Air-Kerma dose (Gy)	**0.70±0.04**	**0.80±0.04**	**0.71±0.04**	**Air-Kerma dose (Gy)**	**0.70±0.04**	**0.80±0.04**	**0.71±0.04**

Except for the doses estimated using the samples positioned on the back of the phantoms and irradiated anterior-posterior which appear lower, due likely to the attenuation of the photon field caused by the presence of the phantoms, the remaining doses are, generally, higher – up to 35 % in some cases (e.g., front of RA phantom for AP irradiation) using the OSL method and on average ~ 80 % using the TL method– than the delivered air-Kerma doses. Two reasons were initially considered to explain the differences. The first is that the fading correction factors applied to the initial dose values may have been highly inaccurate resulting in the over-estimation of the absorbed doses. To exemplify this and determine the extent of uncertainties in

the accuracy of the dose estimates that would be introduced when a universal fading correction formula is used the specific fading of TL and OSL was measured for each one of the samples. The new dose values (Table 11.18) were found to be only slightly different (i.e., maximum difference of ~ 10 %) from the initial values (Table 11.17) confirming previous suggestions (Bassinet, *et al*., 2014; Ekendahl and Judas, 2011) that universal fading factors can, to a good approximation, be used to describe the rate of fading of individual SMRs.

Table 11.18: Values of the absorbed doses reconstructed using the OSL and the TL protocols for three locations on the RA and ISO phantom corrected for the fading effect specific to each sample.

OSL METHOD			
Location	**RA phantom**	**RA phantom**	**ISO phantom**
Front	1.10±0.10	1.12±0.10	0.78±0.10
Back	0.37±0.08	1.09±0.09	0.36±0.07
Sides	0.93±0.08	1.08±0.11	0.60±0.10
Air-Kerma dose (Gy)	**0.70±0.04**	**0.80±0.04**	**0.71±0.04**

TL METHOD			
Location	**RA phantom**	**RA phantom**	**ISO phantom**
Front	2.30±0.15	2.50±0.14	2.20±0.10
Back	1.19±0.20	2.45±0.16	0.60±0.10
Sides	2.42±0.15	2.52±0.13	1.80±0.12
Air-Kerma dose (Gy)	**0.70±0.04**	**0.80±0.04**	**0.71±0.04**

The second cause of the over-estimation of the doses may be associated with the energy of the photon source. As revealed in the previous section, the energy of the photons emitted from the ^{137}Cs source (i.e., 664 keV) is high enough to produce an over-response (i.e., the theoretical, calculated, and experimental values of the photon energy response of the SMRs is ~ 1 for ^{137}Cs) which could explain the fact that for the ^{137}Cs irradiation the differences between the delivered and the measured doses are not so pronounced. However, for the irradiations performed using the High 300 Series x-rays with mean energy 147 keV the photon energy response may be higher than 1. By extrapolating the data shown in Figure 11.12 it was found that the photon energy response of the SMRs embedded in the mobile phones is ~ 1.15 at 147 keV. The data shown in Table 6.18 were, therefore, corrected for the effect of the photon-energy dependence of the alumina substrate. The new dose values (Table 11.19), although they appear lower than the

initial estimates (Table 11.17) they are still higher than the delivered air-Kerma doses (i.e., ~20 % for the OSL method and up to ~ 70 % for the TL). It is speculated that backscattered radiation generated by the phantoms can increase the energy deposited to the dosemeters resulting also in higher doses.

Table 11.19: Values of the absorbed doses reconstructed using the OSL and the TL protocols for three locations on the RA and ISO phantom corrected for the photon-energy dependence effect of the alumina SMRs.

OSL METHOD				TL METHOD			
Location	**RA phantom**	**RA phantom**	**ISO phantom**	**Location**	**RA phantom**	**RA phantom**	**ISO phantom**
Front	0.96±0.12	0.97±0.10	0.78±0.10	Front	2.00±0.12	2.17±0.15	2.20±0.10
Back	0.32±0.08	0.95±0.09	0.36±0.07	Back	1.03±0.17	2.13±0.13	0.60±0.10
Sides	0.81±0.08	0.94±0.11	0.60±0.10	Sides	2.10±0.15	2.19±0.13	1.80±0.12
Air-Kerma dose (Gy)	**0.70±0.04**	**0.80±0.04**	**0.71±0.04**	**Air-Kerma dose (Gy)**	**0.70±0.04**	**0.80±0.04**	**0.71±0.04**

To further investigate the validity of the dose reconstruction process and of the corrections applied a comparison of the doses measured using SMRs with those registered by the TLDs was made. As seen in Table 11.20, the doses reconstructed using the OSL method are, with a few exceptions, consistent with the values of the $H_p(0.07)$ and $H_p(10)$ doses. It could, thus, be argued that the SMRs from mobile phones analysed using the OSL method can be used to monitor personal doses as long as specific details, such as the energy of the radiation field and the location of the mobile phone on the individual's body, of the exposure are known. Moreover, the facts that (1) the TLD doses for the back of the phantoms irradiated anterior-posterior are lower than the air-Kerma doses, and (2) the $H_p(0.07)$ doses, representing the doses to the skin, are higher than the air-Kerma doses support the earlier suggestions about the influence of the attenuation and backscatter properties of the phantom on the measured doses.

Table 11.20: Comparison between the doses reconstructed using SMRs (analysed with the OSL method) and the doses registered by the TLDs for three locations about the RA and ISO phantom.

RA Phantom-AP irradiation Air-Kerma dose: 0.70±0.04 Gy				**RA Phantom-ROT irradiation** Air-Kerma dose: 0.80±0.05 Gy				**ISO Phantom-AP irradiation** Air-Kerma dose: 0.71±0.04 Gy			
Region	**SMRs (Gy)**	**$H_p(10)$ (Sv)**	**$H_p(0.07)$ (Sv)**	**Region**	**SMRs (Gy)**	**$H_p(10)$ (Sv)**	**$H_p(0.07)$ (Sv)**	**Region**	**SMRs (Gy)**	**$H_p(10)$ (Sv)**	**$H_p(0.07)$ (Sv)**
Front	0.96±0.12	0.65±0.10	0.78±0.10	Front	0.97±0.10	0.78±0.10	0.98±0.10	Front	0.78±0.10	0.63±0.10	0.78±0.10
Back	0.32±0.08	0.27±0.09	0.32±0.07	Back	0.95±0.09	0.81±0.09	1.00±0.07	Back	0.36±0.07	0.32±0.09	0.40±0.07
Sides	0.81±0.08	0.53±0.11	0.66±0.10	Sides	0.94±0.11	0.72±0.11	0.89±0.10	Sides	0.46±0.10	0.56±0.11	0.73±0.10

On the other hand, the TL method failed to give the correct values of the absorbed doses. Since the possible uncertainties that could be introduced by the fading of the samples and the energy of the radiation field were examined and presumably (based on the results obtained using the OSL method) were accounted for correctly it is speculated that there should be a luminescence property which changes either during the delay period or during measurement and presumably manifests itself during the acquisition of the TL only. Nevertheless, by the time of completion of the thesis, it was not made possible to identify what causes the delayed TL response to appear significantly higher than what it would be expected based on the anomalous fading behaviour. It is speculated that the over-estimation of the absorbed doses may be caused by the considerably different dose rate used in the phantom experiments than the one used in laboratory irradiations. If this is the case, then, it has to be answered why the OSL response does not present similar behaviour.

11.10 Dose reconstruction using mobile phones: Simulation approach

11.10.1 Introduction

In addition to experiments, Monte Carlo modelling (Eakins and Kouroukla, 2015) of different exposure situations was also performed, considering various photon exposures of mobile phones positioned free-in-space, on a slab phantom, and at different locations around a voxel phantom model of the ICRP reference male (ICRP, 2008). The doses per applied fluence in resistors within these phones were determined, and compared against one another and against the concurrent doses per applied fluence in the various organs of the body, as well as against estimates of the whole-body average absorbed doses per fluence. Some of the doses to the organs of the body are directly comparable to those in the ICRP reference values set (ICRP, 2010), providing important quality assurance of the calculation method. However, additional geometries were used that replicate accident/terrorist scenarios that could not be taken directly from the reference data, and have not been considered elsewhere (Zankl, 1999; Hervé *et al*, 2007). First, the effects of phone's geometry on dosimetry were investigated with particular interest on the positions of the resistors within the phone and whether the phone is exposed from the front or the back. Finally, the impact of the phone location was examined, with the implications of this for accurate retrospective dosimetry considered. Estimates were then given for the magnitudes of the uncertainties that might result when this information is not available, with the subsequent limitations on the emergency dosimetry service then discussed. The physical feasibility of some potential emergency scenarios was also briefly considered.

The main objective of the Monte Carlo modelling was to derive correction / calibration factors that can be applied to ensure that the luminescence readings from phones give good estimates of whole body doses, where the particular emphasis is on avoiding significant underestimates (or at least accounting for them). In fact, several calibration factors can be derived to cope with different generic photon irradiation conditions, the correct application of which would require knowledge of the geometry of the exposure. Of course, it is unlikely that such information will be available in all emergency scenarios, but for specific investigations of the doses received by

small numbers of individuals, detailed data on the direction of exposure may be obtainable and prove useful.

11.10.2 Phone positioned in free space

In the first instance, radiation transport simulations were performed for photon source exposures of the phone located off-phantom, i.e. in free space. In photon-only transport mode, the phone was surrounded by vacuum, with doses estimated via MCNP *f6:p* kerma tallies under the assumptions of the kerma approximation. In the more physically realistic coupled electron-photon mode calculations, however, the phone was surrounded by a mass-thickness of air sufficient to induce secondary charged particle equilibrium from the source in question, with doses to the resistors estimated using MCNP **f8:p,e* event tallies.

Initially, plane-parallel exposures of the phone were performed from its front, i.e. with photons impinging perpendicularly to its glass screen, using monoenergetic sources with energies from 20 to 2000 keV. The doses to the resistors were calculated, and the results normalised to the photon fluence in the case where all materials have been set to vacuum; these applied fluences were the same for all of the *mode p* calculations, because a common planar source of fixed size was used throughout, but differed in the case of the electron-photon calculations because the size of the source had to increase proportionally with the volume of the surrounding air to ensure that the in- and out-scatter of secondary electrons was accounted for correctly.

Figure 11.15 shows the dose per fluence results as a function of energy for both resistors and both transport modes. From the four datasets, a number of observations are evident:

1. The dose responses of the resistors vary with energy. This general result was also confirmed experimentally above, and is a consequence both of the energy-dependence of response of the Al_2O_3 itself, and of the energy-dependent attenuations of the materials that surround the resistors within the phone.

2. For a given transport mode, the results for R1 and R2 agree well as a function of energy. Specifically, the largest difference within each mode-dependent pair of

datasets is ~ 7 % and the mean difference is ~ 3%, both of which should be taken in context with the statistical uncertainties on the individual datapoints, which are of a similar magnitude.

3. Although the *mode p* and *mode p e* datasets are in good agreement at low energies, elsewhere they diverge, in agreement with the results for the photon energy response presented in section 11.7. The greatest discrepancies between the data occur for the 100 keV exposure, where a difference of over 20 % is found.

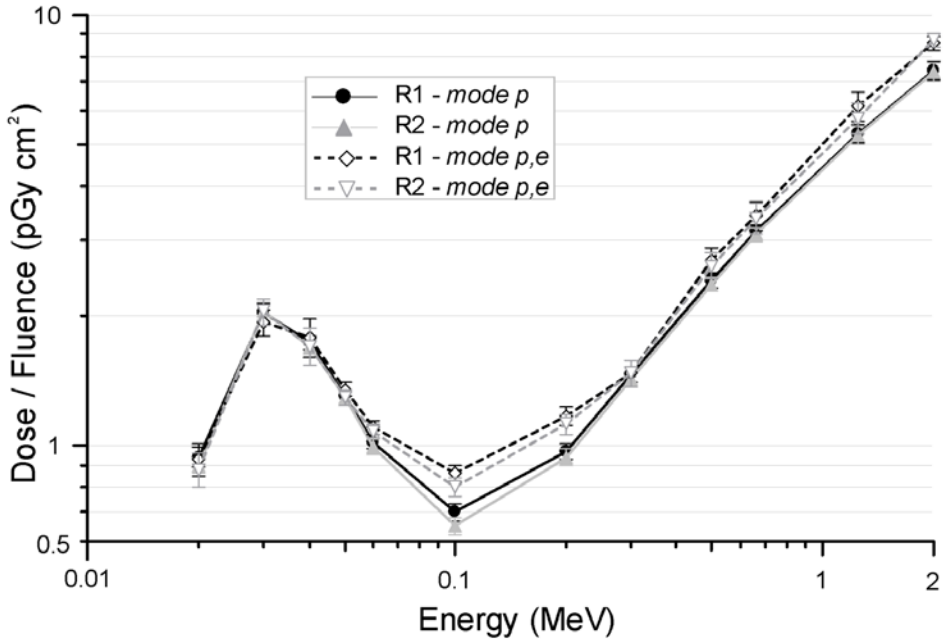

Figure 11.15: Dose per fluence results as a function of energy for both resistors and both transport modes for a free-in-space phone exposed from the front.

Nevertheless, this final result was surprising, since although discrepancies are sometimes observed at high energies due to misapplications of the kerma approximation as secondary electron ranges increase, equivalence is typically exhibited at lower energies. To investigate the cause of these differences, a number of alternative phone models were developed so that individual parameters could be varied: modifications included using different compositions or densities for the circuit board, metal covers, battery, or the contacts. In every case, both *mode p*

and *mode p e* calculations were performed (results are not presented). In addition, MCNP '*f1*' current tallies were defined on each of the six faces of the resistors to determine the numbers of photons and electrons passing through them, with the 'cell flagging' option also employed to ascertain whether the particles had encountered the resistor previously during their histories. The general conclusion drawn from these simulations was that the differences between the *mode p* and *mode p e* data shown in Figure 11.15 were caused primarily by the presence of the metal contacts that surround the aluminium oxide (Figure 11.8). In particular, it was shown that if the materials of these contacts were changed to air (i.e. the contacts were essentially removed from the geometry) the doses to the resistors in both *mode p* and *mode p e* agreed. Furthermore, it was found that although the photon fluxes across a given surface of a resistor were fairly consistent in both cases and for both *mode p* and *mode p e* calculations, using air 'contacts' led to an increase in the number of electrons that crossed the rear surface of the resistor, which is the surface with greatest area touching the contacts; for the 100 keV source, this enhancement was ~ 70 %. The 'cell flagging' showed that almost all of these electrons had previously left the resistor volume. These results imply that the metal contacts caused about ~ 70% of the electrons to be scattered back into the Al_2O_3, where they deposit dose. Since this backscattering appears only to affect the electrons significantly, it explains why the *mode p e* results were greater than the *mode p* results. The magnitude of the backscatter will depend on electron energy, due to the dependence on this of both the electrons' ranges through the media and their scattering angles following atomic interactions: at low energies, for instance, it is likely that the ranges of the secondary electrons created in the Al_2O_3 may be too short for significant backscatter subsequently to arise. For higher energies the longer range electrons may penetrate the metal contact more efficiently and hence be backscattered less.

The above situation represents a breakdown of the kerma conditions occurring on the micro-scale at the interface between two materials of different densities and effective atomic numbers (Z_{eff}), and demonstrates why the *mode p e* calculations are important and more accurate than *mode p*. But more than this, the result indicates a significant observation: the presence (and composition) or absence of the metal contacts surrounding the resistors in a phone could directly affect the dosimetry by up to a few tens of percent. This is important, because the components, materials, and even presence of the contacts are not universal across different phones and different manufacturers; the effect could also depend on the size of the resistors relative to their

contacts, where the metal to alumina ratio may be higher or lower. The implication, therefore, is that rather than highlighting a limitation to the modelling, the potential for dose enhancement that arises from the possible use of metal contacts should be used to inform the overall uncertainty budget of the retrospective dosimetry method.

Whilst personal dosemeters ought to be worn on the body with their reference direction facing outwards and roughly towards the source, no such assumption can be made about mobile phones because they are likely to be placed in a pocket with no consideration of their orientation. Plane-parallel exposures of the phone were hence also modelled from its rear, i.e. with photons impinging perpendicularly to its back plastic case behind the battery, using monoenergetic sources with energies from 20 to 2000 keV. Figure 11.16 shows the dose per fluence results as a function of energy for both resistors and both transport modes. Again, a number of observations may be made:

1. At low energies, i.e. below about 100 keV, the results for R1 from the *mode p* calculations agree with those from the *mode p e* calculations; likewise, the results for R2 from the *mode p* calculations similarly agree with those from the *mode p e* calculations. However, the results for R1 differ from those for R2, which are significantly higher. It is suggested that the reason for this discrepancy is the positioning of R1 behind the battery: the ~ 1.3 g cm^{-2} mass-thickness of material provided by the battery provides an effective shield for R1 for exposures from the rear, but R2 is not protected in this line-of-sight manner. The doses deposited in R2 are therefore considerably greater than those deposited in R1; at 30 keV, for example, the dose per fluence to R1 is almost 90 % lower than that to R2.

2. At higher energies, the results from the *mode p* calculations for R1 and R2 are closer in magnitude: above 100 keV, the differences between the R1 and R2 results are < 5%, which are commensurate with the statistical uncertainties on the data. This is also true for the results from the *mode p e* calculations. These agreements are as expected: for photons of increasing penetration, the effects of shielding of R1 by the battery are gradually diminished.

3. The results from the *mode p e* calculations do not always agree with those from the *mode p* calculations at higher energies, with discrepancies of several tens of percent exhibited at 100 and 200 keV. Similarly to exposures from the front, the explanation of this is a breakdown of the kerma equilibrium on the micro-scale due to the inhomogenous distribution of materials of different Z_{eff} and density surrounding the resistors. Specifically, differences in electron ranges, absorptions, transmissions and backscattering as a function of energy can lead to a net in- or out-flux of secondary electrons through the tallied volumes, so that neglecting the transport of electrons and making the kerma approximation can lead to errors in the estimates of absorbed dose to the aluminium oxide.

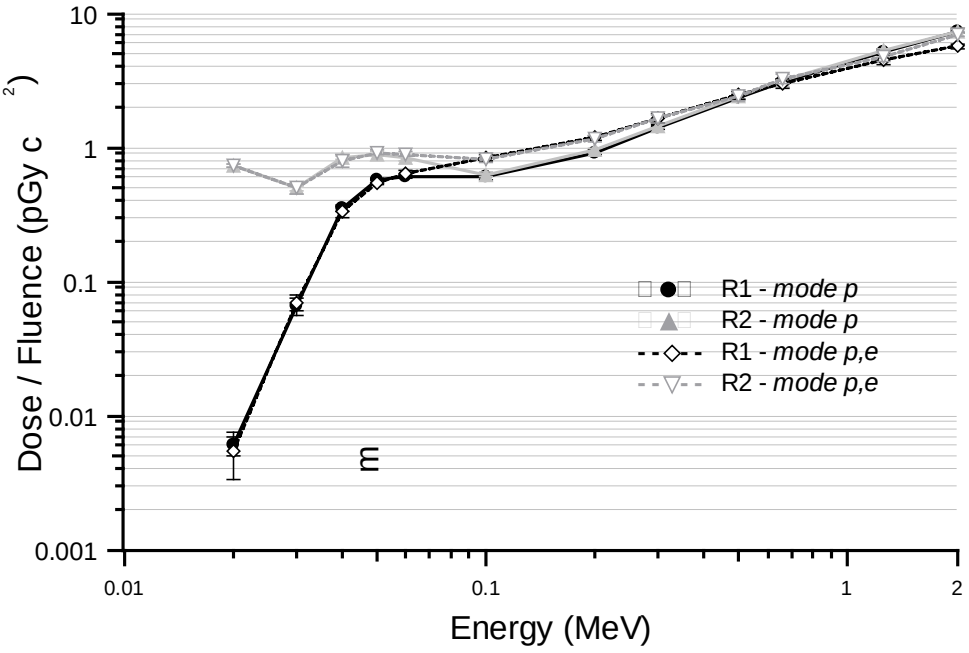

Figure 11.16: Dose per fluence results as a function of energy for both resistors and both transport modes for a free-in-space phone exposed from the back.

Despite the differences highlighted in '3)', and the similar observations made for the phone exposed from the front, only *mode p* calculations have been performed for the work described in subsequent sections of this study, with the general validity of the kerma approximation assumed.

The adoption of this photon-only mode conveys significant advantages in terms of calculation efficiencies, and hence on the precision of the results, which will be essential later when the geometry is greatly enlarged to include a voxel phantom. The approximation is made, however, with the caveat that the discrepancies shown here between the *mode p* and *mode p e* data must subsequently be added to the overall uncertainty budget of the dose reconstruction method. This transfer of this uncertainty is justified, and indeed necessary, from the lack of consistency in the use or presence of metal contacts in different mobile phones, which will represent a genuine source of uncertainty in the determination of doses from measurements of different resistors, as well as perturbing the self-calibration process used in SAR dose reconstruction (Bøtter-Jensen *et al*, 2003) due to the complete or partial removal of the contacts that is likely to take place after the exposure to the accident dose but before the exposure to the calibration dose.

Using the *mode p* data given in Figures 11.15 and 11.16, Table 11.21 shows the mean doses per fluence, $[D_{R12}^{M}/\Phi]$, for each exposure averaged over R1 and R2, as well as the differences between the R1 and R2 doses per fluence given relative to these means, $\delta = |D_{R1}\text{-}D_{R2}| \div D_{R12}^{M}$. As expected, the R1 and R2 results were seen to agree well in general, apart from for low energy exposures from the rear. Also shown in Table 11.2 are the quantities $\Delta_{f,r}$ defined at a given energy as the magnitude of the difference between the mean dose per fluence results for front (subscript '*f*') and rear (subscript '*r*') exposures given relative to the smallest dose per fluence deposited in either resistor for either exposure direction, that is:

$$\Delta_{f,r} = \left| \frac{[D_{R12}^{M}/\Phi]_f - [D_{R12}^{M}/\Phi]_r}{Min\{[D_i/\Phi]_j : i=R1,R2\ ; j=f,r\}} \right| \qquad (1)$$

The parameter $\Delta_{f,r}$ is just one way of indicating the divergences in the sets of results: at low energies it is clear that the direction of exposure significantly affects the dosimetry, but at higher energies the impact of the orientation of the phone relative to the source becomes less significant; above 300 keV, the issue of whether the phone is exposed from the front or from the rear is essentially irrelevant, with the resulting dosimetry affected by less than 1 %. At the energies of the radionuclide sources that may be considered most important for emergency dosimetry (e.g. ^{137}Cs, ^{60}Co or ^{192}Ir) the battery of the mobile phone does not appear to perturb the response significantly, but it is clear that it could have a big impact on the accuracy of dosimetry

for low energy exposures. If a phone had a bulkier battery, however, then its shielding effect would be maintained to higher photon energies, though this may not be of particular concern because phone designs are, in general, becoming slimmer with time. Whilst ^{137}Cs, ^{60}Co or ^{192}Ir may be the sources considered to be most effective for someone planning a malign exposure of the public, it must also be borne in mind not only that such individuals are likely to make use of whatever is available, but also that emergency dosimetry may be required following non-malign exposures of the public: other sources must therefore be considered, such as a low energy photon emitter such as ^{241}Am or an x-ray tube.

Table 11.21: Mean doses deposited per fluence in resistors of mobile phones exposed to photons from the front or rear.

Energy (MeV)	*Front Exposure*		*Rear Exposure*		*Both Exposures*
	$[D_{R12}{}^{M}/\Phi]_f$	δ_f [(a)]	$[D_{R12}{}^{M}/\Phi]_r$	δ_r [(a)]	$\Delta_{f,r}$ [(b)]
	pSv cm^2		pSv cm^2		
0.02	0.92 (0.05)	0.04	0.37 (0.02)	1.97	98.8
0.03	2.04 (0.10)	0.01	0.28 (0.01)	1.53	26.4
0.04	1.71 (0.07)	0.02	0.59 (0.03)	0.82	3.19
0.05	1.30 (0.05)	0.01	0.73 (0.03)	0.45	1.01
0.06	1.01 (0.04)	0.03	0.72 (0.03)	0.30	0.478
0.10	0.67 (0.03)	0.07	0.62 (0.02)	0.06	0.096
0.20	0.96 (0.04)	0.03	0.94 (0.04)	0.04	0.019
0.30	1.44 (0.06)	0.02	1.43 (0.06)	0.02	0.009
0.50	2.39 (0.10)	0.02	2.39 (0.10)	0.02	0.002
0.66 (^{137}Cs)	3.11 (0.12)	0.02	3.11 (0.12)	0.01	0.001
1.25 (^{60}Co)	5.27 (0.26)	0.01	5.26 (0.21)	0.02	0.002
2.00	7.39 (0.37)	0.01	7.37 (0.29)	0.01	0.002

[(a)] Defined for a given orientation as the difference between the R1 and R2 dose per fluence results as a fraction of their mean, δ

[(b)] Defined as the magnitude of the difference between the mean dose per fluence results for front and rear exposures given relative to the smallest dose per fluence deposited in either resistor for either exposure direction

Overall from Figures 11.15 and 11.16 and Table 11.21, no clear systematic relationships were generally apparent when R1 versus R2 results were compared, either in terms of their positions within the phone or of the orientation of the phone relative to the exposure; the exception to this generality is for low-energy exposures of phones from the rear, in which the dose to R1 is significantly lower. These are important conclusions: in general in an emergency, it is unlikely

that it will be known whether the source photons impinged on the front or the back face of a phone, and likely that there will be little time available to accurately analyse or document the precise locations of the resistors within the phones. This latter difficulty is confounded by the fact that several resistors will need to be extracted from each phone to fill the cups necessary for accurate TL/OSL dosimetry, and each of these resistors will inevitably be at a different position. Although only two resistor positions within the phone have been considered in the present Monte Carlo modelling and only two exposure directions, the results found here may indicate that the position of the resistors and the orientation of the phone relative to the source may not greatly impact the doses subsequently found: for photons above ~ 100 keV a combined value of no more than ~ 5 % might be an appropriate assessment of the contribution from these uncertainties to the overall budget of the dosimetry technique. This uncertainty will be much larger for lower energy photons (< 100 keV), for which the position of the resistor has a significant influence on the estimated dose because of the disparate attenuation of the photons by the various components within the phone.

11.10.3 Phone positioned on ISO slab phantom

In addition to the calculations performed above in free-space, simulations were performed with the phone located at the centre of the front face of a 30×30×15 cm^3 water-filled ISO slab phantom. Essentially, the aim of these calculations was to provide a preview and check of the results from the subsequent voxel phantom calculations, which are more advanced and realistic but at the disadvantage of being much more computationally demanding and accordingly yielding results with poorer statistical power; the simpler slab phantom calculations are quicker to perform and lower energy sources could be considered.

The on-phantom calculations were carried out using the photon-only transport mode, with absorbed doses per fluence estimated using *f6:p* tallies normalised to the photon fluence from the source in the absence of the phone and phantom. Six different source energies (0.05, 0.1, 0.2, 0.3, 0.662, and 1.253 MeV) were considered, with four different irradiation geometries:

1. '*AP, Out*': with the phantom exposed from the front (anterior-posterior, AP) and the glass face of the phone facing outwards, i.e. towards the source and away from the phantom;

2. '*PA, Out*': with the phantom exposed from the rear (posterior-anterior, PA) and the glass face of the phone facing outwards, i.e. away from the source and away from the phantom;

3. '*AP, In*': with the phantom exposed from the front (AP) and the glass face of the phone facing inwards, i.e. away from the source and into the phantom;

4. '*PA, In*': with the phantom exposed from the rear (PA) and the glass face of the phone facing inwards, i.e. towards the source and into the phantom.

The dose per fluence results for resistors R1 and R2 are shown in Table 11.22. Three observations are immediately apparent from considering the results. Firstly, for a given exposure, it is seen that the dose deposited in R1 is generally similar to that deposited in R2; this is as expected from the conclusions of the previous section, i.e. that the position of the resistor within the phone does not appear to impact the dosimetry greatly. Also as might be expected, the differences between the R1 and R2 doses decrease with increasing energy, with the greatest discrepancies occurring for the 50 keV exposures, the photons from which would be most significantly affected by their disparate attenuations through the asymmetrically-distributed materials that surround the resistors. Given the broad similarity between the R1 and R2 results above 100 keV, it is reasonable to compute their mean for a given exposure, allowing the trends in Table 11.22 to be better illustrated (Figure 11.17); at lower energy, the usefulness of these mean data should be treated with more skepticism, due to the greater discrepancies in the R1 and R2 results.

Table 11.22: Doses deposited per fluence in resistors of a mobile phone located on an ISO water-filled slab phantom and exposed to plane-parallel photon sources, and the same data given normalised to the mean of the R1 and R2 results for 0.662 MeV exposures at *AP,Out*. Fluence to personal dose equivalent conversion coefficients for AP (i.e. 0^0) exposures are also included for comparison.

Energy, *E* (MeV)	Absorbed Dose / Fluence (pGy cm^{-2}) [(a)]								$H_p(10,0^0)$/ Fluence (pSv cm^{-2})
	Resistor 1				Resistor 2				
	AP, Out	*PA, Out*	*AP, In*	*PA, In*	*AP, Out*	*PA, Out*	*AP, In*	*PA, In*	
0.050	1.39	0.061	0.85	0.20	1.51	0.11	1.28	0.20	0.58
0.100	0.96	0.19	1.02	0.29	1.00	0.24	1.08	0.29	0.67
0.200	1.28	0.38	1.30	0.45	1.26	0.42	1.31	0.44	1.28
0.300	1.73	0.65	1.76	0.66	1.75	0.65	1.80	0.65	1.89
0.662	3.37	1.69	3.39	1.67	3.34	1.67	3.36	1.66	3.77
1.253	5.50	3.20	5.50	3.24	5.43	3.23	5.34	3.20	6.15
	Absorbed Dose / Fluence relative to *AP,Out* exposure to ^{137}Cs [(a)]								
0.050	0.41	0.018	0.25	0.058	0.45	0.033	0.38	0.059	-
0.100	0.29	0.057	0.31	0.088	0.30	0.072	0.32	0.085	-
0.200	0.38	0.11	0.39	0.14	0.38	0.12	0.39	0.13	-
0.300	0.52	0.19	0.53	0.20	0.52	0.19	0.54	0.20	-
0.662	1.00	0.50	1.01	0.50	1.00	0.50	1.00	0.49	-
1.253	1.64	0.95	1.64	0.97	1.62	0.96	1.59	0.95	-

[(a)] Statistical uncertainties on the MCNP data are of the order of a few %.

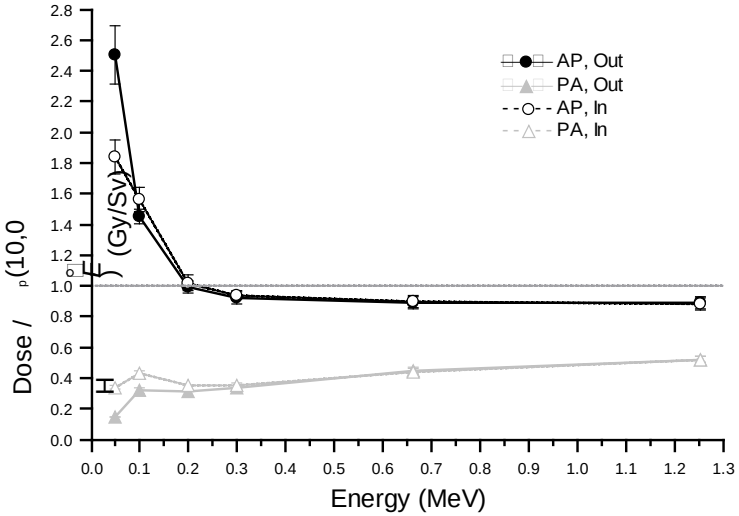

Figure 11.17: Dose per fluence results averaged over both resistors as a function of energy, *E*, and normalized to $H_p(10,0^o,E)/\Phi$, for phones facing both into and away from an ISO slab phantom and exposed to photons from both AP and PA directions.

A second observation from Table 11.22 and Figure 11.17 is that, for a given direction of exposure (i.e. AP or PA), the results at higher energies are fairly insensitive to the orientation of the phone towards or away from the phantom. This conclusion is also partly expected from a consideration of the results presented in the previous section for a phone located off-phantom, but is enhanced in the current situation in a manner that depends on the exposure direction. Specifically, for AP exposures, the effects of the asymmetric nature of the phone are, to an extent, cancelled-out by the production of significant backscattered radiation from the phantom: essentially, the combination of 'direct' photons from the source and 'indirect' photons backscattered from the phantom leads to the situation that, whichever way the phone is orientated, its resistors are simultaneously being exposed from both the most and least shielded directions. It is backscatter that also accounts for the AP doses being higher than those previously calculated for the phone in free space, with differences of up to ~ 70 % found at 0.1 MeV; this result alone demonstrates the problems faced by considering phone doses in isolation, without reference to their locations. For PA exposures, the differences in the shielding of the resistors that are caused by orientating the phone towards or away from the phantom are small compared to the attenuation that results from photons passing through at least 15 cm of water and polymethyl-methacrylate that comprises the ISO slab phantom. The greatest differences between 'In' and 'Out' data for a given exposure direction are at 50 keV, which, again, is as expected: at lower energies even small differences in the attenuation of photons on their paths to the resistors can still be important, so factors such as the location of the battery or circuit board relative to a resistor may still have some significance.

The third observation from Table 11.22 is that the direction of exposure (i.e. AP or PA) drastically affects the dose deposited in the resistors: the results for PA are significantly lower than those for AP. The differences between the AP and PA results are seen to increase with decreasing energy: at 1.253 MeV, for instance, the PA dose is ~ 60 % that of the AP dose, but at 0.1 MeV a difference by a factor of ~ 5 is seen. Again, these differences are expected, and emphasise the significant dependence of the results on the exposure geometry. The implications of this problem are illustrated by comparing (Figure 11.17) the results produced here with the fluence to personal dose equivalent conversion coefficients $H_p(10,0^o,E)/\Phi$ for AP (i.e. 0^o) exposures of energy E (ICRU, 1998), with values for $H_p(10,0^o,E)/\Phi$ at 0.662 and 1.253 MeV

interpolated from the tabulated monoenergetic data. Conversion coefficient data for PA exposures, i.e. $H_p(10,180°,E)/\Phi$, are not included in (ICRU, 1998), so cannot also be considered here or used to provide an alternative comparison; this should not be a significant problem, however, because the $H_p(10,0°,E)/\Phi$ data may be considered to provide a reasonable first estimator of whole body doses for the present purposes, and are in any case primarily being used just to provide a convenient normalisation with which to contrast the datasets. Evidently, personal dose equivalent is underestimated for all geometries and energies apart from AP exposures below 0.2 MeV photons, for which the phone dose overestimates the quantity. Aside from the geometric issues, the non-tissue equivalence of alumina SMRs will also play a part in these differences. For the AP exposures above 0.2 MeV, the underestimate of $H_p(10,0°,E)/\Phi$ by the resistors is not large (up to ~ 10 %) and is fairly constant, leading to the suggestion that a single correction factor could potentially be applied for this irradiation condition to relate a phone dose to the dose received by its owner. However for PA exposures, the personal dose equivalent is underestimated significantly by the resistors and the energy dependence is less flat at higher energies. Of course, these differences for PA exposures have an obvious explanation, and it is acknowledged that using $H_p(10,0°,E)/\Phi$ is not really the correct method for determining risk in this case. But, the comparison does serve to illustrate the considerable impact that the location of the phone can have on the dose it receives, and introduces the scale of the problem that would be encountered if phone doses were automatically associated with doses to the person.

It is noted that the trends highlighted in this section become particularly apparent from the lower half of Table 11.22, in which the data were re-expressed relative to the mean of the R1 and R2 '*AP, Out*' doses per fluence for ^{137}Cs. This normalization is important because it is a measurement that could naturally be picked to provide a convenient calibration for the retrospective dosimetry system (for instance to check the emission rates of any internal radiation sources that might be used by the measurement equipment during the dose reconstruction process, such as that found in the '*Risø TL/OSL Reader*' commonly used in retrospective dosimetry), as it is analogous to the exposure conditions typically used by dosimetry services to calibrate personal dosemeters (IEC, 2012). Indeed, by comparing the data in Tables 11.21 and 11.22, energy-dependent conversion factors may readily be derived for the retrospective

dosimetry system that relate free-in-space phone doses to phone doses received on-phantom; for ^{137}Cs, for example, it is seen that the mean '*AP, Out*' result is approximately 1.08× the mean resistor dose-per-fluence received when the phone is located free-in-space, with the difference caused by backscatter from the phantom. Alternative calibration factors could similarly be derived, such as by considering calibration doses applied to 'free' resistors removed from phones.

11.10.4 Phone positioned on ICRP male voxel phantom

Model set-up

The phone model was embedded within an MCNPX input file that contained a rendering of the voxel phantom corresponding to the ICRP reference male (ICRP, 2008). The entire phantom-phone configuration was surrounded by vacuum, with all calculations performed using photon-only transport (*mode p*) under the general assumptions of the kerma approximation; in real emergency scenarios, secondary charged particle equilibrium incident on the phone is likely to be fulfilled because exposed individuals, and hence their phones, are likely to be considerable distances from the radiation source. This decision was made on the basis of the significant advantages of *mode p* over coupled electron-photon transport in terms of simulation efficiency, especially given the large spatial extent of the voxel geometry, and justified from the reasonable equivalence of the two methods that may be anticipated if the potential dose enhancement from the metal contacts surrounding the resistors has been subsumed within the overall uncertainty budget of the dose reconstruction method (Figures 11.16 and 11.17); dosimetry within the body is discussed further below. Four locations of the phone about the body were considered:

1. '*Chest*', i.e. with the phone centred close to the location of the heart, as shown in Figure 11.18a. This configuration is representative of a phone positioned in an inside jacket or breast pocket.

2. '*Leg*', i.e. with the phone centred just in front of the left thigh, as shown in Figure 11.18b. This configuration is representative of a phone positioned in a trouser front pocket.

3. '*Back*', i.e. with the phone centred just behind the left buttock, as shown in Figure 11.18c. This configuration is representative of a phone positioned in a trouser back pocket.

4. '*Hip*', i.e. with the phone centred close to the left hip, as shown in Figure 11.18d. This configuration is representative of a phone positioned either in the outside pocket of a jacket, or held in the left hand, or inside a handbag or shoulder bag with its strap over the left arm.

The approximate (x,z) positions, in centimetres, of resistor R1 relative to the body's centre line (x=0) and the soles of the feet (z=0) were, respectively, (6, 131), (9, 76), (7, 88) and (19.5, 93) in the four cases. These may be used as reference co-ordinates to illustrate the approximate locations of the phones relative to the body. Taken as a set, it is suggested that the four configurations cover a number of the most likely places for mobile phones to be located about the person. In the Chest, Leg and Back configurations, the glass front of the phone was parallel to the x-z plane (Figures 11.18a-c); in the Hip configuration it was parallel to the y-z plane (Figure 11.18d). In each case, the y positions of R1 were such that the phones were nearly in contact with the skin.

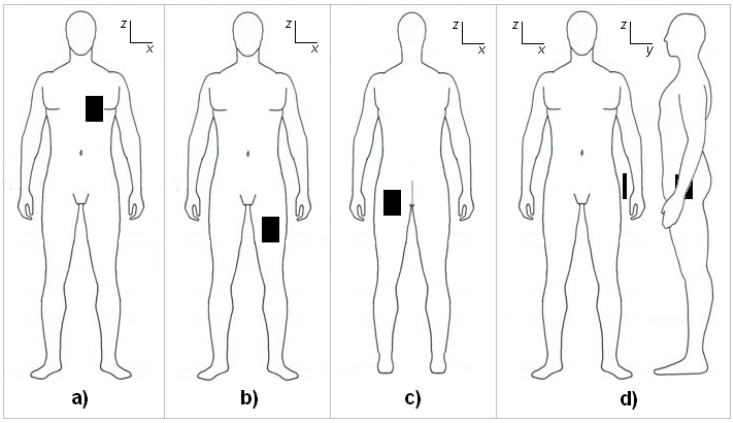

Figure 11.18. Illustration of the approximate locations of the phones (black rectangles) in the four geometries of interest: *a*) Chest, *b*) Leg, *c*) Back and *d*) Hip. [*Original human anatomy outline reproduced from* http://hippie.nu/~unicorn/tut/xhtml/]

For the current analysis, attention was restricted to exposures from Cs-137 (which was assumed to be a pure source of monoenergetic 662 keV photons), Co-60 (which was modelled as an equal distribution of 1173 and 1333 keV photons), and Ir-192 [modelled with an energy spectrum taken from the Brookhaven National Laboratory resource (NNDC)], the strongest photon component of which has an energy of 312 keV). Six exposure geometries, *G*, were considered:

- Four planar sources, from the four cardinal directions: anterior-posterior (AP); posterior-anterior (PA); left-lateral (LLAT); and right-lateral (RLAT). In all cases, the photons were emitted perpendicularly from planes of sufficient spatial extent to completely cover the phantom-phone configuration. These sources could be considered to represent exposures from point sources that are a sufficiently far away from the body to render inverse-square divergences negligible.

- Isotropic (ISO). Photons were emitted isotropically from a spherical shell of radius 102 cm centred such that the phantom-phone configuration is (only just) enclosed completely, to give a field that is isotropic and homogenous everywhere within it. This source could be imagined to represent exposures to an individual who is immersed in an infinite 'cloud' of radionuclide, of uniform spatial dispersion.

- Floor (FLR). Photons were emitted semi-isotropically from a disc of radius 200 cm, orientated in the *x*-*y* plane and centred at the position (0, 0), i.e. on the body's centre line and level with the soles of the feet. This source was considered to represent a scenario in which a radionuclide is spread uniformly across the surface of the ground; the validity of this approximation is discussed later.

A seventh exposure scenario was also considered indirectly: by taking the mean of the AP, PA, LLAT and RLAT data, results could be estimated that may be expected to approximate those from rotational exposures (labelled ROT*, where the asterisk reminds that this is not a true rotational field). Arguably, these results are actually more relevant than those from any of the four planar exposures themselves: in a real emergency, individuals are likely to move both translationally and rotationally relative to the source, leading to them (and their phones) becoming exposed from a wide range of directions. All of the simulations for ^{192}Ir and ^{60}Co were performed with the glass screen of the phone facing away from the phantom; this choice was

fairly arbitrary, however, given the independence of the results shown previously on the orientation of the phone relative to the phantom. As an extra check of this, however, two specific cases of phone orientation were considered during the ^{137}Cs exposures: with the glass front of the phone facing out, i.e. away from the body (labelled '*Out*'); and with the glass front of the phone facing in, i.e. towards from the body (labelled '*In*').

For each exposure, doses were recorded in the cells representing the aluminium oxide substrate of the resistors in the phones, and 27 tissues or organs identified as key for biological dosimetry (ICRP, 2007). These organs or tissues were: adrenal glands, urinary bladder, brain, breast, extra-thoracic region, gall bladder, stomach, small intestine, colon, heart, kidneys, liver, lymphatic nodes, lungs, muscles, oesophagus, oral mucosa, pancreas, salivary glands, skin, spleen, thymus, thyroid, prostate, testes, red bone marrow (RBM) and endosteal (bone surface) tissues. All doses were estimated via *f6:p* kerma tallies defined using the relevant volumes of interest, i.e. the cells representing the resistors and organs, with the exception of RBM and endosteal tissue, for which the dosimetry is more complex. There are two reasons for this complexity. Firstly, the sizes of the 2.137×2.137×8 mm^3 voxels are too large to define in the model the distinct tissues of radiological importance inside the major bones; the materials filling these voxels are defined simply as homogenous mixtures that represent an average of red marrow, yellow marrow, endosteal, and trabecular tissues, and so the doses to just the RBM or endosteal tissue cannot be resolved individually. Secondly, the presence of the interspersed trabecular tissue in real bones undermines the validity of using the kerma approximation for their dosimetry. Specifically, the sharp difference in density and composition at the interface between trabecular bone and RBM, and the inhomogeneity of the RBM / trabeculae structure on the microscopic scale, destroys the secondary-electron equilibrium that may be assumed for most other organs. In particular, photoelectrons are more readily produced in the trabecular bone than in the RBM, and the bone is also a more efficient electron absorber; this is important, because the ranges of the secondary electrons are large compared to the scale of the structures within the bone. To overcome these problems, the average fluences of photons passing through each bone group defined in the phantoms were determined in suitable bins (*f4:p* tallies), and the doses to the RBM or endosteal tissue were calculated by applying appropriate energy-dependent conversion coefficients. For the RBM, these conversion coefficients were derived by considering estimates of the mass-energy absorption coefficients (Hubbell *et al*., 1995) of RBM and the photoelectric enhancement factors

for trabecular tissue given for various bones (King *et al.*, 1985); for the endosteal tissues, the mass-energy absorption coefficients (Hubbell *et al.*, 1995) were again used, with the photoelectric enhancement factors provided in Table D5 of (Cristy *et al.*, 1987). Finally, the overall skeletal RBM or endosteal doses were calculated by weighting the doses from the individual bone groups according to the fractions they contain of the total mass of RBM or endosteal tissue in the body, and summing; these relative fractions are documented in Table 4.2 of ICRP Publication 110 (ICRP, 2008). In the context of the current work, the extra effort on bone dosimetry is particularly worthwhile because one of the most important doses for acute radiation syndrome (ARS) is that to the red bone marrow.

To make a valid comparison across the datasets, each dose was normalised to the relevant fluence from the source in that geometry. For the planar exposures (AP, PA, LLAT and RLAT), this free-in-vacuo fluence was calculated precisely, by taking the reciprocal of the area of the source. For the isotropic exposures, the applied fluence was determined by voiding all materials of the phantom and phone except the volumes representing the resistors, the material of which was set to air; the simulations were then repeated, with the fluence applied by the source estimated from *f4:p* tallies on the 'resistor' volumes. As a check, this calculation was performed for each of the eight resistor positions considered (= 2 resistors × 4 phone locations); all results agreed to within 0.5 %. The applied fluence in the case of the exposures representing ground contamination was more problematic. The intention of the FLR calculations was to recreate a situation in which radioactive contamination is spread over a large area of the ground, i.e. across a surface of effectively infinite extent. In principle, a radionuclide distributed uniformly across a plane of infinite extent and emitting radiation (semi-)isotropically should, in a vacuum, lead to a spatial fluence distribution that is independent of distance from the plane, and would only have a weak dependence on height for strongly penetrating radiation in air. In the Monte Carlo model, however, only a limited approximation to an infinitely extended contaminated ground source could be considered, namely a circular floor of radius 200 cm, because there is an inevitable compromise between accuracy and precision: a floor of increasing area gives improved approximation to an infinite plane, but at the cost of increasingly poorer precision for a given simulation time. Ultimately, this finite source causes the fluence to decrease slightly with distance from the floor. To account for this variation, the dose results from the FLR exposures were normalized, on a case-by-case basis, by the fluences that would be present through each

tallied volume had the phone and phantom not been present. These fluences were estimated by changing all materials within the configuration to air, and tallying the photon fluences (*f4:p*) passing through each of the regions of interest, i.e. the former resistor or organ volumes, as well as through a few 1 cm radius spheres placed strategically to investigate the spatial distribution of fluence more thoroughly. The results from these calculations are not presented here, but to illustrate the scale of the spatial distribution, it is reported that the fluences through the 'Leg' and 'Chest' dosemeters were found to be 66 % and 46 %, respectively, of the fluence 1 cm from the floor. These results also indicate the approximate variation in fluence across the locations of many of the radiosensitive organs of the body, relative to their distances from the source. The fluence at the scalp was 32% of the fluence at the toes. As a check on the accuracy of this method of normalisation, both the organ dose and fluence calculations were repeated for a larger circular floor source of radius 400 cm. The organ doses per fluence data that resulted from the two different source radii were then compared. It was found that although applying the height corrections helped the two datasets to agree, it is not a perfect solution: the differences in organ doses ranged from 1.3 % for the testes to 20 % for the brain, which reflects an anticipated increase in divergence with distance from the floor, with the difference averaged over all organs being 11 %. However, although these differences are significant, they are not large enough to change the overall results and observations that will be seen in the next section.

Results

The absorbed doses per fluence in each of the organs of the phantom are given in Table 11.23 for each of the six exposures to ^{192}Ir, as well as for the ROT* exposure that was estimated by averaging the AP, PA, LLAT and RLAT data. Also contained in Table 11.23 are the results from the FLR exposures to ^{137}Cs and ^{60}Co; the AP, PA, LLAT, RLAT, ISO and ROT* results for these isotopes are not duplicated here as they were all found to agree well with the analogous organ absorbed doses per fluence data published in ICRP 116 (which does not consider either FLR or ^{192}Ir exposures), a resemblance that supports not only the fidelity of the current method of calculation but also the averaging method adopted in this work to estimate the results from

genuine rotational exposures (ROT). In the table, bracketed values denote one standard uncertainty, which quantifies just the statistical fluctuations in the Monte Carlo simulations.

The most important data in Table 11.23 are those in the top few rows, which are: the estimates of the average whole body doses, D_B^G, from exposure geometry G; the associated standard deviations, $\sigma_N(D_B^G)$, that indicate the spreads in the various organ doses around these values; and the doses to the red bone marrow, stomach and small intestine, which are key tissues for acute radiation syndrome. The quantity 'whole body absorbed dose' is not defined in any of the ICRP Publications, but it would seem logical to define it as the total energy deposited in the body divided by the mass of the body. For relevance to acute radiation syndrome (ARS), however, it would seem more appropriate to instead restrict attention just to the most radiosensitive organs and tissues, such as those that contribute to effective dose, with whole body absorbed doses then most accurately estimated by summing the energies deposited in those organs and dividing by the sum of their masses. But, the masses of large organs (e.g. the muscles) would dominate this division, which could potentially lead to a false assessment of risk for some exposures. As a consequence, whole body doses have been estimated here using Equation 2, which takes the average of the absorbed doses to the N organs that contribute to effective dose, including those that are considered part of the 'remainder'. The small standard deviation on the results is taken as establishing that this result is not unduly biased by the high weighting that could be given to some light organs.

$$D_B^G = \frac{\sum_i^N (E_i^G / m_i)}{N} \qquad (2)$$

In Equation 2, E_i^G is the energy deposited in organ i of mass m_i and the summation is over the N most radiosensitive organs specified by ICRP 103 and reported in Table 11.23. As defined by Equation 2, this whole body average absorbed dose D_B^G may perhaps be regarded as a parameter that is somehow analogous to the protection quantity effective dose, but without the latter's tissue (or radiation) weighting factors that are derived from radiobiology to account for the stochastic effects induced at low levels of exposure (ICRP, 2010): for emergency dosimetry, the focus is instead on high doses and their associated tissue reactions. The whole body dose is perhaps the most natural of the parameters to use in deriving a calibration factor for emergency

dosimetry, but potentially it may not be optimal because it includes organs and tissues that are not known to play significant roles in acute radiation syndrome (ARS). Ultimately, it may prove better simply to use the red bone marrow doses, or an average of just red bone marrow, stomach and small intestine, because doses to these organs are considered to be the most impacting for ARS. Some other organs, such as the brain, are also important, but only at very high doses where the effects are likely to lead to rapid death, which would make the OSL method redundant, except perhaps in a forensic sense. Resolution of these issues is beyond the scope of this report, however, and for the present purposes the averaging method of Equation 2 may be considered to provide a sufficiently reasonable estimator of the general risk to an individual from a significant exposure to penetrating radiation, given the wide spatial distribution of these organs in the body and the limited level of precision required for triage dosimetry. Of course, average doses for any alternative groups of organs could also readily be derived using the data shown in Table 11.23 (or ICRP 116), and subsequently contrasted with phone doses using analyses similar to those presented below.

The calculated whole body average doses for Co-60 and Cs-137, which are not provided by ICRP 116 but are important for the current work, are given in Table 11.24 for the seven exposure geometries. Table 11.25 provides essentially the same data as Table 11.23, but for each exposure the most important results are given relative to the whole body dose for that geometry. From Table 11.25 it is immediately apparent how the doses to the key organs deviate from those to the whole body. From the data in Tables 11.23-25 it is evident that for AP exposures to ^{192}Ir, for instance, although the average dose to the body may be close to 1.639 ± 0.002 pGy cm^2, the individual doses received by the various organs cluster around this mean with a distribution that has a standard deviation of 0.298, or ~ 18 % of the mean. Comparing the doses per fluence across each row is also revealing: for example, for AP exposures it is seen that the dose per fluence to the whole body is consistent with that to the stomach to within a few percent; but, for LLAT exposures the dose per fluence to the stomach is ~ 40 % higher than that to the whole body, whilst for RLAT exposures it is ~ 40 % less. On the other hand, the data for the red bone marrow, which is perhaps the most significant organ for ARS, show that an estimate of whole body dose would provide a conservative (over-) estimate for all field orientations except for PA, for which the dose to the red bone marrow is ~ 15 % higher. Similar anomalies are found

elsewhere across the datasets and are significant, and reflect the fact that the radiosensitive organs are not distributed uniformly throughout the body, and hence have different average depths depending on the direction of the radiation field. As a consequence, average body doses cannot necessarily be assumed to be adequate estimators of detriment to a given organ, and are therefore not always reliable assessments of radiological risk.

Table 11.23: Absorbed dose per fluence data for organs exposed to Ir-192 from various geometries, and for FLR exposures to Cs-137 and Co-60. The red bone marrow, stomach and small intestine are considered to be the most significant organs for ARS. The main role of the remaining data is for the computation of whole body doses, $D_B{}^G$, which have been estimated as the averages of the doses to all of the organs.

	Absorbed Dose per fluence (pGy cm^2)								
				^{192}**Iridium**				^{137}**Caesium**	^{60}**Cobalt**
ORGAN	***AP***	***PA***	***LLAT***	***RLAT***	***ISO***	***FLR***	***ROT****	***FLR***	***FLR***
Whole Body ($D_B{}^G$)	*1.639* *(0.002)*	*1.390* *(0.002)*	*1.051* *(0.002)*	*1.020* *(0.002)*	*1.104* *(0.011)*	*0.846* *(0.003)*	*1.275* *(0.002)*	*1.711* *(0.005)*	*3.272* *(0.010)*
$\sigma_N(D_B{}^G)$	*0.298*	*0.302*	*0.308*	*0.349*	*0.158*	*0.201*	*0.148*	*0.340*	*0.510*
RBM	1.430 (0.001)	1.597 (0.001)	0.872 (0.001)	0.884 (0.001)	1.038 (0.004)	0.755 (0.001)	1.195 (0.001)	1.564 (0.001)	3.063 (0.002)
Stomach	1.726 (0.002)	1.142 (0.001)	1.469 (0.001)	0.653 (0.001)	1.005 (0.010)	0.767 (0.002)	1.248 (0.001)	1.570 (0.003)	3.049 (0.006)
S. Intestine	1.750 (0.001)	1.282 (0.001)	1.149 (0.001)	0.912 (0.001)	0.981 (0.010)	0.816 (0.001)	1.273 (0.001)	1.651 (0.002)	3.177 (0.004)
Adrenals	0.984 (0.003)	1.886 (0.004)	0.669 (0.002)	0.672 (0.002)	0.954 (0.010)	0.740 (0.004)	1.052 (0.003)	1.516 (0.007)	2.960 (0.013)
Bladder	1.841 (0.002)	1.311 (0.002)	0.785 (0.001)	0.734 (0.001)	0.961 (0.010)	0.849 (0.002)	1.168 (0.002)	1.719 (0.005)	3.303 (0.009)
Brain	1.192 (0.001)	1.309 (0.001)	1.451 (0.001)	1.465 (0.001)	1.253 (0.012)	0.725 (0.001)	1.354 (0.001)	1.532 (0.003)	3.027 (0.005)
Breast	2.090 (0.003)	0.852 (0.002)	1.237 (0.003)	1.193 (0.003)	1.316 (0.013)	1.078 (0.005)	1.343 (0.003)	2.133 (0.010)	3.881 (0.018)
Extrathoracic	1.680 (0.003)	0.902 (0.002)	1.702 (0.002)	1.705 (0.002)	1.274 (0.013)	0.856 (0.003)	1.497 (0.002)	1.728 (0.006)	3.280 (0.012)
Gall Bladder	1.543 (0.003)	1.208 (0.002)	0.647 (0.002)	1.504 (0.003)	0.954 (0.010)	0.739 (0.003)	1.226 (0.002)	1.516 (0.006)	2.986 (0.013)
Colon	1.723 (0.001)	1.281 (0.001)	1.139 (0.001)	1.004 (0.001)	1.028 (0.010)	0.867 (0.001)	1.287 (0.001)	1.743 (0.002)	3.317 (0.005)
Heart	1.728 (0.001)	1.271 (0.001)	1.064 (0.001)	0.826 (0.001)	1.023 (0.010)	0.630 (0.001)	1.222 (0.001)	1.332 (0.003)	2.698 (0.005)

Kidneys	1.077 (0.001)	1.837 (0.001)	0.839 (0.001)	0.898 (0.001)	0.971 (0.010)	0.755 (0.002)	1.163 (0.001)	1.543 (0.003)	3.006 (0.007)
Liver	1.550 (0.001)	1.308 (0.001)	0.603 (0.000)	1.402 (0.001)	1.002 (0.010)	0.755 (0.001)	1.216 (0.001)	1.546 (0.002)	3.011 (0.004)
Lymph	1.727 (0.001)	1.407 (0.001)	1.049 (0.001)	0.885 (0.001)	1.065 (0.011)	0.864 (0.001)	1.267 (0.001)	1.748 (0.002)	3.334 (0.004)
Lungs	1.662 (0.001)	1.540 (0.001)	0.810 (0.000)	0.805 (0.000)	1.096 (0.011)	0.729 (0.001)	1.204 (0.001)	1.526 (0.002)	3.013 (0.003)
Muscles	1.574 (0.000)	1.615 (0.000)	0.972 (0.000)	0.976 (0.000)	1.180 (0.012)	1.093 (0.000)	1.284 (0.000)	2.160 (0.001)	3.964 (0.001)
Oesophagus	1.591 (0.002)	1.420 (0.002)	0.899 (0.001)	0.816 (0.001)	1.015 (0.010)	0.605 (0.003)	1.181 (0.002)	1.295 (0.006)	2.643 (0.011)
Oral Mucosa	1.540 (0.004)	0.912 (0.003)	1.536 (0.003)	1.540 (0.003)	1.194 (0.012)	0.856 (0.003)	1.382 (0.003)	1.727 (0.006)	3.267 (0.012)
Pancreas	1.552 (0.002)	1.292 (0.002)	0.982 (0.002)	1.041 (0.002)	0.912 (0.009)	0.699 (0.002)	1.217 (0.002)	1.446 (0.004)	2.854 (0.008)
Salivary G.	1.616 (0.002)	1.621 (0.002)	1.511 (0.002)	1.502 (0.002)	1.268 (0.013)	0.874 (0.003)	1.562 (0.002)	1.759 (0.006)	3.316 (0.012)
Skin	1.682 (0.000)	1.652 (0.000)	1.220 (0.000)	1.208 (0.000)	1.384 (0.014)	1.344 (0.000)	1.440 (0.000)	2.580 (0.001)	4.572 (0.002)
Spleen	1.123 (0.002)	1.857 (0.002)	1.105 (0.001)	0.317 (0.001)	1.024 (0.010)	0.806 (0.003)	1.100 (0.002)	1.630 (0.005)	3.132 (0.010)
Thymus	2.086 (0.004)	1.090 (0.003)	0.725 (0.002)	0.658 (0.002)	1.118 (0.011)	0.619 (0.004)	1.140 (0.003)	1.351 (0.008)	2.769 (0.017)
Thyroid	2.122 (0.004)	1.195 (0.003)	1.037 (0.003)	1.134 (0.003)	1.160 (0.012)	0.612 (0.004)	1.372 (0.003)	1.322 (0.008)	2.720 (0.016)
Prostate	1.619 (0.004)	1.519 (0.004)	0.686 (0.002)	0.671 (0.002)	0.928 (0.010)	0.866 (0.005)	1.124 (0.003)	1.754 (0.010)	3.363 (0.019)
Testes	2.018 (0.004)	1.213 (0.003)	0.800 (0.002)	0.720 (0.002)	1.149 (0.012)	1.253 (0.005)	1.188 (0.003)	2.411 (0.010)	4.306 (0.017)
Endosteum	2.021 (0.001)	2.009 (0.000)	1.416 (0.000)	1.426 (0.000)	1.561 (0.005)	1.299 (0.001)	1.718 (0.001)	2.391 (0.002)	4.325 (0.003)

Table 11.24: Estimated whole body absorbed doses per fluence data for exposures to Cs-137 and Co-60 from various geometries, and the standard deviations around these means of the absorbed doses per fluence in the organs specified in ICRP 103.

		Absorbed Dose per fluence (pGy cm^2)						
		AP	***PA***	***LLAT***	***RLAT***	***ISO***	***FLR***	***ROT****
Caesium-137	*Whole Body*	3.015 (0.004)	2.654 (0.004)	2.105 (0.003)	2.051 (0.003)	2.166 (0.021)	1.711 (0.005)	2.456 (0.003)
	$\sigma_N(D_B^G)$	0.457	0.443	0.511	0.585	0.264	0.340	0.244
Cobalt-60	*Whole Body*	5.142 (0.007)	4.686 (0.006)	3.926 (0.005)	3.840 (0.006)	3.971 (0.038)	3.272 (0.010)	4.399 (0.006)
	$\sigma_N(D_B^G)$	0.615	0.576	0.726	0.850	0.395	0.510	0.368

Table 11.25: Selected absorbed dose per fluence data given relative to that for the whole body, for exposures to Ir-192, Cs-137 and Co-60 from various geometries.

	Absorbed Dose per fluence (pGy cm^2)								
	^{132}Iridium							**^{137}Caesium**	**^{60}Cobalt**
ORGAN	***AP***	***PA***	***LLAT***	***RLAT***	***ISO***	***FLR***	***ROT****	***FLR***	***FLR***
Whole Body	*1.00*	*1.00*	*1.00*	*1.00*	*1.00*	*1.00*	*1.00*	*1.00*	*1.00*
$\sigma_N(D_B^G)$	0.18	0.22	0.29	0.34	0.14	0.24	0.12	0.20	0.16
RBM	0.87	1.15	0.83	0.87	0.94	0.89	0.94	0.91	0.94
Stomach	1.05	0.82	1.40	0.64	0.91	0.91	0.98	0.92	0.93
S. Intestine	1.07	0.92	1.09	0.89	0.89	0.96	1.00	0.97	0.97

Of course, this lack of spatial coherency in the results is not surprising and these types of disparity are well-known (ICRP, 2010). Instead, the relevance here lies in the fact that the fortuitous dosimetry method is based on doses absorbed by resistors in phones that are located at specific locations on the body. These doses cannot be expected, therefore, to provide perfect estimates of either whole body absorbed dose, or doses to specific organs within it, especially for those organs far from the site of the phone. To begin to quantify these discrepancies, Tables 11.26-28 show data for the mean absorbed dose per fluence, $(D_{R12}^M)/\Phi$, averaged over the two resistors in phones positioned at the four different locations (Chest, Leg, Back, Hip) and exposed to ^{192}Ir, ^{137}Cs and ^{60}Co photons, respectively, from various geometries (AP, PA, LLAT, RLAT, ISO, FLR and ROT*); as before, bracketed values in the tables denote one standard uncertainty, reflecting only the statistical imprecisions of the Monte Carlo simulations. Ultimately, the factors that govern the ability of a phone to reliably indicate the doses received by specific organs are

the similarities or differences in the degrees to which the photon field is attenuated by the body at the locations of the phone and organ. As might be expected, therefore, a comparison between the data in Table 11.23 (and in ICRP 116) and Table 11.26 shows that the performances of the phones as organ dosemeters vary in a predictable manner according to the location of the phone relative to the organ. For instance, it is seen that for an organ such as the adrenal gland, which is located deep inside the body but closer to the back than to the front, for AP and PA exposures a phone located in the Chest location gives a much poorer dose estimate than a phone located in the Back location. On the other hand, neither location leads to a good estimate of the adrenal gland dose per fluence during LLAT or RLAT exposures. In an ISO or FLR field, however, where there is less dependence on obvious directions of greatest or least shielding, all of the phone locations lead to results that are fairly close (i.e. within ~ 30 %) to the adrenal dose. Of course, doses to the adrenal gland are not considered critical to ARS, but are highlighted here to illustrate the variability in the results. Other correlations or anti-correlations between phone and organ doses may be seen for some of the other locations and exposure types.

Table 11.26: Absolute and relative mean absorbed dose per fluence data for resistors in phones at different locations, exposed to Ir-192 photons from various geometries. The configurations that led to the greatest and smallest results are shown in bold.

Exposure, *G*	**Phone Location**	**Mean absorbed dose per fluence, D_{R12}^{M}/Φ, (pGy cm^2)**	$R_{G,C,O}$ [(a)]	$R_{AP,C,O}$ [(b)]
AP	Chest	1.99 (0.08)	1.00 (0.06)	1.00 (0.06)
	Leg	1.97 (0.09)	0.99 (0.06)	0.99 (0.06)
	Back	0.71 (0.06)	0.36 (0.03)	0.36 (0.03)
	Hip	2.21 (0.16)	1.11 (0.09)	1.11 (0.09)
PA	Chest	0.57 (0.04)	1.00 (0.11)	0.29 (0.03)
	Leg	0.62 (0.05)	1.09 (0.12)	0.31 (0.03)
	Back	1.90 (0.08)	3.33 (0.29)	0.96 (0.06)
	Hip	**2.25 (0.15)**	**3.95 (0.41)**	**1.13 (0.09)**
LLAT	Chest	2.14 (0.12)	1.00 (0.08)	1.08 (0.08)
	Leg	2.09 (0.12)	0.97 (0.08)	1.05 (0.07)
	Back	2.06 (0.12)	0.96 (0.08)	1.04 (0.08)
	Hip	1.93 (0.07)	0.90 (0.06)	0.97 (0.05)
RLAT	Chest	2.03 (0.12)	1.00 (0.08)	1.02 (0.07)
	Leg	1.98 (0.12)	0.97 (0.08)	0.99 (0.07)

	Back	1.89 (0.12)	0.93 (0.08)	0.95 (0.07)
	Hip	**0.12 (0.02)**	**0.06 (0.01)**	**0.06 (0.01)**
ISO	Chest	1.25 (0.08)	1.00 (0.09)	0.63 (0.05)
	Leg	1.17 (0.08)	0.93 (0.09)	0.59 (0.05)
	Back	1.21 (0.08)	0.97 (0.09)	0.61 (0.05)
	Hip	1.21 (0.08)	0.97 (0.09)	0.61 (0.05)
FLR	Chest	0.97 (0.10)	1.00 (0.14)	0.49 (0.05)
	Leg	1.19 (0.08)	1.24 (0.15)	0.60 (0.05)
	Back	1.07 (0.08)	1.11 (0.14)	0.54 (0.05)
	Hip	1.10 (0.08)	1.14 (0.14)	0.56 (0.05)
ROT*	Chest	1.68 (0.20)	1.00 (0.16)	0.85 (0.10)
	Leg	1.66 (0.20)	0.99 (0.16)	0.84 (0.10)
	Back	1.64 (0.20)	0.98 (0.16)	0.82 (0.10)
	Hip	1.63 (0.23)	0.97 (0.18)	0.82 (0.12)

(a) $R_{G,C,O}$ defined as: $(D_{R1,2}{}^{M}/\Phi)[G, location, orientation] / (D_{R1,2}{}^{M}/\Phi)[G, Chest, Out]$.
(b) $R_{AP,C,O}$ defined as: $(D_{R1,2}{}^{M}/\Phi)[G, location, orientation] / (D_{R1,2}{}^{M}/\Phi)[AP, Chest, Out]$.

Table 11.27: Absolute and relative mean absorbed dose per fluence data for resistors in phones at different locations, exposed to Cs-137 photons from various geometries. The configurations that led to the greatest and smallest results are shown in bold.

Exposure, *G*	**Phone Location**	**Mean absorbed dose per fluence, $D_{R12}{}^{M}/\Phi$, (pGy cm^2)**	$R_{G,C,O}$ (a)	$R_{AP,C,O}$ (b)
AP	Chest	3.45 (0.14)	1.00 (0.06)	1.00 (0.06)
	Leg	3.38 (0.14)	0.98 (0.06)	0.98 (0.06)
	Back	1.45 (0.09)	0.42 (0.03)	0.42 (0.03)
	Hip	3.71 (0.25)	1.08 (0.08)	1.08 (0.08)
PA	Chest	1.27 (0.08)	1.00 (0.03)	0.37 (0.03)
	Leg	1.41 (0.09)	1.11 (0.04)	0.41 (0.03)
	Back	3.17 (0.13)	2.49 (0.07)	0.92 (0.05)
	Hip	**3.90 (0.25)**	**3.06 (0.10)**	**1.13 (0.08)**
LLAT	Chest	3.75 (0.21)	1.00 (0.09)	1.09 (0.08)
	Leg	3.62 (0.21)	0.96 (0.08)	1.05 (0.07)
	Back	3.55 (0.21)	0.95 (0.08)	1.03 (0.07)
	Hip	3.36 (0.12)	0.90 (0.06)	0.97 (0.05)
RLAT	Chest	3.77 (0.22)	1.00 (0.09)	1.09 (0.08)
	Leg	3.61 (0.21)	0.96 (0.09)	1.05 (0.07)
	Back	3.49 (0.21)	0.93 (0.08)	1.01 (0.07)
	Hip	**0.31 (0.04)**	**0.08 (0.01)**	**0.09 (0.01)**
ISO	Chest	2.35 (0.15)	1.00 (0.06)	0.68 (0.05)
	Leg	2.24 (0.14)	0.95 (0.06)	0.65 (0.05)
	Back	2.25 (0.14)	0.96 (0.06)	0.65 (0.05)
	Hip	2.31 (0.15)	0.98 (0.06)	0.67 (0.05)
FLR	Chest	1.95 (0.17)	1.00 (0.07)	0.56 (0.05)

	Leg	2.37 (0.15)	1.22 (0.07)	0.69 (0.05)
	Back	1.99 (0.14)	1.02 (0.06)	0.58 (0.05)
	Hip	2.17 (0.16)	1.11 (0.07)	0.63 (0.05)
ROT*	Chest	3.06 (0.34)	1.00 (0.14)	0.89 (0.11)
	Leg	3.01 (0.34)	0.98 (0.14)	0.87 (0.10)
	Back	2.92 (0.33)	0.95 (0.14)	0.84 (0.10)
	Hip	2.82 (0.37)	0.92 (0.14)	0.82 (0.11)

(a) $R_{G,C,O}$ defined as: $(D_{R1,2}{}^{M}/\Phi)[G, location, orientation] / (D_{R1,2}{}^{M}/\Phi)[G, Chest, Out]$.
(b) $R_{AP,C,O}$ defined as: $(D_{R1,2}{}^{M}/\Phi)[G, location, orientation] / (D_{R1,2}{}^{M}/\Phi)[AP, Chest, Out]$.

Table 11.28: Absolute and relative mean absorbed dose per fluence data for resistors in phones at different locations, exposed to Co-60 photons from various geometries. The configurations that led to the greatest and smallest results are shown in bold.

Exposure, *G*	**Phone Location**	**Mean absorbed dose per fluence, $D_{R12}{}^{M}/\Phi$, (pGy cm^2)**	$R_{G,C,O}$ [(a)]	$R_{AP,C,O}$ [(b)]
	Chest	5.59 (0.23)	1.00 (0.06)	1.00 (0.06)
AP	Leg	5.63 (0.24)	1.01 (0.06)	1.01 (0.06)
	Back	2.77 (0.16)	0.50 (0.04)	0.50 (0.04)
	Hip	6.03 (0.42)	1.08 (0.09)	1.08 (0.09)
	Chest	2.64 (0.16)	1.00 (0.09)	0.47 (0.03)
PA	Leg	2.81 (0.16)	1.06 (0.09)	0.50 (0.04)
	Back	5.15 (0.22)	1.95 (0.14)	0.92 (0.05)
	Hip	**6.36 (0.41)**	**2.40 (0.21)**	**1.14 (0.09)**
	Chest	6.10 (0.37)	1.00 (0.08)	1.09 (0.08)
LLAT	Leg	5.72 (0.35)	0.94 (0.08)	1.02 (0.08)
	Back	5.97 (0.36)	0.98 (0.08)	1.07 (0.08)
	Hip	5.49 (0.20)	0.90 (0.06)	0.98 (0.05)
	Chest	6.30 (0.37)	1.00 (0.08)	1.13 (0.08)
RLAT	Leg	6.04 (0.37)	0.96 (0.08)	1.08 (0.08)
	Back	6.11 (0.37)	0.97 (0.08)	1.09 (0.08)
	Hip	**0.96 (0.08)**	**0.15 (0.02)**	**0.17 (0.02)**
	Chest	4.35 (0.28)	1.00 (0.09)	0.78 (0.06)
ISO	Leg	3.94 (0.26)	0.91 (0.08)	0.70 (0.05)
	Back	4.02 (0.25)	0.92 (0.08)	0.72 (0.05)
	Hip	4.22 (0.27)	0.97 (0.09)	0.75 (0.06)
	Chest	3.42 (0.31)	1.00 (0.13)	0.61 (0.06)
FLR	Leg	4.34 (0.28)	1.27 (0.14)	0.78 (0.06)
	Back	3.62 (0.26)	1.06 (0.12)	0.65 (0.05)
	Hip	3.85 (0.28)	1.13 (0.13)	0.69 (0.06)
	Chest	5.16 (0.59)	1.00 (0.16)	0.92 (0.11)
ROT*	Leg	5.05 (0.58)	0.98 (0.16)	0.90 (0.11)
	Back	5.00 (0.58)	0.97 (0.16)	0.89 (0.11)
	Hip	4.71 (0.63)	0.91 (0.16)	0.84 (0.12)

(a) $R_{G,C,O}$ defined as: $(D_{R1,2}{}^{M}/\Phi)[G, location, orientation] / (D_{R1,2}{}^{M}/\Phi)[G, Chest, Out]$.
(b) $R_{AP,C,O}$ defined as: $(D_{R1,2}{}^{M}/\Phi)[G, location, orientation] / (D_{R1,2}{}^{M}/\Phi)[AP, Chest, Out]$.

For a stated exposure geometry, *G*, and phone location and orientation, the fourth columns of Tables 11.26-28 show the values of $R_{G,C,O}$, which is defined as the average dose per fluence in both resistors given relative to the average dose per fluence in both resistors from the same exposure *G* with the phone located at the 'Chest' location and facing Out (i.e. away from the body); of course, only for the ^{137}Cs exposures is the 'orientation' parameter non-redundant here. Similarly, the fifth columns of Tables 11.26-28 provide the values of $R_{AP,C,O}$, defined as the average dose per fluence in both resistors given relative to the result for the AP exposure with the phone located in the 'Chest' location and facing Out. From these, the strong dependence of the dose on the location of the phone and the exposure type is immediately apparent. For example, for an AP exposure, it is seen that phones located in the Chest, Leg or Hip positions generally receive fairly comparable doses; but, phones positioned at the Back location receive doses that are consistently less than these. On the other hand, for a PA exposure, a phone located at the Back or Hip position receives several times the dose absorbed by a phone located at the Chest position. Moreover, for phones at the Hip position, exposures from the left can lead to doses that are an order of magnitude greater than doses following exposure from the right. Conversely, however, the doses received by the phones during the ISO or ROT* exposures appear relatively insensitive to their locations; the doses received by the phones during the FLR exposures are also relatively insensitive to their locations, though for obvious reasons the phones located at the Leg position tended to receive slightly higher doses. Of course in all of these examples, it is the relative differences in attenuation and backscattering of the fields by the body that cause the discrepancies.

The configurations that led to the greatest and smallest results are highlighted in Tables 11.26-28. For each radionuclide, the greatest and least doses per fluence occurred when the phone was located at the Hip, for PA and RLAT exposures respectively. This outcome is predicable from a consideration of directional shielding, as is the observation that the gulf between the two extremes widens with decreasing energy: for Co-60 a difference by a factor of 6.6 is seen, for Cs-137 a factor of ~ 13, but for Ir-192 a factor of ~ 19. This is a highly significant result: if two people were in close proximity during an exposure to iridium-192 but were orientated such that one received an RLAT exposure whilst the other a PA exposure, and if both individuals had their phones located by their left hips, their whole body doses (Table 11.23) would only differ by ~ 40 % but the doses to their phones would be found to differ by ~ 1900 %.

The above types of relationships are illustrated in Figures 11.19-21, which summarise, as a function of exposure type, the dose per fluence results averaged over both resistors (and both phone orientations for ^{137}Cs) for phones in the four locations of interest (Chest, Leg, Back and Hip), for iridium-192, caesium-137 and cobalt-60 respectively. Also shown in Figures 11.19-21 are the corresponding data for the whole body, which were estimated by averaging over the individual organ doses determined in the voxel phantom calculations (Equation 2). Two main conclusions may be drawn from these data. Firstly, it is evident that inaccurate knowledge of the direction of exposure can lead to significant inaccuracy in the reported doses. Secondly, it is evident that, for a given exposure direction, the location of the phone strongly impacts the dose it receives. Table 11.29 summarises these points, by providing the average doses per fluence received by all phones in each of the exposures, $D_P{}^G/\Phi$, along with the standard deviations, $\sigma_{\boldsymbol{D}}{}^{\boldsymbol{G}}$, of the distribution of the four locational results in each case about these means. Also included in Table 11.29 are the whole body doses per fluence for each exposure, $D_B{}^G/\Phi$, calculated by averaging over the individual organ doses. For completeness, Table 11.29 also provides the 'effective doses', E_M, for the exposures, which were calculated by weighting then summing the separate organ doses in the appropriate way (ICRP, 2007); here, the inverted commas and subscript *M* provide the reminder that this quantity is not true effective dose, because only the male ICRP phantom has been considered. Calibration factors, defined as the ratio between the dose per fluence for the whole body and the mean dose per fluence for the phone, are also included in Table 11.29, along with their associated margins of uncertainty; these are discussed further later.

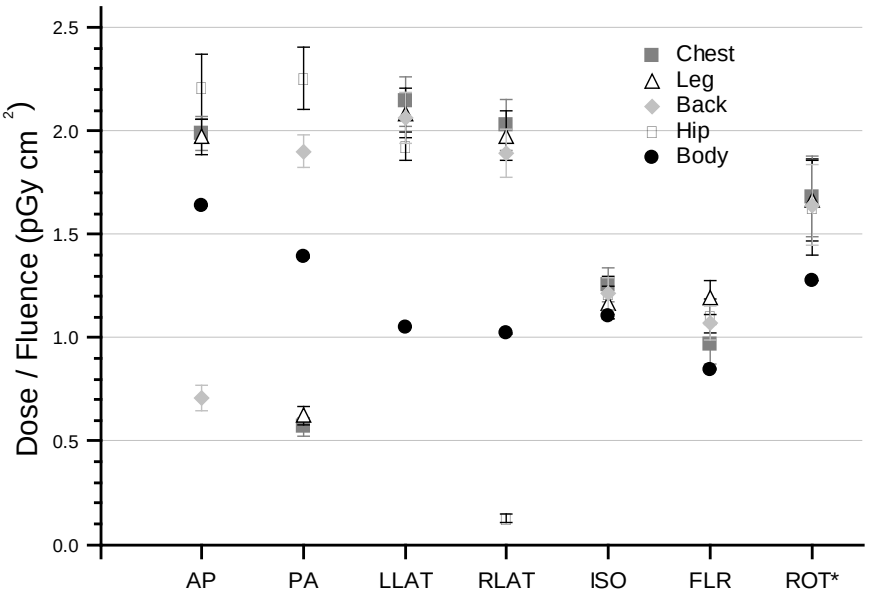

Figure 11.19: Dose per fluence results as a function of exposure type to Ir-192, for the whole body and for phones in the four locations of interest (Chest, Leg, Back and Hip).

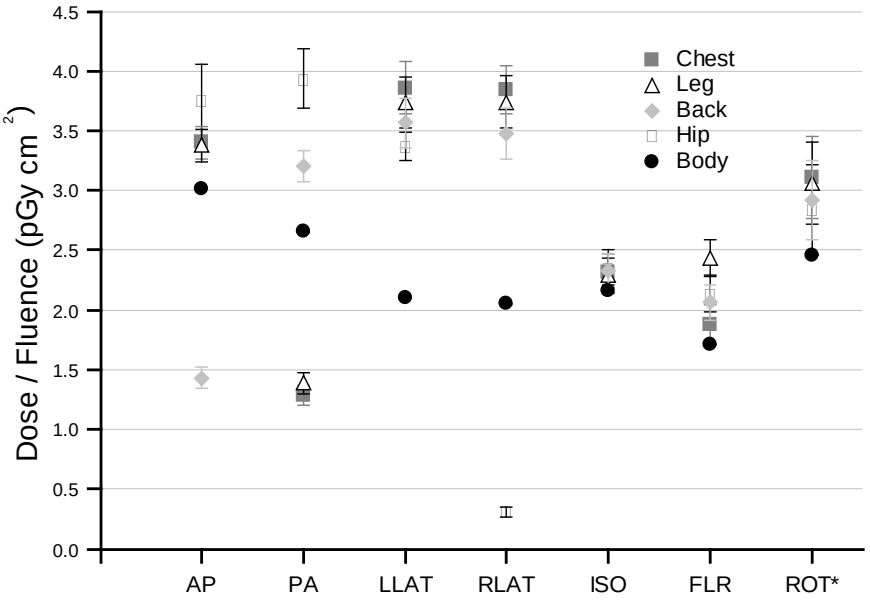

Figure 11.20: Dose per fluence results as a function of exposure type to Cs-137, for the whole body and for phones in the four locations of interest (Chest, Leg, Back and Hip).

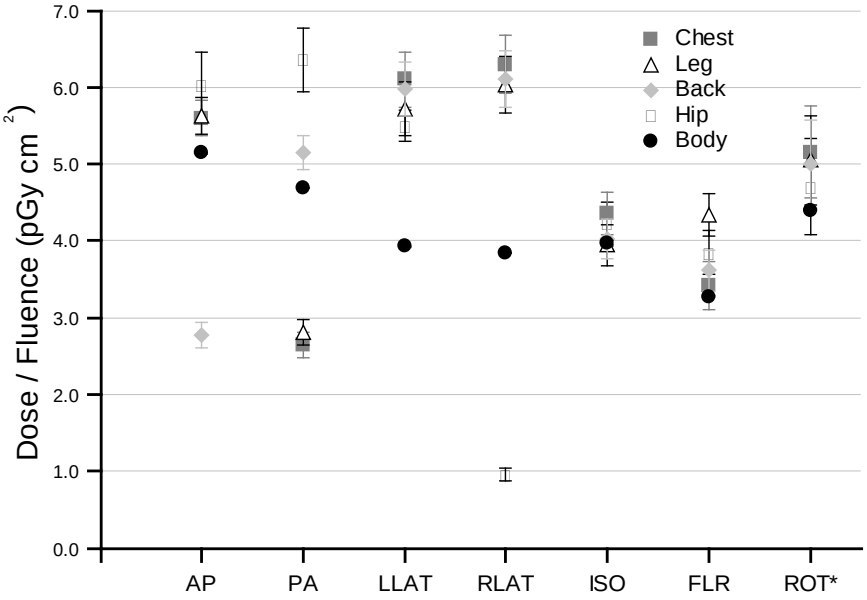

Figure 11.21: Dose per fluence results as a function of exposure type to Co-60, for the whole body and for phones in the four locations of interest (Chest, Leg, Back and Hip).

Table 11.29: Average phone and whole body doses per fluence, calibration factors, and confidence levels for each exposure. Bracketed values denote one standard uncertainty, representing just the statistical variance from the Monte Carlo calculations.

Isotope	Exposure, G	Whole body dose per fluence, D_B^G/Φ (σ_B) (pGy cm^2)	'Effective dose' per fluence, E_M^G/Φ (pSv cm^2)	Mean phone dose per fluence, D_P^G/Φ (σ_P) (pGy cm^2)	Standard Dev. [(a)], σ_{D^G} (pGy cm^2)	Calibration Factor [(b)], C^G	S^G_+ (%) [(c)]	S^G_- (%) [(d)]
Iridium-192	AP	1.64 (0.01)	1.73 (0.01)	1.72 (0.10)	0.680	0.95 (0.06)	22	140
	PA	1.39 (0.01)	1.31 (0.01)	1.34 (0.09)	0.870	1.04 (0.07)	41	130
	LLAT	1.05 (0.01)	1.04 (0.01)	2.05 (0.11)	0.091	0.51 (0.03)	4.1	6.6
	RLAT	1.02 (0.01)	0.94 (0.01)	1.51 (0.10)	0.920	0.68 (0.05)	26	1100
	ISO	1.10 (0.01)	1.01 (0.06)	1.21 (0.08)	0.034	0.91 (0.06)	3.2	3.7
	FLR	0.85 (0.01)	0.85 (0.02)	1.08 (0.08)	0.094	0.78 (0.06)	9.2	12
	ROT*	1.28 (0.01)	1.23 (0.01)	1.65 (0.21)	0.024	0.77 (0.10)	1.7	1.5
Caesium-137	AP	3.02 (0.01)	3.16 (0.02)	3.00 (0.17)	0.98	1.01 (0.06)	21	110
	PA	2.65 (0.01)	2.54 (0.01)	2.46 (0.15)	1.23	1.08 (0.07)	38	93
	LLAT	2.11 (0.01)	2.08 (0.01)	3.63 (0.19)	0.21	0.58 (0.03)	8.2	8.1
	RLAT	2.05 (0.01)	1.92 (0.01)	2.84 (0.19)	1.57	0.72 (0.05)	28	820
	ISO	2.17 (0.02)	2.15 (0.05)	2.32 (0.15)	0.06	0.93 (0.06)	3.3	3.9
	FLR	1.71 (0.01)	1.73 (0.02)	2.13 (0.16)	0.23	0.81 (0.06)	15	18
	ROT*	2.46 (0.01)	2.43 (0.01)	2.98 (0.35)	0.12	0.82 (0.10)	5.3	5.8
Cobalt-60	AP	5.14 (0.01)	5.34 (0.04)	5.01 (0.28)	1.50	1.03 (0.06)	17	81
	PA	4.69 (0.01)	4.55 (0.03)	4.24 (0.26)	1.82	1.11 (0.07)	33	60
	LLAT	3.93 (0.01)	3.90 (0.03)	5.82 (0.33)	0.27	0.68 (0.04)	4.5	6.0
	RLAT	3.84 (0.01)	3.66 (0.03)	4.85 (0.32)	2.60	0.79 (0.05)	23	410
	ISO	3.97 (0.04)	3.96 (0.20)	4.14 (0.27)	0.19	0.96 (0.06)	5.0	4.8
	FLR	3.27 (0.01)	3.30 (0.06)	3.81 (0.28)	0.40	0.86 (0.06)	12	11
	ROT*	4.40 (0.01)	4.36 (0.03)	4.98 (0.60)	0.19	0.88 (0.11)	3.4	5.8

[(a)] Defined for a given exposure as the standard deviation of the distribution of the mean phone doses from the four locations.
[(b)] Defined as the ratio: $C^G = (D_B^G/\Phi) / (D_P^G/\Phi)$.
[(c)] Defined in Equation 4a to provide a conservative estimate of the potential over-response from using C^G.
[(d)] Defined in Equation 4b to provide a conservative estimate of the potential under-response from using C^G.

The results obtained previously from the free-in-space and slab phantom exposures suggested that the absorbed doses are fairly insensitive both to the positions of the resistors within the phone and to whether the phone is exposed from the front or from the back. This justifies the use of the average dose per resistor for a given exposure in Tables 11.26-28, rather than the individual doses to the separate resistors, and the 'Out' orientation of the phone, i.e. with its glass front always facing away from the body. However as a check, both 'In' and 'Out' orientations were modelled for the caesium exposures. The results are not included here explicitly, but it is reported that no unexpected systematic trends or correlations were resolvable when like-for-like datasets from the two orientations were compared, at least within the precision of the typical uncertainties on the individual dose per fluence results from these calculations (~ 5-10 %). This

analysis supports the previous conclusions, and would likely also be demonstrated during Co-60 or Ir-192 exposures.

Although Tables 11.26-28 focus just on the doses averaged over both resistors, it is possible also to analyse the results for the resistors individually. For Cs-137 exposures, the mean of the modulus differences between R1 and R2 doses averaged over the 6 exposures, 4 locations and 2 orientations was 7.9 %, with the overall set of differences in the results distributed around this mean with a (comparable) standard deviation of 6.9. For Co-60 exposures, the analogous data were 7.3 % and 8.0; for Ir-192 exposures, the data were 8.9 % and 9.6. However, there were no obvious trends in any of these datasets, or correlations with any other factors: sometimes the R1 dose was higher than the R2 dose, whilst the converse was true at other times. Overall, no clear systematic relationship was apparent when R1 versus R2 results were compared, in terms of either the location of the phone, its orientation, or the field to which it is exposed, which supports the use of average resistor doses in Tables 11.26-28. As discussed previously, this conclusion is significant for an emergency dosimetry service: in general, it is likely that there would be little time available to accurately analyse or document the precise location of a resistor within a phone; and in any case, during the OSL/TL measurement procedure numbers of resistors are likely to be extracted from the phone and analysed together, rendering an averaging process unavoidable. Although only two resistor positions within the phone have been considered in the present Monte Carlo modelling, the results found here could be taken to indicate that ignorance of their sitting may contribute little to the overall uncertainty budget of the dosimetry technique.

11.10.5 Discussion-Conclusions

A number of conclusions may be drawn from the results presented in this section. Firstly, the position of the resistors within the phone can greatly impact the dosimetry: apart from very low energy exposures, variations of only a few percent have generally been found between R1 and R2 results (Figures 11.15 and 11.17), which are within the levels of statistical fluctuation. However, since this outcome was obtained considering only two positions within the phone it is not inconceivable that greater variations could be found for alternative positions: the dose deposited in a resistor surrounded by large quantities of high-*Z* material very close to the back of

a phone by a battery, say, could still be different from that in a comparatively unshielded resistor closer to the same phone's screen. In fact, measurements of dose deposition as a function of depth within a phone have been considered elsewhere for Cs-137 (Mrozik *et al*., 2014), with discrepancies of over 20 % found between resistors positioned at the front and back of a phone. However, it is remarked that because resistors are typically located on a common PCB, they may all be located at a comparable depth within a given phone. As a consequence, the consistencies shown here for laterally separated resistors are not necessarily in conflict with any differences that might arise due to depth separations: all resistors taken from the same PCB may be expected to exhibit a fairly similar absorbed dose.

Secondly, it is apparent that the PCB itself could significantly affect the results. Specifically, the presence or absence of the metal contacts that surround the resistors was seen to alter the doses that they receive, with their presence enhancing the absorbed dose to a degree that depends on the energy of the source. It is likewise reasonable to assume that the exact compositions of these contacts, in particular their densities and Z_{eff}, would also perturb the dosimetry, although the extent of this has not been investigated in the current work. Given that the resistors in different phones may be connected to their respective PCB using different types of electrical contact, and that it is unlikely that such differences could be taken properly into account during an emergency dosimetry protocol, it may be suggested that this factor could add an uncertainty to the dose estimates that is several tens of percent at some energies.

Thirdly, the orientation of the phone relative to the source was shown not to affect the results greatly for exposures above ~ 100 keV (Figures 11.15-17). This is as expected for resistors located inside a phone, with the small differences that were found readily explainable from a consideration of the disparate attenuation of the field by the asymmetric distribution of materials around the resistors. It might be argued that exposures to sources with energies less than 100 keV are considerably less likely to occur in emergency dosimetry scenarios than exposures to sources greater than this value. Accordingly, the general lack of dependency of the results on the orientation of the phone is extremely fortunate: it would be a difficult problem to correct for otherwise, because when carried in a pocket, say, it is unlikely that an individual would be able to state with certainty the precise orientation of the phone during the exposure.

Finally, it was shown that the parameter that most significantly affects accurate dosimetry is the location of the phone. Comparing results for a phone free in space to one on an ISO slab phantom, the increase in dose due to backscatter is readily apparent and can be by tens of percent. Similarly, attenuation of the field by the phantom when exposed from the rear can change the dose to the phone by more than a factor of two, relative to exposures from the front (Figure 11.17). These differences, the magnitudes of which exhibit a strong energy-dependence, were explored further as functions of both the location of the phone on the body and the direction of exposure (Tables 11.23-11.29 and Figures 11.19-21). Significant differences were found between the doses deposited in phones at different locations, with their resulting estimates for whole body doses being incorrect by up to an order of magnitude. The data in Tables 11.21, 11.22, 11.26-28 and 11.29 may be compared to provide appropriate conversion factors necessary to calibrate a retrospective dosimetry system.

There are many limitations to the approach considered in this work. For a start, only the adult male ICRP phantom was considered, which is positioned standing upright. The phantom is also unclothed, which therefore neglects any shielding or backscatter provided by the very wide variety of garments that individuals might be wearing during a radiological emergency. In addition, all of the phones are located on the left-hand side of the body (from the phantom's point-of-view), the organs of which are not distributed perfectly symmetrically on the left-right axis; this is unlikely to be too significant for the AP, PA, ISO, FLR or ROT* exposures, but would affect the LLAT and RLAT results. Also, only seven exposure geometries were considered, but many more scenarios are feasible, such as a small-volume source positioned close enough to an individual to invalidate the plane parallel conditions assumed here for AP, PA, LLAT and RLAT; in principle, if the geometry of an exposure were known, then a specific model could be used to correct the readings for that case, but the diversity of possible cases is too great to be investigated in detail in advance. Different designs of phone would also lead to different dose depositions in their resistors. Finally, there are clearly an infinite number of positions in which a phone might be located relative to a body, and an infinite number of ways in which it might be turned; mobile phones tend to be significantly asymmetric about their natural rotational axes. Whilst all of these limitations are valid objections, it is suggested that many of them, such as those concerning the exact design of the phone or small rotations of it, are unlikely to change the overall outcomes too significantly, at least within the context of the large

uncertainties reported in the present work and the very crude estimates of dose acceptable for triage dosimetry. But others, such as those arising from the use of the standard ICRP adult male phantom, may be more fundamental and might only properly be resolved by future work that could involve considering voxel phantoms of different age, gender or posture (e.g. sitting or crouching), not all of which exist at present. Nevertheless, compared to these possible alternatives, using a standing adult male gives the configuration with the greatest spatial distribution of phones and organs, so may at least be speculated to provide a worst-case scenario for some of the dose variations highlighted in the current work.

There are currently no criteria against which retrospective / fortuitous dosemeters for triage should be judged, because this is a relatively new field of dosimetry. It would not be reasonable to judge them against the performance criteria required of personal dosemeters, because those dosemeters are worn in more ideal conditions and are designed to meet the specified criteria (IEC, 2012); for instance, a variation in the response by a factor of just 1.5 is permitted for photon personal dosemeters at doses above 10 mSv, but this would not be realistic for mobile phone dosimetry, which is intended only to provide a rough first estimate for individuals receiving high absorbed doses. Instead, since there are no specified criteria, the goal of this work is to show what can be achieved. Because the uncertainties are larger in emergency dosimetry than in routine dosimetry, it is recognised that there may be a need to tailor the calibration for an incident to factors known about the type of exposure, although the situation where a routine system calibration is applied has also been considered.

The calibration factors, C^G, in Table 11.29 are defined for exposure geometry G as the ratio between the dose per fluence for the whole body, (D^G_B/Φ), and the mean dose per fluence for the phone, (D^G_P/Φ), so that $C^G = (D^G_B/\Phi) \div (D^G_P/\Phi)$. These factors attempt to provide a bridge between the doses recorded by the phone, D^G_R, i.e. those that would be reconstructed from the TL or OSL measurement procedure, and those received by the individual, determination of which is of course the ultimate goal of the emergency dosimetry service. The calibration factors should thus be applied to the reconstructed phone doses as the final stage of the TL/OSL dosimetry process to give the corrected doses, D^G_C, via the relationship $D^G_C = D^G_R \times C^G$, which could then be reported as the dose received by the individual. Clearly, the choice of which calibration factor to apply depends upon what is known about the exposure, e.g. whether it is

known to be predominantly AP, PA, LLAT, RLAT, ISO, FLR or ROT. Of course in an ideal situation, perfect knowledge would be available regarding the nature and direction of the radiation exposure, the orientation of the individual relative to this source, and the location of the phone about the body. With such knowledge, the data in Tables 11.23 to 11.28 could be used to relate the phone doses to the doses received either by the whole body or by specific organs within it. In practice, however, it is unlikely that such knowledge will always be available, and the number of phones that might need to be processed in an emergency could be far too large to introduce specific geometry corrections for different individuals. Indeed, even if the general direction of the radiation emission were known in terms of some fixed coordinate system, from a dosimetry service standpoint it is unrealistic to expect that adequate information could always be collected during an emergency to clarify whether this direction was, say, strictly AP, PA, LLAT or RLAT from the perspective of each individual, or where their phone was located relative to it. In any case, movement of the individual or use of the phone during the exposure could negate such information anyhow. In practice therefore, and based on the speculated occurrence of various likely situations, a number of suggestions are hence made, which could perhaps be adopted with the following priorities:

1. In the idealised case that sufficient information is available on the energy and direction of the exposure and the location of the phone, the data of Tables 11.23 (and ICRP 116) and 11.26-28 may readily be used to derive localised organ or whole body doses directly from reconstructed phone doses.

2. Assuming, more realistically, that the location of the phone is not known, but that the direction of the exposure is known and sufficient information can be obtained regarding the relative orientation of the individual during it, the relevant calibration factor from Table 11.29 may be applied. The potential systematic uncertainties in the dose deposited in the individual that then follow from this ignorance of the phone's locations can be estimated using the parameters S^G_+ and S^G_- from Table 11.29, as will be discussed below.

3. If no directional information is available, it may still be reasonable to suggest that three exposure types are most likely:

a. If predominantly aerosol debris is suspected, the conditions of a radioactive cloud may perhaps be assumed most appropriate, and the ISO exposure data in Table 11.29 may be used.
b. For heavy radioactive debris or 'fallout' conditions where ground contamination is suspected, the FLR data in Table 11.29 may be used.
c. For discrete sources located significant distances from the individual, the ROT* data in Table 11.29 may be used, with the assumed effects of movement of the individual mitigating an assumed rotational uniformity of exposure.

4. If no information about the exposure is known, a default of ROT* should perhaps be chosen, as potentially this may be assumed to be the most likely general scenario once air or ground contamination exposures have been ruled out.

For plane parallel exposures of phones located on the front or back of the body at photon energies lower than those considered here, the data given in Table 11.22 for a phone positioned on a slab phantom may be used in conjunction with the organ absorbed doses published in ICRP 116 (ICRP, 2010) to estimate approximate values for dose conversion factors. These dose-per-fluence data are summarised in Table 11.30, where the results have been determined by averaging over both resistors for a phone facing away from the phantom (Table 11.22), and the whole body doses have been calculated using Equation 2; the data could potentially be interpolated, as necessary, to estimate intermediate values. As expected, knowledge of the location of the phone is seen to be critical for accurate conversions from resistor to whole body doses for a given exposure geometry, with factors such as the orientation of the phone and the positions of the resistors within it also known to become increasingly significant at lower energies (Figures 11.15-17). In the event that no energy characteristics of the exposure are known, it may be appropriate either to average over the data given here for ^{192}Ir, ^{137}Cs and ^{60}Co, or else adopt a more conservative approach by choosing the data that correspond to the worst-case scenario. Clearly, the accuracy of the dosimetry could be highly compromised in such circumstances, though by comparing Figures 11.19-21 it is at least noted that some general trends and ratios appear to exist between phone and body doses that are fairly independent of the sources, even if just as a very rough first approximation.

Table 11.30: Absorbed dose per fluence, averaged over both resistors in a phone located on the front or back of a slab phantom and facing away from it, and whole body dose per fluence, from which conversion factors may be derived for low energy AP and PA photon exposures; the 'reversal' of the phone datasets arises from the symmetry of the slab phantom configuration. Bracketed values denote one standard uncertainty, representing just the statistical variance from the Monte Carlo calculations.

	Absorbed dose per fluence (pGy cm^2)					
Energy (keV)	**AP Exposure**			**PA Exposure**		
	Whole Body	***Phone (Front)***	***Phone (Back)***	***Whole Body***	***Phone (Front)***	***Phone (Back)***
50	0.354	1.45 (0.11)	0.086 (0.003)	0.202	0.086 (0.003)	1.45 (0.11)
100	0.494	0.980 (0.035)	0.215 (0.011)	0.353	0.215 (0.011)	0.980 (0.035)
200	0.964	1.27 (0.06)	0.396 (0.004)	0.736	0.396 (0.004)	1.27 (0.06)
300	1.46	1.74 (0.07)	0.650 (0.026)	1.15	0.650 (0.026)	1.74 (0.07)

The parameters S^G_+ and S^G_- in Table 11.29 were introduced in an attempt to provide conservative estimates of the degree of confidence that might be expected from applying the calibration factors, C^G, given incomplete knowledge of the location of the phone and the statistical variances inherent from the Monte Carlo modelling. They are expressed as a percentage of D^G_C, i.e. the (corrected) dose that would be the outcome of the retrospective dose assessment for an individual, and show the amount by which this reported dose could potentially be over- (S^G_+) or under- (S^G_-) estimating the dose actually received by that individual. Specifically, the value of S^G_+ indicates the degree to which the corrected dose could be an over-estimate of the true whole body dose, and is given as a percentage of this corrected dose. Conversely, the parameter S^G_- indicates the degree to which the whole body dose could be under-estimated by the corrected dose, and is similarly normalised to the corrected dose. So, for a given exposure geometry G, the maximum whole body dose, $D^G_{B,max}$, that an individual may actually have received, if a corrected phone dose of D^G_C were reported by the retrospective dosimetry service, could be as large as:

$$D^G_{B,max} = D^G_C + \left(\frac{S^G_-}{100}\right) D^G_C \qquad (3a)$$

Similarly, the minimum whole body dose, $D^G_{B,min}$, that the individual might have received if a corrected phone dose of D^G_C were reported could actually be as low as:

$$D^G_{B,min} = D^G_C - \left(\frac{S^G_+}{100}\right) D^G_C \quad (3b)$$

The two parameters $S^G{}_+$ and $S^G{}_-$ have been defined for a given exposure geometry *G* as:

$$S^G_+ = 100 \times MAX\left\{1 - \frac{(D^G_P/\Phi)}{(D^G_{R12}/\Phi)[G,Location]}\right\} \quad (4a)$$

and

$$S^G_- = 100 \times MAX\left\{\frac{(D^G_P/\Phi)}{(D^G_{R12}/\Phi)[G,Location]} - 1\right\} \quad (4b)$$

where $(D^G{}_P/\Phi)$ is the mean phone dose per fluence from a given exposure geometry *G*, the variable $(D^G{}_{R12}/\Phi)[G,Location]$ is the dose per fluence for *G* averaged over both resistors for a given location (Chest, Leg, Back or Hip), and the set {…} is taken over each of the four locations. In an attempt to mitigate for the asymmetry of the modelled geometry, and given that phones are presumed just as likely to be carried on the right side of the body as the left, the worst-case results for $S^G{}_+$ and $S^G{}_-$ were merged in Table 11.29 for LLAT and RLAT exposures. The maximal term in Equations 4a and 4b originates from the supposition that in a real emergency situation the precise location of a phone will not necessarily be known to the people performing the TL / OSL measurements on its resistors, and hence the people who will be determining the individual's whole body dose from the dose reconstructed from the TL / OSL signal. Accordingly, taken together $S^G{}_+$ and $S^G{}_-$ effectively provide an envelope function reflecting the necessary assumption that the phone could have been located in either of the worst possible positions to provide accurate dosimetry for exposure *G*, considering that this dosimetry uses a method that is based upon applying a standard calibration factor, C^G. For a given exposure, these worst possible positions are the ones that would lead to dose estimates that are furthest from the value that was determined by averaging over all phone locations, upon which the value for C^G was based. In this way, a handle can be gained on the accuracy of the dose reported for an individual, and the degree to which it could be a serious over- or under-estimate of the true dose actually received. Of course, rather than simply making the blanket assumption of a worst-case scenario, other less conservative estimates of the uncertainties resulting from the application of C^G could alternatively be derived, such as making a statistical appraisal of the distributions of results that arise from ignorance of the phone's location. Although $S^G{}_+$ and $S^G{}_-$

are always non-negative, from the definitions in Equations 4a and 4b it is apparent that, whilst S^{G}_{+} can never exceed 100 % for any conceivable exposure, the value of S^{G}_{-} is not similarly constrained: the whole body dose to an individual could potentially be many times larger than the dose deposited in a phone located about their person, and, since S^{G}_{-} is given as a percentage of this phone dose, its value can be greater than 100 %. Naturally, dose under-estimates are of greater importance in terms of health protection, but over-estimates are not without significance.

As an illustrative example of the use of these parameters, it is seen (Table 11.29) that for AP exposures to ^{192}Ir the mean phone dose per fluence averaged over the four locations (D_P^{AP}/Φ) was found to be 1.72 pGy cm^{-2}, which is ~ 15 % lower than the dose per fluence (1.99 pGy cm^{2}) for the phone at the chest. However, the worst over-estimate for this mean value, i.e. the result that had the greatest positive difference from the mean, corresponded to that recorded by the phone in the Hip location, for which a dose per fluence of ($D_{R1,2}^{M}/\Phi$)[*AP*, *Hip*] = 2.21 pGy cm^{-2} was found (Table 11.26), i.e. ~ 28% higher than the mean dose. On the other hand, the worst under-estimate for this mean value, i.e. the result that had the greatest negative difference from the mean, corresponded to that recorded by the phone in the Back location, for which a dose per fluence of ($D_{R1,2}^{M}/\Phi$)[*AP*, *Back*] = 0.71 pGy cm^{-2} was found (Table 11.26), i.e. ~ 59% lower than the mean dose. The actual whole body dose per fluence (Table 11.23) for the AP exposure to ^{192}Ir was found to be (D_B^{AP}/Φ) = 1.64 pGy cm^{-2}. Inserting these values into Equations 4a and 4b therefore suggests that, if the ^{192}Ir exposure were known to be from the AP direction, the whole body dose determined using a phone of unknown location can be trusted only up to an under-estimate accuracy (S^{G}_{-}) of ~ 140 % of the corrected dose, and an over-estimate accuracy (S^{G}_{+}) of ~ 22 % of the corrected dose. So, if the dose reconstructed from the TL / OSL analysis of a phone exposed to an AP field was found to be, say, $D^{AP}_{R} = 1$ Gy, then the whole body dose would be estimated to be $D^{AP}_{C} = D^{AP}_{R} \times C^{AP} = 1 \times 0.95 = 0.95$ Gy, with the actual dose to the individual being expected, with some degree of confidence, to lie within the range from $D^{G}_{B,min}$ = 0.95-(0.22×0.95) = 0.74 Gy to $D^{G}_{B,max}$ = 0.95+(1.4×0.95) = 2.3 Gy. In other words, if the phone had been to its owner's back pocket at the time of the AP exposure, the individual would have received a dose of 2.3 Gy if the phone showed a dose of 1 Gy; but if it had instead been held in the owner's left hand, he would have received a dose of 0.74 Gy if the phone showed a dose of 1 Gy. Since, for the present purposes, it is being assumed that the actual location of the

phone during the exposure is not known to the person performing the analysis, the reported dose (i.e. 0.95 Gy) to the individual would have to be given with the caveat that it could actually lie anywhere within this range of values. Of course, the statistical uncertainty on the calibration factors, which in the current example is ~ 6.3 % (Table 11.29), would also add to the inaccuracies that follow from these systematic uncertainties. Moreover, none of these analyses take into account the systematic uncertainties inherent to the Monte Carlo modelling, such as the uncertainties on the interaction cross-sections (X-5, 2003; Pelowitz, 2011; Eakins, 2009) or material specifications, or any of the other sources of uncertainty that are appropriate for the TL / OSL measurement techniques themselves.

The values of S^G_+ and S^G_- given in Table 11.29 highlight a significant problem in the use of mobile phones as emergency dosemeters in some cases. Specifically, although for ISO, FLR or ROT* exposures the dosimetry may be expected to be reasonably reliable, i.e. being accurate to within a few 10s of percent in all of the circumstances considered, for AP, PA, LLAT or RLAT the dose deposited in the resistors could be a very poor estimator of the dose received by the individual unless it is known exactly where the phone was located during the exposure. Without this location knowledge, a triage service based on TL/OSL analyses of phones would not be able to report doses with the confidence required for emergency dosimetry, and would hence effectively be unusable for mono-directional exposures apart from in identifying negligible doses, for which precise estimates would not be necessary. Fortunately, however, it might be anticipated that ISO, FLR or ROT* exposures of individuals are the ones that are most likely to occur in emergency scenarios. In particular, it is reasonable to suggest that actual emergencies may be most likely to take one of the general forms highlighted in '3)' above, that is: *a*) a plume of radioactive material has been released and has engulfed individuals, in which case ISO exposures are appropriate; *b*) a release of heavy radioactive debris has occurred that has settled as ground contamination, in which case FLR exposures of individuals are relevant; *c*) the source of radiation is located a significant distance away from individuals, who move relative to it during the exposure so that data for ROT* exposures may be considered suitable. In these anticipated scenarios, using mobile phones as emergency dosemeters could be considered reasonably accurate means of assessing whole body doses from external exposures, with uncertainties (i.e. S^G_+ and S^G_-) of only ~ ±5 % for ISO, ~ ±10-20 % for FLR and ~ ±5 % for

ROT* resulting as a consequence of ignorance of the location of the phone during ^{192}Ir, ^{137}Cs or ^{60}Co irradiations; if the ISO, FLR or ROT* nature of the field is also unknown, but mono-directional exposures are still considered unlikely, an overall worst-case uncertainty of ~ ±20 % is perhaps applicable. These uncertainties could rise to ~ ±20-40 % if the other sources of uncertainty discussed in this work are also taken into account, such as the issue regarding the presence / absence of the metal contacts surrounding the resistors, the positions of the resistors within the phone, or the orientation of the phone. Of course, none of these analyses take into account any of the other sources of uncertainty that are appropriate for the TL/OSL measurement techniques themselves. For triage dosimetry, for which nearest-gray assessments of exposures would generally be sufficient, this magnitude of uncertainty on a dose estimate may be considered acceptable, supporting the use of the proposed emergency dosimetry method in the above situations.

Part IV: Summary and Conclusions

Chapter 12: Summary and Conclusions

The primary research objectives of this study were (1) to empirically describe the physical mechanism of luminescence production in the polucrystalline alumina SMRs of a surrogate accident/emergency dosemeter, (2) obtain a more detailed understanding of the characteristics and the physical processes of the athermal or anomalous fading effect, and (3) to characterise the dosimetry properties of alumina SMRs, test their applicability as personal dosemeters under irradiation conditions which correspond more realistically to accidental exposures, and determine appropriate coefficients to convert the dose in the alumina SMRs to dose in air for triage application. The first two research questions were investigated using microscopic and spectroscopic characterisation methods, and a variety of TL and OSL techniques, where the processes that can take place following excitation with ionising radiation were explored both under stimulation with thermal and optical energy and during storage of the material. The implications of these investigations for dosimetry were also speculated. The latter was explored using both experimental and radiation transport simulations. The most important findings to address these issues, as well as future directions that can assist to solve unanswered questions are summarised below.

The technique of scanning electron microscopy was used to examine the microstructural arrangement of the surfaces and sub-surfaces of the alumina substrates and the influence this could have on certain macroscopic properties. The material was found to present a disordered morphology typical of polycrystalline sintered ceramics. A random and inhomogeneous distribution of grains, pores, and grain boundaries are the basic characteristics of the structure of the surfaces as well as of the layers beneath the outer surface, as revealed by examining optically polished samples. Overall, the chemical composition of the substrates is composed of aluminium and oxygen; with oxygen being less than aluminium. Smaller concentrations of other elements – mainly Mg, Ca, and Si– forming a seggregated phase preferentially located near and along the grain boundaries were identified in the electron micrographs. As discussed in Chapter 6, the existence of porosity, and consequently opacity, imposes a significant limitation in the use of the

material as an efficient luminescent emitter since the increased scattering of light at these microstructures reduces the light emission yield.

Closely related with the microstructure and the elemental composition of the alumina substrates, the spectral emission features of the luminescence were studied by means of cathodoluminescence (CL) spectroscopy. A broad emission band in the UV-Blue constitutes the CL emission at RT. The centres responsible for this emission are F-type colour centres resulting from oxygen deficiency which are likely to be a consequence of certain impurities, such as Mg. The F-centre with peak emission around 330 nm seems to contribute most of the luminescence as shown in the radioluminescence (RL) spectra, whereas the emission due to F^{+}-centre at ~ 420 nm appears to be notably thermally quenched even at RT. Although direct indication for the participation of the F-type centres in the production of the TL and OSL signal was not obtained in this study, indirect evidence was acquired by comparing the thermal quenching characteristics of the TL and OSL responses with that of the F-type centres. The close values of the quenching *W* factor calculated for TL and OSL in Chapter 9 and for F-centre (Chapter 6) point to the contribution of the F-centres as recombination sites during thermal and optical stimulation; which is within the detection window usually employed for TL and OSL measurements (typically 300-400 nm).

The nature of the traps where charges are captured after excitation with ionising radiation was investigated using TL and a series of thermal cleaning procedures (Chapter 7). For the main TL peak at ~ 200 ± 5°C (5 °C s^{-1}), which may be used in dosimetry applications, a distribution of traps at closely spaced increasing thermal depths was identified in the temperature region 150-290 °C. The non-first-order kinetics of the 200 °C TL peak with a continuum of trapping states may be another consequence of the polycrystalline and impure nature of the material itself. To calculate more accurately the range of the activation energy of these traps, a fine grain preparation technique was adopted which helps to eliminate the effect of temperature lag being more pronounced in thick samples, such as the 0.3-0.5 mm alumina substrate. Using fine- and coarse-grain samples the ´effective´ trap depth of the energy states responsible for the main TL peak at ~ 200 °C was found to be ~ 1.32 ±0.03 eV. This value predicts an average lifetime for thermal fading at RT of ca 23 years, indicating a relatively thermally stable trap for dose measurements. Generally, the generation of the TL response was interpreted in terms of a semi-

localised trap model where interaction between the various traps is likely. More specifically, during thermal stimulation, the trapped charge population –assumed to be mainly electrons– can be transferred to the recombination sites either via the conduction band or via a subconducting transition.

The second most important stimulated signal from alumina substrates –exploited in the experimental dose reconstruction trials so far– that of OSL arises from the trap distribution which gives rise to the TL signal from ~ 50 to 220 °C. As revealed from the optical bleaching experiments of TL (Chapter 9), blue light stimulation releases electrons from these traps which recombine both radiatively and non-radiatively, causing a reduction in the concentration of holes in the recombination centres, and consequently a reduction of the TL response. The radiative recombination of optically evicted electrons with holes during optical stimulation also results in the production of OSL.

The existence of numerous traps involved in the production of OSL was confirmed by the deconvolution of the OSL decay curves, where a number of components were identified resulting an overall non-exponential decay form (Chapter 8). Following a preheat to 120 °C (10 s) only a thermally stable OSL signal suitable for dosimetry remains which was found to be associated with traps having an average thermal depth of ~ 1.30 ±0.02 eV; a value similar to the ´effective´ thermal depth calculated for the traps giving rise to TL. For the OSL mechanism and due to the unknown optical depth of the relevant traps two cases were considered which both can account for the dependence of the OSL intensity on the sample temperature, T_s. Assuming that the optically sensitive traps lie at optical depths greater than the energy of the stimulating photons (i.e., 2.6 eV for blue light), a thermally activated recombination mechanism involving transitions to an intermediate state (i.e., excited state of the trap) seems very likely. If, however, the optical trap depth is lower than 2.6 eV, OSL could be generated when electrons recombine with holes through transitions into the conduction band. In this case, the temperature dependence effects of the OSL (i.e., increase of rate of decay and enhancement of OSL light sum with increasing stimulation temperature) can be explained by taking into account the variation of the photo-ionisation cross section with temperature. In particular, the probability of optical eviction (i.e., photo-ionisation cross section) of trapped charges increases as the measurement temperature rises due to additional energy provided by the phonons of the alumina lattice. The existence of

electron-phonon interactions was evidenced both in the spectral emission measurements (Chapter 6) – where the broadening of the emission bands attributable, supposedly, to electron-phonon coupling was observed with increasing sample temperature – and in the FTIR measurements (Chapter 6) which showed the presence of several vibrational modes with some corresponding to phonon energies close to 0.10 eV; a value which correlates well with the value of the thermal activation energy calculated for the OSL process.

As demonstrated in previous studies and further in this thesis (Chapter 11), the alumina SMR components present favourable dosimetry characteristics in terms of dose response, reproducibility, and low dose detection capabilities. Nevertheless, the stimulated luminescence signals rapidly fades when there is a delay between the administration of dose and stimulation and, for accurate dose assessments, the time delay must be known. Fading can be thermal in nature, athermal (i.e., anomalous) or a combination of both. The thermal component of fading can be predicted using the kinetic parameters (activation energy, frequency factor, and lifetime) of the TL glow peaks and also be reduced with a suitable thermal cleaning procedure. For OSL, the thermal component of fading was shown to be associated mainly with the low-temperature TL peak at ~ 100 °C, and by preheating the samples to 120 °C it can be removed leaving only the athermal component. The latter, however, is associated with the range of traps which constitute the luminescence signal used in dosimetry and cannot be easily eliminated.

To examine the characteristics of athermal fading different experimental tests were performed. The logarithmic dependence of the TL and OSL signal loss on the elapsed time since irradiation and the rapid fading rate observed at short times followed by slower rate at longer delays are in accordance with both a quantum mechanical tunnelling and a localised transition model. Yet, the quantum mechanical tunnelling model appeared less appropriate when the fading behaviour of the TL Peak 2 was examined over different temperature intervals. In Wheeler's model (1995) the high temperature side of a TL glow peak is expected to fade faster than the low temperature side if the fading is due to a quantum mechanical tunnelling process. In the case of alumina SMRs, the rising part of the TL Peak 2 was affected more during storage and this favours a localised transition model. Another indication that a quantum mechanical tunnelling mechanism may not be the dominant mechanism at RT was obtained from the measurement of the fading while the samples stored in a strong magnetic field (Chapter 10). In this case, the presence of a strong

magnetic field may cause the shrinkage of the localisation length of the electron wavefunction away from the recombination site which in turn would slow down the recombination process and would result in lower rate of fading. Yet, as shown, there was no conclusive difference in the fading for samples stored inside a strong magnetic field.

Perhaps the strongest indication that the mechanism of athermal fading is likely to be different to the widely accepted quantum mechanical tunnelling model comes from the results obtained when the samples were stored at temperatures above RT. Measurement of fading at elevated storage temperature indicated the existence of thermal acceleration of the rate of fading which does not conform with the resonant quantum mechanical tunnelling model. On the other hand, the temperature dependence of athermal fading could be well accounted for by the localised transition model or, as discussed in Chapter 10, by some alternative charge transport processes which include hopping over the potential barrier separating the trap and the recombination centre. According to the localised transition model, the probability of trap emptying is exponentially dependent on temperature and when the latter increases faster rate of fading may be observed since the probability of escape increases. In the hopping process it could be supposed that thermal energy provided by the vibrational modes (i.e., phonons) of the crystal lattice enables a tunnelling process from the traps to the recombination sites. In this case, the higher the temperature of the samples, the stronger the contribution of phonons in the hopping process and, therefore, the higher is the rate of fading. Both thermally-activated processes rely on the existence of vibrational modes which are present in the crystal lattice of the alumina-based SMRs, as evidenced in the FTIR measurements. The linear dependence of the fading rate on the inverse of storage temperature found for both the TL and OSL is also in accordance with a localised transition or a hopping process.

Consequently it is likely that the athermal fading in the alumina substrates is not due to a single mechanism and that the temperature of the samples during storage determines which mechanism prevails. So, for instance, it was found that even when the samples were stored at temperature close to the absolute zero the fading process was slightly slowed down but not eliminated. This observation suggests that the temperature-independent quantum mechanical tunnelling may be responsible for the loss of charges at these temperatures since all the other thermally activated processes are suppressed by the lack of thermal/phonon energy. At temperatures equal or greater

than RT more than one process likely contributes to the athermal fading, but those assisted by the presence of phonons have greater potential.

The last part of this research (Chapter 11) concerned the dosimetry characteristics of SMRs, as well as other issues that need to be taken into consideration when SMRs from mobile phones are used as fortuitous dosemeters. In accordance with previous studies, it was shown that the alumina SMRs despite the less favourable loss of luminescence signal with storage time, demonstrate some of the requirements for dose assessment, such as a linear dose response to 20 Gy and capability of detecting low doses of the order of mGy. Also, it was shown that the measurements protocols suggested by the MULTIBIODOSE project provide an adequate compromise between time needed to complete a measurement cycle and uncertainty in the calculated dose.

Nevertheless, there exist other factors to be considered for accurate dose reconstruction in an emergency situation. Perhaps, two of the most important factors are the energy of the exposure and the location of the device on the individual's body with regards to the direction of the exposure. At low-energy exposures the doses may be over-estimated not only due to the non-flat energy response of the alumina but also due to the presence of several parts – containing heavy elements (e.g., printed circuit board) – of the mobile phones which can increase the amount of energy deposited onto the alumina substrates due to backscatter effects. In addition, MCNP simulations indicated that large discrepancies between SMRs and whole body doses are expected for low-energy exposures: for ^{192}Ir, differences of up to an order-of-magnitude were found between resistor and whole body doses. The location of the phone relative to the source is crucial to determine the effect of the attenuation of the irradiation through an individual's body but also, as demonstrated in the MCNP simulations, to specify the most appropriate dose conversion coefficients that can be applied to estimate whole body doses from OSL / TL determinations, the accurate application of which would depend on the knowledge of the exposure geometry and the degree of conservatism acceptable for the dose assessment

Future Work

For a more complete understanding of the physical mechanism of the generation of luminescence in the alumina substrate of SMR components and, potentially, a more accurate use of the material as accident dosemeter there are certain issues that need to be addressed.

Acquisition of the emission spectra of the steady TL and OSL response following excitation with ionising radiation would help to identify the actual nature of the recombination centres participating during thermal or optical stimulation. This, in turn, could be used to define more accurately the detection window employed during measurements of the TL and OSL.

Thermally stimulated conductivity measurements (TSC) measurements could be helpful to determine the extent to which the delocalised conduction band is a possible route for the thermally excited charges and, therefore, validate the semi-localised transition model suggested for the TL process. Specifically, the existence of TSC peaks at same locations as the TL peaks would strongly indicate the presence of electronic conductivity due electrons transferred into the conduction band during thermal stimulation.

For the OSL mechanism, additional information is likely to be obtained by performing temperature dependence measurements using various wavelengths which may help to differentiate between the Hütt and Spooner models. Also, optically (and thermally stimulated exoelectronic emission may help to understand if electrons are transported directly into the conduction band. Finally, measurement of the optical depth of the traps could clarify the importance of an electron-phonon interaction model.

Concerning the mechanism of athermal stability, a study of the temperature dependence of the effect over a wider temperature range may be able to clarify which of the models suggested in Chapter 10 prevails, depending on the temperature the material is held during storage. In addition, repeated measurement of the fading rate for delay periods longer than the longest time investigated in this thesis (i.e., 1 year) may clarify whether there is a stable signal which could be used for long term retrospective dose estimations.

Additional radiological trials under more realistic exposure conditions incorporating different radiation sources (i.e., energy, particle type) or mixture of sources and different exposure

geometries using anthropomorphic phantoms would better characterise the performance of SMRs as dosemeters and their capability to provide whole body personal doses.

Appendices

Appendix A1

Secondary electron (SE) and backscattered electron (BSE) images of unpolished alumina substrate samples (i.e., type ´0402´ SMR) obtained at different magnification levels using variable electron beam energy.

15 kV

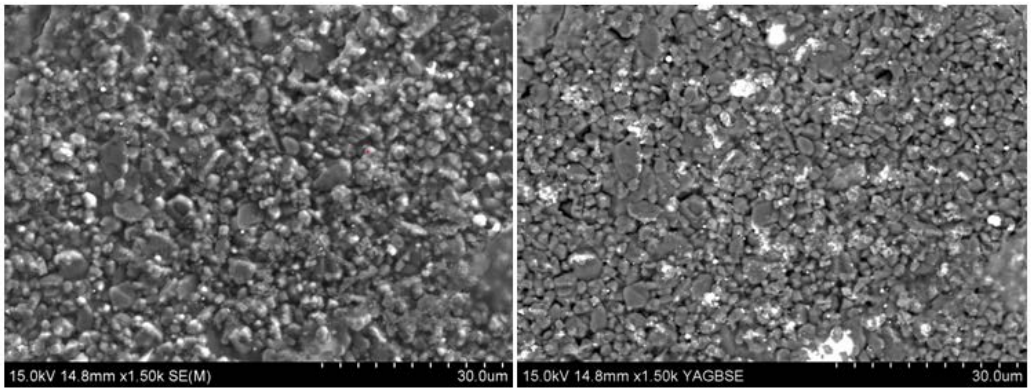

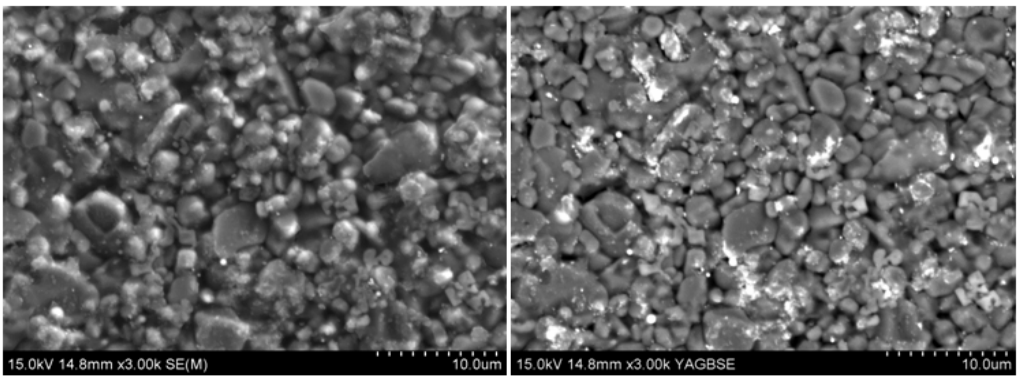

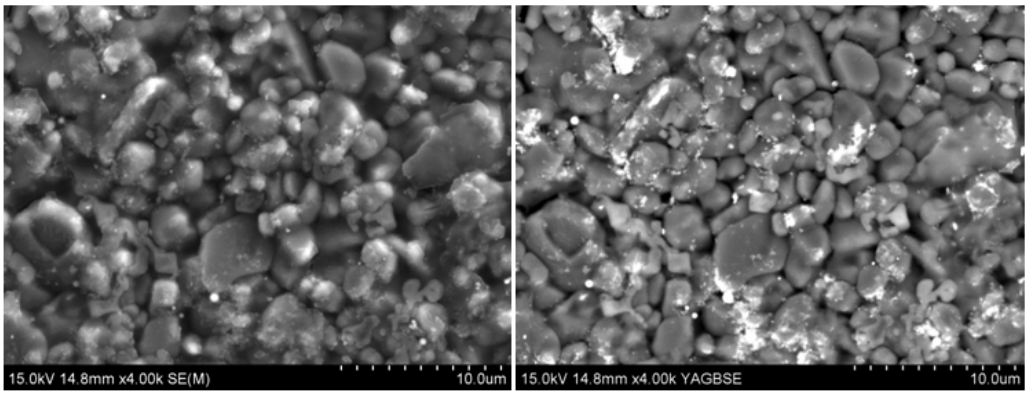
15.0kV 14.8mm x4.00k SE(M)
10.0um
15.0kV 14.8mm x4.00k YAGBSE
10.0um

10 kV

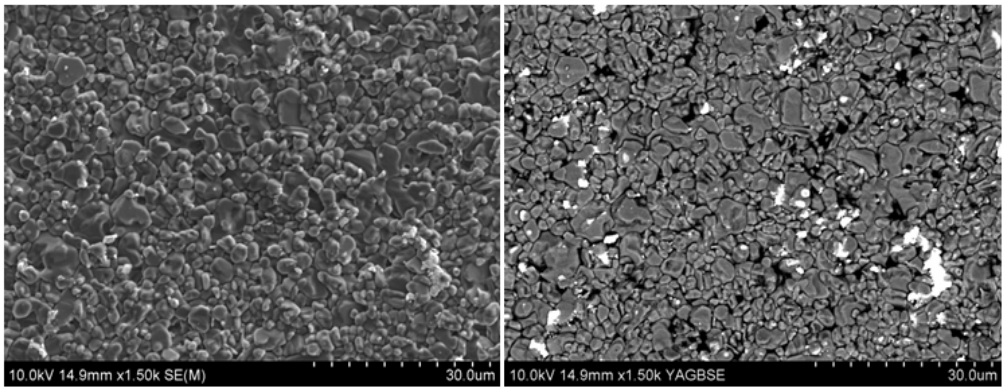
10.0kV 14.9mm x1.50k SE(M)
30.0um
10.0kV 14.9mm x1.50k YAGBSE
30.0um

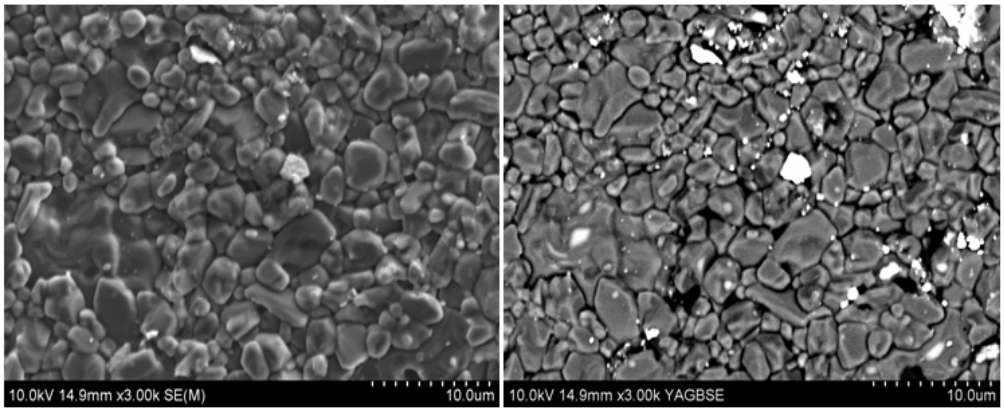
10.0kV 14.9mm x3.00k SE(M)
10.0um
10.0kV 14.9mm x3.00k YAGBSE
10.0um

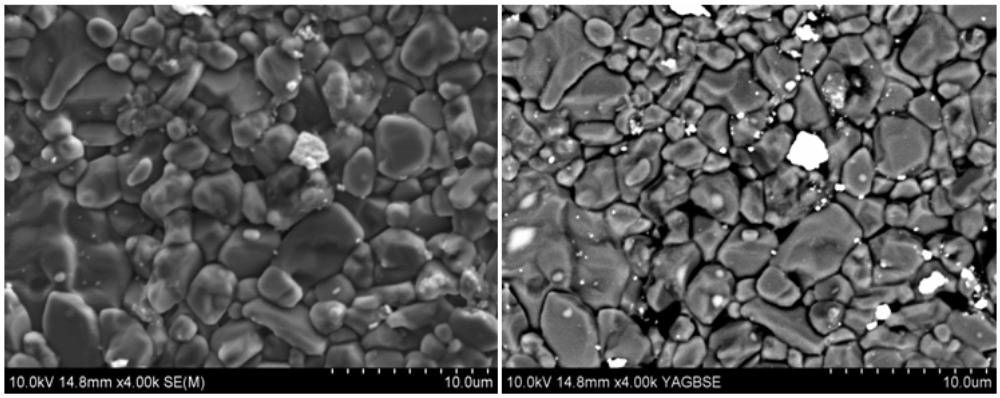
10.0kV 14.8mm x4.00k SE(M)
10.0um
10.0kV 14.8mm x4.00k YAGBSE
10.0um

Appendix A2

Three dimensional radioluminescence (RL) emission spectra as a function of temperature in (a) the low-temperature range between -250 and 20 °C, and (b) in the high-temperature range between 40 and 400 °C.

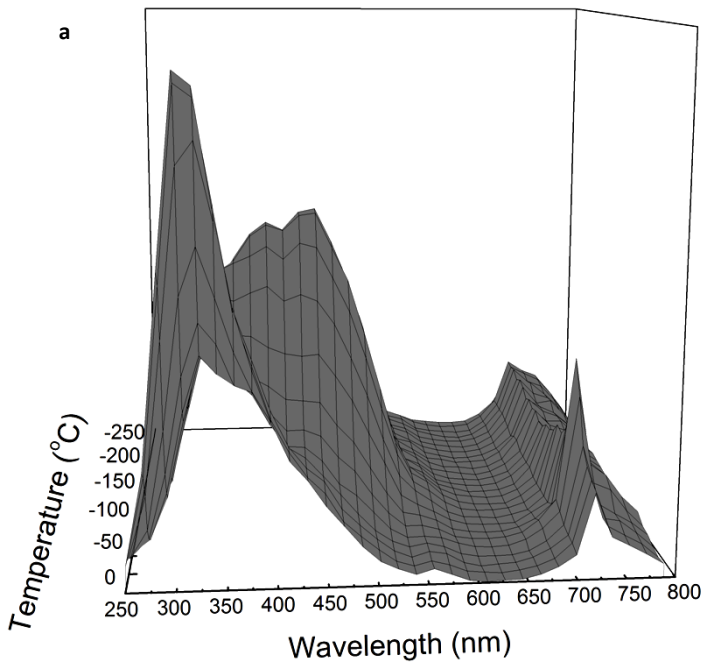

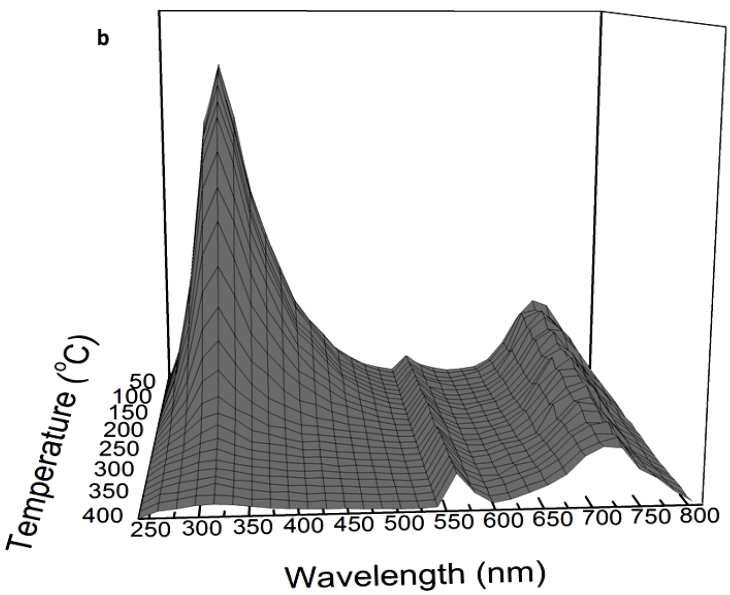
b
Temperature (°C)
50
100
150
200
250
300
350
400
250 300 350 400 450 500 550 600 650 700 750 800
Wavelength (nm)

Appendix A3 – Selected Publications

Some of the research work presented in this thesis has been published.

1. "Luminescence characterisation of alumina substrates using cathodoluminescence microscopy and spectroscopy". E. C. Kouroukla, I. K. Bailiff, I. Terry and L. Bowen. Radiation Measurements 71 (2014) 117-121 doi:10.1016/j.radmeas.2014.03.018

2. "Luminescence-based retrospective dosimetry using Al_2O_3 from mobile phones: a simiulation approach to determine the effects of position." Journal of Radiation Protection 35 (2015) 343-38, http://dx.doi.org/10.1088/0952-4746/35/2/343 1

Bibliography

Agersnap-Larsen, N., Bøtter-Jensen, L., McKeever, S. W. S. (1999). Thermally stimulated conductivity and thermoluminescence from Al_2O_3:C. Radiat. Prot. Dosim. 84 (1-4): 87-90.

Agnew, P. (1992). Displacement thresholds in sapphire. Philos. Mag. A. 65:355-361.

Ainsbury, E. A., Bakhanova, E., Barquinero, J. F., Brai, M., Chumank, V., Correcher, V., Darroudi, F., Fattibene, P., Gruel, G., Guclu, I., Horn, S., Jaworska, A., Kulka, U., Lindholm, C., Lloyd, P., Longo, A., Marrale, M., Monteiro Gil, O., Oestreicher, U., Pajic, J., Rakic, J., Romm, H., Trompier, F., Veronese, I., Voisin, P., Vral, A., Whitehouse, C. A., Wieser, A., Woda, C., Wojcik, A., Rothkamm, K. (2011). Review of retrospective dosimetry techniques for external ionising radiation exposures. Radiat. Prot. Dosim. 147 (4): 573-592.

Aitken, M. J. (1985). Thermoluminescence dating. Academic press Inc, (London), Ltd, London.

Aitken, M. J. and Smith. B. W. (1988). Optical dating: Recuperation after bleaching. Quatern. Sci. Rev. 7 (3-4):387-393.

Akselrod, A. E. and Akselrod, M. S. (2002). Correlation between OSL and the distribution of TL traps in Al_2O_3:C. Radiat. Prot. Dosim. 100 (1-4): 217-220.

Akselrod, A., Akselrod, M. S., Agersnap-Larsen, N., Banerjee, D., Bøtter-Jensen, L., Christensen, P., Lucas, A. C., McKeever, S. W. S., Yoder, R. C. (1999). Optically stimulated luminescence response of Al_2O_3 to beta radiation. Radiat. Prot. Dosim. 85 (1-4): 125-128.

Akselrod, M. S. and Gorelova, E. A. (1993). Deep traps in highly sensitive α-Al_2O_3:C TLD crystals. Nucl. Tracks. Radiat. Meas. 21 : 143-146.

Akselrod, M. S., Agersnap–Larsen, N., Whitley, V., McKeever, S. W. S. (1998). Thermal quenching of F-center luminescence in Al_2O_3:C. J. Appl. Phys. 84 (6): 3364-3373.

Akselrod, M. S., Bøtter-Jensen, L., McKeever, S. W. S. (2006). Optically stimulated luminescence and its use in medical dosimetry. Radiat. Meas. 41: S78-S99.

Akselrod, M. S., Kortov, V. S., Gorelova, E. A. (1993). Preparation and properties of α-Al_2O_3:C. Radiat. Prot. Dosim. 47: 159-164.

Akselrod, M. S., Kortov, V. S., Kravetsky, D. J., Gotlib, V. I. (1990). Highly sensitive thermoluminescence anion-defect α-Al_2O_3:C single crystal detector. Radiat. Prot. Dosim. 33: 119-122.

Akselrod, M. S., McKeever, S. W. S., Moscovitch, M., Emfietzoglou, D., Durham, J. S., Soares, C. G. (1996). A thin layer α-Al_2O_3:C beta TL detector. Radiat. Prot. Dosim. 66 (1-4). 105-110.

Akserlod, M. S. and Kortov, V. S. (1990). Thermoluminescent and exoemission properties of new high- sensitivity TLD α-Al_2O_3:C crystals. Radiat. Prot. Dosim. 33 (2):123-126.

Akserlod, M. S., Kortov, V. S., Kravetsky, D. J., Gotlib, V. I. (1990). High-sensiitivity thermoluminescence anion defective α-Al_2O_3:C single crystals detectors. Radiat. Prot. Dosim 32 (1):15-20.

Alexander, G. A., Swartz, H. M., Amundson, S. A., Blakely, W. F., Buddemeier, B., Gallez, B., Dainiak, N., Goans, R. A., Hayes, R. B., Lowry, P. C., Noska, M. A., Okunieff, P., Salner, A. L., Schauer, D. A., Trompier, F., Turteltaub, K. W., Voisin, P., Wiley Jr, A. L., Wilkins, R. (2007). BiodosEPR-2006 Meeting: Acute dosimetry consensus committee recommendations on biodosimetry applications in events involving uses of radiation by terrorists and radiation accidents. Radiat. Meas. 42 (6-7): 972-996.

Alpen, E. L. (1990). Radiation biophysics. 2nd ed. San Diego, CA, Academic Press.

Altay, A. and Gulgun, M. A. (2003). Microstructural evolution of calcium-doped α-alumina. J. Am. Soc. 86 (4): 623-629.

Arnold, A. G. and Compton, W. D. (1958). Threshold energy for lattice displacement in α-Al_2O_3. Phys. Rev. Lett. 4 (2): 66-68.

Atkinson, K. J. W., Grimes, R. W., Levy, M. R., Coull, Z. L., English, T. (2003). Accommodation of impurities in α-Al_2O_3, α-Cr_2O_3 and α-Fe_2O_3. J. Europ. Ceram. Soc. 23: 3059-3070.

Attix, F. H. (1968). Basic γ-ray dosimetry. Health Phys. Pergammon Press 15: 49-56.

Auclair, R., Lamothe, M., Huot, S. (2003). Measurement of anomalous fading for feldspar IRSL using SAR. Radiat. Meas. 37 (4-5): 487-492.

Aznar, M. C., Andersen, C. E., Bøtter-Jensen, L., Back, S. A., Mattsson, S., Kiaer-Krsitoffersen, F., Medlin, J. (2004). Real-time optical-fibre luminescence dosimetry for radiotherapy: Physical characteristics and applications in proton beams. Phys. Med. Biol. 49 (9): 1655-1669.

Azorin, J. (1986). Determination of thermoluminescence parameters from glow curves I. A review. Nuclear Tracks 11 (3): 159-166.

Bailey, R. M. (1998). The form of the optically stimulated luminescence signal of quartz: Implications for dating. PhD Thesis. Royal Holloway, University of London.

Bailiff, I. K., Stepanenko, V. F., Goksu, H. Y., Bøtter-Jensen, L., Brodski, L., Chumak, V., Correcher, V., Delgado, A., Golikov, V., Jungner, H., Khamidova, L. G., Kolizshenkov, T. V., Likhtarev, I., Meckbach, R., Petrov, S. A., Sholom, S. (2004a). Comparison of retrospective luminescence dosimetry with computational modeling in two highly contaminated settlements downwind of the Chernobyl NPP. Health Phys. 86 (1): 25-41.

Bailiff, I. K. (1995).The use of ceramics for retrospective dosimetry in the Chernobyl exclusion zone. Radiat. Meas. 24 (4): 507-511.

Bailiff, I. K. (1996). The use of luminescence techniques with ceramics for retrospective dosimetry. In: The Radiological Consequences of the Chernobyl Accident, Eds A. Karaoglou, G. Desmet, G. N. Kelly and H. G. Menzel, pp. 985–994.

Bailiff, I. K. (1997). Retrospective dosimetry with ceramics. Radiat. Meas. 27 (5-6): 923-941.

Bailiff, I. K. (1999). The development of retrospective luminescence dosimetry for dose reconstruction in areas downwind of Chernobyl. Radiat. Prot. Dosim. 84 (1-4): 411-419.

Bailiff, I. K. and Clark, R. J. (1999). A preliminary study of fast time-resolved luminescence in Al_2O_3:C. Rad. Prot. Dosim. 84 (1-4):457-460.

Bailiff, I. K. and Poolton, N. R. J. (1991). Studies of charge transfer mechanisms in feldspars. Nucl. Tracks Radiat. Meas. 18 (1-2): 111-118.

Bailiff, I. K., Correcher, V., Delgado, A., Göksu, Y., Habner, S. (2002). Luminescence characteristics of dental ceramics for retrospective dosimetry: A preliminary study. Radiat. Prot. Dosim. 101 (1-4): 519-524.

Bailiff, I. K., Stepanenko, V. F., Göksu, H. Y., Jungner, H., Balmukhanov, S. B., Balmukhanov, T. S., Khamidova, L. G., Kisilev, V. I, Kolyado, I. B., Kolizshenkov, T. V., Shoikhet, Y. N., Tsyb, A. F. (2004b). The application of retrospective luminescence dosimetry in areas affected by fallout from the Semipalatinsk nuclear test site: an evaluation of potential. Health Phys. 87 (6): 625-4.

Baril, M. R. and Huntley, D. J. (2003). Optical excitation spectra of trapped electron in irradiated feldspars. J. Phys.: Condens. Matter 15: 8011–8027

Barthe, J., Kamenopoulou, V., Portal, G. (1989). Dose evaluation from textile fibers: a post-determination of ESR initial signal. Appl. Radiat. Isot. 40 (10-12): 1029-1033.

Bassinet C., Woda C., Bortolin E., Della Monaca S., Fattibene P., Quattrini M. C., Bulanek B., Ekendahl D., Burbridge C. I., Cauwels V., Kouroukla E., Geber-Bergstrand T., Mrozik A., Marczewska B., Bilski P., Sholom S., McKeever S. W. S., Smith R. W., Veronese I., Galli A., Panzeri L., Martini M. (2014). Retrospective radiation dosimetry using OSL of electronic components: Results of an inter-laboratory comparison. Radiat. Meas. In press

Bassinet, C., Piraut, N., Baumann, M., Clairand, I. (2014). Radiation accident dosimetry: TL properties of mobile phone screen glass. Radiat. Meas. In press.

Bassinet, C., Trompier, F., Clairand, I. (2010a). Radiation accident dosimetry on glass by TL and EPR spectrometry. Health Phys. 98 (2): 400-405.

Bassinet, C., Trompier, F., Clairand, I. (2010b). Radiation accident dosimetry on electronic components by OSL. Health Phys. 98 (2): 440-445.

Beerten K. and Vanhavere F. (2010). Photon energy dependence of three fortuitous dosemeters from personal electronic devices measured by optically stimulated luminescence. Radiat. Prot. Dosim. 140 (3): 294-299.

Beerten, K., Woda C., Vanhavere, F., (2009). Thermoluminescence dosimetry of electronic components from personal objects. Radiat. Meas. 44 (5-6): 620-625.

Blasse, G. and Grabmaier, B. C. (1994). Luminescent materials. Springer-Verlang.

Boch, P. and Niepce, J. C. (2007). Ceramic materials. Processes, properties and applications. ISTE LTd.

Bonnelle, C. (2010). Multiphonon-induced charge trapping-detrapping and damage in insulators. Phys. Rev. B. 81: 054307.

Bonnelle, C. And Jonnard, P. (2010). Dynamics of charge trapping by electron-irradiated alumina. Phys. Rev. B. 82: 075132.

Bonnelle, C. and Jonnard, P. (2010). Dynamics of charge trapping by electron irradiated alumina. Phys. Rev. B. 82: 075132-8.

Bøtter-Jensen L. (1997). Luminescence techniques: instrumentation and methods. Radiat. Meas. 27:749-768.

Bøtter-Jensen, L. and McKeever, S. W. S. (1996). Optically stimulated luminescence dosimetry using natural and synthetic material. Radiat. Prot. Dosim. 65 (1-4): 273-280.

Bøtter-Jensen, L., Agersnap-Larsen, N., Markey, B. G. (1997). Al_2O_3:C as a sensitive OSL dosemeter for rapid assessment of environmental photon dose rates. Radiat. Meas. 27 (2): 295-298.

Bøtter-Jensen, L., Banerjee, D., Jungner, H., Murray, A. S. (1999). Retrospective assessment of environmental dose rates using optically stimulated luminescence from α-Al_2O_3:C and quartz. Radiat. Prot. Dosim. 84 (1-4): 537-542.

Bøtter-Jensen, L., S.W.S. McKeever, S. W. S., Wintle, A. G. (2003). Optically Stimulated Luminescence Dosimetry 1st edn. Elsevier Science BV.

Brewer, J. D., Jeffries, J. D., Summers, G. P. (1980). Low-temperature fluorescence in sapphire. Phys. Rev. B. 22 (10): 4900-4906.

Brooks, R. J., Finch, A. A., Hole, D. E., Townsend, P. D., Wu, Z. L. (2002). The red to near infra-red luminescence in alkali feldspar. Contrib. Mineral. Petrol. 143 (4): 484-494.

Bruce, J., Galloway, R. B., Harper, K., Spink, E. (1999). Bleaching and phototransfer of thermoluminescence in limestone. Radiat. Meas. 30 (4): 497-504.

Bull, C. and Garlick, G. F. J. (1950). Proceedings of the Physical Society of London 63: 1283-1291.

Bull, R. K., McKeever, S. W. S., Chen, R., Mathur, V. K., Rjodes, J., Brown, M. D. (1986). Thermoluminescence kinetics for multi-peak glow curves produced by the release of electrons and holes. J. Phys. D: Appl. Phys. **19**, 1321 – 1334.

Bulur, E. (1996). An alternative technique for optically stimulated luminescence (OSL) experiment. Radiat. Meas. 26: 701-709.

Bulur, E., Goksu, H. Y., Wahl, W. (1998). Infrared (IR) stimulated luminescence from α-Al_2O_3:C. Radiat. Meas. 2(6): 625-638.

Burbidge, C. I. and Duller, G. A. T. (2003). Combined gamma and beta dosimetry, using Al_2O_3:C, for in situ measurements on a sequence of archaeological deposits. Radiat. Meas. 37(4-5): 285-291.

Caracelli, I., Terille, M. C., Mascarenhas, S. (1986). Electron spin resonance dosimetric properties of bone. Health Phys. 50 (2): 259-263.

Carter, C. B. and Nortor, M. G. (2007). Ceramic materials. Science and Engineering. Springer.

Catlow, C., James, R., Mackrodt, W. C., Stewart, R. F. (1982). Defect energetics in α-Al_2O_3 and rutile TiO_2. Phys. Rev. B 25 (2): 1006-1026.

Chase, W. J. and Hirning, C. R. (2008). Application of radiation physics in the design of Harshaw 8828 beta-gamma TLD. Radiat. Meas. 43 (2-6): 525-532.

Chen, R. and Hag-Yahya, A. (1997). A new possible interpretation of the anomalous fading in thermoluminescent materials as normal fading in disguise. Radiat. Meas. 27 (2): 205-210.

Chen, R. and Kirsh, Y. (1981). Analysis of thermally stimulated processes. Pergamon Press Ltd., Oxford, England.

Chen, R. and McKeever, S. W. S. (1997). Theory of Thermoluminescence and Related Phenomena. World Scientific Publishing Co. Pte. Ltd., London.

Chen, R. and Pagonis, V. (2011). Thermally and Optically Stimulated Luminescence. A simulation approach. John Wiley & Sons Ltd, West Sussex.

Chen, R. and Winer, S. A. A. (1970). Effects of various heating rates on glow curves. J. App. Phys. 41(13): 5227-5232.

Chen, R., Fogel, G., Lee, C. K. (1996). A new look at the models of the superlinear dose dependence of thermoluminescence. Radiat. Prot. Dosim. 65 (1-4): 63-68.

Chen, R., Hornyak, W. N., Mathur, V. K. (1990). Competition between excitation and bleaching of thermoluminescence. J. Phys. D: Appl. Phys. 23 (6): 724-728.

Chen, R., Leung, P. L., Stokes, M. J. (2000). Apparent anomalous fading of thermoluminescence associated with competition with radiationless transitions. Radiat. Meas. 32(5-6): 505-511.

Chithambo, M. L. and Seneza, E. Z. (2014). Kinetics and dosimetric features of secondary thermoluminescence in carbon-doped aluminium oxide. Phys. B. 439: 165-168.

Choi, J. H., Duller, G. A. T., Winlte, A. G. (2006). Analysis of quartz LM-OSL curves. Anc. TL. 24 (1): 9-20.

Clark, R. J. and Sanderson, D. C. W. (1994). Photostimulated luminescence excitation spectroscopy of feldspars and micas. Radiat. Meas. 23 (2-3): 641-646.

Colak, S. and Ozbey, T. (2011). An ESR study on biological dosimeters: Human hair. Radiat. Meas. 46 (5): 465-472.

Correcher, V., Gomez-Ros, J. M., Garcia-Guinea, J., Lis, M., Sanchez-Munoz, L. (2008). Calculation of the activation energy in a continuous trap distribution system of a charoite silicate using initial rise and TL glow curve fitting methods. Radiat. Meas. 43: 269-272.

Cristy, M., and Eckerman, K. F. (1987). Specific absorbed fractions of energy at various ages from internal photon sources. ORNL Report: ORNL/TM-8381/V1.

Cruscinska, A. (2010). On some fundamental features of optically stimulated luminescence measurements. Radiat. Meas. 45 (9): 991-999.

Cui J. and Zhang L., (2008). Metallurgical recovery of metals from electronic waste. J. Hazard. Mat. 158 (2-3): 228-256.

Curie, D. (1963). Luminescence in crystals. Methuen & CO LTD, London.

Dallas, G. I., Polymeris, G. S., Afouxenidis, D., Tsirliganis, N. C., Tsagas, N. F., Kitis, G. (2010). Correlation between TL and OSL signals in $KMgF_3:Ce^{3+}$: Bleaching study of individual glow peaks. Radiat. Meas. 45 (3-6): 537-539.

Davies, J. E. (1979). On the use of dental ceramics as a possible second-line approach to accident irradiation dosimetry. Radioprotection 14 (2): 89-97.

Denis, G., Rodriguez, M. G., Akselrod, M. S., Underwood, T. H., Yukihara, E. G. (2011). Time-resolved measurements of optically stimulated luminescence of Al_2O_3:C and Al_2O_3:C,Mg. RadiaT. Meas. 46 (12): 1457-1461.

Desrosiers, M. and Schauer, D. A. (2001). Electron paramagnetic resonance (EPR) biodosimetry. Nucl. Instr. Meth. Phys. Res. B. 184 (1-2): 219-228.

Desrosiers, M. F. and Wadley, S. (2006). Time dependence of the radiation-induced EPR signal in sucrose. Radiat. Prot. Dosim. 118 (4): 479-481.

Discher, M. and Woda, C. (2013). Thermoluminescence of glass display from mobile phones for retrospective and emergency dosimetry. Radiat. Meas. 53-54: 12-21.

Discher, M., Woda, C., Fiedler, I. (2013). Improvement of dose determination using glass display of mobile phones for accident dosimetry. Radiat. Meas. 56 : 240-243.

Draeger, B. G. and Summers, G. P. (1979). Defects in unirradiated α-Al_2O_3. Phys. Rev. B. 19 (2): 1172-1177.

Duggan, L., Budzanowski, M., Przegietka, K., Reitsema, N., Wong, J., Kron, T. (2000). The light sensitivity of thermoluminescent materials; LiF:Mg,Cu,P, LiF:Mg,Ti, and Al_2O_3:C. Radiat. Meas. 32: 335-342.

Eakins, J. S. (2009). On the effect of updated MCNP photon cross section data on the simulated response of the HPA TLD. Radiat. Prot. Dosim. 134, 66-71.

Eakins, J. S. (2010). The design of the new HPA personal thermoluminescent dosemeter. HPA-CRCE-007.

Ekendahl, D., Judas, L., Sukupova, L. (2013). OSL and TL retrospective dosimetry with a fluorapatite glass-ceramic used for dental restorations. Radiat. Meas. 58 :138-144.

Ekendhal, D., Judas L. (2012). Retrospective dosimetry with alumina substrate from electronic components. Radiat. Prot. Dosim. 150 (2): 134-141.

El-Faramawy, N. A., Göksu, H. Y., Pazner, W. (2004). Thermoluminescence dosimetric properties of a new thin beta detector (LiF:Mg, Cu, P; GR-200F) in comparison with highly sensitive Al_2O_3:C beta dosimeters. J. Radiol. Prot. 24(3): 273-282.

Emin, D. (1975). Transport properties of small polarons. J. Solid. State Chem. 12 (3-4): 246-252.

Engin, B., Aydas C., Demirtas, H. (2006). ESR dosimetric properties of window glass. Nucl. Instr. Meth. B 243 (1): 149-155.

EUR 5358, Commission of the European Community, (1975). Technical recommendations for the use of thermoluminescence for dosimetry in individual monitoring for photons and electrons from external sources.

Evans, B.D. and Stapelbroek, M. (1978). Optical properties of the F^+ center in crystalline Al_2O_3. Phys. Rev. B 18: 7089-7098.

Fattibene, P. and Callens, F. (2010). EPR dosimetry with tooth enamel: A review. Appl. Radiat. Isot. 68 (11): 2033-2116.

Fattibene, P., Duckworth, T. L., Desrosiers, M. F. (1996). Critical evaluation of the sugar-EPR dosimetry system. Appl. Radiat. Isot. 47 (11-12): 1375-1379.

Fattibene, P., Trompier, F., Wieser, A., Brai, M., Ciesielski, B., De Angelis, C., Della Monaca, S., Garcia, T., Gustafsson, H., Hole, E. O., Juniewicz, M., Krefft, K., Longo, A., Leveque, P., Lund, E., Marrale, M., Michalec, B., Mierzwin´ska, G., Rao, J. L., Romanyukha, A. A., Tuner, H. (2014). EPR dosimetry intercomparison using smart phone touch screen glass. Radiat. Envir. Biophys. 53 (2): 311-320.

Fiedler, I. and Woda, C. (2011). Thermoluminescence of chip inductors from mobile phones for retrospective and accident dosimetry. Radiat. Meas. 46: 1862-1865.

Filin, A. I., Kukushkin, I. V., Larionon, A. V., Klitzing, K. Von. (1995). Wave function of 2D electrons in a parallel magnetic field. JETP Lett, 61 (8): 706-711.

Flerov, V. I., Flerov, A. V., Flerov, S. I. (1996). Photoinduced thermoluminescence in corundum. Radiat. Meas. 26 (2): 253-258.

Franklin, A. D., Hornyak, W. F., Chen, R. (1993). A one trap, two luminescence centre TL model. Rad. Prot. Dosim. 47(1-4): 17-22.

Fu, X., Zhang, J-F., Zhou, L. P. (2012). Comparison of the properties of various optically stimulated luminescence signals from potassium feldspar. Radiat. Meas. 47 (3): 210-218.

Furetta, C. (2010). Handbook of thermoluminescence. 2nd ed. World Scientific Publishing Co Pte Ltd. London.

Furetta, C., Kitis, G., Kuo, C. H. (2000). Kinetic parameters of CVD diamond by computerized glow-curve deconvolution (CGCD). Nucl. Instr. and Meth. in Phys. Res. B 160: 65-72.

Gancheva, V., Yordanov, N. D., Karakirova, Y. (2006). EPR investigation of the gamma radiation response of different types of glasses. Spectr. Acta. A 63 (4): 875-878.

Garlick, G. F. J. and Gibson, A. F. (1948). The electron trap mechanism of luminescence in sulphide and silicate phosphors. Proc. Phys. Soc. 60: 574-590.

Gaza, R., McKeever, S. W. S., Akselrod, M. S., Akselrod, A., Underwood, T., Yoder, C., Andersen, C. E., Aznar, M. C., Marckmann, C. J., Bøtter-Jensen, L. (2004). A fiber-dosimetry method based on OSL from Al_2O_3:C for radiotherapy applications. Radiat. Meas. 38(4-6): 809-812.

Gaza, R., Yukihara, E. G., McKeever, S. W. S. (2004). The response of thermally and optically stimulated luminescence from Al_2O_3:C to high-energy heavy charged particles. Radiat. Meas. 38(4-6): 417-420.

Ghamnia, M., Jardin, C., Bouslama, M. (2003). Luminescent centres F and F^+ detected by cathodoluminescence technique. J. Electr. Spectr. Relat. Phenom. 133 (1-3): 55-63.

Ghamnia, M., Jardin, C., Martinez, L., Bouslama, M., Durupt, P. (1997). Electronic spectroscopy (AES, EELS) and cathodoluminescec (CL) for from α-Al_2O_3 characterization. Vac. 48 (2): 129-134.

Goedicke, C. (2006). Assessments of environmental dose rates in luminescence readers using α-Al_2O_3:C. Radiat. Meas. 41: 36-39.

Göksu, H. Y. (1997). Luminescence methods in retrospective dosimetry using porcelain. In: Proc. Second Hiroshima Int. Symp. on Effects of Low-level Radiation for Residents near the Semipalatinsk Nuclear Test Site, Ed. M. Hoshi, 23–25 July 1996, Hiroshima, Japan, pp. 251–260.

Göksu, H. Y. and Bailiff, I. K. (2006). Luminescence dosimetry using building materials and personal objects. Radiat. Prot. Dosim. 119 (1-4): 413-420.

Göksu, H. Y., Degteva, M. O., Bougrov, N. G., Meckbach, R., Haskell, E. H., Bailiff, I. K., Bøtter-Jensen, L., Jungner, H., Jacob, P. (2002). First international intercomparison of luminescence techniques using samples from the Techa river valley. Health Phys. 82 (1): 94-101.

Göksu, H. Y., Regulla, D. F., Vogenauer, A. (1993). Reconstruction of gamma dose distribution in salt at radioactive waste disposal sites by the water insoluble fraction. Radiat. Prot. Dosim. 47 (1-4): 331–333.

Goksu, H. Y., Semiochkita, N., Shiskina, E. A., Wieser, a., El-Faramawy, N. A., Degteva, M. O, Jacob, P, Ivanov, D. V. (2002). Thin layer α-Al_2O_3:C beta dosemeters for the assessment of current dose rate in teeth due to ^{90}Sr intake, and comparison with electron paramagnetic resonance dosimetry. Radiat. Prot. Dosim. 101 (1-4): 507-513.

Goksu, H.Y., Bulur, E., Wahl, W. (1999). Environmental beta dosimetry using thin layer of α-Al_2O_3:C TL detectors. Radiat. Prot. Dosim. 84 (1-4): 451-457.

Göksu, Y. H. (2003). Telephone chip cards as individuals dosemeters. Radiat. Meas. 37: 617-620.

Goldstein, J. I., Newbury, D. E., Echlin, P., Joy, D. C., Fiori, C., Lifshin, E. (1981). Scanning electron microscopy and x-ray microanalysis. Plenum Press, New York.

Gucsik, A. (2009). Cathodoluminescence and its Applications in the Planetary Sciences. Springer-Verlang, Berlin

Guide to the ´´Risø TL/OSL reader´´ (2013), DTU Denmark.

Halperin, A., and Braner, A. A. (1960). Evaluation of Thermal Activation Energies from Glow Curves. Phys. Rev. 117(2): 408-415.

Hannay, N. (1975). Treatise on Solid Sate Chemistry. Volume 2. Defects in Solids. Plenum Press. London.

Hasan, F. A, Keck, B. D., Hartmetz, C. H., Sears, D. W. G. (1986). Anomalous fading of thermoluminescence in meteorites. J. Lumin. 34: 327-335.

Hasan, F.A, Keck, B. D., Hartmetz, C., Sears, D. W. G. (1986). Anomalous fading of thermoluminescence in meteorites. J. Lumin. 34 (6): 327-335.

Hashizume, T., Maruyama, T., Shiragai, A., Tanaka, E., Izawa, M., Kawamura, S., Nagaoka, S. (1967). Estimation of the air doses from the atomic bombs in Hiroshima and Nagasaki. Health Phys. 13: 149-169.

Haskell, E. H. (1993). Accident dosimetry using environmental materials. Radiat. Prot. Dosim. 47 (1-4): 297–303.

Haskell, E. H. (1993). Retrospective accident dosimetry using environmental materials. Radiat. Prot. Dosi. 47 (1-4): 297-303.

Haskell, E. H., Bailiff, I. K., Kenner, G. H., Kaipa, P. L., Wrenn, M. E. (1994). Thermoluminescence measurements if gamma ray doses attributable to fallout from the Nevada Test Site using building bricks as natural dosemeters. Health Phys. 66 (4): 380–391.

Herve, M. L., Clairand, I., Trompier, F., Tikunov, D., Bottollier-Depois, J. F. (2007). Relation between organ and whole body doses and local doses measured by ESR for standard and realistic neutron and photon overexposures. Radiat. Prot. Dosim. 125 (1): 355-360.

Holt, D. B., Muir, M. D., Grant, P. R. (1974). Quantitative scanning electron microscopy. Academic Press Inc. London, Ltd.

Hoogenstraaten, W. (1958). Electron traps in ZnS phosphors. Philips Research Report 13: 515-693.

Horn, S., Barnard, S., Rothkamm, K. (2011). Gamma-H2AX-based dose estimation for whole and partial body radiation exposure. PLoS ONE 6 (9): 25113.

http://www.panasonic.com/industrial/components/pdf/AOA0000CE1.pdf. Panasonic Thick Film Chip Resistors.

https://cna.ca/issues-policy/radiation/quantifying-radiation

Hubbell, J. H., and Seltzer, S. M. (1995). Tables of X-Ray mass attenuation coefficients and mass energy-absorption coefficients from 1 keV to 20 MeV for elements Z = 1 to 92 and 48 additional substances of dosimetric Interest. NIST Report: NISTIR 5632.

Huntley, D. J., Lian, B. V. (2006). Some observations on tunnelling of trapped electrons in feldspars and their implications for optical dating. Quatern. Sci. Rev. 25 (19-20): 2503-2512.

Huntley, D.J. and Lamothe, M. (2001). Ubiquity of anomalous fading in K-feldspars and the measurement and correction for it in optical dating. Can. J. Earth. Sci. 38 (7): 1093-1106.

Hurd, C. M. (1985). Quantum tunnelling and the temperature dependence DC conduction in low-conductivity semiconductors. J. Phys. C: Solid State Phys. 18 (35): 6487-6499.

Hutt, G., Brodski, L., Bailiff, I. K., Göksu, Y., Haskell, E., Jungner, H. Stoneham, D. (1993). TL accident dosimetry using environmental materials collected from regions downwind of Chernobyl: a preliminary evaluation. Radiat. Prot. Dosim. 47 (1-4): 307–311.

Hutt, G., Jaek, I., Tchonka, J. (1988). Optical dating: K-feldspars optical response stimulation spectra. Quatern. Sci. Rev. 7: 381-385.

IAEA, 2000. Calibration of radiation protection monitoring instruments. IAEA Safety Reports Series No 16.

International Atomic Energy Agency (IAEA), 2011. Cytogenetic dosimetry: applications in preparedness for and response to radiation emergencies. Emergency Preparedness and Response Series. IAEA, Vienna, Austria.

IAEA Safety Standards Series No GS-G-1.5 (2004). Regulatory control of radiation sources. International Atomic Energy Agency, Vienna.

IAEA Safety Standards Series No RS-G-1.10 (2006). Safety of radiation generators and sealed radioactive sources. International Atomic Energy Agency, Vienna.

International Atomic Energy Agency (IAEA) IAEA-TECDOC-1331 (2002). Use of electron paramagnetic resonance dosimetry with tooth enamel for retrospective dose assessment. International Atomic Energy Agency, Vienna.

Ichikawa, H., Higashimura, T., Shidei, T. (1966). Thermoluminescence dosimetry of gamma rays from atomic bombs in Hiroshima and Nagashaki. Health Phys. 12: 395-405.

ICRP 1991. Recommendations of the International Commission on Radiological Protection. ICRP Publication 60, Ann. ICRP 21 (1–3).

ICRP 1996. Conversion coefficients for use in radiological protection against external radiation. ICRP Publication 74, Ann. ICRP 26 (3/4).

ICRP 2003. Relative Biological Effectiveness (RBE), Quality Factor (Q), and Radiation Weighting Factor (w_R). ICRP Publication 92, Ann. ICRP 33 (4).

ICRP 2007. The 2007 Recommendations of the International Commission on Radiological Protection. ICRP Publication 103, Ann. ICRP 37 (2-4).

ICRP 2008. Adult Reference Computational Phantoms. ICRP Publication 110.

ICRP 2010. Conversion Coefficients for Radiological Protection Quantities for External Radiation Exposures. ICRP Publication 116.

ICRU 1972. Measurement of low-level radioactivity. ICRU report 22.

ICRU 1984. Stopping powers for electrons and positrons. ICRU report 37.

ICRU 1993b. Quantities and Units in Radiation Protection Dosimetry. International Commission on Radiation Units and Measurements, Bethesda, MD.

ICRU 1998. Conversion coefficients for use in radiological protection against external radiation. ICRU report 57.

ICRU 2002. Retrospective assessment of exposures to ionizing radiation. Bethesda, MD: International Commission on Radiation Units and Measurements. Report 68, No. 2.

Imatoukene, D., Abdelaziz, F., *et al*. (2008). Development of new system for environmental monitoring based on detectors. Radiat. Meas. 43(2-6): 668-671.

Inrig E. L., Godfrey-Smith D. I., Khanna S. (2008). Optically stimulated luminescence of electronic components for forensic, retrospective and accident dosimetry. Radiat. Meas. 44 (2-6): 726-730.

Inrig, E. L. (2009). Retrospective radiation dosimetry using optically stimulated luminescence of electronic components. MSc Thesis. Royal Military College of Canada.

International Electrotechnical Commission (IEC), 2012. Radiation protection instrumentation – Passive integrating dosimetry systems for environmental and personal monitoring. IEC Report 62387-1.

International Organisation for Standardization (1999). X and gamma reference radiation for calibrating dosemeters and doserate meters and for determining their response as a function of photon energy –Part 3: Calibration of area and personal dosemeters and the measurement of their response as a function of energy and angle of incidence. BS ISO 4037-3.

IUPAC, (1997). Compendium of Chemical Terminology, 2nd ed. (the ´´Gold Book´´). Compilde by A. D. McNaught and A. Wilkinson. Blackell Scientific Publications, Oxford.

Izak-Biran, T. and Moscovitch, M. (1996). Light-induced TL and light-induced fading of TL in α-Al_2O_3:C. Radiat. Meas. 26 (2):259-264.

Jacobs, P. W. M. and Kotomin, E. A. (1994). Modelling of point defects in corundum crystals. J. Am. Soc. 77 (10): 2505-2508.

Jain, M. and Ankjaergaard, C. (2011).Towards a non-fading signal in feldspar: Insight into charge transport and tunnelling from time-resolved optically stimulated luminescence. Radiat. Meas. 46 (3): 292-309.

Jain, P., Bøtter-Jensen, L., Murray, A., Essery, R. (2007). A peak structure in isothermal signals in quartz: Origin and implications. J. Lumin. 127: 678-688.

Jaworska, A. (2009). Types of radiation mass casualties and their management. Ant Int Super Sanita 45 (2): 246-250.

Jones, I. M., Galick, H., Kato, P., Langlois, R. G., Mendelsohn, M. L., Murphy, G. A., Pleshanov, P., Ramsey, M. J., Thomas, C. B., Tucker, J. D., Tureva, L., Vorobtsova, I., Nelson, D. O. (2002). Three somatic genetic biomarkers and covariates in radiation exposed Russian clean-up workers of the Chernobyl nuclear reactor, 6–13 years after exposure. Radiat. Res. 158: 424-442.

Jonnard, P., Bonnelle, C., Blaise, G., Remond, G., Roques-Cames, C. (2000). F^+ and F centers in α-Al2O3 by electron-induced x-ray emission spectroscopy and cathodoluminescence. J. Appl. Phys. 88 (11): 6413-6417.

Jung, H., Lee, K. J., Kim, J. L., Lee, S. Y. (2004). Development of a personal dosimeter badge system using sintered LiF:Mg, Cu, Na, Si TL detectors for photon fields. Radiat. Meas. 38 (1): 71-80.

Jursinic, P. A. (2007). Characterization of optically stimulated luminescent dosimeters, OSLDs, for clinical dosimetric measurements. Med. Phys. 34(12): 4594-4604.

Kamenopoulou, V., Barthe, J., Hickman, C., Portal, C. (1986). Accidental gamma irradiation dosimetry using clothing. Radiat. Prot. Dosim. 17 (1-4): 185-188.

Kang, S. J. L. (2005). Sintering. Densification, grain growth, and microstructure. Elsevier.

Kars, R. H., Poolton, N. R. J., Jain, M., Ankjaergaard, C., Dorenbos, P., Wallinga, J. (2013). On the trap depth of the IR-sensitive trap in Na- and K-feldspar. Radiat. Meas. 59: 103-113.

Katona, T., M. Osvay, Deme, S., Kovacs, A. (2007). Environmental dosimetry using high-sensitivity TL detectors. Radiat. Phys. Chem. 76(8-9): 1511-1514.

King, S.D., and Spiers, F.W. (1985). Photoelectron enhancement of the absorbed dose from X-rays to human bone marrow: experimental and theoretical studies. Br. J. Radiol. 58, pp. 345–356.

Kirsh, Y. (1992). Kinetic Analysis of Thermoluminescence. Phys. Stat. Sol. (a) 129 (1):15-48.

Kitis, G. and Gomez-Ros, G. M. (2000). Thermoluminescence glow-curve deconvolution functions for mixed order of kinetics and continuous trap distribution. Nucl. Instr. and Meth. Phys. Res. A. 440 (1): 224-241.

Kitis, G. and Tuyn, J. W. N. (1999). Correction for temperature lag and thermal gradient effects arising during thermoluminescence readout. Radiat. Prot. Dos. 84 (1-4): 371-374.

Kitis, G., Bousbouras, Antypas, C., Charalambous, S. (1991). Anomalous fading in apatite. Nucl. Tracks Radiat. Meas. 18: 61-65.

Kitis, G., Chen, R, Tuyn, J. W. N. (2008). Thermoluminescence glow peak shape methods based on mixed order kinetics. Phys. Stat. Sol. (a) 205 (5): 1181-1189.

Kitis, G., Gomez Ros, J. M., Tuyn, J. W. C. (1998). Thermoluminescence glow-curve deconvolution functions for first, second and general order of kinetics. J. Phys. D: Appl. Phys. 31: 2636-2641.

Kitis, G., Kiyak, N., Polymeris, G. S., Tsirliganis, N. C. (2010). The correlation of fast OSL component with the TL peak at 325 °C in quartz of various origins. J. Lumin. 130 (2): 298-303.

Kitis, G., Papadopoulos, J. G., Charalambous, S., Tuyn, J. W. N. (1994). The influence of heating rate on the response and trapping parameters of α-Al_2O_3:C. Radiat. Prot. Dosim. 55 (3): 183-190.

Kitis, G., Polymeris, G. S., Pagonis, V., Tsirliganis, N. C. (2012). Anomalous fading of OSL signals originating from very deep traps in Durango apatite. Radiat. Meas. 49: 73-81.

Kitis, G., Spyropulu, M., Papadopoulos, G., Charalambous, S. (1994). Heating rate effects on the TL glow-peaks of three thermoluminesent phosphors. Nucl. Instr. and Meth. in Phys. Res. B. 73 (3): 367-372.

Knoll, G. F. (2000). Radiation detection and measurement. 3rd ed. John Wiley & Sons, USA.

Kodama, Y., Pawel, D., Nakamura, N., Preston, D., Honda, T., Itoh, M., Nakano, M., Ohtaki, K., Funamoto, S., Awa, A. A. (2001). Stable chromosome aberrations in atomic bomb survivors: results from 25 years of investigation. Radiat. Res. 156: 337-346.

Kortov, V. S., Ermakov, A. E., Zatsepin, A. F., Nikiforov, S. V. (2008). Luminescence properties of nanostructured alumina ceramic. Radiat. Meas. 43: 341-344.

Kortov, V. S., Nikiforoc, S. V., Sadykova, E. Z. (2005). Specific features of the thermoluminescence kinetics of shallow traps in anion-defective single crystals of aluminium oxide. Funct. Mat. 12 (2): 282-285.

Kotomin, E. A. and Popov, A. I. (1998). Radiation-induced point defects in simple oxides. Nucl. Instr. Meth. Phys. Res. B 141:1-15.

Kotomin, E. A., Popov, A. I., Stashans, A. (1994). A novel model for $F^+ \rightarrow F$ photoconversion in corundum crystals. J. Phys:Condens. Matter 6: L569-L573.

Kouroukla, E. C., Bailiff, I. K., Terry, I., Bowen, L. (2014). Luminescence characterisation of alumina substrates using cathodoluminescence microscopy and spectroscopy. Radiat. Meas. In press.

Kristianpoller, N., Chen, R., Israeli, M. (1976). Dose dependence of thermoluminescence peaks. J. Phys. D: Appl. 7 (7): 1063-1072.

Kristianpoller., N., Rehavi, P., Shmilevich, A., Weiss, D., Chen, R. (1998). Radiation effects in pure and doped Al_2O_3 crystals. Nucl. Instr. Meth. Phys. Res B 141 (1):343-346.

Kroger, F. A. (1984). Defect related properties of doped alumina. Solid State Ionics 12:189-199.

Kuhns, C. K., Agersnap Larsen, N., McKeever, S. W. S. (2000). Characteristics of LM-OSL from several types of quartz. Radiat. Meas. 32 (5-6): 413-418.

Kulis, P. A., Springis, M. J., Tale, I. A., Vainer, V. S., Valbis, J. A. (1981). Impurity-assocciated colour centres in Mg- and Ca-doped Al_2O_3 crystals. Phys. Stat. Sol B. 104 (2):719-725.

Kumar, M., Kher, R. K., Bhatt, B. C., Sunta, C. M. (2006). Thermally stimulated luminescence arising simultaneously from localized and delocalized recombination processes. J. Phys. D: Appl. Phys. 39 (13): 2670-2679.

Kumar, M., Kher, R. K., Bhatt, B. C., Sunta, C. M. (2007). A comparative study of the models dealing with localized and semi-delocalized transitions in thermally stimulated luminescence. J. Phys. D: Appl. Phys. 40 (19): 5865-5872.

Lapraz, D., Iacconi, P., Daviller, D, Guilhot, B. (1991). Thermostimulated luminescence and fluorescence of α-Al_2O_3:Cr^{3+} samples (ruby) . Influence of the Cr^{3+} concentration. Phys. Stat. Sol. A. 126 (2): 521-531.

Lee, K. H. and Crawford, J. H. (1978). Additive coloration of sapphire. Appl. Phys. Lett. 33: 273.

Lee, K. H. and Crawford, J. H. (1979). Lumiescence of the F center in sapphire. Phys. Rev. B 19 (6): 3217-3221.

Lee, S. Y. and Lee, K. J. (2001). Development of a personal dosimetry system based on optically stimulated luminescence of α-Al_2O_3:C for mixed radiation fields. Appl. Rad. Isot. 54: 675-685.

Leverenz, H. W. (1968). An introduction to luminescence of solids. Dover Publications, New York.

Levin, I. and Brandon D. (1998). Metastable alumina polymorphs: crustal structures and transition sequences. J. Am. Ceram. Soc., 81 (8): 1995-2012.

Levy, P. W. (1984). Thermoluminescence systems with two or more glow peaks described by anomalous kinetic parameters. Nucl. Instr. and Meth. in Phys. Res. B. 1 (2-3): 436-444.

Li J., Lu H., Guo J., Xu Z., Zhou Y. (2007). Recycle technology for recovering resources and products from waste printed circuit boards. Environ. Sci. Technol. 41 (6): 1995-2000.

Li, B. and Li, S. H. (2011). Thermal stability of infrared stimulated luminescence of sedimentary K-feldspar. Radiat. Meas. 46 (1): 29-36.

Li, S. H., Tso, M. Y. W., Wong, N. W. L. (1997). Parameters of OSL traps determined with various linear heating rates. Radiat. Meas. 27 (1): 43-47.

Li, S-H., Tso, M. Y. W., Nelson, N. W. L. (1997). Parameters of OSL traps determined with various linear heating rates. Radiat. Meas. 27 (1): 43-47.

Lim, C. S., Lee, S. B., Jin, G. H. (2011). Performance of optically stimulated luminescence Al_2O_3 dosimeter for low doses of diagnostic energy X-rays. Appl. Radiat. Isot. 69(10): 1486-1489.

Luff, B. J. and Townsend, P. D. (1993). High sensitivity thermoluminescence spectrometer. Meas. Sci. Technol. 4 (1): 65-71.

Mandowski, A. (2005). Semi-localized transitions model for thermoluminescence. J. Phys. D: Appl. Phys. 38 (1): 17-21.

Markey, B. G., McKeever, S. W. S., Akselrod, M. S., Bøtter-Jensen, L. (1996). The temperature dependence of optically stimulated luminescence from α-Al_2O_3:C. Radiat. Prot. Dosim. 65 (1-4): 184-189.

Markey. B. G., Colyott, L. E., McKeever, S. W. S. (1995). Time-resolved optically stimulated luminescence from α-Al_2O_3:C. Radiat. Meas. 24 (4): 457-463.

Marzougui, K., Soliman, Y. S., Farah, K., Mansor, A., Hamzaoui, A. H., Ben Nessib, N. (2012). EPR study of table sugar rod and powder as high dose dosimeters. Radiat. Meas. 47 (10): 988-991.

Mathur, V. K., Barkyoumb, J. H., Yukihara, E. H., Göksu, Y. H. (2007). Radiation sensitivity of memory chip module of an ID card. Radiat. Meas. 42 (1): 43-48.

McKeever, S. W. S. (1980). On the analysis of complex thermoluminescence. Glow curves: Resolution into individual components. Phys. Stat. Sol. (a) 62: 331-340.

McKeever, S. W. S. (1985). Thermoluminescence of solids. Cambridge University Press, Cambridge.

McKeever, S. W. S. (1994). Models for optical bleaching of thermoluminescence in sediments. Radiat. Meas. 23 (2-3): 267-275.

McKeever, S. W. S. and Akelrod, M. S. (1999). Radiation dosimetry using pulsed optically stimulated dosimetry of α-Al_2O_3:C. Radiat. Prot. Dosim. 84 (1-4): 317-320.

McKeever, S. W. S. and Chen, R. (1997). Luminescence models. Radiat. Meas. 27 (5-6): 625-661.

McKeever, S. W. S., Akelrod, M. S., Markey, B. G. (1996). Pulsed optically stimulated dosimetry using α-Al_2O_3:C. Radiat. Prot. Dosim. 65 (1-4): 267-272.

McKeever, S. W. S., Akserlod, M. S., Markey, B. G. (1996). Pulsed optically stimulated luminescence dosimetry using alpha-Al_2O_3:C. Radiat. Prot. Dosim. 65 (1-4): 267-272.

McKeever, S. W. S., Alserlod, M. S., Colyott, L. E., Agersnap-Larsen, N., Polf, J. C., Whitley, V. (1999). Characterisation of Al_2O_3 for use in thermally and optically stimulated luminescence dosimetry. Radiat. Prot. Dosim 84 (1-4): 163-168.

McKeever, S. W. S., and Morris, M. F. (1994). Computer simulations of optical bleaching of TL and OSL signals. Radiat. Meas. 23 (6): 301-306.

McKeever, S. W. S., Bøtter-Jensen, L., Agersnap Larsen, N., Duller, G. A. T. (1997). Temperature dependence of OSL decay curves: experimental and theoretical aspects. Radiat. Meas. 27(2): 161-170.

McKeever, S. W. S., Bøtter-Jensen, L., Agersnap Larsen, N., Duller, G. A. T. (1997). Temperature dependence of OSL decay curves: Experimental and theoretical aspects. Radiat. Meas. 27 (2): 161-170.

McKeever, S. W. S., Moscovitch, M., Townsend, P. D. (1995). Thermoluminescence dosimetry materials: Properties and Uses. Nuclear Technology Publishing, England.

MCNP5 Manual – X-5 Monte Carlo Team, (2008). MCNP – A General Monte Carlo N-Particle Transport Code, Version 5. Volume 1: Overview and theory. Los Alamos National Laboratory.

Mikhailik, V. B., Di Stefano, P. C. F., Balcerzyk, H., Mykhaylyk, M. S., Wahl, R. (2011). Studies of concentration dependencies in the luminescence of Ti-doped Al_2O_3. J. Appl. Phys. 109: 531161-6.

Mishra, D. R., Kulkarni, M. S., Muthe, K. D., Thinaharan, C., Roy, M., Kulshreshtha, S. K., Kannan, S., Bhatt, B. C., Gupta, S. K., Sharma, D. N. (2007). Luminescence properties of Al_2O_3:C crystal with intense low temperature TL peak. Radiat. Meas. 42 (2): 170-176.

Mishra, D. R., Soni, A., Rawat, N. S., Kulkarni, M. S., Bhatt, B. C., Sharma, D. N. (2011). Method of measuring thermal assistance energy associated with OSL traps in α-Al_2O_3:C phosphor. Radiat. Meas. 46 (8): 635-642.

Mittani, J. C. R., Silva, A. A. R., Vanhaver, F., Akselrod, M. S., Yukihara, E. G. (2007). Investigation of neutron converters for production of optically stimulated luminescence (OSL)

neutron dosimeters using Al_2O_3:C. Nucl. Instr. Meth. Phys. Res. B: Beam Interactions with Materials and Atoms 260(2): 663-671.

Miyake, M., Liu, K. J., Walzcak, T. M., Swartz, H. M. (2000). In vivo EPR dosimetry of accidental exposures to radiation: experimental results indicating the feasibility of practical use in human subjects. Appl. Radiat. Isot. 52 (5): 1031-1038.

Molnar, G., Benabdesselam, M., Borossay, J., Lapraz, D., Iacconi, P., Kortov, V. S., Surdo, A. I. (2001). Photoluminescence and thermoluminescence of titanium ions in sapphire crystals. Radiat. Meas. 33: 663-667.

Molnar, G., Papin, A., Grosseau, P., Guilhot, B., Borossay, J., Benabdesselam, M., Iacconi, P., Lapraz, D. (1999). Thermally stimulated luminescence and exoelectron emission mechanism of the 430 K (D') dosimetric peak of a-Al_2O_3. Radiat. Prot. Dosim 84 (1-4): 253-256.

Moscovitch, M., Tawil, R. A., Svinkin, M. (1993). Light induced fading in α-Al_2O_3:C. Radiat. Prot. Dosim. 47 (1-4): 251-253.

Moulson, A. J. and Herbert, J. M. (2003). Electroceramics. Second edition. Wiley.

Mrozik, A., Marczewska, B., Bilski, P., Gieszczyk, W. (2014). Investigation of OSL signal of resistors from mobile phones for accidental dosimetry. Radiat. Meas. In press.

Mukherjee, B., Lambert, J., Hentschel, R., Negodin, E., Farr, J. (2011). An ultra sensitive fast neutron area monitor using gadolinium covered aluminium oxide dosimeter (TLD-500) chips. Radiat. Meas. 46(12): 1698-1700.

Murray, A. S. and Wintle, A. G. (1998). Factors controlling the shape of the OSL decay curve in quartz. Radiat. Meas. 29 (1): 65-79.

Murray, A. S., Buylaert, J. P., Thomsen, K. J., Jain, M. (2009). The effect of preheating on the IRSL signal from feldspar. Radiat. Meas. 44 (5-6): 554-559.

Muthe, K. P., Kulkarni, M. S., Rawat, N. S., Mishra, D. R., Bhatt, B. C., Singh, A., Gupta, S. K. (2008). Melt processing of alumina in graphite ambient for dosimetric applications. J. Lumin. 128 (3): 445-450.

Nagabhushana, K. R., Lakshminarasappa, B. N., Revahnasiddaiah, D. (2008). Thermally stimulated luminescence studies in combustion synthesized polycrystalline aluminium oxide. Bull. Mater. Sci., 31 (4): 669-672.

Nakajima T. (1987). External dose to a Japanese tourist from the Chernobyl reactor accident. Health Phys. 53 (4): 405-407.

Nakajima, T. (1995). ESR of sugar as a personnel monitor for radiation emergencies. Appl. Radiat. Isot. 46 (8): 819-825.

Nakamura, N., Miyazawa, C., Akiyama, M., Sawada, S., Awa, A. A. (1998). A close correlation between electron spin resonance (ESR) dosimetry from tooth enamel and cytogenetic dosimetry from lymphocytes of Hiroshima atomic-bomb survivors. Int. J. Radiat. Biol. 73 (6): 619-627.

Nassau, K. (1978). The origins of colors in minerals. American Mineralogist 63: 219-229.

National Nuclear Data Center (NNDC). NNDC Chart of nuclides. Brookhaven National Laboratory website: http://www.nndc.bnl.gov/chart/

Nikiforov, S. V., Milman, I. I., Kortov, V. S. (2001). Thermal and optical ionization of F-centers in the luminescence mechanism of anion-defective corundum crystals. Radiat. Meas. 33 (5): 537-541.

Noras, J. M. (1980). Photoionisation and phonon coupling. J. Phys. C: Solid. St. Phys. 13 (25): 4779-4789.

Ogundare, F. O., Chitambo, M. L., Oniya, E. O. (2006). Anomalous behaviour of thermoluminescence from quartz: A case of glow peaks from a Nigerian quartz. Radiat. Meas. 41 (5): 549-553.

Olster, L., Weiss, D., Kristianpoller, N. (1994). A study of photostimulated thermoluminescence in C-doped α-Al_2O_3 crystals. J. Phys. D:Appl. Phys. 27 (8): 1732-1736.

Pagonis, V., Ankjærgaard, C., Jain, M., Chen, R. (2013). Thermal dependence of time-resolved blue light stimulated luminescence in α-Al_2O_3:C. J. Lumin. 136: 270-277.

Pagonis, V., Chen, R., Lawless, J. L. (2007). A quantitative kinetic model for Al_2O_3:C TL response to ionizing radiation. Radiat. Meas. 42 (2): 198-204.

Pagonis, V., Kitis, G., Furetta, C. (2006). Numerical and Practical Exercises in Thermoluminescence. Springer Science and Business Media, Inc., USA.

Pascu, A., Vasiliniuc, S., Zeciu-Dolha, M., Timar-Gabor, A. (2013). The potential of luminescence signals from electronic components for accident dosimetry. Radiat. Meas. 56: 384-388.

Pashchenko, L. P. and Barboza-Flores, M. (1995). Thermoluminescence α-Al_2O_3:C detectors (TLD-500K): Some results of a long-term testing. Radiat. Meas. 24 (4): 427-429.

Peelen, J. G. J. (1977). Alumina: sintering and optical properties. PhD Thesis. Eindhoven University of Technology.

Pelowitz, D. B., (2011). MCNPX User's manual, Version 2.7.0. LANL Report: LA-CP-11-00438.

Peto, A. (1996). Luminescence emission spectra of several Al_2O_3 TL materials.

Petrov, S. A. and Bailiff, I. K. (1996). Thermal quenching and the initial rise technique of trap depth evaluation. J. Lum. 65: 289-291.

Pickard, P. S. (1970). Analysis of Electron Trapping in Alumina Using Thermally Stimulated Electrical Currents. Journal of Applied Physics 41 (6): 2636-2643.

Pinto, T. N. O., Cecatti, S. G. P., Gonchi, C. C., Caldas, L. V. E., Fundacentro, A., Trabalcho, M. D., Paulo, S., Brazil, S. P. (2008). Application of the OSL technique for beta dosimetry. Radiat. Meas. 43 (2-6): 332-334.

Podgorsak, E. B. (2006). Radiation physics for medical physicists. Springer-Verlag Berlin, Heidelberg.

Podgorsak, E. B. (technical editor) (2005). Radiation oncology physics: A handbook for teachers and students. IAEA. Austria.

Pokorny, P. and Ibarra, A. (1993). On the origin of the thermoluminescence of Al_2O_3Cr,Ni. J. Phys.: Condens. Matter 5 (40): 7387-7396.

Pokorny. P. and Ibarra A. (1994).Impurity effects on the thermoluminescence of Al_2O_3. Journal of Applied Physics 75 (2): 1088-1092.

Polymeris, G. S., Kitis, G., Tsirliganis, N. (2006). A comparative study of anomalous fading effects of TL and OSL signals of Durango apatite. Phys. Stat. Sol (a) 203 (3): 578-590.

Polymeris, G. S., Kitis, G., Tsirliganis, N. C. (2006). Correlation between TL and OSL properties of CaF_2:N. Nucl. Instr. Meth. Phys. Res. B. 251 (1): 133-142.

Poolton, N. R. J., Bøtter-Jensen, L., Duller, G. A. T. (1995a). Thermal quenching of luminescence processes in feldspars. Radiat. Meas. 24 (1): 57-66.

Poolton, N. R. J., Bøtter-Jensen, L., Johnsen, O. (1995b). Thermo-optical properties of optically stimulated luminescence in feldspars. Radiat. Meas. 24 (4): 531-534.

Poolton, N. R. J., Kars, R. H., Wallinga, J., Bos, A. J. (2009). Direct evidence for the participation of band-tails and excited-state tunnelling in the luminescence of irradiated feldspar. J. Phys. Condens. Matter. 21 (48): 485505-485515.

Rahaman, M. N. (2005). Ceramic processing and sintering. Second edition. Taylor & Francis e-library.

Ramzaev, V., Bøtter-Jensen, L., Thomsen, K. J., Andersson, K. G., Murray, A. S. (2008). An assessment of cumulative external doses from Chernobyl fallout for a forested area in Russia using the optically stimulated luminescence from quartz inclusions in bricks. J. Envir. Rad. 99 (7): 1154-1164.

Randall, J. T. and Wilkins, M. H. F. (1945). Phosphorescence and electron traps I. The study of trap distributions. Proc. Roy. Soc. London 184: 366-389.

Randall, J. T. and Wilkins, M. H. F. (1945). Phosphorescence and electron traps I. The study of trap distributions. Proc. Roy. Soc. London 184: 366-389. Singh, S. D. (2013). A review on the lifetime of trapped electrons relevant to TL glow peaks. Int. J. Lumin. Appl. 3 (1): 11-14.

Reft, C. S. (2009). The energy dependence and dose response of a commercial optically stimulated luminescent detector for kilovoltage photon, megavoltage photon, and electron, proton, and carbon beams. Med. Phys. 36 (5): 1690.

Rhodes, E. J. (1988). Methodological considerations in the optical dating of quartz. Quatern. Sci. Rev. 7 (3-4):395-400.

Richter, D., Richter, A., *et al*. (2013). Lexsyg – A new system for luminescence research. Geochronometria. 40 (4): 220-228.

Ridley, B. K. (1988). Quantum processes in semiconductors. 2nd ed. Oxford Science Publications.

Riedel, R. and Chen, I. W. (2010). Ceramics science and technology Volume 2: properties. Wiley.

Rodriguez, M. G., Denis, G., Underwood, T. H., Yukihara, E. G. (2011). Thermoluminescence, optically stimulated luminescence and radioluminescence properties of Al_2O_3 :C,Mg. Radiat. Meas. 46 (12): 1469-1473.

Romanyukha, A. A., Seltzer, S. M., Desrosiers, M., Ignatiev. E. A., Ivanov, D. V., Bayankin, S., Degteva, M. O., Eichmiller, F. C., Wieser, A., Jacob, P. (2001) Correction factors in the EPR dose reconstruction for residents of the middle and lower Techa riverside. Health Phys. 81 (5): 554-566.

Romanyukha, A. and Trompier, F. (2011). Electron paramagnetic resonance retrospective dosimetry. Conc. Trends Med. Rad. Dosim. AIP Conf. Proc. 1345: 120-128.

Romanyukha, A., Trompier, F., Reyes, R. A., Melanson, M. A., (2011). EPR measurements of fingernails in Q-band. Radiat. Meas. 46 (9): 888-892.

Rothkamm, K. and Horn, S. (2009). Gamma-H2AX as protein biomarker for radiation exposure. Ann. Ist. Super Sanita 45 (3): 265-271.

Rothkamm, K., Beinke, C., Romm, H., Badie, C., Balagurunathan, Y., Barnard, S., Bernard, N., Boulay-Greene, H., Brengues, M., De Amicis, A., De SAnctis, S., Greither, R., Herodin, F.,

Jones, A., Kabacik, S., Knie, T., Kulka, U., Lista, F., Martigne, P., Missel, A., Moquet, J., Oestreicher, O., Peinnequin A., Poyot, T., Roessler, U., Scherthan, H., Terbrueggen, B., Thierens, H., Valente, M., Vral, A., Zenhausern, F., Meineke, V., Braselmann, H., Abend, M. (2014). Comparison of established and emerging biodosimetry assays. Radiat. Res. 180 (2): 111-119.

Rothkamm, K., Horn, S., Scherthan, H., Rössler, U., De Amicis, A., Barnard, S., Kulka, U., Lista, F., Meineke, V., Braselmann, H., Beinke, C., Abend, M. (2013). Laboratory inrercomparison on the ɣ-H2AX foci assay. Radiat. Res. 180 (2): 149-155.

Salomaa, S., Lindholm, C., Tankimanova, M. K., Mamyrbaeva, Z., Koivistoinen, A., Hulten, M., Mustonen, R., Dubrova, Y. E., Bersimbaev, R. I. (2002). Stable chromosome aberrations in the lymphocytes of a population living in the vicinity of the Semipalatinsk nuclear test site. Radiat. Res. 158: 591-596.

Sato, H., Takatsuji, T., Takasa, J., Emdo, S., Hoshi, M., Sharifov, V. F., Veselkina, I. I., Pilenko, I. V., Kalimullin, W. A., Masyakin, V. B., Yoshikawa, I., Nagamoto, T., Okajima, S. (2002). Measuring the external exposure dose in the contaminated area near the Chernobyl nuclear power station using the thermoluminescence of quartz in bricks. Health. Phys. 83 (2): 227-236.

Sato, T., Kobayashi, S., Michizono, S., Saito, Y. (1999). Measurements of secondary electron-emission coefficients and cathodoluminescence spectra for annealed alumina ceramics. Appl. Surf. Sci. 144-145: 324-328.

Sawakuchi, G. O., Yukihara, E. G., McKeever, S. W. S., Benton, E. R. (2008a). Optically stimulated luminescence fluence response of dosimeters exposed to different types of radiation. Radiat. Meas. 43 (2-6): 450-454.

Sawakuchi, G. O., Yukihara, E. G., McKeever, S. W. S., Benton, E. R., Gaza, R., Uchihori, U., Yasuda, N., Kitamura, H. (2008b). Relative optically stimulated luminescence and thermoluminescence efficiencies of Al_2O_3C dosimeters to heavy charged particles with energies relevant to space and radiotherapy dosimetry. J. Appl. Phys. 104 (12): 124903.

Schauer, D. A., Desrosiers, M. F., Kuppusamy, P., Zweier, J. L. (1996). Radiation dosimetry of an accidental overexposure using EPR spectrometry and imaging of human bone. Appl. Radiat. Isot. 47 (11-12): 1345-1350.

Sears, D. W. G., Myers, B. M., Hartmetz, C. P., Hasan, F. A. (1990). Structural and anomalous fading of thermoluminescence of oligoclase. Nucl. Tracks Radiat. Meas. 17 (4): 583-586.

Shackelford, J. F. and Doremus, R. H. (2008). Ceramic and glass materials. Structure, properties and processing. Springer.

Shani, G. (2000). Radiation dosimetry instrumentation and methods. 2nd ed. CRC Press LLC, Florida.

Shepherd, L. A. (1997). Detection of anomalous fading in archaeological ceramics. Radiat. Meas. 27 (2): 199-204.

Sholom, S. and Chumak, V. (2010). EPR emergency dosimetry with plastic components of personal goods. Health Phys. 98 (2): 388-394.

Sholom, S. and McKeever, S. W. S. (2014). Emergency OSL dosimetry with commonplace materials. Radiat. Meas. 61: 33-51.

Sholom, S. V., Voloskiv, V. N., Chumak, V. V. (2000). Retrospective dosimetry at low contamination Chernobyl territories using luminescent technique with quartz. In: Proceedings of the 10th international congress of the International Radiation Protection Association on harmonization of radiation, human life and the ecosystem.

Sholom, S., Desrosiers, M., Bouville, A., Luckyanov, N., Chumak, V., Simon, S. L. (2007). EPR tooth dosimetry of Semipalatinsk area inhabitants. Radiat. Meas. 42 (6): 1037-1040.

Simon, S. L., Bailiff, I., Bouville, A., Fattibene, P., Kleinerman, R. A., Lloyd, D. C., McKeever, S. W. S., Romanyukha, A., Sevan'kaev, A. V., Tucker, J. D., Wieser, A. (2007). BiodosEPR-2006 consensus committee report on biodosimetric methods to evaluate radiation doses at long times after exposure. Radiat. Meas. 42 (6-7): 948-971.

Simon, S. L., Bouville, A., Kleinerman, R. (2010). Current use and future trends of biodosimetry in studies of long-term health risk following radiation exposure. Health Phys. 98 (2): 109-117.

Singarayer, J. S. (2002). Linearly modulated optically stimulated luminescence of sedimentary quartz: Physical mechanisms and implications for dating. PhD Thesis. Linacre College, Oxford.

Singh, A. K., Menon, S. N., Dhabekar, B., Kadam, S., Chougaonkar, M. P., Mayya, Y.S. (2012). TL-OSL correlation studies of $LiMgPO_4$:Tb,B dosimetric phosphor. Nucl Instr. Meth. Phys. Res. B. 274: 177-181.

Singh, T. B., Mashangva, M., Gartia, R. K. (2013). Trap spectroscopy and thermoluminescence of persistent luminescent materials. Ind. J. Pure. Appl. Phys. 51: 223-229.

Soni, A., Mishra, D. R., Bhatt, B. C., Gupta, S. K., Rawat, N. S., Kulkarni, M. S., Sharma, D. N. (2012). Characterization of deep energy levels in α-Al_2O_3:C using thermally assisted OSL. Radiat. Meas. 47 (2): 111-120.

Soni, K. K., Thompson, A. M., Harmer, M. P., Williams, D. B. (1995).Solute segregation to grain boundaries in MgO-doped alumina. Appl. Phys. Lett. 66 (21): 2795-2797.

Spooner, N. A. (1992). Optical dating: Preliminary results on the anomalous fading of luminescence from feldspars. Quatern. Sci. Rev. 11 (1-2): 139-145.

Spooner, N. A. (1993). The validity of optical dating based on feldspar. PhD Thesis. Linacre College, Oxford.

Spooner, N. A. (1993). The validity of optical dating based on feldspar. PhD Thesis. Linacre College, Oxford.

Spooner, N. A. (1994). On the optical dating signal from quartz. Radiat. Meas. 23 (2-3): 593-600.

Spooner, N. A., Prescott, J. R., Hutton, J. T. (1988). The effect of illumination wavelength on the bleaching of the thermoluminescence (TL) of quartz. Quat. Sci. Rev. 7 (3-4): 325-329.

Springis, M., Kulis, P., Veispals, A., Tale, I. (1995). Photo- and thermostimulated processes in α-Al_2O_3. Radiat. Meas. 24 (4): 453-456.

Stashans, A., Kotomin, E., Calais, J. L. (1994). Calculations of the ground and excited states of F-type centers in corundum crystals. Phys. Rev. B 49 (21): 14854-14858.

Stoneham, D. (1985). The use of porcelain slices as a low-dose background dosemeter. Nucl. Tracks Radiat. Meas. 10 (4-6): 509-512.

Stoneham, D., Bailiff, I. K., Brodski, L., Göksu, H. Y., Haskell, E. H., Hutt, G., Jungner, H., Nagatomo, T. (1993). TL accident dosimetry measurements on samples from the town of Pripyat. Nucl. Tracks Radiat. Meas. 21 (1): 195-200.

Stoneham, M. (2001). Theories of defects in solids. Oxford Classic Texts in the Physical Sciences.

Summers, G.P. (1984). Thermoluminescence in single crystal α-Al_2O_3. Radiat. Prot. Dosim. 8: (1-2): 69-80.

Surdo, A. I. and Kortov, V. S. (2004). Exciton mechanism of energy transfer to F-centers in dosimetric corundum crystals. Radiat. Meas. 38 (4-6): 667-671.

Surdo, A. I., Kortov, V. S., Sharafutdinov, F. F. (1999). Luminescence of anion-defective corundum with titanium impurity. Radiat. Prot. Dosim. 84 (1-4): 261-263.

Surdo, A. I., Pustovarov, V. A., Kortov, V. S., Kishka, A. S., Zinin, E. I. (2005). Luminescence in anion-defective crystals over the nano-, micro- and millisecond intervals. Nucl. Instr. Meth. Phys. Res. Section A: Accelerators, Spectrometers, Detectors and Associated Equipment 543 (1): 234-238.

Swartz, H. M, Burke, G., Coey, M., Demidenko, E., Dong, R., Grinberg, O., Hilton, J., Iwasaki, I., Lesniewski, P., Kmiec, M., Lo, K-M, Nicolalde, R. J., Ruuge, A., Sakata, Y., Sucheta, A., Walczak, T., Williams, B. B., Mitchell, C., Romanyukha, A., Schauer, D. A. (2007). *In vivo* EPR for dosimetry. Radiat. Meas. 42 (6-7): 1075-1084.

Takahashi, F., Yanaquchi, Y., Iwasaki, M., Miyazawa, C., Hamada, T. (2001). Relations between tooth enamel dose and organ doses for electron spin resonance dosimetry against external photon exposure. Radiat. Prot. Dosim. 95 (2): 101-108.

Takahashi, F., Yanaquchi, Y., Iwasaki, M., Miyazawa, C., Hamada, T., Funabiki, J., Saito, K. (2003). Analyses of absorbed dose to tooth enamel against external photon exposure. Radiat. Prot. Dosim. 103 (2): 125-130.

Templer, R. H. (1985). The removal of anomalous fading in zircon. Nucl. Tracks. 10 (4-6): 531-537.

Templer, R. H. (1986). The localized transition model of anomalous fading. Rad. Prot. Dosim. 17: 493-497.

Tepe Cam, S., Polat, M., Seyhan, N. (2014). The use of human hair as biodosimeter. Appl. Radiat. Isot. 94: 272-281.

Thomsen, K. J., Botter-Jensen, L., Murray, A. S. (2002). Household and workplace chemicals as retrospective luminescence dosemeters. Radiat. Prot. Dosim. 101 (1-4): 515-518.

Thomsen, K. J., Murray, A. S., Jain, M., Bøtter-Jense, L. (2008). Laboratory fading rates of various luminescence signals from feldspar-rich sediments extracts. Radiat. Meas. 43: 1474-1486.

Townsend, P. D. (1968). Thermoluminescence of geological materials (ed. McDougall, D.J.). Academic Press, London, New York.

Trompier F., *et al*. (2012). Retrospective dose assessment in a radiation mass casualty by EPR and OSL in mobile phones. 13th International Congress of the IRPA, May 2012. www.irpa13glasgow.com

Trompier, F., Bassinet, C., Clairand, I. (2010). Radiation accident dosimetry on plastics by EPR spectrometry. Health Phys. 98 (2): 388-394.

Trompier, F., Bassinet, C., Wieser, A., De Angelis, C., Viscomi, D., Fattibene, P. (2009). Radiation-induced signals analysed by EPR spectrometry applied to fortuitous dosimetry. Ant Int Super Sanita 45 (3): 287-296.

Trompier, F., Della Monaca, S., Fattibene, P., Clairand, I. (2011). EPR dosimetry of glass substrate of mobile phone LCDs. Radiat. Meas. 46 (9): 827-831.

Trompier, F., Romanyukha, A., Kornak, L., Calas, C., Leblanc, B., Mitchell, C., Swartz, H., Clairand, I. (2009). Electron paramagnetic resonance radiation dosimetry in fingernails. Radiat. Meas. 44 (1): 6-10.

Tsirliganis, N., Polymeris, G. S., Loukou, Z., Kitis, G. (2006). Anomalous fading of TL, Blue-SL, and IR-SL signals of fluorapatite. Radiat. Meas. 41: 954-960.

Tyler, S. and McKeever, S. W. S. (1988). Anomalous fading of TL in oligoclase. Nucl. Tracks Radiat. Meas. 14 (1-2): 149-154.

Uzum, E., Yarar, Y., Yazici, A. N. (2011). Electron immigration from shallow traps to deep traps by tunnel mechanism on Seydisehir aluminas. J. Lumin. 131: 2625-2629.

Veronese, I., Galli, A., Cantone, M.C., Martini, M., Vernizzi, F., Guzzi, G. (2010). Study of TSL and OSL properties of dental ceramics for accidental dosimetry applications. Radiat. Meas. 45 (1): 35-41.

Viamonte, A., Rosa, L. A. R., Buckley, L. A., Cherpak, A., Cygler, J. E. (2008). Radiotherapy dosimetry using a commercial OSL system. Med. Phys. 35(4): 1261.

Visocekas, R. (2000). Monitoring anomalous fading of TL of feldspars by using far-red emission as a gauge. Radiat. Meas. 32; 499-504.

Visocekas, R. and Ouchene, M. (1983). Tunneling afterglow and anomalous fading in dosimetry with $CaSO_4$:Dy. Nucl. Instr. Meth. 214: 553-555.

Visocekas, R., Ceva, T., Marti, C., Lefaucheux, F., Robert, M. C. (1976). Tunneling processes in afterglow of calcite. Phys. Stat. Sol. (a) 35: 315-327.

Walker, F. D., Colyott, L. D., Agersnap Larsen, N., McKeever, S. W. S. (1996). The wavelength dependence of light-induced fading of thermoluminescence from α-Al_2O_3. Radiat. Meas. 26 (5): 711-718.

Walker, F. D., Colyott, L. E., Agersnap-Larsen, N., McKeever, S. W. S. (1996). The wavelength dependence of light-induced fading of thermoluminescence from α-Al_2O_3:C. Radiat. Meas. 26 (5): 711-718.

Wheeler, G. C. W. S. (1990). Luminescence studies relevant to archaeological dating. PhD Thesis. Linacre College, Oxford.

Wheeler, G. C. W. S. (1990). Luminescence studies relevant to archaeological dating. PhD Thesis. Linacre College, Oxford.

Whitley, V. H. and McKeever S. W. S. (2000). Photoionization of deep centers in Al_2O_3. J. Appl. Phys. 87 (1): 249-256.

Wieser, A., Vasilenko, E., Fattibene, P., Bayankin, S., El-Faramawy, N., Ivanov, D., Jacob, P., Knyazev, V., Onori, S., Pressello, M. C., Romanyukha, A., Smetanin, M., Ulanovsky, A. (2006). Comparison of EPR occupational lifetime external dose assessments for Mayak nuclear workers and film badge dose data. Radiat. Environ. Biophys. 44 (4): 279-288.

Williams P. (2010). Valorization of printed circuit boards from waste electrical and electronic equipment by pyrolysis. Waste Biom. Valor. 1 (1): 107-120.

Williams, B. B., Dong, R., Kmiec, M., Burke, G., Demidenko, E., Gladstone, E., Nicolalde, R. J., Sucheta, A., Lesniewski, P., Swartz, H. M. (2010). Development of in vivo tooth EPR for individual dose estimation and screening. Health Phys. 98 (2): 327-338.

Williams, B. B., Flood, A. B., Salikhov, I., Kobayashi, K., Dong, R., Rychert, K., Du, G., Schreiberm W., Swartz, H. M. (2014). In vivo EPR tooth dosimetry for triage after a radiation event involving large populations. Radiat. Environ. Biophys. 53 (2): 335-346.

Wintle, A. G. (1977). Detailed study of a thermoluminescent mineral exhibiting anomalous fading. J. Lumin. 15: 385-393.

Wintle, A. G. and Murray, A. S. (1997). The relationship between quartz thermoluminescence, photo-transferred thermoluminescence, and optically stimulated luminescence. Radiat. Meas. 27 (4): 611-624.

Wintle, A. G. and Murray, A. S. (2000). Quartz OSL: Effects of thermal treatment and their relevance to laboratory dating procedures. Radiat. Meas. 32 (5-6): 387-400.

Woda, C. and Spottl, T. (2009). On the use of wire-bond chip card modules for retrospective and accident dosimetry. Radiat. Meas. 44 (5-6): 548-553.

Woda, C., Bassinet, C., Bortolin, E., Della Monaca, S., Fattibene, P. (2009). Radiation-induced damage analysed by luminescence methods in retrospective dosimetry and emergency response. Ant Int Super Sanita 45 (3): 297-306.

Woda, C., Greilich, S., Beerten, K. (2010). On the OSL curve shape and preheat treatment of electronic components from portable electronic devices. Radiat. Meas. 45 (3-6): 746-748.

Woda, C., Ulanovsky, A., Bougrov, N. G., Fiedler, I., Degteva, M. O., Jacob, P. (2011). Luminescence dosimetry in a contaminated settlement of the Techa River valley, Southern Urals, Russia. Radiat. Meas. 46 (3): 277-285.

Wu, K., Sun, C. P., Shi, Y. (1995). Dosimetric properties of watch glass: a potential practical ESR dosemeter for nuclear accidents. Radiat. Prot. Dosim. 59 (3): 223-225.

Yacobi, B. G. and Holt, D. B. (1990). Cathodoluminescence Microscopy of Inorganic Solids. Plenum Press, New York.

Yacobi, G. B. and Holt D. B. (1990). Cathodoluminescence microscopy of inorganic solids. Plenum press, New York.

Yamane L. H., Moraes V. T., Espinosa D. C. R., Tenorio J. A. S. (2011). Recycling of WEEE: Characterisation of spent printed circuit boards from mobile phones and computers. Waste Manag. 31 (12): 2553-2558.

Yang, X. B., Li, H. J., Bi, Q. Y., Cheng, Y., Tang, Q., Xu, J. (2008). Influence of carbon on the thermoluminescence and optically stimulated luminescence of α-Al_2O_3:C crystals. J. Appl. Phys. 104: (12): 1231121-1231126.

Yasuda, H., Kobayashi, I., Morishima, H. (2002). Decaying Patterns of Optically Stimulated Luminescence from Al_2O_3:C for Different Quality Radiations. J. Nucl. Sci. Techn. 39(2): 211-213.

Yazici, A. N., Chen, R., Solak, S., Yegingil, Z. (2002). The analysis of thermoluminescent glow peaks of CaF_2:Dy (TLD-200) after β-irradiation. J. Phys. D: App. Phys. 35: 2526-2535.

Yazici, A. N., Solak, S., Ozturk, Z., Topaksu, M., Yegingil, Z. (2003). The analysis of dosimetric thermoluminescent glow peak of a-Al_2O_3:C after different dose levels by β-irradiation. J. Phys. D: Appl. Phys. 36: 181-191.

Yong, L. C., Wagiran, H., Ismail, A. K. (2013). Thermoluminescence performance of carbon-doped aluminium oxide for dose measurement by various preparation methods. J. Teknol. 62 (3): 109-113.

Yukihara, E. G. and McKeever, S. W. S. (2006). Spectroscopy and optically stimulated luminescence of Al_2O_3 :C using time-resolved measurements. J. Appl. Phys. 100 (8): 083512-083512-9.

Yukihara, E. G. and McKeever, S. W. S. (2008). Optically stimulated luminescence (OSL) dosimetry in medicine. Phys. Med. Biol. 53: 351-379.

Yukihara, E. G. and McKeever, S. W. S. (2011). Optically stimulated luminescence. Fundamentals and applications. John Wiley & Sons, Ltd.

Yukihara, E. G., Gasparian, P. B. R., Sawakuchi, G. O., Ruan, C., Ahmad, S., Kalavagunta, C., Clouse, W. J., Sahoo, N., Titt, U. (2010). Medical applications of optically stimulated luminescence dosimeters (OSLDs). Radiat. Meas. 45(3-6): 658-662.

Yukihara, E. G., Gaza, R., McKeever, S. W. S., Soares, C. G. (2004a). Optically stimulated luminescence and thermoluminescence efficiencies for high-energy heavy charged particle irradiation in Al_2O_3:C. Radiat. Meas. 38(1): 59-70.

Yukihara, E. G., Mittani, J. C., Vanhavere, F., Akselrod, M. S. (2008). Development of new optically stimulated luminescence (OSL) neutron dosimeters. Radiat. Meas. 43(2-6): 309-314.

Yukihara, E. G., Sawakuchi, G. O., Guduru, S., McKeever, S. W. S., Gaza, R., Benton, E. R., Yasuda, N., Uchihori, Y., Kitamura, H. (2006). Application of the optically stimulated luminescence (OSL) technique in space dosimetry. Radiat. Meas. 41(9-10): 1126-1135.

Yukihara, E. G., Whitley, V. H., McKeever, S. W. S., Akselrod, A. E., Akselrod, M. S. (2004b). Effect of high-dose irradiation on the optically stimulated luminescence of Al_2O_3:C. Radiat. Meas. 38: 317-330.

Yukihara, E. G., Whitley, V. H., Polf, J. C., Klein, D. M., McKeever, S. W. S., Akselrod, A. E., Akselrod, M. S. (2003). The effect of deep trap population on the thermoluminescence of Al_2O_3:C. Radiat. Meas. 37: 627-638.

Zahedifar, M., Eshraghi, L., Sadeghi, E. (2012). Thermoluminescence kinetics analysis of α-Al_2O_3:C at different dose levels and populations of trapping states and a model for its dose response. Radiat. Meas. 47 (10): 957-964.

Zankl, M. (1999). Personal dose equivalent for photons and its variation with dosemeter position. Health Physics, 76 (2) pp. 162-170.

Zinkle, S. J. and Kinoshita, C. (1997). Defect production in ceramics. J. Nucl. Mat. 251 (11): 200-217.